ACTIVE AND LONG-LIVED PERMANENT FOREARC DEFORMATION DRIVEN BY THE SUBDUCTION SEISMIC CYCLE

A Dissertation

Presented to the Faculty of the Graduate School

of Cornell University

in Partial Fulfillment of the Requirements for the Degree of

Doctor of Philosophy

by

Felipe Alejandro Aron Melo

August 2014

ACTIVE AND LONG-LIVED PERMANENT FOREARC DEFORMATION DRIVEN BY THE SUBDUCTION SEISMIC CYCLE

Felipe Alejandro Aron Melo, Ph. D.

Cornell University 2014

I have used geological, geophysical and engineering methods to explore mechanisms of upper plate, brittle deformation at active forearc regions. My dissertation particularly addresses the permanent deformation style experienced by the forearc following great subduction ruptures, such as the 2010 M_w8.8 Maule, Chile and 2011 M_w9.0 Tohoku, Japan earthquakes. These events triggered large, shallow seismicity on upper plate normal faults above the rupture reaching M_w7.0.

First I present new structural data from the Chilean Coastal Cordillera over the rupture zone of the Maule earthquake. The study area contains the Pichilemu normal fault, which produced the large crustal aftershocks of the megathrust event. Normal faults are the major neotectonic structural elements but reverse faults also exist. Crustal seismicity and GPS surface displacements show that the forearc experiences pulses of rapid coseismic extension, parallel to the heave of the megathrust, and slow interseismic, convergence-parallel shortening. These cycles, over geologic time, build the forearc structural grain, reactivating structures properly-oriented respect to the deformation field of each stage of the interplate cycle. Great subduction events may play a fundamental role in constructing the crustal architecture of extensional forearc regions. Static mechanical models of coseismic and interseismic upper plate deformation are used to explore for distinct features that could result from brittle fracturing over the two stages of the interplate cycle. I show that the semi-elliptical

outline of the first-order normal faults along the Coastal Cordillera may define the location of a characteristic, long-lived megathrust segment. Finally, using data from the Global CMT catalog I analyzed the seismic behavior through time of forearc regions that have experienced great subduction ruptures >M_w7.7 worldwide. Between 61% and 83% of the cases where upper plate earthquakes exhibited periods of increased seismicity above background levels occurred contemporaneous to megathrust ruptures. That correlation is stronger for normal fault events than reverse or strike-slip crustal earthquakes. More importantly, for any given megathrust the summation of the M_w accounted by the forearc normal fault aftershocks appears to have a positive linear correlation with the M_w of the subduction earthquake – the larger the megathrust the larger the energy released by forearc events.

BIOGRAPHICAL SKETCH

Felipe Aron was born August 02, 1982 in Concepción, Chile to Carmen Gloria Melo and Alejandro Aron. At the early age of eight months, he moved with his family to Kiel, Germany and lived there for four years, while his father was pursuing a Ph. D. in marine biology. That time marks the beginning of Felipe's curiosity about the Earth. Surrounded mostly by graduate students, Felipe started to become fascinated about stories of mysterious and marvelous worlds in the bottom of the oceans or at the top of mountains. His grandmother remembers how surprised she was that, while they were examining an atlas and a globe with topographic relief, four-year-old Felipe stubbornly asked her to explain the origin of the Andes and Himalayas, and take him to those places. During his school days Felipe generally showed interest in subjects related to natural sciences. He was motivated early on by an elementary school teacher named Patricia Pinto, although at some point he was also attracted to other disciplines such as philosophy and architecture. The main reason why he sorted out those adolescent indecisions and finally decided to study earth sciences was probably because of his father – a marine biologist who is passionate about geology. He always managed a way to include a visit to a volcano or another cool geologic site during family vacations, passing on that passion to his children Bárbara and Felipe.

Felipe entered college in the year 2001 and his first scientific experiences date back to the year 2004, when he met José Cembrano and Gabriel González. Besides being good friends, they have been academic and personal mentors to Felipe throughout his entire career. In 2005, Felipe travelled to Germany with his friend and academic partner Erik Jensen to attend for the first time to an international conference, thanks to support obtained by Christoph Heubeck. A year later, Felipe headed to

Liverpool, U.K. to study, along with José and David Prior, material sciences and fracture processes in steels using SEM and EBSD microscopy. In 2006 Felipe started his thesis project supervised by Gabriel and by Eugenio A. Veloso (co-advisor), studying the relationship between modern deformation and volcanism in the Central Andes. In the year 2008 Felipe earned a B.S. and a Professional Title degree (Geologist) from Universidad Católica del Norte (UCN) in Antofagasta, Chile, ranking first among all the students of his matriculating class. After graduation, while he was deciding about his future academic path, he worked as a mining geologist for a small company and also as a free-lance consultant.

In 2008 Rick Allmendinger, a good friend of Gabriel and José, was in Antofagasta teaching his advanced structural geology course – a class that Felipe took three times when he was in college! Rick and Gabriel had a conversation in which they decided that Felipe should move on to Cornell to pursue a doctoral degree. In 2009 Felipe received the prestigious Becas Chile fellowship from the Chilean government to pursue his Ph. D. studies and a few months after, he and Alejandra Escandón decided to get married and move to the United States. He entered the graduate program at Cornell in the Fall of 2009. In his dissertation, supervised by Rick, Matt Pritchard and Tony Ingraffea, Felipe has used geological, geophysical and engineering methods to study mechanisms of upper plate permanent deformation and active seismicity at forearc regions, throughout the subduction seismic cycle. In addition to sitting in the comfort of his lab, working on the computer, he spent 59 days doing structural fieldwork over the area affected by the 2010 M_w 8.8 Maule earthquake. Felipe maintains an active collaboration with his colleagues in Chile and has also been involved with two other research groups at Cornell, analyzing earthquake-triggered volcanic deformation – with Matt Pritchard's group – and the paleo-morphology of the Columbia Hills in Mars, with Shoshanna Cole at the

Department of Astronomy. Felipe is the 2012 recipient of the Meyer Bender Memorial, Class of ’28 Scholarship for academic and community excellence, awarded by the EAS Department, and the Outstanding Student Paper Award (OSPA) from the American Geophysical Union (AGU) for his presentation at the 2011 Fall Meeting.

Upon graduation, Felipe will hit the road along with his wife Alejandra and drive across the country, from Ithaca to Palo Alto, to begin a post-doctoral position with George Hilley at Stanford University.

Dedicated to the Pachamama and its mysterious marvels, sources of inspiration for this piece of work

ACKNOWLEDGMENTS

I hope that in the following lines I can say thanks and express my sincere gratitude to all the people that have contribute greatly to my personal and/or academic experience over these almost five years at Cornell. First and foremost, I thank my advisor Richard Allmendinger who more than a supervisor and mentor has become a very good friend. I've really enjoyed our passionate conversations in the lab, holding a cup of coffee, in the field, his house or my place, whether they were about geology, politics, life, the world energy crisis, education, etc. As he knows, we bear different and somewhat contrasting personalities, but I think that this is exactly what has made us friends. I feel very honored and lucky of having been his student – Rick has taught me the skills I need to become a well-rounded and rigorous scientist, and to think critically about a problem, considering all the alternative explanations. Even if I protested sometimes, I very much appreciate that he sat through countless practice sessions of my talks and read several drafts of my papers to teach me how to present my research in a simple, clean and successful manner.

Matthew Pritchard was an excellent advisor and also a source of inspiration to my work. Through many conversations, meetings or over his classes, he introduced me to most of the quantitative techniques that I've used during my Ph. D., which are now my background set of tools to start building my next academic endeavor. Matt's insightful comments were always right on-spot in pointing out the strengths and weaknesses of my work, and his recommendations improved greatly all my contributions. I also appreciate that he invited me to participate as a collaborator in one of his projects, analyzing volcanic deformation produced by earthquakes. Anthony Ingraffea introduced me to the world of engineering and to think about problems in solid

mechanics from the perspective of a “digital twin”. My very first numerical model was part of his Fracture Mechanics class, one of the best that I’ve taken. One of the many and important thinks that I learned from him, besides to always follow Tony’s rules for constructing a computational model, is the tremendous potential of combining expertize from the earth and engineering sciences. I also enjoyed very much our conversations about fracking and other topics on which he has become passionate about. Tony’s wise comments and recommendations were an excellent complement to my research and I’m honored of having been his last Ph. D. advisee before a well-deserved retirement.

Since the beginning of my academic career, José Cembrano (Pontificia Universidad Católica de Chile, PUC) and Gabriel González (Universidad Católica del Norte, UCN) have been my mentors, friends and sources of inspiration. Their support and good advice have been crucial during hard and difficult experiences in my life. I enjoy very much working with them and I look forward to our future projects. Also, I thank José for having accepted to be a member *ex officio* of my committee. He provided insightful and constructive comments to my dissertation and helped to improve greatly the final version of this thesis. I appreciate that he came from Chile just to attend to my defense and share with me this important moment.

All of my research projects during my Ph. D. were possible thanks to a collaboration with my friends and colleagues at two academic institutions in Chile and at Cornell including, besides the people already mentioned above, Felipe Astudillo (UCN), Gonzalo Yáñez (PUC), Erik Jensen (UCN), and Gloria Arancibia (PUC), and my fellow students Shoshanna Cole (Department of Astronomy, Cornell), Jennifer Jay and Scott Henderson (both at Earth and Atmospheric Sciences, Cornell), and Mauricio Bucca (Department of Sociology, Cornell). Jack Loveless, former Rick’s grad student,

who I met back in 2004 when I assisted him during his Ph. D. field work in Chile, has contributed directly and indirectly to my research. Besides being a good friend and source of personal and academic advice, many of the ideas that I explored in my dissertation were inspired in his previous works in extensional tectonics over the northern Chile forearc.

Muawia Barazangi took good care of my education and many aspects of my life here in Ithaca. He has become one of my substitute fathers away from home. I will never forget his appearances in my lab, sweetening my day with a treat or asking me to get a haircut, if I was making progress with my work and to turn down the volume of the music. His continuous insistence encouraged me to elaborate the first paper of my Ph. D. He taught me that I always have to find a good geologic reason to justify my research projects. But perhaps one of the most important lessons that I learned from Muawia comes from an advice that Rick gave me early in my Ph. D. – "no matter what you are trying to do, always think about what Muawia would say". Teresa Jordan also took good care of my life in Ithaca and along with Rick, she was, and always will be, part of my extended family. I sincerely appreciate her critic comments during my Andes Seminar presentations. She always asked the most difficult question! but at the same time that helped me to think critically about my work.

Many members of the Earth and Atmospheric Sciences department (EAS) were fundamental in helping me with my grad school experience. I specially would like to thank the staff including Savannah Williams, Carolyn Clark (former member), Steve Gallow, Amy Colvin and Judy Starr for their support. Their superb work is crucial in maintaining such a wonderful atmosphere in our small community. Many faculty members at EAS and Civil Engineering enriched both my personal and academic experience at Cornell including: Byan Isacks, Sue Kay, Bob Kay, Dan Karig, Rowena

Lohman, Katie Keranen, Jason Phipps-Morgan (former member), Chris Andronicos (former member), Larry Brown, Heinrich Bahlburg (visiting professor from Universität Münster), Steve Colucci, John Thompson, Geoffrey Abers, Louis Derry, Philip Liu and Derek Warner. I feel lucky and honored to have had many of them listening to my Andes Seminars and I appreciate their advice and constructive comments to my work.

...I get by with a little help from my friends...; I sincerely thank Nico Cosentino, Miguel Pérez, Naomi Kirk-Lawlor, Ryan Gordon, Diego Quiros, Rachel Scanza and Spike, Adriano Quiroga, Jennifer Jay and Kendrick, Patricio Winckler, Scott Henderson, Paulina Cox, José Muñoz, Marta del Campo, Francisco Delgado, Silvia Marrillaga, Marcelo Aguiar, Francisco Díaz, Agustina González, Rodrigo Labatut, Ignacio Sepúlveda, Alejandra Escárez, Jorge Mexia, Eliana Monteverde, Rosario Donoso, Francisca Alliende, Christian Pichard and Chris Siron for their unconditional friendship and constant support during my time away from home. I also thank former and current fellow Cornell grad students Bill Barnhart, Phoebe Judge, Amanda Baker, Kristopher Baker (Civil Engineering), Veronica Prush, Timothy Reber, Chen Chen, Sander Hunter, Brad Wham, Chelsea Scott, Erin Camp, Holly Taylor, John Mason, Chen Chen (CC) for enhancing my overall student experience.

Many people have had a deep influence in the development of my scientific career including David Prior, Misael Camus, Peter Molnar, Christoph Heubeck and George Hilley.

I'm very thankful to students, friends and colleagues in Chile and Perú including Carlos Benavente, Camilo Rojas, Raquel Arriaza, Violeta Véliz, Pamela Pérez, Rodrigo Gomila, Sonia Martínez, Diego Mackenna, Nicolás Pérez, Pablo Galleguillos, Bárbara Aron and Nico Silva (Surfarm) for their helpful assistance in my field

campaigns. I thank Horacio Parragué for sharing with me his neat aerial pictures of my field areas. Marianne Métois kindly provided a compilation of interseismic GPS velocities over the Maule earthquake region. I sincerely thank the Editors Stephen T. Johnston (GSA Bulletin) and Thomas Parsons (JGR-Solid Earth), and the reviewers Lucinda Leonard, Hiroyuki Tsutsumi and two anonymous for their thorough, meticulous and constructive comments on my manuscripts. I gratefully acknowledge support and funding from the U.S. National Science Foundation grants EAR-0738507 and EAR-1118678 (to Rick Allmendinger), Cornell University and Pontificia Universidad Católica de Chile (PUC) for my work in the Andean forearc. My Ph. D. studies were mostly funded by CONICYT *Beca Chile* (2009, Chilean Government).

My beloved family, Carmen Gloria Melo, Alejandro Aron, Bárbara Aron and Señora María, has been a constant source of encouragement, support and love, making me who I am. My infinite thanks to all of you for having pushed me through my grad school experience. My final words are for the love of my life, my wife M. S. Alejandra Escandón. I'm extremely proud of all what you've done to successfully fulfill your academic and professional life at Cornell. Five years ago we decided to start an adventure. We left the comfort of our homes in Chile and came to Ithaca for a new life together, with a bag full of uncertainties and hopes. The family that we have constructed is proof that this adventure ended up well. Thank you for being the pillar that support my life, my partner and for your endless patience and love.

TABLE OF CONTENTS

LIST OF FIGURES

LIST OF TABLES

CHAPTER 1

INTRODUCTION

One of the most outstanding scientific characteristics of the 2010 M_w 8.8 Maule, Chile subduction earthquake is that it triggered large and shallow upper plate normal fault earthquakes, reaching M_w 7.0 (Fig. 1.1) (e.g., *Farías et al.*, 2011; *Ryder et al.*, 2012; *Ruiz et al.*, 2014). These events were nucleated in previously undescribed forearc structures that cut the Chilean Coastal Cordillera overlying the rupture, over the near field of the megathrust. Of particular interest is a major NW-striking structure near the northern end of the Maule earthquake rupture so-called Pichilemu normal fault, which is oblique to the NNE-trending plate boundary and produced the larger aftershocks. About a year later, a similar phenomenon occurred after the 2011 M_w 9.0 Tōhoku megathrust earthquake in Japan (e.g., *Toda et al.*, 2011; *Mizoguchi et al.*, 2012; *Kato et al.*, 2013; *Toda and Tsutsumi*, 2013).

From a geologic perspective, in terms of the permanent, brittle deformation experienced by the upper plate, these triggered events may play a fundamental role in constructing and controlling the style and evolution of the current structural grain. Therefore, if we interpret the forearc faults as long-term strain markers of subduction events, they may be used to investigate, for example, characteristics of the interplate seismic cycle such as long-lived segmentation and recurrence. But perhaps more importantly, the large magnitude and shallow depth of these crustal aftershocks pose a significant threat to population and complex infrastructure (Fig. 1.1), so understanding the behavior of the intraplate structures becomes important for seismic hazards purposes as well (*Gürpinar*, 2005).

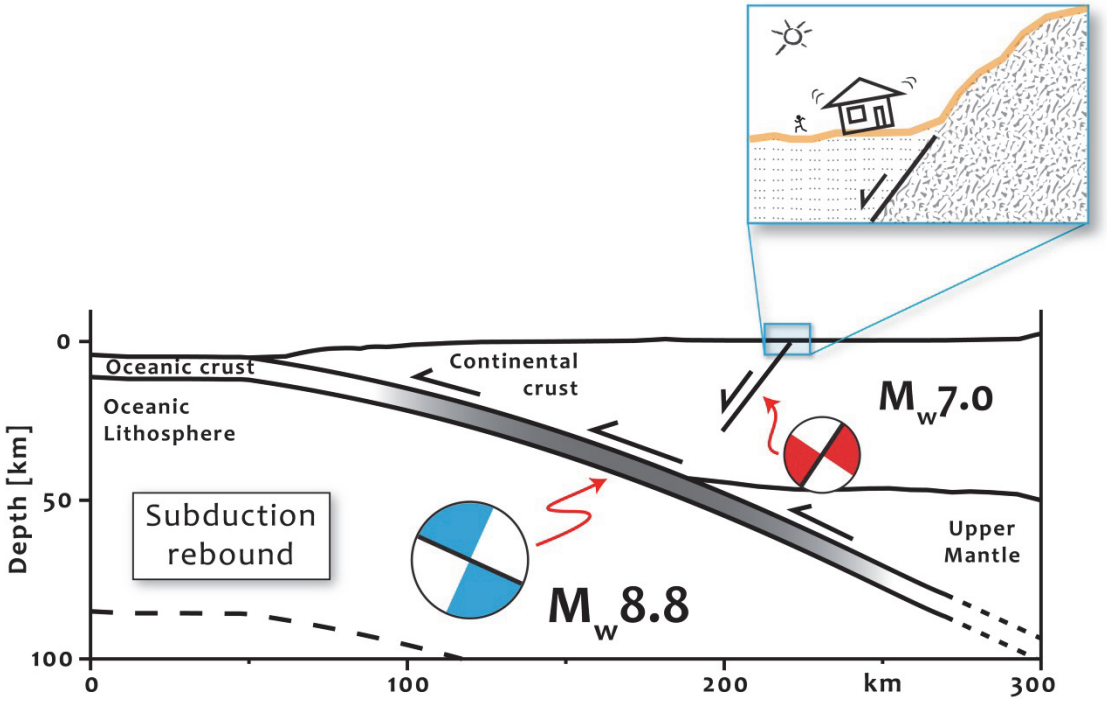

Figure 1.1: Cartoon cross section at the center of the 2010 Maule earthquake rupture in central Chile showing a simplified view of the main structural components of a subduction tectonic system addressed in this Dissertation.

In this dissertation I explore how the activity of upper plate, forearc faults relates to the occurrence of great subduction in the near-field of the event and variations of the elastic and brittle deformation styles throughout the interplate seismic cycle. I particularly focus my research in understanding how those processes affect the construction of the structural edifice at the leading edge of the plate boundary. First, I present extensive new observations on the structural geology and neotectonics of the forearc region affected by the 2010 Maule earthquake, providing the structural background and geologic framework for the study. Previous geologic information over the rupture region was particularly sparse compared to other portions of the plate boundary (Aron et al., 2012, 2013a). Then I show a comparison of this long-term deformation signature with geophysical observation of intraplate seismicity and kinematic models of GPS velocities and displacements, across the subduction cycle in the Maule earthquake segment (Fig. 1.2). Static mechanical models of coseismic and interseismic upper plate deformation are used to explore for distinct features that could result from brittle fracturing over these two stages of the interplate cycle. Those findings enable the testing of the hypothesis of long-lived seismic segmentation of the Maule rupture area. Finally, I show the results of an analysis over near-field regions that have experienced great subduction ruptures worldwide since 1976, to assess the character and style of the seismic behavior of the upper plate crust in relation to the stress release by megathrust events. In agreement with a recent study by Gomberg and Sherrod (2014), I found that most of the analyzed subduction events produced an increase in seismic activity in the upper plate following the megathrust events, reactivating properly-oriented forearc structures. My study goes further in exploring the kinematic style of these triggered events, and how that evolves through the different stages of the subduction seismic cycle. Despite the data quality of the World catalog in regions with poor station coverage and the natural variability in the dataset,

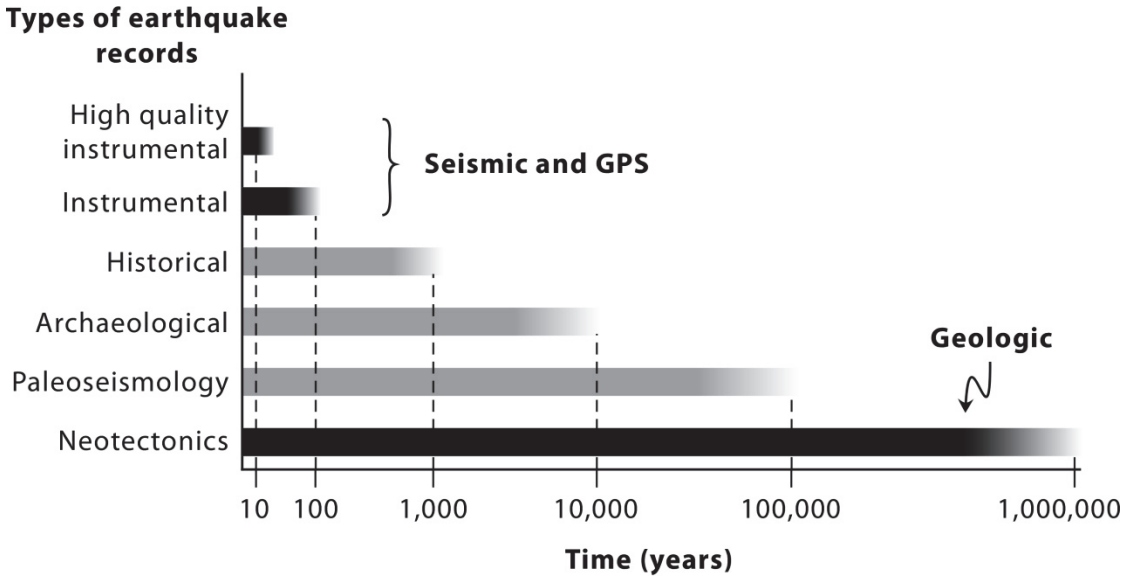

Figure 1.2: Time window of observations, methods and modelling used in this Dissertation, emphasizing in black the chronological separation and distribution of the main disciplines and data sources applied to the study (modified after *Gürpinar*, 1989; *Levret*, 2000; *Caputo and Helly*, 2008; *Tikoff et al.*, 2013).

I will show that different plate boundaries bear similar characteristics regarding the subduction-triggered, upper plate earthquakes such as preferred kinematic style, predominantly normal faulting, and fault orientations respect to the stress field imposed by megathrust earthquakes.

1.1 Structural background

Geologists working in the Andean forearc have long known that normal faults showing neotectonic displacements are an important structural element of the Coastal Cordillera, but the relation of their activity to the subduction seismic cycle is still unclear. Over a significant portion of the Northern, Central and Southern Andes forearc, these structures run parallel and oblique to the plate boundary (e.g., *Arabasz*, 1971; *Sébrier et al.*, 1985; *González et al.*, 2003; *Heinze*, 2003; *Marquardt et al.*, 2004; *Audin et al.*, 2008; *Allmendinger and González*, 2010; *Saillard et al.*, 2011; *Aron et al.*, 2012, 2013a) – though some regions show a puzzling coexistence of normal and reverse faults, and tectonic inversions of the structures (e.g., *Lavenu and Encinas*, 2005; *Melnick et al.*, 2006; *Allmendinger and González*, 2010). The long-term direction of upper plate extension determined by these major normal faults is approximately parallel to the convergence vector (e.g., *Lavenu et al.*, 1999; *Heinze*, 2003; *Cembrano et al.*, 2007).

A similar extensional structural pattern of the foearc can be observed at several other subduction boundaries such as in northern New Zealand (e.g., *Cashman and Kelsey*, 1990; *Chanier et al.*, 1999), Central America near the Nicoya Peninsula (e.g., *Kuijpers*, 1980; *McIntosh et al.*, 1993; *Marshall and Anderson*, 1995) and central-southern Japan (e.g., *Fournier et al.*, 1995; *Yamaji et al.*, 2003). Yet, other subduction zones show different kinematic styles dominating the forearc structural grain. For

example, over accreting plate margins trench-parallel thrust faults affect the toe of the upper plate wedge, consistent with convergence-parallel shortening, as observed in Japan (e.g., *Shiki and Misawa*, 1982; *Taira*, 2001; *Moore et al.*, 2007), Sumatra (e.g., *Sibuet et al.*, 2007; *Mosher et al.*, 2008), the Aleutians (e.g., *von Huene and Klaeschen*, 1999), New Zealand (e.g., *Nicol et al.*, 2007) and Southern Chile (e.g., *Melnick et al.*, 2006, 2009). Also, in regions where subduction is highly oblique to the margin the forearc structure is strongly controlled by major strike-slip fault slivers, which produce a wide region of deformation and strain partitioning in the upper plate. The most representative cases of this architecture are the Mentawai fault and other major structures SW of the Sumatra intra-arc sytem, which interrupt the forearc of the Java-Sumatra-Andaman subduction zone (e.g., *Karig et al.*, 1979; *Diament et al.*, 1992; *Malod and Kemal*, 1996; *Berglar et al.*, 2010; *Weller et al.*, 2012). And perhaps more intriguing, the forearc near concave-towards-the-trench bends at curved plate boundaries, such as northern Chile and Cascadia, is affected by reverse faults nearly orthogonal to the coastline accommodating margin-parallel shortening (e.g., *Johnson et al.*, 2004; *Allmendinger et al.*, 2005).

The crustal normal fault aftershocks that followed the Maule and Tōhoku earthquakes are, to date, some of the most significant evidence of intraplate seismicity instrumentally recorded at any forearc region. Based on those observations, my dissertation explores the mechanisms that control the behavior and activity of crustal normal faults above the interplate seismogenic zone, acknowledging the profound influence that great subduction earthquakes produce on the state of stress in the upper plate. Thus, the findings might be more pertinent to extensional margins. Nonetheless, the behavior of reverse and strike-slip forearc faults, in the context of the subduction seismic cycle, is as well addressed in my work.

1.2 Upper plate faulting and the subduction seismic cycle

Despite the fact that most of the upper plate deformation above a megathrust seismogenic/locking zone is accommodated either elastically or viscoelastically (e.g., *Wang et al.*, 2012), crustal earthquakes, faults or tension cracks are evidence of an important anelastic component to the strain field (*Aron and Allmendinger*, 2011; *Baker et al.*, 2013) – they are the permanent, brittle deformation signatures of the loading processes affecting the forearc.

Normal faulting in the forearc has been normally attributed to subduction erosion (e.g., *von Huene and Scholl*, 1991; *Ranero and von Huene*, 2000; *von Huene and Ranero*, 2003; *Saffer and Tobin*, 2011) or, in accreting margins, to local features related to anticlinal folding above propagating thrust faults in the accretionary wedge (e.g., *Melnick et al.*, 2006). However, some authors have attempted to address this problem acknowledging the importance of cyclic variations in the deformation style experienced by the upper plate at different stages of the subduction seismic cycle (e.g., *Delouis et al.*, 1998; *Klotz et al.*, 2006; *Allmendinger and González*, 2010; *Loveless et al.*, 2010a; *Toda and Tsutsumi*, 2013). During the interseismic period, the upper plate is slowly shortened parallel to convergence, at rates of a few centimeters per year, whereas following a megathrust event the upper plate stretches by meters per minute in the direction of the subduction rebound (*Wang*, 2007; *Wang et al.*, 2012). Postseismic processes such as aseismic afterslip, interplate thrust aftershocks and viscoelastic deformation continue to accommodate forearc extension for years after the earthquake (e.g., *Hu et al.*, 2004), but this extensional field is progressively overcome through time as interseismic shortening builds up again thanks to a full- to partially coupled plate interface. Postseismic deformation has commonly similar orientation to the coseismic field and the two are indistinguishable in the geologic

record – the main concern of my dissertation –, so when I refer to the concept of coseismic deformation I'm usually including these two stages (Fig. 1.2).

Coulomb stress increment (*King et al.*, 1994) provides a convenient tool to conceptualize the relationship between stress transfer from the interplate contact to the upper plate structures. *Delouis et al.* (1998) and *Loveless et al.* (2010a) used this method to propose conceptual models that relate the activity of upper plate faults to the stages of the subduction seismic cycle. *Delouis et al.* (1998) suggest that during the interseismic period the major normal faults remain aseismic due to decrease of normal-fault Coulomb stress under contraction. Subduction earthquakes produce instantaneous positive increments of normal-fault Coulomb stress, surpassing what was negatively induced interseismically. If these positive gains of Coulomb stress progress over more cycles, eventually the structures will reach the normal-fault shear strength and slip. Instead, *Loveless et al.* (2010a) propose that during the interseismic period, normal-fault Coulomb stress on the faults increases positively, and that subduction earthquakes can increase both normal- and/or reverse-fault Coulomb stresses, depending on the location of the forearc structures respect to the megathrust slip. If the later model is correct, normal faulting in the upper plate would occur either coseismically or interseismically; reverse faulting on upper plate faults should occur only following a subduction earthquake event.

Based on their work, I propose an alternative, conceptual model to explain how shear stress on forearc structures evolves throughout many interplate seismic cycles and reach the shear strength to produce slip. This model is a more nuanced explanation, accounting for short- and long-term signals of upper plate deformation captured in the geologic, geodetic and seismic records over the studied regions. Therefore, although it is based on short-term kinematic and mechanical models and

observations, this interpretation intends to represent the most likely scenario over neotectonic, geologic time scales (Fig. 1.2), which smooths out local tectonic and structural anomalies that could modify greatly the state of stress of the crust and so, the structural behavior of the upper plate.

1.3. Subduction segmentation

In the Atacama Desert in northern Chile, *Loveless et al.* (2005, 2009) suggested that a semi-elliptical pattern of coseismic tension cracks over the forearc, preserved over millions of years, delineates the average long-term, behavior of rupture segments. The segment boundaries are marked by bimodal, margin-oblique orientations of cracks determined by intersection of two adjacent semi-ellipses. These cracks indicate the long-term direction of coseismic extension because Mode I fractures form perpendicular to the minimum principal stress and parallel to the maximum stress. The elliptical pattern shown by the fractures would reflect a maximum accumulated slip concentration near the center of the fault, dying out towards the fault terminations, which persistently ruptures the same segment over geologic time (*Scholz*, 2002). That pattern of long-term slip gradient generates the concentric elliptical field of extension above the megathrust.

My thesis follows up on this idea but, instead of using coseismic tension cracks, I extend the analysis to normal faults, structural features that also produce large amounts of sub-horizontal stretching. I test the hypothesis that in the region in central Chile affected by the 2010 Maule earthquake, great megathrusts similar to this event appear to have ruptured the segment repeatedly over time, thus enhancing the morphological and structural expression of appropriately-oriented forearc structures. I incorporate in this analysis all the geological and structural information available for

the study region, including the new field data collected during my Ph. D. research. Mechanical models of Coulomb stress suggest that, similar to the cracks in northern Chile, a semi-elliptical pattern over the forearc of normal faults enclosing the rupture area represents the best-fitting structural arrangement favored to slip after a megathrust event.

One important question which deserves further study is if the semi-elliptical pattern shown by normal faults in the Maule earthquake region may be subject to a positive feedback loop. Lateral inhomogeneities of the upper plate, such as faults oblique to the plate boundary and lithologic contacts, may cause long-lived seismic segmentation over subduction zones, by mechanically decoupling discrete blocks along the strike of the trench (e.g., *Collot et al.*, 2004; *Tassara*, 2010; see also references listed by *Loveless et al.*, 2010b in Table 1). The margin-oblique normal faults or other material discontinuities at segment boundaries may be inherited from tectonic processes previous to the onset of subduction and/or segmentation. Over geologic time, because they are also appropriately oriented to the coseismic extensional strain field imposed by repetition of thousands or even millions of subduction ruptures, they will be more likely to reactivate, enhance its morpho-structural expression and therefore delineate the boundary of a long-lived segment. The reactivated NW-striking Pichilemu normal fault at the northern end of the 2010 Maule rupture may be an exemplar of this configuration. The alternative end member scenario is that, instead of contributing to produce seismic segmentation, the faults are just “indicators” or a result of the process, similarly to the coseismic tension cracks, so segmentation – if really occurs – might be controlled by factors independent of the upper plate architecture. One possible approach to attack these problems is numerical modelling such as the Finite Elements Method (FEM), involving concepts of fracture mechanics and multi-scale (time and space) theory.

1.4 Worldwide view of triggered forearc seismicity

Although the most outstanding examples of near field, upper plate seismicity triggered by subduction earthquakes are the normal fault aftershocks generated by the 2010 Maule and 2011 Tōhoku events (e.g., *Toda et al.*, 2011; *Hasegawa et al.*, 2012; *Lange et al.*, 2012; *Rietbrock et al.*, 2012), other megathrust earthquakes have shown crustal reactivations of normal, strike-slip and reverse kinematics as well. For example, the 2004-2005 Sumatra-Andaman-Nias sequence produced normal fault aftershocks but also large strike-slip events in the forearc structures (*Lay et al.*, 2005; *Oishi and Sato*, 2007). Similarly, the Chololo normal fault in southern Perú was reactivated showing left-lateral displacements following the 2001 Pisco earthquake (*Audin et al.*, 2008). In both cases, the extensional axes of the forearc events are consistent with stretching direction sub-parallel to the subduction rebound; therefore these preexisting structures were properly oriented for strike-slipping under the loading conditions imposed by the megathrust. Reverse fault triggering tends to occur in the upper plate at the toe of the forearc wedge, up dip from the maximum slip zone of the megathrust (*Li et al.*, 2014), because this portion of the upper plate experiences shortening parallel to the heave of the megathrust rebound. There are several cases of documented thrust splay fault reactivations after subduction earthquakes, including the events following the great 1964 Alaska (*Plafker*, 1967) and 2004 Sumatra-Andaman earthquakes (*Sibuet et al.*, 2007).

Using the entire Global CMT catalog of earthquakes (*Ekström et al.*, 2012) and simple methods of statistical seismology, I will show that subduction events globally produce an increase of seismic activity above background levels in the near field volume of the upper plate (*Aron et al.*, 2013b), which agrees very well with the

findings of a recent and independent study by *Gomberg and Sherrod* (2014). But more importantly, my study goes further in analyzing the kinematic style of these triggered events, and how that evolves through the different stages of the seismic cycle, so the results have broader implications in: (a) understanding the mechanics involved in permanent deformation processes of the upper plate under the loading conditions imposed by the megathrust, (b) addressing the importance of the inherited forearc structure to accommodate the loading imposed by the megathrust and (c), assessing the likelihood of which specific forearc structures might be more suitable to reactivate after subduction events.

1.5 Thesis outline

This dissertation is organized in three main chapters which are written as individual journal articles so each one stands by its own. However these three sections are interconnected and the reader will find that the main research lines expressed in this introduction are progressively built up throughout the dissertation and attacked from different perspectives, using a suite of alternative methods from the geological, engineering and geophysical sciences.

Chapter 2 presents new field data on the structural geology and neotectonics from the part of the Chilean Coastal Cordillera that overlies the area ruptured by the 2010 Mw8.8 Maule earthquake. In this contribution I provide the first comprehensive structural dataset of that study regions, which should serve as a reference work for any subsequent study in this area that needs information about the forearc structure. This segment includes the aforementioned Pichilemu normal fault, the intraplate structure reactivated after the megathrust event which held the large crustal events. This fault shows a repeated history of rupture throughout at least the Quaternary. In general, as

with other parts of the Coastal Cordillera and consistent with the kinematics of the crustal aftershocks of the 2010 Maule event, Quaternary normal faults dominate the young architecture of those regions. The forearc overlying the Maule rupture indicates that the occurrence of great subduction events may play a fundamental role in constructing the crustal architecture of extensional forearc regions. Besides the fact that the majority of the areas covered in our work are previously undescribed, this work is of interest to a broader audience in that we relate our geological findings to geophysical signals of forearc deformation – seismic and GPS – throughout the interplate seismic cycle over the Maule earthquake region. I present a conceptual model of how long term faulting in the Coastal Cordillera may be related to great earthquakes on this subduction segment. This chapter has been accepted for publication soon in the *Geological Society of America Bulletin*.

Chapter 3 examines the consequences of the 2010 Maule earthquake for the permanent deformation of the forearc. I combine geophysical and geological data with principles of linear elasticity, dislocation theory and Coulomb rock fracture criteria to explore how permanent upper plate deformation relates to release of elastic strain energy during great earthquakes. Modelling the infinitesimal static strain and stress fields imposed on the upper plate by the interplate megathrust, I provide a mechanical explanation for continental, large intraplate normal faulting triggered by the great megathrusts like the Maule earthquake. By comparing the coseismic and interseismic crustal deformation signals, we propose that cyclical unloading of the upper plate during great subduction earthquakes may generate a permanent, distinctive extensional pattern in the structural grain to the forearc. This pattern may represent the average behavior over many thousands of subduction seismic cycles throughout the geologic time and we suggest that might be used to identify characteristic, long-lived rupture segments. This work, originally published in the *Journal of Geophysical Research –*

Solid Earth, is unique in examining the question of whether upper plate faults can be used to identify long-lived rupture segments.

Finally, in Chapter 4 I use data from the Global CMT catalog to test the hypothesis proposed in the first two parts of my dissertation that in the Maule earthquake region, and perhaps elsewhere, subduction earthquakes may be an important mechanism to reactivate faults in the upper plate, producing permanent deformation of the forearc and shaping its structural grain. If the hypothesis holds true, one would expect to see a perturbation in the seismic behavior of the upper plate following megathrust earthquakes. I examine globally the style and character of near-field, upper plate earthquakes associated with great subduction events ($\geq M_w$ 7.7) since 1976. I use standard techniques in statistical seismology to answer the following questions: After a great megathrust earthquake, (1) is there an increase in upper plate seismicity rate? (2) Is there an increase in the moment released by upper plate events? And (3), is there a change in the kinematic style of the upper plate seismicity? I show evidence that most of the surveyed subduction events triggered upper plate seismicity on properly-oriented structures in the near-field overlying the rupture, predominantly normal faulting but in some cases thrust and strike-slip as well. I discuss the implications of these findings for the long-term structural configuration of the forearc. But perhaps more importantly, I show that the magnitude of these triggered, normal fault events scales proportionally to the size of the megathrust, which may have important implications for seismic hazard assessments in non-collisional, convergent margins. This chapter is in preparation to be submitted to a peer-reviewed journal after the release date of this Ph. D. thesis.

REFERENCES

Allmendinger, R. W., and G. González (2010), Invited review paper: Neogene to Quaternary tectonics of the coastal Cordillera, northern Chile, *Tectonophysics*, *495*(1–2), 93–110, doi:10.1016/j.tecto.2009.04.019.

Allmendinger, R. W., G. González, J. Yu, G. Hoke, and B. Isacks (2005), Trench-parallel shortening in the Northern Chilean Forearc: Tectonic and climatic implications, *Geol. Soc. Am. Bull.*, *117*(1-2), 89–104, doi:10.1130/B25505.1.

Arabasz, W. J. (1971), Geological and geophysical studies of the Atacama fault zone in northern Chile, PhD, Calif. Inst. of Technol., Pasadena, California.

Aron, F., and R. W. Allmendinger (2011), Breaking the Outer Forearc: The Permanent Legacy of a Subduction Earthquake, in *paper presented at 2011 Fall Meeting, AGU, San Francisco, Calif., 5-9 Dec*.

Aron, F., J. Cembrano, R. W. Allmendinger, F. Astudillo, and G. Arancibia (2012), Structural Geology of the Active Forearc above the Maule Megathrust: Traces of a Long-lived Subduction Segment, in *paper presented at 2012 XIII Chilean Geological Congress, Antofagasta, Chile, 5-9 Aug.*

Aron, F., F. Astudillo, J. Cembrano, and G. Arancibia (2013a), Constructing forearc architecture with megathrusts: geological and geophysical examples from the 2010 Maule earthquake region, in *paper presented at 2013 125th Anniversary GSA Annual Meeting, Denver, Colorado, 27-30 October*.

Aron, F., R. W. Allmendinger, and E. Jensen (2013b), Global Correlation between the Size of Subduction Earthquakes and the Magnitude of Crustal Normal Fault Aftershocks in the Forearc, in *paper presented at 2013 Fall Meeting, AGU, San Francisco, Calif., 9-13 Dec*.

Audin, L., P. Lacan, H. Tavera, and F. Bondoux (2008), Upper plate deformation and seismic barrier in front of Nazca subduction zone: The Chololo Fault System and active tectonics along the Coastal Cordillera, southern Peru, *Tectonophysics*, *459*(1–4), 174–185, doi:10.1016/j.tecto.2007.11.070.

Baker, A., R. W. Allmendinger, L. A. Owen, and J. A. Rech (2013), Permanent deformation caused by subduction earthquakes in northern Chile, *Nat. Geosci.*, *advance online publication*, doi:10.1038/ngeo1789.

Berglar, K., C. Gaedicke, D. Franke, S. Ladage, F. Klingelhoefer, and Y. S. Djajadihardja (2010), Structural evolution and strike-slip tectonics off north-western Sumatra, *Tectonophysics*, *480*(1–4), 119–132, doi:10.1016/j.tecto.2009.10.003.

Caputo, R., and B. Helly (2008), The use of distinct disciplines to investigate past earthquakes, *Tectonophysics*, *453*(1–4), 7–19, doi:10.1016/j.tecto.2007.05.007.

Cashman, S. M., and H. M. Kelsey (1990), Forearc uplift and extension, southern Hawke's Bay, New Zealand: Mid-Pleistocene to present, *Tectonics*, *9*(1), 23–44, doi:10.1029/TC009i001p00023.

Cembrano, J., A. Lavenu, G. Yañez, R. Riquelme, M. Garcia, G. González, and G. Hérail (2007), Neotectonics, in *The Geology of Chile*, edited by T. Moreno, W. Gibbons, and G. S. of London, pp. 231–261, Geological Society of London, London, Tulsa. UK.

Chanier, F., J. Ferrière, and J. Angelier (1999), Extensional deformation across an active margin, relations with subsidence, uplift, and rotations: The Hikurangi subduction, New Zealand, *Tectonics*, *18*(5), 862–876, doi:10.1029/1999TC900028.

Collot, J.-Y., B. Marcaillou, F. Sage, F. Michaud, W. Agudelo, P. Charvis, D. Graindorge, M.-A. Gutscher, and G. Spence (2004), Are rupture zone limits of great subduction earthquakes controlled by upper plate structures? Evidence from multichannel seismic reflection data acquired across the northern Ecuador–southwest Colombia margin, *J. Geophys. Res. Solid Earth*, *109*(B11), B11103, doi:10.1029/2004JB003060.

Delouis, B., H. Philip, L. Dorbath, and A. Cisternas (1998), Recent crustal deformation in the Antofagasta region (northern Chile) and the subduction process, *Geophys. J. Int.*, *132*(2), 302–338.

Diament, M., H. Harjono, K. Karta, C. Deplus, D. Dahrin, M. T. Zen, M. Gérard, O. Lassal, A. Martin, and J. Malod (1992), Mentawai fault zone off Sumatra: A new key to the geodynamics of western Indonesia, *Geology*, *20*(3), 259–262, doi:10.1130/0091-7613(1992)020<0259:MFZOSA>2.3.CO;2.

Ekström, G., M. Nettles, and A. M. Dziewoński (2012), The global CMT project 2004–2010: Centroid-moment tensors for 13,017 earthquakes, *Phys. Earth Planet. Inter.*, *200–201*, 1–9, doi:10.1016/j.pepi.2012.04.002.

Farías, M., D. Comte, S. Roecker, D. Carrizo, and M. Pardo (2011), Crustal extensional faulting triggered by the 2010 Chilean earthquake: The Pichilemu Seismic Sequence, *Tectonics*, *30*(6), TC6010, doi:10.1029/2011TC002888.

Fournier, M., L. Jolivet, and O. Fabbri (1995), Neogene stress field in SW Japan and mechanism of deformation during the Sea of Japan opening, *J. Geophys. Res. Solid Earth*, *100*(B12), 24295–24314, doi:10.1029/95JB01973.

Gomberg, J., and B. Sherrod (2014), Crustal earthquake triggering by modern great earthquakes on subduction zone thrusts, *J. Geophys. Res. Solid Earth*, *119*(2), 2012JB009826, doi:10.1002/2012JB009826.

González, G., J. Cembrano, D. Carrizo, A. Macci, and H. Schneider (2003), The link between forearc tectonics and Pliocene-Quaternary deformation of the Coastal Cordillera, northern Chile, *J. South Am. Earth Sci.*, *16*(5), 321–342, doi:10.1016/S0895-9811(03)00100-7.

Gürpinar, A. (1989), Importance of Historical Earthquakes in Research in the Sitting of Nuclear Facilities, in *GPSN, INMG, LNEC, CSN, Proc. Workshop "Historical Earthquakes in the Ibero-Maghrebian Region. Methodological approach and case studies,"* pp. 3–7, Lisbon.

Gürpinar, A. (2005), The importance of paleoseismology in seismic hazard studies for critical facilities, *Tectonophysics*, *408*(1–4), 23–28, doi:10.1016/j.tecto.2005.05.042.

Hasegawa, A., K. Yoshida, Y. Asano, T. Okada, T. Iinuma, and Y. Ito (2012), Change in stress field after the 2011 great Tohoku-Oki earthquake, *Earth Planet. Sci. Lett.*, *355–356*, 231–243, doi:10.1016/j.epsl.2012.08.042.

Heinze, B. (2003), Active Intraplate Faulting in the Forearc of North Central Chile (30°-31° S). Implications from Neotectonic Field Studies, GPS Data, and Elastic Dislocation Modeling, PhD, Free University, Berlin, March.

Hu, Y., K. Wang, J. He, J. Klotz, and G. Khazaradze (2004), Three-dimensional viscoelastic finite element model for postseismic deformation of the great 1960 Chile earthquake, *J. Geophys. Res.*, *109*(B12), B12403, doi:10.1029/2004JB003163.

Von Huene, R., and D. Klaeschen (1999), Opposing gradients of permanent strain in the aseismic zone and elastic strain across the seismogenic zone of the Kodiak shelf and slope, Alaska, *Tectonics*, *18*(2), 248–262, doi:10.1029/1998TC900022.

Von Huene, R., and C. R. Ranero (2003), Subduction erosion and basal friction along the sediment-starved convergent margin off Antofagasta, Chile, *J. Geophys. Res. Solid Earth*, *108*(B2), n/a–n/a, doi:10.1029/2001JB001569.

Von Huene, R., and D. W. Scholl (1991), Observations at convergent margins concerning sediment subduction, subduction erosion, and the growth of continental crust, *Rev. Geophys.*, *29*(3), 279–316, doi:10.1029/91RG00969.

Johnson, S. Y., R. J. Blakely, W. J. Stephenson, S. V. Dadisman, and M. A. Fisher (2004), Active shortening of the Cascadia forearc and implications for seismic hazards of the Puget Lowland, *Tectonics*, *23*(1), TC1011, doi:10.1029/2003TC001507.

Karig, D. E., S. Suparka, G. F. Moore, and P. E. Hehanussa (1979), Structure and Cenozoic evolution of the Sunda arc in the central Sumatra region, in *Geological and Geophysical Investigations of Continental Margins, Memoir*, vol. 29, edited by J. S. Watkins, L. Montadert, and P. W. Dickerson, pp. 223–237, American Association of Petroleum Geologists, Tulsa, OK.

Kato, A. et al. (2013), Imaging the source regions of normal faulting sequences induced by the 2011 M9.0 Tohoku-Oki earthquake, *Geophys. Res. Lett.*, *40*(2), 273–278, doi:10.1002/grl.50104.

King, G. C. P., R. S. Stein, and J. Lin (1994), Static stress changes and the triggering of earthquakes, *Bull. Seismol. Soc. Am.*, *84*(3), 935–953.

Klotz, J., A. Abolghasem, G. Khazaradze, B. Heinze, T. Vietor, R. Hackney, K. B. R. Maturana, J. Viramonte, and R. Perdomo (2006), Long-Term Signals in the Present-Day Deformation Field of the Central and Southern Andes and Constraints on the Viscosity of the Earth's Upper Mantle, in *The Andes: Active subduction orogeny*, edited by O. Oncken, G. Chong, G. Franz, P. Giese, H.-J. Götze, V. A. Ramos, M. R. Strecker, and P. J. Wigger, pp. 65–89, Springer, Berlin.

Kuijpers, E. P. (1980), The geologic history of the Nicoya Ophiolite Complex, Costa Rica, and its geotectonic significance, *Tectonophysics*, *68*(3–4), 233–255, doi:10.1016/0040-1951(80)90178-X.

Lange, D. et al. (2012), Aftershock seismicity of the 27 February 2010 Mw 8.8 Maule earthquake rupture zone, *Earth Planet. Sci. Lett.*, *317–318*, 413–425, doi:10.1016/j.epsl.2011.11.034.

Lavenu, A., and A. Encinas (2005), Deformación frágil de los depósitos neógenos de la cuenca de Navidad (Cordillera de la Costa, 34°S, Chile central), *Rev. Geológica Chile Andean Geol.*, *32*, 229–248, doi:10.4067/S0716-02082005000200004.

Lavenu, A., C. Marquardt, D. Comte, M. Pardo, L. Ortlieb, and T. Monfret (1999), Quaternary Extensional Deformation and Recent Vertical Motion Along the Chilean Coast (between 23° S and 47° S), in *Fourth International Symposium on Andean Geodynamics (ISAG)*, pp. 424–427, Göettingen.

Lay, T. et al. (2005), The Great Sumatra-Andaman Earthquake of 26 December 2004, *Science*, *308*(5725), 1127–1133, doi:10.1126/science.1112250.

Levret, A. (2000), Histoire et aléa sismique, in *Actes des Ve Rencontres du groupe APS*, pp. 107–118, Perpignan, France.

Li, S., M. Moreno, M. Rosenau, D. Melnick, and O. Oncken (2014), Splay fault triggering by great subduction earthquakes inferred from finite element models, *Geophys. Res. Lett.*, *41*(2), 2013GL058598, doi:10.1002/2013GL058598.

Loveless, J. P., G. D. Hoke, R. W. Allmendinger, G. González, B. L. Isacks, and D. A. Carrizo (2005), Pervasive cracking of the northern Chilean Coastal Cordillera: New evidence for forearc extension, *Geology*, *33*(12), 973–976, doi:10.1130/G22004.1.

Loveless, J. P., R. W. Allmendinger, M. E. Pritchard, J. L. Garroway, and G. Gonzalez (2009), Surface cracks record long-term seismic segmentation of the Andean margin, *Geology*, *37*(1), 23–26, doi:10.1130/G25170A.1.

Loveless, J. P., R. W. Allmendinger, M. E. Pritchard, and G. González (2010a), Normal and reverse faulting driven by the subduction zone earthquake cycle in the northern Chilean fore arc, *Tectonics*, *29*(2), TC2001–.

Loveless, J. P., M. E. Pritchard, and N. Kukowski (2010b), Testing mechanisms of subduction zone segmentation and seismogenesis with slip distributions from recent Andean earthquakes, *Tectonophysics*, *495*(1–2), 15–33, doi:10.1016/j.tecto.2009.05.008.

Malod, J. A., and B. M. Kemal (1996), The Sumatra margin: oblique subduction and lateral displacement of the accretionary prism, *Geol. Soc. Lond. Spec. Publ.*, *106*(1), 19–28, doi:10.1144/GSL.SP.1996.106.01.03.

Marquardt, C., A. Lavenu, L. Ortlieb, E. Godoy, and D. Comte (2004), Coastal neotectonics in Southern Central Andes: uplift and deformation of marine terraces in Northern Chile (27°S), *Tectonophysics*, *394*(3–4), 193–219, doi:10.1016/j.tecto.2004.07.059.

Marshall, J. S., and R. S. Anderson (1995), Quaternary uplift and seismic cycle deformation, Península de Nicoya, Costa Rica, *Geol. Soc. Am. Bull.*, *107*(4), 463–473, doi:10.1130/0016-7606(1995)107<0463:QUASCD>2.3.CO;2.

McIntosh, K., E. Silver, and T. Shipley (1993), Evidence and mechanisms for forearc extension at the accretionary Costa Rica Convergent Margin, *Tectonics*, *12*(6), 1380–1392, doi:10.1029/93TC01792.

Melnick, D., B. Bookhagen, H. P. Echtler, and M. R. Strecker (2006), Coastal deformation and great subduction earthquakes, Isla Santa María, Chile (37°S), *Geol. Soc. Am. Bull.*, *118*(11-12), 1463–1480, doi:10.1130/B25865.1.

Melnick, D., B. Bookhagen, M. R. Strecker, and H. P. Echtler (2009), Segmentation of megathrust rupture zones from fore-arc deformation patterns over hundreds to millions of years, Arauco peninsula, Chile, *J. Geophys. Res. Solid Earth*, *114*(B1), B01407, doi:10.1029/2008JB005788.

Mizoguchi, K., S. Uehara, and K. Ueta (2012), Surface Fault Ruptures and Slip Distributions of the Mw 6.6 11 April 2011 Hamadoori, Fukushima Prefecture, Northeast Japan, Earthquake, *Bull. Seismol. Soc. Am.*, *102*(5), 1949–1956, doi:10.1785/0120110308.

Moore, G. F., N. L. Bangs, A. Taira, S. Kuramoto, E. Pangborn, and H. J. Tobin (2007), Three-Dimensional Splay Fault Geometry and Implications for Tsunami Generation, *Science*, *318*(5853), 1128–1131, doi:10.1126/science.1147195.

Mosher, D. C., J. A. Austin Jr., D. Fisher, and S. P. S. Gulick (2008), Deformation of the northern Sumatra accretionary prism from high-resolution seismic reflection profiles and ROV observations, *Mar. Geol.*, *252*(3–4), 89–99, doi:10.1016/j.margeo.2008.03.014.

Nicol, A., C. Mazengarb, F. Chanier, G. Rait, C. Uruski, and L. Wallace (2007), Tectonic evolution of the active Hikurangi subduction margin, New Zealand, since the Oligocene, *Tectonics*, *26*(4), TC4002, doi:10.1029/2006TC002090.

Oishi, M., and T. Sato (2007), Moment release budget at oblique convergence margin as revealed by the 2004 Sumatra-Andaman earthquake, *Earth Planets Space*, *59*(8), 913–921.

Plafker, G. (1967), Surface faults on Montague Island associated with the 1964 Alaska earthquake, *US Geol. Surv. Prof. Pap.*, *543-G*, 42 p.

Ranero, C. R., and R. von Huene (2000), Subduction erosion along the Middle America convergent margin, *Nature*, *404*(6779), 748–752, doi:10.1038/35008046.

Rietbrock, A., I. Ryder, G. Hayes, C. Haberland, D. Comte, S. Roecker, and H. Lyon-Caen (2012), Aftershock seismicity of the 2010 Maule Mw=8.8, Chile, earthquake: Correlation between co-seismic slip models and aftershock distribution?, *Geophys. Res. Lett.*, *39*(8), L08310, doi:10.1029/2012GL051308.

Ruiz, J. A., G. P. Hayes, D. Carrizo, H. Kanamori, A. Socquet, and D. Comte (2014), Seismological analyses of the 2010 March 11, Pichilemu, Chile Mw 7.0 and Mw 6.9 coastal intraplate earthquakes, *Geophys. J. Int.*, *197*(1), 414–434, doi:10.1093/gji/ggt513.

Ryder, I., A. Rietbrock, K. Kelson, R. Bürgmann, M. Floyd, A. Socquet, C. Vigny, and D. Carrizo (2012), Large extensional aftershocks in the continental forearc triggered by the 2010 Maule earthquake, Chile, *Geophys. J. Int.*, *188*(3), 879–890, doi:10.1111/j.1365-246X.2011.05321.x.

Saffer, D. M., and H. J. Tobin (2011), Hydrogeology and Mechanics of Subduction Zone Forearcs: Fluid Flow and Pore Pressure, *Annu. Rev. Earth Planet. Sci.*, *39*(1), 157–186, doi:10.1146/annurev-earth-040610-133408.

Saillard, M., S. R. Hall, L. Audin, D. L. Farber, V. Regard, and G. Hérail (2011), Andean coastal uplift and active tectonics in southern Peru: 10Be surface exposure dating of differentially uplifted marine terrace sequences (San Juan de Marcona, ~ 15.4°S), *Geomorphology*, *128*(3–4), 178–190, doi:10.1016/j.geomorph.2011.01.004.

Scholz, C. H. (2002), *The mechanics of earthquakes and faulting*, Cambridge University Press.

Sébrier, M., J. L. Mercier, F. Mégard, G. Laubacher, and E. Carey-Gailhardis (1985), Quaternary normal and reverse faulting and the state of stress in the central Andes of south Peru, *Tectonics*, *4*(7), 739–780, doi:10.1029/TC004i007p00739.

Shiki, T., and Y. Misawa (1982), Forearc geological structure of the Japanese Islands, *Geol. Soc. Lond. Spec. Publ.*, *10*(1), 63–73, doi:10.1144/GSL.SP.1982.010.01.04.

Sibuet, J.-C. et al. (2007), 26th December 2004 great Sumatra–Andaman earthquake: Co-seismic and post-seismic motions in northern Sumatra, *Earth Planet. Sci. Lett.*, *263*(1–2), 88–103, doi:10.1016/j.epsl.2007.09.005.

Taira, A. (2001), Tectonic Evolution of the Japanese Island Arc System, *Annu. Rev. Earth Planet. Sci.*, *29*(1), 109–134.

Tassara, A. (2010), Control of forearc density structure on megathrust shear strength along the Chilean subduction zone, *Tectonophysics*, *495*(1–2), 34–47, doi:10.1016/j.tecto.2010.06.004.

Tikoff, B., T. Blenkinsop, S. C. Kruckenberg, S. Morgan, J. Newman, and S. Wojtal (2013), A perspective on the emergence of modern structural geology: Celebrating the feedbacks between historical-based and process-based approaches, *Geol. Soc. Am. Spec. Pap.*, *500*, 65–119, doi:10.1130/2013.2500(03).

Toda, S., and H. Tsutsumi (2013), Simultaneous Reactivation of Two, Subparallel, Inland Normal Faults during the Mw 6.6 11 April 2011 Iwaki Earthquake Triggered by the Mw 9.0 Tohoku-oki, Japan, Earthquake, *Bull. Seismol. Soc. Am.*, *103*(2B), 1584–1602, doi:10.1785/0120120281.

Toda, S., R. S. Stein, and J. Lin (2011), Widespread seismicity excitation throughout central Japan following the 2011 M=9.0 Tohoku earthquake and its interpretation by Coulomb stress transfer, *Geophys. Res. Lett.*, *38*, L00G03–, doi:10.1029/2011GL047834.

Wang, K. (2007), Elastic and viscoelastic models of crustal deformation in subduction earthquake cycles, in *The Seismogenic Zone of Subduction Thrust Faults*, edited by T. H. Dixon and J. C. Moore, pp. 540–575, Columbia University Press, New York, NY.

Wang, K., Y. Hu, and J. He (2012), Deformation cycles of subduction earthquakes in a viscoelastic Earth, *Nature*, *484*(7394), 327–332, doi:10.1038/nature11032.

Weller, O., D. Lange, F. Tilmann, D. Natawidjaja, A. Rietbrock, R. Collings, and L. Gregory (2012), The structure of the Sumatran Fault revealed by local seismicity, *Geophys. Res. Lett.*, *39*(1), L01306, doi:10.1029/2011GL050440.

Yamaji, A., T. Sakai, K. Arai, and Y. Okamura (2003), Unstable forearc stress in the eastern Nankai subduction zone for the last 2 million years, *Tectonophysics*, *369*(1–2), 103–120, doi:10.1016/S0040-1951(03)00212-9.

CHAPTER 2

CONSTRUCTING FOREARC ARCHITECTURE OVER MEGATHRUST SEISMIC CYCLES: GEOLOGICAL SNAPSHOTS FROM THE MAULE EARTHQUAKE REGION, CHILE*

2.1 Abstract

We present new field structural data from the Chilean Coastal Cordillera located above the northern and central parts of the interplate contact ruptured by the 2010 M_w8.8 Maule earthquake. The northern study area contains the NW-striking Pichilemu normal fault, an intraplate structure reactivated after the megathrust event by crustal earthquakes up to M_w7.0. The structural style of this region is dominated by kilometer-scale normal faults which have been active at least throughout the Quaternary. The orientations of these main faults define three structural systems: (1) NE- and (2) NW-striking margin-oblique faults, and (3) N- to NNE-striking margin-parallel faults. From north to south, these three systems vary their predominant occurrence starting with bimodal orientations of groups (1) and (2), followed by predominantly single N-NNE (3) orientations. Reverse faults coexist in time and space with the normal structures but are scarce and display variable, apparently random orientations. The shallow crustal normal faults, including the Pichilemu fault, show a persistent kinematic history probably spanning thousands of subduction seismic cycles. Though historically smaller in magnitude than the triggered normal-faults, interseismic forearc thrust events have been recorded above the rupture area prior to the Maule earthquake.

*Originally in final review as: Aron, F., J. Cembrano, F. Astudillo, R. W. Allmendinger, and G. Arancibia (Accepted), Constructing forearc architecture over megathrust seismic cycles: geological snapshots from the Maule earthquake region, Chile, *Geol. Soc. Am. Bull.* Geological Society of America.

The Quaternary reverse faults identified in our study regions may be preserving the interseismic – slow strain rate –, permanent deformation signature in the structural grain. Analogous observations along the 2011 Tohoku earthquake rupture in Japan imply that such a link between the short- and long-term deformation patterns of the forearc is not exclusive of the Maule earthquake region.

2.2 Introduction

Though better instrumented than any other great subduction earthquake along the Nazca-South America plate boundary, the 2010 M_w8.8 Maule megathrust event in central Chile struck a region with very sparse geological information. Beginning twelve days after the main event and continuing for more than thirty nine weeks, the M_w7.0 Pichilemu normal fault sequence demonstrated that at least some of the extensional structures of the forearc are seismically active, following great subduction earthquakes (Fig. 2.1) (*Arriagada et al.*, 2011; *Farías et al.*, 2011; *Ryder et al.*, 2012; *Aron et al.*, 2013; *Ruiz et al.*, 2014). A similar phenomenon was widely observed after the 2011 Tohoku earthquake (e.g., *Mizoguchi et al.*, 2012; *Fukushima et al.*, 2013; *Kato et al.*, 2013; *Kobayashi et al.*, 2013; *Toda and Tsutsumi*, 2013). Thus, in light of these observations, important questions to address are: Do normal faults like Pichilemu represent a singular phenomenon for the main structural style of this region? And, how is the subduction seismic cycle reflected in the long-term structural grain of the forearc?

In other portions of the Andean Coastal Cordillera the forearc architecture is dominated by active, kilometer-scale normal faults (e.g., *Heinze*, 2003; *Cembrano et al.*, 2007; *Allmendinger and González*, 2010). Mechanical models of the deformation field throughout the seismic cycle suggest that extensional kinematics along the outer

Figure 2.1: (a) Regional map of the 2010, Mw 8.8 Maule subduction earthquake rupture area, approximately outlined by the black oval, showing major faults with known kinematics documented by previous work (*Katz*, 1971; *Thiele and Morel*, 1981; *Gana et al.*, 1996; *Wall et al.*, 1996; *SERNAGEOMIN*, 2003; *Melnick et al.*, 2006, 2009; *Geersen et al.*, 2011). Black and gray dots are all the epicenters of upper plate earthquakes over the Coastal Cordillera, displayed with their moment magnitude and focal mechanisms for the larger events, from the Global CMT catalog between January 1, 1976 and May 31, 2013 (excluding "fixed" locations). The dates of upper plate events prior to the Maule earthquake are shown. The boxes indicate the locations of the two study regions (Fig. 2.1b and c). VP and AP stand for Valparaíso and Arauco peninsula respectively. The Santa María island referred in the text is located in the gulf between AP and the city of Concepción. (b) Map of the O'Higgins study region showing geologic units and faults as mapped on the 1 to 1-million scale Chilean Geologic map (*SERNAGEOMIN*, 2003); dots show locations visited in our study. (c) Map of the Maule study region; same features as in (b). Simplified geologic units in both of the study areas, from older to younger: Pz4ab (Silurian?-Carboniferous), metamorphic rocks; CPg (Carboniferous-Permian), intrusive rocks; PzTr4 (Paleozoic-Triassic), metamorphic rocks; Tr1m (Upper Triassic), marine and transitional strata; TrJg (Triassic-Jurassic), intrusive rocks; Jig (Lower Jurassic), intrusive rocks; J3i (Jurassic), volcanic sequences; Ks1m (Upper Cretaceous), marine-beach strata; MP1m (Upper Miocene-Pliocene), marine-beach sedimentary sequences, marine terrace deposits (Navidad Fm.); PPl1c (Pliocene-Pleistocene), continental sedimentary rocks, river deposits; PPl1m (Pliocene-Pleistocene), marine-beach sedimentary sequences, marine terrace deposits; Pl3t (Pleistocene), pyroclastic deposits; Q1 (Pleistocene-Holocene?), marine-beach sedimentary sequences, marine terrace deposits and continental river deposits; Qm (Pleistocene-Holocene?), marine-beach sedimentary sequences, marine terrace deposits; Qe (Pleistocene-Holocene), eolian dune deposits.

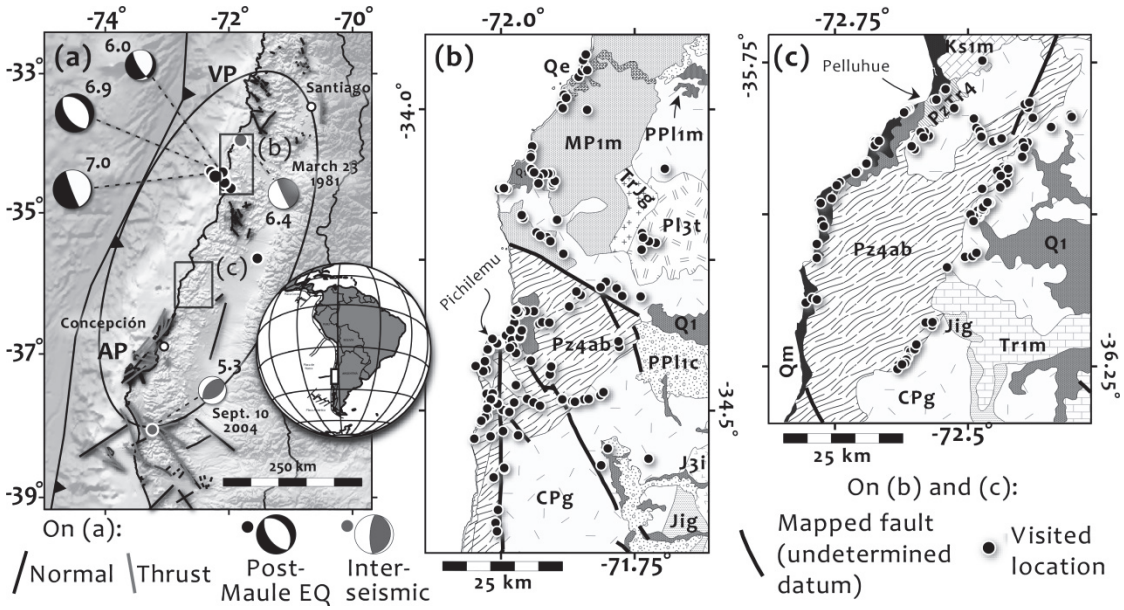
(a)
-74°
-72°
-70°
-33°
-35°
-37°
-39°
6.0
6.9
7.0
VP
Santiago
(b)
March 23 1981
6.4
(c)
Concepción
AP
5.3
Sept. 10 2004
250 km
(b)
-72.0°
-34.0°
-34.5°
Qe
MP1m
PPl1m
TrJg
Pl3t
Pichilemu
Q1
Pz4ab
PPl1c
J3i
CPg
Jig
25 km
-71.75°
(c)
-72.75°
-35.75°
-36.25°
-72.5°
Ks1m
Pelluhue
Pz4ab
Q1
Qm
Jig
Tr1m
CPg
25 km
On (a):
Normal
Thrust
Post-Maule EQ
Inter-seismic
On (b) and (c):
Mapped fault (undetermined datum)
Visited location

forearc are most likely generated by great, Maule-type subduction earthquakes (e.g., *Farías et al.*, 2011; *Aron et al.*, 2013). Similar conclusions are reached based on stress inversions of upper plate earthquakes throughout the interplate seismic cycle in the Tohoku earthquake region (e.g., *Hasegawa et al.*, 2012; *Yoshida et al.*, 2012). However, the gaps in geological information in the Coastal Cordillera overlying the Maule rupture zone limit our ability to define possible correlations between the long-term structural grain and the deformation processes associated with the megathrusts cycle.

We present new field data on the structural geology across the Coastal Cordillera of the O'Higgins and Maule regions in central Chile (Fig. 2.1). These regions overlie the northern and central portions of the Maule rupture area. As with other parts of the Coastal Cordillera and consistent with the kinematics of the large crustal aftershocks of the 2010 Maule event, Quaternary normal faults dominate the young structural architecture. We compare our geological findings with geophysical signals of forearc deformation throughout the interplate seismic cycle over the Maule earthquake region. Finally, we discuss the role of great subduction ruptures in constructing the current structural edifice of the upper plate.

2.3 Tectonic and geologic settings

The Coastal Cordillera lies at the leading edge of South America where it overlies the interplate zone of seismic coupling between the Nazca and South American Plates, as shown by the interplate aftershock distribution from the Maule earthquake and geodetically determined locking inversions (e.g., *Moreno et al.*, 2010; *Lange et al.*, 2012). The convergence rate calculated from GPS is about 63 mm/a in a direction 080° (*Kendrick et al.*, 2003). The segment of the plate boundary between 33° and 37°S

latitude trends 023°, about 15° clockwise from segments to the north and south (Fig. 2.1a). Thus the convergence direction is more than 30° from orthogonal. Despite that relatively large amount of obliquity, there is no compelling evidence of forearc slivers unlike the region farther south (e.g., *Cembrano et al.*, 1996).

The South American margin in this segment represents a transition from a tectonically eroding margin north of 33°S to an accreting margin south of 37°S. This transition is reflected in the basement geology of the Coastal Cordillera (*Kay et al.*, 2005): the north end of the segment consists of Mesozoic magmatic rocks dating from the beginning of the Andean Orogeny whereas farther south, the basement rocks are pre-Andean, upper Paleozoic metamorphic and igneous rocks (e.g., *Hervé et al.*, 2007 and references therein). Thus, the stresses related to the interplate coupling act on an extremely heterogeneous suite of metamorphic and igneous rocks that long predate the modern Andean convergent system. The eastward step of the coastline in this segment may be in part due to the increasing northward removal of material by tectonic erosion (*Kay et al.*, 2005) and/or by a southward decrease in the magnitude of shortening in this part of the Andes (*Vietor and Echtler*, 2006). As we show below, forearc normal faults are characteristic of the majority of the segment suggesting that they are unrelated to tectonic erosion (e.g., *von Huene and Ranero*, 2003) and are more likely associated with loading processes related to the megathrust seismic cycle.

The Coastal Cordillera rises to elevations of nearly 1,000 m. Most discrete morphological features are probably produced by Neogene fault scarps and, on the western side of the range, flights of marine terraces. Superimposed on these features are major cross cutting river valleys, most of which have their origins in the coastal ranges rather than the high Andes. Because this area has relatively high rainfall and significant agricultural activity, outcrops are mainly limited to road cuts, occasional

river cuts, and coastal exposures. Poor access across private land and through dense vegetation is one of the main reasons for the lack of geologic mapping in this area. At the time of the Maule earthquake, the 1:1,000,000 Chilean geologic map (*SERNAGEOMIN*, 2003) represented the most detailed geological knowledge for the majority of the forearc overlying the rupture zone (Fig.2.1).

2.4 Previous work on forearc structures

Some parts of the forearc above the rupture zone have been studied in more detail (Fig. 2.1a). The area due north of the study region shown in Fig. 2.1b (so-called the O'Higgins region) is covered by the 1:100,000 Chilean geologic map sheets San Antonio-Melipilla (*Wall et al.*, 1996) and Valparaíso-Curacaví (*Gana et al.*, 1996). The latter includes the Valparaíso Peninsula which coincides with the northern limit of the Maule rupture (VP in Fig. 2.1a). The main structures in these maps are NW- and NE-striking normal faults (e.g., Maipo, Melipilla and Puangue faults); no reverse faults are shown. *Lavenu and Cembrano* (1999) and *Lavenu and Encinas* (2005) reported Neogene-Quaternary displacements on some of these normal faults. Others displace Miocene-Pliocene beach-marine sedimentary sequences of the Navidad and La Cueva Formations (*Darwin*, 1846; *Gana et al.*, 1996; *Gutiérrez et al.*, 2013), which were deposited on top of a paleo-abrasion platform cut into Paleozoic intrusive rocks (Figs. 2.1b-c). These authors also described a puzzling coexistence of normal and reverse displacements, and tectonic inversions of the faults.

Farther south, near the center of the segment and between the O'Higgins and Maule study regions (Figs. 2.1b-c), *Thiele and Morel* (1981) showed that ~N-striking normal faults dominate the structural grain of the Coastal Cordillera (e.g., El Guindo fault system). Additionally, they found minor NW- and NE-striking normal faults, and

one major ~N-striking reverse fault. The timing of these structures is not well constrained (the maximum estimated age is Late Jurassic) but the authors reported probable Neogene-Quaternary activity of minor normal faults. They suggested that the main, N-striking faults have reactivated pre-Triassic shear zones. *Katz* (1971) also presented a map showing margin-parallel normal faults affecting the central portion of the Maule earthquake segment (north and south of Maule study region shown in Fig. 2.1c). He further suggested that the entire outer forearc region is under extension.

The southern end of the Maule earthquake rupture, including the Arauco Peninsula (AP in Fig. 2.1a), has been more extensively studied compared to the rest of the segment. Based on field and seismic reflection data, *Melnick et al.* (2006, 2009) suggested that reverse faults represent the main tectonic style in the Arauco Peninsula, in contrast to the normal-fault dominated structural grain of the Valparaíso Peninsula and the rest of the Coastal Cordillera. However, they also show coexistence of normal and reverse faults, and inversion of the structures. Many of the deeper structures shown are normal faults affecting the basement and the sedimentary cover. *Geersen et al*. (2011) described structures in the accretionary wedge offshore that may be the continuation of some upper plate thrust faults onshore. Their published seismic reflection profiles show coexistence of normal and reverse faults as well. *Lavenu and Cembrano* (1999) used mesoscopic fault-slip data measured in Quaternary rocks of the Arauco Peninsula to invert for stress tensors, showing an overall E-W extension. *Melnick et al.* (2006), working on Santa María island (see caption of Fig. 2.1a for location), described domino-style, high angle normal faults. These structures cut Late Pleistocene sedimentary rocks and generate growth strata, though they attribute the normal faulting to stretching on the crest of an anticline overlying a blind reverse fault. Some of the structures were reactivated as normal faults after the Maule earthquake with surface rupture (*Melnick et al.*, 2012). Similar to the region around the Valparaíso

Peninsula, the main structures in this area are NW- and NE-striking faults.

2.5 Surficial architectural style of the Coastal Cordillera

We spent 59 days in the field making detailed structural observations at all the locations shown in Figures 2.1b-c (O'Higgins and Maule study regions respectively), the majority of which are previously undescribed. Topographic data from ASTER digital elevation models were used to resolve kilometer-scale features in the morphology. Although fresh fault scarps corresponding to individual earthquakes are virtually nonexistent, at neotectonic time scales (10^3 – 10^6 years) (*Tikoff et al.*, 2013) the average topography, which smooths out very young climatic and tectonic activity, reflects architectural patterns that may relate to long-term deformation (*Burbank and Anderson*, 2011). Thus, we support and correlate our field data with simple DEM (30-meter resolution) analysis of the structural relief, especially in areas lacking adequate exposures.

2.5.1 Structural geology of the O'Higgins Region

2.5.1.1. Boca de Rapel-Matanzas domain

The northern limit of the O'Higgins region (Fig. 2.1b) is characterized by two nearly orthogonal fault sets striking NE and NW (Fig. 2. 2; Appendix Fig. A1). Both fault sets displace the sub-horizontal strata of the Miocene Navidad Formation and the Pliocene La Cueva Formation (*Gutiérrez et al.*, 2013), and the underlying paleo-abrasion platform that cuts the intrusive basement rocks. These fault sets also displace coastal terraces which presumably may be correlated to Pleistocene terraces found at the Arauco Peninsula farther south (*Kaizuka et al.*, 1973; *Melnick et al.*, 2009). NE-striking normal faults are well exposed in the coastal cliffs and have a general strike

Figure 2.2: Structural map of O'Higgins study region showing the faults mapped in our study. The numbered white dots are key field localities described in the manuscript (Table 2.1). Faults of undetermined kinematics were observed in the field but they do not show compelling indicators of the sense of slip. Lineaments from the Chilean geologic map are labeled 1:1 million (*SERNAGEOMIN*, 2003). Lower hemisphere stereonets display orientation of the main faults, keyed by numbers to the map; letters indicate more than one structure at a numbered site. Faults are grouped according to the main structural domains or sub-regions addressed in Section 2.5.1 of the manuscript. The arrows indicate movement of the hanging wall. The locations of the cross sections AA' and BB' (Figs. 2.6, 2.7) are also shown. Relief from ASTER GDEM, a product of the Japanese Ministry of Economy, Trade, and Industry (METI) and NASA.

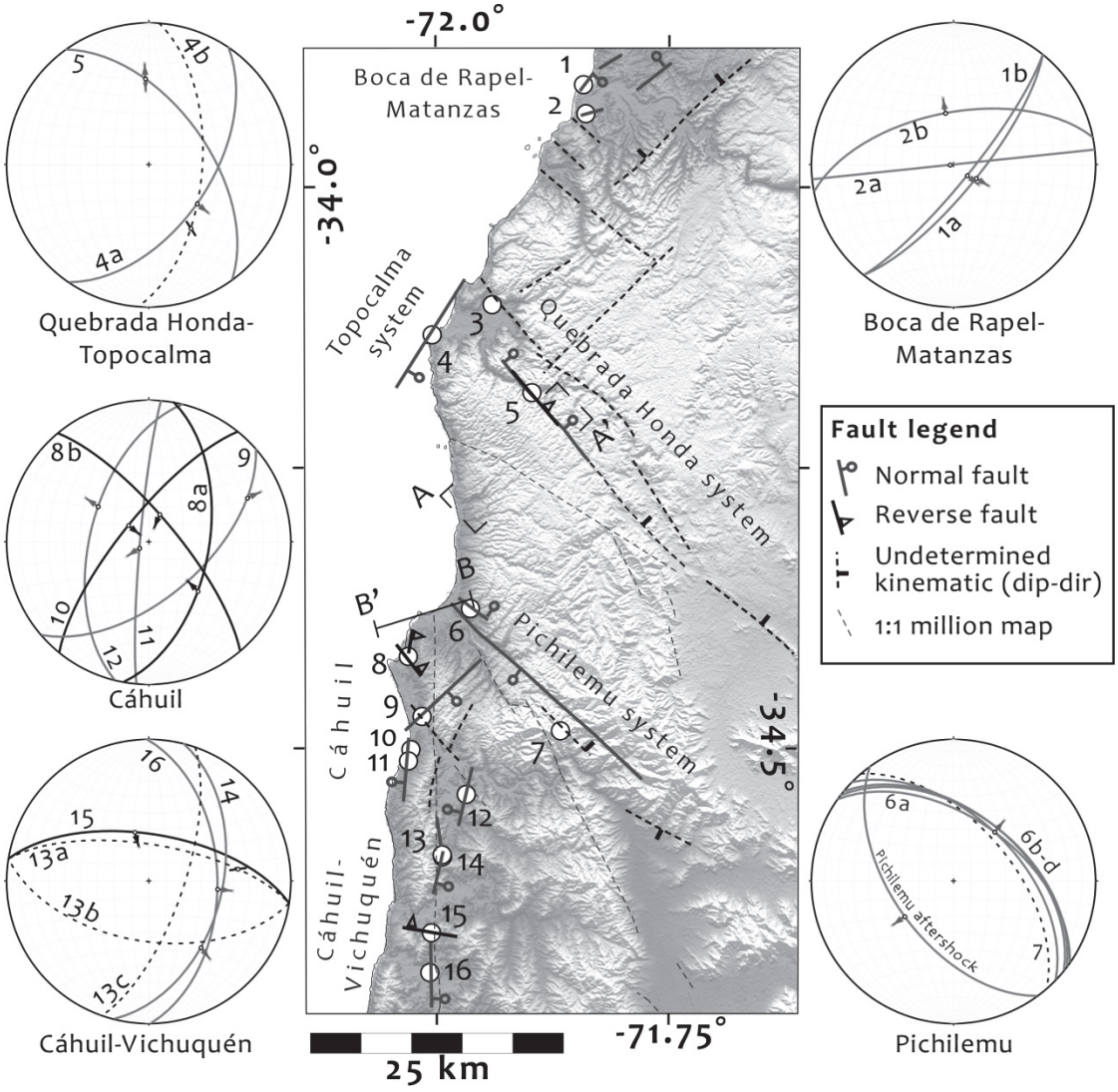
-72.0°
-34.0°
-34.5°
-71.75°
Boca de Rapel-Matanzas
Topocalma system
Quebrada Honda system
Pichilemu system
Cáhuil
Cáhuil-Vichuquén
A
A'
B
B'
1
2
3
4
5
6
7
8
9
10
11
12
13
14
15
16
25 km
Fault legend
Normal fault
Reverse fault
Undetermined kinematic (dip-dir)
1:1 million map
Quebrada Honda-Topocalma
Boca de Rapel-Matanzas
Cáhuil
Cáhuil-Vichuquén
Pichilemu
Pichilemu aftershock

Table 2.1: Fault field data O'Higgins study region

Site	Location		Strike/dip, rake [RHR] (degrees)	Motion	Vertical offset (m)	Dip slip (m)	Damage width (m)	Figures	Observations
	Long (°W)	Lat (°S)							
Boca de Rapel-Matanzas									
1a	71.84°	33.91°	039/75, 88	normal	11	N.D.*	N.D.	2.3, A1a-b	Secondary structure, main fault in outcrop
1b	71.84°	33.91°	039/80, 90	normal	0.2	N.D.	N.D.	A1c	Subsidiary minor fault
2a	71.84°	33.93°	084/90, 92	normal	1.5	N.D.	N.D.	A2a	Secondary faults
2b	71.84°	33.93°	259/60, 91	normal	>2	N.D.	N.D.	A2b	Secondary fault
Topocalma and Quebrada Honda Systems									
3	71.94°	34.10°	N.A.†	N.A.	N.D.	N.D.	N.D.	A3	Fault breccia probably intersection of main faults
4a	72.00°	34.13°	034/54, 93	normal	N.D.	N.D.	N.D.	2.4, A4-5	Main relief-controller fault
4b	72.00°	34.13°	004/59, 124	undet.	N.D.	N.D.	N.D.	N.F.§	Secondary structure
5	71.90°	34.18°	324/56, 55	normal	N.D.	N.D.	5.8	2.5, 2.6, 2.7 A6	Main relief-controller fault. Probable invertion
Pichilemu System									
6a	71.96°	34.38°	305/53, 93	normal	5.2	N.D.	N.D.	2.7, A9a-b	Secondary structure, main fault in outcrop
6b	71.96°	34.38°	314/53	normal	0.36	0.45	N.D.	2.11, A9a-b	Subsidiary minor fault

Table 2.1. Cont.

6c	71.96°	34.38°	307/50	normal	0.23	0.3	N.D.	2.11, A9a-b	Subsidiary minor fault
6d	71.96°	34.38°	309/50	normal	N.D.	0.75	N.D.	A9c	Subsidiary minor fault
7	71.87°	34.48°	319/57	undet.	N.D.	N.D.	0.43	N.F.	Secondary structure
Cáhuil									
8a	72.03°	34.42°	010/55, 112	reverse	N.D.	N.D.	N.D.	N.F.	Subsidiary minor fault
8b	72.03°	34.42°	320/75, 82	reverse	>2	N.D.	N.D.	A10	Secondary fault
9	72.02°	34.47°	049/58, 30	normal	N.D.	N.D.	1.7	2.8, A11	Main relief-controller fault
10	72.03°	34.50°	219/75, 90	reverse	N.D.	0.21	N.D.	A12	Minor fault
11	72.03°	34.51°	185/85, 86	normal	N.D.	N.D.	0.1-0.8	A13	Main-secondary fault
12	71.97°	34.54°	194/56, 102	normal	N.D.	N.D.	2.3	N.F.	Main-secondary fault
Cahuil-Vichuquén									
13a	71.99°	34.59°	279/69, 140	undet.	N.D.	N.D.	N.D.	N.F.	Secondary structure
13b	71.99°	34.59°	099/55	undet.	N.D.	N.D.	0.8	N.F.	Secondary structure
13c	71.99°	34.59°	019/70	undet.	N.D.	N.D.	N.D.	N.F.	Secondary structure
14	71.99°	34.60°	014/47, 118	normal	N.D.	N.D.	N.D.	A14	Main-secondary fault
15	72.01°	34.66°	279/63, 78	reverse	1.8	N.D.	N.D.	N.F.	Secondary structure
16	72.01°	34.70°	359/50, 95	normal	N.D.	N.D.	N.D.	N.F.	Main-secondary fault

*N.D. = not determined.
†N.A. = not applicable.
§N.F. = no figure provided.

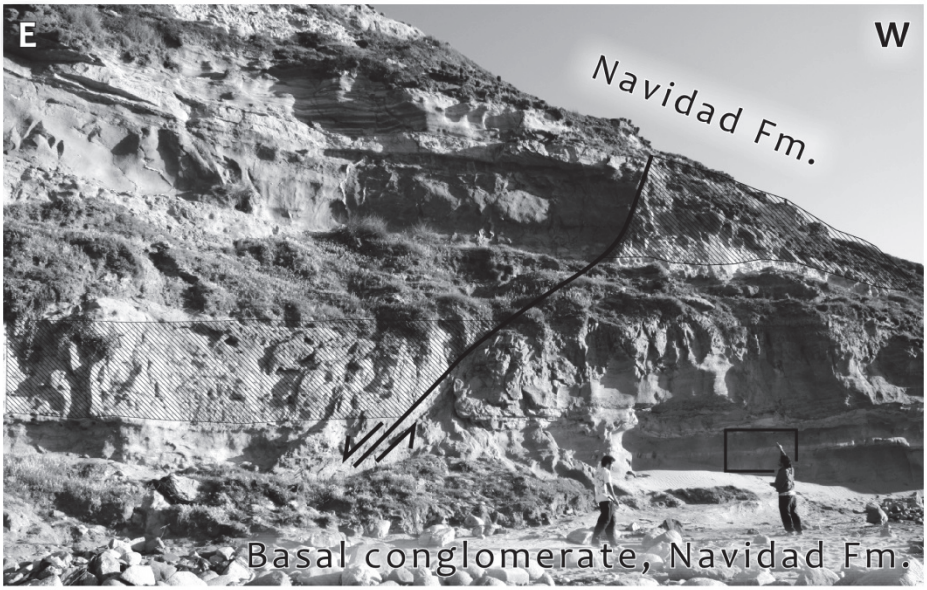

Figure 2.3: Photo of coastal cliff exposure at site 1 displaying a NE-trending normal fault cutting the Navidad Fm. (Fig. 2.2; Fault 1a in Table 2.1). Diagonal hatches emphasize a layer displaced by the fault. Refer to Appendix Fig. A1 for a color version of this figure. The little box in the footwall shows the location of Fig. A1c.

and dip of N39°E/75°SE. Some exhibit throws of ~10 m (Fig. 2.3; site 1 in Fig. 2.2, fault 1a Table 2.1). Inland, more NE-striking structures of this system interrupt the landscape as can be seen in the texture of the topography (Fig. 2.2). We found a pair of adjacent minor, almost vertical ENE-normal faults with throws less than 5 m, which deform and displace the Navidad Formation (site 2 in Fig. 2.2 and Table 2.1; Appendix Fig. A2). The NW-striking faults progressively offset the sedimentary strata and the underlying abrasion platform, and generate a flight of morphological, marine terraces towards the south (Appendix Fig. A1a). We could not find good outcrops of the NW-striking fault planes in the Boca de Rapel-Matanzas domain.

2.5.1.2 Topocalma and Quebrada Honda systems

Farther south, the two orthogonal fault sets mentioned above are better developed (sites 3-5 in Fig. 2.2 and Table 2.1). At the coast, one of the major NE-striking normal faults produces hundreds of meters of separation of the erosional contact between the Paleozoic intrusive rocks and the Navidad-La Cueva Fms. (Fig. 2.4; site 4 in Fig. 2.2, fault 4a in Table 2.1). The profile along the beach cliff shows the erosional contact tilted towards the fault. Also, the dip of the marine terrace surface in the hanging wall is controlled by the rollover into the structure (Fig. 2.4 and Appendix Figs. A4-5).

In a river canyon at site 5 in Fig. 2.2, an outcrop of a NW-striking, steeply NE-dipping fault displays a thick damage zone (Fig. 2.5) with oblique sense of slip as shown by the 55° rake of the slickenlines (site 5 in Table 2.1; refer also to Appendix figures). On a regional scale, the Quebrada Honda fault has a continuous, generally SW-side-up scarp along its trace (Fig. 2.2), offsetting the base of the Miocene-Pliocene Navidad Fm. (Fig. 2.6). However, the fresh, steep topographic scarp along the creek faces to the southwest, suggesting that the most recent displacements on the fault have uplifted the northeastern block by approximately 50 m (Fig. 2.6).

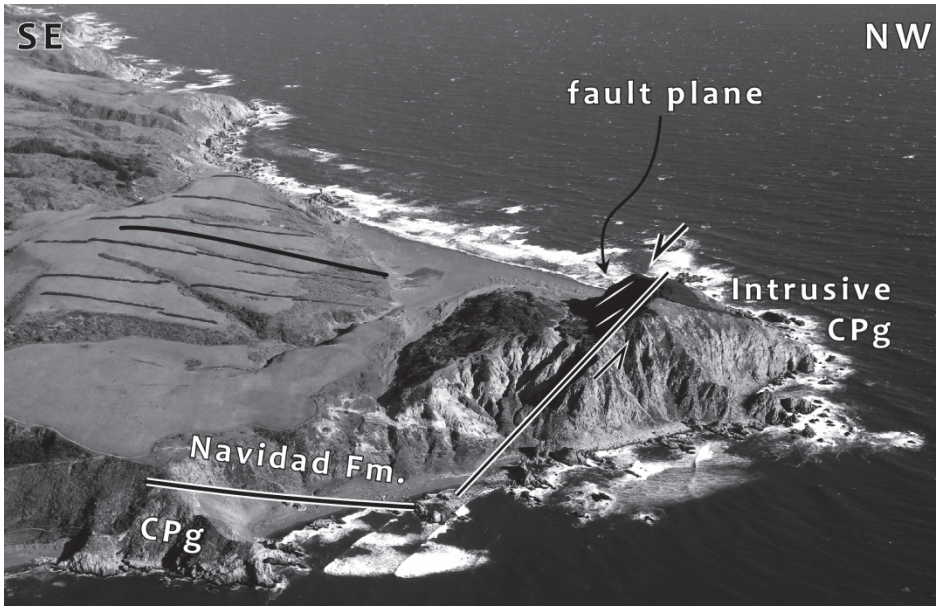

Figure 2.4: Aerial view looking SW of the Topocalma fault described at site 4 (Fig. 2.2; Table 2.1). Note the rollover into the fault plane denoted by the topography and the strata of the Navidad Fm. Black line on the center-left side of the picture outlines the slope of the surface and white-black line at the bottom- left corresponds to the erosional contact between the sedimentary strata and the intrusive basement. The top of the hill in the coastal cliff behind the fault is at about 100 m of elevation. *Photo by Horacio Parragué*. Refer to Appendix Fig. A4b for a color version of this picture.

Figure 2.5: River valley outcrop at site 5 (Fig. 2.2, Table 2.1) showing the fault plane of the Quebrada Honda fault with a thick damage zone. See also Appendix Fig. A6.

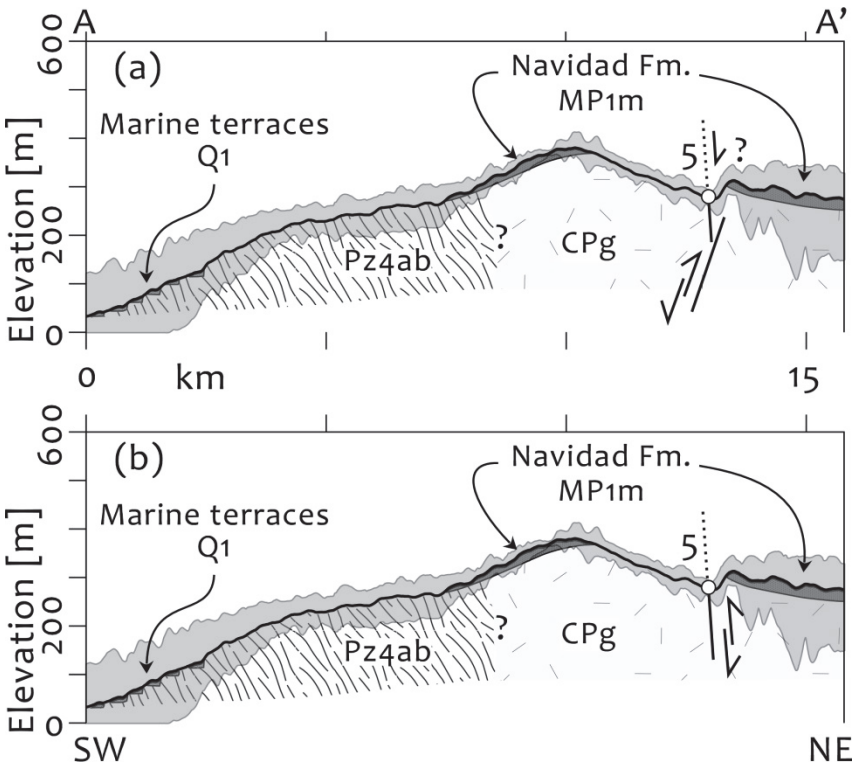

Figure 2.6: Section A-A' (location in Fig. 2.2) showing two possible interpretations for the geometry and kinematics history of the Quebrada Honda fault at site 5 (Figs. 2.2, 2.5; Table 2.1). The thick black line represents the average topography of the swath profile and gray shaded areas bound the maximum and minimum altitudes along the profile. Alternative (a): site 5 structure is interpreted as a subsidiary, antithetic structure of a major normal fault that dips SW (*Farías et al.*, 2011). The offset of the base of the Navidad Fm. indicates previous thrust displacements of the main fault. (b) Our preferred interpretation in which the site 5 fault represents the geometry of the main structure that runs along the river valley (Fig. 2.2). The offset of the Navidad Fm. and the topographic altitude of the footwall imply that the structure has moved predominantly as a normal fault over geologic time. However, the steep morphologic scarp at the creek in front of site 5 may be generated by a recent tectonic inversion of the structure.

Farías et al. (2011) interpreted that this step in the topography was controlled by a NW-striking, SW-dipping normal fault. Our field evidence suggests at least two possible interpretations of the Quebrada Honda fault system. The fault outcrop at site 5 may be an antithetic, subsidiary fault affecting the hanging wall of the main structure as proposed by *Farías et al.* (2011) (Fig. 2.6a). However, the SW-side-up offset of the base of the Navidad Fm. indicates previous thrust kinematics of Neogene age. Alternatively, if the fault outcrop at site 5 represents the main structure, then the most recent activity of the Quebrada Honda system would be controlled by a steep reverse fault that dips northeast and generates the fresh scarp at the creek (Fig. 2.6b). Yet, as evidenced by the displacement of the Navidad Fm. and the main topographic relief change between the two blocks, the structure has moved predominantly as a normal fault in the past. Both interpretations imply a tectonic inversion of the fault, but we think that the latter is the most straight-forward interpretation (Fig. 2.6b).

Finally, near the coast at site 3, along an structure of undetermined kinematics parallel to the Quebrada Honda fault system (see Fig. 2.2 and Table 2.1), we found an outcrop of a mineralized fault breccia with clasts that range between a few cm and 4 m in diameter. This breccia shows signs of alteration and mineralization processes that may have occurred at deeper levels of the structure, thus suggesting a protracted, long-lived history of deformation. Though partially covered by the vegetation, the width of the damage zone appears to exceed 20 m (Appendix Fig. A3). We speculate, based on nothing more than topographic lineaments, that it may mark the intersection of two faults that strike NW and NE.

2.5.1.3 Pichilemu fault system

The Pichilemu fault, which produced the largest continental earthquakes triggered by the Maule event, is parallel to the Quebrada Honda fault (Fig. 2.2). The aftershocks

of the Pichilemu events show that the rupture plane has a strike of 324°-335° and a dip of 40°-53°SW, and extends down almost to the plate interface (*Farías et al.*, 2011; *Ryder et al.*, 2012), which lies approximately at 33 km depth at the epicentral location (*Hayes et al.*, 2012). Maximum surface displacements measured by InSAR and GPS reached about 0.6 m of vertical offset for the main event, and finite slip invertions estimate maximum normal-fault displacements of about 3 m (2.4 m along the vertical component) at 10-11 km depth, and probably a complex rupture process involving a main fault and a subsidiary synthetic structure (*Ryder et al.*, 2012; *Ruiz et al.*, 2014). On the surface, the aftershocks of the Pichilemu earthquake correlate spatially with a 321°, SW-dipping normal fault that nearly coincides with one of the structures shown in the 1:1 million Chilean geologic map (SERNAGEOMIN, 2003) (Figs. 2.1-2.2). The footwall has been uplifted to an altitude of about 550 m and generates a NW-SE-trending ridge which is bounded along the southwestern side by the fault trace (Fig. 2.2). The altitude of the hanging wall gently increases, parallel to the direction of the fault trace, from 0 m at the coastline in front of the structure to a maximum of nearly 300 m at 25 km inland, with a general slope angle of 0.7°. Instead, the footwall shows a more abrupt profile moving away from coast, reaching its maximum altitudes just 8 km inland with an approximate fault-parallel slope angle of 3.9°. This configuration also produces variations in the vertical separation of the two blocks of the structure. Across the section of the fault around site 7 in Figure 2.2 the maximum vertical separation – determined from the highest altitudes at each block – is approximately 138 m, whereas closer to the coast, across a section near site 6, is 410 m. Although we cannot determine the exact origin of this relief, some possible explanations (or a combination of them) are: (a) an overall long-term uplift of the Coastal Cordillera and marine erosion affecting the two blocks of the structure but penetrating farther inland over the relatively depressed hanging wall, (b) NW tilting of the hanging wall block

towards the ocean produced by rotation about the pole of the fault or (c), long-term variation of displacement along the trace of the structure.

Along the coast, the footwall ridge of the Pichilemu fault displays a flight of at least 3 distinct paleo-marine abrasion platforms cutting across the Mid-Upper Paleozoic metamorphic complex, with a thin cover of Pleistocene-Holocene(?) marine-beach strata (Fig. 2.7 and Appendix Figs. A7). The platforms currently stand at 32, 45 and 67 m elevation and demonstrate repeated activity of the Pichilemu fault during the Quaternary. In contrast, the hanging wall has a single marine terrace which displays a gentle rollover into the normal fault (Figs. 2.7 and Appendix Fig. A8). No outcrops of the main fault were found and our field observations agree with published reports that there was no surface breakage associated with the 2010 Pichilemu earthquakes (*Arriagada et al.*, 2011; *Farías et al.*, 2011). However, the geological relations presented here show that the Pichilemu fault has repeatedly broken the surface in the past and has moved as a normal fault.

Near the trace of the Pichilemu fault zone and on both sides of it, we found antithetic normal faults subsidiary to the main structure (sites 6 and 7 in Fig. 2.2 and Table 2.1). In the footwall, normal faults cut both the Pleistocene-Holocene(?) strata and the underlying abrasion platform located at 45 m. a. s. l., with throws up to 5 m (6a-d in Fig. 2.2 and Table 2.1; see also Fig. 2.7 and Appendix Fig. A9). At site 7, the structure cuts the metamorphic basement but no clear kinematic indicators were observed at the outcrop. Both the spatial distribution with respect to the main fault and the kinematics exhibited by the faults at site 6 suggest that the antithetic faults belong to the Pichilemu fault system.

2.5.1.4 Cáhuil structural domain

Unlike the regions father north, the Cáhuil segment displays more compelling

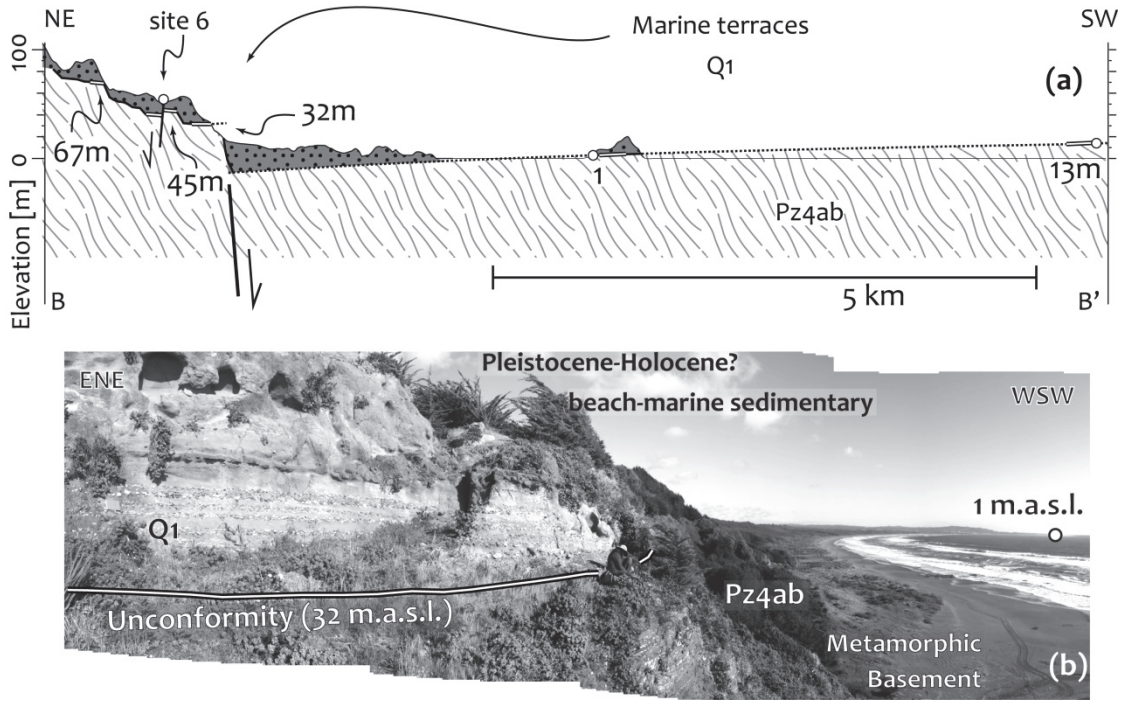

Figure 2.7: (a) Section B-B' (location in Fig. 2.2) across the Pichilemu fault showing the 3 distinct marine paleo-abrasion platforms and terraces developed in the footwall at, 32, 45, 67 meters above present sea level. The hanging wall has a single platform developed which shows a gentle rollover into the normal fault (13 to 1 m. a. s. l.). Refer to Appendix Figs. A7-8 for more morphologic and stratigraphic evidence of young deformation due to the Pichilemu fault captured on both sides of the structure. (b) Photo of sub-horizontal erosional contact (paleo-abrasion platform) between the Paleozoic metamorphic basement and the Quaternary paleo-beach deposits in the footwall of the Pichilemu fault at 32 m. a. s. l. The picture was taken from the lowest terrace in the footwall shown in the cross section (a), looking towards the hanging wall, where the unconformity lies at 1 m. a. s. l. at the end point of the beach.

evidence of horizontal shortening (site 8 in Fig. 2.2 and Table 2.1). Near the coast, a thrust fault with ramp-and-flat geometry places metamorphic basement on top of the Pleistocene-Holocene(?) beach strata (Appendix Fig. A10). The main structure at the outcrop strikes NW (8b in Table 2.1) and offsets the paleo-abrasion platform more than 2 m. In the footwall of the fault we identified a colluvial wedge from the eroded scarp, with centimeter- to decimeter-scale, angular clasts of metamorphic basement in a sandy matrix. The wedge interfingers with sand lenses of the Pleistocene-Holocene(?) beach-sedimentary unit south of the structure. More examples of minor young reverse faults offsetting the beach strata by tens of centimeters can be observed at site 10 (Table 2.1).

Overall, the Cáhuil domain shows a transition in the architectural pattern from mainly margin-oblique normal faults, striking both NW and NE, to nearly margin-parallel, ~NS-trending structures (sites 9, 11-12 in Fig. 2.2 and Table 2.1). The normal fault found at the quarry of site 9 is parallel to the NE-striking Topocalma fault (section 2.5.1.2) and affects the Paleozoic intrusive unit (Fig. 2.8). The curvature of the topographic surface in the hanging wall of this fault suggest a roll over anticline, similarly to what was observed at the Topocalma beach, but exposures are not sufficient to confirm this interpretation (compare Figs. 2.4 and 2.8a). At sites 11 and 12 ~NS-striking faults cut the metamorphic basement and the gouge exhibits a sigmoidal fabric that we use as a kinematic indicator of normal faulting (Appendix Fig. A13).

2.5.1.5 Cáhuil-Vichuquén domain

One of the most prominent geomorphic features in the Cáhuil-Vichuquén domain is a ~NS-trending ridge, which runs parallel and near to the coast (Fig. 2.2). The Cáhuil-Vichuquén ridge reaches maximum elevation and width of about 380 m and 7

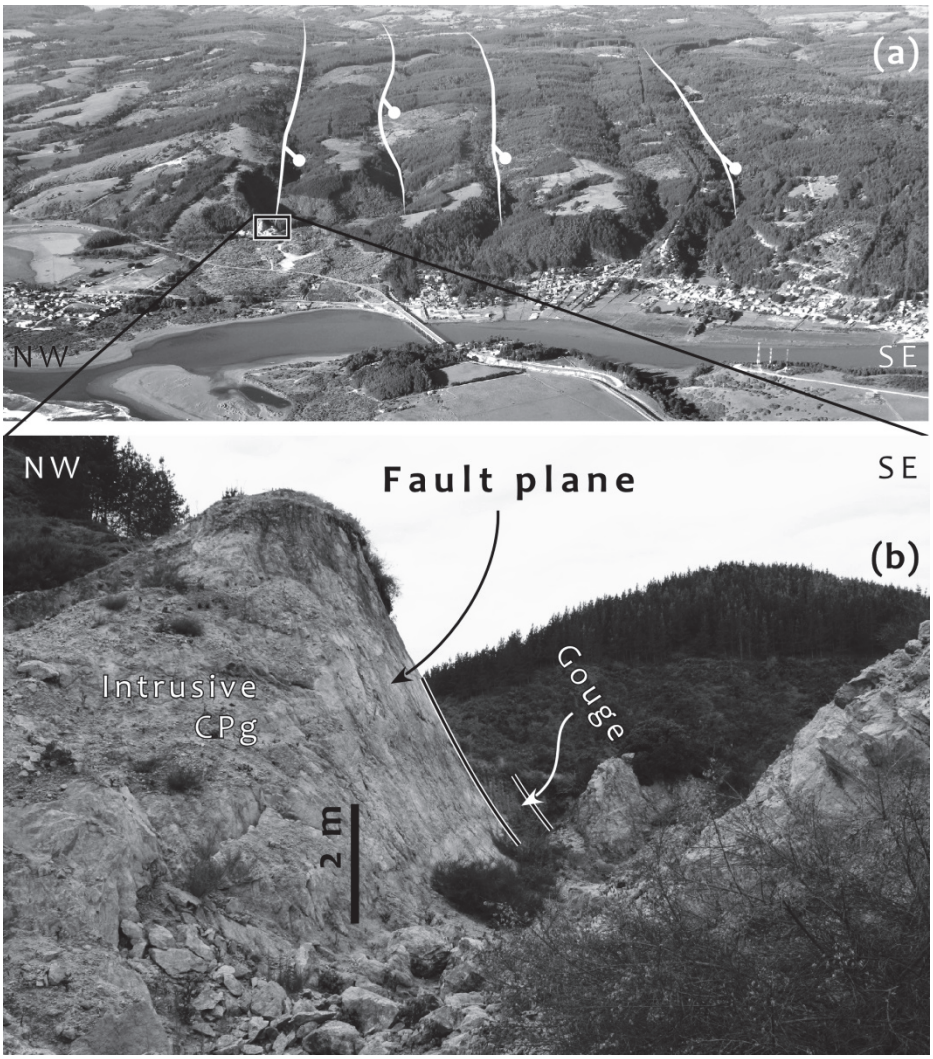

Figure 2.8: (a) Aerial view looking NE to a set of parallel, possibly domino-style major normal faults that affect the Cáhuil region in and around site 9 (Fig. 2.2; Table 2.1). *Photo by Horacio Parragué*. The little box shows the location of the picture below. (b) Outcrop view in a quarry near Cáhuil town of the major normal fault on the left of the aerial picture shown in (a). Refer to Appendix Fig. A11 for a color version.

km, respectively. A flight of marine terraces on the western flank records the Quaternary uplift. The eastern flank has a single, steep scarp that separates the ridge from an intermontane basin farther east (Fig. 2.2). Two major fault sets affect the intrusive and metamorphic basement as well as the overlying cover: a ~NS-striking, E-dipping fault parallel to the ridge, and mainly EW-striking faults dipping both N and S (sites 13-16 in Fig. 2.2 and Table 2.1; refer also to Appendix figures). The EW structures appear to have reverse displacement (site 15) whereas the NS faults show normal offset (sites 14 and 16) and may be the prolongation of the NS-system in the Cáhuil segment farther north (Section 2.5.1.4).

The ridge constitutes the uplifted footwall block of an asymmetric half-graben, formed by a normal fault along its eastern flank. The fault coincides with a Paleozoic-Mesozoic shear zone that dips to the east and bounds the scarp (e.g., *Lavenu and Encinas*, 2005; *Richter et al.*, 2007; *Willner et al.*, 2009). This shear zone has had both a brittle and a ductile protracted history and coincides with the contact between early Paleozoic metamorphic basement in the footwall and a late Paleozoic intrusive in the hanging wall (Fig. 2.1), a geometry also described by *Thiele and Morel* (1981) farther south.

2.5.2 Structural geology of the Maule Region

Compared to the O'Higgins region, the Maule region (Fig. 2.1c) has much more limited bedrock exposure and pre-existing study. The structural grain here is dominated by sharp and relatively straight fault line scarps which, we will show below, are best interpreted to mark normal fault-bounded half grabens. The main geomorphic feature of this region is a NNE-trending, margin-parallel asymmetric ridge, here named the Maule Ridge, that separates coastal and intermontane environments similar to, but much wider than, the Cáhuil-Vichuquén domain (Figs.

2.2, 2.9). The ridge is bounded to the west by a stepped morphology formed by marine terraces and on the east by a steep scarp. The average altitude of the ridge is about 500 m, with a maximum of almost 800 m (Figs. 2.9, 2.10). This ridge forms the backbone of the Coastal Cordillera over the center of the Maule earthquake rupture area.

2.5.2.1 Western flank

The western flank of the Maule ridge slopes gently westward, shaped by the formation of marine terraces and controlled by long-term uplift (Figs. 2.9, 2.10), which is likely caused by activity of the Maule fault system (see Section 2.5.2.2). As in the Cáhuil-Vichuquén region, the coastal terraces consist of Pleistocene-Holocene(?) paleo-beach sequences of units Q1 and Qm. Most fault outcrops along the western flank contain no reliable slip indicators (sites 17-19 in Fig. 2.9 and Table 2.2) but, along the beach, two conjugate NW-striking reverse faults offset the erosional contact between the Paleozoic metamorphic basement and the Q1 and Qm beach-marine sequences (sites 20-21 in Fig. 2.9 and Table 2.2). Angular, virtually untransported rubble sourced from the hanging wall now lies in the footwall and interfingers with deposits of both Quaternary units (Fig. 2.11). At site 20 the measured vertical fault offset is 2.6 m and at site 21 the displacement magnitude is unclear (Appendix Figs. A15-16).

2.5.2.2 Maule fault system

The central and eastern parts of the northern Maule ridge are affected by two sets of structures: one transverse to the main trend of the structural relief, with margin-oblique faults striking NE to ENE (sites 22-24, 27 in Figs. 2.9-2.10a and Table 2.2) and another striking NNE to NE, parallel to the steep eastern scarp (sites 25-26 in Fig. 2.9 and Table 2.2).

The average topography across the first set (sites 22-24, Fig. 2.10a) delineates two

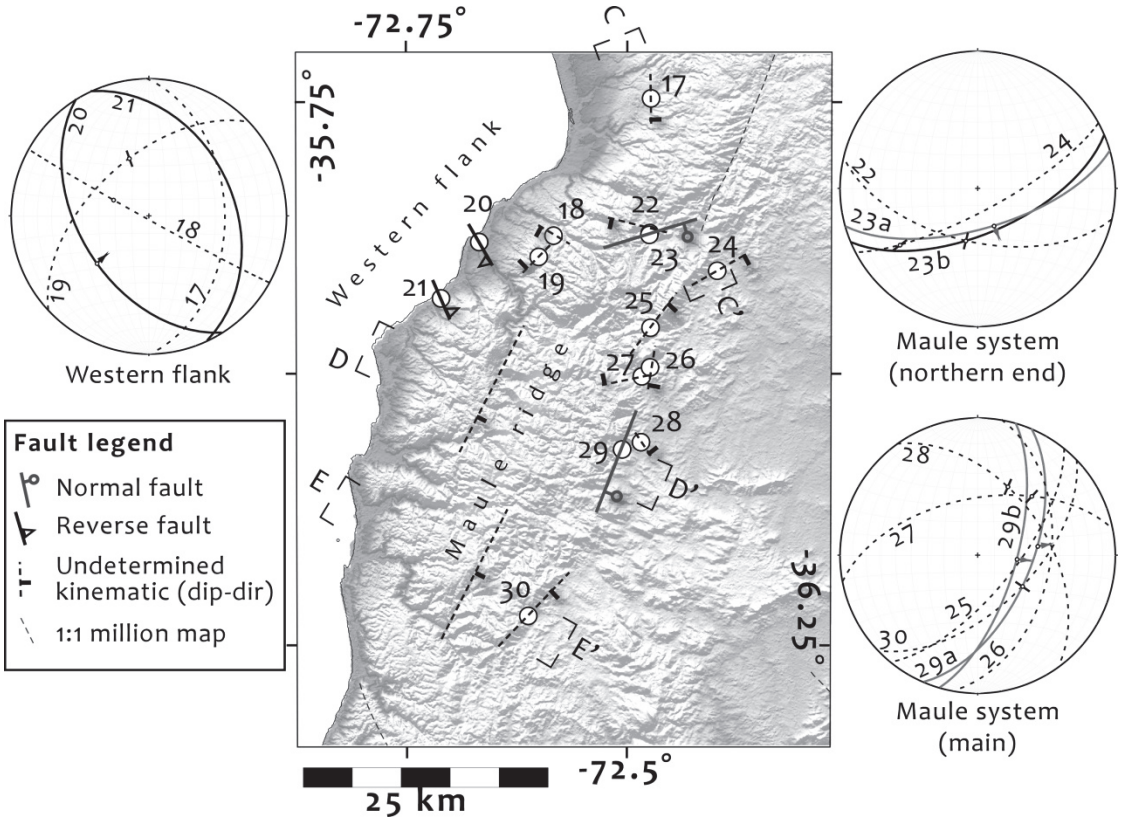

Figure 2.9: Structural map of Maule study region showing the newly mapped faults. Ornamentation as in Figure 2.2. See Section 2.5.2 for discussion. The location of the cross sections C-C', D-D' and E-E' of Fig. 2.10 are also shown.

Table 2.2: Fault field data Maule study region

Site	Location		Strike/dip, rake [RHR]	Motion	Vertical offset	Dip slip	Damage width	Figures	Observations
	Long (°W)	Lat (°S)	(degrees)		(m)	(m)	(m)		
West flank									
17	72.47°	35.75°	359/44	undet.	N.D.	N.D.	1.1	2.10a	Secondary structure
18	72.58°	35.87°	119/88, 113	undet.	N.D.	N.D.	0.28	N.F.	Secondary structure
19	72.60°	35.89°	227/56, 104	undet.	N.D.	N.D.	0.07	N.F.	Secondary structure
20	72.67°	35.88°	148/48, 83	reverse	2.6	N.D.	0.42	2.11, A15	Secondary fault
21	72.71°	35.93°	335/38	reverse	N.D.	N.D.	0.31	A16	Secondary fault
Maule fault system									
22	72.47°	35.87°	103/58, 90	undet.	N.D.	N.D.	0.9	2.10a, A17	Main structure
23a	72.47°	35.87°	074/66, 87	normal	N.D.	N.D.	7.8	2.10a, 2.12, 2.17 A18-21	Main relief-controller structure
23b	72.47°	35.87°	067/63	reverse	0.13	N.D.	N.D.	N.F.	Subsidiary minor fault
24	72.40°	35.91°	062/76, 148	undet.	N.D.	N.D.	0.86	2.10a	Secondary structure
25	72.47°	35.96°	039/68	undet.	N.D.	N.D.	0.39	N.F.	Secondary structure
26	72.47°	35.99°	010/46	undet.	N.D.	N.D.	N.D.	N.F.	Secondary structure
27	72.48°	36.00°	259/56, 127	undet.	N.D.	N.D.	N.D.	N.F.	Secondary structure
28	72.48°	36.06°	324/49, 69	undet.	N.D.	N.D.	N.D.	N.F.	Subsidiary minor fault
29a	72.51°	36.07°	023/58, 72	normal	N.D.	N.D.	2.8	2.10b, A22-23	Main relief-controller
29b	72.51°	36.07°	016/67, 86	normal	N.D.	N.D.	N.D.	N.F.	Secondary fault
30	72.61°	36.22°	046/58, 84	undet.	N.D.	N.D.	0.16	2.10c	Secondary structure

Note: Same footnotes as in Table 2.1.

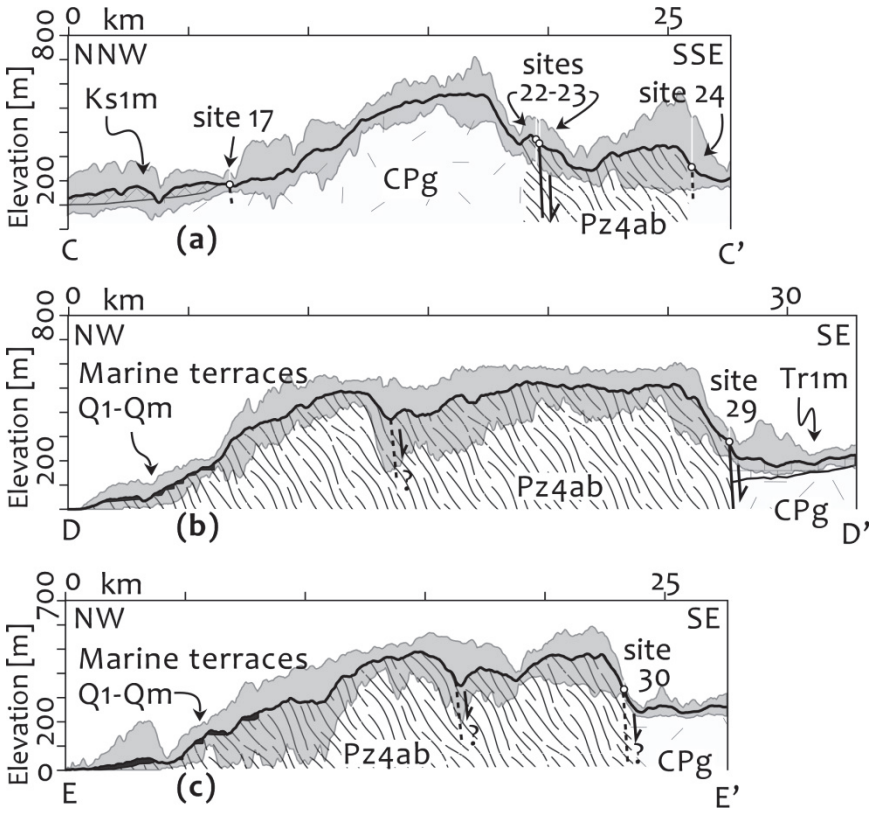

Figure 2.10: Sections C-C', D-D' and E-E' (location in Fig. 2.9) across the Maule ridge show, from north to south, the main features in the structural relief of this region. The thick black line represents the average topography of the swath profile and gray shaded areas bound the maximum and minimum altitudes along the profile.

subparallel asymmetric ridges with steep SE-facing flanks and gentle slope towards the northwest. Here, the structures are oblique to the main margin-parallel fault system resembling a fault transfer zone configuration (Fig. 2.9). At its northern end the Maule Ridge is comprised of a dominant and a subsidiary ridge farther east, both with a NE-striking, SE-dipping along their eastern margins (sites 22, 23 and 24) (Figs. 2.9, 2.10a and 2.12). We were not able to find outcrops along the prominent NNE-striking topographic lineament between sites 23 and 24. However, just to the south (site 25), an E-dipping fault sub-parallel to the main ridge separates metamorphic rocks in the footwall from intrusive rocks in the hanging wall (Figs. 2.1c and 2.9).

Farther south (sites 28-30, Figs. 2.9, 2.10b-c; Table 2.2), a major structure we call the Maule fault system coincides with a west-side-up step in the average topography of about 300 m; the crest of the ridge shows a southward narrowing plateau slightly tilted to the west (Figs. 2.9, 2.10b-c). The narrowing of the ridge occurs as it approaches the coast and its western flank is modified by marine terraces. At the base of the scarp at site 29, a pair of NNE-striking, E-dipping faults cut the metamorphic basement and deflects the fabric towards the fault planes, indicating a normal sense of movement (Table 2.2 and Appendix Figs. A22-23). At site 30, a NE-striking, E-dipping fault occurs near the base of the scarp but lacks compelling kinematic indicators. We interpret the structures at both sites 29 and 30 as part of a major normal fault zone, responsible for constructing the relief of the ridge. The Maule fault system follows the contact between the mid-Paleozoic metamorphic basement units in the footwall and both upper Paleozoic intrusive and lower Mesozoic sedimentary units in the hanging wall (Figs. 2.1c and 2.10b-c). At site 28 in the hanging wall, a NW-trending, SE-dipping fault cuts the intrusive unit; its age, kinematics, and relation to the Maule fault system are unclear (Table 2.2).

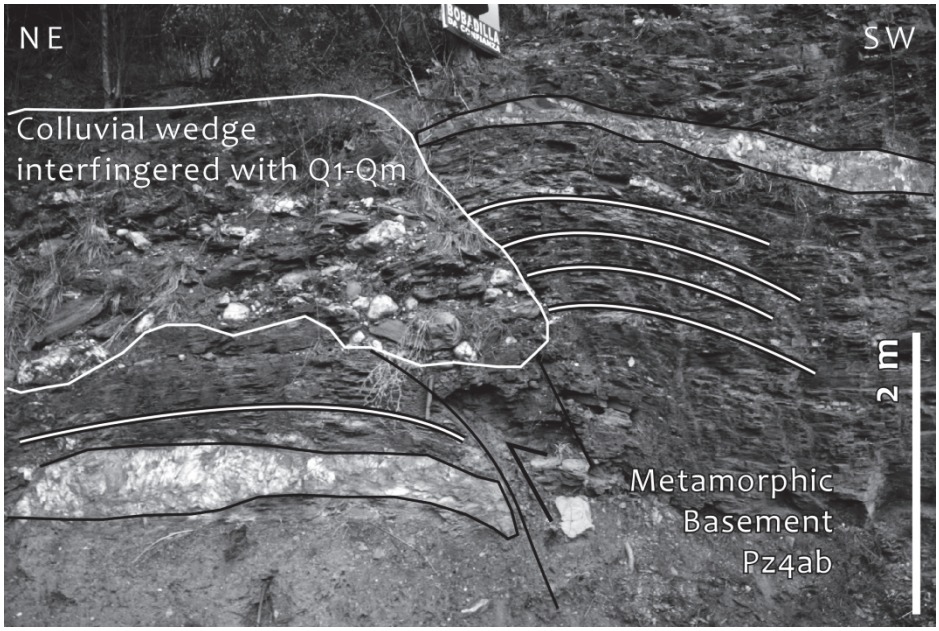

Figure 2.11: Photo of metamorphic basement thrust on top of Pleistocene-Holocene? sedimentary, paleo-beach deposits (site 20, Fig.2.9; Table 2.2). The white marker emphasizes a quartz vein in the metamorphic unit displaced by the fault. Just to the left of the photo, the colluvial wedge generated at the base of the scarp interfingers with Quaternary paleo-beach sedimentary rocks, which lie sub-horizontally on an abrasion platform cut on metamorphic basement rocks. The fault contact at the base of the hanging wall shows evidence of erosion and subsequent deposition in situ of the material reworked by coastal abrasion, generating a minor escarpment retreat. Refer to Appendix Fig. A15 for a color version.

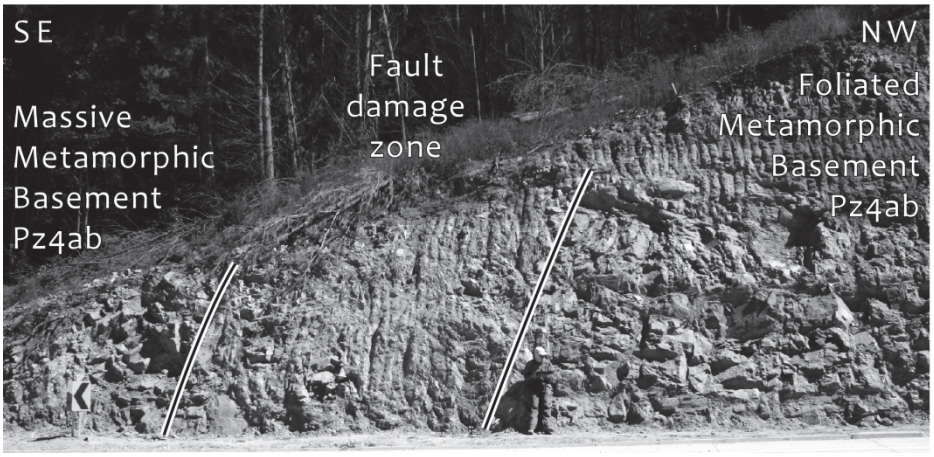

Figure 2.12: Photo of major fault in metamorphic basement at site 23 (Fault 23a in Table 2.2; Figs. 2.9-2.10; see also Appendix Figs. A18-21). This fault corresponds to the largest structure found in the northern portion of the Maule ridge. The fault coincides spatially with the location of a SE-facing, steep morphological scarp which limits a NE-trending ridge (Fig. 2.10a). Refer to Appendix Fig. A18 for a color version.

2.6 Discussion

2.6.1 Geological, long-term age constraints

Numerous faults that control the structural relief of the study regions show evidence of Neogene to Recent activity. At the Boca de Rapel-Matanzas domain and at Topocalma, the faults displace the Miocene-Pliocene Navidad-La Cueva Fms. (Figs. 2.3-2.4). Their activity has probably continued into the Quaternary as they displace marine terraces close to the coastal cliff. The morphology of tilted, well-preserved topographic surfaces along the Topocalma, and probably the Quebrada Honda and Cáhuil Quarry faults suggest the formation of either hanging wall rollover anticlines or domino-style rotated blocks (Figs. 2.4, 2.6 and 2.8). These tilted surfaces are undated but, given the high erosion and incision rates in the Coastal Cordillera in this latitude, at least 0.15-0.5 mm/a over the Quaternary (e.g., *Scholl et al.*, 1970; *Lowrie and Hey*, 1981; *Rehak et al.*, 2010; *Carretier et al.*, 2013), we assume that they are no older than Pleistocene. In addition to the post-Maule earthquake seismicity in 2010, the Pichilemu fault shows a history of Pleistocene-Holocene(?) uplift of paleo-beach sequences in the footwall (Fig. 2.7), demonstrating repeated normal fault offsets. In the Cáhuil domain and western flank of the Maule ridge, reverse faults displace Pleistocene-Holocene(?) sedimentary rocks by more than 2 m (Fig. 2.11).

Inland, the margin-parallel faults bounding the high topographic ridges do not yield reliable age constraints due to the absence of marine sedimentation (Cáhuil-Vichuquén and Maule fault systems). Most fault outcrops found in this study show Paleozoic basement on both sides of the structure. Thus, the dip of the fault, combined with the structural relief produced at the fault trace, is a crude proxy for late Cenozoic normal-fault activity assuming similar erosion rates of the Paleozoic units in the hanging wall and footwall (Fig. 2.10).

The dominant extensional structural pattern and age of deformation found in our work are consistent with observations in other forearc regions overlying the 2010 Maule earthquake rupture area (*Katz*, 1971; *Thiele and Morel*, 1981; *Gana et al.*, 1996; *Wall et al.*, 1996; *Lavenu and Cembrano*, 1999; *Lavenu and Encinas*, 2005) and elsewhere in the Andean Coastal Cordillera (e.g., *Niemeyer et al.*, 1996; *Heinze*, 2003; *Marquardt et al.*, 2004; *Audin et al.*, 2008; *Allmendinger and González*, 2010), with the exception of the Arauco peninsula, at the southern end of the rupture (Section 2.4). There, Melnick and coworkers have argued that Neogene-Quaternary reverse faulting has played a predominant role in shaping the current structural grain (e.g., *Melnick et al.*, 2006, 2009).

2.6.2 Seismic and geodetic short-term record

Though both young normal and reverse faults occur in the Coastal Cordillera overlying the Maule earthquake rupture segment, the resolution of the geologic record is, in general, too low to define how these structures relate to the seismic cycle of the plate boundary. Thus, we must turn to the record of crustal seismicity and its relation to the seismic cycle of the subduction megathrust. The Pichilemu sequence of normal fault aftershocks triggered by the Maule earthquake demonstrates co/post-seismic normal faulting (Fig. 2.1a). For megathrust events, postseismic deformation processes such as aseismic afterslip, interplate thrust aftershocks and viscoelastic deformation, have commonly similar orientation to the coseismic field but the strain rates in the upper plate, as captured by GPS displacements, are orders of magnitude smaller (e.g., *Wang et al.*, 2012; *Bedford et al.*, 2013). The two stages are indistinguishable in the geologic record – the main concern of this contribution –, so when we refer to the concept of coseismic deformation we are usually including both stages. Unlike other examples of megathrust earthquakes showing important coseismic splay faulting (e.g.,

Plafker, 1967), there is no conclusive evidence of upper plate reverse fault earthquakes that occurred during the co- and post-seismic period of the 2010 Maule event, at least over the Coastal Cordillera. *Melnick et al.* (2012) proposed that one of the branches of the Santa María fault system was reactivated by the Maule earthquake as a splay thrust fault. However, the evidence presented can equally well be interpreted as coseismic normal fault reactivation of a fault plane that acts as a reverse fault during the interseismic period (*Allmendinger et al.*, 2013).

Thirty years prior to the Maule event a shallow M_w 6.4 thrust earthquake (16 km depth) was recorded near the Valparaíso peninsula in 1981, (Fig. 2.1a). Also during the interseismic period, local networks in the area of the Arauco Peninsula detected shallow thrust seismicity < M 5, below the threshold of the global catalog on some structures underneath the Santa María island (*Bohm et al.*, 2002; *Melnick et al.*, 2006).

Similar coseismic-postseismic/interseismic alternation of forearc kinematics has been observed at other subduction zones (e.g., *Oishi and Sato*, 2007; *Audin et al.*, 2008; *Asano et al.*, 2011; *Kato et al.*, 2011, 2013; *Toda et al.*, 2011; *Hardebeck*, 2012; *Hasegawa et al.*, 2012; *Imanishi et al.*, 2012; *Yoshida et al.*, 2012). Although both reverse and normal faulting occurred in the upper plate after the 2010 Tohoku earthquake, the larger M_w 7.0 normal fault aftershocks are comparable to the 2010 Maule earthquake crustal events (e.g., *Toda and Tsutsumi*, 2013). Studies of total moment released by interseismic vs. coseismic forearc seismicity suggest that coseismic faulting may exceed interseismic activity (*Hardebeck*, 2012; e.g., *Hasegawa et al.*, 2012; *Yoshida et al.*, 2012). However, this interpretation has to be taken with caution because the information available in the instrumental record provides only a very narrow time window of observation for the megathrust interseismic period, sampling just a small fraction of the potential crustal earthquakes that could have

occurred over that stage.

Like the sparse earthquake record, GPS data from the Maule segment (e.g., *Ruegg et al.*, 2002, 2009; *Vigny et al.*, 2011; *Métois et al.*, 2012; *Moreno et al.*, 2012) document interseismic shortening and co/post-seismic extension of the Coastal Cordillera (Fig. 2.13; Appendix Figs. A24-25). Although these data are generally interpreted in terms of elastic and/or viscoelastic deformation (e.g., *Wang et al.*, 2012), *Aron et al.* (2013) showed that the coseismic GPS extensional strain is of the same order of magnitude as the permanent strain from the Pichilemu normal fault earthquake sequence. Though small, over geologic time this permanent deformation must sum up to produce the Neogene structures and much of the regional-scale morphology of the Coastal Cordillera. Likewise, the reverse fault earthquakes indicate some small portion of the interseismic cycle is non-elastic.

2.6.3 Deformation at intermediate time scales

To date, the upper crustal faults in the Coastal Cordillera overlying the Maule rupture segment lack paleoseismic study so we must draw on insight from other, similar margins. In northern Chile, *Cortés et al.* (2012) concluded that upper plate normal faults have recurrence intervals of 5 ± 3.5 ka, about one order of magnitude longer than the interplate cycle. Likewise, in Japan *Toda and Tsutsumi* (2013) suggested that upper plate faults in the forearc have a recurrence time corresponding to approximately ten M 9 subduction earthquake cycles.

Respect to the megathrust seismic cycle over the Maule segment, the previous great earthquake that may have ruptured the same area and reached a similar magnitude than the 2010 event occurred in 1835 (*Darwin*, 1845). Before that, two great earthquakes reported by Spanish conquistadors in 1657 and 1751 are potential candidates for an older predecessor (*Nishenko*, 1985; *Beck et al.*, 1998; *Campos et al.*,

2002; *Scholz and Campos*, 2012); yet, because of the qualitative nature of the historical record, there are discrepancies on their magnitude and exact rupture extension/location. On the other hand, considering an estimated average slip for the 2010 Maule earthquake of 6.5-6.8 m (*Tong et al.*, 2010; *Pollitz et al.*, 2011) and assuming 100% of interplate coupling, under the current convergence rate of 63 mm/a (*Kendrick et al.*, 2003) it would take at least 103-108 years to accumulate the necessary slip deficit for an equivalent event. This estimation falls within the 84-178 years recurrence range observed in the historical record.

If the crustal structures of the Coastal Cordillera over the Maule earthquake region behave similarly to the other mentioned margins, it would suggest that the major faults we have described are reactivated about every 840-1,780 years. Assuming 0.6 to 2.4 m of vertical displacement for each event (see Section 2.5.1.3) and pure seismic behavior of the structure, the current offset of the Pichilemu blocks could have been constructed in a period ranging from 0.2 to 1.5 Ma.

Unfortunately, in our specific study areas reports of absolute ages on morphologic surfaces or Quaternary units affected by faults are virtually nonexistent, so we cannot have a more detailed control on active deformation. However, in the region in-and-around the Arauco Peninsula, just south of the Maule study area (Fig. 2.1), there are numerous studies reporting Quaternary uplift rates based on well-constrained ages of marine terraces (which are in fact very similar to the terraces in our study areas), paleosols and strandlines (e.g., *Stefer et al.*, 2010 and references therein). Most of them agree that the average, long-term background uplift of the Coastal Cordillera is about 0.5-0.6 mm/a (*Rehak et al.*, 2010; e.g., *Stefer et al.*, 2010). However, the Quaternary uplift rates increase by an order of magnitude, ranging between 2 and 5 mm/a, over the hanging wall of mapped, kilometer-scale thrust faults with documented

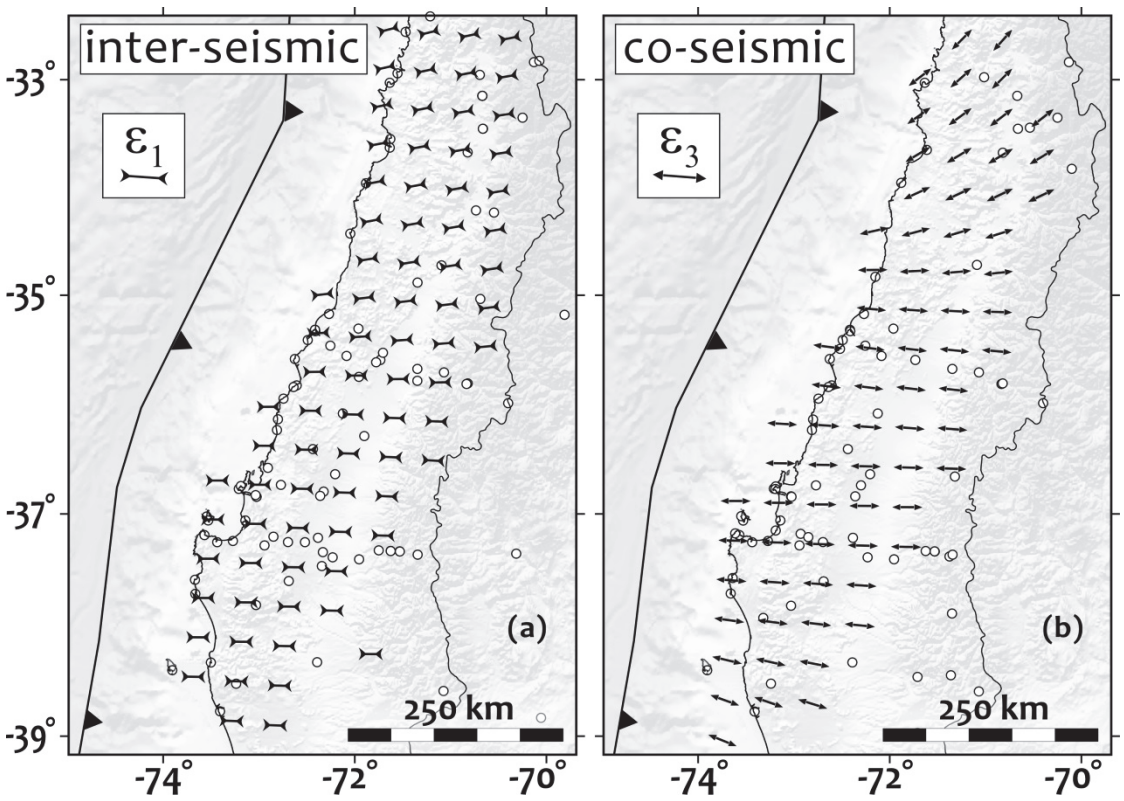

Figure 2.13: Maps of the Maule earthquake rupture area showing the orientation of the largest principal axes of surface infinitesimal strain for: (a) interseismic and (b) coseismic stages of the subduction seismic cycle, calculated from published GPS velocities and instantaneous displacements respectively. The circles show the station location. We resolve the strain field over a 2D regular grid using standard methods to invert strain from GPS vectors (*Cardozo and Allmendinger*, 2009; *Allmendinger et al.*, 2012). Coseismic GPS displacements are from Vigny et al. (2011) and Moreno et al. (2012) (Appendix Fig. A24). The interseismic GPS compilation is courtesy of Marianne Métois and spans about 12 years of data (*Métois et al.*, 2012) (Appendix Fig. A25). Note that convergence-parallel shortening (large ε_1) dominates the interseismic period while the coseismic GPS vectors capture rapid extension parallel to the heave of the megathrust or subduction rebound (large ε_3). See Appendix Figures A24-25 for maps showing interseismic and coseismic calculations of the first invariant of strain (dilatation) over the rupture area.

Pleistocene activity (e.g., *Kaizuka et al.*, 1973; *Nelson and Manley*, 1992; *Bookhagen et al.*, 2006; *Melnick et al.*, 2006; *Stefer et al.*, 2010) – these structures are contributing greatly to construct the current relief of the coastal ranges. Preliminary results of a study dating coastal terraces show that the MIS-5 terrace (71-130 ka; *Lisiecki and Raymo*, 2005) has a continuous expression over the entire 2010 Maule earthquake rupture area and that in some places is offset by major, kilometer-scale normal faults (*Jara-Muñoz et al.*, 2014). It is likely that MIS-5 unit corresponds to one of the coastal terraces affected by crustal faulting described in our work, but we cannot make further correlations because exact locations of their measurements are not available yet. But more importantly, their work also suggests that the northern end of the Maule segment, near the O'Higgins study region, may undergo uplift rates of about 1.8 mm/a over the Quaternary, similarly to what has been observed in the Arauco Peninsula (*Melnick et al.*, 2006). As discussed above, our crude estimation of vertical offset rates for the Pichilemu normal fault, attributed to recurrent Pleistocene reactivations of the structure, ranges between 0.3 and 2.9 mm/a.

2.6.4 From one seismic cycle to long-term deformation

Coulomb stress increments (*King et al.*, 1994) are a convenient way to conceptualize the relationship between plate boundary seismicity and upper plate crustal faulting. In northern Chile, *Delouis et al.* (1998) and *Loveless et al.* (2010) used this method to propose conceptual models of how crustal faulting in the Coastal Cordillera may relate, in the long-term, to megathrust earthquakes. Based on their contributions, the signals of short- and long-term forearc deformation discussed in our work, and Coulomb stress analysis (*Farías et al.*, 2011; e.g., *Toda et al.*, 2011; *Aron et al.*, 2013), we present an alternative multi-scale conceptual model to explain how shear stresses on forearc structures evolve throughout many interplate seismic cycles

in the Maule megathrust segment (Fig. 2.14). The scenarios we present here should also apply to many other convergent margins. Our model is a more nuanced interpretation, intending to represent the most likely scenario over neotectonic time scales, which smooths out local tectonic and structural anomalies that could modify greatly the state of stress of the crust; so, the structural behavior of the upper plate.

Our scenario for the current, geologically instantaneous state of the segment is quite straightforward: GPS and crustal seismicity demonstrate slow interseismic horizontal shortening and rapid co/post-seismic extension (Figs. 2.1, 2.13 and 2.14a). Over a longer time span, faults should develop as shown in Figure 2.14b. The specific behavior of the forearc structures would depend on their location with respect to the distribution of interplate interseismic locking and subsequent megathrust slip, as well as fault strength, orientation, fluid pressure, healing, friction evolution and the ambient stress state. Those variables control the slope of effective shear stress on forearc faults during the interseismic period, the magnitude of normal- and/or reverse-fault shear stress generated by a subduction earthquake, and the recurrence time of intraplate faulting. Consistent with negative Coulomb stresses for normal faulting, stress inversions of upper plate earthquakes and theoretic approximations, interseismic normal faulting in the forearc structures, especially at nucleation depths below 5 km depth, appears unlikely and any reactivation would be as thrusting (*Yoshida et al.*, 2012; *Aron et al.*, 2013; *Sibson*, 2013). Although probably depending on local geologic or short-term conditions, there are exceptions such as the Iwaki area in Japan where normal faulting predominates even over the interseismic period (*Imanishi et al.*, 2012). During the co- and post-seismic periods, the faults of the upper plate overlying and inboard of the megathrust slip zone would be encouraged to slip principally as normal faults if the shear stress on them exceeds the critical shear strength (*Farías et al.*, 2011; *Toda et al.*, 2011; *Hasegawa et al.*, 2012; *Aron et al.*, 2013; *Toda and*

Tsutsumi, 2013). Splay reverse faults would be expected in the upper plate above the megathrust up dip from the main slip zone (*Li et al.*, 2014), similar to what occurred after the 1964 Alaska and 2004 Sumatra-Andaman earthquakes (*Plafker*, 1967; *Sibuet et al.*, 2007).

For the pure normal faulting case, there would be a progressive increase through time in the effective normal-fault shear stress, until it reaches the shear strength (Fig. 2.14b). In each cycle, positive gains during subduction earthquakes would have to be larger than the interseismic negative loading. According to very limited paleoseismological studies from other margins, this process could take about 10 subduction seismic cycles (*Cortés et al.*, 2012; *Toda and Tsutsumi*, 2013), though, as mentioned above, changes in the mechanical behavior of the intraplate structures can retard or hasten their reactivation. For example, longer recurrence times would result from increasing the negative slope of the interseismic shear stress, reducing the positive coseismic gains of normal-fault shear stress or from potential negative coseismic normal stress gains.

Forearc structures with pure thrust kinematics require a progressive increase of reverse-fault effective shear stress (decrease of normal-fault shear), facilitated by small or negative gains of normal-fault shear during subduction events (Fig. 2.14b). Over many megathrust cycles the net reverse shear stress imposed on the faults overtakes the normal shear. Details of Holocene thrust faulting activity are lacking but we assume that recurrence times should be on the same order of magnitude as the crustal normal faults. Finally, the bottom graph of Figure 2.14b shows an example of stress evolution on upper-plate faults with documented, long-term tectonic inversions; e.g., as observed with the Quebrada Honda fault (Section 2.5.1.2) or of the type described by *Lavenu and Encinas* (2005) and *Allmendinger and González* (2010).

Figure 2.14: Conceptual multi-scale model integrating instantaneous and long term permanent deformation in the Coastal Cordillera as a function of the subduction earthquake cycle. (a) Seismicity and GPS data shows cycles of interseismic, convergence-parallel shortening and coseismic extension of the upper plate (Figs. 2.1 and 2.13). (b) The three graphs show the shear stress evolution (τ_N and τ_R are for normal and reverse faulting respectively) over neotectonic time scales on the upper plate faults for different fault kinematics scenarios. Zero shear stress means "ambient levels". The white circles indicate a faulting event. The dotted lines with a question mark in the upper and central panels represent the scenario of potential increments of negative normal-fault Coulomb stress (or positive reverse-fault) on upper plate structures properly-oriented and located respect to the compressive stresses imposed by a megathrust event, such as splay, thrust faults.

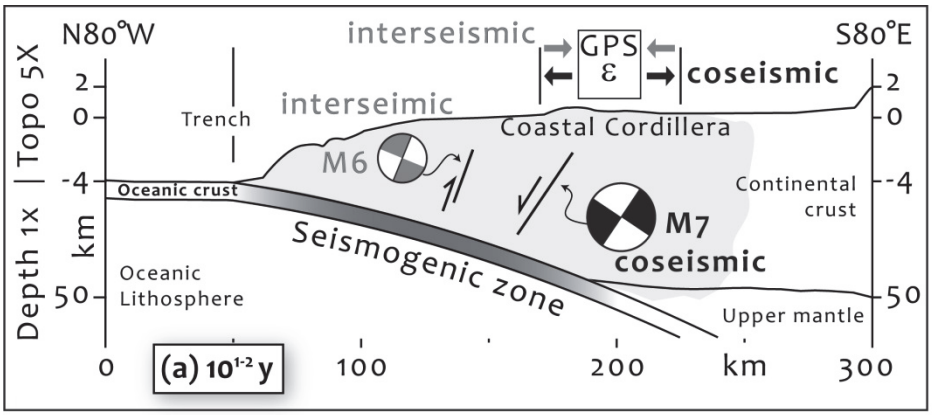
N80°W
S80°E
interseismic
GPS
ε
coseismic
interseimic
Trench
Coastal Cordillera
M6
Continental crust
Oceanic crust
M7
coseismic
Seismogenic zone
Oceanic Lithosphere
Upper mantle
Depth 1x | Topo 5X
km
2
0
-4
50
0
(a) 10^1-2 y
100
200
km
300

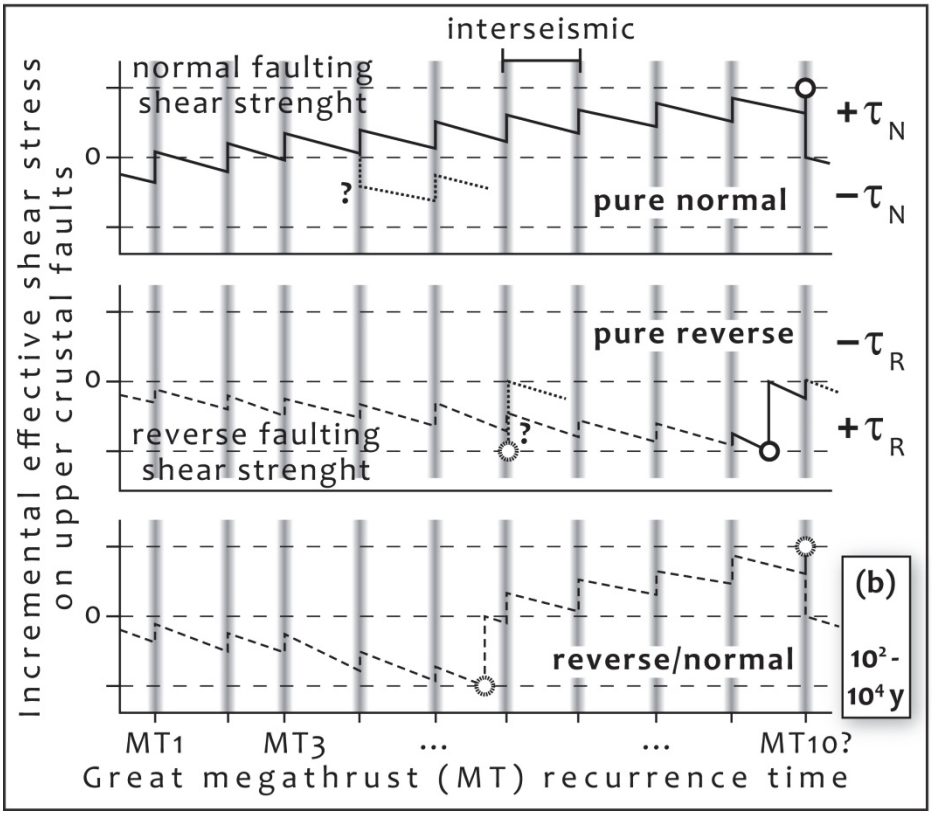
interseismic
normal faulting
shear strenght
+τN
0
?
pure normal
−τN
pure reverse
−τR
0
reverse faulting
shear strenght
?
+τR
Incremental effective shear stress on upper crustal faults
0
reverse/normal
(b)
10²-10⁴ y
MT1
MT3
...
...
MT10?
Great megathrust (MT) recurrence time

This would require a change in the predominant mechanical behavior of the structures between the two described end-members throughout their history (e.g., by modifying the rupture position of megathrust events or the coupling distribution on the subduction interface).

Over geologic time, the cyclic pulses of contraction and extension experienced by the upper plate during thousands of subduction cycles build the forearc structural grain and morphology. Because materials are much weaker under tension than they are under compression, we expect the permanent interseismic strain, especially in forearc basement rocks, to be smaller in magnitude than the coseismic strain. In the area we have described it appears that horizontal extension dominates, which is consistent with evidence from northern Chile and Japan (e.g., *Loveless et al.*, 2005; *Baker et al.*, 2013; *Toda and Tsutsumi*, 2013).

2.7 Conclusions

The neotectonic structural style of the Coastal Cordillera in both of our study areas is dominated by kilometer-scale normal faults which have been active at least throughout the Neogene and Quaternary. The Pichilemu fault which was reactivated by the 2010 Maule earthquake, as well as other shallow crustal normal faults, shows a consistent kinematic history over thousands of subduction seismic cycles. Major crustal discontinuities inherited from pre-Andean geologic processes such as Paleozoic ductile shear zones or lithological contacts are used by the current tectonic stresses to accommodate permanent, brittle deformation. Reverse faults are contemporaneous to the normal faults but generally scarce. Some of the structures show long-term inversions of fault kinematics. Our findings are consistent with what has been observed in other regions of the Maule earthquake rupture area and elsewhere in the

Andean Coastal Cordillera

At instrumental time scales, both crustal seismicity and GPS surface displacements show that the subduction seismic cycle produces pulses of episodic rapid coseismic extension and slow interseismic, convergence-parallel shortening of the upper plate. These pulses of contraction and extension, over geologic time, build the forearc structural grain and morphology, reactivating structures favorably-oriented with respect to the stress field imposed at each stage of the megathrust seismic cycle. Analogous observations along the 2011 Tohoku earthquake rupture in Japan indicate that the occurrence of great subduction events may play a fundamental role in constructing the crustal architecture of extensional forearc regions.

REFERENCES

Allmendinger, R. W., and G. González (2010), Invited review paper: Neogene to Quaternary tectonics of the coastal Cordillera, northern Chile, *Tectonophysics*, *495*(1-2), 93–110, doi:10.1016/j.tecto.2009.04.019.

Allmendinger, R. W., N. Cardozo, and D. M. Fisher (2012), *Structural Geology Algorithms: Vectors and Tensors*, Cambridge University Press, New York.

Allmendinger, R. W., G. González, J. Cembrano, F. Aron, and G. Yáñez (2013), Splay fault slip during the Mw 8.8 2010 Maule Chile earthquake: COMMENT, *Geology*, *41*(12), e309–e309, doi:10.1130/G34326C.1.

Aron, F., R. W. Allmendinger, J. Cembrano, G. González, and G. Yáñez (2013), Permanent fore-arc extension and seismic segmentation: Insights from the 2010 Maule earthquake, Chile, *Journal of Geophysical Research: Solid Earth*, *118*(2), 724–739, doi:10.1029/2012JB009339.

Arriagada, C. et al. (2011), Nature and tectonic significance of co-seismic structures associated with the Mw 8.8 Maule earthquake, central-southern Chile forearc, *J. Struct. Geol.*, *33*(5), 891–897, doi:10.1016/j.jsg.2011.03.004.

Asano, Y., T. Saito, Y. Ito, K. Shiomi, H. Hirose, T. Matsumoto, S. Aoi, S. Hori, and S. Sekiguchi (2011), Spatial distribution and focal mechanisms of aftershocks of the 2011 off the Pacific coast of Tohoku Earthquake, *Earth, Planets and Space*, *63*(7), 669–673, doi:10.5047/eps.2011.06.016.

Audin, L., P. Lacan, H. Tavera, and F. Bondoux (2008), Upper plate deformation and seismic barrier in front of Nazca subduction zone: The Chololo Fault System and active tectonics along the Coastal Cordillera, southern Peru, *Tectonophysics*, *459*(1-4), 174–185.

Baker, A., R. W. Allmendinger, L. A. Owen, and J. A. Rech (2013), Permanent deformation caused by subduction earthquakes in northern Chile, *Nature Geosci*, *advance online publication*, doi:10.1038/ngeo1789.

Beck, S., S. Barrientos, E. Kausel, and M. Reyes (1998), Source characteristics of historic earthquakes along the central Chile subduction Askew et alzone, *Journal of South American Earth Sciences*, *11*(2), 115–129, doi:10.1016/S0895-9811(98)00005-4.

Bedford, J. et al. (2013), A high-resolution, time-variable afterslip model for the 2010 Maule Mw = 8.8, Chile megathrust earthquake, *Earth and Planetary Science Letters*, *383*, 26–36, doi:10.1016/j.epsl.2013.09.020.

Bohm, M., S. Lüth, H. Echtler, G. Asch, K. Bataille, C. Bruhn, A. Rietbrock, and P. Wigger (2002), The Southern Andes between 36° and 40°S latitude: seismicity and average seismic velocities, *Tectonophysics*, *356*(4), 275–289, doi:10.1016/S0040-1951(02)00399-2.

Bookhagen, B., H. P. Echtler, D. Melnick, M. R. Strecker, and J. Q. G. Spencer (2006), Using uplifted Holocene beach berms for paleoseismic analysis on the Santa María Island, south-central Chile, *Geophys. Res. Lett.*, *33*(15), L15302, doi:10.1029/2006GL026734.

Burbank, D. W., and R. S. Anderson (2011), *Tectonic Geomorphology*, 2nd ed., Wiley-Blackwell, West Sussex, UK.

Campos, J., D. Hatzfeld, R. Madariaga, G. Lopez, E. Kausel, A. Zollo, G. Iannacone, R. Fromm, S. Barrientos, and H. Lyon-Caen (2002), A seismological study of the 1835 seismic gap in south-central Chile, *Physics of the Earth and Planetary Interiors*, *132*(1–3), 177–195, doi:10.1016/S0031-9201(02)00051-1.

Cardozo, N., and R. W. Allmendinger (2009), SSPX: A program to compute strain from displacement/velocity data, *Computers & Geosciences*, *35*(6), 1343 – 1357, doi:DOI: 10.1016/j.cageo.2008.05.008.

Carretier, S. et al. (2013), Slope and climate variability control of erosion in the Andes of central Chile, *Geology*, *41*(2), 195–198, doi:10.1130/G33735.1.

Cembrano, J., F. Hervé, and A. Lavenu (1996), The Liquiñe Ofqui fault zone: a long-lived intra-arc fault system in southern Chile, *Tectonophysics*, *259*(1–3), 55–66, doi:10.1016/0040-1951(95)00066-6.

Cembrano, J., A. Lavenu, G. Yañez, R. Riquelme, M. Garcia, G. González, and G. Hérail (2007), Neotectonics, in *The Geology of Chile*, edited by T. Moreno, W. Gibbons, and G. S. of London, pp. 231–261, Geological Society of London, London, Tulsa. UK.

Cortés, J., G. González, S. A. Binnie, R. Robinson, S. P. H. T. Freeman, and G. Vargas (2012), Paleoseismology of the Mejillones Fault, northern Chile: Insights from cosmogenic 10Be and optically stimulated luminescence determinations, *Tectonics*, *31*(2), TC2017, doi:10.1029/2011TC002877.

Darwin, C. (1845), *Journal of researches into the natural history and geology of the countries visited during the voyage of H.M.S. Beagle round the world*, 2nd. ed., John Murray, London.

Darwin, C. (1846), *Geological observations on South America. Being the third part of the geology of the voyage of the Beagle, under the command of Capt. Fitzroy, R.N. during the years 1832 to 1836*, Smith Elder and Co., London.

Delouis, B., H. Philip, L. Dorbath, and A. Cisternas (1998), Recent crustal deformation in the Antofagasta region (northern Chile) and the subduction process, *Geophys. J. Int.*, *132*(2), 302–338, doi:10.1046/j.1365-246x.1998.00439.x.

Farías, M., D. Comte, S. Roecker, D. Carrizo, and M. Pardo (2011), Crustal extensional faulting triggered by the 2010 Chilean earthquake: The Pichilemu Seismic Sequence, *Tectonics*, *30*(6), TC6010–, doi:10.1029/2011TC002888.

Fukushima, Y., Y. Takada, and M. Hashimoto (2013), Complex Ruptures of the 11 April 2011 Mw 6.6 Iwaki Earthquake Triggered by the 11 March 2011 Mw 9.0 Tohoku Earthquake, Japan, *Bulletin of the Seismological Society of America*, *103*(2B), 1572–1583, doi:10.1785/0120120140.

Gana, P., R. Wall, and A. Gutiérrez (1996), *Mapa geológico del área Valparaíso-Curacaví, Regiones de Valparaíso y Metropolitana.*, Geological map Scale 1:100,000, Servicio Nacional de Geología y Minería, Santiago, Chile.

Geersen, J., J. H. Behrmann, D. Völker, S. Krastel, C. R. Ranero, J. Diaz-Naveas, and W. Weinrebe (2011), Active tectonics of the South Chilean marine fore arc (35°S–40°S), *Tectonics*, *30*(3), TC3006, doi:10.1029/2010TC002777.

Gutiérrez, N. M., L. F. Hinojosa, J. P. Le Roux, and V. Pedroza (2013), Evidence for an Early-Middle Miocene age of the Navidad Formation (central Chile): Paleontological, paleoclimatic and tectonic implications, *Andean Geology*, *40*(1), doi:10.5027/andgeoV40n1-a03.

Hardebeck, J. L. (2012), Coseismic and postseismic stress rotations due to great subduction zone earthquakes, *Geophysical Research Letters*, *39*(21), n/a–n/a, doi:10.1029/2012GL053438.

Hasegawa, A., K. Yoshida, Y. Asano, T. Okada, T. Iinuma, and Y. Ito (2012), Change in stress field after the 2011 great Tohoku-Oki earthquake, *Earth and Planetary Science Letters*, *355–356*, 231–243, doi:10.1016/j.epsl.2012.08.042.

Hayes, G. P., D. J. Wald, and R. L. Johnson (2012), Slab1.0: A three-dimensional model of global subduction zone geometries, *Journal of Geophysical Research: Solid Earth*, *117*(B1), B01302–, doi:10.1029/2011JB008524.

Heinze, B. (2003), Active Intraplate Faulting in the Forearc of North Central Chile (30°-31° S). Implications from Neotectonic Field Studies, GPS Data, and Elastic Dislocation Modeling, PhD, Free University, Berlin, March.

Hervé, F., V. Faundez, M. Calderón, H.-J. Massonne, and A. P. Willner (2007), Metamorphic and plutonic basement complexes, in *The Geology of Chile*, edited by T. Moreno, W. Gibbons, and G. S. of London, pp. 231–261, Geological Society of London, London, Tulsa. UK.

Von Huene, R., and C. R. Ranero (2003), Subduction erosion and basal friction along the sediment-starved convergent margin off Antofagasta, Chile, *Journal of Geophysical Research: Solid Earth*, *108*(B2), n/a–n/a, doi:10.1029/2001JB001569.

Imanishi, K., R. Ando, and Y. Kuwahara (2012), Unusual shallow normal-faulting earthquake sequence in compressional northeast Japan activated after the 2011 off the Pacific coast of Tohoku earthquake, *Geophysical Research Letters*, *39*(9), n/a–n/a, doi:10.1029/2012GL051491.

Jara-Muñoz, J., D. Melnick, D. Brill, and M. Strecker (2014), Linking short- and long-term deformation along an active margin: regional tectono-geomorphic patterns in light of the 2010 Maule Chile earthquake (M8.8), in *EGU General Assembly Conference Abstracts*, vol. 16, p. 4604.

Kaizuka, S., T. Matsuda, M. Nogami, and N. Yonekura (1973), Quaternary tectonic and recent seismic crustal movements in the arauco peninsula and its environs, central chile, *Geographical reports of Tokyo Metropolitan University*, *8*, 1–49.

Kato, A., S. Sakai, and K. Obara (2011), A normal-faulting seismic sequence triggered by the 2011 off the Pacific coast of Tohoku Earthquake: Wholesale stress regime changes in the upper plate, *Earth, Planets and Space*, *63*(7), 745–748, doi:10.5047/eps.2011.06.014.

Kato, A. et al. (2013), Imaging the source regions of normal faulting sequences induced by the 2011 M9.0 Tohoku-Oki earthquake, *Geophysical Research Letters*, *40*(2), 273–278, doi:10.1002/grl.50104.

Katz, H. R. (1971), Continental Margin in Chile-Is Tectonic Style Compressional or Extensional?, *AAPG Bulletin*, *55*(10), 1753–1758, doi:10.1306/819A3DA2-16C5-11D7-8645000102C1865D.

Kay, S. M., E. Godoy, and A. Kurtz (2005), Episodic arc migration, crustal thickening, subduction erosion, and magmatism in the south-central Andes, *Geological Society of America Bulletin*, *117*(1-2), 67–88, doi:10.1130/B25431.1.

Kendrick, E., M. Bevis, R. Smalley, B. Brooks, R. B. Vargas, E. Lauría, and L. P. S. Fortes (2003), The Nazca-South America Euler vector and its rate of change, *J. South Amer. Earth Sci.*, *16*(2), 125–131, doi:10.1016/S0895-9811(03)00028-2.

King, G. C. P., R. S. Stein, and J. Lin (1994), Static stress changes and the triggering of earthquakes, *Bull. Seismol. Soc. Am.*, *84*(3), 935–953.

Kobayashi, T., M. Tobita, M. Koarai, T. Okatani, S. Akira, Y. Noguchi, M. Yamanaka, and B. Miyahara (2013), InSAR-derived crustal deformation and fault models of normal faulting earthquake (M_j 7.0) in the Fukushima-Hamadori area, *Earth, Planets and Space*, *64*(12), 1209–1221, doi:10.5047/eps.2012.08.015.

Lange, D. et al. (2012), Aftershock seismicity of the 27 February 2010 Mw 8.8 Maule earthquake rupture zone, *Earth and Planetary Science Letters*, *317–318*, 413–425, doi:10.1016/j.epsl.2011.11.034.

Lavenu, A., and J. Cembrano (1999), Compressional- and transpressional-stress pattern for Pliocene and Quaternary brittle deformation in fore arc and intra-arc zones (Andes of Central and Southern Chile), *J. Struct. Geol.*, *21*(12), 1669–1691, doi:10.1016/S0191-8141(99)00111-X.

Lavenu, A., and A. Encinas (2005), Deformación frágil de los depósitos neógenos de la cuenca de Navidad (Cordillera de la Costa, 34°S, Chile central), *Rev. Geol. Chile*, *32*, 229–248, doi:10.4067/S0716-02082005000200004.

Li, S., M. Moreno, M. Rosenau, D. Melnick, and O. Oncken (2014), Splay fault triggering by great subduction earthquakes inferred from finite element models, *Geophys. Res. Lett.*, *41*(2), 2013GL058598, doi:10.1002/2013GL058598.

Lisiecki, L. E., and M. E. Raymo (2005), A Pliocene-Pleistocene stack of 57 globally distributed benthic δ18O records, *Paleoceanography*, *20*(1), PA1003, doi:10.1029/2004PA001071.

Loveless, J. P., G. D. Hoke, R. W. Allmendinger, G. Gonzalez, B. L. Isacks, and D. A. Carrizo (2005), Pervasive cracking of the northern Chilean Coastal Cordillera: New evidence for forearc extension, *Geology*, *33*(12), 973–976, doi:10.1130/G22004.1.

Loveless, J. P., R. W. Allmendinger, M. E. Pritchard, and G. González (2010), Normal and reverse faulting driven by the subduction zone earthquake cycle in the northern Chilean fore arc, *Tectonics*, *29*(2), TC2001–.

Lowrie, A., and R. Hey (1981), Geological and geophysical variations along the western margin of Chile near lat 33° to 36° S and their relation to Nazca plate subduction, *Geological Society of America Memoirs*, *154*, 741–754, doi:10.1130/MEM154-p741.

Marquardt, C., A. Lavenu, L. Ortlieb, E. Godoy, and D. Comte (2004), Coastal neotectonics in Southern Central Andes: uplift and deformation of marine terraces in Northern Chile (27°S), *Tectonophysics*, *394*(3-4), 193 – 219, doi:10.1016/j.tecto.2004.07.059.

Melnick, D., B. Bookhagen, H. P. Echtler, and M. R. Strecker (2006), Coastal deformation and great subduction earthquakes, Isla Santa María, Chile (37°S), *Geological Society of America Bulletin*, *118*(11-12), 1463–1480, doi:10.1130/B25865.1.

Melnick, D., B. Bookhagen, M. R. Strecker, and H. P. Echtler (2009), Segmentation of megathrust rupture zones from fore-arc deformation patterns over hundreds to millions of years, Arauco peninsula, Chile, *J. Geophys. Res.*, *114*, 23 PP., doi:200910.1029/2008JB005788.

Melnick, D., M. Moreno, M. Motagh, M. Cisternas, and R. L. Wesson (2012), Splay Fault Slip During the Mw 8.8 2010 Maule Chile Earthquake, *Geology*, *40*(3), 251–254, doi:10.1130/G32712.1.

Métois, M., A. Socquet, and C. Vigny (2012), Interseismic coupling, segmentation and mechanical behavior of the central Chile subduction zone, *J. Geophys. Res.*, *117*, 16 PP., doi:10.1029/2011JB008736.

Mizoguchi, K., S. Uehara, and K. Ueta (2012), Surface Fault Ruptures and Slip Distributions of the Mw 6.6 11 April 2011 Hamadoori, Fukushima Prefecture, Northeast Japan, Earthquake, *Bulletin of the Seismological Society of America*, *102*(5), 1949–1956, doi:10.1785/0120110308.

Moreno, M., M. Rosenau, and O. Oncken (2010), 2010 Maule earthquake slip correlates with pre-seismic locking of Andean subduction zone, *Nature*, *467*(7312), 198–202, doi:10.1038/nature09349.

Moreno, M. et al. (2012), Toward understanding tectonic control on the Mw 8.8 2010 Maule Chile earthquake, *Earth Planet. Sci. Lett.*, *321–322*(0), 152–165, doi:10.1016/j.epsl.2012.01.006.

Nelson, A. R., and W. F. Manley (1992), Holocene coseismic and aseismic uplift of Isla Mocha, south-central Chile, *Quaternary International*, *15–16*, 61–76, doi:10.1016/1040-6182(92)90036-2.

Niemeyer, H., G. González, and E. Martinez-De Los Rios (1996), Evolución tectónica cenozoica del margen continental activo de Antofagasta, norte de Chile, *Andean Geology (formely Revista Geológica de Chile)*, *23*(2), 165–186, doi:10.5027/andgeoV23n2-a05.

Nishenko, S. P. (1985), Seismic potential for large and great interplate earthquakes along the Chilean and Southern Peruvian Margins of South America: A quantitative reappraisal, *J. Geophys. Res.*, *90*(B5), 3589–3615, doi:10.1029/JB090iB05p03589.

Oishi, M., and T. Sato (2007), Moment release budget at oblique convergence margin as revealed by the 2004 Sumatra-Andaman earthquake, *Earth, Planets and Space*, *59*(8), 913–921.

Plafker, G. (1967), Surface faults on Montague Island associated with the 1964 Alaska earthquake, *U.S. Geol. Surv. Prof. Pap.*, *543-G*, 42 p.

Pollitz, F. F. et al. (2011), Coseismic slip distribution of the February 27, 2010 Mw 8.8 Maule, Chile earthquake, *Geophys. Res. Lett.*, *38*(9), L09309, doi:10.1029/2011GL047065.

Rehak, K., S. Niedermann, F. Preusser, M. R. Strecker, and H. P. Echtler (2010), Late Pleistocene landscape evolution in south-central Chile constrained by luminescence and stable cosmogenic nuclide dating, *Geological Society of America Bulletin*, *122*(7-8), 1235–1247, doi:10.1130/B26545.1.

Richter, P. P., U. Ring, A. P. Willner, and B. Leiss (2007), Structural contacts in subduction complexes and their tectonic significance: the Late Palaeozoic coastal accretionary wedge of central Chile, *Journal of the Geological Society*, *164*(1), 203–214, doi:10.1144/0016-76492005-181.

Ruegg, J. C., J. Campos, R. Madariaga, E. Kausel, J. B. de Chabalier, R. Armijo, D. Dimitrov, I. Georgiev, and S. Barrientos (2002), Interseismic strain accumulation in south central Chile from GPS measurements, 1996-1999, *Geophys. Res. Lett.*, *29*(11), 1517–, doi:10.1029/2001GL013438.

Ruegg, J. C., A. Rudloff, C. Vigny, R. Madariaga, J. B. de Chabalier, J. Campos, E. Kausel, S. Barrientos, and D. Dimitrov (2009), Interseismic strain accumulation measured by GPS in the seismic gap between Constitución and Concepción in Chile, *Phys. Earth Planet. Inter.*, *175*(1-2), 78–85, doi:10.1016/j.pepi.2008.02.015.

Ruiz, J. A., G. P. Hayes, D. Carrizo, H. Kanamori, A. Socquet, and D. Comte (2014), Seismological analyses of the 2010 March 11, Pichilemu, Chile Mw 7.0 and Mw 6.9 coastal intraplate earthquakes, *Geophys. J. Int.*, *197*(1), 414–434, doi:10.1093/gji/ggt513.

Ryder, I., A. Rietbrock, K. Kelson, R. Bürgmann, M. Floyd, A. Socquet, C. Vigny, and D. Carrizo (2012), Large extensional aftershocks in the continental forearc triggered by the 2010 Maule earthquake, Chile, *Geophys. J. Int.*, *188*(3), 879–890, doi:10.1111/j.1365-246X.2011.05321.x.

Scholl, D. W., M. N. Christensen, R. V. Huene, and M. S. Marlow (1970), Peru-Chile Trench Sediments and Sea-Floor Spreading, *Geological Society of America Bulletin*, *81*(5), 1339–1360, doi:10.1130/0016-7606(1970)81[1339:PTSASS]2.0.CO;2.

Scholz, C. H., and J. Campos (2012), The seismic coupling of subduction zones revisited, *J. Geophys. Res.*, *117*(B5), B05310, doi:10.1029/2011JB009003.

SERNAGEOMIN (2003), *Mapa Geológico de Chile: versión digital*, Geological map Scale 1:1,000,000, Servicio Nacional de Geología y Minería, Santiago, Chile.

Sibson, R. H. (2013), Stress switching in subduction forearcs: Implications for overpressure containment and strength cycling on megathrusts, *Tectonophysics*, *600*, 142–152, doi:10.1016/j.tecto.2013.02.035.

Sibuet, J.-C. et al. (2007), 26th December 2004 great Sumatra–Andaman earthquake: Co-seismic and post-seismic motions in northern Sumatra, *Earth and Planetary Science Letters*, *263*(1–2), 88–103, doi:10.1016/j.epsl.2007.09.005.

Stefer, S., J. Moernaut, D. Melnick, H. P. Echtler, H. W. Arz, F. Lamy, M. De Batist, O. Oncken, and G. H. Haug (2010), Forearc uplift rates deduced from sediment cores of two coastal lakes in south-central Chile, *Tectonophysics*, *495*(1–2), 129–143, doi:10.1016/j.tecto.2009.05.006.

Thiele, R., and R. Morel (1981), Tectónica Triásico-Jurásica en la Cordillera de la Costa, al norte y sur del río Mataquito (34°45' - 35°15' Lat. S), Chile, *Andean geology*, *8*(2-3), 46–61, doi:10.5027/andgeoV8n2-3-a04.

Tikoff, B., T. Blenkinsop, S. C. Kruckenberg, S. Morgan, J. Newman, and S. Wojtal (2013), A perspective on the emergence of modern structural geology: Celebrating the feedbacks between historical-based and process-based approaches, *Geological Society of America Special Papers*, *500*, 65–119, doi:10.1130/2013.2500(03).

Toda, S., and H. Tsutsumi (2013), Simultaneous Reactivation of Two, Subparallel, Inland Normal Faults during the Mw 6.6 11 April 2011 Iwaki Earthquake Triggered by the Mw 9.0 Tohoku-oki, Japan, Earthquake, *Bulletin of the Seismological Society of America*, *103*(2B), 1584–1602, doi:10.1785/0120120281.

Toda, S., R. S. Stein, and J. Lin (2011), Widespread seismicity excitation throughout central Japan following the 2011 M=9.0 Tohoku earthquake and its interpretation by Coulomb stress transfer, *Geophys. Res. Lett.*, *38*, L00G03–, doi:10.1029/2011GL047834.

Tong, X. et al. (2010), The 2010 Maule, Chile earthquake: Downdip rupture limit revealed by space geodesy, *Geophys. Res. Lett.*, *37*(24), L24311, doi:10.1029/2010GL045805.

Vietor, T., and H. Echtler (2006), Episodic Neogene Southward Growth of the Andean Subduction Orogen between 30°S and 40°S — Plate Motions, Mantle Flow, Climate, and Upper-Plate Structure, in *The Andes*, edited by O. Oncken, G. Chong, G. Franz, P. Giese, H.-J. Götze, V. A. Ramos, M. R. Strecker, and P. Wigger, pp. 375–400, Springer Berlin Heidelberg.

Vigny, C. et al. (2011), The 2010 Mw 8.8 Maule Megathrust Earthquake of Central Chile, Monitored by GPS, *Science*, *332*(6036), 1417–1421, doi:10.1126/science.1204132.

Wall, R., P. Gana, and A. Gutiérrez (1996), *Mapa geológico del área de San Antonio-Melipilla, Regiones de Valparaiso, Metropolitana y del Libertador Bernardo O'Higgins.*, Geological map Scale 1:100,000, Servicio Nacional de Geología y Minería, Santiago, Chile.

Wang, K., Y. Hu, and J. He (2012), Deformation cycles of subduction earthquakes in a viscoelastic Earth, *Nature*, *484*(7394), 327–332, doi:10.1038/nature11032.

Willner, A. P., P. P. Richter, and U. Ring (2009), Structural overprint of a late Paleozoic accretionary system in north-central Chile (34°-35°S) during post-accretional deformation, *Andean geology*, *36*(1), 17–36, doi:10.5027/andgeoV36n1-a02.

Yoshida, K., A. Hasegawa, T. Okada, T. Iinuma, Y. Ito, and Y. Asano (2012), Stress before and after the 2011 great Tohoku-oki earthquake and induced earthquakes in inland areas of eastern Japan, *Geophysical Research Letters*, *39*(3), n/a–n/a, doi:10.1029/2011GL049729.

CHAPTER 3

PERMANENT FOREARC EXTENSION AND SEISMIC SEGMENTATION: INSIGHTS FROM THE 2010 MAULE EARTHQUAKE, CHILE*

3.1 Abstract

Geologists have long known that young normal faults are an important structural element of the Andean Coastal Cordillera, but their relationship to the subduction seismic cycle is still unclear. Some of the largest aftershocks of the 2010 M_w8.8 Maule earthquake in central Chile were nucleated on upper plate normal faults, including the M_w6.9 and 7.0 events of the Pichilemu earthquake sequence. We use the available coseismic GPS displacements, moment tensor sums, and slip distribution models for the Maule earthquake to compute the static strain and stress fields imposed on the upper plate by slip on the subduction interface. The extensional strains calculated from coseismic GPS and from a moment tensor sum of the Pichilemu events have similar orientations and orders of magnitude. The normal Coulomb stress increment (CSI) on the Pichilemu fault has maximum positive stresses as high as 4.9 MPa. Regionally, the Maule event produced a semi-elliptical, radial pattern of static extension and deviatoric tension (CSI >1.5 MPa) along the Coastal Cordillera enclosing the rupture area. This elliptical pattern mimics the trends of the major upper crustal structures. The static deformation field produced by a great subduction earthquake is an effective mechanism for generating permanent extension above the seismogenic zone,

*Originally published as: Aron, F., R. W. Allmendinger, J. Cembrano, G. González, and G. Yáñez (2013), Permanent fore-arc extension and seismic segmentation: Insights from the 2010 Maule earthquake, Chile, *Journal of Geophysical Research: Solid Earth*, *118*(2), 724–739, doi:10.1029/2012JB009339. Reprinted with permission of the American Geophysical Union.

reactivating suitably-oriented, long-lived normal faults. We suggest that the semi-elliptical outline of the first-order structures along the Coastal Cordillera may define the location of a characteristic, long-lived megathrust segment. This observation implies a persistence at least over the Quaternary of great subduction ruptures along the Maule segment.

3.2 Introduction

On February 27, 2010, approximately 600 km of the Nazca-South America plate boundary ruptured to generate the M_w 8.8 Maule earthquake on the subduction megathrust beneath central Chile (Fig. 3.1). Curiously, the two largest aftershocks were intraplate normal fault earthquakes with magnitudes of M_w 7.4 and M_w 7.0, the first located in the outer rise of the down-going oceanic slab and the second within the upper plate forearc, directly above the rupture area (Fig. 3.1 and Appendix section B1). In many parts of the Chilean Coastal Cordillera, where it overlies the zone of interplate seismogenic coupling, Neogene-Quaternary normal faults outnumber reverse faults, especially north of 33°S but also in the Maule segment (*Katz*, 1971; *Benado*, 2000; *Heinze*, 2003; e.g., *Allmendinger and González*, 2010; *Aron et al.*, 2012). The 2011 M_w 9.0 Tōhoku, Japan, subduction zone earthquake was also accompanied by a significant number of upper plate normal aftershocks (e.g., *Lay et al.*, 2011; *Toda et al.*, 2011a, 2011b). How do upper plate normal faults relate to interplate boundary thrusting, and are there specific conditions that favor formation of normal faults?

Figure 3.1: Shaded relief of the Maule earthquake region in central Chile. The rupture segment is approximately enclosed by the black ellipse. The circles show the location of intraplate normal aftershocks from February 27, 2010, to July 31, 2012, reported in the Global CMT catalog. The aftershocks size is scaled by moment magnitude and the color code is explained in the Appendix section B1. Also, the focal mechanisms and moment magnitudes of the 5th largest aftershocks are shown. The lines over the continent correspond to upper-crustal faults (*Katz*, 1971; *Gana et al.*, 1996; *Wall et al.*, 1996; *SERNAGEOMIN*, 2003; *Melnick et al.*, 2006, 2009; *Geersen et al.*, 2011; *Aron et al.*, 2012). Red, blue and gray are normal, reverse and undetermined faults respectively. The weight of the lines distinguishes between certain and inferred structures. The box depicts the Pichilemu sequence area enlarged in Figure 3.3. The black line at the east delineates the Chile-Argentina border and the approximate location of the ~NS-running volcanic arc. Digital elevation model based on ETOPO2 (*NOAA*, 2006).

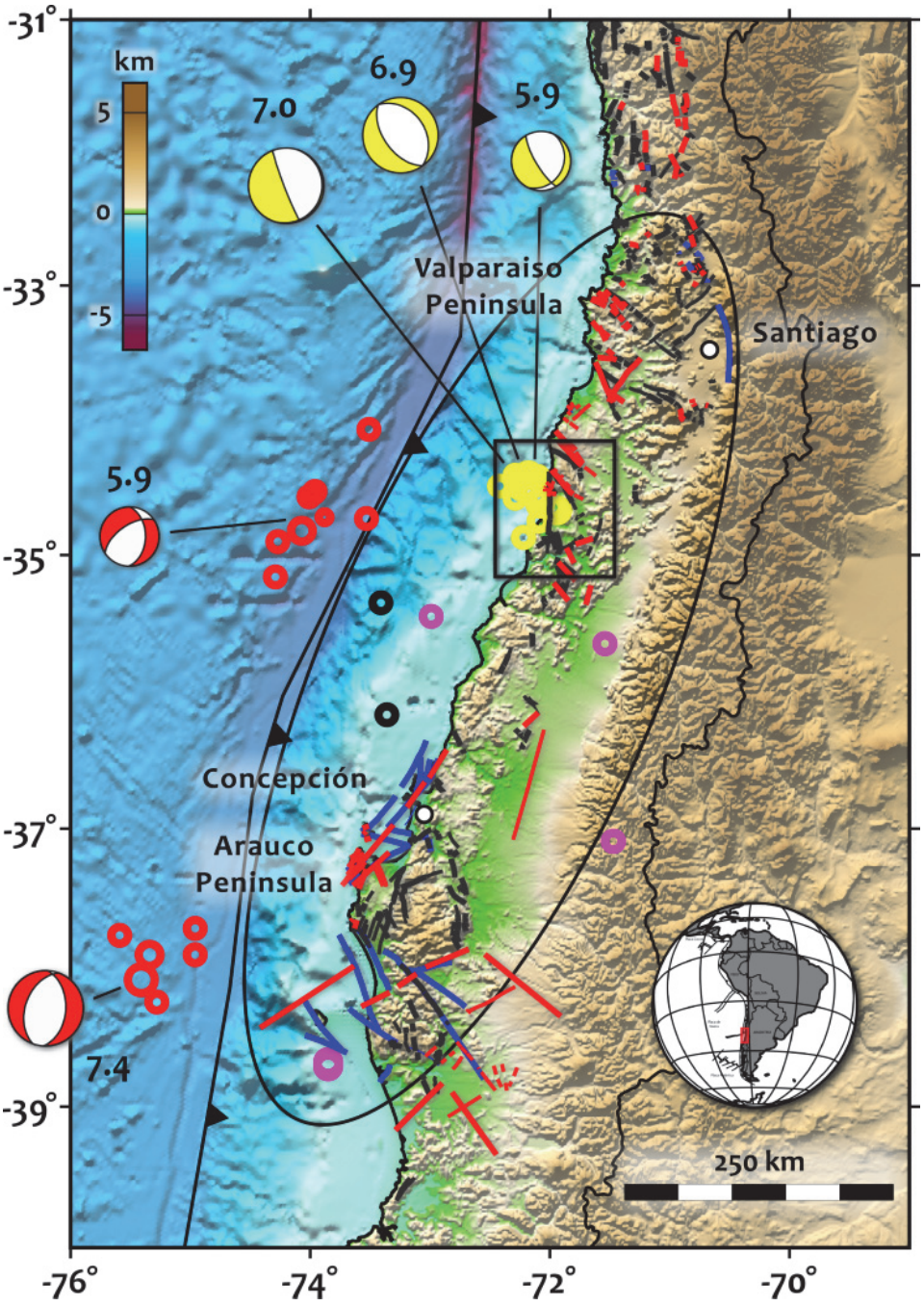
km
5
0
-5
7.0
6.9
5.9
5.9
7.4
Valparaiso
Peninsula
Santiago
Concepción
Arauco
Peninsula
250 km
-31°
-33°
-35°
-37°
-39°
-76°
-74°
-72°
-70°

For the Chilean margin, a common answer to this question is that upper plate normal faults in the north are strictly related to subduction erosion (e.g., *Armijo and Thiele*, 1990; *von Huene and Ranero*, 2003), and that any normal faults in the accretionary part of the Chilean forearc, south of 33°S, are local features related to anticlinal folding above propagating thrust faults in the accretionary wedge (*Melnick et al.*, 2006). This common view, however, does not explain several key observations, including (1) local network seismic data that show that the Pichilemu fault cuts most of the crust (*Farías et al.*, 2011), (2) existence of young normal faults in Paleozoic bedrock outside of the accretionary wedge, (3) normal fault focal mechanisms accompanying many great subduction earthquakes, or (4) the relatively common observation that upper plate faults have moved as both normal and reverse faults during their long-term history (*Melnick et al.*, 2006; *Allmendinger and González*, 2010). We suggest here a more nuanced explanation that acknowledges the profound influence that great subduction earthquakes, like the Maule megathrust, produce on the state of stress in the upper plate, even in accreting plate margins.

We combine geophysical and geological data with principles of linear elasticity, dislocation theory and Coulomb rock fracture criteria to explore how permanent upper plate deformation relates to release of elastic strain energy during great earthquakes. Modeling the infinitesimal static strain and stress fields imposed on the upper plate by the interplate megathrust, we provide a mechanical explanation for continental M_w 7.0 intraplate normal faulting triggered by the Maule earthquake. By comparing the coseismic and interseismic crustal deformation signals, we propose that cyclical unloading of the upper plate during great subduction earthquakes may generate a permanent, distinctive extensional pattern in the structural grain to the forearc. This pattern may represent the average behavior over many thousands of subduction seismic cycles throughout the geologic time and we suggest that might be used to

identify characteristic, long-lived rupture segments.

3.3 Tectonic and Structural Settings

Subduction zones are one of the most tectonically active provinces in the planet. The plate convergence forces, at least in the upper brittle part of the lithosphere, are transmitted to both plates in the form of shear stresses (*McCaffrey*, 1994; *Lallemand et al.*, 2005; *Lamb*, 2006) on a "dual behavior" locking-slipping fault that constitutes the seismogenic portion of the plates interface (Fig. 3.2) (*Scholz*, 2002). The dual behavior is reflected in the seismic cycle. This can be divided into an interseismic period of full to partial coupling of the interface, with a duration in the scale of the hundreds of years for time intervals between events of magnitude > M_w 8.5 (*Rikitake*, 1976; e.g., *Minoura et al.*, 2001; *Satake and Atwater*, 2007), and a coseismic-post-seismic period, minutes-to-months long (*Reid*, 1910; *Scholz*, 2002). The later encompasses rapid slip on the subduction megathrust and continuous accommodation of strain due to aseismic afterslip and thrust aftershocks. The two periods of the seismic cycle differ in the time scale and in the direction of the applied shear, which is approximately opposite in sense (Fig. 3.2). Postseismic deformation has been recognized as increasingly important (e.g., *Hu et al.*, 2004) but commonly has similar orientation to the coseismic deformation and the two are indistinguishable in the geologic record, which is our main concern here.

The Nazca-South America plate boundary accounts for 16 out of 89 of all the earthquakes greater than M_w 8.0 ever recorded up to July 31th 2012 (source USGS). Three of those are in the top fifteen, including the largest recorded in modern history (Valdivia M_w 9.5; *Kanamori* (1977)). The 2010 Maule earthquake, which is the focus of this paper, is the sixth largest since 1900.

Figure 3.2: Cross section, perpendicular to the Nazca-South America subduction zone, across the forearc of the Southern Andes. The figure shows the schematic orientation of the external (boundary) shear loads, denoted by black thin arrows, applied at the bottom of the upper plate during the interseismic (A) and coseismic (B) periods of the subduction cycle. The gray zone indicates the "dual-behavior" seismogenic zone. The gray gradient of the seismogenic zone as well as the relative size of the black arrows, represent simplistically the depth variation and distribution of both the coupling of the interface (A) and the megathurst slip (B). The black thick arrows and the parallel text indicate the displacement vector rate of the bottom of the forearc wedge (upper plate) for the 2 seismic periods, estimated from: (A) the plate convergence vector (references in Fig. 3.1) projected on the cross-section, and (B) the order of magnitude of the slip on megathrust planes during great subduction earthquakes. The main tectonic features of the Andean forearc are also shown. The inset graph on A represents the interseismic synthetic coupling function modeled in this study (see Appendix section B4.2). The topography is from ETOPO2 and the geometry of the top of the slab (oceanic lithosphere) is based on the Slab1.0 model by *Hayes et al.* (2012). The continental crust thickness is consistent with crustal depths reported by *Fromm et al.* (2004), *Krawczyk et al.* (2006) and *McGlashan et al.* (2008) for this region. The cross-section was traced at the center of the 2010 M_w 8.8 Maule rupture (Fig. 3.1) and intersects the coastline approximately at 72.6°W, 35.8°S.

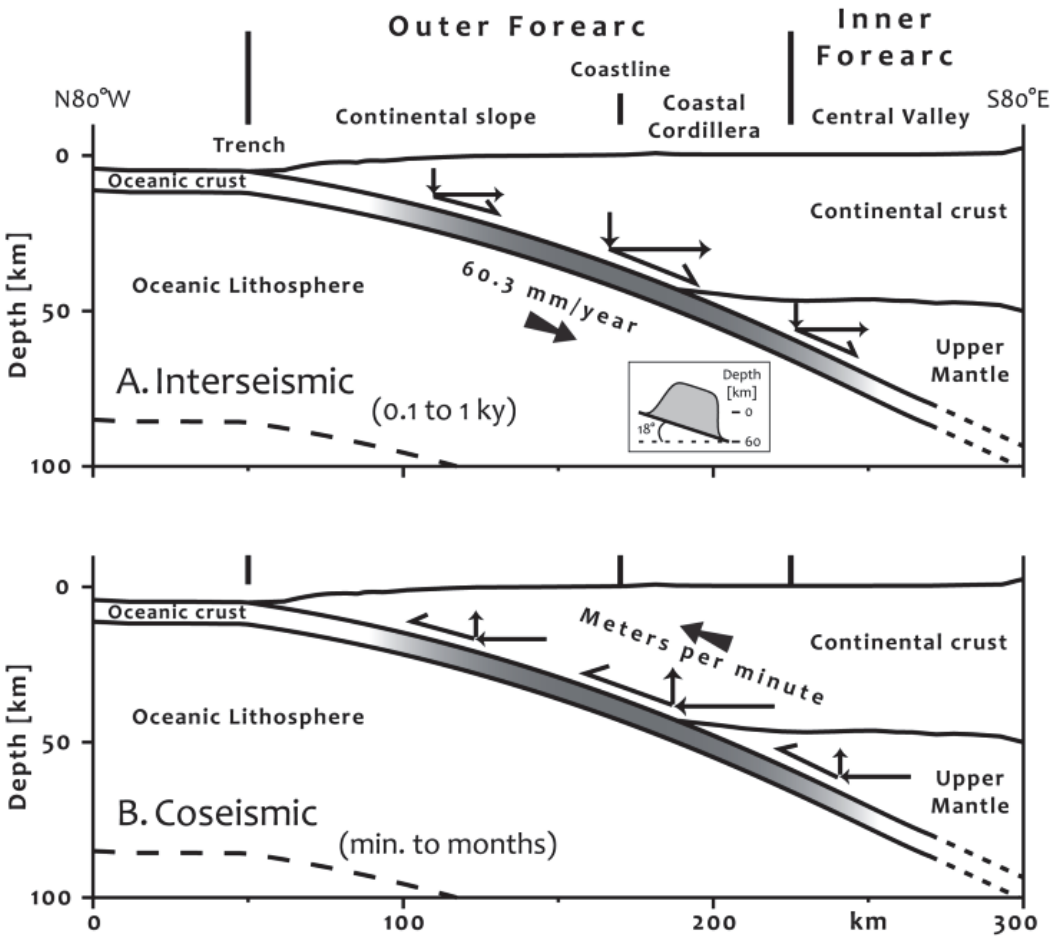
Outer Forearc
Inner Forearc
Coastline
N80°W
S80°E
Continental slope
Coastal Cordillera
Central Valley
Trench
Oceanic crust
Continental crust
Oceanic Lithosphere
60.3 mm/year
Upper Mantle
A. Interseismic
(0.1 to 1 ky)
Depth [km]
18°
0
60
Depth [km]
0
50
100
Meters per minute
B. Coseismic
(min. to months)
0
100
200
km
300

The upper plate deformation in a "Chilean" type of subduction zone has been characterized as highly compressional (*Uyeda*, 1982) with compression parallel to the convergence vector as determined by plate boundary related earthquakes and forearc GPS data (*Bevis et al.*, 2001; *Kendrick et al.*, 2001; *Klotz et al.*, 2001, 2006; *Ruegg et al.*, 2002, 2009; *Brooks et al.*, 2003), that record strong coupling of the plates down to approximately 50 km depth (*Tichelaar and Ruff*, 1991, 1993; *Suarez and Comte*, 1993; *Bevis et al.*, 2001; *Khazaradze and Klotz*, 2003; *Moreno et al.*, 2010, 2011, 2012). In other words, the maximum long- and short-term compressive stresses in the continent are both approximately parallel to the convergence vector (Fig. 3.2). In contrast, during the very short-term coseismic deformation, the portion of the forearc above the rupture area extends in the direction of the megathrust rebound (e.g., *Klotz et al.*, 1999, 2006).

Despite the highly compressive nature of the leading edge of the South American plate, a significant portion of the Central and Southern Andes, the outer forearc (Fig. 3.2), is dominated by kilometer-scale normal faults that run parallel and oblique to the plate boundary along the Coastal Cordillera. Structural studies documenting normal faulting are common north of the Maule rupture area (*Arabasz*, 1971; *Armijo and Thiele*, 1990; *Delouis et al.*, 1998; *Marquardt*, 1999; *Benado*, 2000; *González et al.*, 2003, 2006; *Heinze*, 2003; *Marquardt et al.*, 2004; *Allmendinger et al.*, 2005; e.g., *Allmendinger and González*, 2010; *Loveless et al.*, 2010), but some evidence for extensional structures in the Maule region is also available (*Katz*, 1971; *Wall et al.*, 1996; *Gana et al.*, 1996; *Lavenu and Cembrano*, 1999; *Lavenu et al.*, 1999; *Lavenu and Encinas*, 2005; *Melnick et al.*, 2006, 2009; *Cembrano et al.*, 2007; *Geersen et al.*, 2011; e.g., *Aron et al.*, 2012). *Melnick et al*. (2006, 2009) states that reverse faults in the Arauco Peninsula at the southern end of the Maule rupture seem to be relatively more abundant than the normal faults, especially compared to the Valparaiso

Peninsula (northern end), and in general to the rest of the Coastal Cordillera. However, they also show a puzzling coexistence of normal and reverse faults and inversion of the structures.

The normal fault-dominated structural style is active today and extends back in time to at least the Quaternary in the Maule region. For example, the Pichilemu normal fault shows evidence of successive offsets of a Pleistocene-Holocene? marine abrasion platform (*Aron et al.*, 2012). Some of these structures, like Pichilemu, may cut the upper crust all the way down until the plate interface, but others appear limited to just the upper crust (e.g., *Allmendinger and González*, 2010). The long-term direction of extension along the outer forearc (Miocene to Present) determined by these structures is approximately parallel to the convergence vector (*Lavenu et al.*, 1999; *Heinze*, 2003; e.g., *Cembrano et al.*, 2007), i.e., the orientation of the maximum compressive traction applied to the body during the time-dominant interseismic period (Fig. 3.2). There are, however, distinctive regions, such as between Valparaiso and Pichilemu or near the Mejillones peninsula, where these structures are more oblique to the continental margin.

Published explanations of forearc normal faulting include: (a) changes in the flat-ramp geometry of the slab (*Armijo and Thiele*, 1990), (b) subduction erosion and underplating (*von Huene and Lallemand*, 1990; *von Huene and Scholl*, 1991; *Delouis et al.*, 1998; *von Huene and Ranero*, 2003; *Hoffmann-Rothe et al.*, 2006), (c) crustal strain imbalance between the interseismic (accumulation) and the coseismic (release) periods that leads to plastic-permanent deformation (*Klotz et al.*, 2006), (d) elastic flexure and bending moment tension of the plates during the period of fully coupling (*Delouis et al.*, 1998; *González et al.*, 2003; *Loveless and Pritchard*, 2008; *Allmendinger and González*, 2010; *Loveless et al.*, 2010), and (e) an extensional static

or dynamic stress field produced by the elastic rebound during a great subduction earthquake (*Delouis et al.*, 1998; *Loveless and Pritchard*, 2008; *Allmendinger and González*, 2010; *Loveless et al.*, 2010). The last three hypotheses consider the earthquake cycle to be the driving mechanism for long-term deformation in the outer fore arc.

3.4 The Maule Earthquake

Rapid moment tensor solutions published for the 2010 Maule earthquake show a M_w 8.8 thrust fault focal mechanism, with a centroid located at 35.85°S, 72.72°W and 35 km depth (USGS; http://earthquake.usgs.gov/earthquakes/eqinthenews/2010/us2010tfan/neic_tfan_cmt.php), or at 35.98°S, 73.15°W and 23.2 km depth (Global CMT catalog; http://www.globalcmt.org/CMTsearch.html, Event name: 201002270634A). This megathrust earthquake filled the seismic gap from the 1835 earthquake (*Darwin*, 1845), and re-ruptured a segment that experienced a M 8 earthquake in 1928 (*Lomnitz*, 1970; *Kelleher*, 1972; *Nishenko*, 1985, 1991; *Beck et al.*, 1998; *Campos et al.*, 2002; *Ruegg et al.*, 2002, 2009). The Maule earthquake was located just north of the M_w 9.5 Valdivia earthquake in 1960. Inversions obtained from pre-earthquake geodetic data indicate that the seismogenic plate interface in the Maule area was strongly coupled up to the date of the event (*Ruegg et al.*, 2009; *Madariaga et al.*, 2010; *Moreno et al.*, 2010).

Several finite fault slip solutions for the Maule earthquake have been released, e.g.: G. Hayes (unpublished data, 2010; available online from the USGS web site: http://earthquake.usgs.gov/earthquakes/eqinthenews/2010/us2010tfan/finite_fault.php), G. Shao *et al.* (unpublished data, 2010; available online from UCSB web site: http://www.geol.ucsb.edu/faculty/ji/big_earthquakes/2010/02/27/chile_2_27.html), A.

Sladen (unpublished data, 2010; available online from Caltech web site: http://www.tectonics.caltech.edu/slip_history/2010_chile/index.html), *Delouis et al.* (2010), *Lay et al.* (2010), *Tong et al.* (2010), *Lorito et al.* (2011), *Pollitz et al.* (2011), *Vigny et al.* (2011) and *Moreno et al.* (2012) (see Appendix section B2). These models, based on inversions of teleseismic, geodetic and/or tsunami data, estimate a length of rupture of about 600-650 km, a width of approximately 200 km, strikes ranging between N16°-19°E and dips between 15°-18°E for the fault plane; some also solve for varying strike and dip for the different fault patches. The main slip is principally reverse with some variable and small components of strike-slip.

Most of the aftershocks $M_w > 4.8$ that followed the main shock reported by the Global CMT and NEIC (http://earthquake.usgs.gov/earthquakes/eqarchives/epic/epic_rect.php) agencies were thrust events that nucleated at the plate interface. However, approximately nineteen yielded normal focal mechanisms with hypocenters located within the upper plate of the outer forearc at depths varying between 12 and 20 km. An additional fifteen normal mechanisms were located in the lower plate (outer rise) near the trench (Fig. 3.1 and Appendix section B1). The thrust earthquakes occurring after the main shock produce discrete slip that fills both the areas of low slip (*Rietbrock et al.*, 2012) and the coseismically stressed areas on the plate interface, around the zones that concentrate most of the slip of the first motion (barriers). The normal earthquakes represent brittle intraplate deformation. It is notable that the outer rise earthquakes are located mostly along the traces of fracture zones in the subducting plate near the trench, at the north-central and southern parts of the segment (Fig. 3.1).

A cluster of upper crustal aftershocks located near the northern end of the rupture area, the Pichilemu sequence (*Arriagada et al.*, 2011; *Farías et al.*, 2011; *Ryder et al.*,

2012), started six days after the Maule earthquake and lasted for 269 days (Figs. 3.1, 3.3 and Appendix section B1). This cluster can be divided in three groups according to the strike of the nodal planes and to the alignment of the individual events: 1) the NNE-NE, 2) the ~NS and 3) the NNW-NW sequences. Some of the epicenters and the nodal planes, obtained from the moment tensor orientations of these earthquakes, coincide with the location and strike of major faults of the Coastal Cordillera that appear in the 1-million scale Chilean geological map (*SERNAGEOMIN*, 2003). Our recent field observations (*Aron et al.*, 2012) indicate that these large aftershocks were nucleated in a 321°-striking, SW-dipping normal fault that nearly coincides with one of the structures of the Chilean geologic map (Fig. 3.3). The maximum expression of the crustal normal fault cluster was on March 11th (twelve days after the main shock) with a M_w 6.9 and a M_w 7.0 events (12.9 and 16.3 km depth, respectively) which belong to the third sequence mentioned above (Figs. 3.1 and 3.3).

3.5 Kinematics of the Pichilemu Events

3.5.1 Moment Tensor Summation in Pichilemu and GPS Strain

Using data from the Global Centroid Moment Tensor catalog we sum the moment tensors for the Pichilemu sequence which is dominated by the two main shocks, M_w 6.9 and M_w 7.0 of March 11, 2010. The principal infinitesimal extension axis of the summed moment tensor has a trend and plunge of about 240°, 30° (Fig. 3.4). Unlike the orientation, the magnitude of strain from a moment tensor sum is particularly dicey given the uncertainty surrounding the volume of the region affected by the earthquakes. We calculate strain for a range of volumes, from an unrealistically small 10x10x10 km^3 to an unrealistically large 100x100x30 km^3. In between those extremes, the principal extensional strain varies from about 10^{-5} to 10^{-4} (Fig. 3.5).

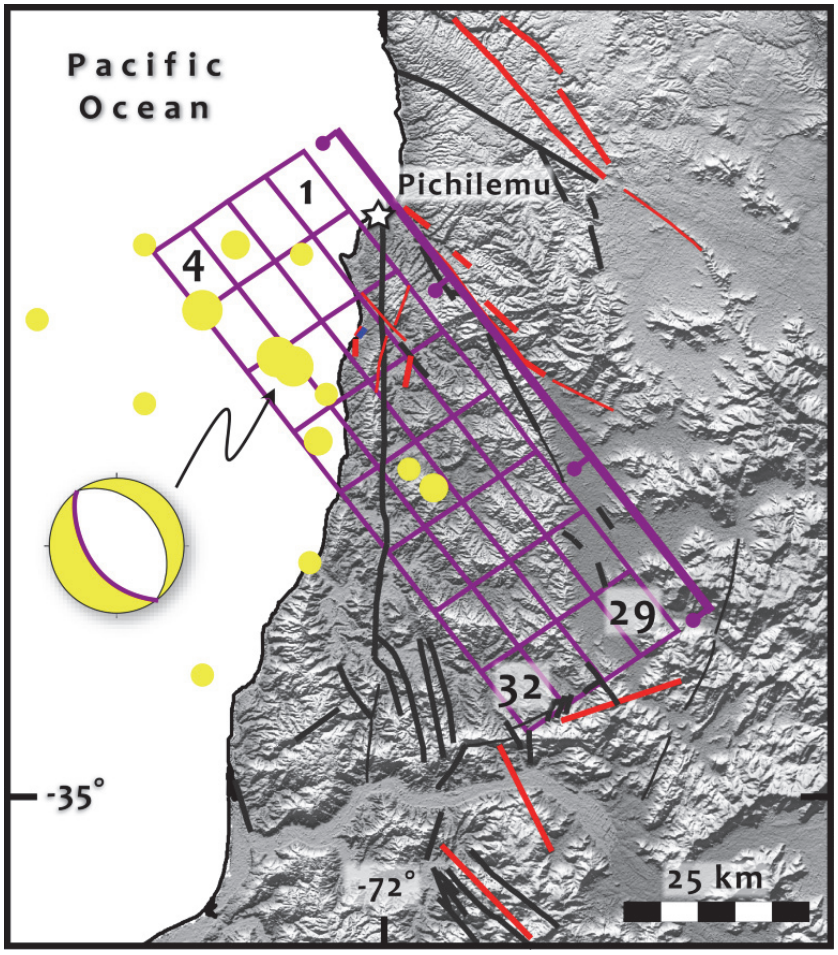

Figure 3.3: Close-up to the Pichilemu area. The blue grid corresponds to the horizontal projection of the normal fault modeled in this study, subdivided in 32 patches. The numerical order of the patches is referred to in the text and Table 3.2. The stereonet (lower hemisphere) shows the fault plane solution of the main aftershock that we use to determine the Pichilemu fault geometry. The red and gray lines are mapped crustal faults (one coincides with the modeled fault trace). Colored dots are explained in Appendix section B1. The geographic location of the Pichilemu area is shown in Figure 3.1 and the star indicates the location of the Pichilemu town. Altitude data from ASTER GDEM, which is a product of METI and NASA.

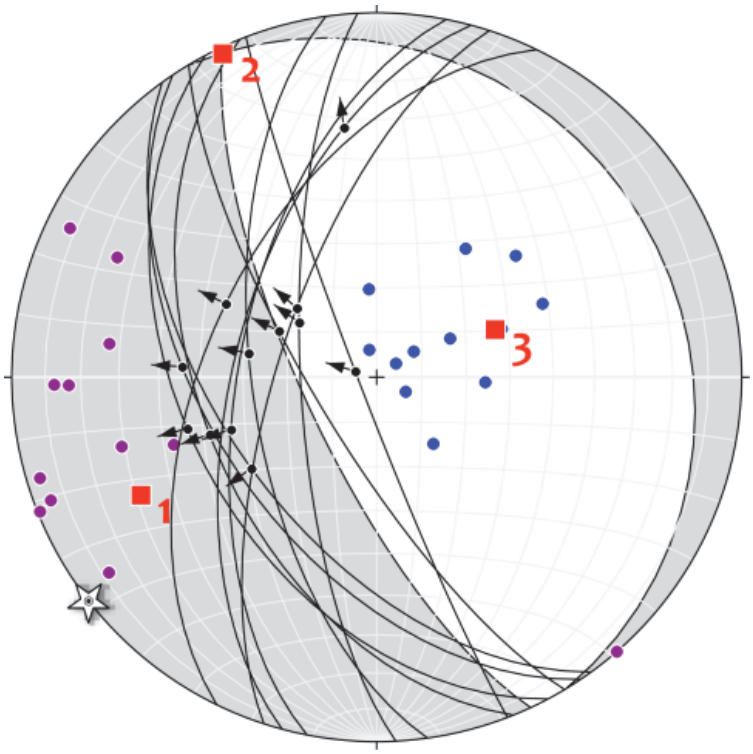

Figure 3.4: Kinematics of the Pichilemu aftershock sequence depicted in a lower hemisphere projection. All events with M_w>=5 are shown. The dots show P and T axes of individual events; we have selected the nodal planes (great circles) and slip directions (arrows) most likely to represent the fault plane based on distribution of aftershocks described by *Comte et al.* (2010) and *Farías et al.* (2011). Principal axes of the symmetric moment tensor (i.e., the infinitesimal strain tensor) are shown by large red boxes. The numbers indicate: 1 - principal extension axis, 3 - principal shortening axis, and 2 - intermediate axis underlying fault plane solution derived from the moment tensor sum. The white star shows the orientation of the principal infinitesimal extension axes calculated from the seven nearest GPS stations.

Coseismic GPS provides a different measure of strain, one restricted just to the surface on which the GPS stations lie. Because of the two dimensional nature of the rupture area and the fact that Pichilemu lies at the northern end of rupture, the traditional geophysical approach of constructing a 1D transect of displacement versus distance does not work. Furthermore, there were no GPS stations within 55 km of Pichilemu, itself. Therefore, we invert the coseismic displacement field (*Vigny et al.*, 2011; *Moreno et al.*, 2012) for a distance weighted, best-fitting displacement gradient tensor from which we extract the infinitesimal strain tensor (*Allmendinger et al.*, 2009; *Cardozo and Allmendinger*, 2009). The analysis shows that the highest extension magnitudes are located just to the south of Pichilemu (Fig. 3.6). The regionally smoothed principal extension axis orientation is 080-260°, with a magnitude of 1.4 x 10^{-5}.

Using just the seven nearest stations — three to the north and four to the south of Pichilemu (Fig. 3.6) — we calculate a best fit principal extension axis oriented with an azimuth of 063-243°, and a magnitude of 2.3 x 10^{-5} (Fig. 3.6). As in the case of earthquakes, the magnitude of strain determined from GPS vectors is subject to several limitations: stations are not uniformly distributed, the strain is not homogeneous, and the magnitude depends on the length scale over which it is measured. Nonetheless, we note that the coseismic extension measured by GPS and the strain due to the Pichilemu earthquakes sequence, have very similar orientations and are well within an order of magnitude of each other (Figs. 3.4 and 3.5).

3.5.2 Regional Strain Field

Our second approach to the coseismic deformation caused by the Maule event is to calculate the infinitesimal strain field in three dimensions from discrete displacements of the upper crust (following methods described by *Allmendinger et al.*,

2009; *Cardozo and Allmendinger*, 2009). We use a distance-weighted least squares inversion to obtain displacement gradient tensors calculated over a regular grid. Note that the size of the grid only influences the visual smoothness of the solution but does not affect the magnitudes or orientations calculated.

To see the complete upper plate kinematic field, we combine the observed GPS with the slip vectors on the fault patches from the different published Maule slip models in a South America fixed reference frame. The displacements utilized were: (a) The coseismic static GPS displacements published by *Vigny et al.* (2011) and *Moreno et al.* (2012) (Fig. 3.6); and (b) slip vectors from the finite fault models published by G. Hayes, G. Shao *et al.* and A. Sladen (all unpublished data, 2010; refer to section 3.4 for web sites) (Appendix section B2). These three slip models were chosen to avoid circular calculations because they are only based on seismic data and not GPS data.

In this way we constrained the inversion of the applied displacements from above and below the deformed body, i.e. the outer forearc wedge. The inclusion of the interface slip distribution not only constrains the 3-dimensional displacement gradients, but also offers much better resolution for the strain calculation in the volume above the rupture area.

Like the GPS vectors, alone, the inversion of coseismic GPS displacements and static fault slip displacements show a widespread volume of a positive extensional field, covering the entire forearc above the Maule segment (Fig. 3.7 and Appendix section B3). The models produced a radial pattern of static extension (predominantly trench-perpendicular) and semi-elliptical pattern of shortening axes enclosing the rupture area and the zones of maximum slip (Fig. 3.7 and Appendix section B3). We return to this pattern in the discussion section.

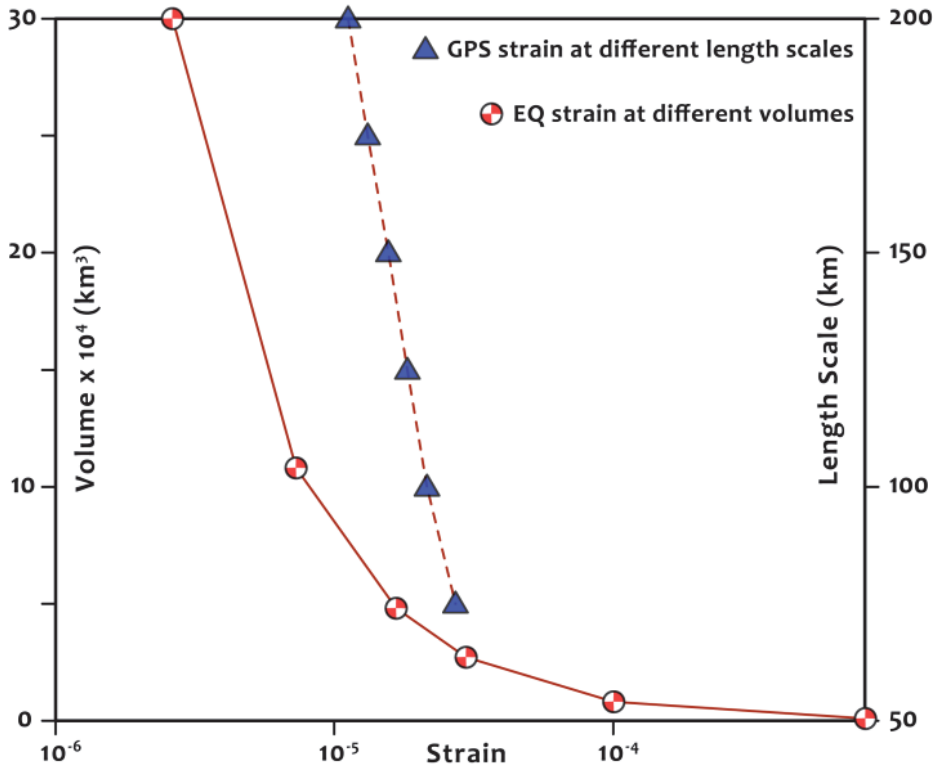

Figure 3.5: Static coseismic strain calculated from an earthquake moment tensor sum for the Pichilemu sequence (Fig. 3.3), and from coseismic GPS data from *Vigny et al.* (2011) and *Moreno et al*. (2012). Graph shows the dependence of the magnitude of the coseismic strain on the volume of the region (in the case of earthquakes) or distance weighting factor (in the case of GPS). Nonetheless, for reasonable volumes and length scales, the strain from both earthquakes and coseismic GPS is on the order of 10^{-4} to 10^{-5}.

Figure 3.6: Regional static coseismic extensional strain field over the continent, calculated from coseismic GPS (*Vigny et al.*, 2011; *Moreno et al.*, 2012). The box delineates the Pichilemu area which is affected by the greatest extension at the Earth surface. The 2-dimensional station displacements are exaggerated by a factor of 3 x 10^4. The net strain magnitudes are relative to the distance weighting factor used (Alpha). To generate this plot we use an Alpha value of 80 km and a grid space of 15 by 15 km; the grid size only affects the smoothness of the plot, not the magnitude or orientation. The coseismic displacement vectors are referenced with respect to stable South America.

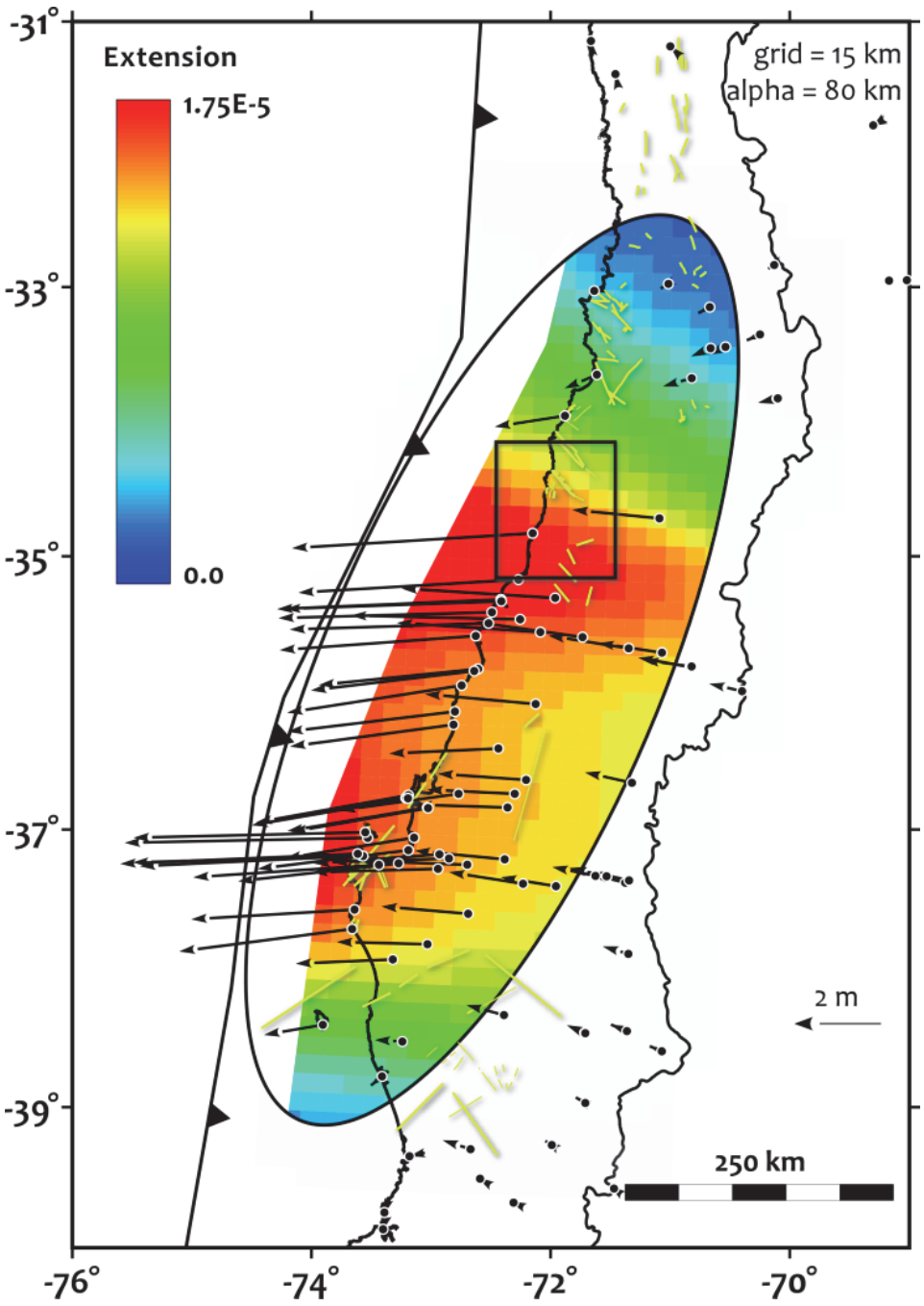
Extension
1.75E-5
0.0
grid = 15 km
alpha = 80 km
2 m
250 km
-31°
-33°
-35°
-37°
-39°
-76°
-74°
-72°
-70°

Figure 3.7: Regional coseismic infinitesimal strain field above the Maule segment. Here we use static GPS displacements and slip on the megathrust from the teleseismic finite fault model by G. Hayes (unpublished data, 2010). All the displacement vectors (slip and GPS) are referenced with respect to stable South America. Green-blue crosses represent the orientation of the infinitesimal strain tensor at each horizontal grid element. Green is principal extensional and blue principal shortening axes. Note the semi-elliptical pattern outlined in the continent by the shortening axes. Note also the orthogonality relations between the crustal faults (yellow lines) and the extensional axes. Almost all of the coseismic static strain over the continent is extensional, oriented orthogonal and oblique to the plate boundary, and is concentrated along the forearc. More results using the teleseismic fault slip models by G. Shao *et al.* (unpublished data, 2010) and A. Sladen (unpublished data, 2010) can be found in the Appendix section B3.

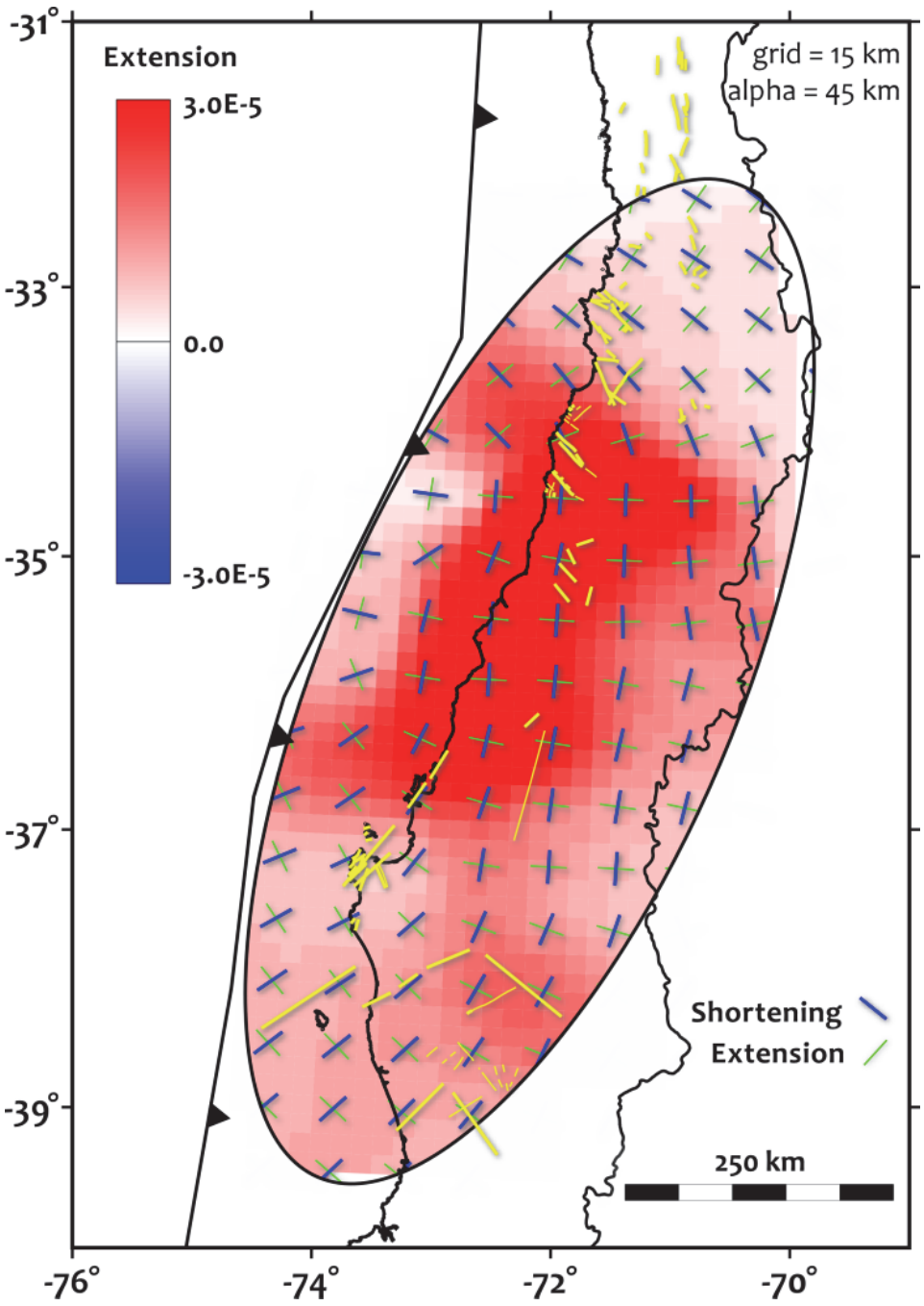
Extension
3.0E-5
0.0
-3.0E-5
grid = 15 km
alpha = 45 km
Shortening
Extension
250 km
-31°
-33°
-35°
-37°
-39°
-76°
-74°
-72°
-70°

3.6 Coulomb Stress Increment

3.6.1 Theoretical Background

We also take a static mechanical approach to determine the coseismic deformation field by using an analytical solution based on Volterra's theory of dislocations (*Volterra*, 1907). This theory was first developed to study earthquakes by *Steketee* (1958) and completely defined by *Okada* (1992). The fault plane is represented mathematically as a dislocation in an infinite, homogeneous elastic half-space. The shear vectors on the source fault (or megathrust), or distributed slip vectors in the case of finite discrete fault models, produce opposite displacement couples of the blocks separated by the dislocation, and generates an elastic perturbation or distortion of the material surrounding the discontinuity (Fig. 3.2). This process is expressed in an internal displacement field (*Okada*, 1992).

The determination of the coseismic internal deformation field using theory of dislocations and subsequently the Coulomb stress increment or Coulomb stress change (hereafter CSI) resolved on receiver faults (like Pichilemu), has been extensively and successfully utilized to assess how the coseismic stress transfer affects the structures near the source fault, and how it triggers new earthquakes (aftershocks) around the source (e.g., *Chinnery*, 1963; *Press*, 1965; *Das and Scholz*, 1981; *Oppenheimer et al.*, 1988; *King et al.*, 1994; *Stein et al.*, 1994; *Harris*, 1998; *Stein*, 1999; *Lin and Stein*, 2004; *Freed*, 2005; *Toda et al.*, 2011a). A brief summary of the mechanical theory behind these methods is given in the Appendix (section B4) of the article.

Here, we produce coseismic forward models of the static CSI on the Pichilemu receiver fault and coincident nodal planes of the M_w 6.9 and M_w 7.0 normal events of March 11th (Figs. 3.1, 3.3 and Table 3.1; see also Appendix section B1). Also, we compute the strike of "optimally oriented" normal faults on horizontal grids at

different depths covering the entire forearc above the Maule rupture area. The optimal orientation is defined by the maximum value of CSI modeled at each grid element, which is also shown in our results as color contoured maps, along a normal slip vector with rake = −90° (Appendix section B4.1).

Because the determination of coseismic slip is an inverse algebraic problem with no unique solution, we test all the available finite fault models that have published the slip distribution data (papers by: *Delouis et al.* (2010), *Lorito et al.* (2011), *Vigny et al*. (2011) and *Moreno et al*. (2012), and web open sources by: G. Hayes, G. Shao *et al.* and A. Sladen; 2010) (Appendix section B2). Models for great ruptures that are based only on teleseismic data, do not reliably solve for the slip distribution (*Pritchard et al.*, 2007). Although our calculations use all the fault slip models mentioned, we prefer the fault slip models which are based on a much more comprehensive data matrix for the slip inversion (i.e., models by: *Lorito et al.*, 2011; *Vigny et al.*, 2011; *Moreno et al.*, 2012). The *Lamé* constants were determined using average values for upper crustal materials of Elastic modulus and Poisson's ratio (*Turcotte and Schubert*, 2002). The static coefficient of friction (μ') was set following the criteria adopted by *Byerlee* (1978) and *Sibson* (1985) for preexisting faults and intact rocks (Table 3.1; see Appendix for mathematical details about how the material properties parameters relate to the CSI on receiver faults). The selection of the nodal plane, location and dimensions of the Pichilemu normal receiver fault, which cuts through the entire upper plate, were based on the information reported in the Chilean geological map (*SERNAGEOMIN*, 2003), the works by *Farías et al.* (2011) and *Ryder et al.* (2012), and in our field observations (*Aron et al.*, 2012) (Fig. 3.3).

Table 3.1: Input parameters used in our mechanical modeling

Source fault slip	Material properties[b]			Pichilemu receiver normal fault parameters (rake: -90°)[c]					
	E [GPa]	ν	μ'	Strike	Dip	Length [km]	Width [km]	T D [km]	U W c
Finite fault models[a]	75	.25	.75	N36°W	55°SW	70	35.4	1	72.1°W, 34.2°S

[a]Delouis et al. (2010), Hayes (2010), Shao et al. (2010), Sladen (2010), Lorito et al. (2011), Vigny et al. (2011), Moreno et al. (2012) and synthetic interseismic locking.
[b]*E*: elastic modulus, ν: Poisson's ratio (*Lamé* constants parameters).
[c]T D: Top tip line depth, U W c: coordinate of upper west corner. The fault was subdivided in an 8 (L) by 4 (W) grid.

Table 3.2: Summarized results of the coseismic CSI resolved on the Pichilemu normal fault[a]

Finite source fault Model	CSI (MPa)					
	Max all (patch)	Min all (patch)	Average	Max safe	Min safe	Average safe
Hayes (2010)	9.30 (4)	0.93 (29)	2.26	2.63 (11)	0.93 (29)	1.69
Sladen (2010)	0.70 (12)	0.13 (32)	0.43	0.62 (25)	0.13 (32)	0.40
Shao et al. (2010)	3.72 (4)	0.36 (29)	1.49	2.27 (16)	0.36 (29)	1.24
Delouis et al. (2010)	4.00 (16)	0.59 (1)	2.00	4.00 (16)	0.59 (1)	1.84
Lorito et al. (2011)	3.56 (12)	0.52 (3)	1.95	3.04 (20)	1.42 (2)	1.88
Vigny et al. (2011)	4.58 (8)	1.70 (29)	2.43	2.72 (1)	1.70 (29)	2.28
Moreno et al. (2012)	4.87 (24)	-120.26 (8)	-2.37	4.87 (24)	2.38 (1)	3.16

[a]The Pichilemu fault was subdivided in 32 patches (4 along dip by 8 along strike, see Fig. 3.5). Maximum, minimum and average CSI values are for the entire set of results (columns 2-4) and for the "safe area" (5-7) explained in the text.

The receiver fault was subdivided in 32 patches to obtain more precise and detailed calculations of the CSI distribution on the fault plane, and to avoid that possible singularities in the calculation of the CSI near the source slip model were included in the complete fault plane average (Fig. 3.3). We assumed no external stress acting on the elastic half-space to assess exclusively the coseismic deformation.

Somewhat similar analyses of CSI have been carried out by *Farías et al.* (2011) and *Ryder et al.* (2012). Our approach differs in that we compute alternative models offering a statistical range of possible solutions; we model the reactivated structure in detail and include an analysis of GPS and moment tensor data lacking in these other articles. Moreover, in the following sections, we provide a mechanical comparison to the interseismic period and a regional perspective about the genetic relation between the structural grain of the forearc and the seismic cycle.

3.6.2 The Interseismic CSI Analysis

To explore the potential of the interseismic deformation field to generate forearc permanent extension compared to the coseismic field, we simulate a simple dislocation model of the Maule segment throughout an interseismic period of 150 years, which falls within the recurrence times of subduction earthquakes estimated for the Andes (*Lomnitz*, 1970; *Nishenko*, 1985, 1991; e.g., *Comte and Pardo*, 1991). We based our simulation on a "backslip" model (*Savage*, 1983), hypothesizing that the finite upper plate deformation field over Maule is created by shear stress transfer at the plates interface (Fig. 3.2). This external shear acts constantly during the entire interseismic cycle due to the interplate locking and the continuous plate convergence.

Here we present a synthetic semi-2D approximation of the subduction interface along the Maule segment, divided in 3 segments with variable strike, which mimics the trend of the trench (Appendix section B2, Figure B9). This approach does not

include the sophisticated interseismic coupling models of *Moreno et al.* (2010). Though crude, our model is consistent with the overall interseismic stress field determined by other methods which consider second-order effects such as: strain rate, rheology inhomogeneities, elasto-plastic and viscous behaviors of the material, and thermal effects near the volcanic arc (e.g., *Yáñez and Cembrano*, 2004). The mathematical specifications and theoretical foundations behind our approach are explained in the Appendix, section B4.2.

The upper tip line of the plate interface lies on the trench axis (~4.5 km depth) and we extend the full-to-partially coupled zone (>25%; see Appendix Figure B12) down to the seismogenic zone depth (~50 km), in agreement to the reported data for Maule (*Tichelaar and Ruff*, 1991, 1993; *Suarez and Comte*, 1993; *Khazaradze and Klotz*, 2003; *Ruegg et al.*, 2009; *Moreno et al.*, 2010, 2012; *Métois et al.*, 2012). We used a constant value of 18° for the dip angle of the 3 segments (Fig. 3.2 and Appendix Figure B9) based on the recent world slab model contributed by *Hayes et al.* (2012). The interseismic slip deficit vector has a rake of −77° and a maximum magnitude of 9.75 m (6.5 mm/year over 150 years), according to the Nazca-South America convergence vectors reported for the latitudes of Maule (*Angermann et al.*, 1999; *Norabuena et al.*, 1999; *Kendrick et al.*, 2003). The plate interface was discretized in 11 down-dip elements and 13, 19 and 13 along-slip elements for the south, central and northern segments. In our reconstruction we avoid superposition of elements and gaps of patches on the subduction interface (Appendix Figure B9). Similar to the coseismic modeling, the calculation of the upper plate stress field and the CSI on the intraplate faults uses the material properties listed in Table 3.1; we imposed no external fields to assess specifically the interseismic deformation generated by the stress transfer at the plates interface. Our use of dislocations and CSI to determine the stress field assumes that interseismic deformation is a result of a

static mechanics and not dynamics over the 150 years of slow shortening.

For the coseismic and interseismic periods, both calculations — the internal deformation field and the CSI — were run with the Matlab code Coulomb 3.2., developed by the "Team Coulomb", USGS.

3.6.3 Results from the Maule Seismic Segment

3.6.3.1 The Pichilemu Normal Fault

The coseismic stress tensor, resolved in the rake direction of the normal fault responsible of the Pichilemu aftershocks (CSI along a -90° rake), encourages slip on the structure (Fig. 3.8). For all the models tested (Table 3.2), we obtained positive values of CSI ranging from a minimum of 0.13 MPa, to a maximum of 9.30 MPa (note that the very high negative value showed in Table 3.2 is clearly a model artifact). The maximum values are some of the highest CSI estimations reported in any study and agree with maximums estimated by *Ryder et al.* (2012). However, the lower left corner of the modeled Pichilemu fault almost intersects the slip area of the subduction megathrust; it is possible that the CSI calculation on the patches of that corner are biased by singularities caused by proximity to the source (Fig. 3.3). To avoid this potential artifact, we omit some of the Pichilemu fault patches from the calculation to produce a more realistic estimate of a CSI maximum value of 4.87 MPa and the same minimum value as before (colums 5-7 or "safe area" in Table 3.2).

3.6.3.2 Regional Coseismic Coulomb Stress Increment

To extend these results to the entire forearc, we calculate the CSI and strike of the optimally oriented normal faults over a horizontal grid divided in 30 by 30 km elements, at different depths, covering the region affected by the Maule earthquake (Fig. 3.9a). Our resulting preferred fault orientation and stress magnitude are similar for each of the input slip models and calculation depths so we show the regional model

Figure 3.8: Coseismic CSI resolved on the Pichilemu normal receiver fault. The results from the fault slip models by *Lorito et al.* (2011) (a), *Moreno et al*. (2012) (b) and *Vigny et al*. (2011) (c) are shown here as representative examples (all based on geodetic data). The close-up area is the same as that on Figure 3.3. Positive stress values (red colors) mean faulting enhancement in a -90° rake direction (normal). Note that the negative values of CSI in model (b) are singularities because of the proximity of these patches to the source fault. For details about the fault geometry please refer to Figure 3.3, Table 3.1 and section 3.6.1. Numerical results of maximum and average CSI across the fault plane can be found in Table 3.2. More solutions for different slip models are found in the Appendix section B5.

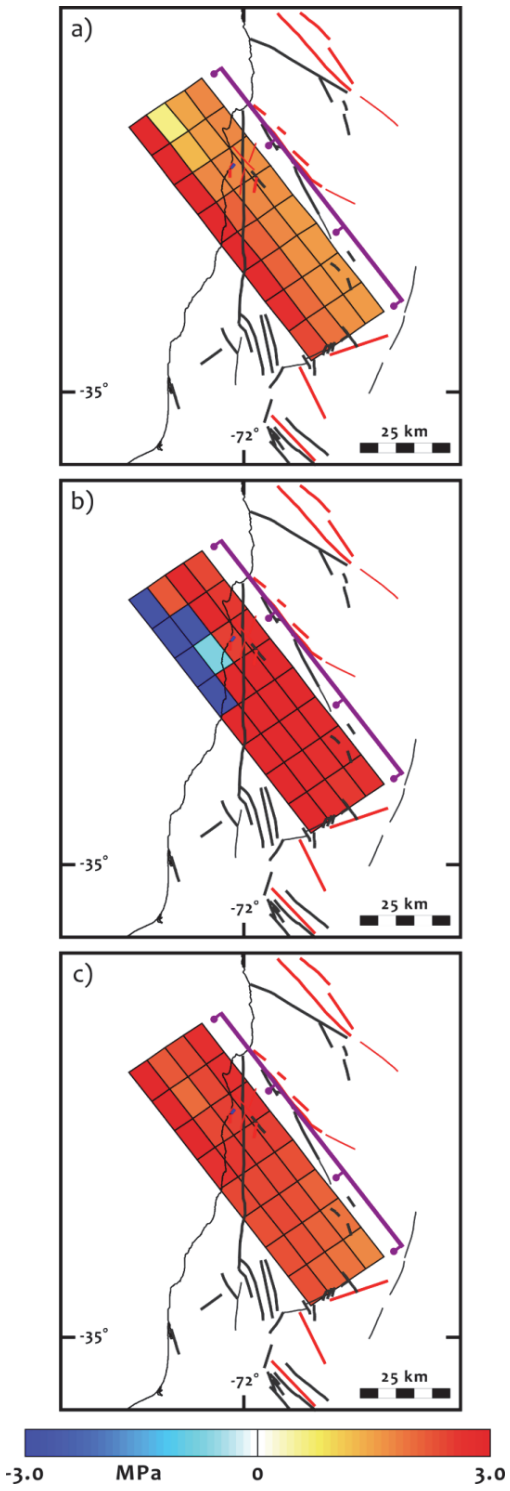
a)
-35°
-72°
25 km
b)
-35°
-72°
25 km
c)
-35°
-72°
25 km
-3.0
MPa
0
3.0

using the slip distribution by *Vigny et al*. (2011), computed for 10 km depth (Fig. 3.9a) (and relegate the remaining models to the Appendix data section B6). As in the analysis of the Pichilemu fault, the regions of very high CSI near the trench (both, positive and negative) are caused by singularities where the source slip model intersects the calculation surface. Near the toe of the upper plate wedge, a region in the submarine portion of the forearc shows negative values of CSI (Fig. 3.10a). The negative stress field suggests enhanced development of reverse faulting in the region overlying that part of the subduction zone that experienced an up-dip decrease in slip on the seaward side of the slip maximum, generating a negative slip gradient. This result agrees with the observations of *Melnick et al.* (2012).

Most of the onshore forearc above the rupture, however, is highly affected by a coseismic tensional field (compare Figs. 3.7 and 3.9a), consistent with the infinitesimal strain analysis. This widespread field extends down to the plate interface. The volume of continent in and around the Pichilemu sequence, approximately $7.5x10^5$ km^3, was highly stressed, with positive values of CSI on optimally oriented normal faults exceeding 1.5 MPa (Figs. 3.9a and 3.10a). The coseismic stress field encourages normal faulting oriented sub-parallel and oblique to the plate boundary in all of the onshore forearc. Like the strain field (Fig. 3.7), the maximum values of CSI, all greater than 1.0 MPa, on optimally oriented normal faults are concentrated along the Coastal Cordillera (Fig. 3.9a). The strikes of these idealized faults form a semi-elliptical pattern around the zones of maximum slip on the finite fault models (Fig. 3.9a and Appendix section B6). The modeled normal faults at the southern end are mostly oblique with respect to the continental margin striking ~NE, sub-parallel to the margin along the center of the rupture and again, oblique at the northern end striking ~NW (Fig. 3.9a). More importantly, many mapped upper plate faults coincide in orientation with the model fault traces (Fig. 3.11 and Appendix section B7);

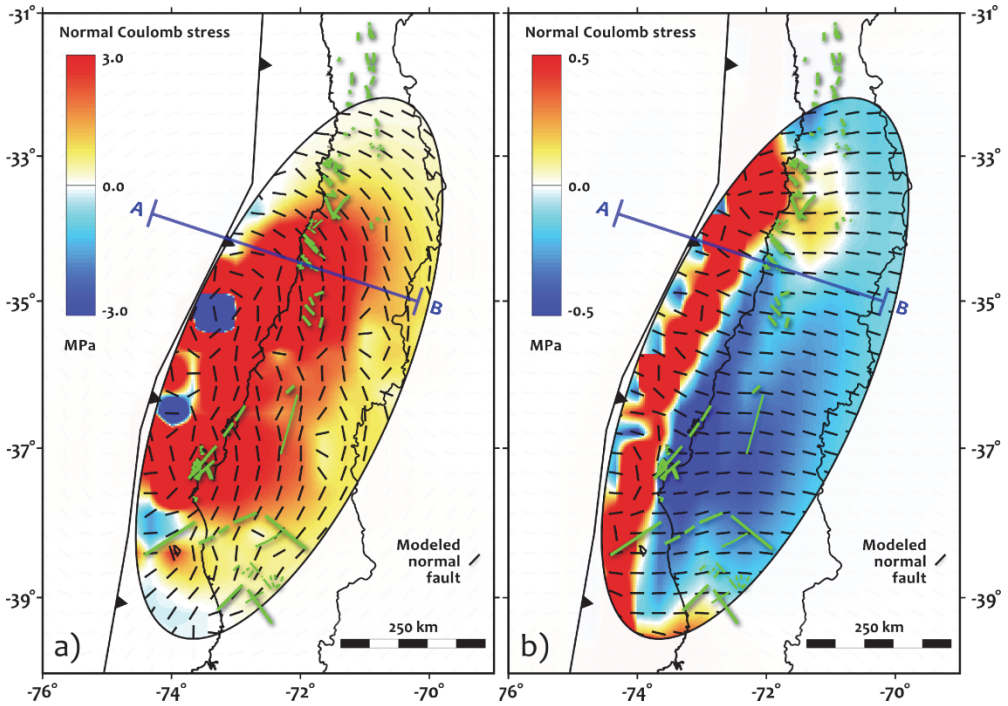

Figure 3.9: Coseismic (a) and interseismic (b) regional CSI over the continent resolved on "optimally-oriented" modeled normal faults (rake -90°), calculated at 10 km depth, above the Maule subduction segment.

(a): We use here the results of the slip model by *Vigny et al*. (2011) to exemplify the stress field imposed in the upper-crust by the Maule earthquake. Please refer to Appendix section B6.1 for more results using different fault slip models. The black lines represent the strike of the modeled faults at each element of the horizontal grid and the green lines are mapped normal faults. Positive CSI values (red colors) mean that normal faulting is enhanced. The magnitude of each square of the grid is determined by the stress resolved on the modeled fault which optimal orientation determines the highest possible value of CSI at the specific location of the element (see Appendix section B4.1).

(b): Interseismic coupling model the CSI resolved on optimally-oriented structures over the upper plate results in suppressed normal faulting. Most of the forearc is affected by a negative field (blue) and the modeled faults do not match the crustal structures.

In both maps the blue heavy line across the Pichilemu region shows the location of the cross sections in Figure 3.10.

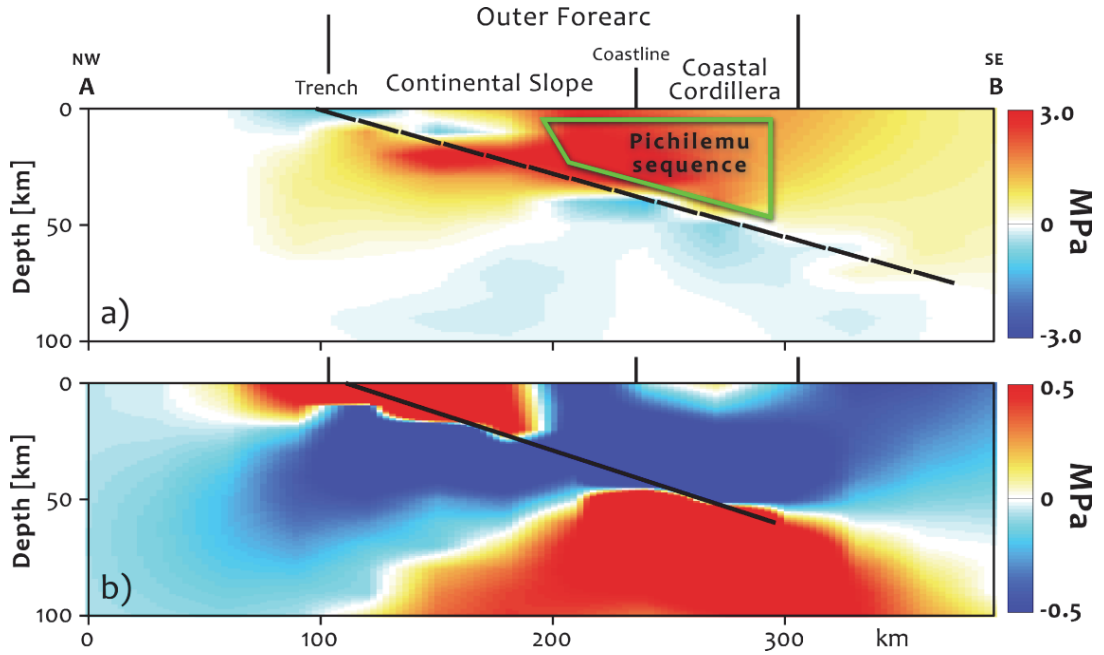

Figure 3.10: Cross-section of CSI magnitude resolved on optimally-oriented normal faults across the forearc at the Pichilemu region, perpendicular to the plate boundary (location of the profile and color code explanation in Fig. 3.9). The thick black line represents the megathrust geometry in cross-section for the coseismic slip (a) and the interseismic coupling models (b).

(a) Results from the same input source showed in Figure 3.9 (*Vigny et al.*, 2011). The green polygon encloses the zone of hypocentral locations of the Pichilemu sequence. More solution can be found in the Appendix section B6.2.

(b) For the interseismic period note also the widely extended and prevailing compressive stress field that affect the forearc wedge during that stage.

at the northern and southern ends of the segment, mapped faults show bimodal patterns in the structural grain with some striking sub-parallel to the modeled structures and some sub-perpendicular (Figs. 3.1, 3.11 and Appendix section B7). The orientation of the Pichilemu fault fits well with the modeled strikes.

We also modeled the optimal orientations and CSI magnitude for thrust and strike-slip faults in the upper plate. With the exception of a few small areas, reverse faulting is retarded by the coseismic stress field, and strike-slip is enhanced but the CSI is generally much smaller than the estimations for normal faults along the Coastal Cordillera.

3.6.3.3 Regional Interseismic Coulomb Stress Increment

In contrast to the coseismic deformation, the interseismic deformation field suppresses normal faulting in the majority of the upper-crustal wedge (Figs. 3.9b and 3.10b). The finite CSI on optimally oriented normal faults yields a negative field over the entire upper plate (Fig. 3.9b) for a 10 km calculation depth (30 by 30 km each grid element). Along the outer forearc normal faults are negatively stressed by values < −0.125 MPa and at depths greater than 10 km, the CSI reaches values < −0.5 MPa (Fig. 3.10b).

Additionally, for most of the Coastal Cordillera the optimal modeled strike of the normal faults is nearly orthogonal to the plate boundary (Fig. 3.9b). In fact, the calculated orientations and negative CSI magnitudes imply that permanent reverse faults in the upper plate should strike nearly parallel to the trench. The reverse faults mapped by *Melnick et al.* (2006, 2009) fit the interseismic pattern very well. The small positive stressed area located on the continent, in front of the northern and southern bends of the plate boundary (Fig. 3.9b), may be caused either by the change in geometry of the slab or by a model artifact.

Figure 3.11: Angular misfit between the strikes of known normal faults along the Coastal Cordillera of the Maule segment (green lines) and the optimally oriented normal faults resulted from the fault slip model by *Vigny et al*. (2011) (white lines). See the caption for Figure B30 in Appendix section B7.1 for the explanation of which faults appear in this analysis. The grid squares (30 by 30 km) are defined by the modeled faults. When more than one mapped faults are present at the same square we calculate a weighted average to determine the orientation of the long-term strike of the structures that corresponds to the specific grid element. The angular misfit of strike at each grid square is represented by colors with the population of results binned in four groups of 22.5°, from 0° to 90° of misfit. Blue represents a small misfit (< 22.5°) therefore a good agreement in orientation. Red corresponds to misfits larger than 67.5°. The pie chart shows the relative abundance of the grid elements that belong to the four groups of angular misfit. More results for this statistical analysis using all the fault slip models can be found in the Appendix section B7.2.

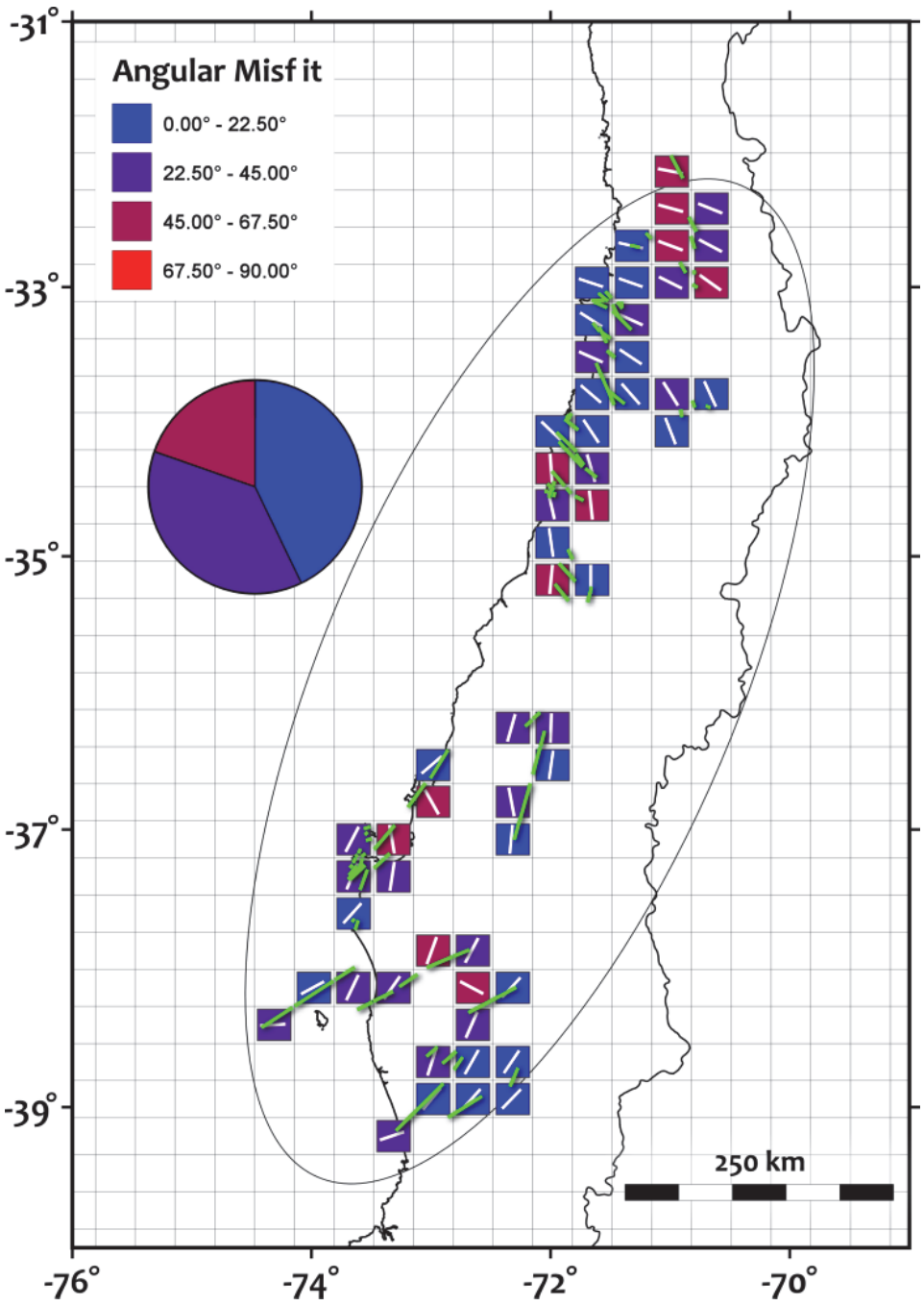
Angular Misf it
0.00° - 22.50°
22.50° - 45.00°
45.00° - 67.50°
67.50° - 90.00°
-31°
-33°
-35°
-37°
-39°
-76°
-74°
-72°
-70°
250 km

Similar to the coseismic modeling, a small portion at the toe of the upper plate wedge near the trench behaves in an opposite way than the rest of the forearc, showing positively stressed zones for normal faulting. In this case, the up-dip low coupling zone of the plates interface generates a positive gradient of backslip and presumably, extension in the upper plate (see Figs. 3.2 and Appendix section B4.2).

3.7 Discussion

3.7.1 Permanent Coseismic Extension

Much of coseismic extension documented here is accommodated by elastic rebound but part was produced by the permanent reactivation of the normal faults in the Pichilemu region (Figs. 3.4-3.6 and Table 3.2). To generate a M_w 7.0 earthquake, almost the entire plane that we modeled should have ruptured with 0.5 m of average slip, a non-trivial coseismic deformation considering the surface area of this structure (70 by 35.4 km) and the surface area of the megathrust (~600 by 200 km) (Fig. 3.3 and Table 3.1). The principal extensional axes obtained from both the moment tensor summation of earthquakes in Pichilemu and from the coseismic surface GPS, coincide in orientation and magnitude of strain (Figs. 3.4-3.5). The similarity in magnitude is significant because it suggests a non-trivial plastic response to coseismic extension. The Tōhoku subduction earthquake was likewise followed by significant upper plate normal fault aftershocks (*Lay et al.*, 2011; *Toda et al.*, 2011a, 2011b), suggesting a plastic component to coseismic rebound.

3.7.2 Interseismic vs. Coseismic Deformation

CSI calculations have been used elsewhere in the Andean Cordillera to suggest that the interseismic deformation field caused by the stress transfer at the locked inter-

plate surface produces tension at shallow crustal levels (< ~2.5 km depth), which could load the normal faults and bring the structures to fracture (*Loveless and Pritchard*, 2008; *Loveless et al.*, 2010). These interseismic estimations for CSI accumulation near the surface reach maximum values of about 0.5 MPa on fixed, homogeneously oriented normal faults, over a 1 km depth horizontal grid and during a ~100-150 year interseismic period. Below this depth the CSI becomes negative for normal faulting.

Our simulation for the Maule segment indicates that normal faulting is mostly suppressed along the Coastal Cordillera during the interseismic period (Figs. 3.9b and 3.10b). The only possible region of interseismic forearc extension along the Coastal Cordillera is restricted to a shallow and small region, not deeper than ~1 km, where the CSI is close to 0 (Fig. 3.10b). Large intraplate normal faults generally nucleate at levels deeper than 5 km (*Jackson and McKenzie*, 1983; *Jackson*, 1987; *Scholz*, 1988, 2002; *Jackson and White*, 1989; *Jackson et al.*, 2008). Likewise, the hypocenters of the sequence of normal aftershocks that followed the Maule earthquake range between 12 and 30 km depth (see Appendix section B1).

Field studies carried out by *González et al.* (2003), *Loveless and Pritchard* (2008), *Allmendinger and González* (2010) and *Loveless et al.* (2010) in the Atacama Desert, show minor reverse reactivation on the NS and trench-oblique structures of the Coastal Cordillera. Likewise *Melnick et al.* (2006, 2009) describe reverse reactivation of normal faults on Santa Maria Island and in the Arauco Peninsula at the south end of the Maule rupture (Fig. 3.1 and Appendix section B7.1). Our field data from the Pichilemu region also documents centimeter- to meter-scale reverse faults, mostly oriented NS, cut Pleistocene-Holocene? sedimentary sequences which are subsidiary to the NW-striking normal faults of the region (*Aron et al.*, 2012). Our interseismic

model is consistent with these field data as the magnitude of stress obtained is small (CSI ~ |0.5| MPa) compared to the coseismic period with optimal orientation of reverse faults is mainly NS (Figs. 3.9b-3.10b).

Loveless and Pritchard (2008) and *Loveless et al.* (2010) proposed that coseismic deformation generated by the 1995 Antofagasta M_w 8.1 earthquake in northern Chile could trigger both, normal and reverse intraplate faulting in the Coastal Cordillera depending on the slip distribution on the megathrust. The coseismic CSI calculated for the Maule earthquake shows that reverse faulting in the subaerial part of the forearc is unlikely during a subduction earthquake. Six out of the seven finite fault models generate vast regions of values of CSI greater than 1.5 MPa on optimally oriented faults over the outer forearc, all the way to the subduction interface (Figs. 3.8, 3.9a-3.10a and Appendix section B6). Positive CSI averaged across the Pichilemu fault ranged from 1.2 to 3.2 MPa with maximum CSI values of 2.3 to 4.9 MPa (Fig. 3.8 and Table 3.2). Reverse faulting can indeed be triggered by the megathrust but it is restricted to the toe of the continental wedge, along the submarine portion of the outer forearc. In this region, the negative slip gradient of the rupture induces compression in the upper plate and likely reactivation of thrust "splay faults". This result is consistent with recent observations reported for the Maule earthquake region (*Melnick et al.*, 2012) and for other subduction ruptures (e.g., *Plafker*, 1967). Additionally, as described below, preexisting oblique faults striking towards the center of the rupture zone may also be reactivated if they are very near failure already.

3.7.3 Breaking the Forearc

The CSIs that we have documented are probably not sufficient to make very many new large structures, but in the forearc basement, we have abundant evidence of pre-

existing planes of weakness, like the Pichilemu fault. Those pre-existing planes may be the result of older Cenozoic tectonics produced during Andean subduction or they may well take their heritage from tectonics affecting the Paleozoic basement of the forearc (*Yáñez et al.*, 1998; e.g., *Lavenu and Encinas*, 2005). Regardless of the origin of the fractures, only those that are suitably oriented in the stress fields related to current subduction processes will be reactivated and thus will have marked topographic expression or structural relief.

The permanent deformation of any particular place along the forearc should represent a combination of coseismic normal faulting and interseismic reverse faulting behaviors. Local variations in interseismic coupling and coseismic slip on the megathrust, as well as the availability of suitably oriented planes of weakness, will probably determine which style is more prevalent. In general, interseismic reverse fault reactivation will mostly occur on planes parallel or sub-parallel to the margin, though strike- or oblique-slip on extremely weak planes might also occur. For coseismic deformation, normal displacement may occur on faults parallel the margin in the center of the rupture segment; at the ends of the rupture segments faults oblique to the margin and at a high angle to coseismic extension direction are likely to be reactivated as at Pichilemu.

Other than the Pichilemu structure and the Arauco Peninsula, fault activity and kinematics is not well known for the Maule rupture area. Based on the normal aftershocks that follow the Maule earthquake (Fig. 3.1, Appendix Table B1 and Appendix Figure B1) and on analogous examples elsewhere in the Coastal Cordillera (*Heinze*, 2003; e.g., *González et al.*, 2006) and along the Maule rupture area (*Katz*, 1971; *Gana et al.*, 1996; *Wall et al.*, 1996; *Lavenu and Cembrano*, 1999; *Lavenu et al.*, 1999; e.g., *Aron et al.*, 2012), it is likely that, the principal structural style, at least

above the northern half the Maule segment, is extensional and active, although reverse faults also exist. Reverse faults coexisting with larger scale normal faults along the Coastal Cordillera (e.g., *Melnick et al.*, 2006, 2009; *Moreno et al.*, 2008) may reflect the permanent signature of the compressive interseismic period as well as coseismic splay faults in the toe of the accretionary wedge (*Melnick et al.*, 2012). Alternatively, surface normal faults described by *Melnick et al*. (2012) may represent coseismic normal fault reactivation of reverse faults with documented interseismic activity (*Melnick et al.*, 2006, 2009) as there was no documented co/post-seismic reverse fault seismicity associated with the structure.

Why were other pre-existing intraplate faults not triggered by the Maule earthquake, at least with magnitudes large enough for focal mechanisms to be calculated? In northern Chile, recent work by *Cortés et al*. (2012) suggests that upper plate forearc normal faults have recurrence intervals more than one order of magnitude longer than the plate boundary seismic cycle. Thus, if subduction earthquakes are responsible for the permanent upper plate extension, many cycles are necessary to accumulate shear loading and break the Coastal Cordillera or reactivate upper plate normal faults. The coseismic loading of a single event, mostly controlled by the slip distribution on the megathrust, is not homogeneously distributed over the forearc (Figs. 3.9a-3.10a), contributing to possible variations in the recurrence times for the different intraplate faults.

3.7.4 Long-term Strain Markers and Seismic Segmentation

Loveless et al. (2005, 2009) suggested that the semi-elliptical pattern of coseismic cracks in the Atacama Desert in northern Chile delineates the long term, average behavior of rupture segments. We postulate that a semi-elliptical map pattern of normal faults might likewise indicate average rupture segments (Figs. 3.11 and 3.12).

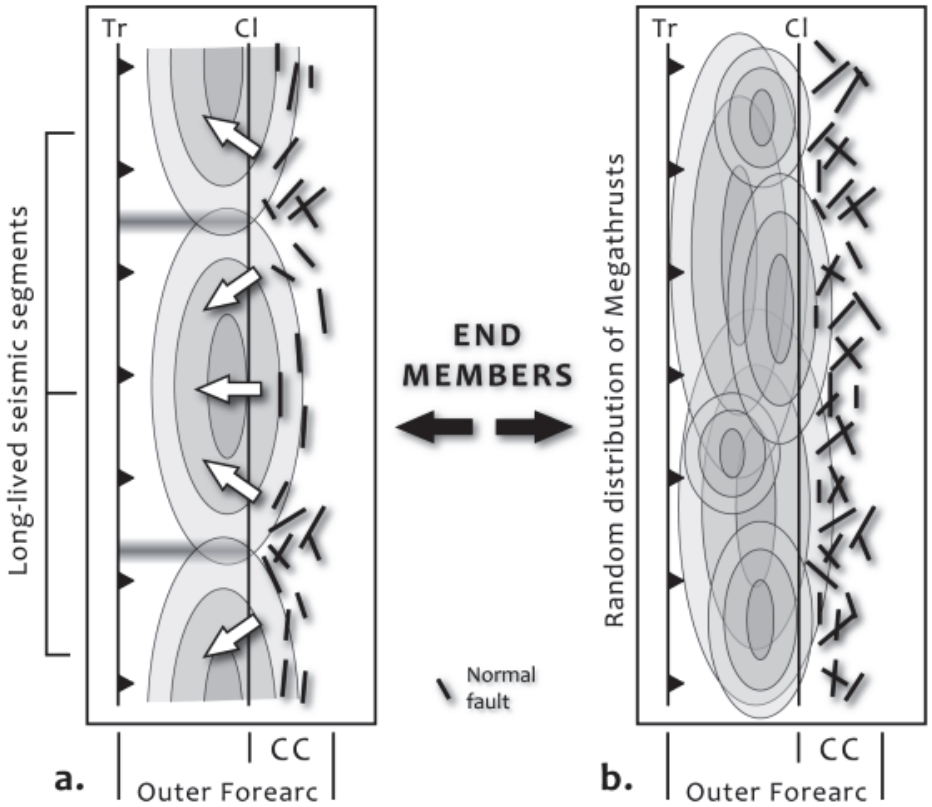

Figure 3.12: Cartoon maps showing end-members of the possible behavior of earthquakes at subduction zones and the associated result in the structural grain. (a) Long-lived and fixed segments produce a semi-elliptical geometric configuration of large normal faults, enclosing the rupture area, which results from the average slip cyclically accumulated over geologic time. The bimodal orientations represent segment boundary zones. (b) Random distribution of oblique and trench-parallel structures resulting from the coseismic deformation imposed by megathrust segments that change location over time. The ellipses represent the hypothetical pattern of the finite slip distribution on the megathrust (darker colors are higher slip) and the white arrows in member (a) indicate the long-term extensional axis of the continent resulted from this pattern. Tr, Cl and CC stands for trench, coastline and Coastal Cordillera respectively.

As geologists studying features that develop over a million year or more, and thousands to tens of thousands of earthquake cycles, we define an "average rupture segment" as one that, *over geologic time*, tends to rupture repeatedly. Thus, the accumulation of permanent deformation of the upper plate should reflect that average behavior. This view is quite different than the more typical geophysical view of a single earthquake cycle, a characteristic earthquake, or historical record spanning two or three events. On the scale of just a few events, segments may shift around or only parts of segments will rupture (as with the case of the 1928 earthquake of the northern part of the Maule segment) and from time to time extremely large events may rupture several segments. The long term, permanent record of deformation of the upper plate should smooth out that short-term behavior and reflect features of the upper plate that tend to control segmentation.

With this concept in mind, we ask the question of whether there is an identifiable average behavior in this part of the Chilean forearc and, if so, whether the Maule rupture may be relatively close to the average segment. The answer, at this point, is a qualified "maybe yes". Maule mostly ruptured an oblique bend in the coastline between south of Valparaiso to the Arauco Peninsula, overshooting the peninsula by a small amount (Fig. 3.1 and Appendix section B2). Others have already postulated that peninsulas might control long-term segmentation (e.g., *Song and Simons*, 2003; *Wells et al.*, 2003). At a more detailed scale, we have calculated the misfit between known normal faults in the Coastal Cordillera of the Maule segment and the ideal semi-elliptical pattern calculated from the slip models (Fig. 3.11). This exercise is hampered by lack of detailed geologic mapping and disagreement by existing coworkers over the quality of the existing mapping and significance of known normal faults. Given these uncertainties, the modeled semi-elliptical pattern is in good agreement with faults of known normal displacement (e.g., Pichilemu) and with faults that arguably *may* have

normal component of slip (Fig. 3.11 and Appendix section B7). Note that, if the rupture segments are long-lived, at the boundaries there should be a bimodal population of faults (Fig. 3.12) and to evaluate the goodness of fit for a single segment, faults produced by adjoining segments should not be included. This is the case with the northern and southern ends of the Maule segment (Figs. 3.1 and 3.9a; Figure B29 Appendix) which coincides with the boundary of the 1960 M_w 9.5, Valdivia earthquake (*Plafker and Savage*, 1970; *Kanamori*, 1977; *Cifuentes*, 1989) and the segment which ruptured in 1906 M_w 8.6 and 1985 M_w 7.8 Valparaiso earthquakes (*Christensen and Ruff*, 1986; *Comte et al.*, 1986; *Barrientos*, 1988).

It is probable that the largest, frequently repeated earthquakes are responsible for the majority of the forearc, upper plate deformation. For the Maule rupture region it appears that, on average over geologic time, and consistent with recent observations made by *Moreno et al.* (2012), great subduction earthquakes tend to rupture the same segment repeatedly. However, definitive test of the concept in Figure 3.12 must await better and more complete mapping of the Chilean Coastal Cordillera.

3.8 Conclusions

We have demonstrated that the static coseismic deformation field, imposed in the upper plate by a great subduction earthquake, is an effective mechanism for generating convergence-parallel permanent extension above the seismogenic zone. This large and widely distributed extensional field is consistent with the large upper plate normal aftershocks generated by the Maule earthquake and probably the normal aftershocks that followed the Tōhoku earthquake, as well. Long-lived normal faults in the outer forearc wedge are likely reactivated whenever the slip on subduction megathrust segments is appropriately oriented to provide the proper loading conditions.

The semi-elliptically oriented coseismic stress field generated by slip on the Maule megathrust mimics the semi-elliptical outline of the first-order normal faults along the Coastal Cordillera. The interseismic deformation field produces convergence-parallel shortening and enhanced minor reverse faulting in the upper crust, which agrees with geological observations of the forearc. As upper plate normal faulting is suppressed during the interseismic period, recurrence of discrete events like great subduction earthquakes probably plays a major role in the genesis of permanent extensional provinces along the leading edge of non-collisional convergent margins.

Such architectural patterns may be persistent over many thousands of cycles in the region overlying the Maule rupture zone. A hypothesis meriting further testing is that the semi-elliptical outline of the first-order structures along the Coastal Cordillera may indicate the cyclic accumulation of slip on segments that tend to rupture repeatedly over geologic time, thus enhancing the morphological and structural expression of appropriately-oriented structures. The 2010 Maule earthquake may be representative of the average great earthquake in this segment.

REFERENCES

Allmendinger, R. W., and G. González (2010), Invited review paper: Neogene to Quaternary tectonics of the coastal Cordillera, northern Chile, *Tectonophysics*, *495*(1-2), 93–110, doi:10.1016/j.tecto.2009.04.019.

Allmendinger, R. W., G. González, J. Yu, G. Hoke, and B. Isacks (2005), Trench-parallel shortening in the Northern Chilean Forearc: Tectonic and climatic implications, *Geol. Soc. Am. Bull.*, *117*(1-2), 89–104, doi:10.1130/B25505.1.

Allmendinger, R. W., J. P. Loveless, M. E. Pritchard, and B. Meade (2009), From decades to epochs: Spanning the gap between geodesy and structural geology of active mountain belts, *Journal of Structural Geology*, *31*(11), 1409 – 1422, doi:DOI: 10.1016/j.jsg.2009.08.008.

Angermann, D., J. Klotz, and C. Reigber (1999), Space-geodetic estimation of the nazca-south america euler vector, *Earth Planet. Sci. Lett.*, *171*(3), 329–334, doi:10.1016/S0012-821X(99)00173-9.

Arabasz, W. J. (1971), Geological and geophysical studies of the Atacama fault zone in northern Chile, PhD, Calif. Inst. of Technol., Pasadena, California.

Armijo, R., and R. Thiele (1990), Active faulting in northern Chile: ramp stacking and lateral decoupling along a subduction plate boundary?, *Earth Planet. Sci. Lett.*, *98*(1), 40 – 61, doi:10.1016/0012-821X(90)90087-E.

Aron, F., J. Cembrano, R. W. Allmendinger, F. Astudillo, and G. Arancibia (2012), Structural Geology of the Active Forearc above the Maule Megathrust: Traces of a Long-lived Subduction Segment, in *paper presented at 2012 XIII Chilean Geological Congress, Antofagasta, Chile, 5-9 Aug.*

Arriagada, C. et al. (2011), Nature and tectonic significance of co-seismic structures associated with the Mw 8.8 Maule earthquake, central-southern Chile forearc, *J. Struct. Geol.*, *33*(5), 891–897, doi:10.1016/j.jsg.2011.03.004.

Barrientos, S. (1988), Slip distribution of the 1985 Central Chile earthquake, *Tectonophysics*, *145*(3–4), 225–241, doi:10.1016/0040-1951(88)90197-7.

Beck, S., S. Barrientos, E. Kausel, and M. Reyes (1998), Source characteristics of historic earthquakes along the central Chile subduction Askew et alzone, *J. South Amer. Earth Sci.*, *11*(2), 115–129, doi:10.1016/S0895-9811(98)00005-4.

Benado, D. (2000), Estructuras y estratigrafía básica de terrazas marinas en el sector costero de Altos de Talinay y Bahía Tongoy: Implicancia neotectónica, PhD, Departamento de Geología, University of Chile, Santiago, Chile.

Bevis, M., E. Kendrick, R. Smalley Jr., B. Brooks, R. Allmendinger, and B. Isacks (2001), On the strength of interplate coupling and the rate of back arc convergence in the central Andes: An analysis of the interseismic velocity field, *Geochem. Geophys. Geosyst.*, *2*(11), 1067–, doi:10.1029/2001GC000198.

Brooks, B. A., M. Bevis, R. Smalley Jr., E. Kendrick, R. Manceda, E. Lauría, R. Maturana, and M. Araujo (2003), Crustal motion in the Southern Andes (26°-36°S): Do the Andes behave like a microplate?, *Geochem. Geophys. Geosyst.*, *4*(10), 1085–, doi:10.1029/2003GC000505.

Byerlee, J. (1978), Friction of rocks, *Pure Appl. Geophys.*, *116*(4-5), 615–626, doi:10.1007/BF00876528.

Campos, J., D. Hatzfeld, R. Madariaga, G. Lopez, E. Kausel, A. Zollo, G. Iannacone, R. Fromm, S. Barrientos, and H. Lyon-Caen (2002), A seismological study of the 1835 seismic gap in south-central Chile, *Phys. Earth Planet. Inter.*, *132*(1-3), 177–195, doi:10.1016/S0031-9201(02)00051-1.

Cardozo, N., and R. W. Allmendinger (2009), SSPX: A program to compute strain from displacement/velocity data, *Computers & Geosciences*, *35*(6), 1343 – 1357, doi:DOI: 10.1016/j.cageo.2008.05.008.

Cembrano, J., A. Lavenu, G. Yañez, R. Riquelme, M. Garcia, G. González, and G. Hérail (2007), Neotectonics, in *The Geology of Chile*, edited by T. Moreno, W. Gibbons, and G. S. of London, pp. 231–261, Geological Society of London, London, Tulsa. UK.

Chinnery, M. A. (1963), The stress changes that accompany strike-slip faulting, *Bull. Seismol. Soc. Am.*, *53*(5), 921–932.

Christensen, D. H., and L. J. Ruff (1986), Rupture process of the March 3, 1985 Chilean earthquake, *Geophys. Res. Lett.*, *13*(8), 721–724, doi:198610.1029/GL013i008p00721.

Cifuentes, I. L. (1989), The 1960 Chilean Earthquakes, *J. Geophys. Res.*, *94*(B1), 665–680, doi:198910.1029/JB094iB01p00665.

Comte, D., and M. Pardo (1991), Reappraisal of great historical earthquakes in the northern Chile and southern Peru seismic gaps, *Natural Hazards*, *4*(1), 23–44.

Comte, D., A. Eisenberg, E. Lorca, M. Pardo, L. Ponce, R. Saragoni, S. K. Singh, and G. Suárez (1986), The 1985 Central Chile Earthquake: A Repeat of Previous Great Earthquakes in the Region?, *Science*, *233*(4762), 449–453, doi:10.1126/science.233.4762.449.

Comte, D., M. Farías, S. Roecker, D. Carrizo, and M. H. Pardo (2010), Crustal Normal Faulting Triggered by the Mw=8.8 Maule Megathrust Subduction Earthquake in Central Chile, in *paper presented at 2010 Fall Meeting, AGU, San Francisco, Calif., 13-17 Dec*.

Cortés, J., G. González, S. A. Binnie, R. Robinson, S. P. H. T. Freeman, and G. Vargas (2012), Paleoseismology of the Mejillones Fault, northern Chile: Insights from cosmogenic 10Be and optically stimulated luminescence determinations, *Tectonics*, *31*(2), TC2017, doi:10.1029/2011TC002877.

Darwin, C. (1845), *Journal of researches into the natural history and geology of the countries visited during the voyage of H.M.S. Beagle round the world*, 2nd. ed., John Murray, London.

Das, S., and C. H. Scholz (1981), Off-fault aftershock clusters caused by shear stress increase?, *Bull. Seismol. Soc. Am.*, *71*(5), 1669–1675.

Delouis, B., H. Philip, L. Dorbath, and A. Cisternas (1998), Recent crustal deformation in the Antofagasta region (northern Chile) and the subduction process, *Geophys. J. Int.*, *132*(2), 302–338, doi:10.1046/j.1365-246x.1998.00439.x.

Delouis, B., J.-M. Nocquet, and M. Vallée (2010), Slip distribution of the February 27, 2010 Mw = 8.8 Maule Earthquake, central Chile, from static and high-rate GPS, InSAR, and broadband teleseismic data, *Geophys. Res. Lett.*, *37*(17), L17305–, doi:10.1029/2010GL043899.

Farías, M., D. Comte, S. Roecker, D. Carrizo, and M. Pardo (2011), Crustal extensional faulting triggered by the 2010 Chilean earthquake: The Pichilemu Seismic Sequence, *Tectonics*, *30*(6), TC6010–, doi:10.1029/2011TC002888.

Freed, A. M. (2005), Earthquake triggering by static, dynamic, and postseismic stress transfer, *Annu. Rev. Earth Planet. Sci.*, *33*(1), 335–367, doi:10.1146/annurev.earth.33.092203.122505.

Fromm, R., G. Zandt, and S. L. Beck (2004), Crustal thickness beneath the Andes and Sierras Pampeanas at 30°S inferred from Pn apparent phase velocities, *Geophys. Res. Lett.*, *31*(6), L06625–, doi:10.1029/2003GL019231.

Gana, P., R. Wall, and A. Gutiérrez (1996), *Mapa geológico del área Valparaíso-Curacaví, Regiones de Valparaíso y Metropolitana.*, Geological map Scale 1:100,000, Servicio Nacional de Geología y Minería, Santiago, Chile.

Geersen, J., J. H. Behrmann, D. Völker, S. Krastel, C. R. Ranero, J. Diaz-Naveas, and W. Weinrebe (2011), Active tectonics of the South Chilean marine fore arc (35°S–40°S), *Tectonics*, *30*(3), TC3006, doi:10.1029/2010TC002777.

González, G., J. Cembrano, D. Carrizo, A. Macci, and H. Schneider (2003), The link between forearc tectonics and Pliocene-Quaternary deformation of the Coastal Cordillera, northern Chile, *J. South Amer. Earth Sci.*, *16*(5), 321–342, doi:10.1016/S0895-9811(03)00100-7.

González, G., T. Dunai, D. Carrizo, and R. Allmendinger (2006), Young displacements on the Atacama Fault System, northern Chile from field observations and cosmogenic 21Ne concentrations, *Tectonics*, *25*(3), TC3006–, doi:10.1029/2005TC001846.

Harris, R. A. (1998), Introduction to special section: Stress triggers, stress shadows, and implications for seismic hazard, *J. Geophys. Res.*, *103*(B10), 24,347–24,358, doi:10.1029/98JB01576.

Hayes, G. P., D. J. Wald, and R. L. Johnson (2012), Slab1.0: A three-dimensional model of global subduction zone geometries, *J. Geophys. Res.*, *117*(B1), B01302–, doi:10.1029/2011JB008524.

Heinze, B. (2003), Active Intraplate Faulting in the Forearc of North Central Chile (30°-31° S). Implications from Neotectonic Field Studies, GPS Data, and Elastic Dislocation Modeling, PhD, Free University, Berlin, March.

Hoffmann-Rothe, A., N. Kukowski, G. Dresen, H. Echtler, O. Oncken, J. Klotz, E. Scheuber, and A. Kellner (2006), Oblique Convergence along the Chilean Margin: Partitioning, Margin-Parallel Faulting and Force Interaction at the Plate Interface, in *The Andes: Active subduction orogeny*, edited by O. Oncken, G. Chong, G. Franz, P. Giese, H.-J. Götze, V. A. Ramos, M. R. Strecker, and P. J. Wigger, pp. 125–146, Springer, Berlin.

Hu, Y., K. Wang, J. He, J. Klotz, and G. Khazaradze (2004), Three-dimensional viscoelastic finite element model for postseismic deformation of the great 1960 Chile earthquake, *J. Geophys. Res.*, *109*(B12), B12403, doi:10.1029/2004JB003163.

Von Huene, R., and S. Lallemand (1990), Tectonic erosion along the Japan and Peru convergent margins, *Geol. Soc. Am. Bull.*, *102*(6), 704–720, doi:10.1130/0016-7606(1990)102<0704:TEATJA>2.3.CO;2.

Von Huene, R., and C. R. Ranero (2003), Subduction erosion and basal friction along the sediment-starved convergent margin off Antofagasta, Chile, *J. Geophys. Res.*, *108*(B2), 2079–, doi:10.1029/2001JB001569.

Von Huene, R., and D. W. Scholl (1991), Observations at convergent margins concerning sediment subduction, subduction erosion, and the growth of continental crust, *Rev. Geophys.*, *29*(3), 279–316, doi:10.1029/91RG00969.

Jackson, J. A. (1987), Active normal faulting and crustal extension, *Geol. Soc. Spec. Publ.*, *28*(1), 3–17, doi:10.1144/GSL.SP.1987.028.01.02.

Jackson, J. A., and D. McKenzie (1983), The geometrical evolution of normal fault systems, *J. Struct. Geol.*, *5*(5), 471–482, doi:10.1016/0191-8141(83)90053-6.

Jackson, J. A., and N. J. White (1989), Normal faulting in the upper continental crust: observations from regions of active extension, *J. Struct. Geol.*, *11*(1-2), 15–36, doi:10.1016/0191-8141(89)90033-3.

Jackson, J. A., D. McKenzie, K. Priestley, and B. Emmerson (2008), New views on the structure and rheology of the lithosphere, *J. Geol. Soc. (London, U.K.)*, *165*(2), 453–465, doi:10.1144/0016-76492007-109.

Kanamori, H. (1977), The Energy Release in Great Earthquakes, *J. Geophys. Res.*, *82*(20), 2981–2987, doi:197710.1029/JB082i020p02981.

Katz, H. R. (1971), Continental Margin in Chile-Is Tectonic Style Compressional or Extensional?, *AAPG Bulletin*, *55*(10), 1753–1758, doi:10.1306/819A3DA2-16C5-11D7-8645000102C1865D.

Kelleher, J. A. (1972), Rupture Zones of Large South American Earthquakes and Some Predictions, *J. Geophys. Res.*, *77*(11), 2087–2103, doi:10.1029/JB077i011p02087.

Kendrick, E., M. Bevis, R. Smalley Jr., and B. Brooks (2001), An integrated crustal velocity field for the central Andes, *Geochem. Geophys. Geosyst.*, *2*(11), 1066–, doi:10.1029/2001GC000191.

Kendrick, E., M. Bevis, R. Smalley, B. Brooks, R. B. Vargas, E. Lauría, and L. P. S. Fortes (2003), The Nazca-South America Euler vector and its rate of change, *J. South Amer. Earth Sci.*, *16*(2), 125–131, doi:10.1016/S0895-9811(03)00028-2.

Khazaradze, G., and J. Klotz (2003), Short- and long-term effects of GPS measured crustal deformation rates along the south central Andes, *J. Geophys. Res.*, *108*(B6), 2289–, doi:10.1029/2002JB001879.

King, G. C. P., R. S. Stein, and J. Lin (1994), Static stress changes and the triggering of earthquakes, *Bull. Seismol. Soc. Am.*, *84*(3), 935–953.

Klotz, J. et al. (1999), GPS-derived Deformation of the Central Andes Including the 1995 Antofagasta M w = 8.0 Earthquake, *Pure Appl. Geophys.*, *154*(3-4), 709–730, doi:10.1007/s000240050249.

Klotz, J., G. Khazaradze, D. Angermann, C. Reigber, R. Perdomo, and O. Cifuentes (2001), Earthquake cycle dominates contemporary crustal deformation in Central and Southern Andes, *Earth Planet. Sci. Lett.*, *193*(3-4), 437–446, doi:10.1016/S0012-821X(01)00532-5.

Klotz, J., A. Abolghasem, G. Khazaradze, B. Heinze, T. Vietor, R. Hackney, K. B. R. Maturana, J. Viramonte, and R. Perdomo (2006), Long-Term Signals in the Present-Day Deformation Field of the Central and Southern Andes and Constraints on the Viscosity of the Earth's Upper Mantle, in *The Andes: Active subduction orogeny*, edited by O. Oncken, G. Chong, G. Franz, P. Giese, H.-J. Götze, V. A. Ramos, M. R. Strecker, and P. J. Wigger, pp. 65–89, Springer, Berlin.

Krawczyk, C. M., J. Mechie, S. Lüth, Z. Tašárová, P. Wigger, M. Stiller, H. Brasse, H. P. Echtler, M. Araneda, and K. Bataille (2006), Geophysical Signatures and Active Tectonics at the South-Central Chilean Margin, in *The Andes: Active subduction orogeny*, edited by O. Oncken, G. Chong, G. Franz, P. Giese, H.-J. Götze, V. A. Ramos, M. R. Strecker, and P. Wigger, pp. 171–192, Springer Berlin Heidelberg.

Lallemand, S., A. Heuret, and D. Boutelier (2005), On the relationships between slab dip, back-arc stress, upper plate absolute motion, and crustal nature in subduction zones, *Geochem. Geophys. Geosyst.*, *6*(9), Q09006–, doi:10.1029/2005GC000917.

Lamb, S. (2006), Shear stresses on megathrusts: Implications for mountain building behind subduction zones, *J. Geophys. Res.*, *111*(B7), B07401–, doi:10.1029/2005JB003916.

Lavenu, A., and J. Cembrano (1999), Compressional- and transpressional-stress pattern for Pliocene and Quaternary brittle deformation in fore arc and intra-arc zones (Andes of Central and Southern Chile), *J. Struct. Geol.*, *21*(12), 1669–1691, doi:10.1016/S0191-8141(99)00111-X.

Lavenu, A., and A. Encinas (2005), Deformación frágil de los depósitos neógenos de la cuenca de Navidad (Cordillera de la Costa, 34°S, Chile central), *Rev. Geol. Chile*, *32*, 229–248, doi:10.4067/S0716-02082005000200004.

Lavenu, A., C. Marquardt, D. Comte, M. Pardo, L. Ortlieb, and T. Monfret (1999), Quaternary Extensional Deformation and Recent Vertical Motion Along the Chilean Coast (between 23° S and 47° S), in *Fourth International Symposium on Andean Geodynamics (ISAG)*, pp. 424–427, Göettingen.

Lay, T., C. J. Ammon, H. Kanamori, K. D. Koper, O. Sufri, and A. R. Hutko (2010), Teleseismic inversion for rupture process of the 27 February 2010 Chile (Mw 8.8) earthquake, *Geophys. Res. Lett.*, *37*(13), L13301–, doi:10.1029/2010GL043379.

Lay, T., C. J. Ammon, H. Kanamori, M. J. Kim, and L. Xue (2011), Outer trenchslope faulting and the 2011 Mw 9.0 off the Pacific coast of Tohoku Earthquake, *Earth Planets Space*, *63*(7), 713–718.

Lin, J., and R. S. Stein (2004), Stress triggering in thrust and subduction earthquakes and stress interaction between the southern San Andreas and nearby thrust and strike-slip faults, *J. Geophys. Res.*, *109*, B02303–, doi:200410.1029/2003JB002607.

Lomnitz, C. (1970), Major earthquakes and tsunamis in Chile during the period 1535 to 1955, *Int. J. Earth Sci.*, *59*(3), 938–960, doi:10.1007/BF02042278.

Lorito, S., F. Romano, S. Atzori, X. Tong, A. Avallone, J. McCloskey, M. Cocco, E. Boschi, and A. Piatanesi (2011), Limited overlap between the seismic gap and coseismic slip of the great 2010 Chile earthquake, *Nat. Geosci.*, *4*(3), 173–177, doi:10.1038/ngeo1073.

Loveless, J. P., and M. E. Pritchard (2008), Motion on upper-plate faults during subduction zone earthquakes: Case of the Atacama Fault System, northern Chile, *Geochem. Geophys. Geosyst.*, *9*(12), Q12017–, doi:10.1029/2008GC002155.

Loveless, J. P., G. D. Hoke, R. W. Allmendinger, G. Gonzalez, B. L. Isacks, and D. A. Carrizo (2005), Pervasive cracking of the northern Chilean Coastal Cordillera: New evidence for forearc extension, *Geology*, *33*(12), 973–976, doi:10.1130/G22004.1.

Loveless, J. P., R. W. Allmendinger, M. E. Pritchard, J. L. Garroway, and G. Gonzalez (2009), Surface cracks record long-term seismic segmentation of the Andean margin, *Geology*, *37*(1), 23–26, doi:10.1130/G25170A.1.

Loveless, J. P., R. W. Allmendinger, M. E. Pritchard, and G. González (2010), Normal and reverse faulting driven by the subduction zone earthquake cycle in the northern Chilean fore arc, *Tectonics*, *29*(2), TC2001–, doi:10.1029/2009TC002465.

Madariaga, R., M. Métois, C. Vigny, and J. Campos (2010), Central Chile Finally Breaks, *Science*, *328*(5975), 181–182, doi:10.1126/science.1189197.

Marquardt, C. (1999), Neotectónica de la franja costera y aportes a la geología regional entre Caldera y Caleta Pajonal (27°00'-27°45'), III Región de Atacama, Master, University of Chile, Santiago, Chile.

Marquardt, C., A. Lavenu, L. Ortlieb, E. Godoy, and D. Comte (2004), Coastal neotectonics in Southern Central Andes: uplift and deformation of marine terraces in Northern Chile (27°S), *Tectonophysics*, *394*(3-4), 193 – 219, doi:10.1016/j.tecto.2004.07.059.

McCaffrey, R. (1994), Global variability in subduction thrust zone-forearc systems, *Pure Appl. Geophys.*, *142*(1), 173–224, doi:10.1007/BF00875971.

McGlashan, N., L. Brown, and S. Kay (2008), Crustal thickness in the central Andes from teleseismically recorded depth phase precursors, *Geophys. J. Int.*, *175*(3), 1013–1022, doi:10.1111/j.1365-246X.2008.03897.x.

Melnick, D., B. Bookhagen, H. P. Echtler, and M. R. Strecker (2006), Coastal deformation and great subduction earthquakes, Isla Santa María, Chile (37°S), *Geological Society of America Bulletin*, *118*(11-12), 1463–1480, doi:10.1130/B25865.1.

Melnick, D., B. Bookhagen, M. R. Strecker, and H. P. Echtler (2009), Segmentation of megathrust rupture zones from fore-arc deformation patterns over hundreds to millions of years, Arauco peninsula, Chile, *J. Geophys. Res.*, *114*, 23 PP., doi:200910.1029/2008JB005788.

Melnick, D., M. Moreno, M. Motagh, M. Cisternas, and R. L. Wesson (2012), Splay Fault Slip During the Mw 8.8 2010 Maule Chile Earthquake, *Geology*, *40*(3), 251–254, doi:10.1130/G32712.1.

Métois, M., A. Socquet, and C. Vigny (2012), Interseismic coupling, segmentation and mechanical behavior of the central Chile subduction zone, *J. Geophys. Res.*, *117*, 16 PP., doi:10.1029/2011JB008736.

Minoura, K., F. Imamura, D. Sugawara, Y. Koni, and T. Iwashita (2001), The 869 Jogan tsunami deposit and recurrence interval of large-scale tsunami on the Pacific coast of northeast J apan, *Journal of Natural Disaster Science*, *23*(2), 83–88.

Moreno, M., M. Rosenau, and O. Oncken (2010), 2010 Maule earthquake slip correlates with pre-seismic locking of Andean subduction zone, *Nature*, *467*(7312), 198–202, doi:10.1038/nature09349.

Moreno, M. et al. (2011), Heterogeneous plate locking in the South–Central Chile subduction zone: Building up the next great earthquake, *Earth Planet. Sci. Lett.*, *305*(3–4), 413–424, doi:10.1016/j.epsl.2011.03.025.

Moreno, M. et al. (2012), Toward understanding tectonic control on the Mw 8.8 2010 Maule Chile earthquake, *Earth Planet. Sci. Lett.*, *321–322*(0), 152–165, doi:10.1016/j.epsl.2012.01.006.

Moreno, M. S., J. Klotz, D. Melnick, H. Echtler, and K. Bataille (2008), Active faulting and heterogeneous deformation across a megathrust segment boundary from GPS data, south central Chile (36–39°S), *Geochemistry Geophysics Geosystems*, *9*(12), Q12024, doi:10.1029/2008GC002198.

Nishenko, S. P. (1985), Seismic potential for large and great interplate earthquakes along the Chilean and southern Peruvian margins of South America: a quantitative reappraisal, *J. Geophys. Res.*, *90*(B5), 3589–3615, doi:10.1029/JB090iB05p03589.

Nishenko, S. P. (1991), Circum-Pacific seismic potential: 1989-1999, *Pure Appl. Geophys.*, *135*(2), 169–259, doi:10.1007/BF00880240.

NOAA, N. G. D. C. (2006), *ETOPO2v2 Global Gridded 2-minute Database*, National Geophysical Data Center, National Oceanic and Atmospheric Administration, U.S. Dept. of Commerce.

Norabuena, E. O., T. H. Dixon, S. Stein, and C. G. A. Harrison (1999), Decelerating Nazca-South America and Nazca-Pacific Plate motions, *Geophys. Res. Lett.*, *26*(22), 3405–3408, doi:10.1029/1999GL005394.

Okada, Y. (1992), Internal deformation due to shear and tensile faults in a half-space, *Bull. Seismol. Soc. Am.*, *82*(2), 1018–1040.

Oppenheimer, D. H., P. A. Reasenberg, and R. W. Simpson (1988), Fault Plane Solutions for the 1984 Morgan Hill, California, Earthquake Sequence: Evidence for the State of Stress on the Calaveras Fault, *J. Geophys. Res.*, *93*(B8), PP. 9007–9026, doi:10.1029/JB093iB08p09007.

Plafker, G. (1967), Surface faults on Montague Island associated with the 1964 Alaska earthquake, *U.S. Geol. Surv. Prof. Pap.*, *543-G*, 42 p.

Plafker, G., and J. C. Savage (1970), Mechanism of the Chilean Earthquakes of May 21 and 22, 1960, *Geol. Soc. Am. Bull.*, *81*(4), 1001–1030, doi:10.1130/0016-7606(1970)81[1001:MOTCEO]2.0.CO;2.

Pollitz, F. F. et al. (2011), Coseismic slip distribution of the February 27, 2010 Mw 8.8 Maule, Chile earthquake, *Geophys. Res. Lett.*, *38*(9), L09309–, doi:10.1029/2011GL047065.

Press, F. (1965), Displacements, Strains, and Tilts at Teleseismic Distances, *J. Geophys. Res.*, *70*(10), 2395–2412, doi:10.1029/JZ070i010p02395.

Pritchard, M. E., E. O. Norabuena, C. Ji, R. Boroschek, D. Comte, M. Simons, T. H. Dixon, and P. A. Rosen (2007), Geodetic, teleseismic, and strong motion constraints on slip from recent southern Peru subduction zone earthquakes, *J. Geophys. Res.*, *112*(B3), B03307, doi:10.1029/2006JB004294.

Reid, H. F. (1910), *The mechanics of the earthquake.*, The California earthquake of April 18, 1906, Report of the State Earthquake Investigation Committee. 1908-10. California., Carnegie institution of Washington, Washington, D.C.

Rietbrock, A., I. Ryder, G. Hayes, C. Haberland, D. Comte, S. Roecker, and H. Lyon-Caen (2012), Aftershock seismicity of the 2010 Maule Mw=8.8, Chile, earthquake: Correlation between co-seismic slip models and aftershock distribution?, *Geophys. Res. Lett.*, *39*(8), L08310, doi:10.1029/2012GL051308.

Rikitake, T. (1976), Recurrence of great earthquakes at subduction zones, *Tectonophysics*, *35*(4), 335–362, doi:10.1016/0040-1951(76)90075-5.

Ruegg, J. C., J. Campos, R. Madariaga, E. Kausel, J. B. de Chabalier, R. Armijo, D. Dimitrov, I. Georgiev, and S. Barrientos (2002), Interseismic strain accumulation in south central Chile from GPS measurements, 1996-1999, *Geophys. Res. Lett.*, *29*(11), 1517–, doi:10.1029/2001GL013438.

Ruegg, J. C., A. Rudloff, C. Vigny, R. Madariaga, J. B. de Chabalier, J. Campos, E. Kausel, S. Barrientos, and D. Dimitrov (2009), Interseismic strain accumulation measured by GPS in the seismic gap between Constitución and Concepción in Chile, *Phys. Earth Planet. Inter.*, *175*(1-2), 78–85, doi:10.1016/j.pepi.2008.02.015.

Ryder, I., A. Rietbrock, K. Kelson, R. Bürgmann, M. Floyd, A. Socquet, C. Vigny, and D. Carrizo (2012), Large extensional aftershocks in the continental forearc triggered by the 2010 Maule earthquake, Chile, *Geophys. J. Int.*, *188*(3), 879–890, doi:10.1111/j.1365-246X.2011.05321.x.

Satake, K., and B. F. Atwater (2007), Long-Term Perspectives on Giant Earthquakes and Tsunamis at Subduction Zones, *Annu. Rev. Earth Planet. Sci.*, *35*(1), 349–374, doi:10.1146/annurev.earth.35.031306.140302.

Savage, J. C. (1983), A Dislocation Model of Strain Accumulation and Release at a Subduction Zone, *J. Geophys. Res.*, *88*(B6), 4984–4996, doi:10.1029/JB088iB06p04984.

Scholz, C. (1988), The brittle-plastic transition and the depth of seismic faulting, *Geol. Rundsch.*, *77*(1), 319–328, doi:10.1007/BF01848693.

Scholz, C. H. (2002), *The mechanics of earthquakes and faulting*, 2nd Edition., Cambridge University Press, Cambridge, UK.

SERNAGEOMIN (2003), *Mapa Geológico de Chile: versión digital*, Geological map Scale 1:1,000,000, Servicio Nacional de Geología y Minería, Santiago, Chile.

Sibson, R. H. (1985), A note on fault reactivation, *J. Struct. Geol.*, *7*(6), 751–754, doi:10.1016/0191-8141(85)90150-6.

Song, T.-R. A., and M. Simons (2003), Large Trench-Parallel Gravity Variations Predict Seismogenic Behavior in Subduction Zones, *Science*, *301*(5633), 630–633, doi:10.1126/science.1085557.

Stein, R. S. (1999), The role of stress transfer in earthquake occurrence, *Nature*, *402*(6762), 605–609, doi:10.1038/45144.

Stein, R. S., G. C. P. King, and J. Lin (1994), Stress Triggering of the 1994 M = 6.7 Northridge, California, Earthquake by Its Predecessors, *Science*, *265*(5177), 1432–1435, doi:10.1126/science.265.5177.1432.

Steketee, J. A. (1958), On Volterra's dislocations in a semi-infinite elastic medium, *Can. J. Phys.*, *36*(2), 192–205, doi:10.1139/p58-024.

Suarez, G., and D. Comte (1993), Comment on: Seismic Coupling Along the Chilean Subduction Zone; by B. W. Tichelaar and L. R. Ruff, *J. Geophys. Res.*, *98*(B9), 15825–15828, doi:10.1029/93JB00234.

Tichelaar, B. W., and L. J. Ruff (1991), Seismic Coupling Along the Chilean Subduction Zone, *J. Geophys. Res.*, *96*(B7), 11997–12022, doi:10.1029/91JB00200.

Tichelaar, B. W., and L. J. Ruff (1993), Depth of Seismic Coupling Along Subduction Zones, *J. Geophys. Res.*, *98*(B2), 2017–2037, doi:10.1029/92JB02045.

Toda, S., J. Lin, and R. S. Stein (2011a), Using the 2011 Mw 9.0 off the Pacific coast of Tohoku Earthquake to test the Coulomb stress triggering hypothesis and to calculate faults brought closer to failure, *Earth, Planets and Space*, *63*(7), 725–730, doi:10.5047/eps.2011.05.010.

Toda, S., R. S. Stein, and J. Lin (2011b), Widespread seismicity excitation throughout central Japan following the 2011 M=9.0 Tohoku earthquake and its interpretation by Coulomb stress transfer, *Geophys. Res. Lett.*, *38*, L00G03–, doi:10.1029/2011GL047834.

Tong, X. et al. (2010), The 2010 Maule, Chile earthquake: Downdip rupture limit revealed by space geodesy, *Geophys. Res. Lett.*, *37*(24), L24311–, doi:10.1029/2010GL045805.

Turcotte, D. L., and G. Schubert (2002), *Geodynamics*, 2nd Edition., Cambridge University Press, Cambridge; New York.

Uyeda, S. (1982), Subduction zones: An introduction to comparative subductology, *Tectonophysics*, *81*(3-4), 133–159, doi:10.1016/0040-1951(82)90126-3.

Vigny, C. et al. (2011), The 2010 Mw 8.8 Maule Megathrust Earthquake of Central Chile, Monitored by GPS, *Science*, *332*(6036), 1417–1421, doi:10.1126/science.1204132.

Volterra, V. (1907), Sur l'equilibre des corps multiplement connexes, *Ann. sci. école norm. supérieure, III. Ser*, *24*, 401–517.

Wall, R., P. Gana, and A. Gutiérrez (1996), *Mapa geológico del área de San Antonio-Melipilla, Regiones de Valparaiso, Metropolitana y del Libertador Bernardo O'Higgins.*, Geological map Scale 1:100,000, Servicio Nacional de Geología y Minería, Santiago, Chile.

Wells, R. E., R. J. Blakely, Y. Sugiyama, D. W. Scholl, and P. A. Dinterman (2003), Basin-centered asperities in great subduction zone earthquakes: A link between slip, subsidence, and subduction erosion?, *J. Geophys. Res.*, *108*(B10), 2507, doi:10.1029/2002JB002072.

Yáñez, G., and J. Cembrano (2004), Role of viscous plate coupling in the late Tertiary Andean tectonics, *J. Geophys. Res.*, *109*, 21 PP., doi:10.1029/2003JB002494.

Yáñez, G. A., P. Gana, and R. Fernández (1998), Origen y significado geológico de la Anomalía Melipilla, Chile central, *Rev. Geol. Chile*, *25*(2), 175–198, doi:10.4067/S0716-02081998000200005.

CHAPTER 4

SHALLOW UPPER PLATE SEISMICITY OVER ACTIVE SUBDUCTION REGIONS

4.1 Abstract

The great 2010, M_w 8.8 Maule and 2011, M_w 9.0 Tohoku earthquakes in Chile and Japan triggered large, shallow seismicity on upper plate faults in the near-field above the rupture, reaching up to M_w 7.0. We use the entire Global CMT catalog of earthquakes to examine the style and character of upper plate earthquakes associated with great subduction events worldwide $\geq M_w$ 7.7, since 1976 (44 events). The intraplate events selected have hypocentral locations inside the forearc wedge above the rupture; our search spans the full time series of the catalog, capturing the seismic behavior of the upper plate over all the stages of the subduction seismic cycle. Within the detection limits of the catalog, between 61% and 83% of the cases were upper plate earthquakes exhibit periods of increase seismicity rate and magnitude above background levels occurred contemporaneous to megathrust ruptures. That correlation is stronger for normal fault events than reverse or strike-slip earthquakes. For any given subduction zone, the summation of the Mo accounted by the forearc normal fault aftershocks appears to have a positive correlation with the Mo of the subduction earthquake – the larger the megathrust earthquake the larger the energy released by forearc aftershocks. More importantly, our results suggest that great subduction events may be important contributors of stress to produce permanent extension in the forearc.

4.2 Introduction

Following the 2010 Maule and 2011 Tohoku earthquakes, the upper plate overlying the rupture areas experienced a significant change in their seismic behavior. Both the rate of seismicity and total moment released by the forearc, intraplate events exceeded by far what had been observed in these regions preceding the main shocks (e.g., *Toda et al.*, 2011; *Hasegawa et al.*, 2012; *Lange et al.*, 2012). But how likely are large, upper plate aftershocks after a great megathrust event? And is there a characteristic kinematic style of those triggered earthquakes?

In a recent study, also using data from the world catalog, *Gomberg and Sherrod* (2014) found evidence that, over a 1-year time window, the rate of seismicity in the overriding plate and in some examples, the magnitude reached by upper plate earthquakes, increased with respect to background activity after great subduction ruptures ($M > 8.6$). In the cases of the Maule and Tohoku earthquakes, the large triggered earthquakes were normal fault events (e.g., *Farías et al.*, 2011; *Toda and Tsutsumi*, 2013; *Aron et al.*, 2013), in contrast to the compressional style of upper plate seismicity observed before the megathrust earthquakes (e.g., *Hardebeck*, 2012; e.g., *Hasegawa et al.*, 2012; *Yoshida et al.*, 2012). Other plate boundaries that have experienced great subduction earthquakes, as the case of the 1964 Alaska and 2004 Sumatra-Andaman earthquakes, show evidence of reverse, splay-fault reactivation as well as strike-slip kinematics in the upper plate following the main shocks (e.g., *Plafker*, 1967; *Lay et al.*, 2005; *Sibuet et al.*, 2007).

Previously, we suggested that in the Maule earthquake region and perhaps elsewhere, subduction earthquakes may be an important mechanism to reactivate faults in the upper plate, producing permanent deformation of the forearc and shaping its structural grain (*Aron et al.*, 2013, Accepted). If the hypothesis holds true, one

would expect to see a perturbation in the seismic behavior of the upper plate following megathrust earthquakes. Here we use the Global CMT catalog (*Ekström et al.*, 2012) to examine the style and character of near-field, upper plate earthquakes associated with great subduction events. We test the hypothesis using standard techniques in statistical seismology to answer the following questions: After a great megathrust earthquake, (1) is there an increase in upper plate seismicity? (2) Is there an increase in the moment released by upper plate events? And (3), is there a change in the kinematic style of the upper plate seismicity?

We show evidence that most of the great subduction events triggered upper plate seismicity in the near-field overlying the rupture, predominantly normal faulting but in some cases thrust and strike-slip as well. We show how the magnitude of these triggered events scales proportionally to the size of the megathrust. Finally, we discuss the implications of our findings for the long-term structural configuration of the forearc and seismic hazard assessments.

Our contribution goes further than *Gomberg and Sherrod* (2014) in analyzing the kinematic style of these triggered events, and how that evolves through the different stages of the seismic cycle. Thus, the results presented here have broader implications in: (a) understanding the mechanics involved in permanent deformation processes of the upper plate under the loading conditions imposed by the plate interface, (b) addressing the importance of the inherited forearc structure to accommodate the loading imposed by the megathrust, and (c) assessing the likelihood of which specific forearc structures might be more suitable to reactivate after subduction events.

4.3 Methods

4.3.1 Subduction earthquakes and near-field volume

We have searched the entire Global CMT catalog between January 1, 1976 and May 31, 2013 for subduction zones that have experienced large to great subduction earthquakes, with moment magnitudes equal or greater than 7.7, and found 44 events (Fig. 4.1 and Table 4.1). With almost 40 years of data, we have good coverage of coseismic and post-seismic phases of the great subduction events but we have a narrow window of observation for the interseismic period. Although there are different methods to determine the volume of influence of an earthquake or near-field (e.g., *van Stiphout et al.*, 2012), here we use a window-oriented approach to define that volume based on a factor (β) of the megathrust rupture length (L) (e.g., *Parsons and Velasco*, 2011; *Tahir et al.*, 2012; *Zakharova et al.*, 2013). In map view, the extent of the near-field area is given by the distance along strike: $D_{as} = \beta L$, centered on the centroid epicenter, and the distance from the trench to the volcanic arc, perpendicular to the margin, so the segment encloses the entire forearc-arc region of the plate boundary over the subduction ruptures (Fig. 4.1 and Appendix Figures C). We have chosen the centroid location reported by the catalog instead of the hypocenter because it is most likely to represent the center of the final slip distribution instead of the rupture initiation (e.g., *Smith and Ekström*, 1997), which in some cases can be far off from the center of the entire rupture area (e.g., *Ammon et al.*, 2005). The parameter L for each megathrust earthquake was determined from the M_w using empirical scaling laws (*Wells and Coppersmith*, 1994) and we set $\beta = 3$ following the criteria to determine near-field areas of earthquakes adopted by *Parsons and Velasco* (2011). Where active volcanic edifices are absent, we use the horizontal projection of the 110 km depth contour of the Slab1.0 surface (*Hayes et al.*, 2012) to limit the forearc-arc extension.

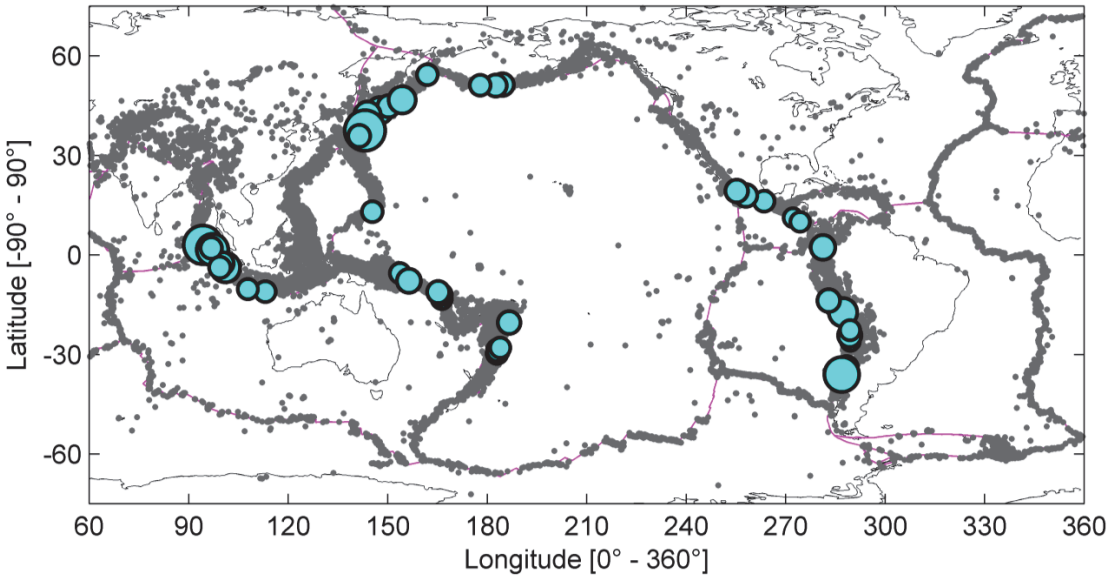

Figure 4.1: World map showing in light blue the epicenters of subduction earthquakes ≥ M_w 7.7 identified in Global CMT catalog between January 1, 1976 and May 31, 2013 (Table 4.1 in main manuscript). In gray are shown all the earthquakes recorded by catalog.

Table 4.1: Location and general information of the great subduction earthquakes identified in the catalog.

Slab1.0 Region	Nr	Date	Time (UTC)	° Lat	° Long	Depth [km]	Mw
	1	1986/05/07	22:47:10.2	51.3	-175.4	31.3	8.0
ALU	2	1996/06/10	04:03:35.4	51.1	-177.4	29.0	7.9
	3	2003/11/17	06:43:06.8	51.1	177.9	21.7	7.8
IZU	4	1993/08/08	08:34:25.0	13.1	145.3	59.3	7.8
	5	1976/01/14	15:56:34.9	-29.7	-177.0	46.7	7.8
KER	6	1976/01/14	16:47:33.5	-28.7	-176.8	17.7	7.9
	7	1986/10/20	06:46:10.4	-27.9	-176.1	50.4	7.7
	8	2006/05/03	15:26:40.3	-20.4	-173.5	67.8	8.0
	9	1978/06/12	08:14:26.4	38.0	142.1	37.7	7.7
	10	1994/10/04	13:22:58.3	43.6	147.6	68.2	8.3
	11	1994/12/28	12:19:23.6	40.6	143.0	27.7	7.8
	12	1995/12/03	18:01:07.7	44.8	150.2	25.9	7.9
KUR	13	1997/12/05	11:26:54.7	54.3	161.9	33.6	7.8
	14	2003/09/25	19:50:06.4	42.2	143.8	28.2	8.3
	15	2006/11/15	11:14:17.8	46.7	154.3	13.5	8.3
	16	2011/03/11	05:46:23.0	37.5	143.1	20.0	9.1
	17	2011/03/11	06:15:45.0	35.9	141.4	29.0	7.9
	18	1978/11/29	19:52:47.6	16.2	-96.6	16.1	7.8
	19	1985/09/19	13:17:47.8	17.9	-102.0	21.3	8.0
MEX	20	1992/09/02	00:15:57.5	11.2	-87.8	15.0	7.7
	21	1995/10/09	15:35:55.7	19.3	-104.8	15.0	8.0
	22	2012/09/05	14:42:07.9	10.0	-85.6	29.7	7.7

Table 4.1. Cont.

	23	1979/12/12	07:59:03.3	2.3	-78.8	19.7	8.1
	24	1983/10/04	18:52:12.9	-26.0	-70.6	38.7	7.7
	25	1985/03/03	22:47:06.9	-33.9	-71.7	40.7	8.0
	26	1995/07/30	05:11:23.5	-24.2	-70.7	28.7	8.0
SAM	27	1996/11/12	16:59:44.0	-15.0	-75.4	37.4	7.7
	28	2001/06/23	20:33:14.1	-17.3	-72.7	29.6	8.4
	29	2007/08/15	23:40:57.9	-13.7	-77.0	33.8	8.0
	30	2007/11/14	15:40:50.5	-22.6	-70.6	37.6	7.8
	31	2010/02/27	06:34:15.6	-36.0	-73.2	23.2	8.8
	32	1994/06/02	18:17:36.8	-11.0	113.0	15.0	7.8
	33	2000/06/04	16:28:26.2	-4.7	101.9	43.9	7.9
	34	2004/12/26	00:58:50.0	3.1	94.3	28.6	9.0
	35	2005/03/28	16:09:36.5	1.7	97.1	25.8	8.6
SUM	36	2006/07/17	08:19:28.8	-10.3	107.8	20.0	7.7
	37	2007/09/12	11:10:26.8	-3.8	101.0	24.4	8.5
	38	2007/09/12	23:49:03.7	-2.5	100.1	43.1	7.9
	39	2010/04/06	22:15:01.6	2.1	96.7	17.6	7.8
	40	2010/10/25	14:42:22.5	-3.7	99.3	12.0	7.9
	41	1980/07/17	19:42:23.2	-12.4	165.9	34.0	7.8
	42	1997/04/21	12:02:26.4	-13.2	166.2	51.2	7.7
VAN	43	2009/10/07	22:18:51.2	-11.9	166.0	41.7	7.8
	44	2013/02/06	01:12:25.8	-11.2	165.2	20.2	7.9

When two or more individual near-field areas intersect or superimpose, we combine them in a single region which encloses all of the intersected segments and subduction events. Finally, we checked manually to see if both the cloud of interplate aftershocks of the main shocks and the ruptures areas of major events worldwide reported by *Tarr et al.* (2009) are contained within our segments. The criteria applied here to determine near-field areas resulted in 18 segments (Tables 4.2, 4.3), covering approximately 45% of the world forearc regions (Appendix Figures C).

4.3.2 Upper plate vs. megathrust seismicity and kinematics

After determining the near-field segments, we scan the catalog for all the events that fall inside those regions. The Slab1.0 surface is used to separate earthquakes nucleated on the plate interface from events nucleated in the upper plate wedge, considering a safe range of depth-tolerance of ±10 km above and below the slab. That depth range constraints the width of the 3-D volume of the slab or megathrust. Then we apply an eigen decomposition to calculate the principal axes of the earthquakes from the moment tensor components reported by the catalog according to the expression: $M_{ij}\,\boldsymbol{X_k} = \lambda_k \boldsymbol{X_k}$; i, j, k = 1-3, where M_{ij} is the moment tensor of the earthquake, $\boldsymbol{X_k}$ are the three eigenvectors corresponding to the **P**, **T** and **B** axes, and λ_k the corresponding eigenvalues. The orientation of the principal axes of the event are used to categorize the kinematics between normal, reverse and strike-slip faults, following the criteria proposed by *Frohlich* (1992). Therefore, subduction events are reverse fault earthquakes contained inside the slab volume with one of the nodal planes coinciding in orientation with Slab1.0, within ±15° of strike and dip tolerance. Although no uncertainties are reported for the Slab1.0 model, we assume that the chosen width of 20 km, centered at the slab surface, is a conservative estimate given the contour intervals of 20 km provided by the model (*Hayes et al.*, 2012; *Gomberg*

and Sherrod, 2014). However, a larger uncertainties may arise from the depths estimates reported by the CMT catalog which error can exceed the ±10 km (*Engdahl et al.*, 1998), so we acknowledge that some events in might be misclassified.

With respect to the magnitude of the earthquakes, when our analysis requires summation of events we determine a total scalar moment using the expression (*Stein and Wysession*, 2003):

$$Mo_{\,total} = \left(\sum_{ij} {M_{ij}}_{\,total}^{\,2} \right)^{1/2} / \sqrt{2} \tag{1}$$

where:

$$M_{ij\,total} = \sum_{n=1}^{Nr\ EQs} M_{ij}^{(n)} \tag{2}$$

is the total moment tensor sum over the time range. Finally, we calculate the moment magnitude associated to the total scalar moment in dyne-cm according to:

$$M_{w\,total} = (2/3\ \log_{10} Mo_{\,total}) - 10.7 \tag{3}$$

Tables 4.2 and 4.3 show the total accumulated scalar moment and moment magnitude for each of the near-field segments, over the entire time-range of the catalog, for upper plate and subduction events. Using this approach to calculate the scalar moment and moment magnitude we can estimate the errors from the uncertainties reported in the catalog for the individual components of the moment tensor using standard methods for Gaussian error propagation (*Bevington and Robinson*, 2002).

Table 4.2: General information of the near-field subduction segments determined in our study, excluding fixed events

			Fix NO			
Segment*	Earthquake Nr**	Area km^2	***Mo tot. MT	Mw tot. MT	Mo tot. UP	Mw tot. UP
ALU_seg1	1, 2	224205.0	2.6E+28	8.2	6.8E+26	7.2
ALU_seg2	3	115653.8	7.3E+27	7.9	5.2E+26	7.1
IZU_seg1	4	91428.4	6.4E+27	7.8	2.0E+25	6.2
KER_seg1	8	141314.7	1.3E+28	8.0	7.1E+25	6.5
KER_seg2	5, 6, 7	163815.0	2.4E+28	8.2	1.2E+27	7.4
KUR_seg1	13	160436.6	6.3E+27	7.8	1.6E+24	5.4
KUR_seg2	9, 10, 11, 12, 14, 15, 16, 17	1165889.8	6.8E+29	9.2	8.7E+26	7.3
MEX_seg1	19, 21	272548.4	3.8E+28	8.3	1.4E+26	6.7
MEX_seg2	18	140928.0	6.1E+27	7.8	3.5E+26	7.0
MEX_seg3	20, 22	143592.0	9.1E+27	7.9	1.9E+27	7.5
SAM_seg1	25, 31	608520.8	3.1E+29	9.0	1.1E+27	7.3
SAM_seg2	24, 26, 30	299436.3	3.2E+28	8.3	8.1E+24	5.9
SAM_seg3	27, 28, 29	501317.1	9.6E+28	8.6	9.4E+26	7.3
SAM_seg4	23	216672.0	2.0E+28	8.2	1.0E+27	7.3
SUM_seg1	32	139726.1	6.0E+27	7.8	--	--
SUM_seg2	36	136524.1	5.6E+27	7.8	5.0E+24	5.8
SUM_seg3	33, 34, 35, 37, 38, 39, 40	932533.5	1.1E+30	9.3	3.8E+27	7.7
VAN_seg1	41, 42, 43, 44	106494.4	4.1E+28	8.4	1.2E+27	7.3

*See Appendix Figures C for locations of the subduction segments.
**Numbers are the same as in Table 4.1.
*** The total moment of the segment is normalized by the area for comparison between the different regions.

Table 4.3: General information of the near-field subduction segments determined in our study, including fixed events

			Fix YES			
Segment	Earthquake Nr	Area km^2	Mo tot. MT	Mw tot. MT	Mo tot. UP	Mw tot. UP
ALU_seg1	1, 2	224205.0	2.6E+28	8.2	1.3E+27	7.4
ALU_seg2	3	115653.8	7.9E+27	7.9	5.9E+26	7.1
IZU_seg1	4	91428.4	6.4E+27	7.8	4.1E+25	6.4
KER_seg1	8	141314.7	1.3E+28	8.1	1.4E+26	6.7
KER_seg2	5, 6, 7	163815.0	2.5E+28	8.2	1.5E+27	7.4
KUR_seg1	13	160436.6	6.3E+27	7.8	2.7E+24	5.6
KUR_seg2	9, 10, 11, 12, 14, 15, 16, 17	1165889.8	6.8E+29	9.2	1.5E+27	7.4
MEX_seg1	19, 21	272548.4	3.8E+28	8.3	2.6E+26	6.9
MEX_seg2	18	140928.0	6.9E+27	7.9	3.7E+26	7.0
MEX_seg3	20, 22	143592.0	9.1E+27	7.9	2.0E+27	7.5
SAM_seg1	25, 31	608520.8	3.1E+29	9.0	1.2E+27	7.4
SAM_seg2	24, 26, 30	299436.3	3.2E+28	8.3	5.9E+25	6.5
SAM_seg3	27, 28, 29	501317.1	9.7E+28	8.6	9.4E+26	7.3
SAM_seg4	23	216672.0	2.0E+28	8.2	1.1E+27	7.3
SUM_seg1	32	139726.1	6.0E+27	7.8	1.9E+25	6.2
SUM_seg2	36	136524.1	5.7E+27	7.8	5.8E+24	5.8
SUM_seg3	33, 34, 35, 37, 38, 39, 40	932533.5	1.1E+30	9.3	4.5E+27	7.7
VAN_seg1	41, 42, 43, 44	106494.4	4.2E+28	8.4	1.2E+27	7.4

Note: Same footnotes as in Table 4.2

We report all our calculations for both the full dataset of earthquakes and a subset excluding events which depths were fixed ("FIX") and not a result of the inversion or modelling of broad-band P waveforms ("FREE" or "BDY").

4.3.3 Time series analysis

We analyze how the occurrence of the 44 identified megathrust earthquakes correlates over time with the following upper plate variables: (a) increments in number of seismic events, (b) increments in moment release rate and (c), kinematic style of those events at each of the 18 near-field segments (Tables 4.2 and 4.3; Figs. 4.2-4.4). All of the series tested are referenced to the same origin time and range from January 1, 1976 (day 0) to May 31, 2013 (day 13,665). In each segment, the time is discretized in bins of equal width and same center points for both series – upper plate and subduction events. At each time bin, we count the number of events and calculate the total moment and moment magnitude of the bin from equations (1-3).

When an event greater or equal to M_w 7.7 occurs in the subduction earthquakes series that day marks the start of a new time window which is used to search for triggered activity in the upper plate. Depending on the size of that window, over that period more than one great subduction earthquake can affect the near-field segment. In our analysis we considered this time range as the coseismic/post-seismic period of the specific subduction event(s) inside the segment. Therefore, the earthquakes contained in the rest of the bins of the time series are considered part of the interseismic stage of the plate boundary seismic cycle (Fig. 4.2-4.4). A number of possible time windows have been proposed in the literature for the extent of aftershock activity after an earthquake, ranging from days to tens of years from the main shock (e.g., *Molchan and Dmitrieva*, 1992; *Felzer et al.*, 2003; *Parsons and Velasco*, 2011; *Michael*, 2012; *Tahir et al.*, 2012; *van Stiphout et al.*, 2012; *Zakharova et al.*, 2013).

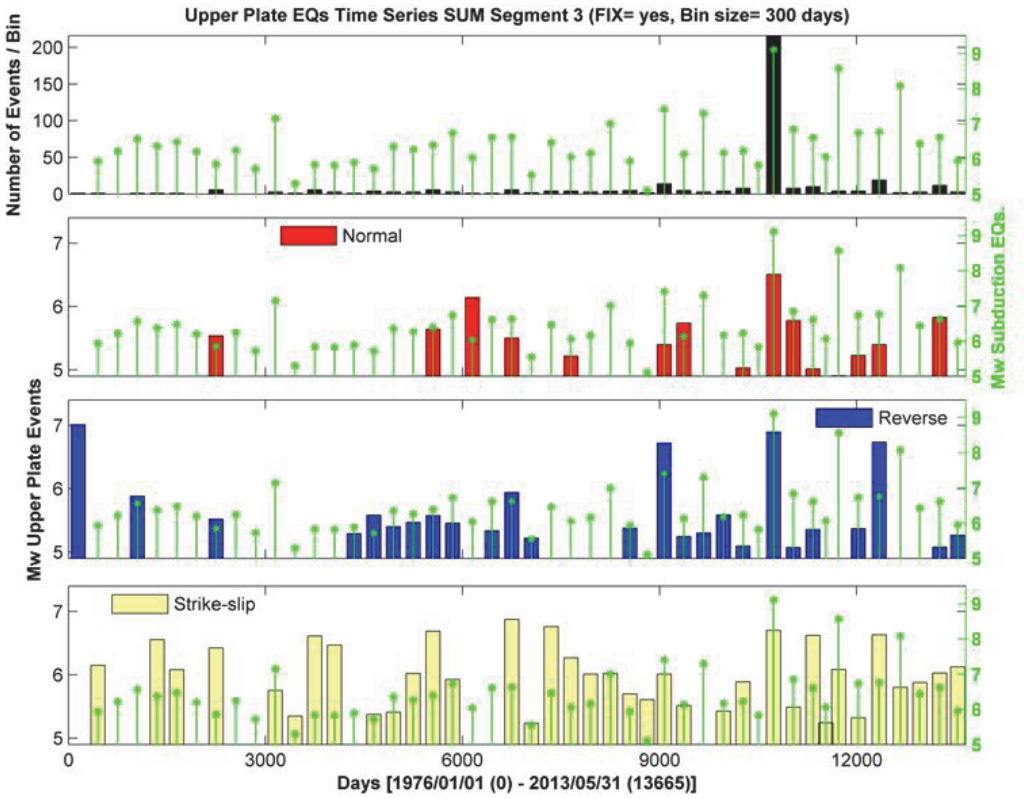

Figure 4.2: Time series of upper plate earthquakes over the SUM_seg3 segment (Tables 4.2, 4.3) expressed in terms of seismicity rate Nr/t (number of events per bin) and $M_{w\,total}$ for normal, reverse and strike-slip events, superimposed by $M_{w\,total}$ of subduction events shown in green (See Appendix Figures C for location).

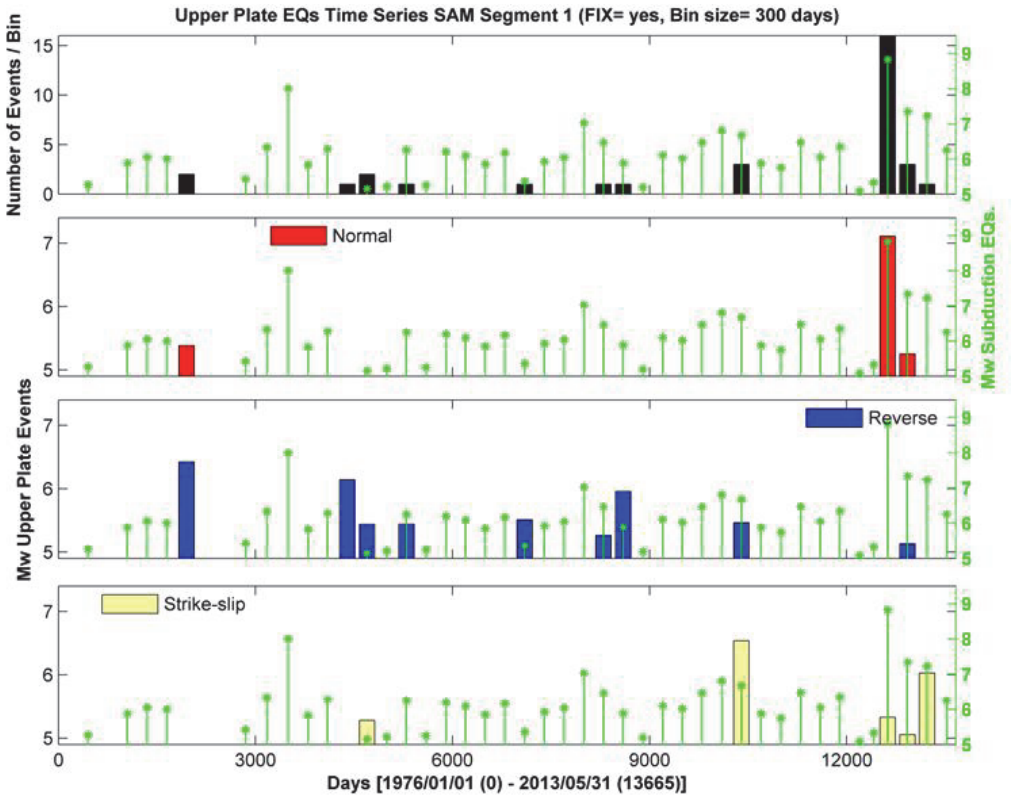

Figure 4.3: Time series of upper plate earthquakes over the SAM_seg1 segment (Tables 4.2, 4.3) expressed in terms of seismicity rate Nr/t (number of events per bin) and $M_{w\,total}$ for normal, reverse and strike-slip events, superimposed by $M_{w\,total}$ of subduction events shown in green (See Appendix Figures C for location).

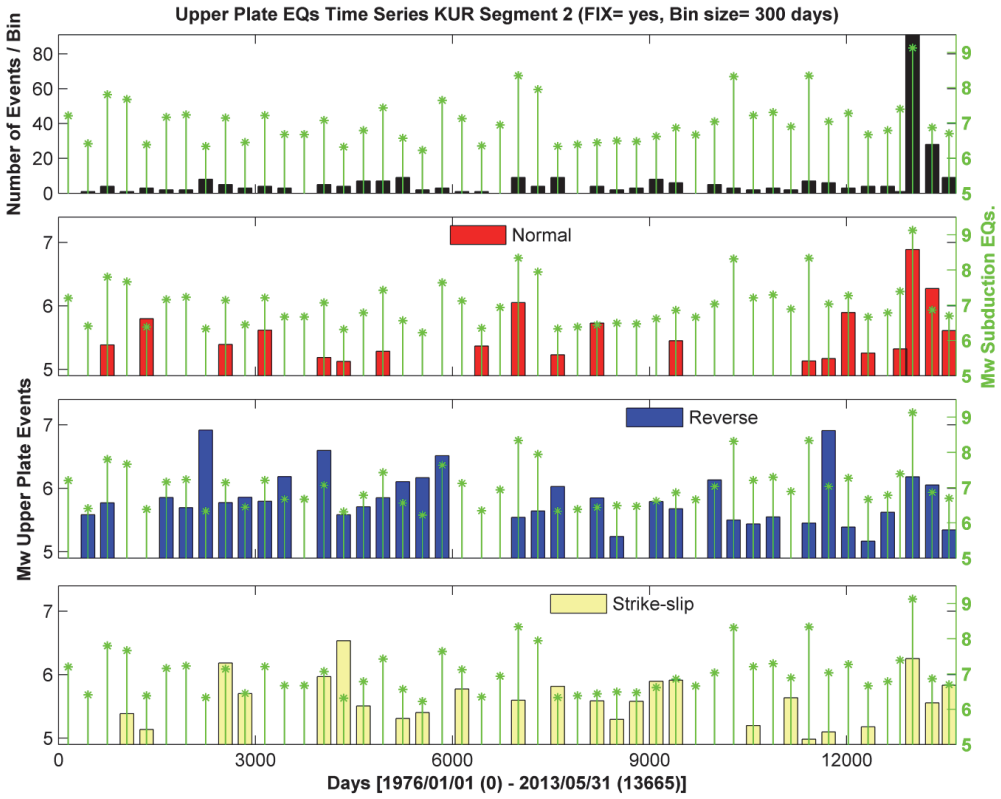

Figure 4.4: Time series of upper plate earthquakes over the KUR_seg2 segment (Tables 4.2, 4.3) expressed in terms of seismicity rate Nr/t (number of events per bin) and $M_{w\,total}$ for normal, reverse and strike-slip events, superimposed by $M_{w\,total}$ of subduction events shown in green (See Appendix Figures C for location).

That variation depends, among other factors, on the theoretical approach used, magnitude of the main shock and on whether aftershocks are considered to be strictly events nucleated on the same fault than the main shock or also triggered seismicity in the volume surrounding the structure. To address that uncertainty, we test how our results evolve and change when varying the time window or bin width (BW) over the domain:

BW = [100,200,300,…1000] days. We set the upper time bound in agreement with empirical and window-oriented aftershocks identification methods (e.g., *Molchan and Dmitrieva*, 1992; *van Stiphout et al.*, 2012), and because longer time windows would increase the smoothing of the signal and also lead to a total number of bins less than ten over the time series of the catalog, affecting the robustness of our statistical analysis.

To further investigate the correlation of the cycles of moment release by subduction events with changes in seismicity rate and moment release rate in the upper plate, we produce a binary analysis of the full time series, searching for pulses of deviation or peaks of these variables from background activity over time. We define the peaks over the series in terms of both $M_{w\,total}$ (see equations 1-3) and number of events per time (Nr/t), as values that exceed a background threshold estimated from 99% confidence intervals (CI) for these variables using nonparametric bootstrap resampling with replacement methods (Fig. 4.5) (*Efron*, 1981). The time series are discretized in equal-sized bins (e.g., Figs. 4.2, 4.4) and we produce a simulation of one thousand iterations, calculating at each run an average, background threshold of $M_{w\,total}$ and Nr/t for the individual segment series using the total population of bins, similar to other approaches to determine background seismicity rates found in recent literature (e.g., *Parsons and Velasco*, 2011; *Gomberg and Sherrod*, 2014). Our analysis differs in that we calculate specific thresholds for each combination of:

corresponding variable ($M_{w\,total}$ and Nr/t), segment, whether fixed events are included or not, independent fault kinematics and bin width (BW). The calculated background levels for each variable using all those combinations are listed in Appendix Tables C1-C3. Finally, we redefined the series in terms of zeroes and ones. We assign the value of 1 or true to bins which variable exceeds the defined background threshold (peak) or 0 otherwise (no-peak).

4.4 Results

4.4.1 Megathrust earthquakes vs. upper plate peaks of seismicity

First we test at each of the selected segments how well correlated in time are peaks of increasing seismicity and moment release rates in the upper plate to peaks in seismic activity of the subduction earthquakes series. We determine a correlation coefficient in our binary analysis as the percentage of all the upper plate peaks which coincide in time with peaks of megathrust moment release, using the following expressions:

$$\rho_{Mw} = \frac{\sum_{i=1}^{\#bins} \mathbf{1}\,\{UP_{Mw\,peak}(i) = 1 \mid MT_{Mw\,peak}(i) = 1\}}{\sum_{i=1}^{\#bins} \mathbf{1}\,\{UP_{Mw\,peak}(i) = 1\}} \quad (4)$$

$$\rho_{Nr} = \frac{\sum_{i=1}^{\#bins} \mathbf{1}\,\{UP_{Nr\,peak}(i) = 1 \mid MT_{Mw\,peak}(i) = 1\}}{\sum_{i=1}^{\#bins} \mathbf{1}\,\{UP_{Nr\,peak}(i) = 1\}} \quad (5)$$

where *UP*, *MT*, refer to upper plate and megathrust series, and *Mw* and *Nr* denotes peaks of the variables $M_{w\,total}$, or Nr/t respectively. The index ρ goes from 0 to 1 and can be read as the percentage of upper plate peaks which occurred in the same time range (bin position) than a peak of total moment magnitude of subduction earthquakes (Fig. 4.5). A value of zero means that all the upper plate peaks do not coincide in time

with peaks of subduction events, i.e., they occurred during the interseismic period or that there were no peaks in the upper plate, whereas $\rho = 1$ indicates a perfect correlation. We made independent calculations for each fault kinematic type (normal, reverse and strike-slip) of upper plate events and values of BW.

The results of maximum ρ_{Mw} and ρ_{Nr} calculated on each the 18 segments are shown in Figures 4.6 and 4.7 (see Appendix Tables C4-C5 for results using all the possible values of BW). Over the majority of the segments, the occurrence of peaks in the upper plate series is strongly correlated with the occurrence of peaks of subduction earthquakes, as shown by the high values of maximum ρ. For the case of ρ_{Mw}, between 61 and 72 % of the segments have at least one kinematic fault type showing values greater than 0.5, depending on whether events with fixed depth are used in the analysis or not (Table 4.4). Furthermore, between 61 and 68 % of the cases have ρ_{Mw} values equal to 1, which means that all the peaks of M_w in the upper plate for that specific fault kinematics are synchronous to peaks of subduction earthquakes. Those correlations are higher in terms of the ρ_{Nr} analysis. For example, between 61 and 78 % of the segments have at least one kinematic type with values equals to 1. As shown in Table 4.4 both the percentage of segments with ρ_{Mw} and ρ_{Nr} greater than 0.5 and equal to 1 are smaller when independent fault mechanisms are analyzed because, in some segments, peaks of upper plate seismicity associated with peaks of subduction earthquakes occur only for one or two kinematic type. However, the peaks of upper plate normal fault earthquakes are generally more strongly correlated to large subduction earthquakes compared to reverse or strike-slip events, independently of whether we include fixed events or not in the analysis (Figs. 4.6, 4.7; Table 4.4).

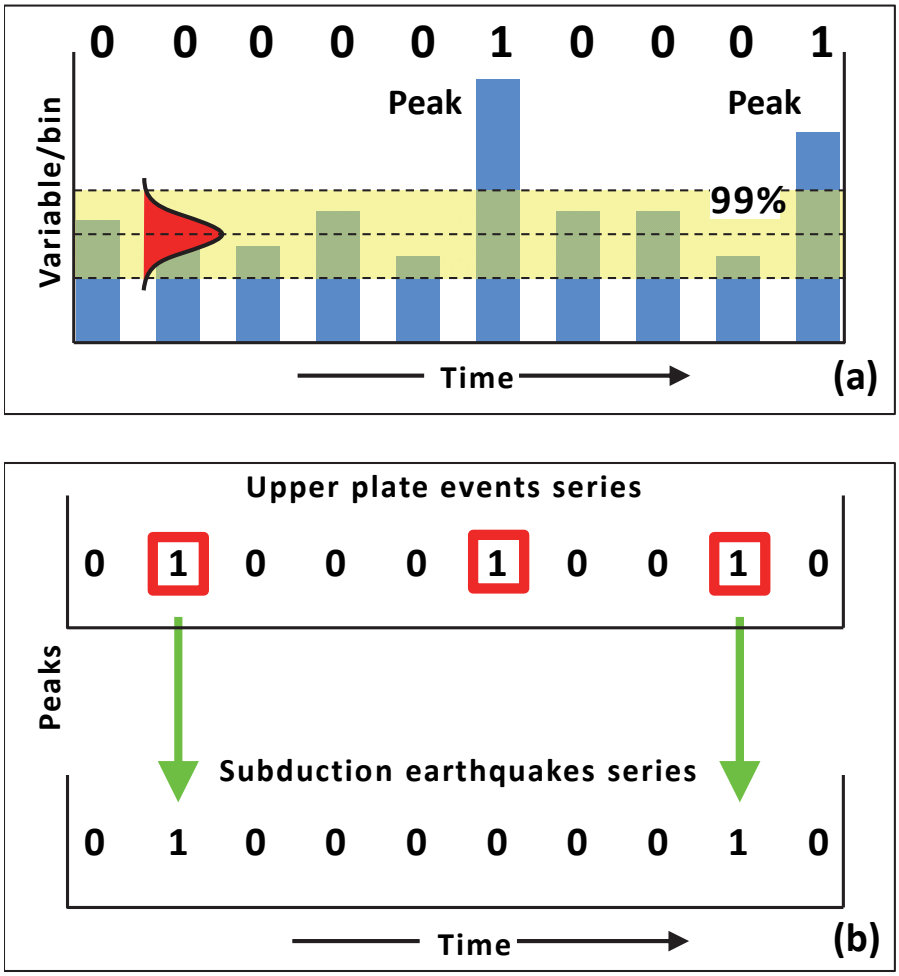

Figure 4.5: (a) Cartoon showing the methodology used to identify peaks of Nr/t (number of events per bin) and $M_{w\,total}$ over the time series. We determine 99% confidence intervals from a normal distribution of means resulting from 1,000 iterations using nonparametric bootstrap resampling with replacement. Values above that interval are considered "peaks" and are assigned a value of 1 or "true". (b) After redefining the series in terms of ones and zeroes we compare the occurrences of peaks in the upper plate (Nr/t and $M_{w\,total}$) with peaks of $M_{w\,total}$ in the subduction earthquakes series. In the example above, there are three peaks in the upper plate; two of them coincide in time with peaks of subduction earthquakes, so the corresponding value of the correlation coefficient ρ will be 2/3 or 0.7.

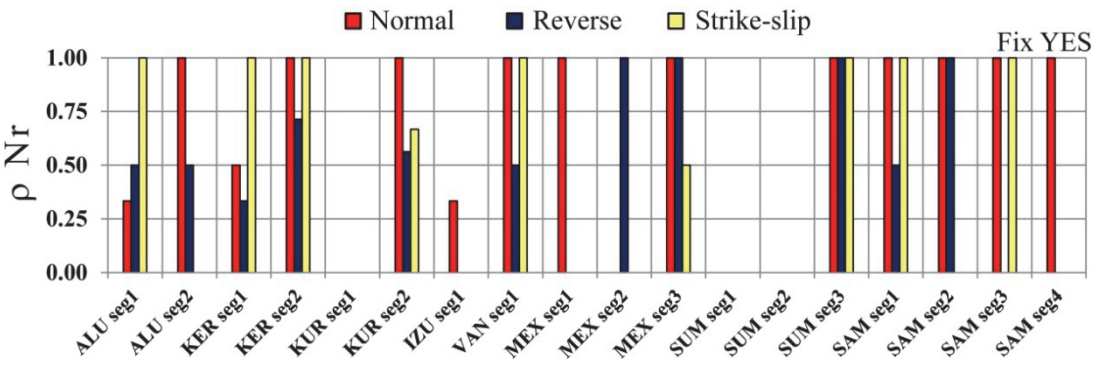

Figure 4.6: Peak correlation analysis of ρ_{Nr} separated by fault kinematics for all subduction segments and the full dataset (fixed and non-fixed events).

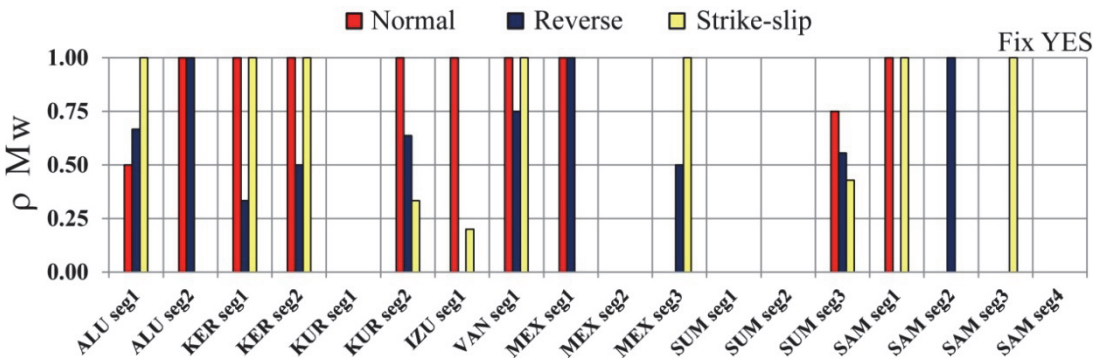

Figure 4.7: Peak correlation analysis of ρ_{Mw} separated by fault kinematic for all subduction segments and the full dataset (fixed and non-fixed events).

4.4.2 Moment magnitude correlation

Our final test to correlate the behavior of upper plate seismicity to occurrence of great subduction earthquakes is to investigate possible scaling relations of moment release between megathrust events and triggered upper plate earthquakes. In Appendix Tables C4-C5 we show that although there are variations, in general the best agreements between megathrust and upper plate peaks are reached when a time window of a thousand days per bin is used, which agrees with maximum time windows of aftershock activity determined from empirical approximations (*Knopoff and Gardner*, 1972; *Gardner and Knopoff*, 1974; *Uhrhammer*, 1986). So, using equations (1-3) and BW = 1,000 we select at each segment the bins in the subduction earthquakes time series with $M_{w\,total} > 7.6$, containing the events listed in Table 4.1, and compare them to the values of $M_{w\,total}$ of the corresponding upper plate time bins, independently for the three kinematic types. The bins are set so they start at the time of occurrence of the megathrust events but, in some cases, more than one subduction earthquake with $M_w > 7.6$ is included when they struck within the period of the selected BW. In any case, the moment magnitude correlation resolved here refers to the activity observed over the entire window of 1,000 days. The results of this analysis are shown in Figures 4.8-4.10 and Table 4.5. Using a least squares fit linear model, an increase of total moment magnitude release by megathrust earthquakes over the BW accounts for a maximum of 47.8% of the variation in the total moment magnitude increase of upper plate normal fault events in the time window. That correlation is much weaker for reverse and strike-slip kinematics, reaching maximum percentage values of R^2 of 8.1% and 6.8% respectively (Table 4.5).

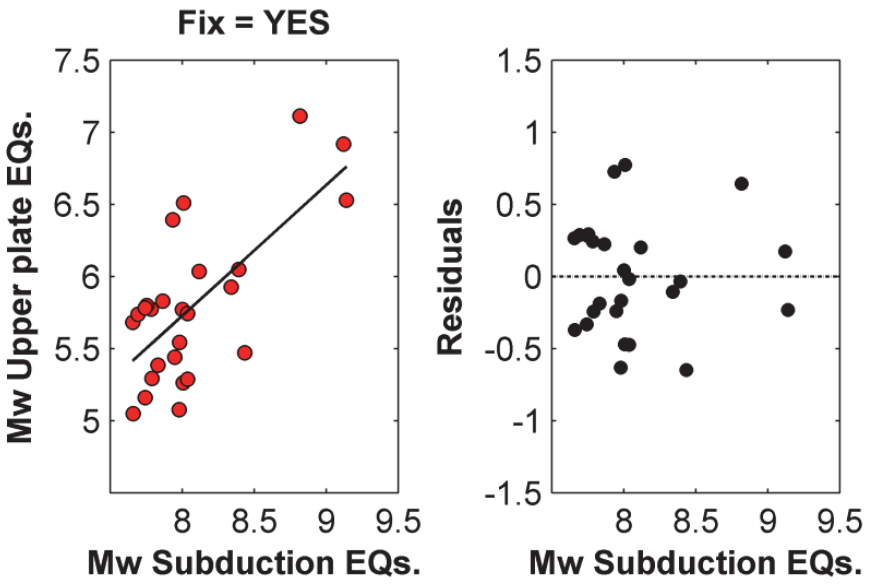

Figure 4.8: Scaling relation between $M_{w\,total}^{MT}$ of peaks greater than 7.7 and $M_{w\,total}^{UP}$ of normal fault aftershocks during the same time span. We use a bin size BW=1,000 for this analysis. The black line shows the linear least square regression line of the population.

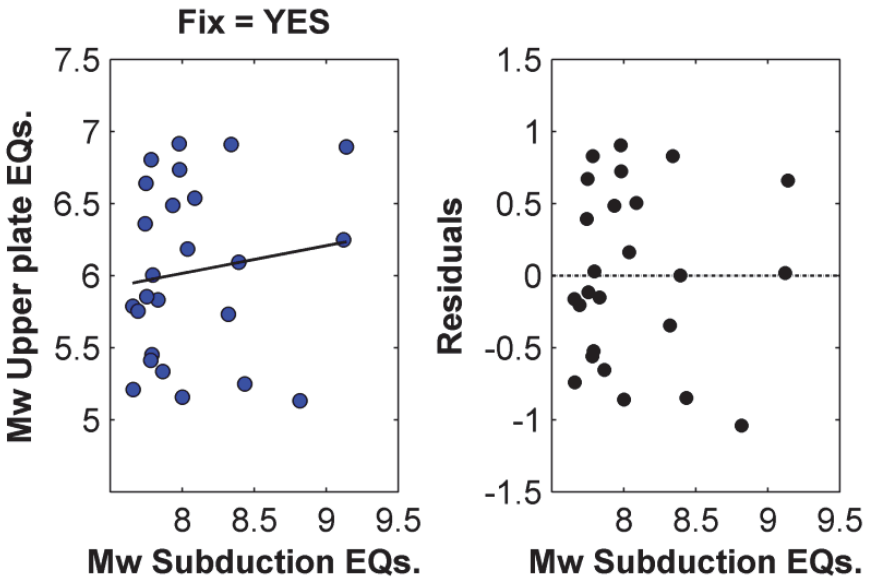

Figure 4.9: Scaling relation between $M_{w\,total}^{MT}$ of peaks greater than 7.7 and $M_{w\,total}^{UP}$ of reverse fault aftershocks during the same time span. We use a bin size BW=1,000 for this analysis. The black line shows the linear least square regression line of the population.

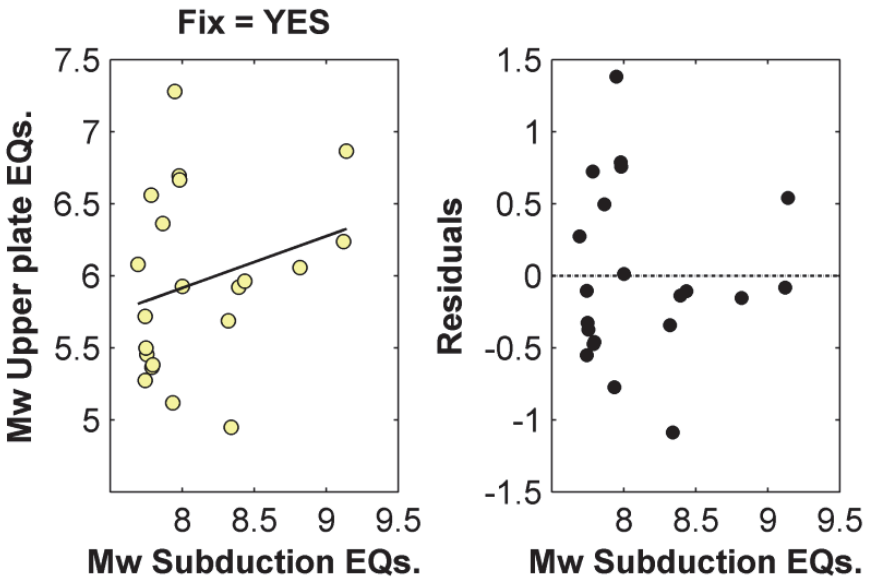

Figure 4.10: Scaling relation between $M_{w\,total}^{MT}$ of peaks greater than 7.7 and $M_{w\,total}^{UP}$ of strike-slip fault aftershocks during the same time span. We use a bin size BW=1,000 for this analysis. The black line shows the linear least square regression line of the population.

Table 4.4: Results of peak correlation analysis

Kinematics	%ρ Mw ≥ 0.5		%ρ Mw = 1		%ρ Nr ≥ 0.5		%ρ Nr = 1	
	Fix NO	Fix YES	Fix NO	Fix YES	Fix NO	Fix YES	Fix NO	Fix YES
All*	61.1	72.2	61.1	66.7	72.2	77.8	61.1	77.8
Normal	44.4	55.6	38.9	44.4	38.9	66.7	38.9	61.1
Reverse	38.9	50.0	16.7	16.7	50.0	55.6	22.2	22.2
Strike-slip	38.9	38.9	33.3	38.9	38.9	50.0	38.9	38.9

*At least one of the kinematic style shows a peak correlation

Table 4.5: % R^2 Mw UP vs Mw MT

Kinematics	Fix NO	Fix YES
Normal	37.9	47.8
Reverse	8.1	1.9
Strike-slip	4.4	6.8

4.5 Discussion

4.5.1 Triggering of upper plate earthquakes

Despite the fact that the studied, near-field subduction segments vary in area, maximum magnitudes reached by earthquakes and number of great megathrust events contained (Tables 4.2, 4.3), the results from the binary analysis over the time series shows that between 77 % to 83 % of the cases, great subduction events are responsible of at least one peak of Nr/t above background in the upper plate. In 61-78 % of the cases, upper plate peaks occurred only contemporaneous to a peak in subduction activity. The range of agreement is given by the results obtained from the full dataset of earthquakes or a subset excluding the fixed events (Table 4.4). The correlations are always better when we use the full dataset however there is a tradeoff in increasing uncertainty by the possibility of incorporating earthquakes to the upper plate that could potentially belong to the slab and vice versa. In terms of the magnitude reached by upper plate events, our analysis shows a strong correlation as well. The percentage of the cases in which peaks above background in the upper plate are accompanied by peaks of subduction earthquakes range between 61 % and 72 %. Although we use different methods, our findings are in agreement with a recent and independent work by *Gomberg and Sherrod* (2014), which suggests that over a ±1-year time window the rate of seismicity in the overriding plate and sometimes the magnitude reached by upper plate earthquakes, increased after great subduction events. By using the full time series of the catalog, we can further suggest that, for the majority of the studied subduction zones, periods of significant seismicity in the forearc are more likely to follow great subduction earthquakes than occur interseismically. But perhaps more importantly, we have found that this relation is stronger in the case of normal fault events which as discussed in the following sections, may have implications for the

mechanisms and style of permanent deformation of the forearc, and seismic hazard.

4.5.2 Kinematics of subduction-triggered events

Our analyses suggest that periods of high intraplate seismicity on forearc normal faults correlate better to an increase in subduction activity compared to reverse and strike-slip kinematics. The most outstanding examples are the upper plate events triggered by the great 2010 Maule and 2011 Tohoku earthquakes (e.g., *Toda et al.*, 2011; *Hasegawa et al.*, 2012; *Lange et al.*, 2012; *Rietbrock et al.*, 2012). The composite focal mechanisms obtained from a moment tensor sum including all the forearc aftershocks of these two events yield similar orientations than that obtained by just adding the normal fault aftershocks, meaning that normal fault reactivations are dominating the moment released by upper plate events (Fig. 4.11). For the case of the Maule earthquake, the major aftershocks were nucleated in a NW-striking, margin-oblique structure so-called Pichilemu normal fault (*Farías et al.*, 2011; *Ryder et al.*, 2012; *Aron et al.*, 2013; *Ruiz et al.*, 2014), which bounds the northern end of the megathrust rupture area that has a general strike of 20°. That structure delineates the termination of a concave to the ocean, semi-elliptical pattern of crustal faults enclosing the Maule segment (*Aron et al.*, 2013). The shallowly plunging T-axis obtained from the moment tensor sum of normal faults aftershocks points towards the zone of maximum slip of the megathrust and its trend has an angle of 44° respect to the trench axis (Fig. 4.11). Likewise, the large normal fault crustal aftershocks following the Tohoku earthquake also occurred in NW-striking, margin oblique structures (Yunodake and Itozawa faults), located at the southern end of the megathrust rupture (*Imanishi et al.*, 2012; *Fukushima et al.*, 2013; *Toda and Tsutsumi*, 2013). These structures outline a similar geometric pattern respect to the rupture area than the Pichilemu fault. The extensional axis of the moment tensor sum trends obliquely to the

trench axis by 31.5° (Fig. 4.11) and points towards the zone of maximum slip of the megathrust located farther north (*Loveless and Meade*, 2011). Estimations of Coulomb stress change on the reactivated crustal faults in Chile and Japan show high stresses for normal faulting, indicating that these structures were properly oriented to slip under the loading conditions imposed by the megathrust earthquakes (e.g., *Farías et al.*, 2011; *Toda et al.*, 2011; *Imanishi et al.*, 2012; *Aron et al.*, 2013). In general, the shallowly plunging extensional axes of the crustal normal fault aftershocks, even when they are not the dominant kinematics of the reactivated crustal events, tend to be oriented at high angle respect to the trench axis, indicating an important component of stretching parallel to the heave of the megathrust (Figs. 4.11, 4.12).

Studies using stress inversions from moment tensors of the world catalog and local networks show coseismic rotations of the principal axes of stress in the upper plate volume overlying the 2004 Mw 9.2 Sumatra-Andaman, 2010 Mw 8.8 Maule and 2011 Mw 9.0 Tohoku ruptures (e.g., *Oishi and Sato*, 2007; *Hardebeck*, 2012; *Hasegawa et al.*, 2012; *Yoshida et al.*, 2012). The maximum compressive stress axis was shallowly plunging before the earthquakes, approximately oriented parallel to the convergence vector, but following the main shock both the maximum and minimum principal stresses rotate so that the least principal stress axis becomes more horizontal, trending sub-perpendicular to the trench, while the compressive axis plunges at a higher angle. That switch in the state of stress occurs because the continent is mostly stretched in the direction of the coseismic rebound or heave of the megathrust, facilitating the reactivation of extensional features including surface tension cracks and shallow, intraplate normal fault earthquakes (*Baker et al.*, 2013; *Sibson*, 2013). Those reactivations tend to occur in pre-existing structures which strike at a high angle to the maximum coseismic stretching orientation.

Figure 4.11: Composited focal mechanisms of upper plate aftershocks for the 2010 Maule and 2011 Tohoku earthquakes (left and right columns respectively) calculated using a moment tensor sum. The first row of stereonets shows the solution using all the events and the lower three are computed for independent kinematics (normal, reverse and strike-slip faults respectively). Kinematic axes of the composited focal mechanisms are shown in green and the numbers are as follows: 1= T, 2= B (null), 3= P. The trend in degrees of the shallowly plunging kinematic axes for each case is shown below the beach balls. Red and blue dots are T- and P-axes respectively for the individual events included in the computation. The black crosses represent the trend of the trench axis for each rupture segment. We use a trench axis of 020° and 019° over the rupture area of the Maule and Tohoku earthquakes respectively. Next to the arcs are the angles between the trend of the shallowly plunging kinematic axes and the trench orientation (obliquity of the kinematic axis). Beach balls are lower hemisphere, equal area projections.

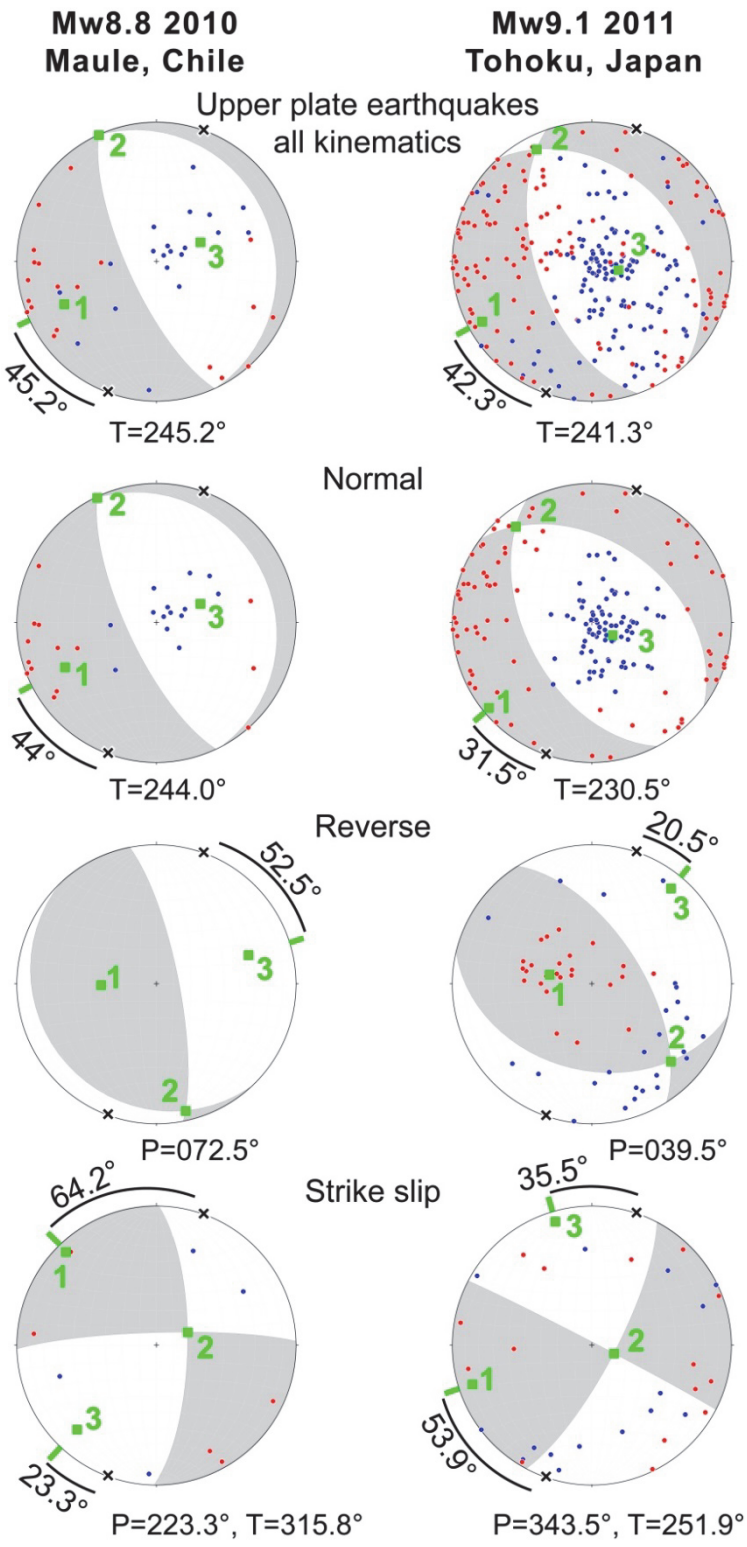
Mw8.8 2010
Maule, Chile
Mw9.1 2011
Tohoku, Japan
Upper plate earthquakes
all kinematics
2
3
1
45.2°
T=245.2°
42.3°
T=241.3°
Normal
44°
T=244.0°
31.5°
T=230.5°
Reverse
52.5°
P=072.5°
20.5°
P=039.5°
Strike slip
64.2°
23.3°
P=223.3°, T=315.8°
35.5°
53.9°
P=343.5°, T=251.9°

Figure 4.12: Composited focal mechanisms of upper plate aftershocks for the 2005 Nias, 2004 Andaman and 2001 Arequipa earthquakes (left, center and right columns respectively) calculated using a moment tensor sum. Symbols, general explanations, color code and notations are the same than Figure 4.11. Here we use general trench axes of 142°, 175° and 132° for the three rupture areas respectively.

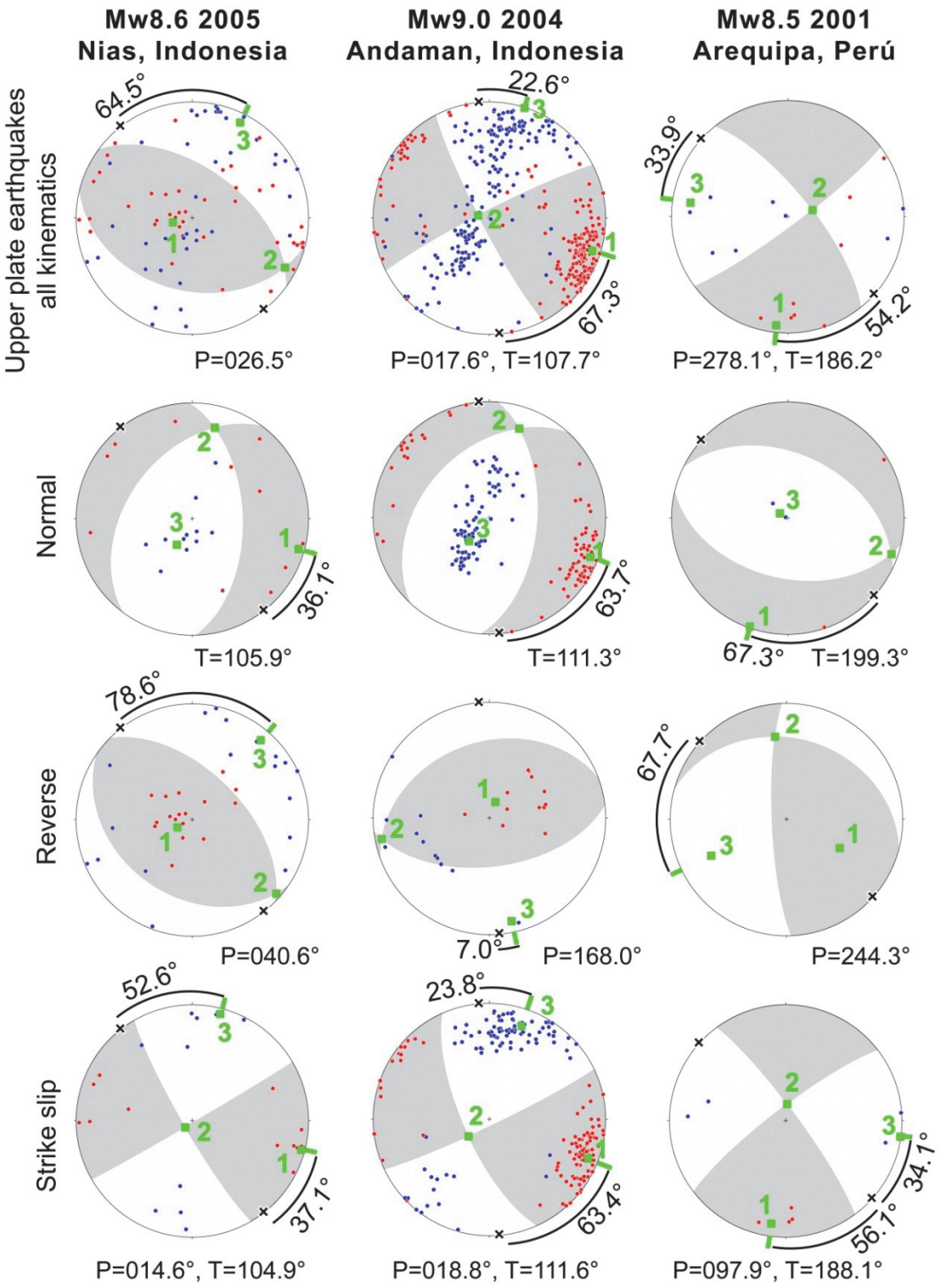
Mw8.6 2005
Nias, Indonesia
Mw9.0 2004
Andaman, Indonesia
Mw8.5 2001
Arequipa, Perú
Upper plate earthquakes
all kinematics
Normal
Reverse
Strike slip
64.5°
22.6°
33.9°
54.2°
67.3°
P=026.5°
P=017.6°, T=107.7°
P=278.1°, T=186.2°
36.1°
63.7°
67.3°
T=105.9°
T=111.3°
T=199.3°
78.6°
67.7°
7.0°
P=040.6°
P=168.0°
P=244.3°
52.6°
23.8°
37.1°
63.4°
34.1°
56.1°
P=014.6°, T=104.9°
P=018.8°, T=111.6°
P=097.9°, T=188.1°

However, out of many suitably oriented faults, only a few generated significant aftershocks after a single subduction event (*Aron et al.*, 2013). Recent paleoseismological studies on forearc normal faults suggest that stress on the upper plate structures needs to build up over many subduction cycles to overcome the shear strength and produce slip (*Cortés et al.*, 2012; *Toda and Tsutsumi*, 2013). Over geologic time this permanent deformation must sum to produce the Neogene structural grain of the forearc (*Aron et al.*, Accepted).

For the case of strike-slip and reverse faults, the correlation with subduction earthquakes is weaker over the time span of the catalog. In fact, they are more likely to occur interseismically (Figs. 4.2-4.4). Nonetheless, we identified several cases where significant triggering of these upper plate structures occurred. In many cases, large M 7 reverse and strike-slip events are observed across the entire magnitude range of analyzed megathrusts, contrary to the normal fault aftershocks which tend to reach maximum magnitudes following the larger megathrusts (Figs. 4.8, 4.9, 4.10). This finding emphasizes the importance of the pre-existing structure, the ambient regional and local stresses, orientation of faults and the location of the structures in space respect to the megathrust slip distribution.

As shown in Figure 4.12 by the composite focal mechanisms calculated from moment tensor sums, the 2004-2005 Sumatra-Andaman-Nias sequence generated large strike-slip and thrust events in the upper plate, dominating the moment released by upper plate aftershocks (*Lay et al.*, 2005; *Oishi and Sato*, 2007; *Sibuet et al.*, 2007). In that region, the upper plate structure is strongly controlled by the Sumatra and Mentawai faults, major right-lateral, trench-parallel systems which produce a wide region of strike-slip deformation and strain partitioning in the arc and forearc (*Karig et al.*, 1979, 1980; *Diament et al.*, 1992; *Malod and Kemal*, 1996; *Berglar et al.*, 2010;

Weller et al., 2012). One of the nodal planes estimated from the moment tensor sum of the upper plate strike-slip aftershocks of both the Andaman and Nias megathrust earthquakes is almost parallel to the trench, coinciding with the strikes of these two major forearc systems (Fig. 4.12).

Another example of important triggering of forearc strike-slip events captured in our search window occurred following the 2001 M_w 8.5 Arequipa earthquake in Southern Perú (Fig. 4.12). Those events were likely nucleated in a set of structures running along the piedmont of the Peruvian Precordillera, between the Cotahuasi-Ocoña and Colca-Majes valleys, near the north-western end of the megathrust rupture area (*Pritchard et al.*, 2007). In that area there are several major structures which strike parallel to the trench such as the Lluclla fault with documented Quaternary normal and strike-slip activity (*Sébrier et al.*, 1985; *Schildgen et al.*, 2009), coinciding in orientation with one of the nodal planes from the composited focal mechanism of upper plate strike-slip events. Similarly, the margin-oblique, NE-striking Chololo fault in Ilo, Perú was as well reactivated after the 2001 Arequipa earthquake showing left-lateral and normal fault components (*Audin et al.*, 2008). This structure has a protracted history of normal fault slip over the Neogene. In most of the examples of megathrust events showing strike-slip crustal aftershocks, the extensional axes of the forearc events are consistent to stretching sub-parallel to the subduction rebound or at high angle to the trench (Fig. 4.12); therefore these preexisting structures were properly oriented to slip parallel to their strikes under the loading conditions imposed by the megathrust earthquakes.

Reverse faults triggered by subduction earthquakes tend to occur in the upper plate at the toe of the forearc wedge, up dip from the slip zone of the megathrust (*Li et al.*, 2014). This portion of the upper plate is more likely to experience shortening

parallel to the heave of the megathrust, highly oblique to the trench (Figs. 4.11, 4.12). Several cases of thrust splay fault reactivations are clear, particularly in the Aleutians region, consistent with what was previously observed after the great 1964 Alaska earthquake (*Plafker*, 1967), and in the outer forearc of the Sumatra subduction zone following the Andaman and Nias great earthquakes (*Sibuet et al.*, 2007).

4.5.3 Implications for seismic hazard

Earthquakes are particularly difficult to predict. In our study we test how a single variable, the occurrence of great megathrust events, may control the occurrence of periods of anomalously high seismicity in the upper plate (*Gomberg and Sherrod*, 2014). Yet, more than a one variable controls the dynamics of earthquakes and several of these variables (or how they interact with each other) are unknown. However, if there is a strong control in the seismic behavior of the forearc by the occurrence of great subduction earthquakes, we suggest that this would more likely apply to extensional kinematics. Perhaps more importantly, our analysis of the total moment magnitude scaling relation suggests that, compared to reverse and strike-slip events, forearc normal fault aftershocks satisfy better a linear relation between the size of megathrust events and that of the upper plate (Table 4.5, Figs. 4.8-4.10). The best fit least squares linear regression model, denoted by the expression: $M_{w\ total}^{UP\ Normal} = -1.53 + 0.91 M_{w\ total}^{MT}$, accounts for 48 % of the variation in the moment magnitude increase of upper plate normal fault events, with a standard error of the regression of 0.38 corresponding to the size of the average residual in the model (Fig. 4.8). For any given peak of subduction earthquakes, the total M_w accounted by triggered upper plate normal events over the coseismic/post-seismic period, calculated from the summation of Mo inside the bin, has a positive correlation with the total M_w of the subduction

earthquakes – the larger the megathrust the larger the energy released by forearc aftershocks. Coulomb stress change has proven to be a successful tool in studying fault interactions and static triggering in the near-field volume surrounding earthquakes (*King et al.*, 1994). For the case of megathrust earthquakes, stress fields encouraging normal faulting would be expected in most of the forearc wedge, especially over the region above the megathrust down dip from the main slip zone (e.g., *Lin and Stein*, 2004). This suggest that, if the magnitudes of the stresses imposed by a subduction earthquake are proportional to the size of the event, the aforementioned scaling relationship should bear for stress magnitude as well, so the larger the normal-fault Coulomb stresses in the upper plate, the larger the potential aftershocks.

Given the relatively large magnitude and shallow depth of these triggered earthquakes, understanding their behavior in the context of the subduction seismic cycle becomes important for seismic hazards evaluation. In general, the M_w 7.0 crustal events in both Chile and Japan struck in sparsely populated areas with relatively good compliance of building codes and basic infrastructure; though a triggered normal fault with surface rupture did occur just 60 km south from the Fukushima nuclear plant. However, as population increases with concomitant land use and development, large crustal aftershocks pose a significant hazard to critical infrastructure (e.g., *Gürpinar*, 2005). As we showed in this work, some upper plate aftershocks can struck even years after a megathrust earthquake, making impossible to predict the exact timing of reactivation. Nevertheless, most of the cases bear a common characteristic: they occur on preexisting structures which were favorably oriented to the stress field imposed by the subduction earthquake. This documented correlation between size of the main shock and that of the intraplate normal aftershocks, along with field studies of these faults, suggest that the forearc structures should be incorporated in any seismic hazard

assessment of subduction zones regions.

4.6 Conclusions

We have shown that for the majority of the cases in the Global CMT catalog, great subduction earthquakes are responsible of peaks of increase in seismicity rate and moment magnitude release by upper plate events. That strong correlation is mainly dominated by normal fault earthquakes. The behavior of the cycle of upper plate normal faults appears to be more controlled by subduction activity than reverse and strike-slip kinematics, and peaks of normal fault events are most likely to occur following great megathrust earthquakes rather than interseismically. Our analysis of total moment magnitude scaling relations, based on the moment summation of coseismic/post-seismic events, suggests that forearc normal fault aftershocks may follow a linear relation between the size of megathrust events and that of the upper plate. That correlation is much weaker in the case of reverse and strike-slip aftershocks.

Great megathrust events not only shake the ground and deform elastically the crust; they also leave a permanent deformation mark in the geological record of the upper plate, especially on the forearc above the seismogenic zone. We propose that the long-lived normal faults of the forearc are the structural elements which better reflect coseismic/post-seismic deformation fields. Therefore, their activity and structural behavior over geologic time should be indicators of long-term permanent strain patterns imposed by repeated subduction earthquake cycles over the megathrust segment.

REFERENCES

Ammon, C. J. et al. (2005), Rupture Process of the 2004 Sumatra-Andaman Earthquake, *Science*, *308*(5725), 1133–1139, doi:10.1126/science.1112260.

Aron, F., J. Cembrano, F. Astudillo, R. W. Allmendinger, and G. Arancibia (Accepted), Constructing forearc architecture over megathrust seismic cycles: geological snapshots from the Maule earthquake region, Chile, *Geol. Soc. Am. Bull.*

Aron, F., R. W. Allmendinger, J. Cembrano, G. González, and G. Yáñez (2013), Permanent fore-arc extension and seismic segmentation: Insights from the 2010 Maule earthquake, Chile, *J. Geophys. Res. Solid Earth*, *118*(2), 724–739, doi:10.1029/2012JB009339.

Audin, L., P. Lacan, H. Tavera, and F. Bondoux (2008), Upper plate deformation and seismic barrier in front of Nazca subduction zone: The Chololo Fault System and active tectonics along the Coastal Cordillera, southern Peru, *Tectonophysics*, *459*(1–4), 174–185, doi:10.1016/j.tecto.2007.11.070.

Baker, A., R. W. Allmendinger, L. A. Owen, and J. A. Rech (2013), Permanent deformation caused by subduction earthquakes in northern Chile, *Nat. Geosci.*, *advance online publication*, doi:10.1038/ngeo1789.

Berglar, K., C. Gaedicke, D. Franke, S. Ladage, F. Klingelhoefer, and Y. S. Djajadihardja (2010), Structural evolution and strike-slip tectonics off north-western Sumatra, *Tectonophysics*, *480*(1–4), 119–132, doi:10.1016/j.tecto.2009.10.003.

Bevington, P., and D. K. Robinson (2002), *Data Reduction and Error Analysis for the Physical Sciences*, 3rd edition., McGraw-Hill Science/Engineering/Math, Boston.

Cortés, J., G. González, S. A. Binnie, R. Robinson, S. P. H. T. Freeman, and G. Vargas (2012), Paleoseismology of the Mejillones Fault, northern Chile: Insights from cosmogenic 10Be and optically stimulated luminescence determinations, *Tectonics*, *31*(2), TC2017, doi:10.1029/2011TC002877.

Diament, M., H. Harjono, K. Karta, C. Deplus, D. Dahrin, M. T. Zen, M. Gérard, O. Lassal, A. Martin, and J. Malod (1992), Mentawai fault zone off Sumatra: A new key to the geodynamics of western Indonesia, *Geology*, *20*(3), 259–262, doi:10.1130/0091-7613(1992)020<0259:MFZOSA>2.3.CO;2.

Efron, B. (1981), Nonparametric estimates of standard error: The jackknife, the bootstrap and other methods, *Biometrika*, *68*(3), 589–599, doi:10.1093/biomet/68.3.589.

Ekström, G., M. Nettles, and A. M. Dziewoński (2012), The global CMT project 2004–2010: Centroid-moment tensors for 13,017 earthquakes, *Phys. Earth Planet. Inter.*, *200–201*, 1–9, doi:10.1016/j.pepi.2012.04.002.

Engdahl, E. R., R. van der Hilst, and R. Buland (1998), Global teleseismic earthquake relocation with improved travel times and procedures for depth determination, *Bull. Seismol. Soc. Am.*, *88*(3), 722–743.

Farías, M., D. Comte, S. Roecker, D. Carrizo, and M. Pardo (2011), Crustal extensional faulting triggered by the 2010 Chilean earthquake: The Pichilemu Seismic Sequence, *Tectonics*, *30*(6), TC6010, doi:10.1029/2011TC002888.

Felzer, K. R., R. E. Abercrombie, and G. Ekström (2003), Secondary Aftershocks and Their Importance for Aftershock Forecasting, *Bull. Seismol. Soc. Am.*, *93*(4), 1433–1448, doi:10.1785/0120020229.

Frohlich, C. (1992), Triangle diagrams: ternary graphs to display similarity and diversity of earthquake focal mechanisms, *Phys. Earth Planet. Inter.*, *75*(1–3), 193–198, doi:10.1016/0031-9201(92)90130-N.

Fukushima, Y., Y. Takada, and M. Hashimoto (2013), Complex Ruptures of the 11 April 2011 Mw 6.6 Iwaki Earthquake Triggered by the 11 March 2011 Mw 9.0 Tohoku Earthquake, Japan, *Bull. Seismol. Soc. Am.*, *103*(2B), 1572–1583, doi:10.1785/0120120140.

Gardner, J. K., and L. Knopoff (1974), Is the sequence of earthquakes in Southern California, with aftershocks removed, Poissonian?, *Bull. Seismol. Soc. Am.*, *64*(5), 1363–1367.

Gomberg, J., and B. Sherrod (2014), Crustal earthquake triggering by modern great earthquakes on subduction zone thrusts, *J. Geophys. Res. Solid Earth*, *119*(2), 2012JB009826, doi:10.1002/2012JB009826.

Gürpinar, A. (2005), The importance of paleoseismology in seismic hazard studies for critical facilities, *Tectonophysics*, *408*(1–4), 23–28, doi:10.1016/j.tecto.2005.05.042.

Hardebeck, J. L. (2012), Coseismic and postseismic stress rotations due to great subduction zone earthquakes, *Geophys. Res. Lett.*, *39*(21), n/a–n/a, doi:10.1029/2012GL053438.

Hasegawa, A., K. Yoshida, Y. Asano, T. Okada, T. Iinuma, and Y. Ito (2012), Change in stress field after the 2011 great Tohoku-Oki earthquake, *Earth Planet. Sci. Lett.*, *355–356*, 231–243, doi:10.1016/j.epsl.2012.08.042.

Hayes, G. P., D. J. Wald, and R. L. Johnson (2012), Slab1.0: A three-dimensional model of global subduction zone geometries, *J. Geophys. Res. Solid Earth*, *117*(B1), B01302–, doi:10.1029/2011JB008524.

Imanishi, K., R. Ando, and Y. Kuwahara (2012), Unusual shallow normal-faulting earthquake sequence in compressional northeast Japan activated after the 2011 off the Pacific coast of Tohoku earthquake, *Geophys. Res. Lett.*, *39*(9), n/a–n/a, doi:10.1029/2012GL051491.

Karig, D. E., S. Suparka, G. F. Moore, and P. E. Hehanussa (1979), Structure and Cenozoic evolution of the Sunda arc in the central Sumatra region, in *Geological and Geophysical Investigations of Continental Margins, Memoir*, vol. 29, edited by J. S. Watkins, L. Montadert, and P. W. Dickerson, pp. 223–237, American Association of Petroleum Geologists, Tulsa, OK.

Karig, D. E., M. B. Lawrence, G. F. Moore, and J. R. Curray (1980), Structural frame work of the fore-arc basin, NW Sumatra, *J. Geol. Soc.*, *137*(1), 77–91, doi:10.1144/gsjgs.137.1.0077.

King, G. C. P., R. S. Stein, and J. Lin (1994), Static stress changes and the triggering of earthquakes, *Bull. Seismol. Soc. Am.*, *84*(3), 935–953.

Knopoff, L., and J. K. Gardner (1972), Higher Seismic Activity During Local Night on the Raw Worldwide Earthquake Catalogue, *Geophys. J. R. Astron. Soc.*, *28*(3), 311–313, doi:10.1111/j.1365-246X.1972.tb06133.x.

Lange, D. et al. (2012), Aftershock seismicity of the 27 February 2010 Mw 8.8 Maule earthquake rupture zone, *Earth Planet. Sci. Lett.*, *317–318*, 413–425, doi:10.1016/j.epsl.2011.11.034.

Lay, T. et al. (2005), The Great Sumatra-Andaman Earthquake of 26 December 2004, *Science*, *308*(5725), 1127–1133, doi:10.1126/science.1112250.

Li, S., M. Moreno, M. Rosenau, D. Melnick, and O. Oncken (2014), Splay fault triggering by great subduction earthquakes inferred from finite element models, *Geophys. Res. Lett.*, *41*(2), 2013GL058598, doi:10.1002/2013GL058598.

Lin, J., and R. S. Stein (2004), Stress triggering in thrust and subduction earthquakes and stress interaction between the southern San Andreas and nearby thrust and strike-slip faults, *J. Geophys. Res. Solid Earth*, *109*(B2), B02303, doi:10.1029/2003JB002607.

Loveless, J. P., and B. J. Meade (2011), Spatial correlation of interseismic coupling and coseismic rupture extent of the 2011 MW = 9.0 Tohoku-oki earthquake, *Geophys. Res. Lett.*, *38*(17), L17306–, doi:10.1029/2011GL048561.

Malod, J. A., and B. M. Kemal (1996), The Sumatra margin: oblique subduction and lateral displacement of the accretionary prism, *Geol. Soc. Lond. Spec. Publ.*, *106*(1), 19–28, doi:10.1144/GSL.SP.1996.106.01.03.

Michael, A. J. (2012), Do Aftershock Probabilities Decay With Time?, *Seismol. Res. Lett.*, *83*(4), 630–632, doi:10.1785/0220120061.

Molchan, G. M., and O. E. Dmitrieva (1992), Aftershock identification: methods and new approaches, *Geophys. J. Int.*, *109*(3), 501–516, doi:10.1111/j.1365-246X.1992.tb00113.x.

Oishi, M., and T. Sato (2007), Moment release budget at oblique convergence margin as revealed by the 2004 Sumatra-Andaman earthquake, *Earth Planets Space*, *59*(8), 913–921.

Parsons, T., and A. A. Velasco (2011), Absence of remotely triggered large earthquakes beyond the mainshock region, *Nat. Geosci.*, *4*(5), 312–316, doi:10.1038/ngeo1110.

Plafker, G. (1967), Surface faults on Montague Island associated with the 1964 Alaska earthquake, *US Geol. Surv. Prof. Pap.*, *543-G*, 42 p.

Pritchard, M. E., E. O. Norabuena, C. Ji, R. Boroschek, D. Comte, M. Simons, T. H. Dixon, and P. A. Rosen (2007), Geodetic, teleseismic, and strong motion constraints on slip from recent southern Peru subduction zone earthquakes, *J. Geophys. Res. Solid Earth*, *112*(B3), B03307, doi:10.1029/2006JB004294.

Rietbrock, A., I. Ryder, G. Hayes, C. Haberland, D. Comte, S. Roecker, and H. Lyon-Caen (2012), Aftershock seismicity of the 2010 Maule Mw=8.8, Chile, earthquake: Correlation between co-seismic slip models and aftershock distribution?, *Geophys. Res. Lett.*, *39*(8), L08310, doi:10.1029/2012GL051308.

Ruiz, J. A., G. P. Hayes, D. Carrizo, H. Kanamori, A. Socquet, and D. Comte (2014), Seismological analyses of the 2010 March 11, Pichilemu, Chile Mw 7.0 and Mw 6.9 coastal intraplate earthquakes, *Geophys. J. Int.*, *197*(1), 414–434, doi:10.1093/gji/ggt513.

Ryder, I., A. Rietbrock, K. Kelson, R. Bürgmann, M. Floyd, A. Socquet, C. Vigny, and D. Carrizo (2012), Large extensional aftershocks in the continental forearc triggered by the 2010 Maule earthquake, Chile, *Geophys. J. Int.*, *188*(3), 879–890, doi:10.1111/j.1365-246X.2011.05321.x.

Schildgen, T. F., K. V. Hodges, K. X. Whipple, M. S. Pringle, M. van Soest, and K. Cornell (2009), Late Cenozoic structural and tectonic development of the western margin of the central Andean Plateau in southwest Peru, *Tectonics*, *28*(4), TC4007, doi:10.1029/2008TC002403.

Sébrier, M., J. L. Mercier, F. Mégard, G. Laubacher, and E. Carey-Gailhardis (1985), Quaternary normal and reverse faulting and the state of stress in the central Andes of south Peru, *Tectonics*, *4*(7), 739–780, doi:10.1029/TC004i007p00739.

Sibson, R. H. (2013), Stress switching in subduction forearcs: Implications for overpressure containment and strength cycling on megathrusts, *Tectonophysics*, *600*, 142–152, doi:10.1016/j.tecto.2013.02.035.

Sibuet, J.-C. et al. (2007), 26th December 2004 great Sumatra–Andaman earthquake: Co-seismic and post-seismic motions in northern Sumatra, *Earth Planet. Sci. Lett.*, *263*(1–2), 88–103, doi:10.1016/j.epsl.2007.09.005.

Smith, G. P., and G. Ekström (1997), Interpretation of earthquake epicenter and CMT centroid locations, in terms of rupture length and direction, *Phys. Earth Planet. Inter.*, *102*(1–2), 123–132, doi:10.1016/S0031-9201(96)03246-3.

Stein, S., and M. E. Wysession (2003), *An Introduction to Seismology, Earthquakes and Earth Structure*, 1st Edition., Blackwell Publishing, Oxford, UK.

Van Stiphout, T., J. Zhuang, and D. Marsan (2012), Seismicity declustering, *Community Online Resour. Stat. Seism. Anal.*, doi:10.5078/corssa-52382934. Available at http://www.corssa.org.

Tahir, M., J.-R. Grasso, and D. Amorèse (2012), The largest aftershock: How strong, how far away, how delayed?, *Geophys. Res. Lett.*, *39*(4), n/a–n/a, doi:10.1029/2011GL050604.

Tarr, A. C., A. Villaseñor, K. P. Furlong, S. Rhea, and H. M. Benz (2009), *Seismicity of the Earth 1900–2007, U.S. Geological Survey. Scientific Investigations Map 3064*, 1 sheet, scale 1:25,000,000, US Geological Survey, Denver, CO.

Toda, S., and H. Tsutsumi (2013), Simultaneous Reactivation of Two, Subparallel, Inland Normal Faults during the Mw 6.6 11 April 2011 Iwaki Earthquake Triggered by the Mw 9.0 Tohoku-oki, Japan, Earthquake, *Bull. Seismol. Soc. Am.*, *103*(2B), 1584–1602, doi:10.1785/0120120281.

Toda, S., R. S. Stein, and J. Lin (2011), Widespread seismicity excitation throughout central Japan following the 2011 M=9.0 Tohoku earthquake and its interpretation by Coulomb stress transfer, *Geophys. Res. Lett.*, *38*, L00G03–, doi:10.1029/2011GL047834.

Uhrhammer, R. (1986), Characteristics of northern and southern California seismicity, *Earthq. Notes*, *57*(21).

Weller, O., D. Lange, F. Tilmann, D. Natawidjaja, A. Rietbrock, R. Collings, and L. Gregory (2012), The structure of the Sumatran Fault revealed by local seismicity, *Geophys. Res. Lett.*, *39*(1), L01306, doi:10.1029/2011GL050440.

Wells, D. L., and K. J. Coppersmith (1994), New empirical relationships among magnitude, rupture length, rupture width, rupture area, and surface displacement, *Bull. Seismol. Soc. Am.*, *84*(4), 974–1002.

Yoshida, K., A. Hasegawa, T. Okada, T. Iinuma, Y. Ito, and Y. Asano (2012), Stress before and after the 2011 great Tohoku-oki earthquake and induced earthquakes in inland areas of eastern Japan, *Geophys. Res. Lett.*, *39*(3), n/a–n/a, doi:10.1029/2011GL049729.

Zakharova, O., S. Hainzl, and C. Bach (2013), Seismic moment ratio of aftershocks with respect to main shocks, *J. Geophys. Res. Solid Earth*, *118*(11), 5856–5864, doi:10.1002/2013JB010191.

APPENDIX A

SUPPLEMENTARY INFORMATION TO CHAPTER 2

This section provides additional field examples of structures found in our field campaigns which complement the observations shown in Chapter 2.

A.1 Additional structural field examples of the O'Higgins study region

Figure 5.1: (a) Aerial view looking south showing the 2 major, orthogonal fault sets affecting the northern portion of the O'Higgins region (Boca de Rapel-Matanzas domain of Fig. 2.2 and Section 2.5.1.1 in main manuscript). Locations of site 1 and site 2 are shown at the lower center (black box) and center of the picture (white dot). The NW-trending set of faults generates a flight of marine terraces to the south, offsetting both the morphologic, marine terraces and the sub-horizontal contact between the basement and the Navidad Fm., shown by the altitude numbers, along the coastal cliff. *Photo by Horacio Parragué*. (b) Color version of Fig. 2.3 in main manuscript. (c) Close up to minor subsidiary normal faults affecting the foot-wall (Fault 1b in Table 2.1).

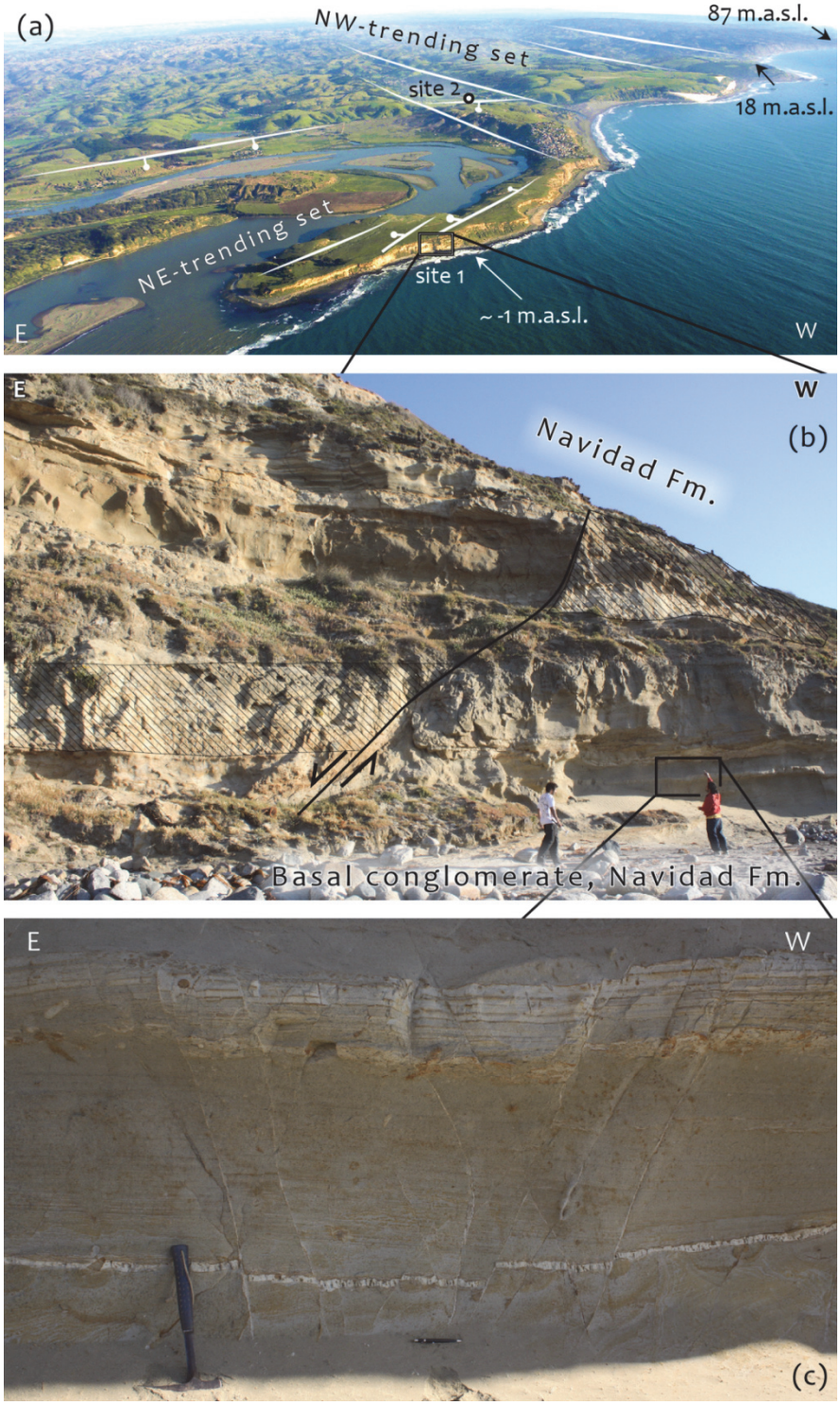
(a)
NW-trending set
site 2
87 m.a.s.l.
18 m.a.s.l.
NE-trending set
site 1
~ -1 m.a.s.l.
E
W
E
W
(b)
Navidad Fm.
Basal conglomerate, Navidad Fm.
E
W
(c)

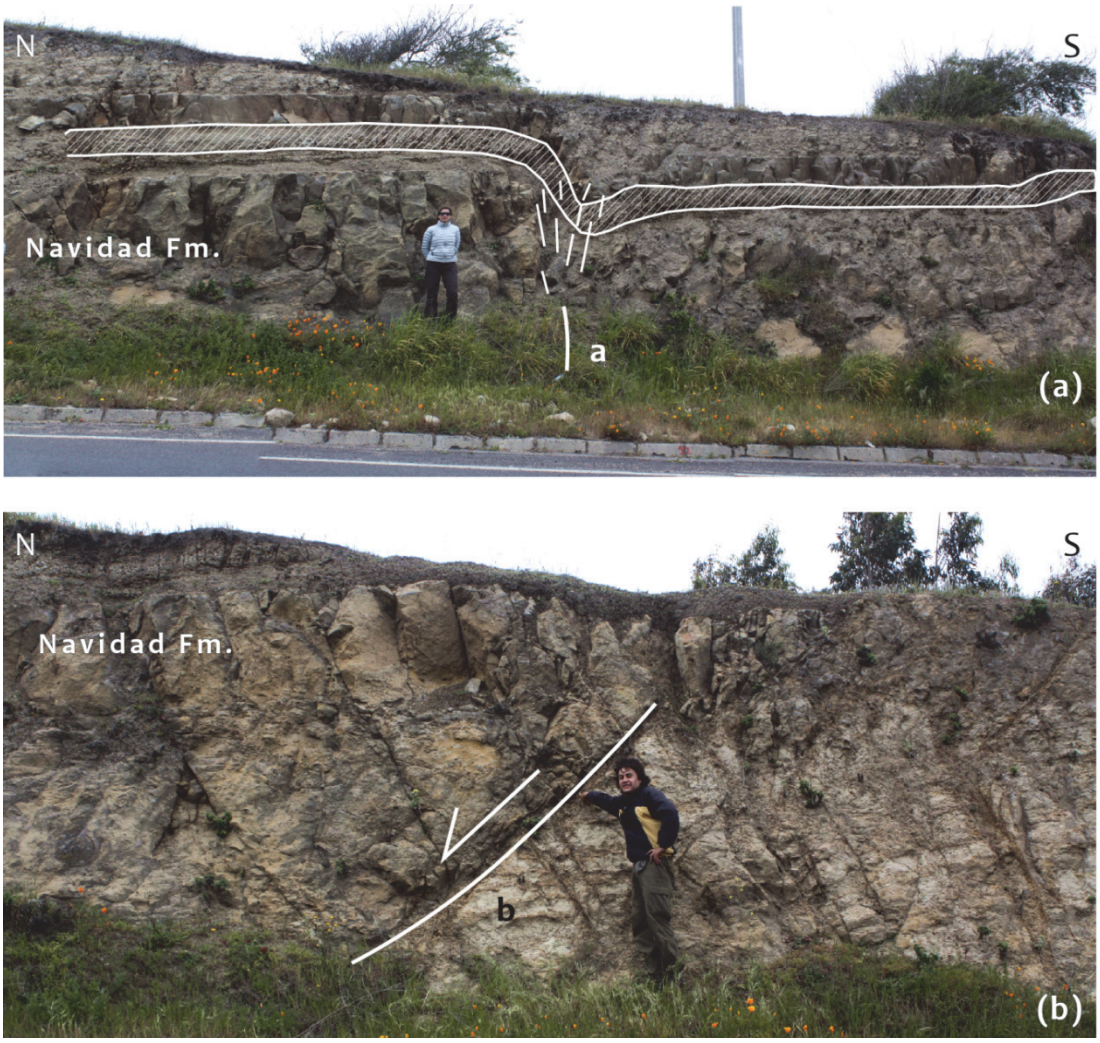

Figure 5.2: Outcrop of normal faults “a” and “b” found in site 2 affecting the Navidad Fm. (Fig. 2.2, Table 2.1 and Section 2.5.1.1 in main manuscript).

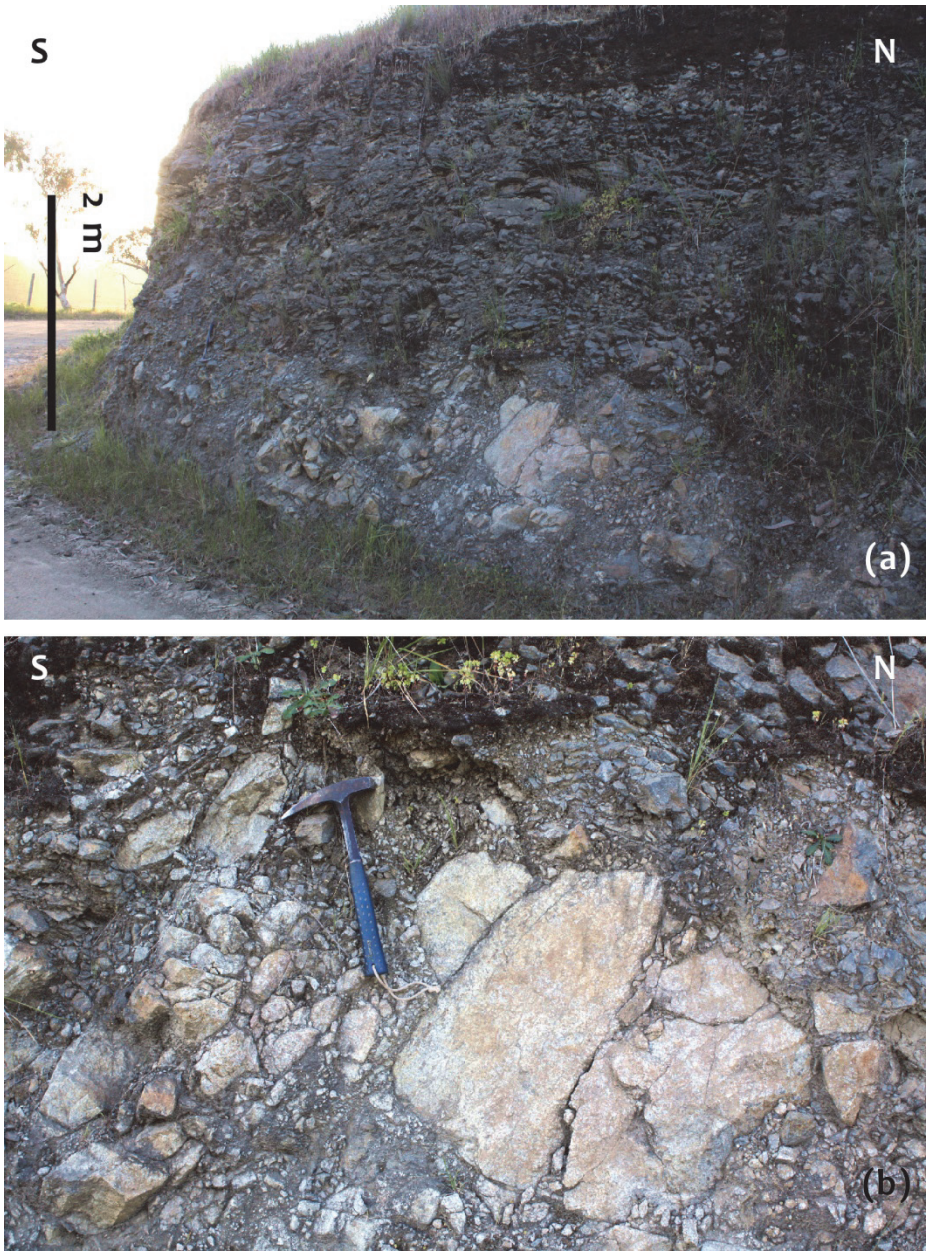

Figure 5.3: (a) Outcrop of fault breccia described in site 3 which may mark the intersection of two orthogonal fault systems (NE- and NW-trending structures). (b) Close up to fault breccia. See Fig. 2.2, Table 2.1 and Section 2.5.1.2 in main manuscript.

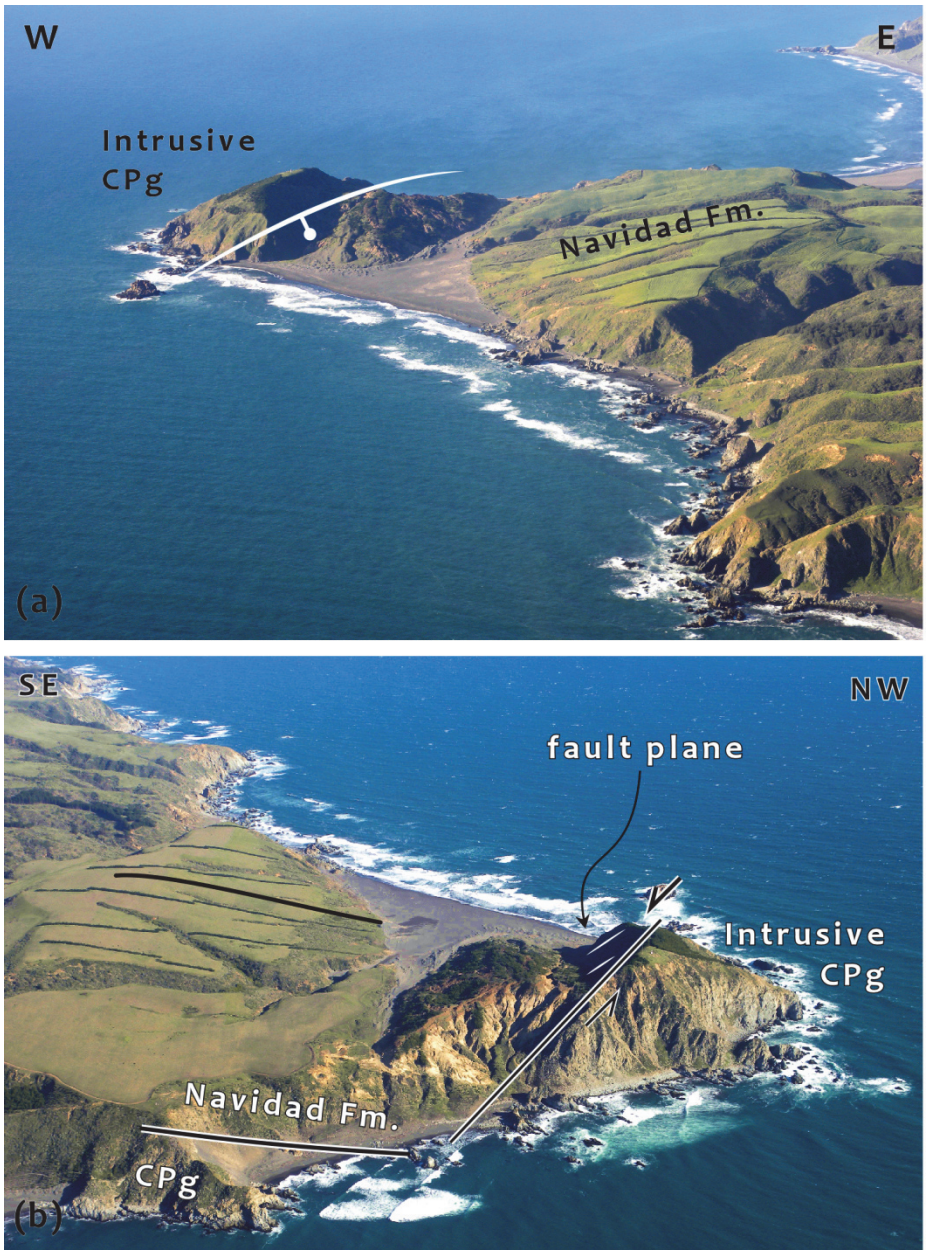

Figure 5.4: (a) Aerial view looking NNW of the Topocalma fault described in site 4 (Fig. 2.2, Table 2.1 and Section 2.5.1.2 in main manuscript). (b) Color version of Figure 2.4 in main manuscript. The top of the hill behind the fresh fault plane of the structure is about 100 m high. *Photos by Horacio Parragué*.

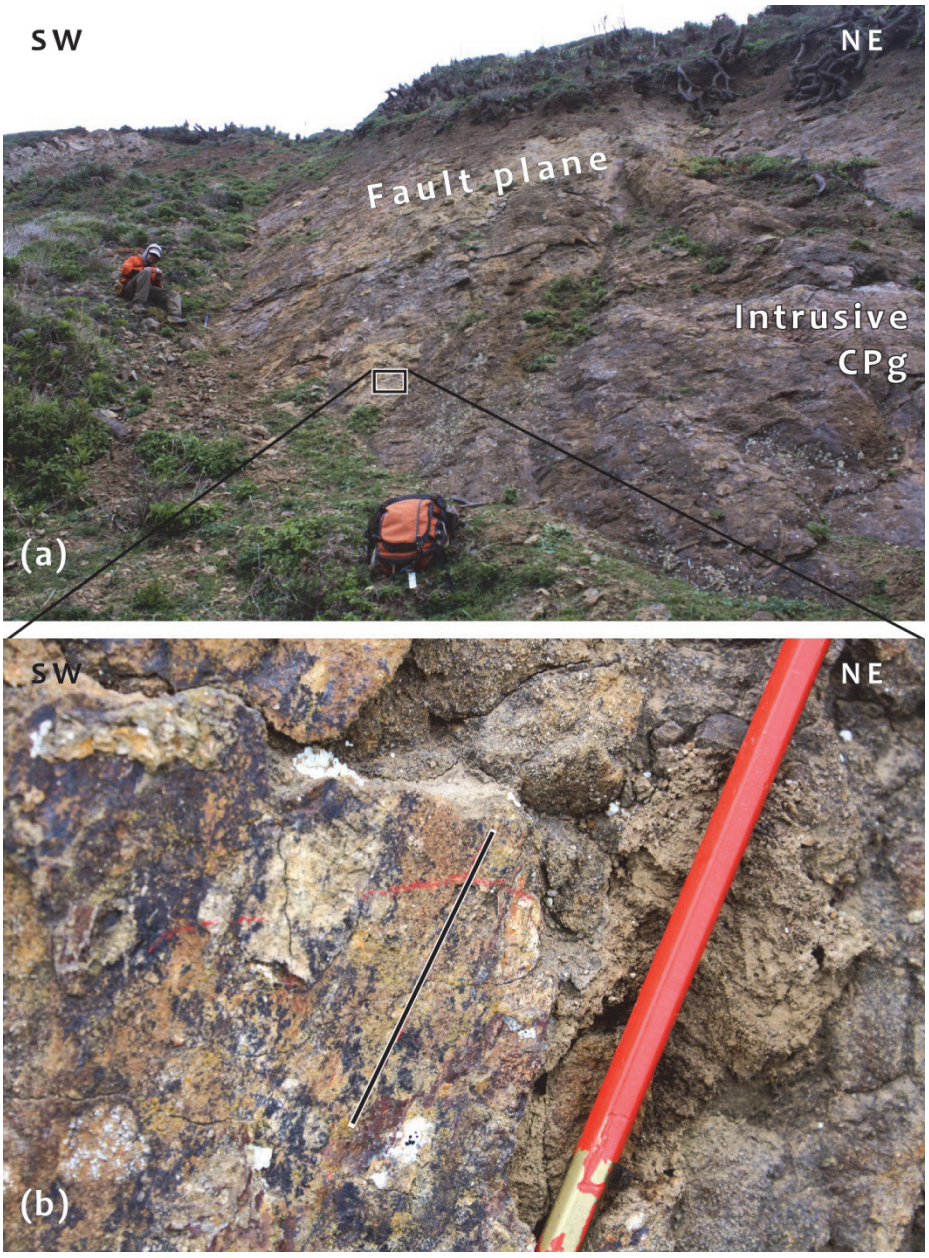

Figure 5.5: (a) Outcrop of the Topocalma fault plane (Fig. 2.2, Table 2.1 and Section 2.5.1.2 in main manuscript; see also Figures 2.4 and A4 for reference). (b) Close up showing slickenlines on the fresh fault plane.

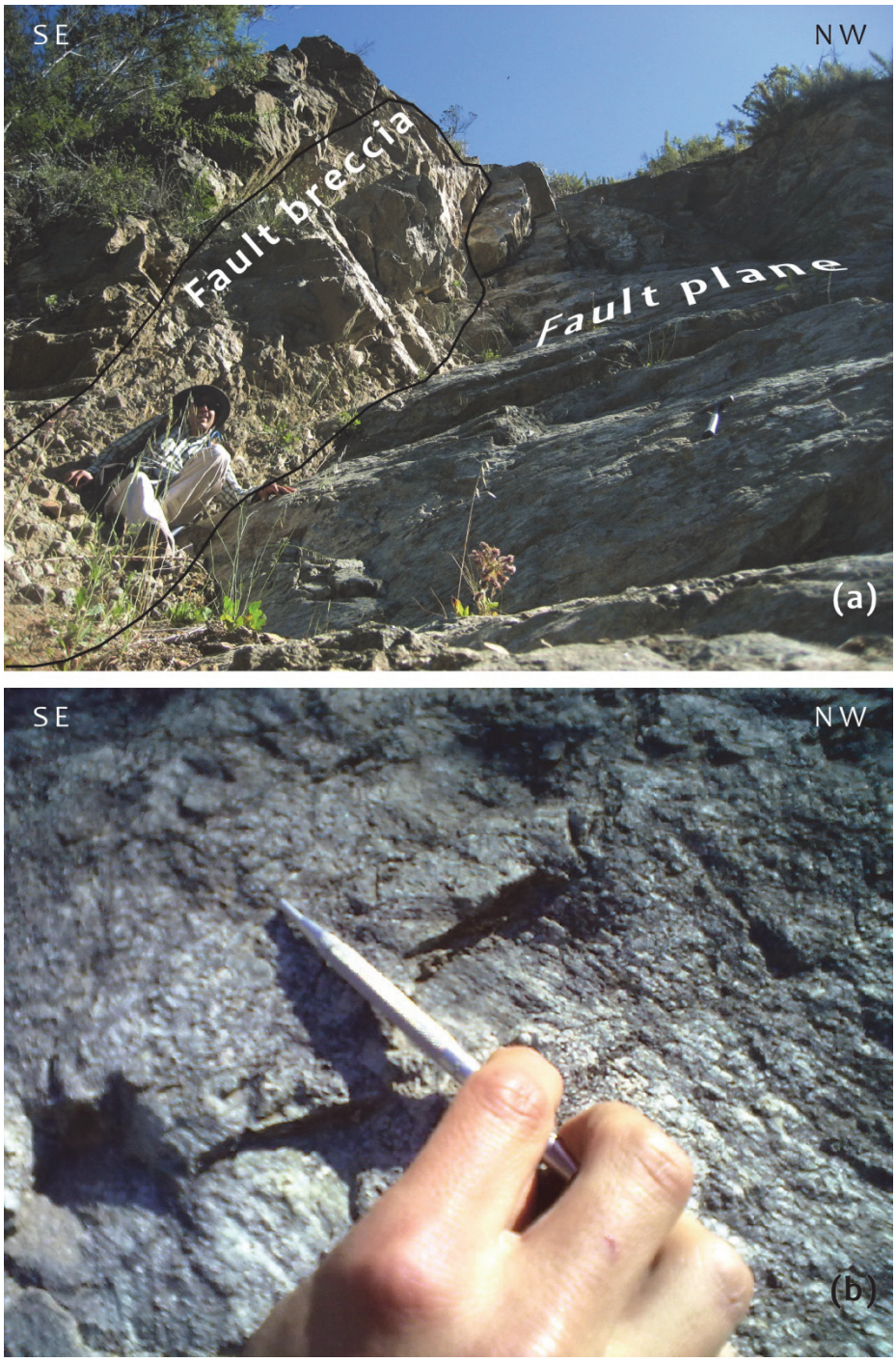

Figure 5.6: (a) Outcrop of the Quebrada Honda fault described in site 5 (Fig. 2.2, Table 2.1 and Section 2.5.1.2 in main manuscript). (a) Color version of Figure 2.5, main manuscript. (b) Close up to striated plane.

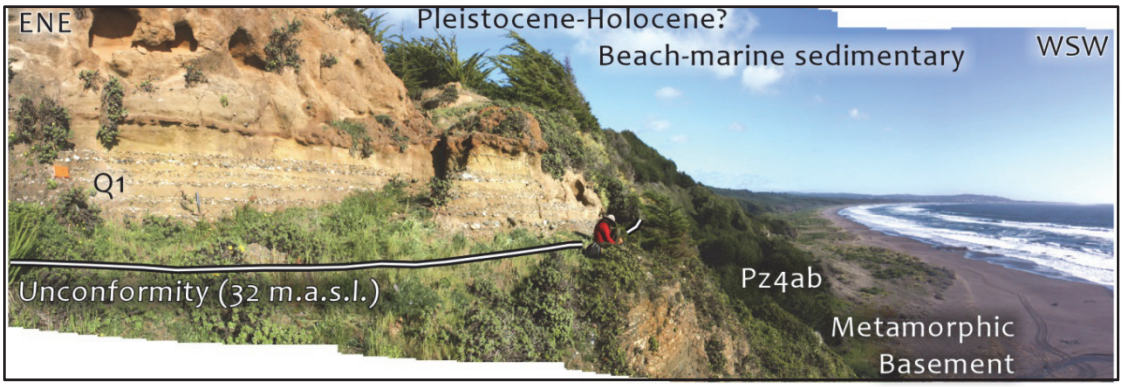

Figure 5.7: Color version of Figure 2.7b in main manuscript.

Figure 5.8: (a) Aerial view looking south, away from the structure, of the hanging-wall of the Pichilemu fault showing a gentle rollover towards the fault, depicted by the Quaternary paleo-abrasion platform as described in Section 2.5.1.3 in main manuscript (see Fig. 2.7a). *Photo by Horacio Parragué*. (b) Outcrop of the contact lying at 1 meter above sea level. Note the foot-wall of the structure in the background across the bay. (c) Aerial view looking straight down to the terrace where the contact lies at 13 m.a.s.l. *Photo by Horacio Parragué*.

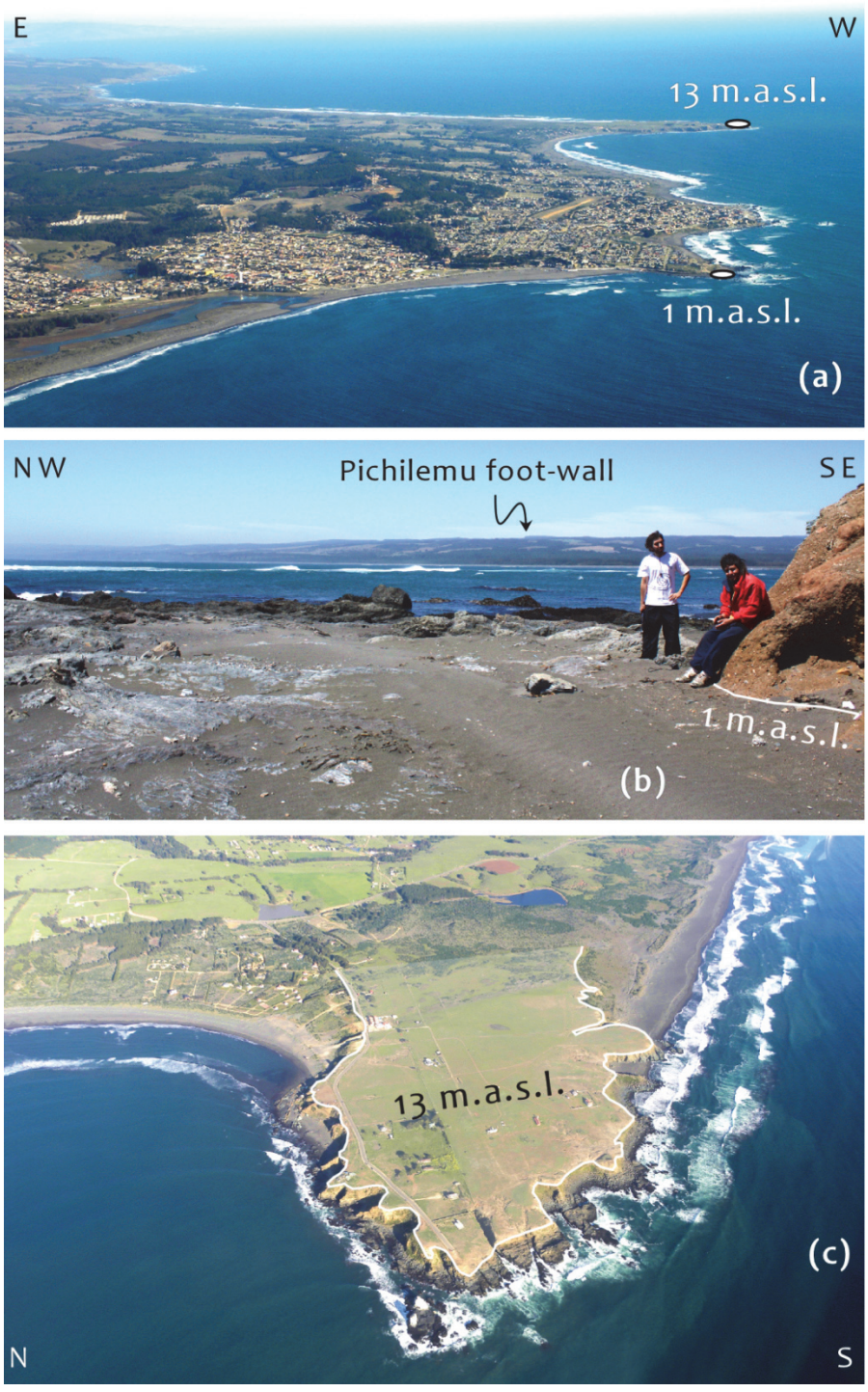
E
W
13 m.a.s.l.
1 m.a.s.l.
(a)
NW
Pichilemu foot-wall
SE
1 m.a.s.l.
(b)
13 m.a.s.l.
(c)
N
S

Figure 5.9: Outcrop of normal faults described in site 6 (Fig. 2.2, Table 2.1 and Section 2.5.1.3 in main manuscript). These structures cut the foot-wall of the Pichilemu fault, close to the trace, and are antithetic to the main structure. They affect the Quaternary sedimentary rocks evidencing young, probably active deformation. Fault “d” showed in picture (c) cuts the foot-wall of fault “a” and is located about 150 m away from that structure.

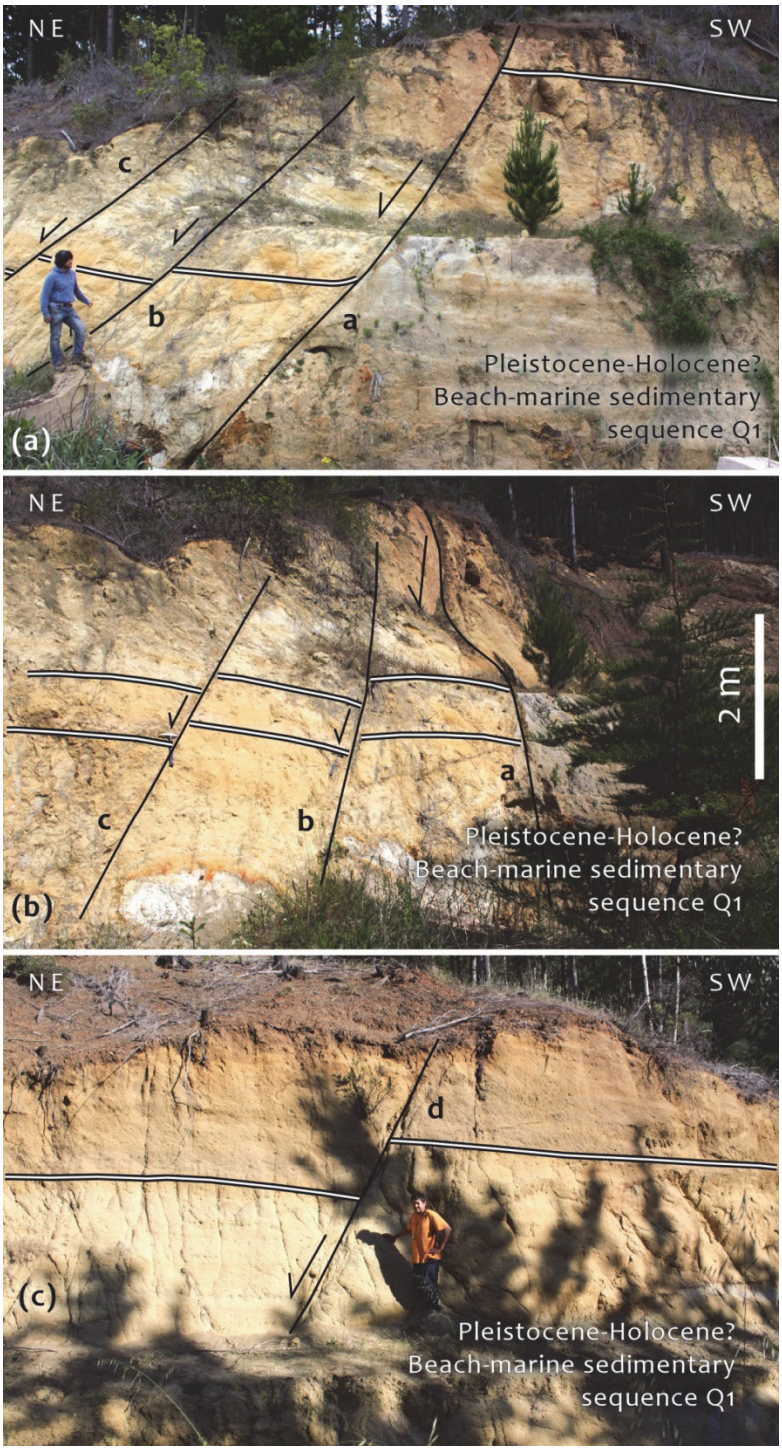
NE
SW
c
b
a
Pleistocene-Holocene?
Beach-marine sedimentary
sequence Q1
(a)
NE
SW
2 m
a
c
b
Pleistocene-Holocene?
Beach-marine sedimentary
sequence Q1
(b)
NE
SW
d
(c)
Pleistocene-Holocene?
Beach-marine sedimentary
sequence Q1

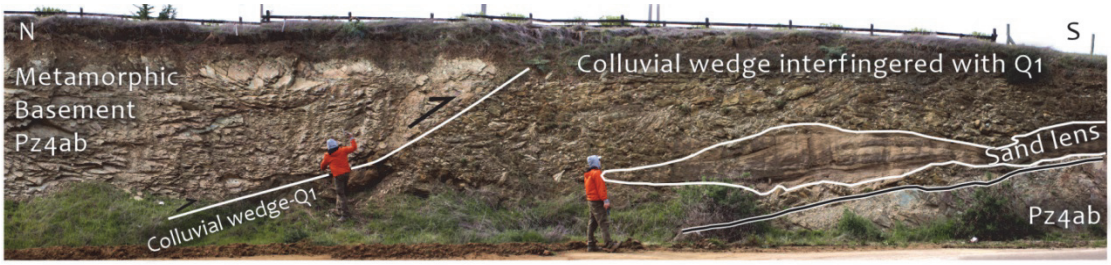

Figure 5.10: Outcrop of reverse fault affecting metamorphic basement and Quaternary sedimentary rocks as described in site 8 (Fig. 2.2, Table 2.1 and Section 2.5.1.4 in main manuscript). Note the colluvial wedge of basement material mixed with sand in the foot-wall in front of the fault.

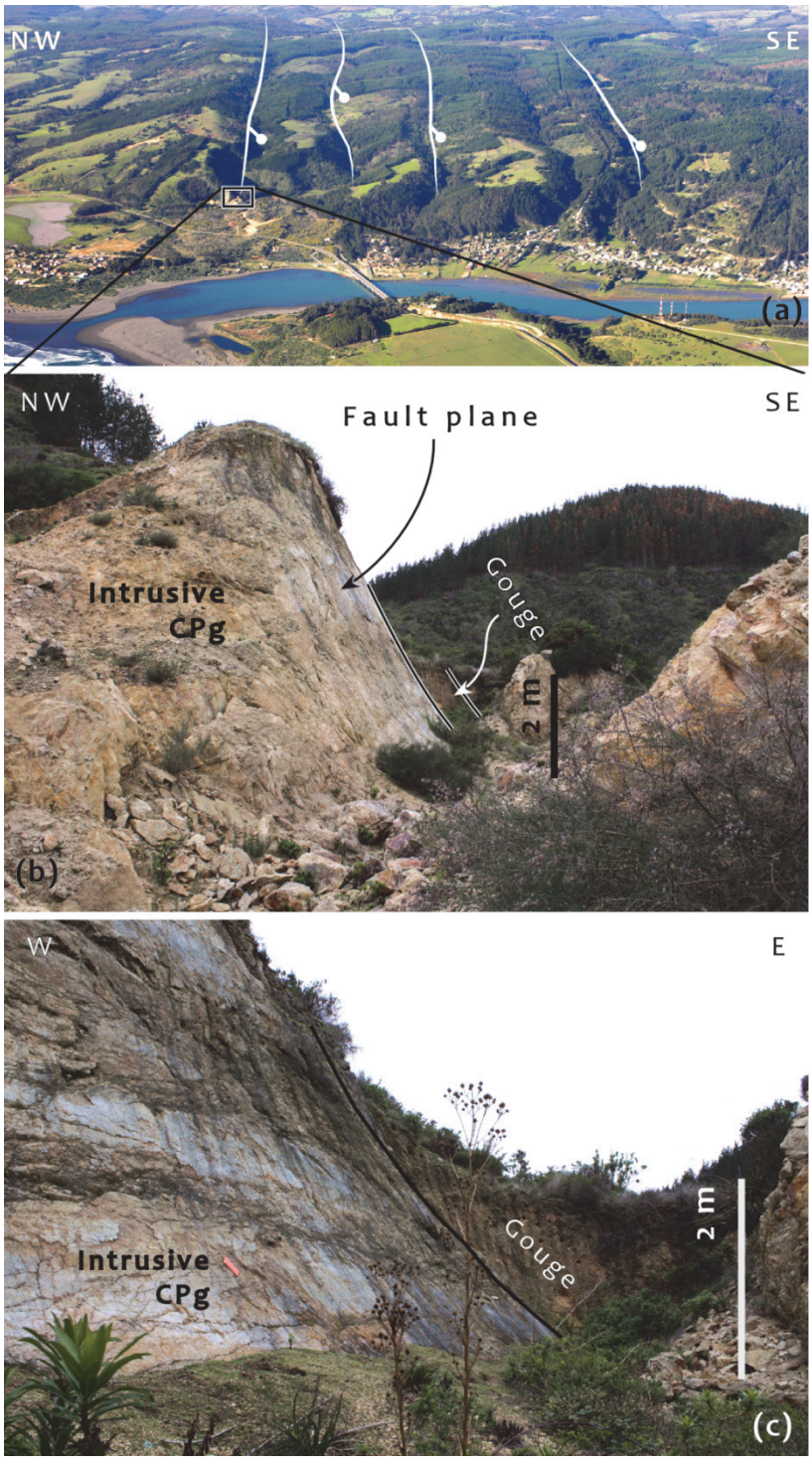

Figure 5.11: (a) and (b) are color versions of Figure 2.8 in main manuscript. (c) Close up to fault plane shown in (b). *Aerial view by Horacio Parragué*.

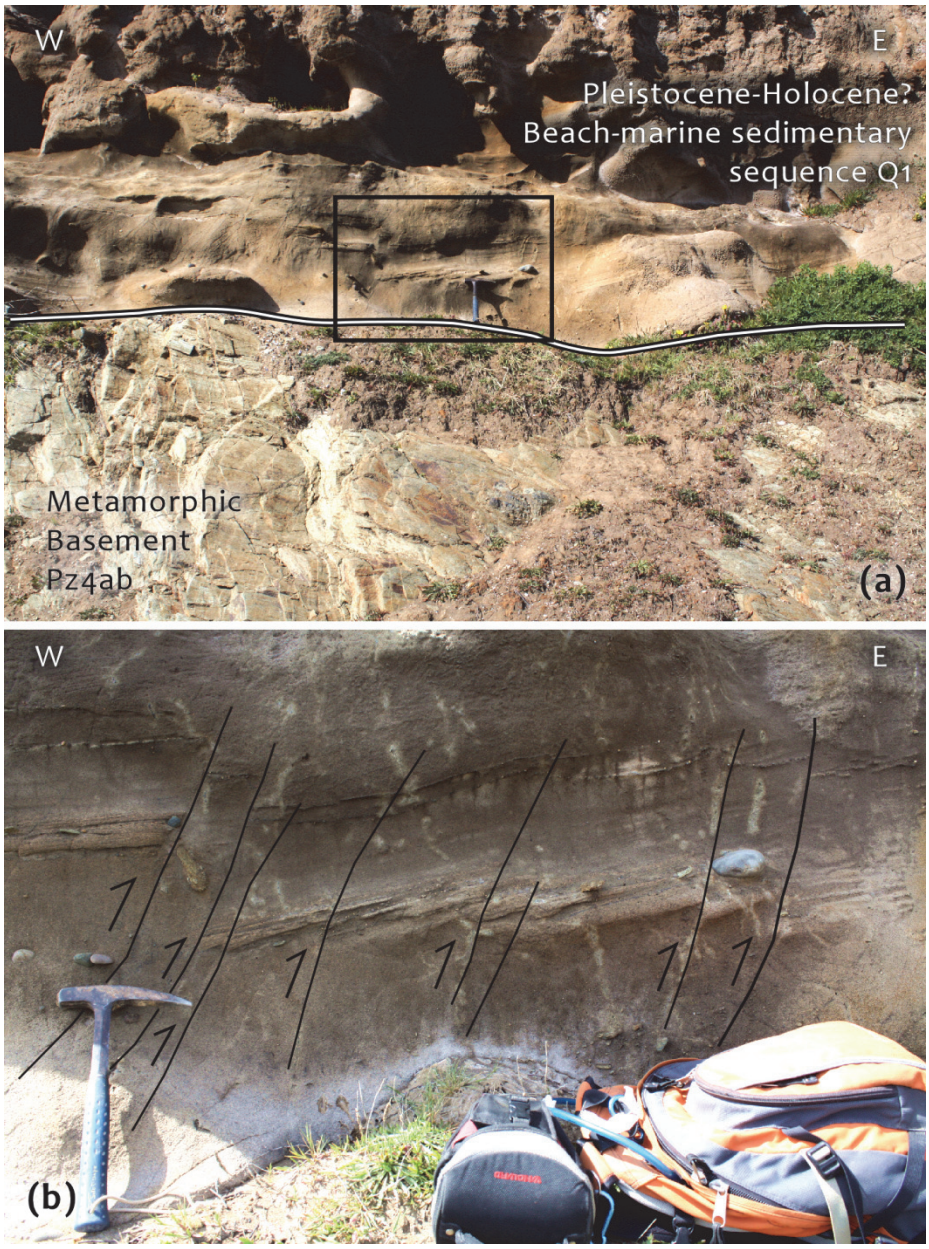

Figure 5.12: Minor centimeter-scale reverse faults affecting the Quaternary sedimentary sequences found at site 10 (Fig. 2.2, Table 2.1 and Section 2.5.1.4 in main manuscript).

Figure 5.13: (a) and (b) show outcrop of a NS-striking, W-dipping normal fault found at the coastal cliff in site 11 (Fig. 2.2, Table 2.1 and Section 2.5.1.4 in main manuscript). (c) and (d) are close ups of the fault zone showing kinematic indicators of normal displacement (sigmoid-shaped fabrics in the gouge and deflection of the schistosity in the foot-wall block).

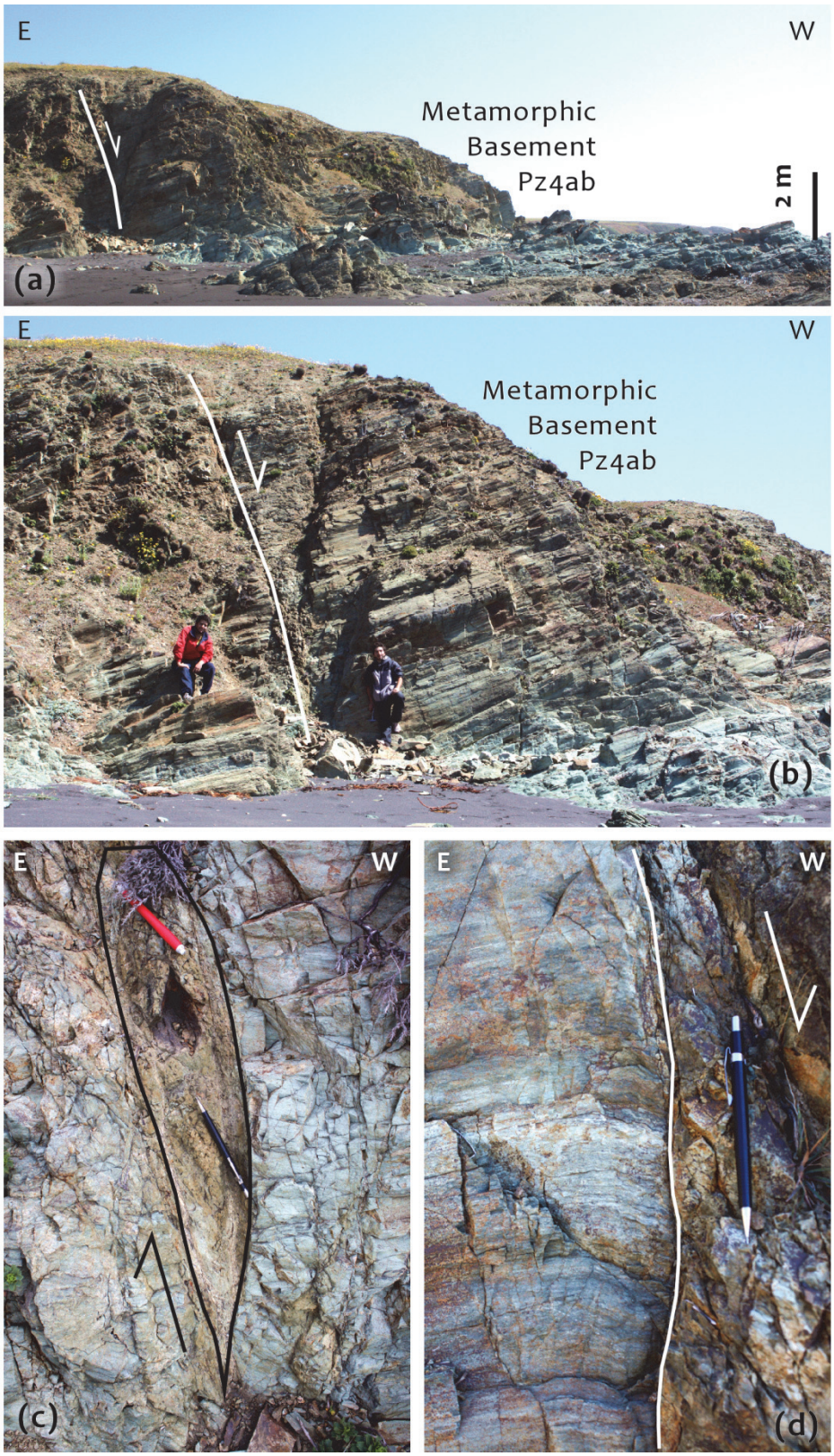
E
W
Metamorphic
Basement
Pz4ab
2 m
(a)
E
W
Metamorphic
Basement
Pz4ab
(b)
E
W
(c)
E
W
(d)

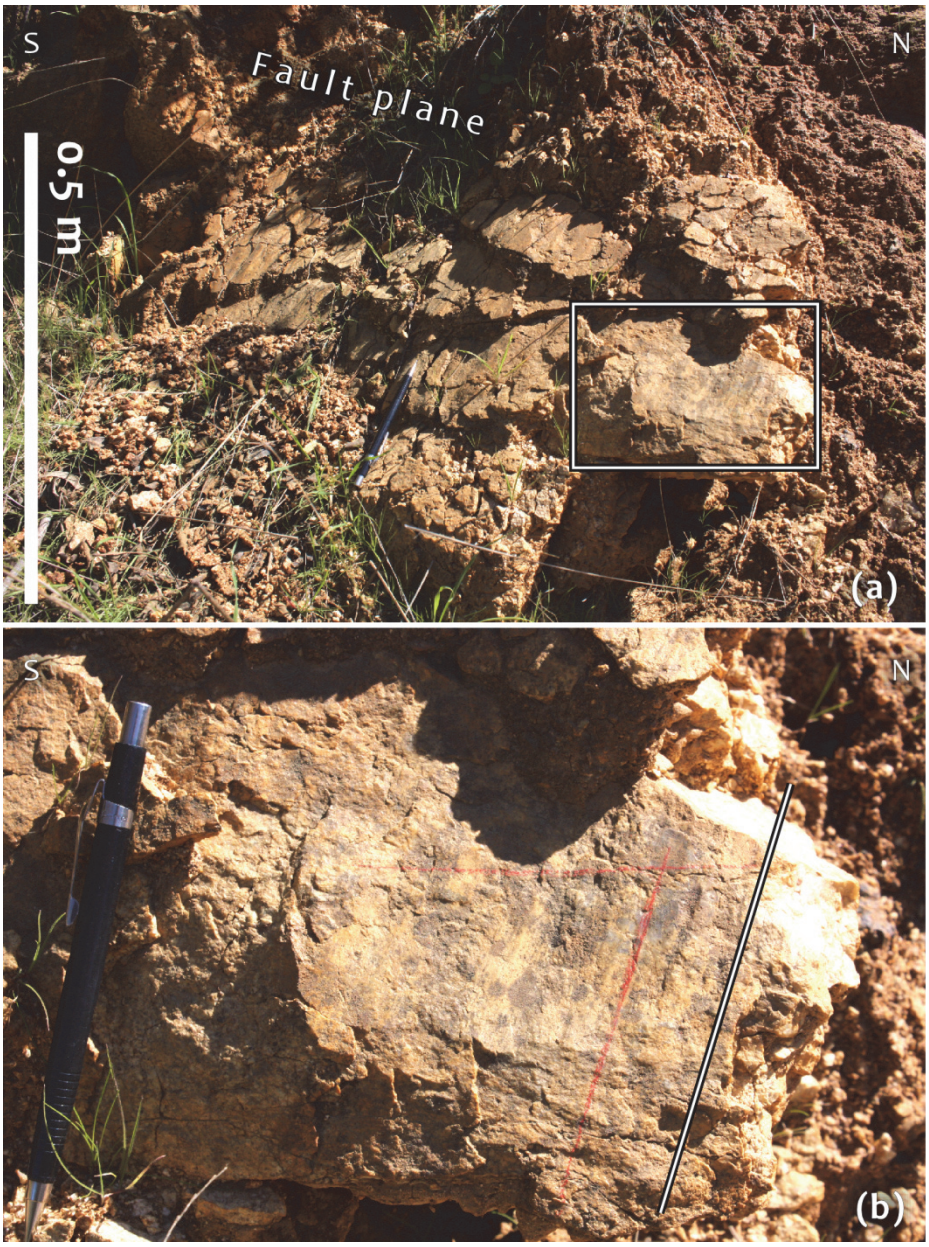

Figure 5.14: (a) Outcrop of one of the normal faults found at the base of the Cáhuil-Vichuquén ridge scarp in site 14 (Fig. 2.2, Table 2.1 and Section 2.5.1.5 in main manuscript). (b) Close up to fault plane with slickensides. The structure affects the Paleozoic metamorphic basement rocks.

A.2 Additional structural field examples of the Maule study region

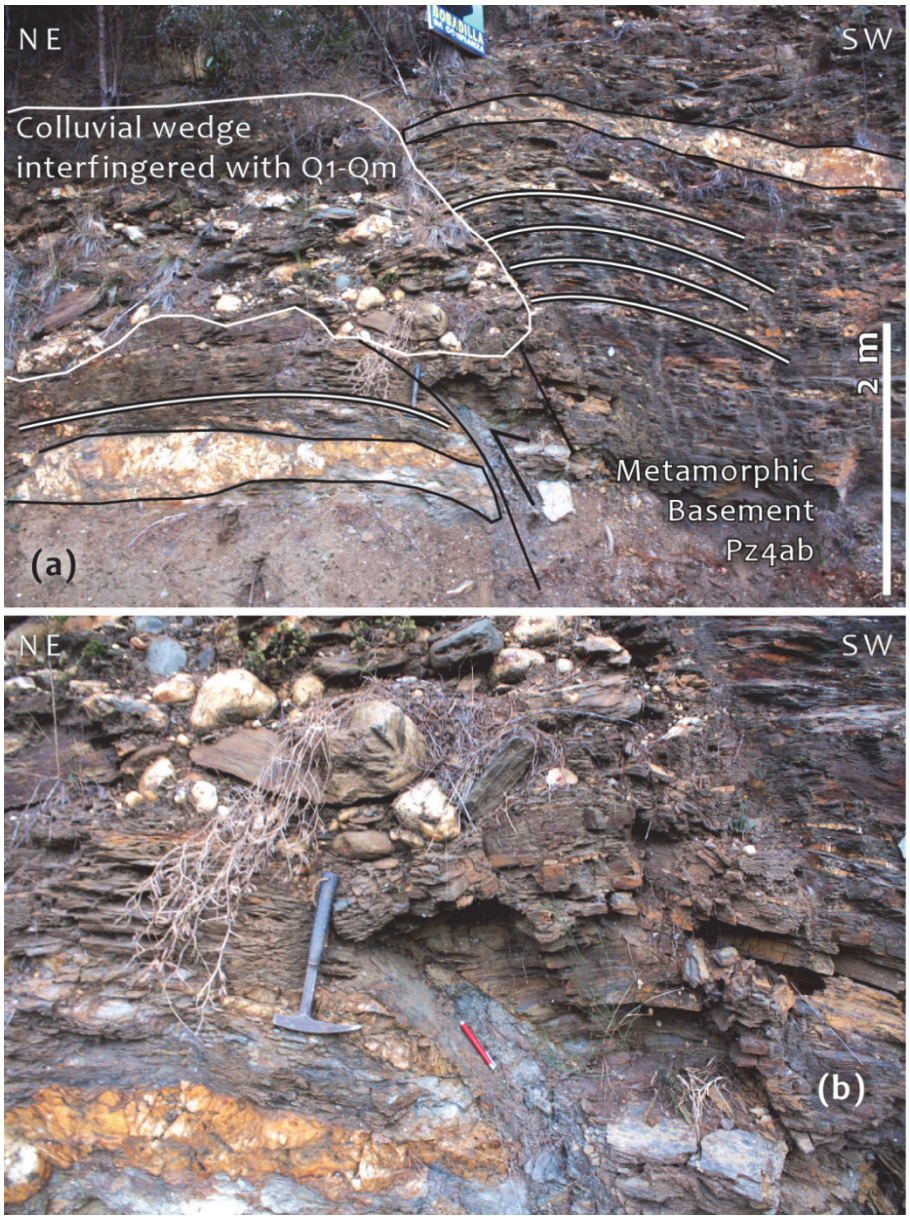

Figure 5.15: (a) Color version of Figure 2.11 in main manuscript (site 20 in Fig. 2.9 and Table 2.2; Section 2.5.2.1 in main manuscript). (b) Close up to fault plane and colluvial wedge in the foot-wall. Outside the pictures to the left, the material of the wedge interfingers with Quaternary paleo-beach sedimentary rocks, which lie on top of a sub-horizontal abrasion platform cut on metamorphic basement rocks.

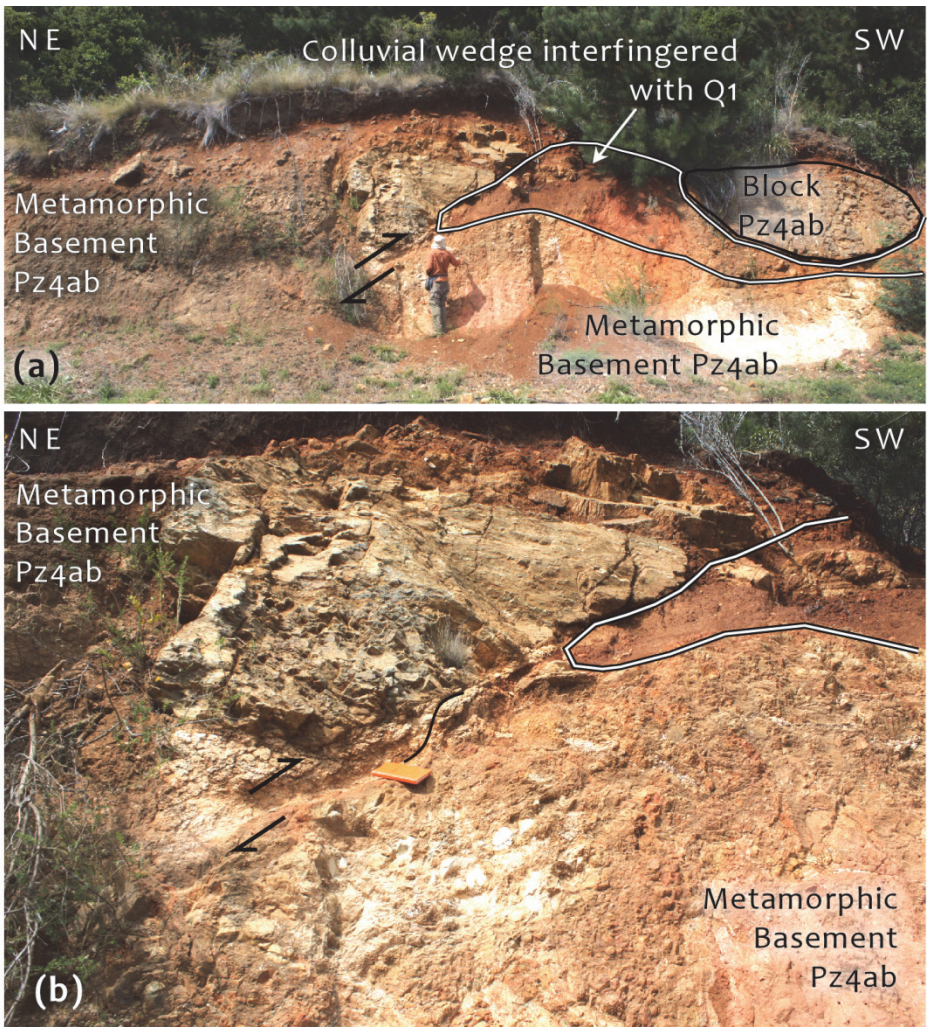

Figure 5.16: (a) Outcrop of reverse fault found at site 21 affecting metamorphic rocks and Quaternary sedimentary units (Fig. 2.9, Table 2.2 and Section 2.5.2.1 in main manuscript). Here the colluvial wedge in front of the scarp interfingers with Quaternary river deposits (Q1). (b) Close up to fault zone around the person at the center of picture in (a).

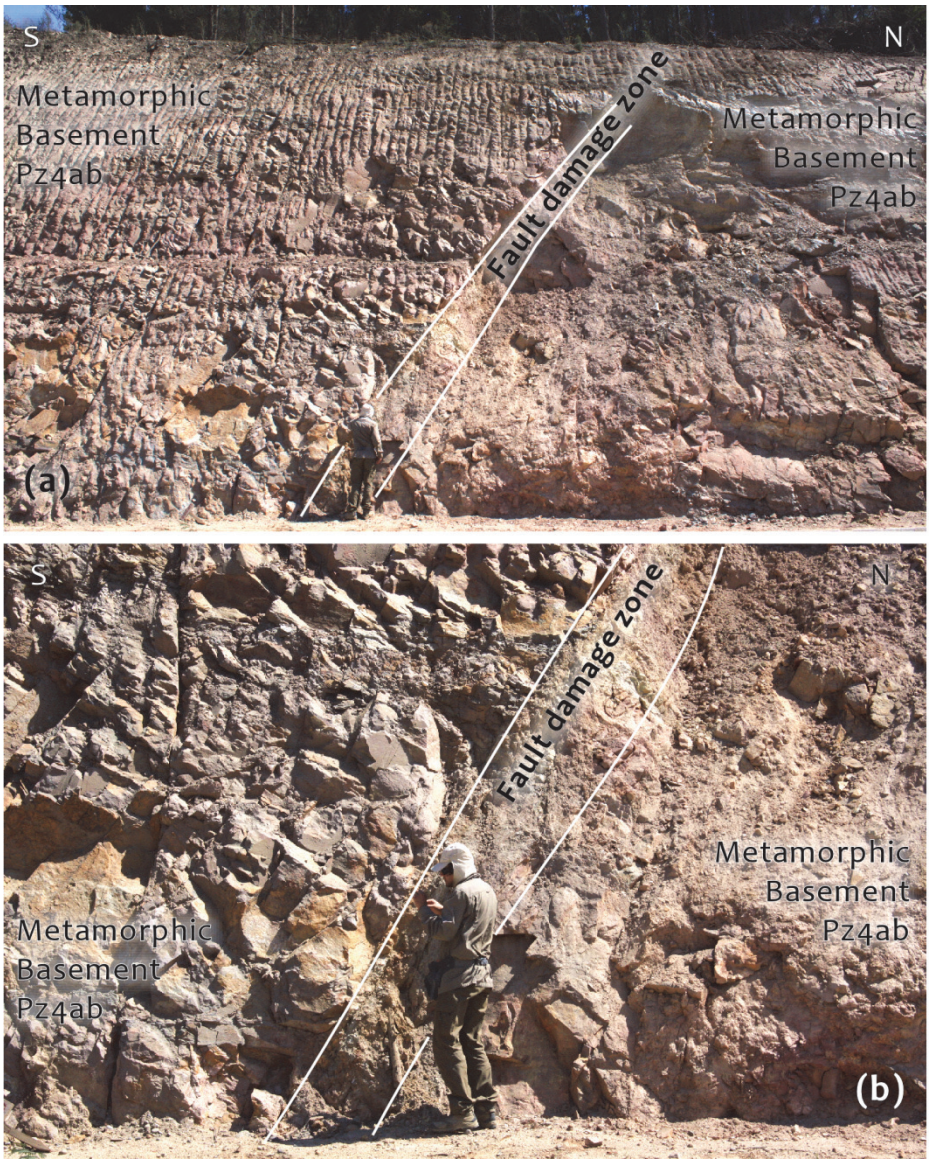

Figure 5.17: (a) Outcrop of major fault affecting metamorphic basement at site 22 (Figs. 2.9-2.10, Table 2.2 and Section 2.5.2.2 in main manuscript). The width of the fault damage zone, as emphasized in the pictures, suggests a significant brittle deformation history accounted by this structure. (b) Close up around the location of the person at the lower center of photo (a).

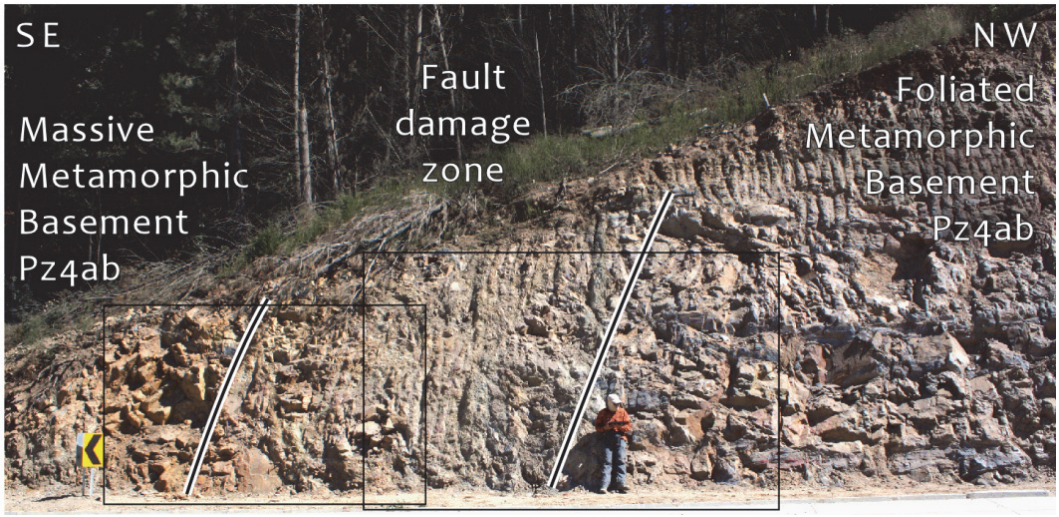

Figure 5.18: Color version of Figure 2.12 in main manuscript (Fault 23a in Figs. 2.9-2.10 and Table 2.2; Section 2.5.2.2 in main manuscript). The boxes on the lower left and lower center of the picture show the location of Figs. A19 and A21 respectively.

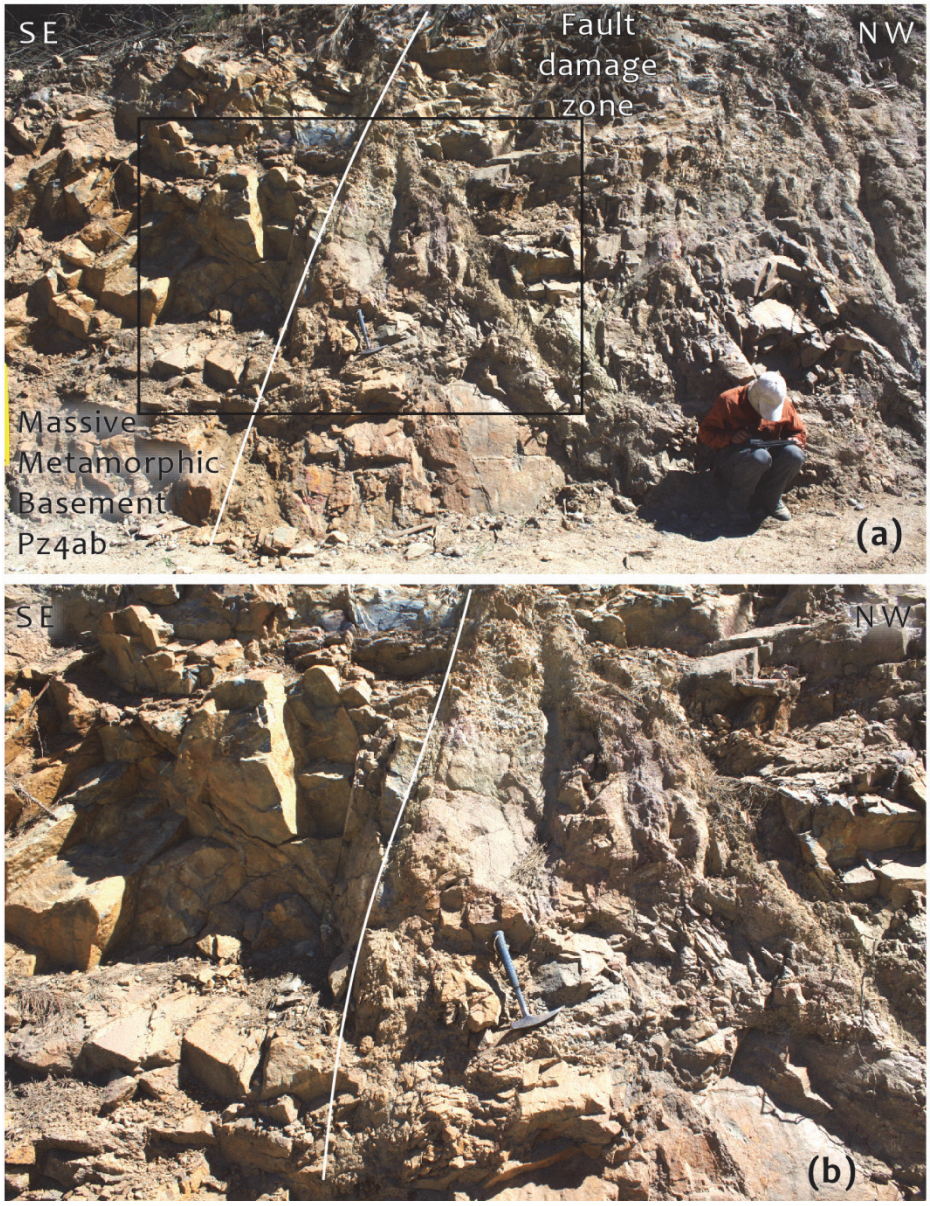

Figure 5.19: (a) Contact between the top of the damage zone and the hanging-wall of the main fault in site 23 (location in Fig. A20). (b) Close up to the black box in (a).

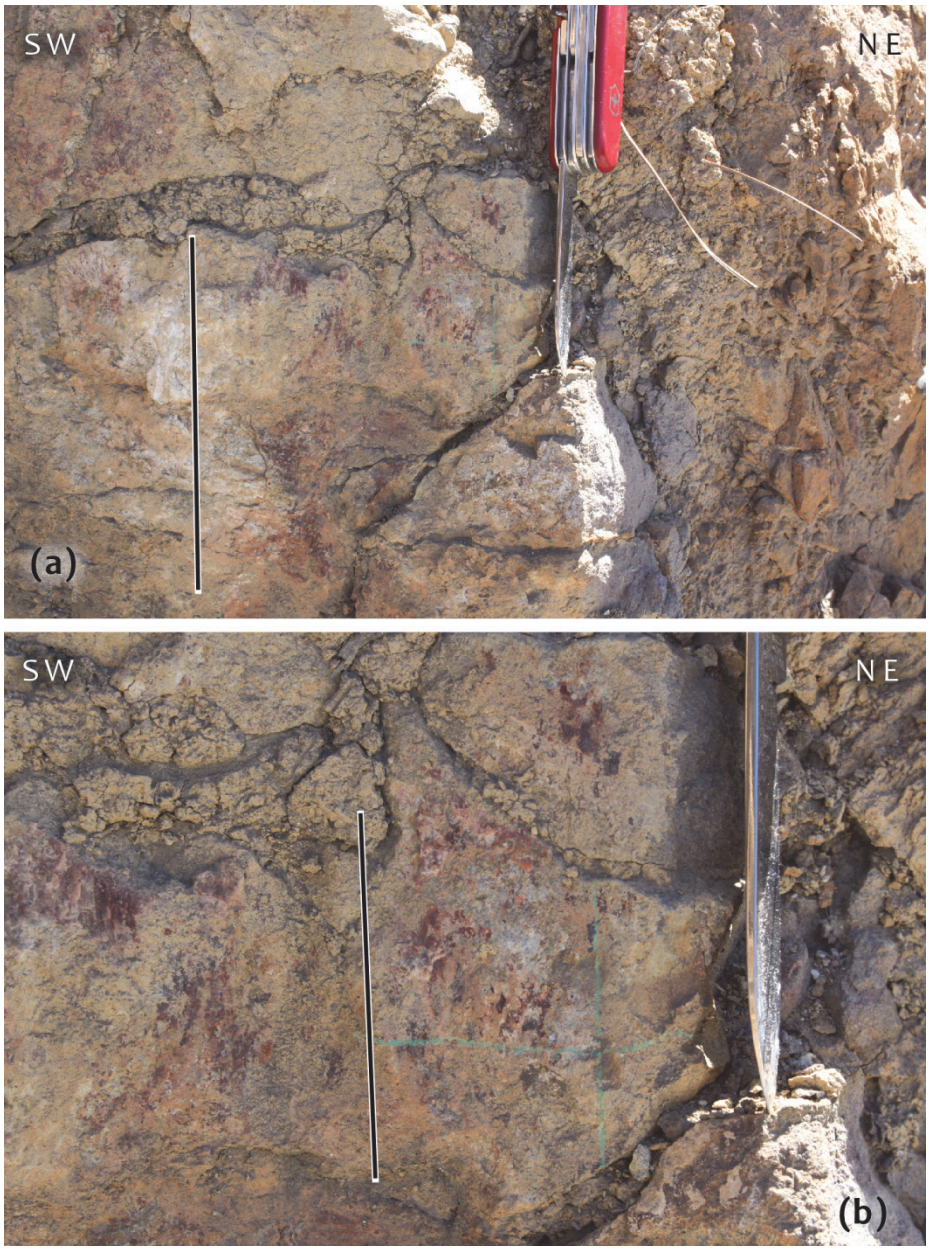

Figure 5.20: (a) and (b) are close up views of a striated plane on the contact shown in Figure A19.

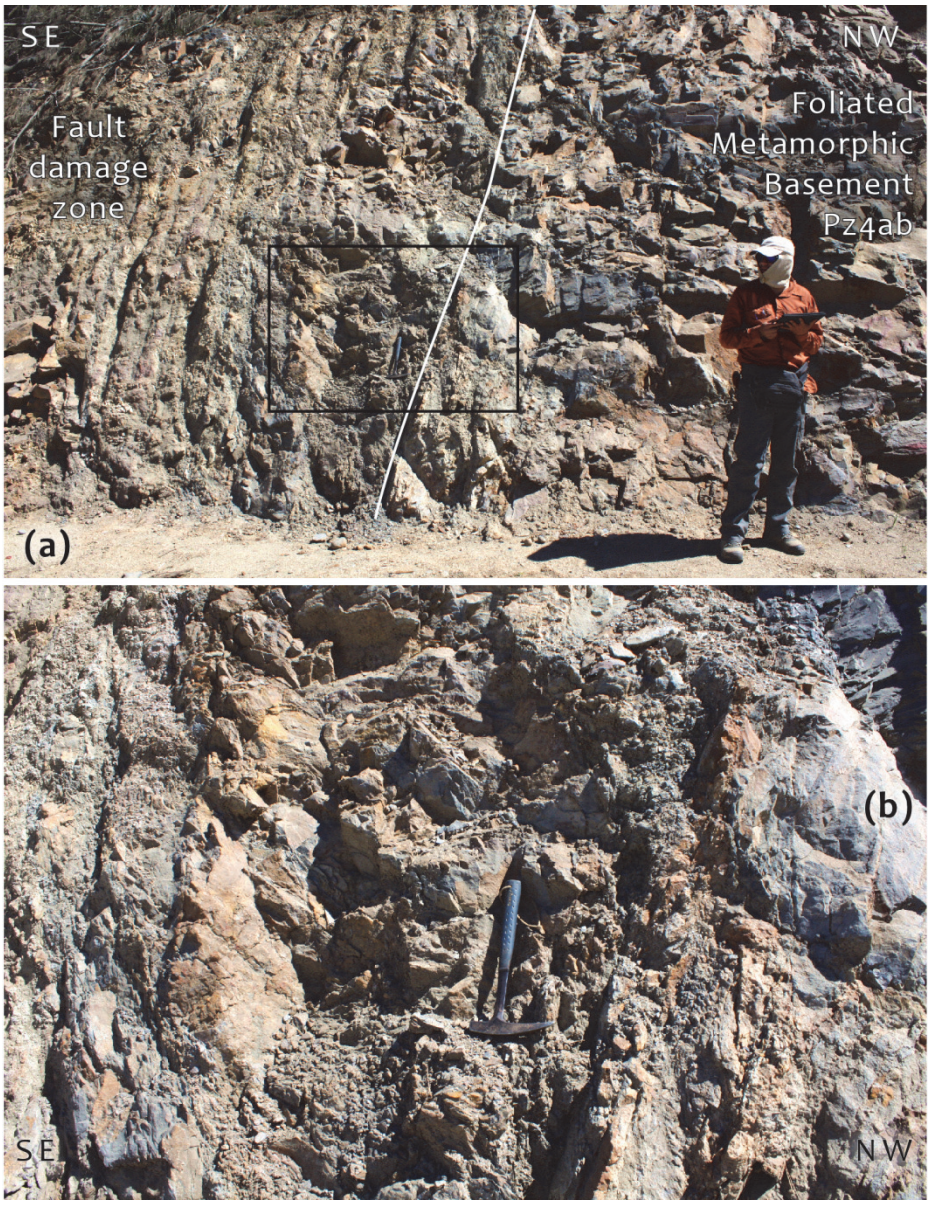

Figure 5.21: (a) Contact between the bottom of the damage zone and the foot-wall of the main fault in site 23 (location in Fig. A20). (b) Close up to the black box in (a).

Figure 5.22: Outcrop of major normal fault bounding the scarp of the Maule ridge at site 29 (Figs. 2.9-2.10, Table 2.2 and Section 2.5.2.2 in main manuscript). The fault zone is bounded by the two white polygons illustrated on the right of the picture. The schistocity of the metamorphic basement in the hanging-wall is deflected close to the fault plane, as emphasized by the ornamentation, indicating normal sense of slip.

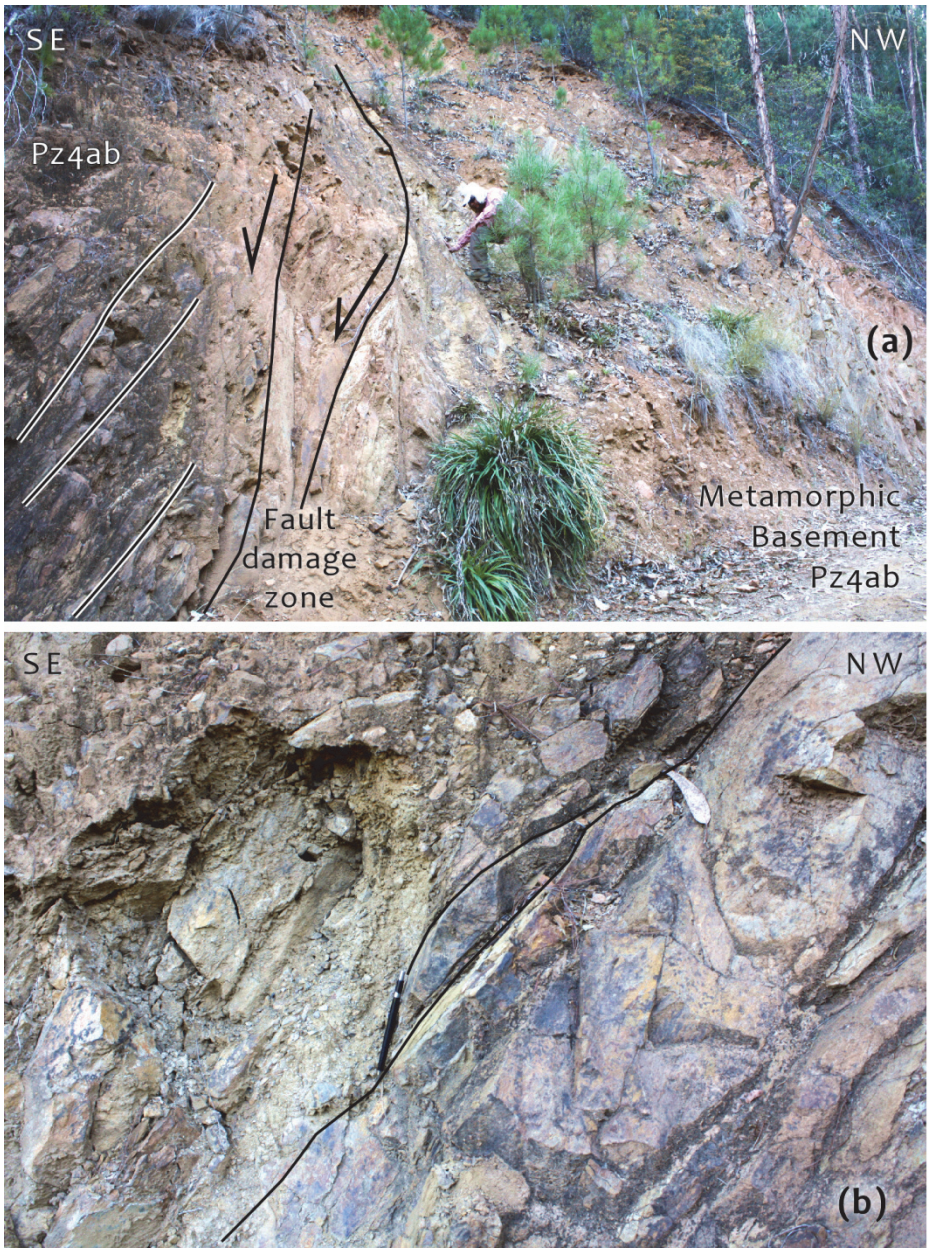

Figure 5.23: (a) Outcrop of fault shown in Fig. A22 emphasizing the damage zone of the structure (site 29 in Figs. 2.9-2.10 and Table 2.2; Section 2.5.2.2 in main manuscript). (b) Close up to the damage zone. Note that the fault gouge and breccia display sigmoid-shaped clasts which indicate shear slip of the structure.

A.3 Infinitesimal 2D strain from GPS over the Maule earthquake rupture area

A.3.1 Coseismic static surface displacements and first invariant of strain

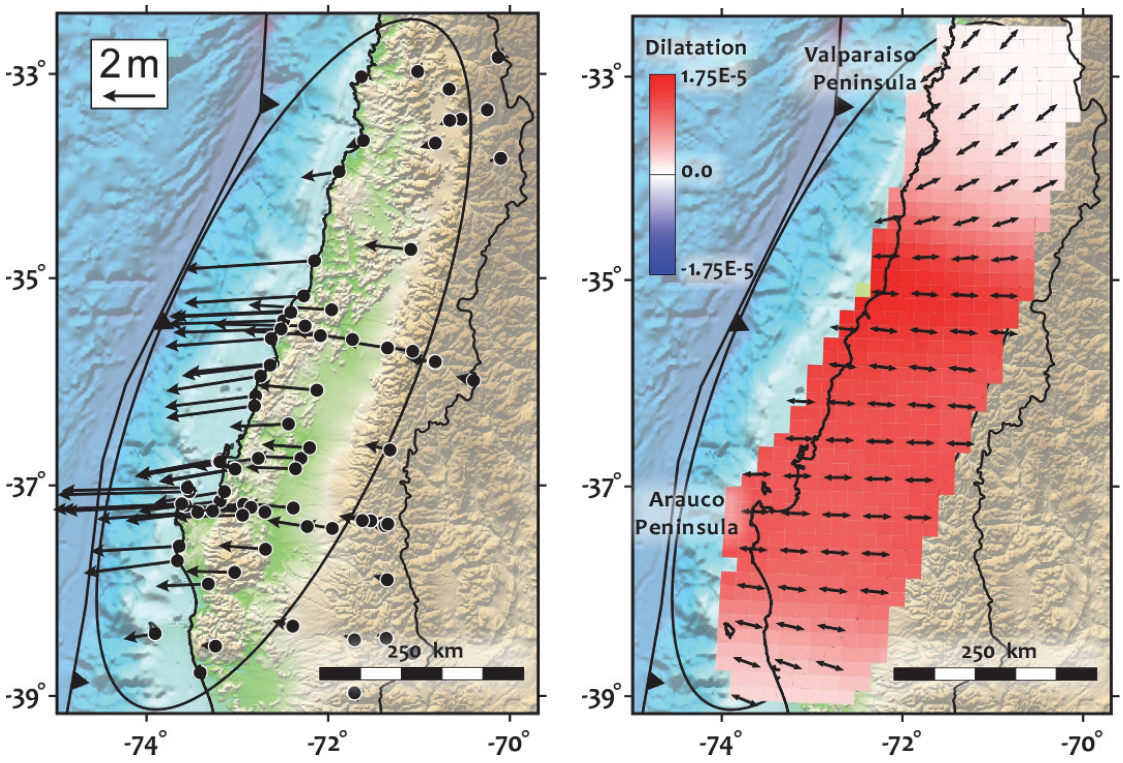

Figure 5.24: Left, coseismic static surface GPS displacements generated by the subduction rebound of the 2010 Maule earthquake. GPS data from *Vigny et al.* (2011) and *Moreno et al.* (2012). Right, 2D infinitesimal strain calculated from these vectors capturing rapid coseismic positive dilatation (in red), caused by an excess of forearc extension. Black arrows represent the horizontal vector field of the principal extension strain (ε_3). See Section 2.6.2 and Figure 2.13 in main manuscript.

A.3.2 Interseismic surface velocities and first invariant of strain

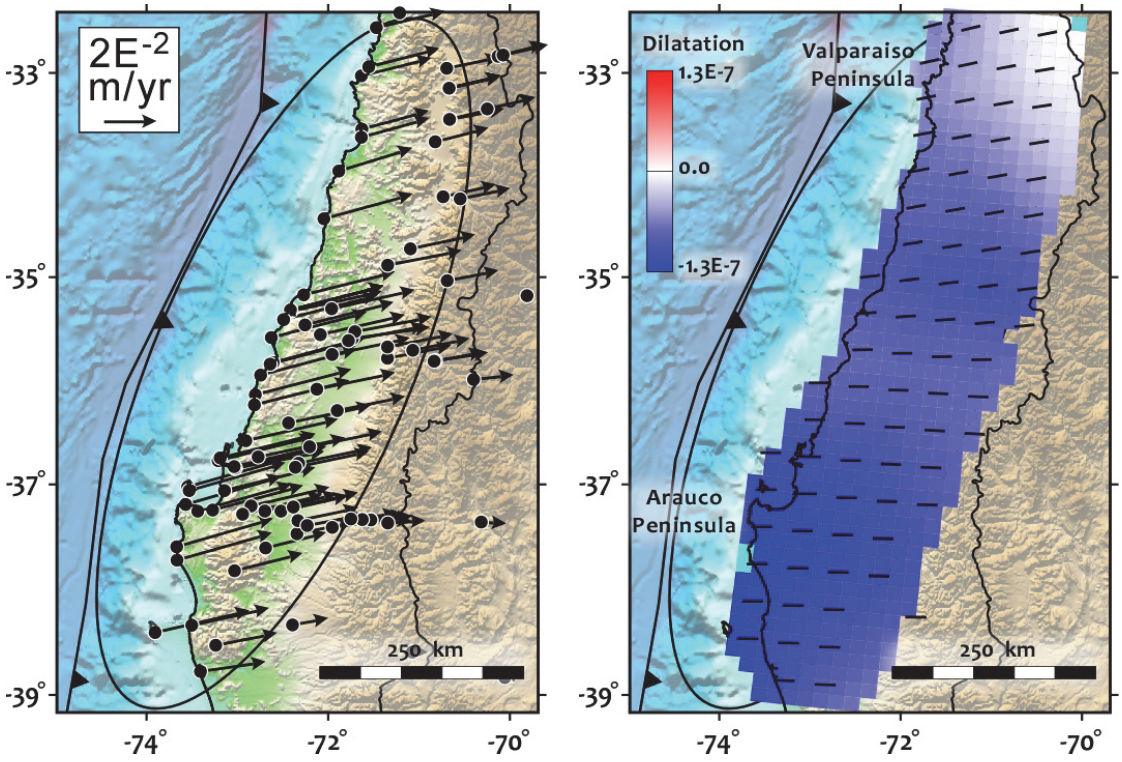

Figure 5.25: Left, compilation of interseismic GPS velocities of the rupture area averaged between 1998 and February 2010, before the Maule earthquake. GPS data courtesy of Marianne Métois (*Métois et al.*, 2012). The velocities before the megathrust show convergence-parallel inland motion of the upper plate. Right, slow shortening shown by the blue colors of the first invariant of strain dominates the interseismic period. Black lines represent the horizontal vector field of the principal shortening strain (ε_1). See Section 2.6.2 and Figure 2.13 in main manuscript.

REFERENCES

Métois, M., A. Socquet, and C. Vigny (2012), Interseismic coupling, segmentation and mechanical behavior of the central Chile subduction zone, *J. Geophys. Res.*, *117*, 16 PP., doi:10.1029/2011JB008736.

Moreno, M. et al. (2012), Toward understanding tectonic control on the Mw 8.8 2010 Maule Chile earthquake, *Earth Planet. Sci. Lett.*, *321–322*(0), 152–165, doi:10.1016/j.epsl.2012.01.006.

Vigny, C. et al. (2011), The 2010 Mw 8.8 Maule Megathrust Earthquake of Central Chile, Monitored by GPS, *Science*, *332*(6036), 1417–1421, doi:10.1126/science.1204132.

APPENDIX B

SUPPLEMENTARY INFORMATION TO CHAPTER 3

B.1 Intraplate normal aftershocks of the Maule earthquake

Table 6.1: Normal intraplate aftershocks of the Maule earthquake from February 27, 2010 to July 31, 2012*

Upper plate				
Long	Lat	Depth	Mw	Event name
Pichilemu sequence				
-71.94	-34.67	12	5.5	201003050334A
-72.29	-34.41	17	5.0	201003111051A
-72.11	-34.54	13	6.9	201003111439A
-72.13	-34.53	16	7.0	201003111455A
-72.08	-34.62	19	5.7	201003112011A
-72.18	-34.41	12	5.7	201003121650A
-71.97	-34.65	19	5.1	201003130712A
-72.07	-34.57	16	5.3	201003131522A
-72.10	-34.42	16	5.2	201003140731A
-72.42	-34.49	31	5.1	201003180318A
-72.22	-34.87	12	5.2	201004011253A
-72.22	-34.48	15	6.0	201005021452A
-72.09	-34.75	12	5.4	201005211852A
-72.29	-34.58	33	5.2	201011280819A
Outside Pichilemu				
-72.99	-35.45	12	5.0	201003021130A
-73.85	-38.71	19	5.5	201003141352A
-73.85	-38.68	13	5.5	201003142004A
-71.47	-37.09	16	5.3	201008150750A
-71.54	-35.65	13	5.3	201102141218A

Table B1. Cont.

Lower plate				
Long	Lat	Depth	Mw	Event name
		Northern cluster		
-73.88	-34.72	17	4.9	201003010530A
-73.53	-34.73	12	5.4	201003010749A
-74.01	-34.57	12	5.1	201003011220A
-73.96	-34.53	12	5.2	201003011436A
-74.27	-34.9	18	5	201003012240A
-73.97	-34.54	12	5.1	201003081303A
-74.29	-35.16	18	5.1	201003100845A
-74.07	-34.82	12	5.9	201010210249A
-73.51	-34.07	12	5.2	201012131851A
		Southern cluster		
-75.41	-38.09	20	7.4	201002270801A
-74.96	-37.91	19	5	201003010858A
-74.96	-37.72	17	5.1	201003040903A
-75.28	-38.25	27	5.1	201003101600A
-75.34	-37.91	20	5.6	201006280059A
-75.59	-37.77	30	5	201111251735A
		Uncertain		
-73.41	-35.35	36	5.1	201003050736A
-73.36	-36.17	29	5.1	201003072346A

*Source: Global CMT catalog. Centroid depth in km.

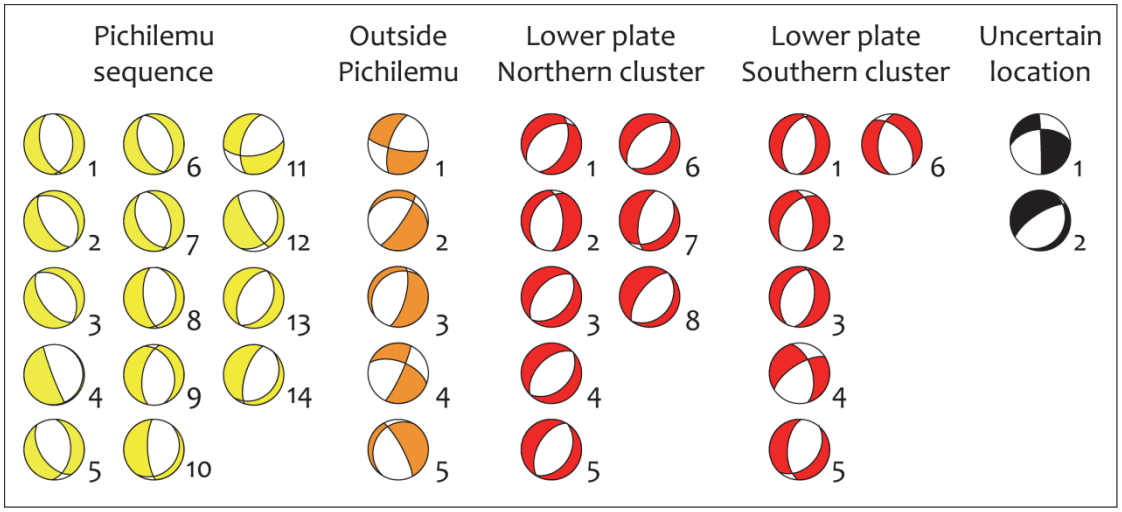

Figure 6.1: Fault plane solutions of the normal aftershocks. Refer to table B.1 for location and moment magnitude. Colors are the same than Figure 3.1 and 3.3 in main manuscript.

B.2 Fault slip models used in strain and CSI calculations

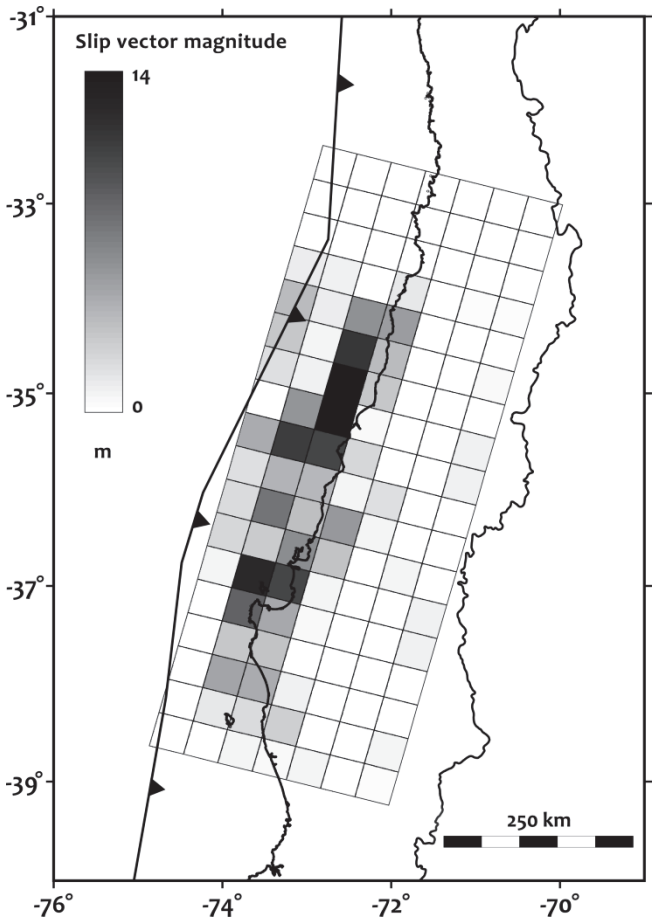

Figure 6.2: Fault slip model by *Delouis et al*. (2010).

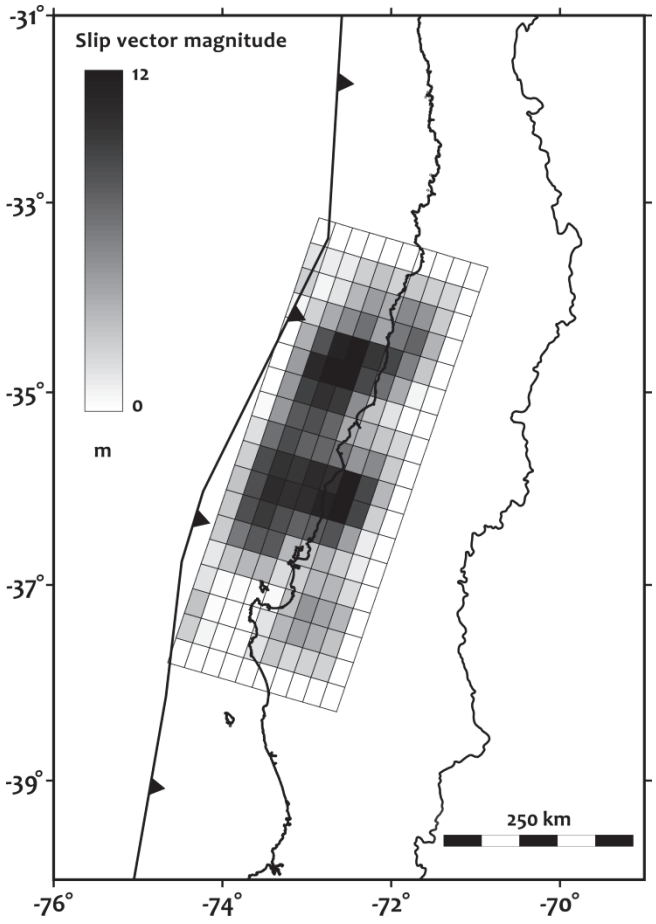

Figure 6.3: Fault slip model by G. Hayes (unpublished data, 2010; available online from the USGS web site: http://earthquake.usgs.gov/earthquakes/eqinthenews/2010/us2010tfan/finite_fault.php)

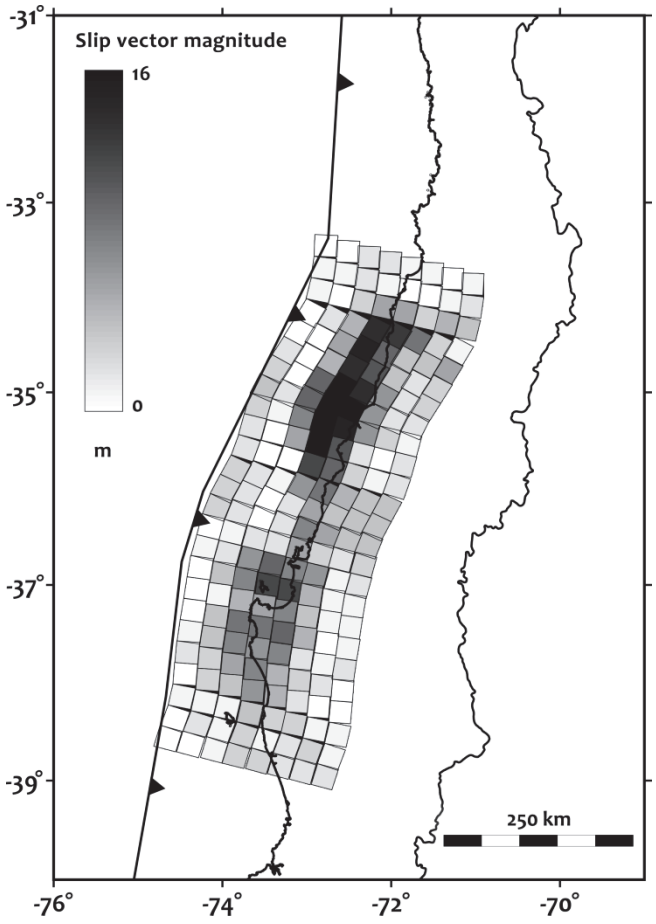

Figure 6.4: Fault slip model by *Lorito et al*. (2011)

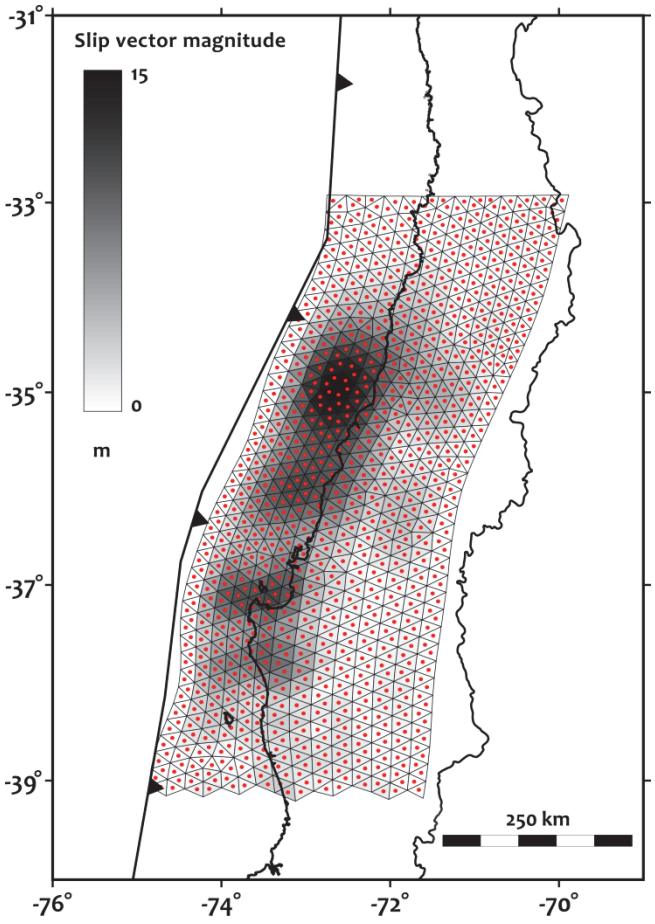

Figure 6.5: Fault slip model by *Moreno et al*. (2012). Red dots indicate that we used a "point source" approach of slip for each triangular patch to model the Coulomb Stress Increment (CSI).

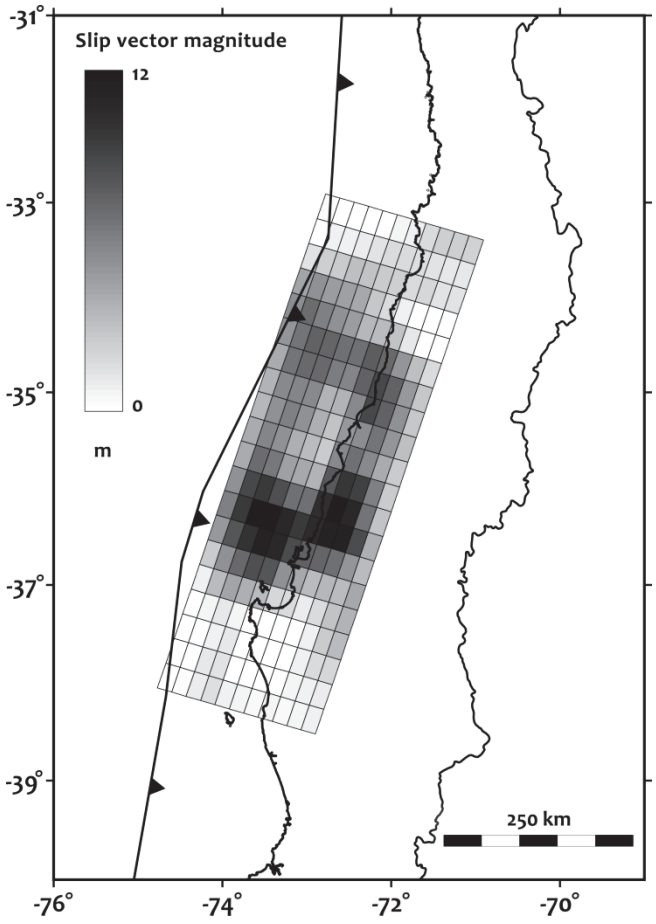

Figure 6.6: Fault slip model by G. Shao et al. (unpublished data, 2010; available online from UCSB web site: http://www.geol.ucsb.edu/faculty/ji/big_earthquakes/2010/02/27/chile_2_27.html).

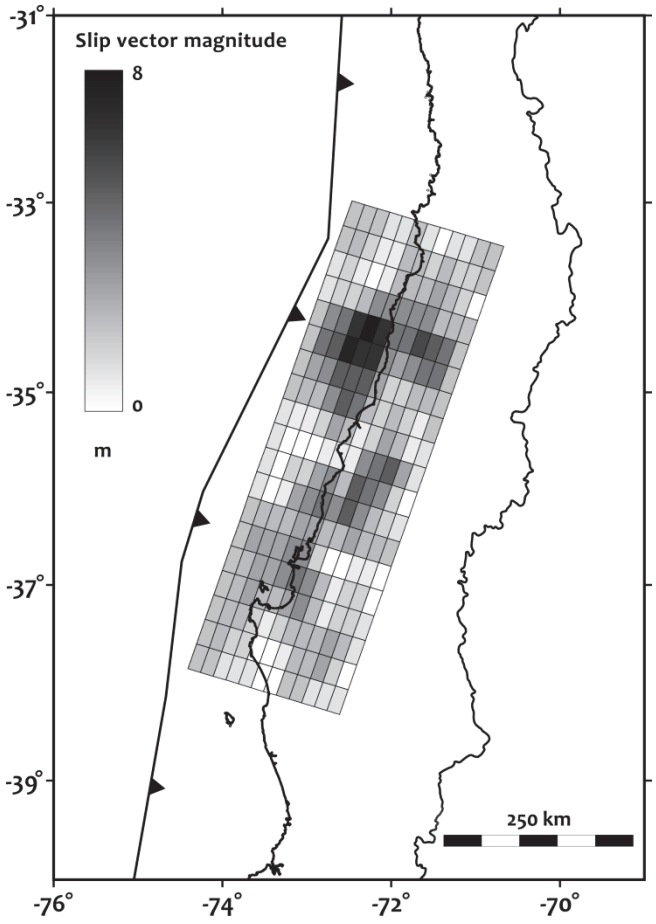

Figure 6.7: Fault slip model by A. Sladen (unpublished data, 2010; available online from Caltech web site: http://www.tectonics.caltech.edu/slip_history/2010_chile/index.html).

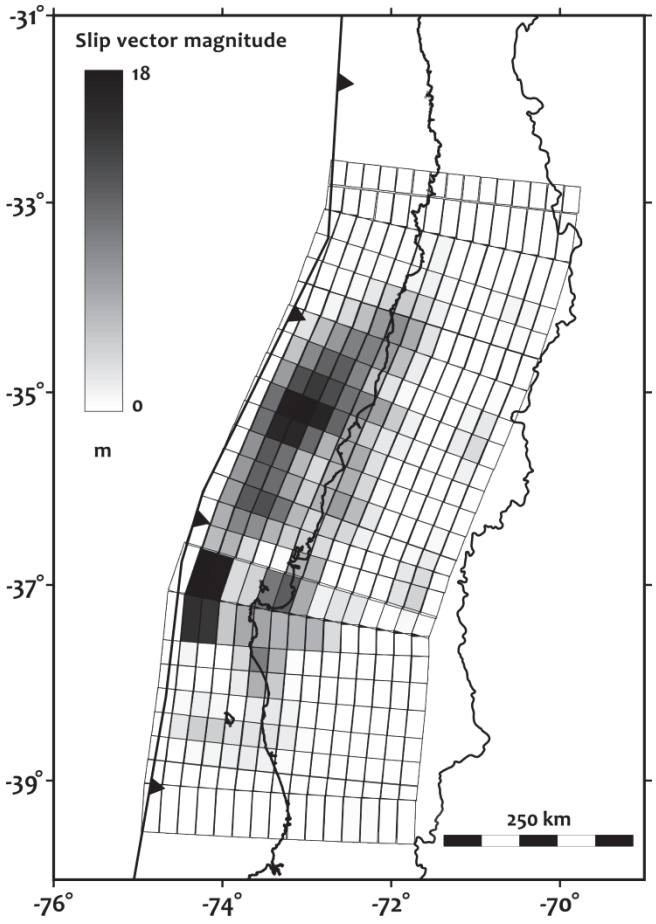

Figure 6.8: Fault slip model by *Vigny et al.* (2011).

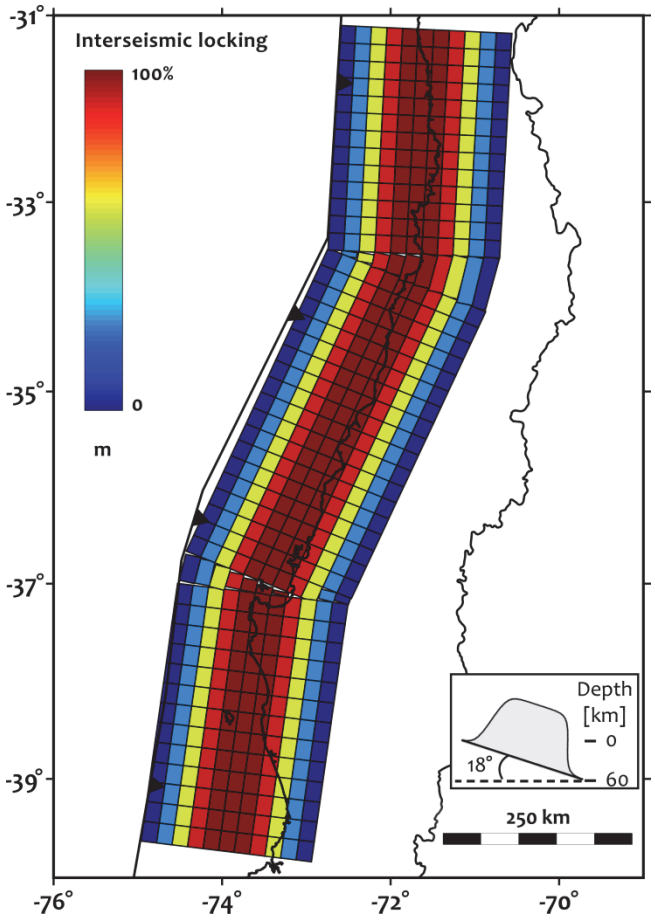

Figure 6.9: Synthetic interseismic coupling of the plate interface used in our model. The inset graph shows the shape of the coupling function in an 18° down-dip profile (see equation (1) in section B.4.2 and Figure B.12).

B.3. Regional strain field calculations

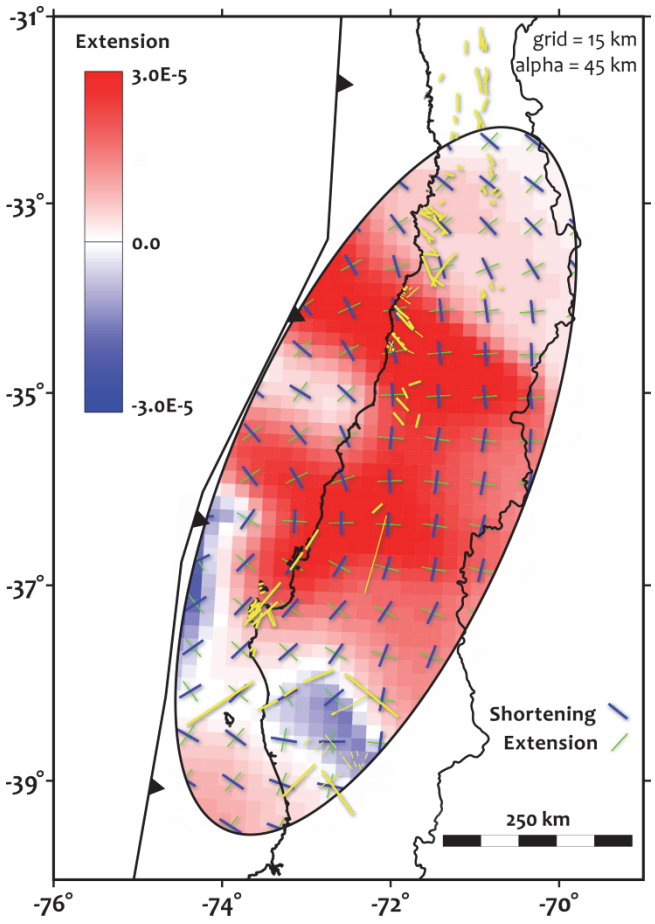

Figure 6.10: Regional coseismic infinitesimal strain field above the Maule segment. Here we use static GPS displacements and slip on the megathrust from the teleseismic finite fault model by G. Shao et al. (unpublished data, 2010; available online from UCSB web site: http://www.geol.ucsb.edu/faculty/ji/big_earthquakes/2010/02/27/chile_2_27.html). Refer to Figure 3.7 in main manuscript for a complete caption.

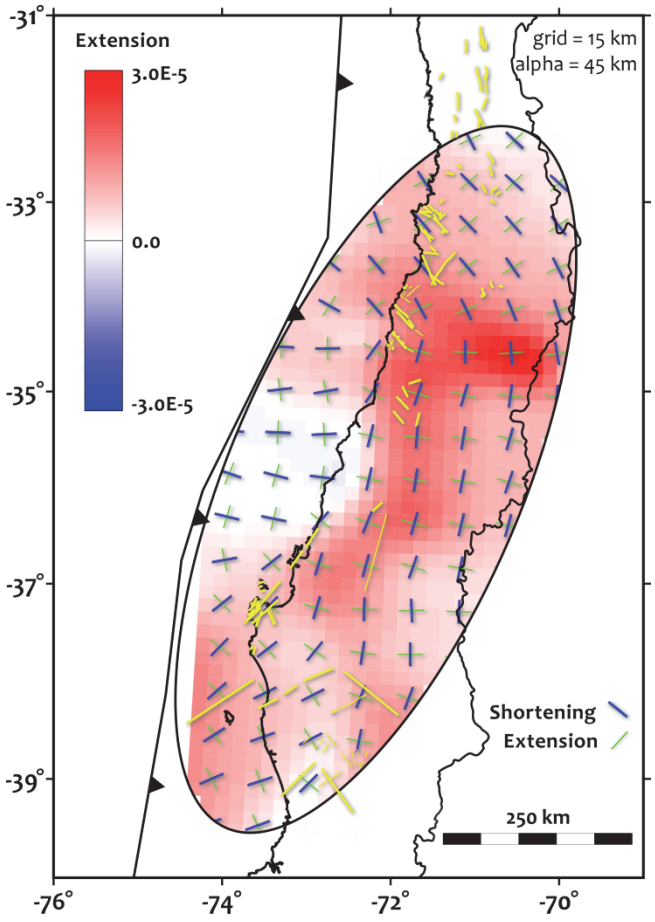

Figure 6.11: Regional coseismic infinitesimal strain field above the Maule segment. Here we use static GPS displacements and slip on the megathrust from the teleseismic finite fault model by A. Sladen (unpublished data, 2010; available online from Caltech web site: http://www.tectonics.caltech.edu/slip_history/2010_chile/index.html). Refer to Figure 3.7 in main manuscript for a complete caption.

B.4. Theoretical foundations behind our mechanical models

B.4.1. Coulomb stress increment and coseismic period

As is it mentioned in the chapter, we use a static mechanical approach to determine the coseismic deformation field by using an analytical solution based on Volterra's theory of dislocations (*Volterra*, 1907). According to this theory, which was first developed to study earthquakes by *Steketee* (1958) and completely defined by *Okada* (1992), the fault plane is represented mathematically as a dislocation in an infinite homogeneous elastic half-space. The shear vectors on the source fault, or distributed slip vectors in the case of finite discrete fault models, produce opposite displacement couples of the blocks separated by the dislocation, and generate a perturbation or distortion of the material surrounding the discontinuity (Figure 3.4 in manuscript). This perturbation is expressed in an internal displacement field (all the analytical expressions are given by *Okada*, 1992).

Basically, the displacement vector $\mathbf{u}_{(x,\ y,\ z)}$ at any point in the half-space, is a function of the following parameters: $\mathbf{u}_{(x,y,z)} = \bar{\mathrm{U}}/2\pi * \boldsymbol{f}_{(x,y,z)}(\theta, L, W, \bar{d}, \lambda, \mu)$, where λ and μ are the *Lamé* constants (material properties), $\mathbf{U}$ is the fault slip vector, $\bar{d}$ the distance from the fault centroid, and θ, L and W are the dip, length and width of the fault respectively. After determining the displacement vector field, the infinitesimal strain and the stress tensors can be obtained invoking linear elasticity and the Hooke's law as constitutive equations, according to the expressions: $\varepsilon_{ij} = 1/2 * (\partial u_i/\partial x_j + \partial u_j/\partial x_i)$ and $\sigma_{ij} = 2\mu\varepsilon_{ij} + \lambda\varepsilon_{kk}\delta_{ij}$, where i, j and $k = 1$ to 3.

Finally, the static coseismic internal stress field (σ_{ij}) generated by the source fault (plate interface megathrust) can be resolved on any other discontinuity that cuts the deformed body (so-called receiver faults) (*Lin and Stein*, 2004). For example, the components of the stress tensor normal and tangential to the intraplate faults of the

outer forearc ($\Delta\sigma_n$ and $\Delta\tau_{slip}$ respectively) can be calculated. Based on the Coulomb rock fracture criteria, these two components can be used to determine if the applied stress field enhances or retards (and how much) the slip on the receiver fault in a specific direction (*King et al.*, 1994). The resultant, named Coulomb stress increment (thereafter CSI) or Coulomb stress change, has units of stress and is defined by: $\mathrm{CSI} = \pm\Delta\tau_{\mathrm{slip}} - \mu'\Delta\sigma_{\mathrm{n}}$.

The shear stress is resolved in the slip direction (positive in the slip sense of interest), the normal stress is positive in compression and μ' corresponds to the effective static friction coefficient of the fault plane (*Scholz*, 2002). The CSI can be positive or negative. If CSI > 0 the slip will be enhanced in the specific evaluated direction; otherwise slip is impeded.

In this paper we produce coseismic forward models of the static CSI resolved on the Pichilemu fault and on optimally oriented extensional structures over horizontal grids at 10 km depth, covering the entire upper plate above the Maule rupture area. The strike of these optimally oriented structures is orthogonal to the minimum principal stress vector ($\Delta\sigma_3$) at each grid element, which is horizontal over most of the upper plate. The dip of the structures is determined based on the Coulomb rock fracture criterion and is a function of μ' and the orientation of the maximum principal stress ($\Delta\sigma_1$) at each grid node (*King et al.*, 1994).

By combining dislocations and Coulomb theories to analyze coseismic deformation, we assume that the faulting process occurs as a result of a linear-elastic fracture mechanics.

Though beyond the scope of this article, an alternative method to calculate the cosesimic and interseismic stress fields using GPS data and finite element models (*Parsons*, 2006) may be used in future work to compare this solution to the results

obtained from a dislocation theory approach. This alternative method has the advantage of being based on direct observations and not in non-unique fault slip models.

B.4.2. The interseismic period: inverted boundary conditions

We simulate a simple dislocation model of the Maule segment throughout an interseismic period of 150 years, based on a "backslip" model (*Savage*, 1983). By using this approach we hypothesize that the finite upper plate deformation field over Maule is created by shear stress transfer at the plates interface (Figure 3.2 main manuscript). This external shear acts constantly during the entire interseismic cycle due to the interplate locking and the continuous plate convergence. The interplate locking or degree of coupling is expressed in terms of the coupling ratio which ranges between 0 (decoupled) and 1 (or 100%; coupled) (*Wang and Dixon*, 2004).

As well as the coseismic slip distribution, this ratio is not homogeneous over the entire interface. Geodetic inversions, which assume that all the surface deformation signal is due to the slip deficit caused by interseismic coupling, show a variety of solutions for different subduction zones or even for the same subduction segments (*Yoshioka et al.*, 1993; e.g., *Bürgmann et al.*, 2005; *Gagnon et al.*, 2005; *Hashimoto et al.*, 2009; *Loveless and Meade*, 2010, 2011; *Moreno et al.*, 2010, 2011, 2012; *Perfettini et al.*, 2010). This variability is explained because here we face an inversion problem with no unique solution and, as *Gagnon et al.* (2005) and *Loveless and Meade* (2011) pointed out, in subduction settings the land coverage of the geodetic signal does not permit robust estimations of coupling offshore.

Theoretical, mechanical and seismological approximations of interseismic coupling simplify the distribution to a semi-2D problem, where the subduction interface is subdivided, down-dip, in: coupled, partially coupled and decoupled zones,

with no significant variations along strike (*Ruff and Kanamori*, 1983; *Tichelaar and Ruff*, 1993, 1991; *Hyndman and Wang*, 1993; *Suarez and Comte*, 1993; *Flück et al.*, 1997; *Oleskevich et al.*, 1999; e.g., *Bevis et al.*, 2001; *Wang et al.*, 2003; *Khazaradze and Klotz*, 2003; *Song and Simons*, 2003; *Wang and Dixon*, 2004; *Loveless et al.*, 2010). These estimations are mainly based in the back slip model by *Savage* (1983), in the correlation between interseismic coupling and the distribution of seismicity on the subduction zone (seismogenic zone), and in the correlation between coupled regions and gravity anomalies. Despite variations in depth constraints, most of the models agree that the mechanical behavior of the interseismic coupling gradually varies downward, starting at the trench, from: (a) an up-dip decoupled to coupled portion, to (b) a fully coupled and to (c) a down-dip decoupled zone below the interplate seismogenic zone (Figure B.9. and Figure 3.2 in main manuscript). Along the Maule segment, the fully coupled portion reaches an approximate maximum of 50 km depth (*Tichelaar and Ruff*, 1991, 1993; *Suarez and Comte*, 1993; *Khazaradze and Klotz*, 2003; *Ruegg et al.*, 2009; *Moreno et al.*, 2010).

Considering the non-uniqueness of the coupling distribution and the *state of the art* in the understanding of this phenomenon, in our mechanical approximation we use a simple 2D "mesa-shaped" function ($cf_{(Ddd)}$) to simulate the down-dip change of coupling (Figure B.12), with no variation along strike:

$$cf_{(Ddd)} = \left(\frac{1}{1+e^{-a(Ddd-c_1)}}\right) * \left(\frac{1}{1+e^{a(Ddd-c_2)}}\right) \quad (1)$$

Ddd is the down-dip depth (x'-axis), c_1 and c_2 are the x'-coordinates of the inflection points in the up- and down-dip transitions zones respectively (50 % of coupling or $cf_{(Ddd)} = 0.5$), and a is the shape factor which is inversely proportional to the width and/or the slope of the transition. This coupling distribution results from the multiplication of two sigmoidally-shaped functions (1). The solution converges

downwards to a maximum coupling ($cf_{(Ddd)} = 1$) from a minimum at the trench ($cf_{(Ddd)} = 0$) (up-dip zone) and then diverges from the maximum to a minimum below the seismogenic zone (Figures B.9 and B.12, and Figure 3.2 in main manuscript). By varying the parameters a, c_1 and c_2 we can control the width and depth of the coupled and decoupled zones, and the sharpness of the transitions.

This approximation uses a similar model to other logistic functions which describe natural processes like the *Gaussian*, the probability and distribution functions, the population growth and decay, and the *Fermi-Dirac* distribution function in thermodynamics, among others. In our case, the sigmoid curves permit a smooth and statistically "normal" mechanic transition between the two extreme rheological behaviors of the coupling factor. We do not know in fact if the transitions are sharp or smooth but in terms of the dislocation model, the smoothness helps to avoid singularities in the computations.

The last step before computing the interseismic deformation model is to calculate the slip-deficit vector ($\mathbf{s}_{defi}$) in the down-dip direction, which is the product of: $\mathbf{s_{defi}} = cf_{(Ddd)} \times \mathbf{cr_{proj}} \times t_{\text{int}}$, where $\mathbf{cr}_{proj}$ is the projected convergence rate vector and t_{int} the time interval of the interseismic period. The vector $\mathbf{s}_{defi}$, extrapolated all over the plate interface, constantly along the trend-axis, generates a displacement vector field (same as $\mathbf{u}_{(x,\ y,\ z)}$ in section B.4.1.) that stands as input parameter for our dislocation model, in a normal kinematic fashion (Figures B.9 and B.12).

By using theory of dislocations and CSI to determine the stress field we assume that interseismic deformation is a result of a static mechanics and not dynamic over the 150 years of slow shortening.

Though too simplistic to represent a real natural distribution of the interseismic coupling and slip deficit (see for example the heterogeneity in the coupling

distribution recently published by (*Moreno et al.*, 2010) for the Maule region), and therefore the upper-plate deformation field in fine detail, our synthetic coupling model accounts for the following advantages:

(1) It is consistent with other conceptual and mechanical approximations.

(2) Reconciles theoretical estimations and non-unique geodetic inversions, assessing a more generic case for coupling distribution.

(3) It considers the the change in strike of the subduction interface along the Maule rupture (Figure B.9).

(4) Whereas our semi-2D approach of the coupling function does not permit to solve for fine variations, especially along the strike axis, we assume that this coarse reconstruction is detailed enough to analyze the interseismic deformation field from the perspective of a regional scale.

Probably, our static and elastic approach is not sufficient to explain the complete mechanical behavior of the upper-plate during the interseismic period. For example we cannot assess the influence of the strain rate in the crustal deformation (Figure 3.2 in main manuscript), neither the respond of different rheological configurations to this field. In these terms, a dynamic approximation which accounts for the incremental deformation over the interseismic time span would be the best mechanical procedure to assess the upper-plate deformation. However, our first-order approximation is consistent with other mechanical approaches that consider second-order effects (for example strain rate, rheology inhomogeneities, elasto-plastic and viscous behaviors of the material, and thermal effects near the volcanic arc) to quantify the interseismic deformation field (e.g., *Yáñez and Cembrano*, 2004).

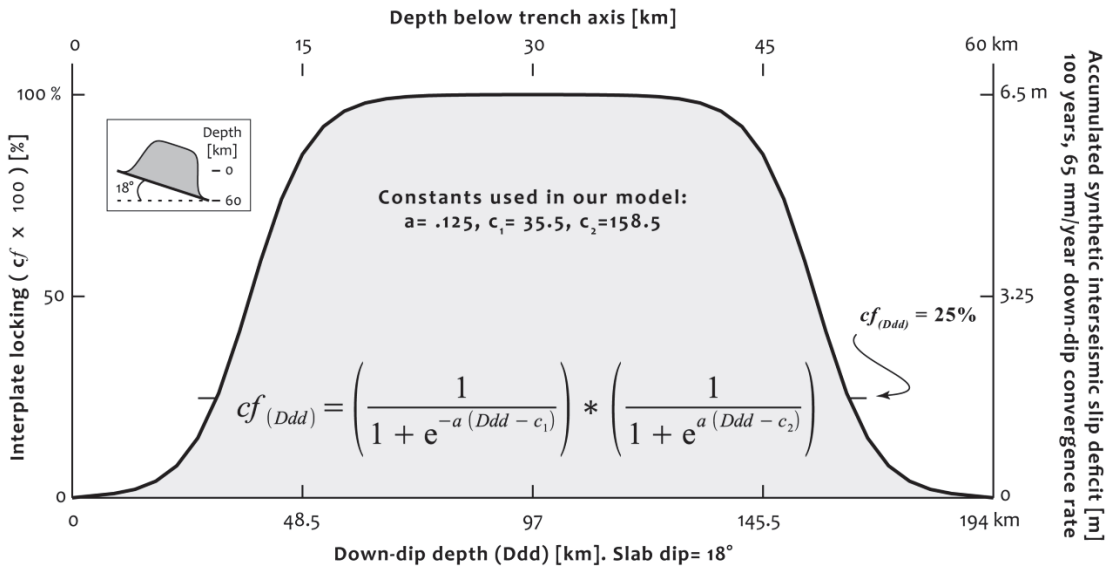

Figure 6.12: Graphical representation of the "mesa-shaped" function (1) that we use to represent the down-dip variation of interseismic coupling ($cf_{(Ddd)}$) on the plates interface. The area of the curve where $cf_{(Ddd)}$ >0.25 defines the fully-coupled portion. The inset shows the function rotated to a *dip direction-slab pole* coordinate system (x'-y'). Refer to section B.4.2. for theoretical foundations behind the determination of interseismic coupling using this technique.

S.5. Coseismic CSI on Pichilemu normal fault

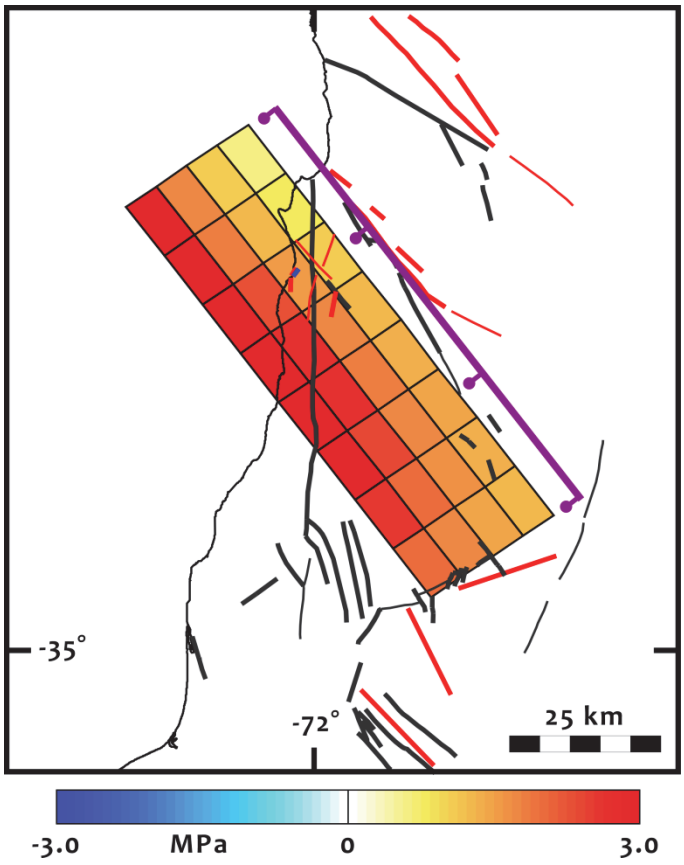

Figure 6.13: Coseismic CSI resolved on the Pichilemu normal fault resultant from the fault slip model by *Delouis et al*. (2010). Refer to Figure 3.8 in main manuscript for a complete caption.

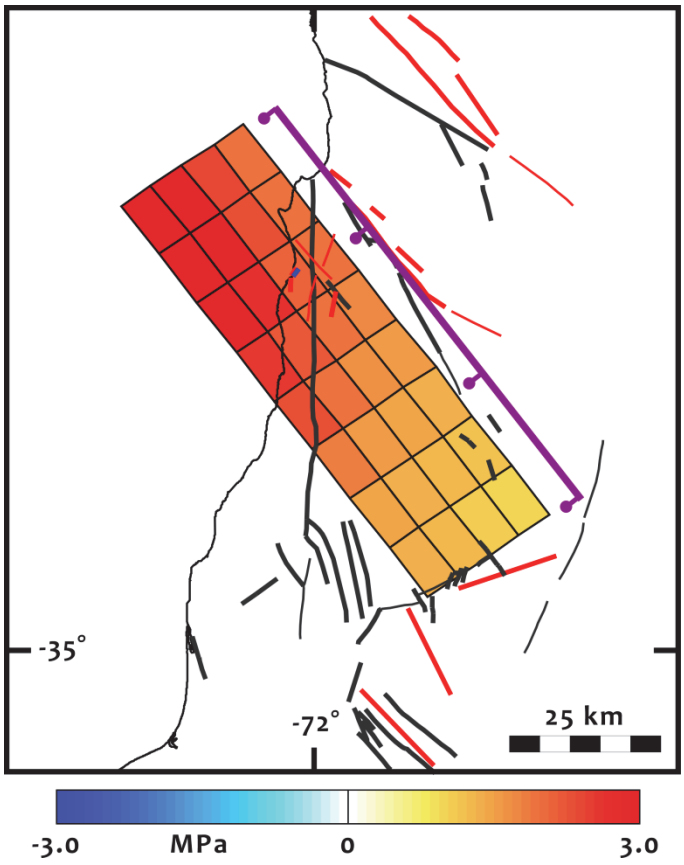

Figure 6.14: Coseismic CSI resolved on the Pichilemu normal fault resultant from the fault slip model by G. Hayes (unpublished data, 2010). Refer to Figure 3.8 in main manuscript for a complete caption.

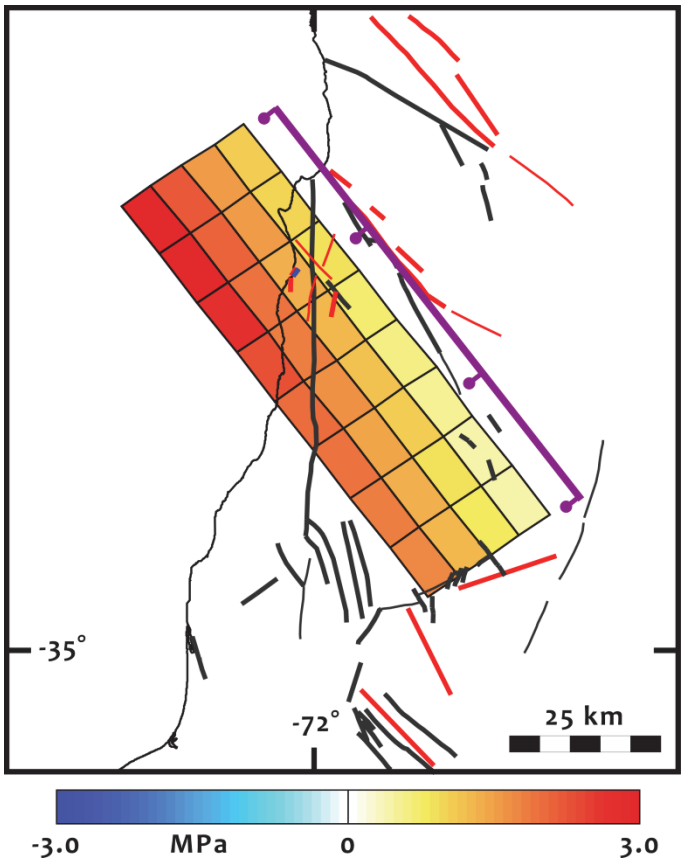

Figure 6.15: Coseismic CSI resolved on the Pichilemu normal fault resultant from the fault slip model by G. Shao et al. (unpublished data, 2010). Refer to Figure 3.8 in main manuscript for a complete caption.

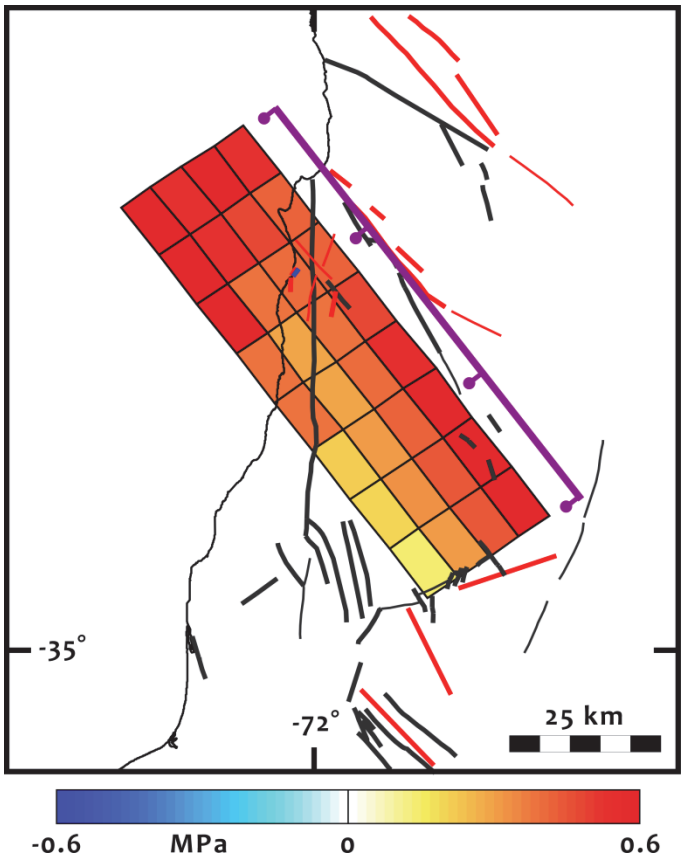

Figure 6.16: Coseismic CSI resolved on the Pichilemu normal fault resultant from the fault slip model by A. Sladen (unpublished data, 2010). Refer to Figure 3.8 in main manuscript for a complete caption.

B.6. Regional coseismic CSI over the Maule rupture area

B.6.1. Maps

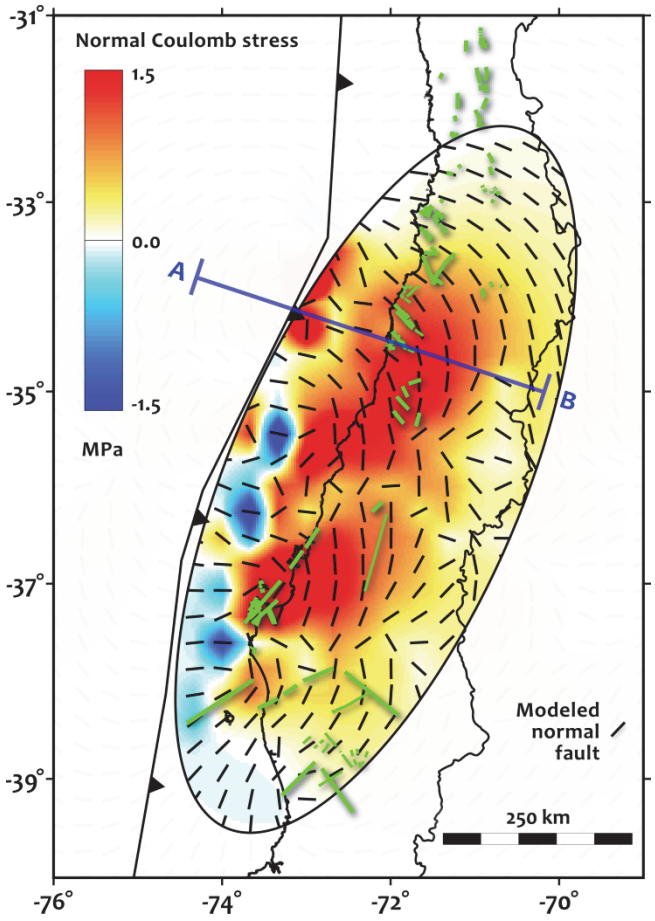

Figure 6.17: Coseismic regional CSI over the continent resolved on "optimally-oriented" modeled normal faults (rake -90°), calculated at 10 km depth, above the Maule subduction segment. Fault slip model by *Delouis et al*. (2010). Refer to Figure 3.9a (main manuscript) for a complete caption.

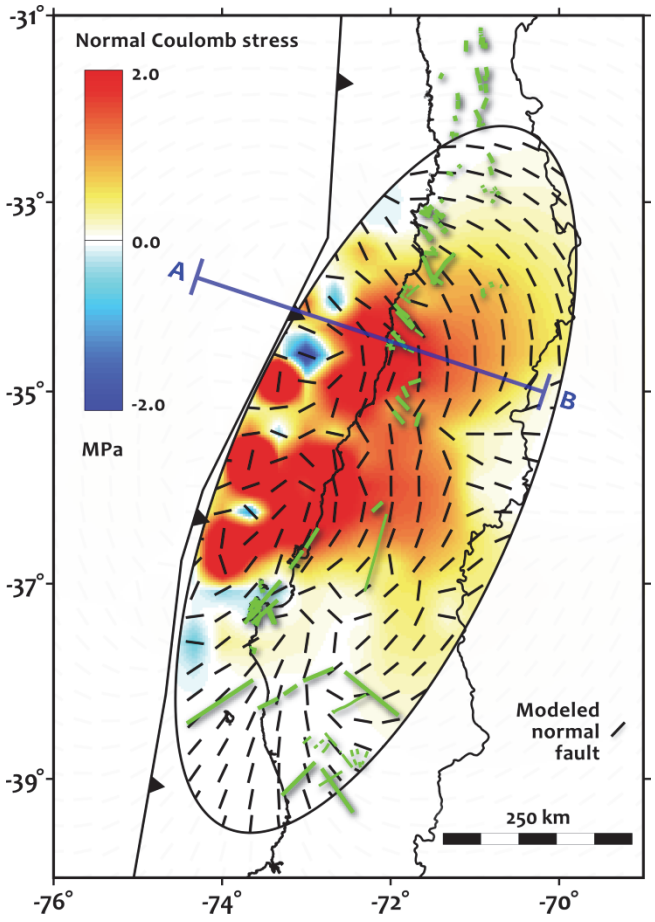

Figure 6.18: Coseismic regional CSI over the continent resolved on "optimally-oriented" modeled normal faults (rake -90°), calculated at 10 km depth, above the Maule subduction segment. Fault slip model by G. Hayes (unpublished data, 2010). Refer to Figure 3.9a (main manuscript) for a complete caption.

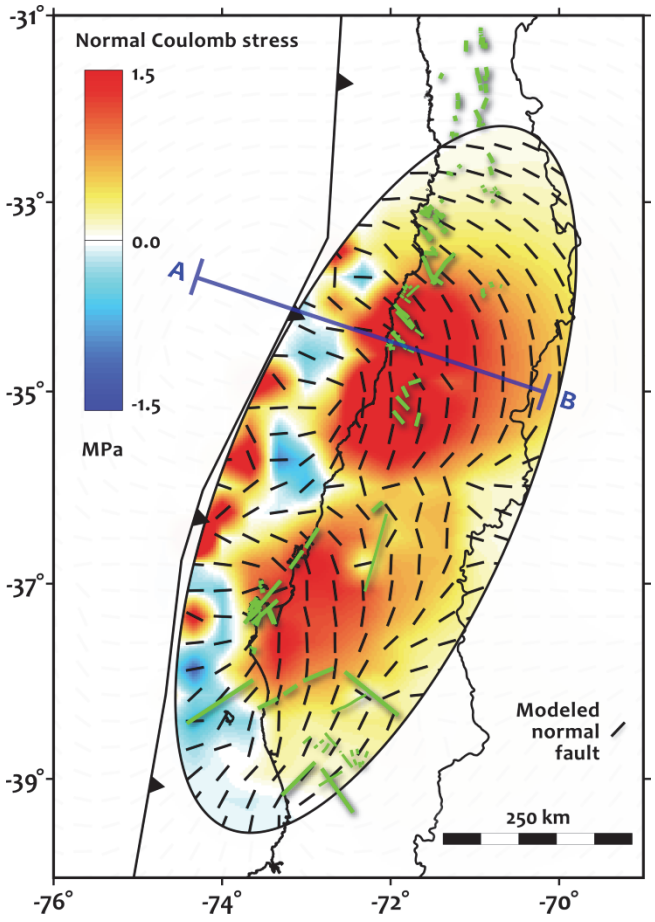

Figure 6.19: Coseismic regional CSI over the continent resolved on "optimally-oriented" modeled normal faults (rake -90°), calculated at 10 km depth, above the Maule subduction segment. Fault slip model by *Lorito et al*. (2011). Refer to Figure 3.9a (main manuscript) for a complete caption.

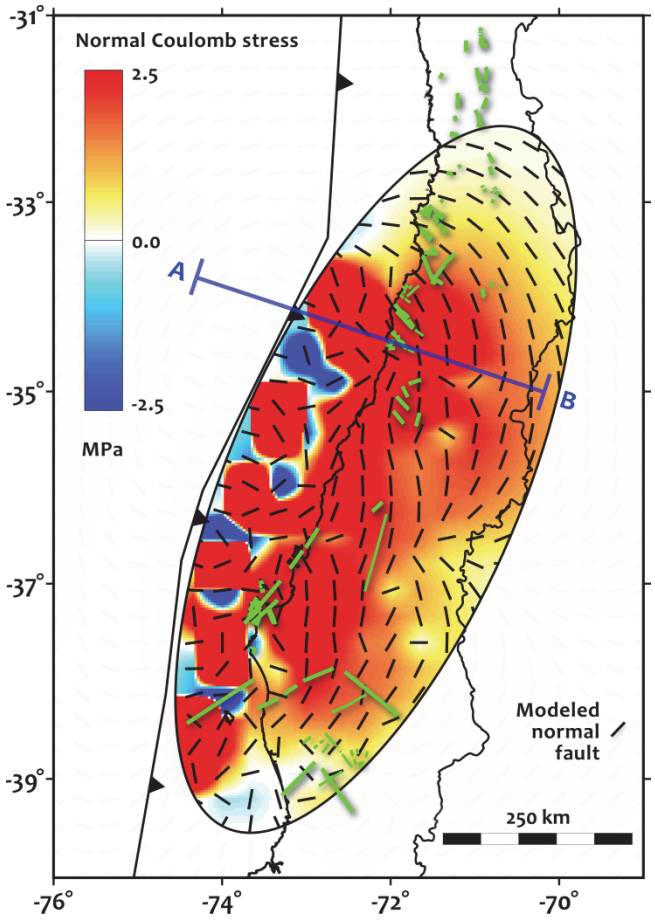

Figure 6.20: Coseismic regional CSI over the continent resolved on "optimally-oriented" modeled normal faults (rake -90°), calculated at 10 km depth, above the Maule subduction segment. Fault slip model by *Moreno et al*. (2012). Refer to Figure 3.9a (main manuscript) for a complete caption.

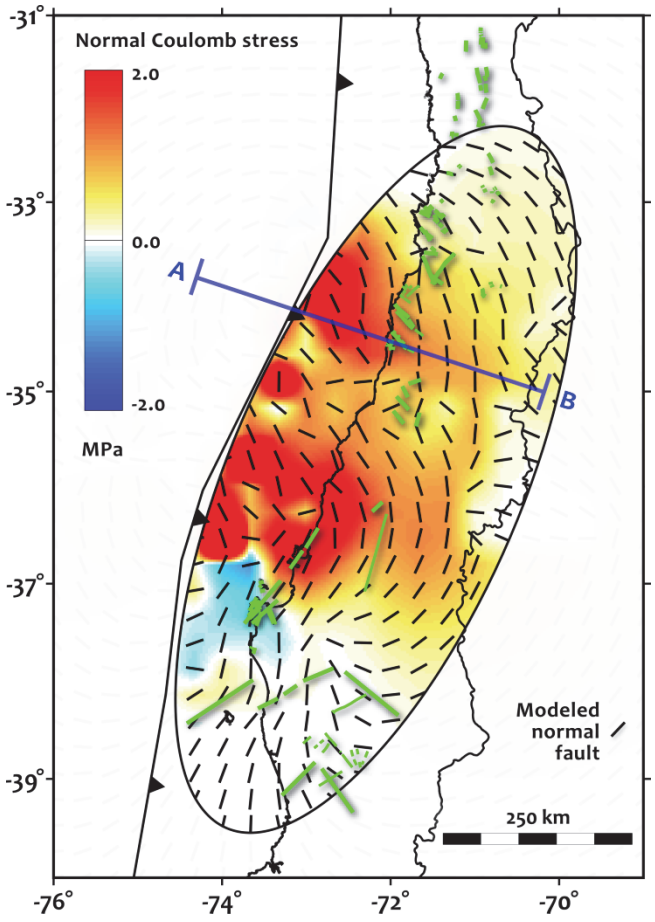

Figure 6.21: Coseismic regional CSI over the continent resolved on "optimally-oriented" modeled normal faults (rake -90°), calculated at 10 km depth, above the Maule subduction segment. Fault slip model by G. Shao et al. (unpublished data, 2010). Refer to Figure 3.9a (main manuscript) for a complete caption.

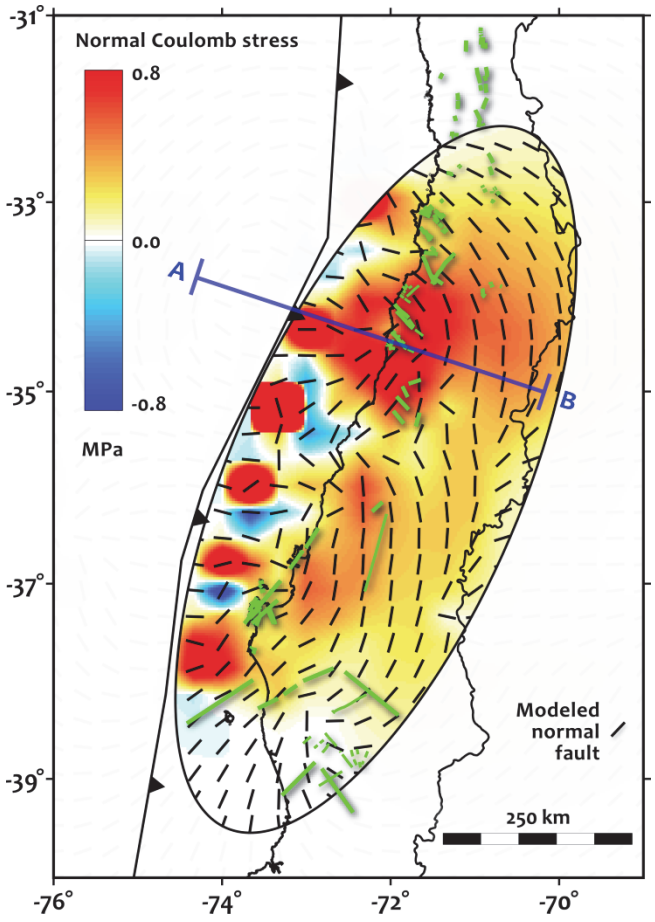

Figure 6.22: Coseismic regional CSI over the continent resolved on "optimally-oriented" modeled normal faults (rake -90°), calculated at 10 km depth, above the Maule subduction segment. Fault slip model by A. Sladen (unpublished data, 2010). Refer to Figure 3.9a (main manuscript) for a complete caption.

B.6.2. Cross sections

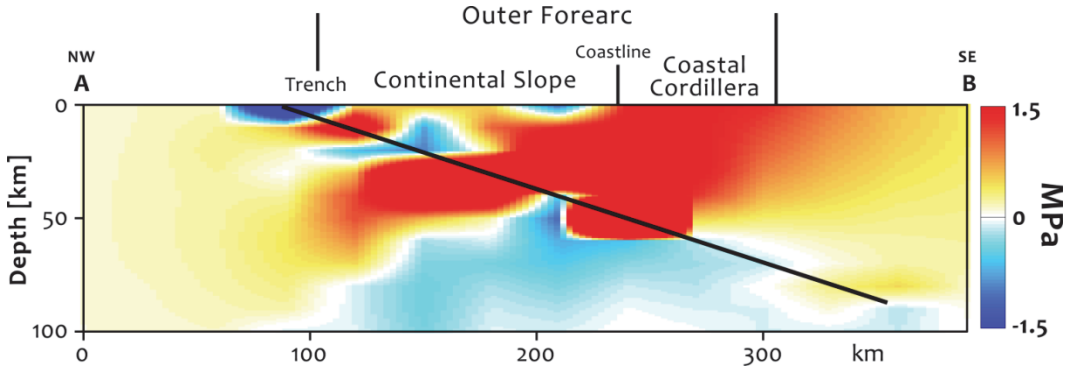

Figure 6.23: Cross-section of CSI magnitude resolved on optimally-oriented normal faults across the forearc at the Pichilemu region, perpendicular to the plate boundary. Fault slip model by *Delouis et al*. (2010). Refer to Figure 3.10 (main manuscript) for a complete caption.

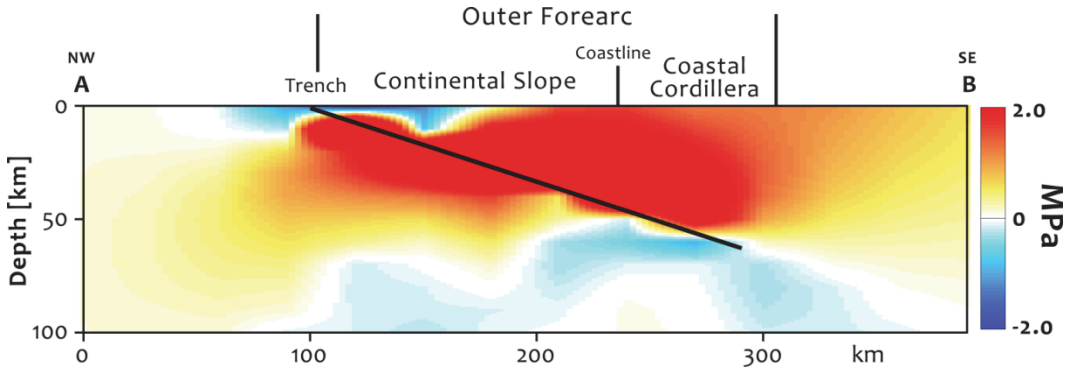

Figure 6.24: Cross-section of CSI magnitude resolved on optimally-oriented normal faults across the forearc at the Pichilemu region, perpendicular to the plate boundary. Fault slip model by G. Hayes (unpublished data, 2010). Refer to Figure 3.10 (main manuscript) for a complete caption.

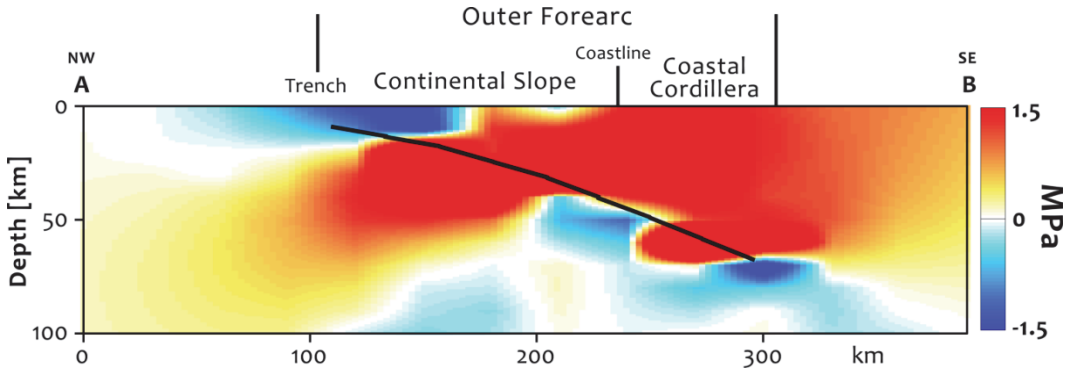

Figure 6.25: Cross-section of CSI magnitude resolved on optimally-oriented normal faults across the forearc at the Pichilemu region, perpendicular to the plate boundary. Fault slip model by *Lorito et al*. (2011). Refer to Figure 3.10 (main manuscript) for a complete caption.

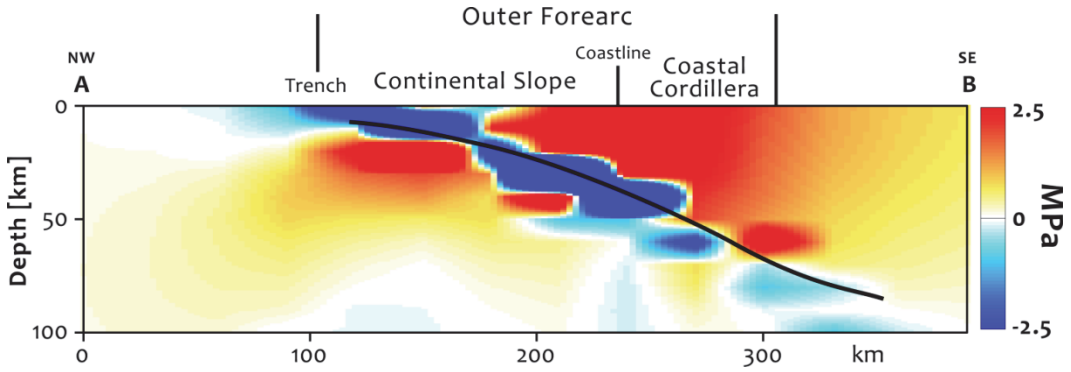

Figure 6.26: Cross-section of CSI magnitude resolved on optimally-oriented normal faults across the forearc at the Pichilemu region, perpendicular to the plate boundary. Fault slip model by *Moreno et al*. (2012). Refer to Figure 3.10 (main manuscript) for a complete caption.

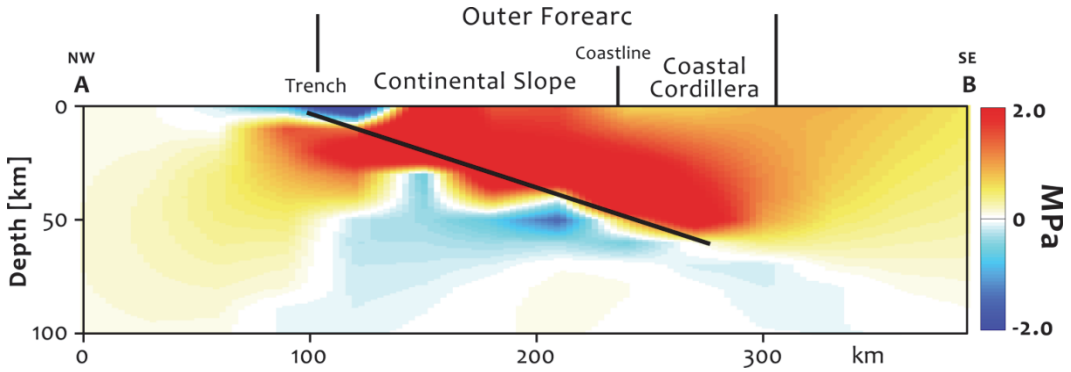

Figure 6.27: Cross-section of CSI magnitude resolved on optimally-oriented normal faults across the forearc at the Pichilemu region, perpendicular to the plate boundary. Fault slip model by G. Shao et al. (unpublished data, 2010). Refer to Figure 3.10 (main manuscript) for a complete caption.

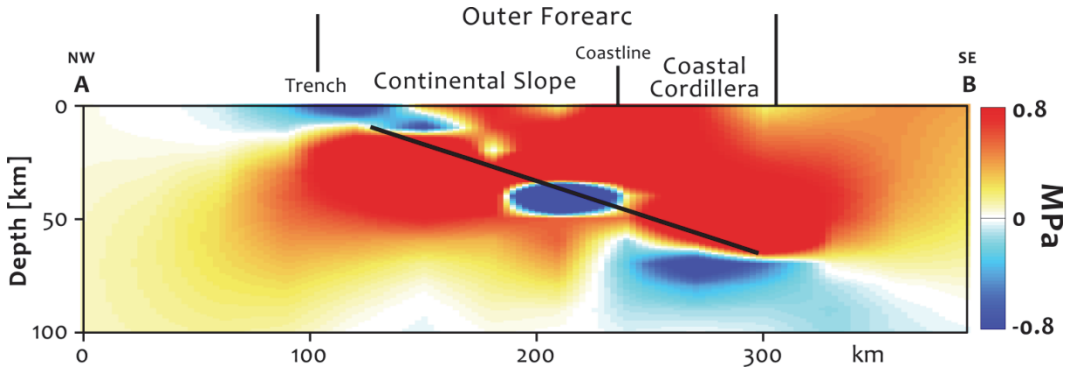

Figure 6.28: Cross-section of CSI magnitude resolved on optimally-oriented normal faults across the forearc at the Pichilemu region, perpendicular to the plate boundary. Fault slip model by A. Sladen (unpublished data, 2010). Refer to Figure 3.10 (main manuscript) for a complete caption.

B.7. Angular misfit analysis

B.7.1. Long-term structural grain

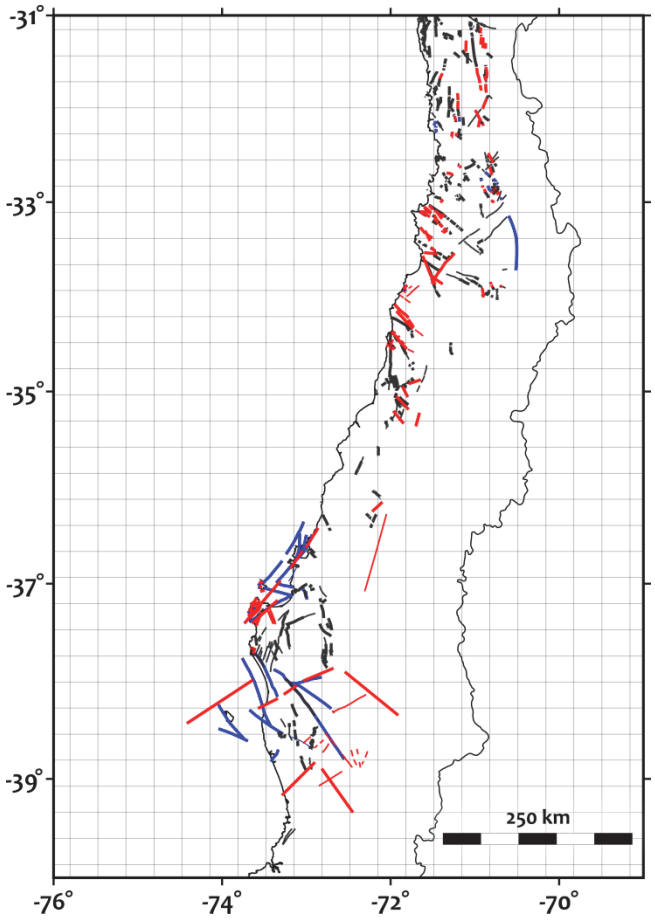

Figure 6.29: Mapped crustal faults of the Coastal Cordillera along the Maule segment (*Katz*, 1971; *Gana et al.*, 1996; *Wall et al.*, 1996; *SERNAGEOMIN*, 2003; *Melnick et al.*, 2006, 2009; *Geersen et al.*, 2011; based on the works by *Aron et al.*, 2012). Red, blue and gray are normal, reverse and undetermined faults. The weight of the lines distinguishes between certain and inferred structures.

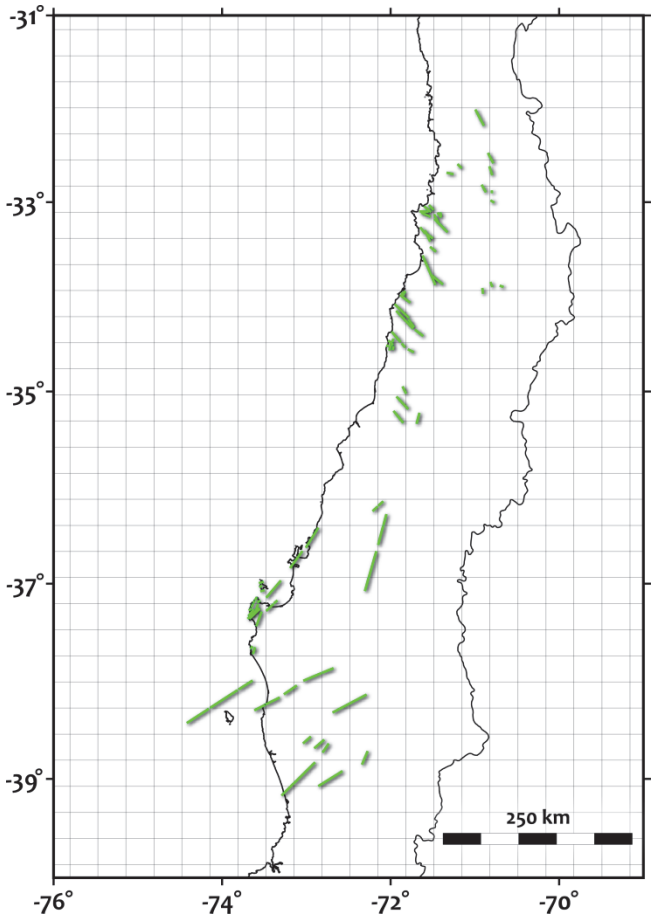

Figure 6.30: Subset of mapped normal faults from Figure B.29 with strikes that delineate a semi-elliptical pattern enclosing the Maule segment. We have eliminated from this figure NW-striking faults at the south end of the Maule segment and NE-striking faults at the north end under the assumption that those faults correspond to repeated ruptures on the Valdivia and Valparaiso segments, respectively (further discussion in section 3.7.4 main manuscript).

B.7.2. Misfit maps

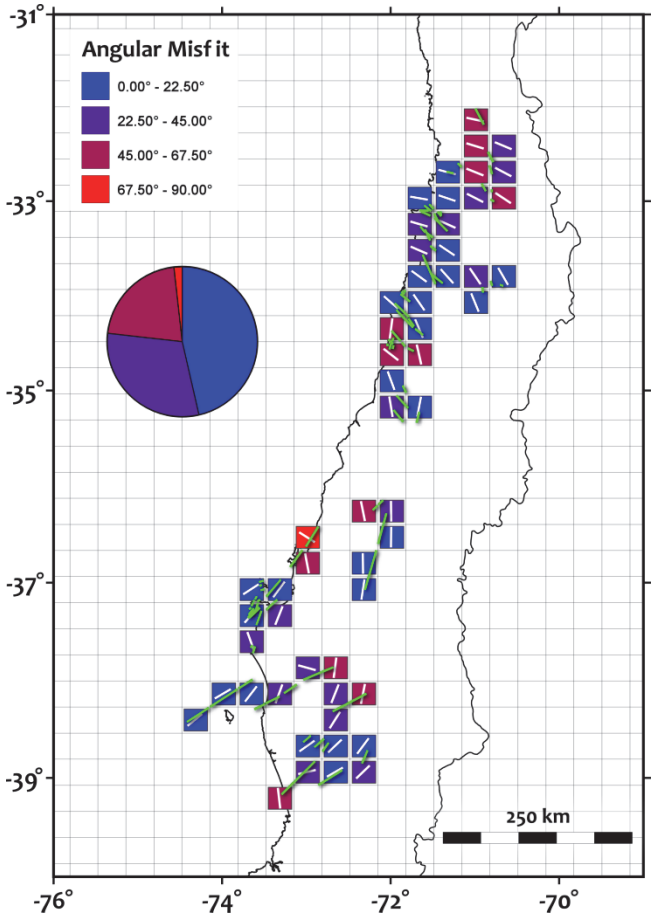

Figure 6.31: Angular misfit between the strikes of known normal faults along the Coastal Cordillera of the Maule segment (green lines from Figure B.30) and the optimally oriented normal faults resulted from the fault slip model by *Delouis et al*. (2010) (white lines). Refer to Figure 3.11 in main manuscript for the complete caption.

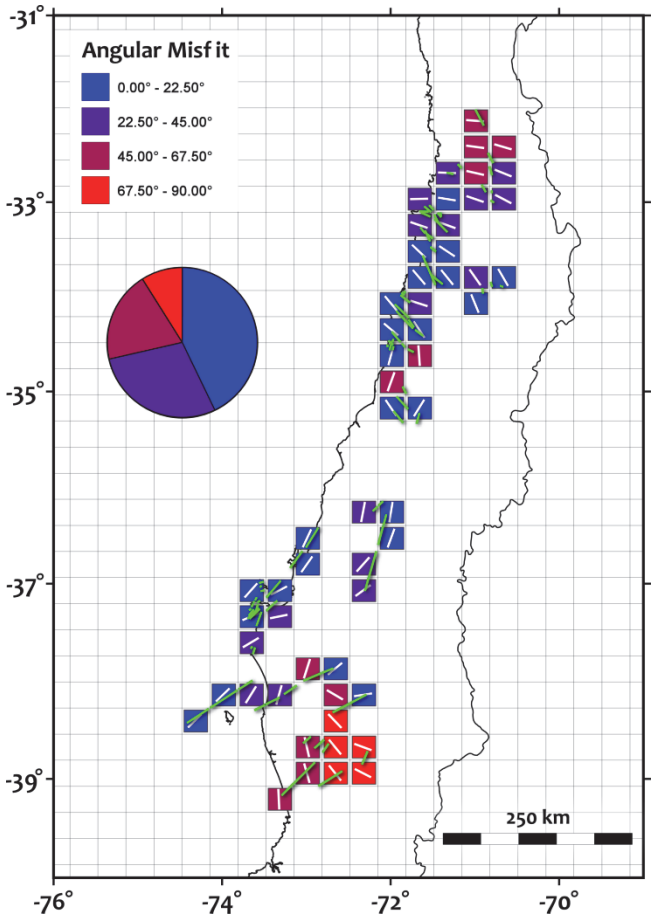

Figure 6.32: Angular misfit between the strikes of known normal faults along the Coastal Cordillera of the Maule segment (green lines from Figure B.30) and the optimally oriented normal faults resulted from the fault slip model by G. Hayes (unpublished data, 2010) (white lines). Refer to Figure 3.11 in main manuscript for the complete caption.

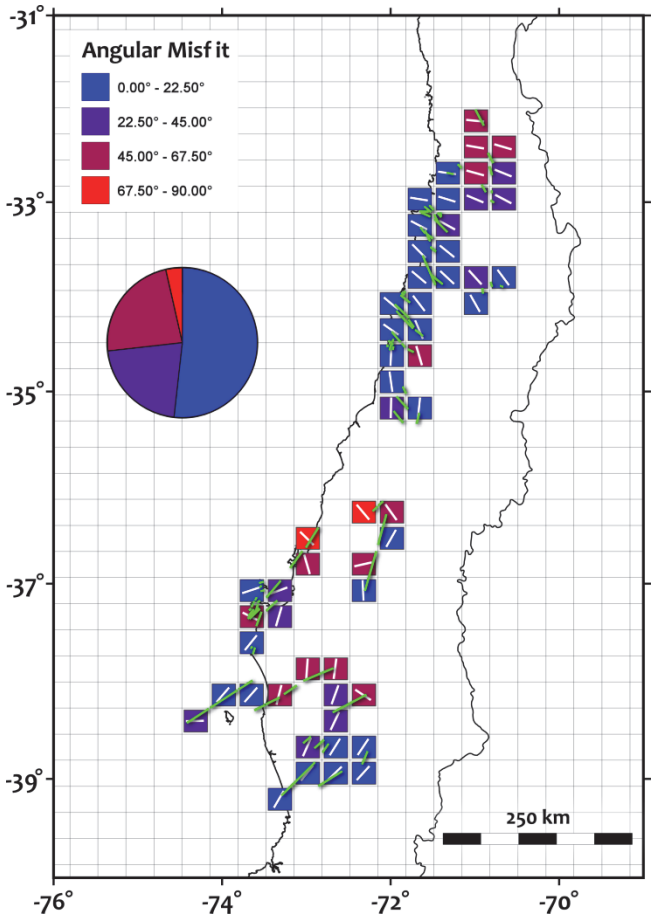

Figure 6.33: Angular misfit between the strikes of known normal faults along the Coastal Cordillera of the Maule segment (green lines from Figure B.30) and the optimally oriented normal faults resulted from the fault slip model by *Lorito et al*. (2011) (white lines). Refer to Figure 3.11 in main manuscript for the complete caption.

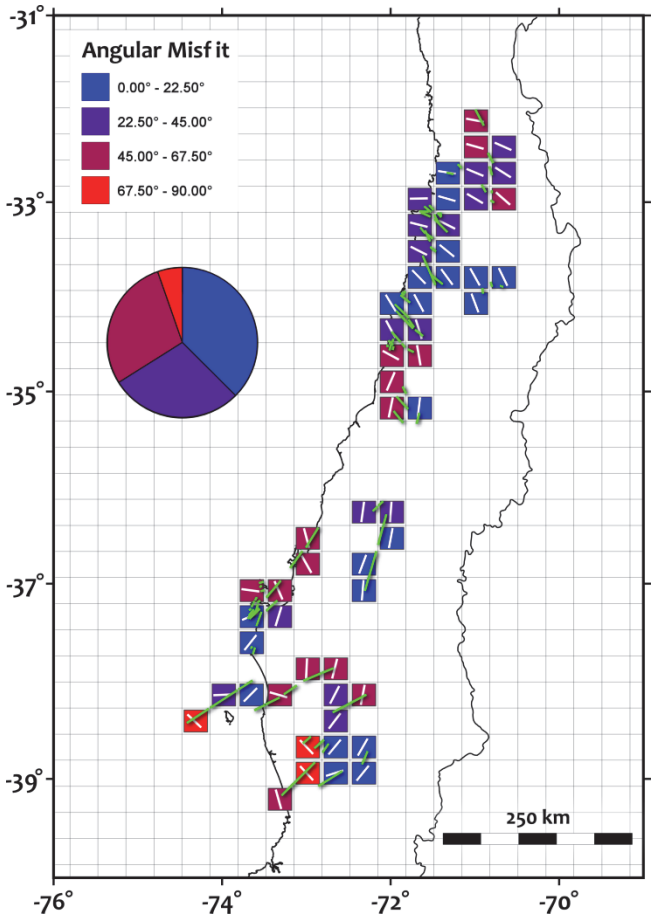

Figure 6.34: Angular misfit between the strikes of known normal faults along the Coastal Cordillera of the Maule segment (green lines from Figure B.30) and the optimally oriented normal faults resulted from the fault slip model by *Moreno et al*. (2012) (white lines). Refer to Figure 3.11 in main manuscript for the complete caption.

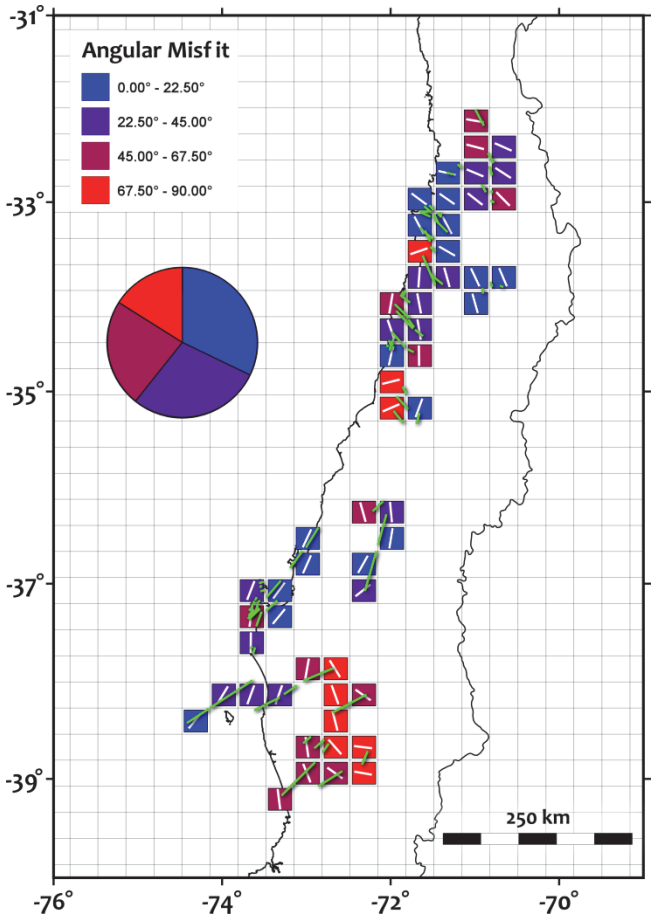

Figure 6.35: Angular misfit between the strikes of known normal faults along the Coastal Cordillera of the Maule segment (green lines from Figure B.30) and the optimally oriented normal faults resulted from the fault slip model by G. Shao et al. (unpublished data, 2010) (white lines). Refer to Figure 3.11 in main manuscript for the complete caption.

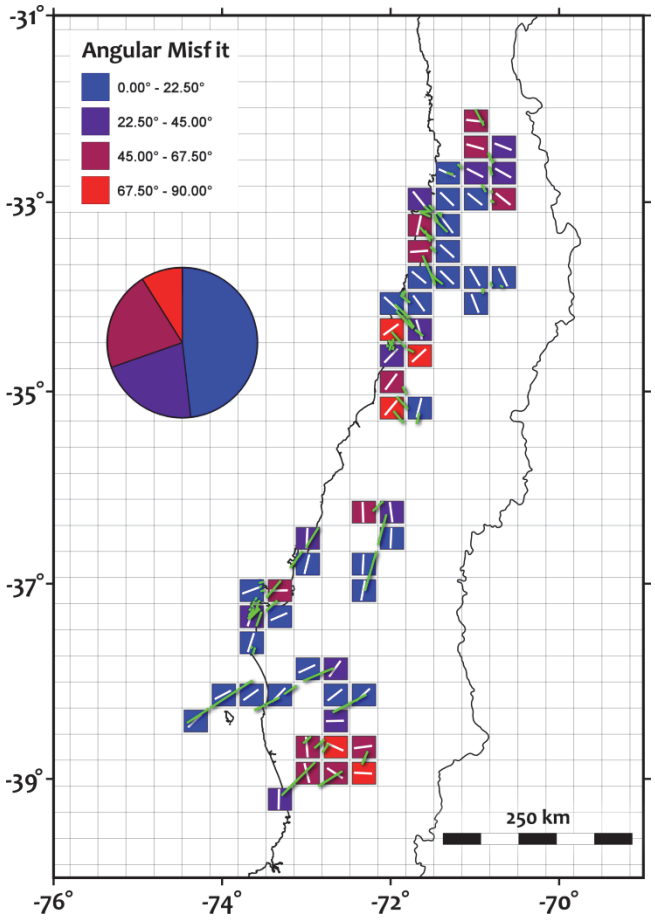

Figure 6.36: Angular misfit between the strikes of known normal faults along the Coastal Cordillera of the Maule segment (green lines from Figure B.30) and the optimally oriented normal faults resulted from the fault slip model by A. Sladen (unpublished data, 2010) (white lines). Refer to Figure 3.11 in main manuscript for the complete caption.

REFERENCES

Aron, F., J. Cembrano, R. W. Allmendinger, F. Astudillo, and G. Arancibia (2012), Structural Geology of the Active Forearc above the Maule Megathrust: Traces of a Long-lived Subduction Segment, in *paper presented at 2012 XIII Chilean Geological Congress, Antofagasta, Chile, 5-9 Aug.*

Bevis, M., E. Kendrick, R. Smalley Jr., B. Brooks, R. Allmendinger, and B. Isacks (2001), On the strength of interplate coupling and the rate of back arc convergence in the central Andes: An analysis of the interseismic velocity field, *Geochem. Geophys. Geosyst.*, *2*(11), 1067–, doi:10.1029/2001GC000198.

Bürgmann, R., M. G. Kogan, G. M. Steblov, G. Hilley, V. E. Levin, and E. Apel (2005), Interseismic coupling and asperity distribution along the Kamchatka subduction zone, *J. Geophys. Res.*, *110*(B7), B07405–, doi:10.1029/2005JB003648.

Delouis, B., J.-M. Nocquet, and M. Vallée (2010), Slip distribution of the February 27, 2010 Mw = 8.8 Maule Earthquake, central Chile, from static and high-rate GPS, InSAR, and broadband teleseismic data, *Geophys. Res. Lett.*, *37*(17), L17305–, doi:10.1029/2010GL043899.

Flück, P., R. D. Hyndman, and K. Wang (1997), Three-dimensional dislocation model for great earthquakes of the Cascadia subduction zone, *J. Geophys. Res.*, *102*(B9), 20539–20550, doi:10.1029/97JB01642.

Gagnon, K., C. D. Chadwell, and E. Norabuena (2005), Measuring the onset of locking in the Peru-Chile trench with GPS and acoustic measurements, *Nature*, *434*(7030), 205–208, doi:10.1038/nature03412.

Gana, P., R. Wall, and A. Gutiérrez (1996), *Mapa geológico del área Valparaíso-Curacaví, Regiones de Valparaíso y Metropolitana.*, Geological map Scale 1:100,000, Servicio Nacional de Geología y Minería, Santiago, Chile.

Geersen, J., J. H. Behrmann, D. Völker, S. Krastel, C. R. Ranero, J. Diaz-Naveas, and W. Weinrebe (2011), Active tectonics of the South Chilean marine fore arc (35°S–40°S), *Tectonics*, *30*(3), TC3006, doi:10.1029/2010TC002777.

Hashimoto, C., A. Noda, T. Sagiya, and M. Matsu'ura (2009), Interplate seismogenic zones along the Kuril-Japan trench inferred from GPS data inversion, *Nat. Geosci.*, *2*(2), 141–144, doi:10.1038/ngeo421.

Hyndman, R. D., and K. Wang (1993), Thermal Constraints on the Zone of Major Thrust Earthquake Failure: The Cascadia Subduction Zone, *J. Geophys. Res.*, *98*(B2), 2039–2060, doi:10.1029/92JB02279.

Katz, H. R. (1971), Continental Margin in Chile-Is Tectonic Style Compressional or Extensional?, *AAPG Bulletin*, *55*(10), 1753–1758, doi:10.1306/819A3DA2-16C5-11D7-8645000102C1865D.

Khazaradze, G., and J. Klotz (2003), Short- and long-term effects of GPS measured crustal deformation rates along the south central Andes, *J. Geophys. Res.*, *108*(B6), 2289–, doi:10.1029/2002JB001879.

King, G. C. P., R. S. Stein, and J. Lin (1994), Static stress changes and the triggering of earthquakes, *Bull. Seismol. Soc. Am.*, *84*(3), 935–953.

Lin, J., and R. S. Stein (2004), Stress triggering in thrust and subduction earthquakes and stress interaction between the southern San Andreas and nearby thrust and strike-slip faults, *J. Geophys. Res.*, *109*, B02303–, doi:200410.1029/2003JB002607.

Lorito, S., F. Romano, S. Atzori, X. Tong, A. Avallone, J. McCloskey, M. Cocco, E. Boschi, and A. Piatanesi (2011), Limited overlap between the seismic gap and coseismic slip of the great 2010 Chile earthquake, *Nat. Geosci.*, *4*(3), 173–177, doi:10.1038/ngeo1073.

Loveless, J. P., and B. J. Meade (2010), Geodetic imaging of plate motions, slip rates, and partitioning of deformation in Japan, *J. Geophys. Res.*, *115*(B2), B02410–, doi:10.1029/2008JB006248.

Loveless, J. P., and B. J. Meade (2011), Spatial correlation of interseismic coupling and coseismic rupture extent of the 2011 MW = 9.0 Tohoku-oki earthquake, *Geophys. Res. Lett.*, *38*(17), L17306–, doi:10.1029/2011GL048561.

Loveless, J. P., R. W. Allmendinger, M. E. Pritchard, and G. González (2010), Normal and reverse faulting driven by the subduction zone earthquake cycle in the northern Chilean fore arc, *Tectonics*, *29*(2), TC2001–, doi:10.1029/2009TC002465.

Melnick, D., B. Bookhagen, H. P. Echtler, and M. R. Strecker (2006), Coastal deformation and great subduction earthquakes, Isla Santa María, Chile (37°S), *Geological Society of America Bulletin*, *118*(11-12), 1463–1480, doi:10.1130/B25865.1.

Melnick, D., B. Bookhagen, M. R. Strecker, and H. P. Echtler (2009), Segmentation of megathrust rupture zones from fore-arc deformation patterns over hundreds to millions of years, Arauco peninsula, Chile, *J. Geophys. Res.*, *114*, 23 PP., doi:200910.1029/2008JB005788.

Moreno, M., M. Rosenau, and O. Oncken (2010), 2010 Maule earthquake slip correlates with pre-seismic locking of Andean subduction zone, *Nature*, *467*(7312), 198–202, doi:10.1038/nature09349.

Moreno, M. et al. (2011), Heterogeneous plate locking in the South–Central Chile subduction zone: Building up the next great earthquake, *Earth Planet. Sci. Lett.*, *305*(3–4), 413–424, doi:10.1016/j.epsl.2011.03.025.

Moreno, M. et al. (2012), Toward understanding tectonic control on the Mw 8.8 2010 Maule Chile earthquake, *Earth Planet. Sci. Lett.*, *321–322*(0), 152–165, doi:10.1016/j.epsl.2012.01.006.

Okada, Y. (1992), Internal deformation due to shear and tensile faults in a half-space, *Bull. Seismol. Soc. Am.*, *82*(2), 1018–1040.

Oleskevich, D. A., R. D. Hyndman, and K. Wang (1999), The updip and downdip limits to great subduction earthquakes: Thermal and structural models of Cascadia, south Alaska, SW Japan, and Chile, *J. Geophys. Res.*, *104*(B7), 14965–14991, doi:10.1029/1999JB900060.

Parsons, T. (2006), Tectonic stressing in California modeled from GPS observations, *J. Geophys. Res.*, *111*, 16 PP., doi:200610.1029/2005JB003946.

Perfettini, H. et al. (2010), Seismic and aseismic slip on the Central Peru megathrust, *Nature*, *465*(7294), 78–81, doi:10.1038/nature09062.

Ruegg, J. C., A. Rudloff, C. Vigny, R. Madariaga, J. B. de Chabalier, J. Campos, E. Kausel, S. Barrientos, and D. Dimitrov (2009), Interseismic strain accumulation measured by GPS in the seismic gap between Constitución and Concepción in Chile, *Phys. Earth Planet. Inter.*, *175*(1-2), 78–85, doi:10.1016/j.pepi.2008.02.015.

Ruff, L., and H. Kanamori (1983), Seismic coupling and uncoupling at subduction zones, *Tectonophysics*, *99*(2-4), 99–117, doi:10.1016/0040-1951(83)90097-5.

Savage, J. C. (1983), A Dislocation Model of Strain Accumulation and Release at a Subduction Zone, *J. Geophys. Res.*, *88*(B6), 4984–4996, doi:10.1029/JB088iB06p04984.

Scholz, C. H. (2002), *The mechanics of earthquakes and faulting*, Cambridge University Press.

SERNAGEOMIN (2003), *Mapa Geológico de Chile: versión digital*, Geological map Scale 1:1,000,000, Servicio Nacional de Geología y Minería, Santiago, Chile.

Song, T.-R. A., and M. Simons (2003), Large Trench-Parallel Gravity Variations Predict Seismogenic Behavior in Subduction Zones, *Science*, *301*(5633), 630–633, doi:10.1126/science.1085557.

Steketee, J. A. (1958), On Volterra's dislocations in a semi-infinite elastic medium, *Can. J. Phys.*, *36*(2), 192–205, doi:10.1139/p58-024.

Suarez, G., and D. Comte (1993), Comment on: Seismic Coupling Along the Chilean Subduction Zone; by B. W. Tichelaar and L. R. Ruff, *J. Geophys. Res.*, *98*(B9), 15825–15828, doi:10.1029/93JB00234.

Tichelaar, B. W., and L. J. Ruff (1991), Seismic Coupling Along the Chilean Subduction Zone, *J. Geophys. Res.*, *96*(B7), 11997–12022, doi:10.1029/91JB00200.

Tichelaar, B. W., and L. J. Ruff (1993), Depth of Seismic Coupling Along Subduction Zones, *J. Geophys. Res.*, *98*(B2), 2017–2037, doi:10.1029/92JB02045.

Vigny, C. et al. (2011), The 2010 Mw 8.8 Maule Megathrust Earthquake of Central Chile, Monitored by GPS, *Science*, *332*(6036), 1417–1421, doi:10.1126/science.1204132.

Volterra, V. (1907), Sur l'equilibre des corps multiplement connexes, *Ann. sci. école norm. supérieure, III. Ser*, *24*, 401–517.

Wall, R., P. Gana, and A. Gutiérrez (1996), *Mapa geológico del área de San Antonio-Melipilla, Regiones de Valparaiso, Metropolitana y del Libertador Bernardo O'Higgins.*, Geological map Scale 1:100,000, Servicio Nacional de Geología y Minería, Santiago, Chile.

Wang, K., and T. Dixon (2004), “Coupling” Semantics and science in earthquake research, *Eos Trans. AGU*, *85*(18), 180, doi:10.1029/2004EO180005.

Wang, K., R. Wells, S. Mazzotti, R. D. Hyndman, and T. Sagiya (2003), A revised dislocation model of interseismic deformation of the Cascadia subduction zone, *J. Geophys. Res.*, *108*(B1), 2026–, doi:10.1029/2001JB001227.

Yáñez, G., and J. Cembrano (2004), Role of viscous plate coupling in the late Tertiary Andean tectonics, *J. Geophys. Res.*, *109*, 21 PP., doi:10.1029/2003JB002494.

Yoshioka, S., T. Yabuki, T. Sagiya, T. Tada, and M. Matsu’ura (1993), Interplate coupling and relative plate motion in the Tokai district, central Japan, deduced from geodetic data inversion using ABIC, *Geophys. J. Int.*, *113*(3), 607–621, doi:10.1111/j.1365-246X.1993.tb04655.x.

APPENDIX C

SUPPLEMENTARY INFORMATION TO CHAPTER 4

C.1. Supplementary tables

Table 7.1: Threshold of background Mw of upper plate events per segment and kinematic type for each value of BW

zone-seg	fix	type	100	200	300	400	500	600	700	800	900	1000	min	max
ALU seg1	no	All	5.83	5.93	6.08	6.10	6.19	6.21	6.32	6.32	6.37	6.42	5.83	6.42
ALU seg1	no	Normal	5.96	5.92	6.00	6.01	6.05	6.04	6.09	6.20	6.19	6.16	5.92	6.20
ALU seg1	no	Reverse	5.86	5.98	6.07	6.13	6.19	6.13	6.29	6.25	6.30	6.34	5.86	6.34
ALU seg1	no	Strslip	5.48	5.46	5.51	5.53	5.53	5.55	5.55	5.55	5.53	5.55	5.46	5.55
ALU seg1	yes	All	5.87	6.00	6.13	6.21	6.32	6.30	6.47	6.49	6.40	6.58	5.87	6.58
ALU seg1	yes	Normal	5.92	5.95	5.96	6.09	6.05	6.16	6.03	6.13	6.15	6.27	5.92	6.27
ALU seg1	yes	Reverse	5.84	5.96	6.04	6.14	6.17	6.13	6.34	6.31	6.36	6.46	5.84	6.46
ALU seg1	yes	Strslip	6.08	6.15	6.12	6.26	6.13	6.31	6.33	6.25	6.42	6.27	6.08	6.42
ALU seg2	no	All	5.94	5.95	6.08	6.13	6.20	6.31	6.33	6.38	6.43	6.53	5.94	6.53
ALU seg2	no	Normal	5.56	5.56	5.56	5.56	5.56	5.56	5.56	5.56	5.56	5.56	5.56	5.56
ALU seg2	no	Reverse	6.00	6.03	6.13	6.14	6.20	6.33	6.38	6.38	6.50	6.54	6.00	6.54
ALU seg2	no	Strslip	6.19	6.01	6.16	6.34	6.13	6.33	6.34	6.35	6.34	6.16	6.01	6.35
ALU seg2	yes	All	5.90	6.02	6.14	6.27	6.34	6.43	6.46	6.45	6.52	6.58	5.90	6.58
ALU seg2	yes	Normal	5.54	5.54	5.52	5.66	5.69	5.54	5.66	5.66	5.66	5.72	5.52	5.72
ALU seg2	yes	Reverse	5.92	6.08	6.12	6.25	6.29	6.39	6.47	6.49	6.56	6.57	5.92	6.57
ALU seg2	yes	Strslip	6.13	6.17	6.01	6.32	6.09	6.33	6.34	6.13	6.34	6.35	6.01	6.35
KER seg1	no	All	5.74	5.77	5.83	5.83	5.83	5.90	5.88	5.96	5.85	5.96	5.74	5.96
KER seg1	no	Normal	6.25	6.25	6.25	6.25	6.25	6.25	6.25	6.25	6.25	6.25	6.25	6.25
KER seg1	no	Reverse	5.60	5.66	5.64	5.69	5.70	5.69	5.69	5.74	5.65	5.69	5.60	5.74
KER seg1	no	Strslip	5.96	5.96	5.96	5.96	5.96	5.96	5.97	5.97	5.96	5.97	5.96	5.97
KER seg1	yes	All	5.64	5.73	5.76	5.83	5.83	5.94	6.00	5.93	5.97	6.06	5.64	6.06
KER seg1	yes	Normal	5.82	5.80	5.78	5.80	5.87	5.87	5.85	5.91	5.82	5.94	5.78	5.94
KER seg1	yes	Reverse	5.60	5.60	5.70	5.69	5.72	5.83	5.82	5.77	5.83	5.87	5.60	5.87
KER seg1	yes	Strslip	5.94	5.90	5.90	5.94	6.00	6.00	5.96	5.97	6.00	6.14	5.90	6.14
KER seg2	no	All	5.93	6.04	6.18	6.23	6.36	6.38	6.42	6.49	6.50	6.59	5.93	6.59

KER seg2	**no**	**Normal**	5.77	5.77	5.76	5.76	5.77	5.75	5.82	5.93	5.82	5.74	5.74	5.93
KER seg2	**no**	**Reverse**	5.97	6.08	6.22	6.21	6.31	6.40	6.45	6.45	6.56	6.57	5.97	6.57
KER seg2	**no**	**Strslip**	6.34	6.34	6.41	6.40	6.44	6.40	6.43	6.43	6.40	6.40	6.34	6.44
KER seg2	**yes**	**All**	5.92	6.02	6.16	6.23	6.29	6.39	6.51	6.50	6.55	6.63	5.92	6.63
KER seg2	**yes**	**Normal**	5.91	6.00	5.94	6.00	6.01	6.01	6.01	6.08	6.11	6.13	5.91	6.13
KER seg2	**yes**	**Reverse**	5.90	6.06	6.12	6.18	6.25	6.35	6.46	6.42	6.57	6.57	5.90	6.57
KER seg2	**yes**	**Strslip**	6.31	6.31	6.43	6.45	6.41	6.39	6.40	6.40	6.52	6.43	6.31	6.52
KUR seg1	**no**	**All**	5.29	5.29	5.29	5.29	5.29	5.29	5.29	5.29	5.29	5.29	5.29	5.29
KUR seg1	**no**	**Normal**	5.08	5.08	5.08	5.08	5.08	5.08	5.08	5.08	5.08	5.08	5.08	5.08
KUR seg1	**no**	**Reverse**	.	.	.	.	.	.	.	.	.	.	0.00	0.00
KUR seg1	**no**	**Strslip**	5.29	5.29	5.29	5.29	5.29	5.29	5.29	5.29	5.29	5.29	5.29	5.29
KUR seg1	**yes**	**All**	5.29	5.25	5.25	5.29	5.25	5.25	5.25	5.27	5.29	5.25	5.25	5.29
KUR seg1	**yes**	**Normal**	5.16	5.16	5.16	5.16	5.16	5.16	5.16	5.16	5.16	5.16	5.16	5.16
KUR seg1	**yes**	**Reverse**	4.95	4.95	4.95	4.95	4.95	4.95	4.95	4.95	4.95	4.95	4.95	4.95
KUR seg1	**yes**	**Strslip**	5.29	5.29	5.29	5.29	5.29	5.29	5.29	5.29	5.29	5.29	5.29	5.29
KUR seg2	**no**	**All**	5.70	5.84	6.06	6.08	6.21	6.32	6.32	6.33	6.42	6.53	5.70	6.53
KUR seg2	**no**	**Normal**	5.75	5.82	5.88	5.90	5.87	5.92	5.91	5.94	5.93	6.02	5.75	6.02
KUR seg2	**no**	**Reverse**	5.67	5.82	5.91	5.96	6.10	6.19	6.24	6.24	6.25	6.33	5.67	6.33
KUR seg2	**no**	**Strslip**	5.78	5.84	5.81	5.92	5.97	6.02	6.05	6.03	6.10	6.22	5.78	6.22
KUR seg2	**yes**	**All**	5.79	5.98	6.18	6.26	6.40	6.48	6.52	6.56	6.63	6.70	5.79	6.70
KUR seg2	**yes**	**Normal**	5.74	5.82	5.89	5.90	5.93	5.96	6.05	5.99	5.98	6.18	5.74	6.18
KUR seg2	**yes**	**Reverse**	5.75	5.91	6.06	6.14	6.21	6.31	6.33	6.44	6.45	6.50	5.75	6.50
KUR seg2	**yes**	**Strslip**	5.70	5.77	5.82	5.87	5.95	5.96	6.06	6.11	6.09	6.18	5.70	6.18
IZU seg1	**no**	**All**	5.41	5.39	5.43	5.48	5.47	5.58	5.63	5.55	5.65	5.67	5.39	5.67
IZU seg1	**no**	**Normal**	5.24	5.25	5.22	5.25	5.27	5.27	5.27	5.26	5.31	5.33	5.22	5.33
IZU seg1	**no**	**Reverse**	5.45	5.45	5.45	5.45	5.45	5.45	5.45	5.45	5.45	5.45	5.45	5.45
IZU seg1	**no**	**Strslip**	5.52	5.54	5.56	5.57	5.66	5.61	5.58	5.56	5.62	5.72	5.52	5.72
IZU seg1	**yes**	**All**	5.48	5.48	5.50	5.54	5.60	5.66	5.71	5.69	5.74	5.77	5.48	5.77
IZU seg1	**yes**	**Normal**	5.24	5.24	5.24	5.25	5.27	5.27	5.27	5.35	5.37	5.30	5.24	5.37
IZU seg1	**yes**	**Reverse**	5.45	5.45	5.45	5.45	5.45	5.45	5.45	5.45	5.45	5.45	5.45	5.45
IZU seg1	**yes**	**Strslip**	5.55	5.58	5.63	5.58	5.70	5.70	5.66	5.66	5.72	5.79	5.55	5.79
VAN seg1	**no**	**All**	6.07	6.16	6.20	6.16	6.15	6.33	6.34	6.40	6.41	6.61	6.07	6.61
VAN seg1	**no**	**Normal**	5.48	5.49	5.48	5.48	5.48	5.48	5.48	5.48	5.48	5.49	5.48	5.49
VAN seg1	**no**	**Reverse**	6.04	6.14	6.05	6.13	6.11	6.08	6.11	6.13	6.11	6.22	6.04	6.22

VAN seg1	**no**	**Strslip**	6.79	6.70	6.92	6.98	6.90	6.92	6.92	6.93	7.30	6.93	6.70	7.30
VAN seg1	**yes**	**All**	5.91	6.09	6.08	6.09	6.13	6.18	6.21	6.41	6.29	6.43	5.91	6.43
VAN seg1	**yes**	**Normal**	5.48	5.49	5.48	5.48	5.48	5.48	5.48	5.49	5.48	5.49	5.48	5.49
VAN seg1	**yes**	**Reverse**	5.89	6.00	5.96	6.01	6.03	6.04	6.03	6.08	6.07	6.21	5.89	6.21
VAN seg1	**yes**	**Strslip**	6.33	6.29	6.30	6.27	6.30	6.39	6.39	6.55	6.53	6.55	6.27	6.55
MEX seg1	**no**	**All**	5.84	5.96	5.99	6.04	6.18	6.12	6.13	6.19	6.23	6.35	5.84	6.35
MEX seg1	**no**	**Normal**	5.97	6.03	6.10	6.20	6.42	6.32	6.30	6.38	6.38	6.47	5.97	6.47
MEX seg1	**no**	**Reverse**	5.81	5.81	5.81	5.81	5.81	5.81	5.81	5.81	5.81	5.81	5.81	5.81
MEX seg1	**no**	**Strslip**	5.17	5.17	5.17	5.17	5.17	5.17	5.17	5.17	5.17	5.17	5.17	5.17
MEX seg1	**yes**	**All**	5.91	5.97	5.96	6.02	6.22	6.12	6.16	6.22	6.33	6.40	5.91	6.40
MEX seg1	**yes**	**Normal**	5.87	5.96	5.94	5.99	6.30	6.16	6.16	6.25	6.31	6.38	5.87	6.38
MEX seg1	**yes**	**Reverse**	6.40	6.50	6.40	6.60	6.40	6.40	6.40	6.40	6.40	6.40	6.40	6.60
MEX seg1	**yes**	**Strslip**	5.17	5.17	5.17	5.17	5.17	5.17	5.17	5.17	5.17	5.17	5.17	5.17
MEX seg2	**no**	**All**	6.02	6.00	6.06	6.09	6.08	6.12	6.15	6.34	6.22	6.28	6.00	6.34
MEX seg2	**no**	**Normal**	5.56	5.56	5.47	5.47	5.47	5.47	5.63	5.63	5.63	5.63	5.47	5.63
MEX seg2	**no**	**Reverse**	6.44	6.64	6.64	6.64	6.50	6.55	6.60	6.82	6.56	6.60	6.44	6.82
MEX seg2	**no**	**Strslip**	5.51	5.51	5.51	5.51	5.51	5.51	5.51	5.51	5.51	5.51	5.51	5.51
MEX seg2	**yes**	**All**	5.91	5.93	5.91	6.03	6.10	6.15	6.08	6.21	6.26	6.25	5.91	6.26
MEX seg2	**yes**	**Normal**	5.80	5.88	5.91	5.88	5.89	5.91	5.97	5.97	6.09	5.97	5.80	6.09
MEX seg2	**yes**	**Reverse**	6.15	6.15	6.10	6.08	6.26	6.16	6.20	6.36	6.36	6.21	6.08	6.36
MEX seg2	**yes**	**Strslip**	5.51	5.51	5.51	5.51	5.51	5.51	5.51	5.51	5.51	5.51	5.51	5.51
MEX seg3	**no**	**All**	6.29	6.29	6.39	6.40	6.42	6.55	6.49	6.62	6.74	6.68	6.29	6.74
MEX seg3	**no**	**Normal**	6.46	6.46	6.46	6.46	6.46	6.46	6.46	6.46	6.46	6.46	6.46	6.46
MEX seg3	**no**	**Reverse**	6.84	6.91	6.87	7.03	7.13	7.21	6.83	7.08	7.19	7.21	6.83	7.21
MEX seg3	**no**	**Strslip**	6.09	6.10	6.18	6.17	6.18	6.18	6.30	6.27	6.18	6.25	6.09	6.30
MEX seg3	**yes**	**All**	6.05	6.10	6.19	6.19	6.35	6.38	6.40	6.51	6.62	6.56	6.05	6.62
MEX seg3	**yes**	**Normal**	5.87	5.86	5.82	5.87	5.88	5.92	5.89	6.08	6.07	5.99	5.82	6.08
MEX seg3	**yes**	**Reverse**	6.46	6.49	6.56	6.56	6.67	6.68	6.56	6.67	6.79	6.81	6.46	6.81
MEX seg3	**yes**	**Strslip**	5.99	5.99	6.11	6.09	6.11	6.19	6.13	6.09	6.22	6.28	5.99	6.28
SUM seg1	**no**	**All**	.	.	.	.	.	.	.	.	.	.	0.00	0.00
SUM seg1	**no**	**Normal**	.	.	.	.	.	.	.	.	.	.	0.00	0.00
SUM seg1	**no**	**Reverse**	.	.	.	.	.	.	.	.	.	.	0.00	0.00
SUM seg1	**no**	**Strslip**	.	.	.	.	.	.	.	.	.	.	0.00	0.00
SUM seg1	**yes**	**All**	6.12	6.12	6.12	6.12	6.12	6.12	6.12	6.12	6.12	6.12	6.12	6.12

SUM seg1	**yes**	**Normal**	.	.	.	.	.	.	.	.	.	.	0.00	0.00
SUM seg1	**yes**	**Reverse**	6.12	6.12	6.12	6.12	6.12	6.12	6.12	6.12	6.12	6.12	6.12	6.12
SUM seg1	**yes**	**Strslip**	.	.	.	.	.	.	.	.	.	.	0.00	0.00
SUM seg2	**no**	**All**	5.63	5.63	5.63	5.63	5.63	5.63	5.63	5.63	5.63	5.63	5.63	5.63
SUM seg2	**no**	**Normal**	.	.	.	.	.	.	.	.	.	.	0.00	0.00
SUM seg2	**no**	**Reverse**	5.63	5.63	5.63	5.63	5.63	5.63	5.63	5.63	5.63	5.63	5.63	5.63
SUM seg2	**no**	**Strslip**	.	.	.	.	.	.	.	.	.	.	0.00	0.00
SUM seg2	**yes**	**All**	5.63	5.53	5.53	5.58	5.63	5.53	5.53	5.53	5.58	5.53	5.53	5.63
SUM seg2	**yes**	**Normal**	.	.	.	.	.	.	.	.	.	.	0.00	0.00
SUM seg2	**yes**	**Reverse**	5.63	5.63	5.53	5.53	5.53	5.53	5.53	5.53	5.53	5.63	5.53	5.63
SUM seg2	**yes**	**Strslip**	.	.	.	.	.	.	.	.	.	.	0.00	0.00
SUM seg3	**no**	**All**	5.90	6.09	6.25	6.36	6.51	6.59	6.64	6.74	6.74	6.83	5.90	6.83
SUM seg3	**no**	**Normal**	5.78	5.88	5.87	5.84	5.95	5.96	6.04	6.06	6.22	6.05	5.78	6.22
SUM seg3	**no**	**Reverse**	5.86	5.96	6.00	6.07	6.18	6.23	6.38	6.37	6.34	6.43	5.86	6.43
SUM seg3	**no**	**Strslip**	5.98	6.13	6.21	6.25	6.41	6.44	6.48	6.56	6.57	6.67	5.98	6.67
SUM seg3	**yes**	**All**	5.89	6.13	6.31	6.45	6.59	6.66	6.71	6.79	6.80	6.88	5.89	6.88
SUM seg3	**yes**	**Normal**	5.73	5.73	5.90	5.88	5.97	5.98	6.00	6.05	6.14	6.09	5.73	6.14
SUM seg3	**yes**	**Reverse**	5.87	5.91	5.96	6.03	6.26	6.26	6.38	6.40	6.48	6.54	5.87	6.54
SUM seg3	**yes**	**Strslip**	5.94	6.06	6.23	6.33	6.44	6.52	6.56	6.62	6.64	6.70	5.94	6.70
SAM seg1	**no**	**All**	6.63	6.84	6.75	6.89	6.92	6.92	6.92	7.00	7.00	7.00	6.63	7.00
SAM seg1	**no**	**Normal**	6.85	7.15	7.15	7.15	7.15	7.15	7.15	7.15	7.15	7.16	6.85	7.16
SAM seg1	**no**	**Reverse**	6.42	6.42	6.42	6.42	6.42	6.42	6.42	6.42	6.42	6.42	6.42	6.42
SAM seg1	**no**	**Strslip**	6.33	6.31	6.31	6.41	6.41	6.54	6.41	6.54	6.54	6.54	6.31	6.54
SAM seg1	**yes**	**All**	6.14	6.32	6.36	6.42	6.55	6.49	6.47	6.67	6.79	6.62	6.14	6.79
SAM seg1	**yes**	**Normal**	7.01	7.16	7.16	7.16	7.15	7.16	7.16	7.16	7.16	7.16	7.01	7.16
SAM seg1	**yes**	**Reverse**	6.01	6.00	6.07	6.08	6.17	6.08	6.09	6.15	6.25	6.15	6.00	6.25
SAM seg1	**yes**	**Strslip**	6.22	6.22	6.15	6.33	6.33	6.33	6.33	6.41	6.42	6.54	6.15	6.54
SAM seg2	**no**	**All**	5.52	5.53	5.53	5.52	5.53	5.55	5.65	5.49	5.52	5.65	5.49	5.65
SAM seg2	**no**	**Normal**	5.24	5.24	5.24	5.24	5.24	5.24	5.24	5.24	5.24	5.24	5.24	5.24
SAM seg2	**no**	**Reverse**	5.54	5.55	5.55	5.54	5.54	5.55	5.65	5.54	5.54	5.65	5.54	5.65
SAM seg2	**no**	**Strslip**	.	.	.	.	.	.	.	.	.	.	0.00	0.00
SAM seg2	**yes**	**All**	5.78	5.82	5.88	5.95	5.99	5.95	5.99	5.91	5.95	6.03	5.78	6.03
SAM seg2	**yes**	**Normal**	5.83	5.84	5.86	5.84	5.85	5.89	5.87	5.91	5.84	5.87	5.83	5.91
SAM seg2	**yes**	**Reverse**	5.56	5.56	5.56	5.61	5.68	5.62	5.73	5.70	5.67	5.88	5.56	5.88

SAM seg2	**yes**	**Strslip**	6.08	6.08	6.08	6.08	6.08	6.08	6.08	6.08	6.08	6.08	6.08	6.08
SAM seg3	**no**	**All**	5.94	6.08	6.15	6.17	6.16	6.17	6.28	6.48	6.35	6.51	5.94	6.51
SAM seg3	**no**	**Normal**	5.66	5.66	5.62	5.67	5.65	5.63	5.64	5.64	5.70	5.64	5.62	5.70
SAM seg3	**no**	**Reverse**	7.16	7.16	7.16	7.16	7.16	7.16	7.16	7.16	7.16	7.16	7.16	7.16
SAM seg3	**no**	**Strslip**	5.65	5.75	5.85	5.86	5.85	5.84	5.89	5.89	5.86	5.89	5.65	5.89
SAM seg3	**yes**	**All**	5.85	6.00	6.14	6.14	6.15	6.18	6.27	6.40	6.37	6.47	5.85	6.47
SAM seg3	**yes**	**Normal**	5.62	5.62	5.61	5.65	5.67	5.62	5.63	5.60	5.70	5.66	5.60	5.70
SAM seg3	**yes**	**Reverse**	6.85	6.85	6.85	7.00	7.00	7.16	6.85	6.85	6.85	7.16	6.85	7.16
SAM seg3	**yes**	**Strslip**	5.60	5.68	5.73	5.74	5.75	5.80	5.86	5.88	5.76	5.85	5.60	5.88
SAM seg4	**no**	**All**	6.15	6.21	6.29	6.33	6.39	6.26	6.37	6.35	6.46	6.46	6.15	6.46
SAM seg4	**no**	**Normal**	6.52	6.65	6.65	6.65	6.52	6.65	6.52	6.52	6.52	6.52	6.52	6.65
SAM seg4	**no**	**Reverse**	6.50	6.56	6.62	6.77	6.75	6.62	6.50	6.77	6.51	6.77	6.50	6.77
SAM seg4	**no**	**Strslip**	5.66	5.66	5.66	5.66	5.66	5.66	5.66	5.66	5.66	5.66	5.66	5.66
SAM seg4	**yes**	**All**	6.17	6.14	6.19	6.32	6.24	6.21	6.42	6.29	6.44	6.34	6.14	6.44
SAM seg4	**yes**	**Normal**	6.78	6.78	6.69	6.60	6.60	6.60	6.60	6.60	6.60	6.69	6.60	6.78
SAM seg4	**yes**	**Reverse**	6.49	6.56	6.40	6.51	6.54	6.52	6.69	6.79	6.40	6.55	6.40	6.79
SAM seg4	**yes**	**Strslip**	5.93	6.01	5.93	5.93	5.93	6.01	5.97	6.01	5.93	5.93	5.93	6.01

Table 7.2: Threshold of background Nr of upper plate events (seismicity rate) per segment and kinematic type for each value of BW

zone-seg	fix	type	100	200	300	400	500	600	700	800	900	1000	min	max
ALU seg1	**no**	**All**	2.1	2.9	4.1	5.2	5.9	6.9	7.7	8.1	10.3	10.3	2.1	10.3
ALU seg1	**no**	**Normal**	1.0	1.0	1.4	1.7	1.6	1.8	1.7	2.0	1.9	2.0	1.0	2.0
ALU seg1	**no**	**Reverse**	2.2	3.0	4.0	5.0	5.2	6.1	7.2	7.4	10.3	9.7	2.2	10.3
ALU seg1	**no**	**Strslip**	1.7	1.5	2.6	2.6	2.6	2.6	2.6	2.6	2.6	2.6	1.5	2.6
ALU seg1	**yes**	**All**	2.8	4.3	5.5	7.6	8.3	9.9	11.7	12.0	13.9	15.7	2.8	15.7
ALU seg1	**yes**	**Normal**	1.0	1.0	1.4	1.7	1.7	1.8	1.6	1.9	1.8	2.0	1.0	2.0
ALU seg1	**yes**	**Reverse**	2.6	3.8	4.9	6.5	7.6	8.0	10.3	10.9	13.4	14.3	2.6	14.3
ALU seg1	**yes**	**Strslip**	2.7	3.1	4.6	4.8	4.9	5.3	4.6	5.3	5.8	5.7	2.7	5.8
ALU seg2	**no**	**All**	2.0	2.1	2.6	2.9	2.9	3.5	5.1	5.0	5.0	5.1	2.0	5.1
ALU seg2	**no**	**Normal**	1.0	1.0	1.0	1.0	1.0	1.0	1.0	1.0	1.0	1.0	1.0	1.0
ALU seg2	**no**	**Reverse**	1.5	1.6	2.0	2.0	2.1	2.5	2.6	2.9	4.1	3.5	1.5	4.1
ALU seg2	**no**	**Strslip**	3.7	3.3	3.7	4.0	3.7	4.0	5.5	4.0	5.5	5.0	3.3	5.5
ALU seg2	**yes**	**All**	2.1	2.5	2.9	3.6	4.0	4.8	6.2	6.3	6.5	7.5	2.1	7.5
ALU seg2	**yes**	**Normal**	1.0	1.0	1.0	1.8	1.8	1.0	2.0	1.8	2.0	1.9	1.0	2.0
ALU seg2	**yes**	**Reverse**	1.4	1.9	2.3	2.9	3.1	3.8	4.3	4.6	5.8	5.9	1.4	5.9
ALU seg2	**yes**	**Strslip**	3.0	3.7	3.0	5.0	3.0	5.0	5.0	5.0	5.0	5.0	3.0	5.0
KER seg1	**no**	**All**	1.6	1.8	2.2	2.2	2.3	2.7	2.4	2.9	2.6	3.2	1.6	3.2
KER seg1	**no**	**Normal**	2.0	2.0	2.0	2.0	2.0	2.0	2.0	2.0	2.0	2.0	2.0	2.0
KER seg1	**no**	**Reverse**	1.0	1.4	1.4	1.8	1.6	1.8	1.8	1.9	1.4	1.6	1.0	1.9
KER seg1	**no**	**Strslip**	3.0	3.0	3.0	3.0	3.0	3.0	4.0	4.0	3.0	4.0	3.0	4.0
KER seg1	**yes**	**All**	1.6	2.0	2.3	2.6	3.2	3.8	4.0	4.3	5.1	5.8	1.6	5.8
KER seg1	**yes**	**Normal**	1.6	1.6	1.5	1.5	1.8	1.8	1.8	2.1	1.7	1.9	1.5	2.1
KER seg1	**yes**	**Reverse**	1.5	1.5	2.1	2.0	2.3	3.1	3.2	3.4	3.9	3.8	1.5	3.9
KER seg1	**yes**	**Strslip**	2.6	2.6	2.6	2.6	4.0	5.0	3.8	4.0	4.0	6.0	2.6	6.0
KER seg2	**no**	**All**	2.3	3.1	4.1	4.6	5.2	6.1	6.7	7.4	8.6	8.7	2.3	8.7
KER seg2	**no**	**Normal**	1.0	1.0	1.0	1.0	1.0	1.0	1.0	1.9	1.0	1.0	1.0	1.9
KER seg2	**no**	**Reverse**	2.4	3.4	4.4	4.6	6.0	6.6	7.2	7.5	9.6	8.8	2.4	9.6
KER seg2	**no**	**Strslip**	3.2	3.2	3.7	3.6	3.6	3.5	3.6	3.6	3.4	3.6	3.2	3.7
KER seg2	**yes**	**All**	3.0	4.3	5.6	6.1	7.4	8.4	9.8	10.1	12.7	13.3	3.0	13.3
KER seg2	**yes**	**Normal**	2.1	2.7	2.1	2.7	2.7	2.7	2.7	3.6	3.5	3.4	2.1	3.6
KER seg2	**yes**	**Reverse**	3.0	4.4	5.5	6.6	7.8	8.8	10.7	9.7	13.6	12.6	3.0	13.6

KER seg2	**yes**	**Strslip**	3.3	3.1	3.6	3.5	3.6	3.5	3.6	3.6	4.0	3.5	3.1	4.0
KUR seg1	**no**	**All**	1.0	1.0	1.0	1.0	1.0	1.0	1.0	1.0	1.0	1.0	1.0	1.0
KUR seg1	**no**	**Normal**	1.0	1.0	1.0	1.0	1.0	1.0	1.0	1.0	1.0	1.0	1.0	1.0
KUR seg1	**no**	**Reverse**	.	.	.	.	.	.	.	.	.	.	0.0	0.0
KUR seg1	**no**	**Strslip**	1.0	1.0	1.0	1.0	1.0	1.0	1.0	1.0	1.0	1.0	1.0	1.0
KUR seg1	**yes**	**All**	1.0	1.0	1.0	1.0	1.0	1.0	1.0	1.0	1.0	1.0	1.0	1.0
KUR seg1	**yes**	**Normal**	1.0	1.0	1.0	1.0	1.0	1.0	1.0	1.0	1.0	1.0	1.0	1.0
KUR seg1	**yes**	**Reverse**	1.0	1.0	1.0	1.0	1.0	1.0	1.0	1.0	1.0	1.0	1.0	1.0
KUR seg1	**yes**	**Strslip**	1.0	1.0	1.0	1.0	1.0	1.0	1.0	1.0	1.0	1.0	1.0	1.0
KUR seg2	**no**	**All**	4.3	7.0	8.9	12.0	13.1	16.9	20.6	24.3	26.3	24.9	4.3	26.3
KUR seg2	**no**	**Normal**	6.4	9.4	8.6	12.7	11.7	12.8	15.7	18.2	16.0	14.9	6.4	18.2
KUR seg2	**no**	**Reverse**	2.2	2.8	3.5	4.4	5.2	6.4	7.2	7.9	8.9	8.5	2.2	8.9
KUR seg2	**no**	**Strslip**	2.2	2.4	2.5	3.4	3.4	3.7	4.1	5.0	5.1	5.4	2.2	5.4
KUR seg2	**yes**	**All**	5.7	9.6	12.4	18.5	20.8	25.2	33.5	36.5	41.8	37.3	5.7	41.8
KUR seg2	**yes**	**Normal**	8.5	12.2	12.4	16.3	14.5	18.8	22.9	23.0	23.6	24.9	8.5	24.9
KUR seg2	**yes**	**Reverse**	2.3	3.5	4.5	6.3	7.0	8.7	9.1	11.4	12.8	11.6	2.3	12.8
KUR seg2	**yes**	**Strslip**	2.4	3.0	3.1	3.8	3.9	4.2	5.7	6.9	6.2	6.3	2.4	6.9
IZU seg1	**no**	**All**	1.4	1.4	1.6	1.9	2.0	2.3	2.4	2.4	2.9	3.0	1.4	3.0
IZU seg1	**no**	**Normal**	1.0	1.0	1.0	1.0	1.6	1.6	1.6	1.6	1.8	2.3	1.0	2.3
IZU seg1	**no**	**Reverse**	1.0	1.0	1.0	1.0	1.0	1.0	1.0	1.0	1.0	1.0	1.0	1.0
IZU seg1	**no**	**Strslip**	1.0	1.0	1.6	1.6	1.8	1.8	1.6	1.6	1.8	2.6	1.0	2.6
IZU seg1	**yes**	**All**	1.8	1.7	2.0	2.2	2.4	2.8	3.2	3.4	3.9	4.4	1.7	4.4
IZU seg1	**yes**	**Normal**	1.4	1.4	1.4	1.4	1.6	2.0	1.7	1.9	2.3	2.5	1.4	2.5
IZU seg1	**yes**	**Reverse**	1.0	1.0	1.0	1.0	1.0	1.0	1.0	1.0	1.0	1.0	1.0	1.0
IZU seg1	**yes**	**Strslip**	1.5	1.5	1.9	1.8	2.4	2.3	2.2	2.5	2.7	3.4	1.5	3.4
VAN seg1	**no**	**All**	7.6	7.9	8.5	8.4	8.4	9.9	10.1	11.0	11.0	12.2	7.6	12.2
VAN seg1	**no**	**Normal**	4.0	4.5	4.0	4.5	5.0	4.5	4.0	5.0	4.0	4.5	4.0	5.0
VAN seg1	**no**	**Reverse**	1.6	1.9	1.6	1.9	1.9	1.9	1.9	2.0	1.9	2.5	1.6	2.5
VAN seg1	**no**	**Strslip**	15.4	11.8	16.9	15.4	15.4	14.8	14.8	14.8	19.0	14.8	11.8	19.0
VAN seg1	**yes**	**All**	5.9	7.6	8.2	8.5	8.4	9.8	10.1	11.8	10.8	12.5	5.9	12.5
VAN seg1	**yes**	**Normal**	5.0	4.0	4.0	4.5	4.0	4.0	4.0	4.5	5.0	4.0	4.0	5.0
VAN seg1	**yes**	**Reverse**	1.5	1.9	1.8	1.9	2.2	2.1	2.1	2.2	2.2	2.8	1.5	2.8
VAN seg1	**yes**	**Strslip**	10.8	10.8	9.5	10.8	10.8	12.0	12.1	14.0	13.6	13.7	9.5	14.0
MEX seg1	**no**	**All**	1.3	1.6	2.1	2.2	2.9	2.7	2.7	3.3	3.8	4.5	1.3	4.5

MEX seg1	**no**	**Normal**	1.4	1.6	2.1	2.3	3.4	2.8	2.7	3.5	4.0	4.8	1.4	4.8
MEX seg1	**no**	**Reverse**	1.0	1.0	1.0	1.0	1.0	1.0	1.0	1.0	1.0	1.0	1.0	1.0
MEX seg1	**no**	**Strslip**	1.0	1.0	1.0	1.0	1.0	1.0	1.0	1.0	1.0	1.0	1.0	1.0
MEX seg1	**yes**	**All**	1.2	1.6	1.8	1.9	2.6	2.5	2.4	3.0	3.5	4.4	1.2	4.4
MEX seg1	**yes**	**Normal**	1.3	1.5	1.8	2.0	3.1	2.5	2.6	3.1	3.7	4.4	1.3	4.4
MEX seg1	**yes**	**Reverse**	1.0	1.0	1.0	1.0	1.0	1.0	1.0	1.0	1.0	1.0	1.0	1.0
MEX seg1	**yes**	**Strslip**	1.0	1.0	1.0	1.0	1.0	1.0	1.0	1.0	1.0	1.0	1.0	1.0
MEX seg2	**no**	**All**	1.4	1.5	1.5	2.0	1.6	2.0	1.8	2.5	1.9	2.3	1.4	2.5
MEX seg2	**no**	**Normal**	1.0	1.0	1.0	1.0	1.0	1.0	2.0	2.0	2.0	2.0	1.0	2.0
MEX seg2	**no**	**Reverse**	1.0	1.8	1.8	1.8	1.6	1.6	1.8	2.0	1.8	1.6	1.0	2.0
MEX seg2	**no**	**Strslip**	2.0	2.0	2.0	2.0	2.0	2.0	2.0	2.0	2.0	2.0	2.0	2.0
MEX seg2	**yes**	**All**	1.4	1.5	1.5	2.1	1.9	2.5	1.9	2.8	2.6	2.7	1.4	2.8
MEX seg2	**yes**	**Normal**	1.0	1.0	1.0	1.0	1.0	1.0	2.0	1.8	2.0	1.9	1.0	2.0
MEX seg2	**yes**	**Reverse**	1.0	1.4	1.4	1.4	1.7	1.6	1.6	1.9	2.3	1.6	1.0	2.3
MEX seg2	**yes**	**Strslip**	2.0	2.0	2.0	2.0	2.0	2.0	2.0	2.0	2.0	2.0	2.0	2.0
MEX seg3	**no**	**All**	1.4	1.6	1.8	1.9	2.0	2.5	2.3	2.4	2.5	2.5	1.4	2.5
MEX seg3	**no**	**Normal**	1.0	1.0	1.0	1.0	1.0	1.0	1.0	2.0	1.0	2.0	1.0	2.0
MEX seg3	**no**	**Reverse**	1.0	1.6	1.6	1.8	2.3	2.6	1.6	1.8	2.0	2.6	1.0	2.6
MEX seg3	**no**	**Strslip**	2.1	2.0	2.4	2.4	2.3	2.3	3.0	3.0	2.5	2.6	2.0	3.0
MEX seg3	**yes**	**All**	2.0	2.3	2.8	2.8	4.1	4.3	4.3	5.1	5.6	5.4	2.0	5.6
MEX seg3	**yes**	**Normal**	1.5	1.5	1.5	1.5	1.5	1.8	1.5	2.0	2.3	1.7	1.5	2.3
MEX seg3	**yes**	**Reverse**	2.1	2.3	2.9	2.5	3.4	3.6	3.0	3.4	4.3	3.5	2.1	4.3
MEX seg3	**yes**	**Strslip**	1.8	1.8	2.4	2.4	3.3	3.6	3.6	2.6	3.7	4.0	1.8	4.0
SUM seg1	**no**	**All**	.	.	.	.	.	.	.	.	.	.	0.0	0.0
SUM seg1	**no**	**Normal**	.	.	.	.	.	.	.	.	.	.	0.0	0.0
SUM seg1	**no**	**Reverse**	.	.	.	.	.	.	.	.	.	.	0.0	0.0
SUM seg1	**no**	**Strslip**	.	.	.	.	.	.	.	.	.	.	0.0	0.0
SUM seg1	**yes**	**All**	1.0	1.0	1.0	1.0	1.0	1.0	1.0	1.0	1.0	1.0	1.0	1.0
SUM seg1	**yes**	**Normal**	.	.	.	.	.	.	.	.	.	.	0.0	0.0
SUM seg1	**yes**	**Reverse**	1.0	1.0	1.0	1.0	1.0	1.0	1.0	1.0	1.0	1.0	1.0	1.0
SUM seg1	**yes**	**Strslip**	.	.	.	.	.	.	.	.	.	.	0.0	0.0
SUM seg2	**no**	**All**	1.0	1.0	1.0	1.0	1.0	1.0	1.0	1.0	1.0	1.0	1.0	1.0
SUM seg2	**no**	**Normal**	.	.	.	.	.	.	.	.	.	.	0.0	0.0
SUM seg2	**no**	**Reverse**	1.0	1.0	1.0	1.0	1.0	1.0	1.0	1.0	1.0	1.0	1.0	1.0

SUM seg2	**no**	**Strslip**	.	.	.	.	.	.	.	.	.	.	0.0	0.0
SUM seg2	**yes**	**All**	1.0	1.0	1.0	1.0	1.0	1.0	1.0	1.0	1.0	1.0	1.0	1.0
SUM seg2	**yes**	**Normal**	.	.	.	.	.	.	.	.	.	.	0.0	0.0
SUM seg2	**yes**	**Reverse**	1.0	1.0	1.0	1.0	1.0	1.0	1.0	1.0	1.0	1.0	1.0	1.0
SUM seg2	**yes**	**Strslip**	.	.	.	.	.	.	.	.	.	.	0.0	0.0
SUM seg3	**no**	**All**	9.7	13.3	18.8	23.7	29.3	35.0	39.5	45.9	48.0	56.0	9.7	56.0
SUM seg3	**no**	**Normal**	10.7	12.7	16.7	16.8	21.7	20.5	26.9	26.7	28.5	27.3	10.7	28.5
SUM seg3	**no**	**Reverse**	3.4	4.1	5.6	7.2	8.0	8.4	9.5	10.4	10.3	11.0	3.4	11.0
SUM seg3	**no**	**Strslip**	7.8	10.0	12.4	14.1	17.1	20.6	25.5	24.3	25.7	30.2	7.8	30.2
SUM seg3	**yes**	**All**	9.7	15.9	26.5	31.1	39.8	46.9	52.0	60.8	65.5	76.8	9.7	76.8
SUM seg3	**yes**	**Normal**	12.9	15.2	23.4	23.2	30.2	28.9	33.0	36.6	38.6	39.9	12.9	39.9
SUM seg3	**yes**	**Reverse**	3.7	5.0	5.9	7.3	9.4	8.8	11.4	11.0	11.8	13.2	3.7	13.2
SUM seg3	**yes**	**Strslip**	7.6	10.4	15.4	18.1	19.7	25.2	30.6	29.6	30.7	36.5	7.6	36.5
SAM seg1	**no**	**All**	5.1	7.1	7.3	9.0	7.6	8.2	7.1	10.0	8.5	10.3	5.1	10.3
SAM seg1	**no**	**Normal**	6.3	9.0	9.0	9.0	8.0	9.0	9.0	9.0	9.0	10.0	6.3	10.0
SAM seg1	**no**	**Reverse**	1.0	1.0	1.0	1.0	1.0	1.0	1.0	1.0	1.0	1.0	1.0	1.0
SAM seg1	**no**	**Strslip**	1.0	1.0	1.0	2.0	1.9	1.8	1.8	2.0	3.0	3.0	1.0	3.0
SAM seg1	**yes**	**All**	4.1	5.5	6.0	7.3	7.1	7.1	7.1	9.7	10.1	10.4	4.1	10.4
SAM seg1	**yes**	**Normal**	9.1	13.0	13.0	13.0	10.0	13.0	13.0	13.0	13.0	14.0	9.1	14.0
SAM seg1	**yes**	**Reverse**	1.4	1.4	1.7	1.8	1.9	1.6	1.7	1.9	2.5	1.9	1.4	2.5
SAM seg1	**yes**	**Strslip**	1.6	1.7	1.7	2.6	2.0	2.0	2.0	3.0	2.8	3.3	1.6	3.3
SAM seg2	**no**	**All**	1.8	1.8	1.7	1.6	1.8	3.0	3.0	1.8	1.6	3.0	1.6	3.0
SAM seg2	**no**	**Normal**	1.0	1.0	1.0	1.0	1.0	1.0	1.0	1.0	1.0	1.0	1.0	1.0
SAM seg2	**no**	**Reverse**	1.8	1.9	1.9	1.8	1.8	3.0	3.0	1.8	2.0	3.0	1.8	3.0
SAM seg2	**no**	**Strslip**	.	.	.	.	.	.	.	.	.	.	0.0	0.0
SAM seg2	**yes**	**All**	1.9	1.9	2.2	2.8	3.3	3.6	4.3	4.1	3.5	6.0	1.9	6.0
SAM seg2	**yes**	**Normal**	1.8	1.8	1.8	1.8	1.6	2.0	2.0	2.0	1.8	2.0	1.6	2.0
SAM seg2	**yes**	**Reverse**	1.5	1.5	1.5	1.7	2.0	2.3	3.0	2.3	2.0	4.0	1.5	4.0
SAM seg2	**yes**	**Strslip**	1.0	1.0	1.0	1.0	1.0	1.0	1.0	1.0	1.0	1.0	1.0	1.0
SAM seg3	**no**	**All**	1.8	2.4	2.8	3.1	2.5	3.3	3.5	4.0	3.6	4.3	1.8	4.3
SAM seg3	**no**	**Normal**	1.0	1.0	1.0	1.0	1.0	1.0	1.0	1.0	1.8	1.0	1.0	1.8
SAM seg3	**no**	**Reverse**	2.0	2.0	2.0	2.0	2.0	2.0	2.0	2.0	2.0	3.0	2.0	3.0
SAM seg3	**no**	**Strslip**	2.1	2.8	3.6	3.5	3.0	3.6	3.8	4.0	3.5	3.8	2.1	4.0
SAM seg3	**yes**	**All**	1.8	2.5	3.0	3.3	3.3	3.3	4.0	4.1	5.1	5.7	1.8	5.7

SAM seg3	**yes**	**Normal**	1.6	1.6	1.6	1.6	1.8	1.6	1.6	1.6	2.6	1.8	1.6	2.6
SAM seg3	**yes**	**Reverse**	2.0	1.8	1.8	1.8	1.8	2.0	1.8	1.8	1.8	3.0	1.8	3.0
SAM seg3	**yes**	**Strslip**	2.0	2.6	3.3	3.3	3.0	3.3	3.7	3.6	3.4	3.6	2.0	3.7
SAM seg4	**no**	**All**	1.5	1.5	1.6	2.1	2.3	1.6	2.0	2.0	2.5	2.3	1.5	2.5
SAM seg4	**no**	**Normal**	1.8	1.8	1.9	2.0	2.0	1.9	2.0	1.8	2.0	1.8	1.8	2.0
SAM seg4	**no**	**Reverse**	1.7	1.7	1.7	2.6	2.4	1.7	1.7	2.2	2.2	2.6	1.7	2.6
SAM seg4	**no**	**Strslip**	1.0	1.0	1.0	1.0	1.0	1.0	1.0	1.0	1.0	1.0	1.0	1.0
SAM seg4	**yes**	**All**	1.9	1.9	2.1	3.1	2.8	2.0	2.5	3.0	3.6	3.1	1.9	3.6
SAM seg4	**yes**	**Normal**	2.5	2.5	2.5	2.5	2.5	2.5	2.5	2.8	3.0	2.5	2.5	3.0
SAM seg4	**yes**	**Reverse**	1.7	1.7	1.9	3.3	3.0	1.7	2.0	3.4	3.0	3.0	1.7	3.4
SAM seg4	**yes**	**Strslip**	1.0	1.0	1.0	1.0	1.0	1.0	1.0	1.0	1.0	1.0	1.0	1.0

Table 7.3: Threshold of background Mw of subduction events (seismicity rate) per segment and kinematic type for each value of BW

zone-seg	fix	type	100	200	300	400	500	600	700	800	900	1000	min	max
ALU seg1	no	All	5.96	6.26	6.38	6.56	6.75	6.93	6.99	7.03	7.14	7.25	5.96	6.26
ALU seg1	no	Normal	5.96	6.26	6.38	6.56	6.75	6.93	6.99	7.03	7.14	7.25	5.96	6.26
ALU seg1	no	Reverse	5.96	6.26	6.38	6.56	6.75	6.93	6.99	7.03	7.14	7.25	5.96	6.26
ALU seg1	no	Strslip	5.96	6.26	6.38	6.56	6.75	6.93	6.99	7.03	7.14	7.25	5.96	6.26
ALU seg1	yes	All	5.97	6.24	6.42	6.55	6.77	6.88	7.01	7.05	7.15	7.28	5.97	6.24
ALU seg1	yes	Normal	5.97	6.24	6.42	6.55	6.77	6.88	7.01	7.05	7.15	7.28	5.97	6.24
ALU seg1	yes	Reverse	5.97	6.24	6.42	6.55	6.77	6.88	7.01	7.05	7.15	7.28	5.97	6.24
ALU seg1	yes	Strslip	5.97	6.24	6.42	6.55	6.77	6.88	7.01	7.05	7.15	7.28	5.97	6.24
ALU seg2	no	All	6.19	6.21	6.21	6.37	6.57	6.56	6.60	6.66	6.70	7.00	6.19	6.21
ALU seg2	no	Normal	6.19	6.21	6.21	6.37	6.57	6.56	6.60	6.66	6.70	7.00	6.19	6.21
ALU seg2	no	Reverse	6.19	6.21	6.21	6.37	6.57	6.56	6.60	6.66	6.70	7.00	6.19	6.21
ALU seg2	no	Strslip	6.19	6.21	6.21	6.37	6.57	6.56	6.60	6.66	6.70	7.00	6.19	6.21
ALU seg2	yes	All	6.21	6.24	6.22	6.42	6.57	6.52	6.66	6.66	6.75	6.92	6.21	6.24
ALU seg2	yes	Normal	6.21	6.24	6.22	6.42	6.57	6.52	6.66	6.66	6.75	6.92	6.21	6.24
ALU seg2	yes	Reverse	6.21	6.24	6.22	6.42	6.57	6.52	6.66	6.66	6.75	6.92	6.21	6.24
ALU seg2	yes	Strslip	6.21	6.24	6.22	6.42	6.57	6.52	6.66	6.66	6.75	6.92	6.21	6.24
KER seg1	no	All	5.87	6.01	6.16	6.25	6.36	6.50	6.56	6.63	6.67	6.87	5.87	6.01
KER seg1	no	Normal	5.87	6.01	6.16	6.25	6.36	6.50	6.56	6.63	6.67	6.87	5.87	6.01
KER seg1	no	Reverse	5.87	6.01	6.16	6.25	6.36	6.50	6.56	6.63	6.67	6.87	5.87	6.01
KER seg1	no	Strslip	5.87	6.01	6.16	6.25	6.36	6.50	6.56	6.63	6.67	6.87	5.87	6.01
KER seg1	yes	All	5.86	6.08	6.26	6.36	6.51	6.59	6.71	6.69	6.85	6.93	5.86	6.08
KER seg1	yes	Normal	5.86	6.08	6.26	6.36	6.51	6.59	6.71	6.69	6.85	6.93	5.86	6.08
KER seg1	yes	Reverse	5.86	6.08	6.26	6.36	6.51	6.59	6.71	6.69	6.85	6.93	5.86	6.08
KER seg1	yes	Strslip	5.86	6.08	6.26	6.36	6.51	6.59	6.71	6.69	6.85	6.93	5.86	6.08
KER seg2	no	All	6.16	6.42	6.63	6.77	6.91	7.02	7.07	7.14	7.19	7.28	6.16	6.42
KER seg2	no	Normal	6.16	6.42	6.63	6.77	6.91	7.02	7.07	7.14	7.19	7.28	6.16	6.42
KER seg2	no	Reverse	6.16	6.42	6.63	6.77	6.91	7.02	7.07	7.14	7.19	7.28	6.16	6.42
KER seg2	no	Strslip	6.16	6.42	6.63	6.77	6.91	7.02	7.07	7.14	7.19	7.28	6.16	6.42
KER seg2	yes	All	6.13	6.42	6.65	6.79	6.95	7.06	7.11	7.15	7.22	7.30	6.13	6.42
KER seg2	yes	Normal	6.13	6.42	6.65	6.79	6.95	7.06	7.11	7.15	7.22	7.30	6.13	6.42
KER seg2	yes	Reverse	6.13	6.42	6.65	6.79	6.95	7.06	7.11	7.15	7.22	7.30	6.13	6.42

KER seg2	**yes**	**Strslip**	6.13	6.42	6.65	6.79	6.95	7.06	7.11	7.15	7.22	7.30	6.13	6.42
KUR seg1	**no**	**All**	5.74	5.83	5.87	6.03	6.08	6.08	6.20	6.33	6.23	6.45	5.74	5.83
KUR seg1	**no**	**Normal**	5.74	5.83	5.87	6.03	6.08	6.08	6.20	6.33	6.23	6.45	5.74	5.83
KUR seg1	**no**	**Reverse**	5.74	5.83	5.87	6.03	6.08	6.08	6.20	6.33	6.23	6.45	5.74	5.83
KUR seg1	**no**	**Strslip**	5.74	5.83	5.87	6.03	6.08	6.08	6.20	6.33	6.23	6.45	5.74	5.83
KUR seg1	**yes**	**All**	5.70	5.79	5.87	6.02	6.00	6.15	6.19	6.38	6.26	6.45	5.70	5.79
KUR seg1	**yes**	**Normal**	5.70	5.79	5.87	6.02	6.00	6.15	6.19	6.38	6.26	6.45	5.70	5.79
KUR seg1	**yes**	**Reverse**	5.70	5.79	5.87	6.02	6.00	6.15	6.19	6.38	6.26	6.45	5.70	5.79
KUR seg1	**yes**	**Strslip**	5.70	5.79	5.87	6.02	6.00	6.15	6.19	6.38	6.26	6.45	5.70	5.79
KUR seg2	**no**	**All**	6.50	6.94	7.26	7.45	7.60	7.77	7.87	7.95	8.05	8.20	6.50	6.94
KUR seg2	**no**	**Normal**	6.50	6.94	7.26	7.45	7.60	7.77	7.87	7.95	8.05	8.20	6.50	6.94
KUR seg2	**no**	**Reverse**	6.50	6.94	7.26	7.45	7.60	7.77	7.87	7.95	8.05	8.20	6.50	6.94
KUR seg2	**no**	**Strslip**	6.50	6.94	7.26	7.45	7.60	7.77	7.87	7.95	8.05	8.20	6.50	6.94
KUR seg2	**yes**	**All**	6.56	6.99	7.27	7.48	7.64	7.79	7.93	7.99	8.09	8.13	6.56	6.99
KUR seg2	**yes**	**Normal**	6.56	6.99	7.27	7.48	7.64	7.79	7.93	7.99	8.09	8.13	6.56	6.99
KUR seg2	**yes**	**Reverse**	6.56	6.99	7.27	7.48	7.64	7.79	7.93	7.99	8.09	8.13	6.56	6.99
KUR seg2	**yes**	**Strslip**	6.56	6.99	7.27	7.48	7.64	7.79	7.93	7.99	8.09	8.13	6.56	6.99
IZU seg1	**no**	**All**	5.78	5.84	5.96	6.08	6.17	6.17	6.40	6.46	6.48	6.53	5.78	5.84
IZU seg1	**no**	**Normal**	5.78	5.84	5.96	6.08	6.17	6.17	6.40	6.46	6.48	6.53	5.78	5.84
IZU seg1	**no**	**Reverse**	5.78	5.84	5.96	6.08	6.17	6.17	6.40	6.46	6.48	6.53	5.78	5.84
IZU seg1	**no**	**Strslip**	5.78	5.84	5.96	6.08	6.17	6.17	6.40	6.46	6.48	6.53	5.78	5.84
IZU seg1	**yes**	**All**	5.76	5.89	5.97	6.11	6.20	6.18	6.40	6.42	6.53	6.54	5.76	5.89
IZU seg1	**yes**	**Normal**	5.76	5.89	5.97	6.11	6.20	6.18	6.40	6.42	6.53	6.54	5.76	5.89
IZU seg1	**yes**	**Reverse**	5.76	5.89	5.97	6.11	6.20	6.18	6.40	6.42	6.53	6.54	5.76	5.89
IZU seg1	**yes**	**Strslip**	5.76	5.89	5.97	6.11	6.20	6.18	6.40	6.42	6.53	6.54	5.76	5.89
VAN seg1	**no**	**All**	6.17	6.40	6.65	6.83	6.93	7.10	7.23	7.34	7.44	7.50	6.17	6.40
VAN seg1	**no**	**Normal**	6.17	6.40	6.65	6.83	6.93	7.10	7.23	7.34	7.44	7.50	6.17	6.40
VAN seg1	**no**	**Reverse**	6.17	6.40	6.65	6.83	6.93	7.10	7.23	7.34	7.44	7.50	6.17	6.40
VAN seg1	**no**	**Strslip**	6.17	6.40	6.65	6.83	6.93	7.10	7.23	7.34	7.44	7.50	6.17	6.40
VAN seg1	**yes**	**All**	6.18	6.47	6.68	6.84	7.01	7.14	7.25	7.38	7.46	7.50	6.18	6.47
VAN seg1	**yes**	**Normal**	6.18	6.47	6.68	6.84	7.01	7.14	7.25	7.38	7.46	7.50	6.18	6.47
VAN seg1	**yes**	**Reverse**	6.18	6.47	6.68	6.84	7.01	7.14	7.25	7.38	7.46	7.50	6.18	6.47
VAN seg1	**yes**	**Strslip**	6.18	6.47	6.68	6.84	7.01	7.14	7.25	7.38	7.46	7.50	6.18	6.47
MEX seg1	**no**	**All**	6.24	6.50	6.66	6.65	6.76	6.93	7.03	7.03	7.13	7.16	6.24	6.50

MEX seg1	**no**	**Normal**	6.24	6.50	6.66	6.65	6.76	6.93	7.03	7.03	7.13	7.16	6.24	6.50
MEX seg1	**no**	**Reverse**	6.24	6.50	6.66	6.65	6.76	6.93	7.03	7.03	7.13	7.16	6.24	6.50
MEX seg1	**no**	**Strslip**	6.24	6.50	6.66	6.65	6.76	6.93	7.03	7.03	7.13	7.16	6.24	6.50
MEX seg1	**yes**	**All**	6.19	6.47	6.68	6.63	6.78	6.95	7.02	7.04	7.16	7.30	6.19	6.47
MEX seg1	**yes**	**Normal**	6.19	6.47	6.68	6.63	6.78	6.95	7.02	7.04	7.16	7.30	6.19	6.47
MEX seg1	**yes**	**Reverse**	6.19	6.47	6.68	6.63	6.78	6.95	7.02	7.04	7.16	7.30	6.19	6.47
MEX seg1	**yes**	**Strslip**	6.19	6.47	6.68	6.63	6.78	6.95	7.02	7.04	7.16	7.30	6.19	6.47
MEX seg2	**no**	**All**	5.80	5.91	6.05	6.13	6.24	6.26	6.31	6.40	6.49	6.59	5.80	5.91
MEX seg2	**no**	**Normal**	5.80	5.91	6.05	6.13	6.24	6.26	6.31	6.40	6.49	6.59	5.80	5.91
MEX seg2	**no**	**Reverse**	5.80	5.91	6.05	6.13	6.24	6.26	6.31	6.40	6.49	6.59	5.80	5.91
MEX seg2	**no**	**Strslip**	5.80	5.91	6.05	6.13	6.24	6.26	6.31	6.40	6.49	6.59	5.80	5.91
MEX seg2	**yes**	**All**	5.87	5.99	6.07	6.22	6.43	6.39	6.44	6.51	6.61	6.71	5.87	5.99
MEX seg2	**yes**	**Normal**	5.87	5.99	6.07	6.22	6.43	6.39	6.44	6.51	6.61	6.71	5.87	5.99
MEX seg2	**yes**	**Reverse**	5.87	5.99	6.07	6.22	6.43	6.39	6.44	6.51	6.61	6.71	5.87	5.99
MEX seg2	**yes**	**Strslip**	5.87	5.99	6.07	6.22	6.43	6.39	6.44	6.51	6.61	6.71	5.87	5.99
MEX seg3	**no**	**All**	5.96	6.15	6.28	6.38	6.54	6.68	6.70	6.83	6.85	6.99	5.96	6.15
MEX seg3	**no**	**Normal**	5.96	6.15	6.28	6.38	6.54	6.68	6.70	6.83	6.85	6.99	5.96	6.15
MEX seg3	**no**	**Reverse**	5.96	6.15	6.28	6.38	6.54	6.68	6.70	6.83	6.85	6.99	5.96	6.15
MEX seg3	**no**	**Strslip**	5.96	6.15	6.28	6.38	6.54	6.68	6.70	6.83	6.85	6.99	5.96	6.15
MEX seg3	**yes**	**All**	5.95	6.11	6.26	6.40	6.54	6.64	6.69	6.82	6.84	6.97	5.95	6.11
MEX seg3	**yes**	**Normal**	5.95	6.11	6.26	6.40	6.54	6.64	6.69	6.82	6.84	6.97	5.95	6.11
MEX seg3	**yes**	**Reverse**	5.95	6.11	6.26	6.40	6.54	6.64	6.69	6.82	6.84	6.97	5.95	6.11
MEX seg3	**yes**	**Strslip**	5.95	6.11	6.26	6.40	6.54	6.64	6.69	6.82	6.84	6.97	5.95	6.11
SUM seg1	**no**	**All**	7.21	7.10	7.10	7.10	7.10	7.79	7.10	7.10	7.10	7.79	7.21	7.10
SUM seg1	**no**	**Normal**	7.21	7.10	7.10	7.10	7.10	7.79	7.10	7.10	7.10	7.79	7.21	7.10
SUM seg1	**no**	**Reverse**	7.21	7.10	7.10	7.10	7.10	7.79	7.10	7.10	7.10	7.79	7.21	7.10
SUM seg1	**no**	**Strslip**	7.21	7.10	7.10	7.10	7.10	7.79	7.10	7.10	7.10	7.79	7.21	7.10
SUM seg1	**yes**	**All**	7.09	6.86	7.21	7.06	7.35	7.23	7.23	7.21	7.21	7.23	7.09	6.86
SUM seg1	**yes**	**Normal**	7.09	6.86	7.21	7.06	7.35	7.23	7.23	7.21	7.21	7.23	7.09	6.86
SUM seg1	**yes**	**Reverse**	7.09	6.86	7.21	7.06	7.35	7.23	7.23	7.21	7.21	7.23	7.09	6.86
SUM seg1	**yes**	**Strslip**	7.09	6.86	7.21	7.06	7.35	7.23	7.23	7.21	7.21	7.23	7.09	6.86
SUM seg2	**no**	**All**	6.04	6.18	6.22	6.29	6.40	6.36	6.48	6.55	6.56	6.54	6.04	6.18
SUM seg2	**no**	**Normal**	6.04	6.18	6.22	6.29	6.40	6.36	6.48	6.55	6.56	6.54	6.04	6.18
SUM seg2	**no**	**Reverse**	6.04	6.18	6.22	6.29	6.40	6.36	6.48	6.55	6.56	6.54	6.04	6.18

SUM seg2	**no**	**Strslip**	6.04	6.18	6.22	6.29	6.40	6.36	6.48	6.55	6.56	6.54	6.04	6.18
SUM seg2	**yes**	**All**	5.96	6.08	6.18	6.20	6.30	6.29	6.40	6.46	6.47	6.51	5.96	6.08
SUM seg2	**yes**	**Normal**	5.96	6.08	6.18	6.20	6.30	6.29	6.40	6.46	6.47	6.51	5.96	6.08
SUM seg2	**yes**	**Reverse**	5.96	6.08	6.18	6.20	6.30	6.29	6.40	6.46	6.47	6.51	5.96	6.08
SUM seg2	**yes**	**Strslip**	5.96	6.08	6.18	6.20	6.30	6.29	6.40	6.46	6.47	6.51	5.96	6.08
SUM seg3	**no**	**All**	6.24	6.60	6.76	6.91	7.15	7.36	7.46	7.49	7.63	7.77	6.24	6.60
SUM seg3	**no**	**Normal**	6.24	6.60	6.76	6.91	7.15	7.36	7.46	7.49	7.63	7.77	6.24	6.60
SUM seg3	**no**	**Reverse**	6.24	6.60	6.76	6.91	7.15	7.36	7.46	7.49	7.63	7.77	6.24	6.60
SUM seg3	**no**	**Strslip**	6.24	6.60	6.76	6.91	7.15	7.36	7.46	7.49	7.63	7.77	6.24	6.60
SUM seg3	**yes**	**All**	6.32	6.64	6.83	7.02	7.18	7.39	7.57	7.51	7.74	7.86	6.32	6.64
SUM seg3	**yes**	**Normal**	6.32	6.64	6.83	7.02	7.18	7.39	7.57	7.51	7.74	7.86	6.32	6.64
SUM seg3	**yes**	**Reverse**	6.32	6.64	6.83	7.02	7.18	7.39	7.57	7.51	7.74	7.86	6.32	6.64
SUM seg3	**yes**	**Strslip**	6.32	6.64	6.83	7.02	7.18	7.39	7.57	7.51	7.74	7.86	6.32	6.64
SAM seg1	**no**	**All**	6.16	6.34	6.51	6.63	6.84	6.97	7.02	7.08	7.28	7.40	6.16	6.34
SAM seg1	**no**	**Normal**	6.16	6.34	6.51	6.63	6.84	6.97	7.02	7.08	7.28	7.40	6.16	6.34
SAM seg1	**no**	**Reverse**	6.16	6.34	6.51	6.63	6.84	6.97	7.02	7.08	7.28	7.40	6.16	6.34
SAM seg1	**no**	**Strslip**	6.16	6.34	6.51	6.63	6.84	6.97	7.02	7.08	7.28	7.40	6.16	6.34
SAM seg1	**yes**	**All**	6.14	6.32	6.58	6.65	6.85	7.00	7.07	7.12	7.37	7.37	6.14	6.32
SAM seg1	**yes**	**Normal**	6.14	6.32	6.58	6.65	6.85	7.00	7.07	7.12	7.37	7.37	6.14	6.32
SAM seg1	**yes**	**Reverse**	6.14	6.32	6.58	6.65	6.85	7.00	7.07	7.12	7.37	7.37	6.14	6.32
SAM seg1	**yes**	**Strslip**	6.14	6.32	6.58	6.65	6.85	7.00	7.07	7.12	7.37	7.37	6.14	6.32
SAM seg2	**no**	**All**	6.22	6.32	6.53	6.73	6.74	7.00	7.11	7.16	7.30	7.19	6.22	6.32
SAM seg2	**no**	**Normal**	6.22	6.32	6.53	6.73	6.74	7.00	7.11	7.16	7.30	7.19	6.22	6.32
SAM seg2	**no**	**Reverse**	6.22	6.32	6.53	6.73	6.74	7.00	7.11	7.16	7.30	7.19	6.22	6.32
SAM seg2	**no**	**Strslip**	6.22	6.32	6.53	6.73	6.74	7.00	7.11	7.16	7.30	7.19	6.22	6.32
SAM seg2	**yes**	**All**	6.18	6.31	6.49	6.70	6.73	6.98	7.09	7.09	7.24	7.20	6.18	6.31
SAM seg2	**yes**	**Normal**	6.18	6.31	6.49	6.70	6.73	6.98	7.09	7.09	7.24	7.20	6.18	6.31
SAM seg2	**yes**	**Reverse**	6.18	6.31	6.49	6.70	6.73	6.98	7.09	7.09	7.24	7.20	6.18	6.31
SAM seg2	**yes**	**Strslip**	6.18	6.31	6.49	6.70	6.73	6.98	7.09	7.09	7.24	7.20	6.18	6.31
SAM seg3	**no**	**All**	6.04	6.21	6.39	6.62	6.76	6.80	6.85	7.06	7.15	7.25	6.04	6.21
SAM seg3	**no**	**Normal**	6.04	6.21	6.39	6.62	6.76	6.80	6.85	7.06	7.15	7.25	6.04	6.21
SAM seg3	**no**	**Reverse**	6.04	6.21	6.39	6.62	6.76	6.80	6.85	7.06	7.15	7.25	6.04	6.21
SAM seg3	**no**	**Strslip**	6.04	6.21	6.39	6.62	6.76	6.80	6.85	7.06	7.15	7.25	6.04	6.21
SAM seg3	**yes**	**All**	6.04	6.17	6.40	6.68	6.78	6.91	7.07	7.17	7.17	7.27	6.04	6.17

SAM seg3	**yes**	**Normal**	6.04	6.17	6.40	6.68	6.78	6.91	7.07	7.17	7.17	7.27	6.04	6.17
SAM seg3	**yes**	**Reverse**	6.04	6.17	6.40	6.68	6.78	6.91	7.07	7.17	7.17	7.27	6.04	6.17
SAM seg3	**yes**	**Strslip**	6.04	6.17	6.40	6.68	6.78	6.91	7.07	7.17	7.17	7.27	6.04	6.17
SAM seg4	**no**	**All**	6.48	6.46	6.54	6.62	6.74	6.68	6.98	6.56	6.82	7.01	6.48	6.46
SAM seg4	**no**	**Normal**	6.48	6.46	6.54	6.62	6.74	6.68	6.98	6.56	6.82	7.01	6.48	6.46
SAM seg4	**no**	**Reverse**	6.48	6.46	6.54	6.62	6.74	6.68	6.98	6.56	6.82	7.01	6.48	6.46
SAM seg4	**no**	**Strslip**	6.48	6.46	6.54	6.62	6.74	6.68	6.98	6.56	6.82	7.01	6.48	6.46
SAM seg4	**yes**	**All**	6.46	6.50	6.48	6.68	6.73	6.67	6.83	6.65	6.83	6.87	6.46	6.50
SAM seg4	**yes**	**Normal**	6.46	6.50	6.48	6.68	6.73	6.67	6.83	6.65	6.83	6.87	6.46	6.50
SAM seg4	**yes**	**Reverse**	6.46	6.50	6.48	6.68	6.73	6.67	6.83	6.65	6.83	6.87	6.46	6.50
SAM seg4	**yes**	**Strslip**	6.46	6.50	6.48	6.68	6.73	6.67	6.83	6.65	6.83	6.87	6.46	6.50

Table 7.4: Variation of ρNr using different bin sizes.

zone-seg	fix	type	Bin 100	Bin 200	Bin 300	Bin 400	Bin 500	Bin 600	Bin 700	Bin 800	Bin 900	Bin 1000	min	max
ALU seg1	no	All	0.57	0.42	0.57	0.60	0.33	0.60	0.50	0.50	0.50	0.50	0.33	0.60
ALU seg1	no	Normal	.	.	0.00	0.00	0.00	0.00	0.00	.	0.33	.	0.00	0.33
ALU seg1	no	Reverse	0.67	0.36	0.50	0.50	0.33	0.33	0.50	0.33	0.50	0.50	0.33	0.67
ALU seg1	no	Strslip	0.00	1.00	0.00	1.00	1.00	1.00	1.00	1.00	0.00	1.00	0.00	1.00
ALU seg1	yes	All	0.50	0.56	0.29	0.60	0.60	0.50	0.33	0.33	0.50	0.33	0.29	0.60
ALU seg1	yes	Normal	.	.	0.00	0.00	0.00	0.33	0.00	0.33	0.33	.	0.00	0.33
ALU seg1	yes	Reverse	0.45	0.44	0.43	0.50	0.50	0.33	0.33	0.33	0.50	0.50	0.33	0.50
ALU seg1	yes	Strslip	0.50	0.50	0.00	1.00	1.00	1.00	1.00	1.00	0.00	1.00	0.00	1.00
ALU seg2	no	All	0.50	0.00	0.33	0.00	0.00	0.00	0.00	0.00	0.50	0.50	0.00	0.50
ALU seg2	no	Normal	.	.	.	.	.	.	.	.	.	.	0.00	0.00
ALU seg2	no	Reverse	0.33	0.50	0.50	0.00	0.00	0.33	0.33	0.33	1.00	0.50	0.00	1.00
ALU seg2	no	Strslip	0.00	0.00	0.00	0.00	0.00	0.00	0.00	0.00	0.00	0.00	0.00	0.00
ALU seg2	yes	All	0.50	0.40	0.40	0.33	0.00	0.25	0.50	0.50	0.33	0.50	0.00	0.50
ALU seg2	yes	Normal	.	.	.	1.00	1.00	.	.	1.00	.	1.00	1.00	1.00
ALU seg2	yes	Reverse	0.40	0.38	0.33	0.25	0.00	0.33	0.50	0.33	0.50	0.00	0.00	0.50
ALU seg2	yes	Strslip	0.00	0.00	0.00	0.00	0.00	0.00	0.00	0.00	0.00	0.00	0.00	0.00
KER seg1	no	All	0.67	0.60	1.00	0.00	0.50	0.33	0.00	0.00	0.50	1.00	0.00	1.00
KER seg1	no	Normal	.	.	.	.	.	.	.	.	.	.	0.00	0.00
KER seg1	no	Reverse	.	0.00	0.00	0.00	0.00	0.00	0.50	0.33	0.00	0.00	0.00	0.50
KER seg1	no	Strslip	.	.	.	.	.	.	.	.	.	.	0.00	0.00
KER seg1	yes	All	0.43	0.50	0.00	0.29	0.25	0.33	0.00	0.00	0.50	0.50	0.00	0.50
KER seg1	yes	Normal	0.50	0.50	0.50	0.50	0.00	0.00	0.00	0.00	0.33	0.25	0.00	0.50
KER seg1	yes	Reverse	0.00	0.33	0.00	0.00	0.00	0.00	0.00	0.00	0.00	0.00	0.00	0.33
KER seg1	yes	Strslip	1.00	1.00	0.00	0.00	1.00	.	0.00	.	1.00	.	0.00	1.00
KER seg2	no	All	0.40	0.25	0.33	0.40	0.25	0.25	0.25	0.00	0.00	0.00	0.00	0.40
KER seg2	no	Normal	.	.	.	.	.	.	.	0.00	.	.	0.00	0.00
KER seg2	no	Reverse	0.50	0.33	0.33	0.50	0.25	0.25	0.00	0.00	0.00	0.00	0.00	0.50
KER seg2	no	Strslip	0.00	0.00	0.00	0.00	1.00	1.00	0.00	1.00	0.00	0.00	0.00	1.00
KER seg2	yes	All	0.25	0.20	0.33	0.00	0.00	0.00	0.33	0.00	0.00	0.00	0.00	0.33
KER seg2	yes	Normal	0.00	1.00	0.00	0.50	0.00	0.00	0.00	0.00	0.00	0.00	0.00	1.00
KER seg2	yes	Reverse	0.71	0.33	0.33	0.00	0.00	0.00	0.00	0.00	0.00	0.00	0.00	0.71

KER seg2	yes	Strslip	0.00	0.00	0.00	0.00	1.00	0.50	0.50	0.50	.	0.50	0.00	1.00
KUR seg1	no	All	.	.	.	.	.	.	.	.	.	.	0.00	0.00
KUR seg1	no	Normal	.	.	.	.	.	.	.	.	.	.	0.00	0.00
KUR seg1	no	Reverse	.	.	.	.	.	.	.	.	.	.	0.00	0.00
KUR seg1	no	Strslip	.	.	.	.	.	.	.	.	.	.	0.00	0.00
KUR seg1	yes	All	.	.	.	.	.	.	.	.	.	.	0.00	0.00
KUR seg1	yes	Normal	.	.	.	.	.	.	.	.	.	.	0.00	0.00
KUR seg1	yes	Reverse	.	.	.	.	.	.	.	.	.	.	0.00	0.00
KUR seg1	yes	Strslip	.	.	.	.	.	.	.	.	.	.	0.00	0.00
KUR seg2	no	All	0.71	0.50	0.33	0.50	0.50	0.50	1.00	1.00	1.00	0.50	0.33	1.00
KUR seg2	no	Normal	1.00	1.00	0.33	0.50	0.50	0.50	1.00	1.00	1.00	0.50	0.33	1.00
KUR seg2	no	Reverse	0.57	0.55	0.29	0.40	0.25	0.33	1.00	0.33	0.33	0.25	0.25	1.00
KUR seg2	no	Strslip	1.00	0.67	0.33	0.50	0.50	0.50	1.00	1.00	1.00	0.50	0.33	1.00
KUR seg2	yes	All	0.71	0.25	0.33	0.50	0.50	0.50	1.00	1.00	1.00	0.50	0.25	1.00
KUR seg2	yes	Normal	1.00	1.00	0.33	0.50	0.50	1.00	1.00	1.00	1.00	0.50	0.33	1.00
KUR seg2	yes	Reverse	0.56	0.50	0.43	0.50	0.29	0.33	0.50	0.50	0.50	0.25	0.25	0.56
KUR seg2	yes	Strslip	0.67	0.40	0.25	0.33	0.25	0.33	0.50	0.50	0.50	0.33	0.25	0.67
IZU seg1	no	All	0.00	0.00	0.00	0.25	0.00	0.00	0.00	0.33	0.50	0.00	0.00	0.50
IZU seg1	no	Normal	.	.	.	.	0.00	0.00	0.00	0.00	0.00	0.00	0.00	0.00
IZU seg1	no	Reverse	.	.	.	.	.	.	.	.	.	.	0.00	0.00
IZU seg1	no	Strslip	.	.	0.00	0.00	0.00	0.00	0.00	0.00	0.00	0.00	0.00	0.00
IZU seg1	yes	All	0.17	0.17	0.14	0.33	0.00	0.00	0.00	0.33	0.25	0.00	0.00	0.33
IZU seg1	yes	Normal	0.00	0.00	0.00	0.00	0.00	0.00	0.00	0.33	0.00	0.00	0.00	0.33
IZU seg1	yes	Reverse	.	.	.	.	.	.	.	.	.	.	0.00	0.00
IZU seg1	yes	Strslip	0.00	0.00	0.00	0.00	0.00	0.00	0.00	0.00	0.00	0.00	0.00	0.00
VAN seg1	no	All	1.00	1.00	1.00	1.00	1.00	1.00	1.00	1.00	1.00	1.00	1.00	1.00
VAN seg1	no	Normal	1.00	1.00	1.00	1.00	.	1.00	1.00	.	1.00	1.00	1.00	1.00
VAN seg1	no	Reverse	0.50	0.33	0.50	0.33	0.33	0.33	0.33	.	0.33	0.00	0.00	0.50
VAN seg1	no	Strslip	1.00	1.00	1.00	1.00	1.00	1.00	1.00	1.00	.	1.00	1.00	1.00
VAN seg1	yes	All	1.00	1.00	1.00	1.00	1.00	1.00	1.00	1.00	1.00	1.00	1.00	1.00
VAN seg1	yes	Normal	.	1.00	1.00	1.00	1.00	1.00	1.00	1.00	.	1.00	1.00	1.00
VAN seg1	yes	Reverse	0.33	0.25	0.33	0.25	0.50	0.00	0.00	0.00	0.00	0.33	0.00	0.50
VAN seg1	yes	Strslip	1.00	1.00	1.00	1.00	1.00	1.00	1.00	1.00	1.00	1.00	1.00	1.00
MEX seg1	no	All	1.00	0.33	0.50	1.00	0.00	0.00	0.00	0.00	0.00	0.00	0.00	1.00

MEX seg1	no	Normal	1.00	0.50	1.00	1.00	0.00	0.00	0.00	0.00	.	0.00	0.00	1.00
MEX seg1	no	Reverse	.	.	.	.	.	.	.	.	.	.	0.00	0.00
MEX seg1	no	Strslip	.	.	.	.	.	.	.	.	.	.	0.00	0.00
MEX seg1	yes	All	1.00	0.50	0.50	0.40	0.00	0.00	0.00	0.00	0.00	0.00	0.00	1.00
MEX seg1	yes	Normal	1.00	0.50	0.50	1.00	0.00	0.00	0.00	0.00	0.00	0.00	0.00	1.00
MEX seg1	yes	Reverse	.	.	.	.	.	.	.	.	.	.	0.00	0.00
MEX seg1	yes	Strslip	.	.	.	.	.	.	.	.	.	.	0.00	0.00
MEX seg2	no	All	0.00	0.50	0.50	0.00	0.00	0.00	0.00	0.00	0.00	0.00	0.00	0.50
MEX seg2	no	Normal	.	.	.	.	.	.	.	.	.	.	0.00	0.00
MEX seg2	no	Reverse	.	1.00	1.00	0.00	0.00	0.00	0.00	.	0.00	0.00	0.00	1.00
MEX seg2	no	Strslip	.	.	.	.	.	.	.	.	.	.	0.00	0.00
MEX seg2	yes	All	0.00	0.33	0.33	0.00	0.17	0.00	0.17	0.00	0.00	0.00	0.00	0.33
MEX seg2	yes	Normal	.	.	.	.	.	.	.	0.00	.	0.00	0.00	0.00
MEX seg2	yes	Reverse	.	1.00	1.00	1.00	0.50	0.50	0.50	0.33	0.00	0.50	0.00	1.00
MEX seg2	yes	Strslip	.	.	.	.	.	.	.	.	.	.	0.00	0.00
MEX seg3	no	All	0.00	0.00	0.00	0.00	0.00	0.00	0.33	0.50	0.50	0.00	0.00	0.50
MEX seg3	no	Normal	.	.	.	.	.	.	.	.	.	.	0.00	0.00
MEX seg3	no	Reverse	.	0.00	0.00	0.00	0.00	0.00	0.00	0.50	.	0.00	0.00	0.50
MEX seg3	no	Strslip	0.00	0.00	0.00	0.00	0.00	0.00	.	.	0.00	0.00	0.00	0.00
MEX seg3	yes	All	0.22	0.33	0.33	0.29	0.50	0.33	0.50	1.00	0.50	0.00	0.00	1.00
MEX seg3	yes	Normal	1.00	1.00	1.00	1.00	1.00	1.00	1.00	.	1.00	0.50	0.50	1.00
MEX seg3	yes	Reverse	0.00	0.50	1.00	0.50	1.00	1.00	1.00	1.00	0.00	0.00	0.00	1.00
MEX seg3	yes	Strslip	0.00	0.00	0.00	0.00	0.00	0.00	0.50	0.33	0.00	0.00	0.00	0.50
SUM seg1	no	All	.	.	.	.	.	.	.	.	.	.	0.00	0.00
SUM seg1	no	Normal	.	.	.	.	.	.	.	.	.	.	0.00	0.00
SUM seg1	no	Reverse	.	.	.	.	.	.	.	.	.	.	0.00	0.00
SUM seg1	no	Strslip	.	.	.	.	.	.	.	.	.	.	0.00	0.00
SUM seg1	yes	All	.	.	.	.	.	.	.	.	.	.	0.00	0.00
SUM seg1	yes	Normal	.	.	.	.	.	.	.	.	.	.	0.00	0.00
SUM seg1	yes	Reverse	.	.	.	.	.	.	.	.	.	.	0.00	0.00
SUM seg1	yes	Strslip	.	.	.	.	.	.	.	.	.	.	0.00	0.00
SUM seg2	no	All	.	.	.	.	.	.	.	.	.	.	0.00	0.00
SUM seg2	no	Normal	.	.	.	.	.	.	.	.	.	.	0.00	0.00
SUM seg2	no	Reverse	.	.	.	.	.	.	.	.	.	.	0.00	0.00

SUM seg2	no	Strslip	.	.	.	.	.	.	.	.	.	.	0.00	0.00
SUM seg2	yes	All	.	.	.	.	.	.	.	.	.	.	0.00	0.00
SUM seg2	yes	Normal	.	.	.	.	.	.	.	.	.	.	0.00	0.00
SUM seg2	yes	Reverse	.	.	.	.	.	.	.	.	.	.	0.00	0.00
SUM seg2	yes	Strslip	.	.	.	.	.	.	.	.	.	.	0.00	0.00
SUM seg3	no	All	1.00	1.00	1.00	1.00	1.00	1.00	1.00	1.00	1.00	1.00	1.00	1.00
SUM seg3	no	Normal	1.00	1.00	1.00	1.00	1.00	1.00	1.00	1.00	1.00	1.00	1.00	1.00
SUM seg3	no	Reverse	0.67	0.75	0.50	1.00	0.50	1.00	1.00	1.00	1.00	1.00	0.50	1.00
SUM seg3	no	Strslip	1.00	1.00	1.00	1.00	1.00	1.00	1.00	1.00	1.00	1.00	1.00	1.00
SUM seg3	yes	All	0.75	0.67	1.00	1.00	1.00	1.00	1.00	1.00	1.00	1.00	0.67	1.00
SUM seg3	yes	Normal	1.00	1.00	1.00	1.00	1.00	1.00	1.00	1.00	1.00	1.00	1.00	1.00
SUM seg3	yes	Reverse	0.60	0.75	0.67	0.67	0.50	1.00	1.00	0.67	1.00	1.00	0.50	1.00
SUM seg3	yes	Strslip	1.00	1.00	1.00	1.00	1.00	1.00	1.00	1.00	1.00	1.00	1.00	1.00
SAM seg1	no	All	1.00	1.00	1.00	1.00	1.00	1.00	1.00	1.00	1.00	1.00	1.00	1.00
SAM seg1	no	Normal	1.00	.	.	.	.	.	.	.	.	.	1.00	1.00
SAM seg1	no	Reverse	.	.	.	.	.	.	.	.	.	.	0.00	0.00
SAM seg1	no	Strslip	.	.	.	.	1.00	1.00	1.00	.	.	.	1.00	1.00
SAM seg1	yes	All	1.00	1.00	1.00	1.00	1.00	1.00	1.00	1.00	1.00	1.00	1.00	1.00
SAM seg1	yes	Normal	1.00	.	.	.	.	.	.	.	.	.	1.00	1.00
SAM seg1	yes	Reverse	0.00	0.00	0.50	0.00	0.33	0.00	0.00	0.00	0.00	0.00	0.00	0.50
SAM seg1	yes	Strslip	1.00	1.00	1.00	1.00	.	.	.	.	1.00	1.00	1.00	1.00
SAM seg2	no	All	0.00	0.00	0.00	0.00	0.00	.	.	0.00	0.00	.	0.00	0.00
SAM seg2	no	Normal	.	.	.	.	.	.	.	.	.	.	0.00	0.00
SAM seg2	no	Reverse	0.00	0.00	0.00	0.00	0.00	.	.	0.00	.	.	0.00	0.00
SAM seg2	no	Strslip	.	.	.	.	.	.	.	.	.	.	0.00	0.00
SAM seg2	yes	All	0.50	0.50	1.00	1.00	1.00	1.00	1.00	1.00	1.00	1.00	0.50	1.00
SAM seg2	yes	Normal	1.00	1.00	1.00	1.00	1.00	.	.	.	1.00	.	1.00	1.00
SAM seg2	yes	Reverse	0.00	0.00	0.00	0.50	.	0.00	.	1.00	.	.	0.00	1.00
SAM seg2	yes	Strslip	.	.	.	.	.	.	.	.	.	.	0.00	0.00
SAM seg3	no	All	0.00	0.00	0.33	0.50	0.33	0.50	0.50	1.00	1.00	1.00	0.00	1.00
SAM seg3	no	Normal	.	.	.	.	.	.	.	.	1.00	.	1.00	1.00
SAM seg3	no	Reverse	.	.	.	.	.	.	.	.	.	.	0.00	0.00
SAM seg3	no	Strslip	0.00	0.00	1.00	1.00	.	1.00	1.00	.	1.00	1.00	0.00	1.00
SAM seg3	yes	All	0.00	0.00	0.50	0.33	0.00	0.33	0.50	0.50	1.00	1.00	0.00	1.00

SAM seg3	yes	Normal	0.00	0.00	0.00	0.00	0.00	0.00	0.00	0.00	1.00	0.50	0.00	1.00
SAM seg3	yes	Reverse	.	0.00	0.00	0.00	0.00	.	0.00	0.00	0.00	.	0.00	0.00
SAM seg3	yes	Strslip	0.00	0.00	1.00	1.00	.	1.00	1.00	1.00	1.00	1.00	0.00	1.00
SAM seg4	no	All	0.00	0.00	0.00	0.00	0.00	0.00	0.00	0.00	0.00	0.00	0.00	0.00
SAM seg4	no	Normal	0.00	0.00	0.00	.	.	0.00	.	0.00	.	1.00	0.00	1.00
SAM seg4	no	Reverse	0.00	0.00	0.00	0.00	0.00	0.00	0.00	0.00	0.00	0.00	0.00	0.00
SAM seg4	no	Strslip	.	.	.	.	.	.	.	.	.	.	0.00	0.00
SAM seg4	yes	All	0.00	0.00	0.00	0.00	0.00	0.00	0.33	0.00	0.00	0.00	0.00	0.33
SAM seg4	yes	Normal	0.00	0.00	0.00	0.00	0.00	0.00	1.00	0.00	.	1.00	0.00	1.00
SAM seg4	yes	Reverse	0.00	0.00	0.00	0.00	0.00	0.00	.	0.00	0.00	0.00	0.00	0.00
SAM seg4	yes	Strslip	.	.	.	.	.	.	.	.	.	.	0.00	0.00

Table 7.5: Variation of ρMw using different bin sizes.

zone-seg	fix	type	Bin 100	Bin 200	Bin 300	Bin 400	Bin 500	Bin 600	Bin 700	Bin 800	Bin 900	Bin 1000	min	max
ALU seg1	no	All	0.33	0.45	0.33	0.44	0.33	0.20	0.20	0.40	0.50	0.40	0.20	0.50
ALU seg1	no	Normal	0.00	0.00	0.00	0.00	0.00	0.00	0.00	0.50	0.50	0.50	0.00	0.50
ALU seg1	no	Reverse	0.42	0.50	0.38	0.43	0.40	0.33	0.25	0.50	0.67	0.50	0.25	0.67
ALU seg1	no	Strslip	1.00	1.00	1.00	1.00	1.00	1.00	1.00	1.00	1.00	1.00	1.00	1.00
ALU seg1	yes	All	0.37	0.46	0.33	0.50	0.50	0.33	0.40	0.50	0.40	0.60	0.33	0.60
ALU seg1	yes	Normal	0.00	0.00	0.00	0.00	0.00	0.00	0.00	0.50	0.50	0.50	0.00	0.50
ALU seg1	yes	Reverse	0.43	0.50	0.40	0.50	0.40	0.43	0.25	0.50	0.67	0.50	0.25	0.67
ALU seg1	yes	Strslip	0.33	0.67	0.50	1.00	1.00	1.00	1.00	1.00	0.50	1.00	0.33	1.00
ALU seg2	no	All	0.25	0.40	0.25	0.25	0.00	0.33	0.00	0.50	0.67	0.33	0.00	0.67
ALU seg2	no	Normal	.	.	.	.	.	.	.	.	.	.	0.00	0.00
ALU seg2	no	Reverse	0.33	0.33	0.33	0.33	0.00	0.50	0.00	0.50	1.00	0.50	0.00	1.00
ALU seg2	no	Strslip	0.00	0.00	0.00	0.00	0.00	0.00	0.00	0.00	0.00	0.00	0.00	0.00
ALU seg2	yes	All	0.14	0.17	0.17	0.00	0.00	0.33	0.00	0.50	0.67	0.33	0.00	0.67
ALU seg2	yes	Normal	0.00	0.00	0.00	1.00	1.00	0.00	1.00	1.00	1.00	.	0.00	1.00
ALU seg2	yes	Reverse	0.17	0.20	0.20	0.00	0.00	0.50	0.00	0.50	1.00	0.50	0.00	1.00
ALU seg2	yes	Strslip	0.00	0.00	0.00	0.00	0.00	0.00	0.00	0.00	0.00	0.00	0.00	0.00
KER seg1	no	All	1.00	0.67	0.67	0.33	0.33	0.50	0.00	0.00	0.33	0.50	0.00	1.00
KER seg1	no	Normal	.	.	.	.	.	.	.	.	.	.	0.00	0.00
KER seg1	no	Reverse	0.00	0.00	0.00	0.00	0.00	0.00	0.00	0.00	0.00	0.00	0.00	0.00
KER seg1	no	Strslip	.	.	.	.	.	.	.	.	.	.	0.00	0.00
KER seg1	yes	All	0.38	0.50	0.25	0.29	0.17	0.25	0.25	0.20	0.33	0.25	0.17	0.50
KER seg1	yes	Normal	1.00	1.00	1.00	0.00	0.00	0.00	0.00	0.00	0.00	0.00	0.00	1.00
KER seg1	yes	Reverse	0.25	0.33	0.00	0.25	0.00	0.00	0.00	0.33	0.00	0.00	0.00	0.33
KER seg1	yes	Strslip	1.00	1.00	0.50	0.00	1.00	1.00	0.00	.	1.00	.	0.00	1.00
KER seg2	no	All	0.23	0.36	0.38	0.67	0.00	0.25	0.00	0.00	0.00	0.00	0.00	0.67
KER seg2	no	Normal	1.00	1.00	1.00	0.00	0.00	0.00	0.00	.	0.00	0.00	0.00	1.00
KER seg2	no	Reverse	0.33	0.50	0.50	0.75	0.33	0.50	0.00	0.00	0.00	0.00	0.00	0.75
KER seg2	no	Strslip	0.00	0.00	1.00	1.00	0.00	0.00	0.00	0.00	0.00	0.00	0.00	1.00
KER seg2	yes	All	0.23	0.45	0.44	0.50	0.50	0.50	0.40	0.20	0.00	0.50	0.00	0.50
KER seg2	yes	Normal	0.50	0.50	0.50	0.00	0.50	0.50	0.00	1.00	0.00	0.00	0.00	1.00
KER seg2	yes	Reverse	0.33	0.50	0.50	0.50	0.20	0.50	0.33	0.33	0.00	0.00	0.00	0.50

KER seg2	yes	Strslip	0.00	0.50	0.50	0.50	1.00	0.50	0.50	0.00	0.00	0.50	0.00	1.00
KUR seg1	no	All	.	.	.	.	.	.	.	.	.	.	0.00	0.00
KUR seg1	no	Normal	.	.	.	.	.	.	.	.	.	.	0.00	0.00
KUR seg1	no	Reverse	.	.	.	.	.	.	.	.	.	.	0.00	0.00
KUR seg1	no	Strslip	.	.	.	.	.	.	.	.	.	.	0.00	0.00
KUR seg1	yes	All	.	0.00	0.00	.	0.00	0.00	0.00	0.00	.	0.00	0.00	0.00
KUR seg1	yes	Normal	.	.	.	.	.	.	.	.	.	.	0.00	0.00
KUR seg1	yes	Reverse	.	.	.	.	.	.	.	.	.	.	0.00	0.00
KUR seg1	yes	Strslip	.	.	.	.	.	.	.	.	.	.	0.00	0.00
KUR seg2	no	All	0.38	0.42	0.25	0.40	0.20	0.17	0.25	0.25	0.33	0.33	0.17	0.42
KUR seg2	no	Normal	0.67	0.75	0.50	0.67	0.67	0.67	1.00	1.00	1.00	0.67	0.50	1.00
KUR seg2	no	Reverse	0.54	0.50	0.33	0.38	0.50	0.33	0.33	0.33	0.33	0.00	0.00	0.54
KUR seg2	no	Strslip	0.20	0.20	0.20	0.20	0.33	0.33	0.33	0.33	0.33	0.33	0.20	0.33
KUR seg2	yes	All	0.42	0.36	0.23	0.38	0.17	0.17	0.33	0.40	0.25	0.50	0.17	0.50
KUR seg2	yes	Normal	0.57	0.60	0.40	0.50	0.50	0.67	1.00	1.00	1.00	0.67	0.40	1.00
KUR seg2	yes	Reverse	0.59	0.64	0.33	0.38	0.17	0.20	0.33	0.25	0.00	0.25	0.00	0.64
KUR seg2	yes	Strslip	0.11	0.11	0.13	0.14	0.20	0.20	0.33	0.25	0.25	0.33	0.11	0.33
IZU seg1	no	All	0.40	0.40	0.40	0.25	0.50	0.50	0.00	0.50	0.67	0.50	0.00	0.67
IZU seg1	no	Normal	0.00	0.00	0.00	0.00	1.00	1.00	0.00	1.00	1.00	1.00	0.00	1.00
IZU seg1	no	Reverse	.	.	.	.	.	.	.	.	.	.	0.00	0.00
IZU seg1	no	Strslip	0.33	0.33	0.33	0.00	0.00	0.00	0.00	0.33	0.00	0.00	0.00	0.33
IZU seg1	yes	All	0.25	0.25	0.29	0.17	0.25	0.33	0.00	0.50	0.00	0.25	0.00	0.50
IZU seg1	yes	Normal	0.33	0.00	0.33	0.00	1.00	1.00	0.00	1.00	1.00	1.00	0.00	1.00
IZU seg1	yes	Reverse	.	.	.	.	.	.	.	.	.	.	0.00	0.00
IZU seg1	yes	Strslip	0.20	0.00	0.00	0.00	0.00	0.00	0.00	0.00	0.00	0.00	0.00	0.20
VAN seg1	no	All	1.00	0.67	0.67	0.67	0.67	0.50	1.00	1.00	1.00	1.00	0.50	1.00
VAN seg1	no	Normal	1.00	.	1.00	1.00	1.00	1.00	1.00	1.00	1.00	.	1.00	1.00
VAN seg1	no	Reverse	1.00	0.50	0.50	0.50	0.50	0.50	1.00	0.50	0.50	0.00	0.00	1.00
VAN seg1	no	Strslip	1.00	1.00	1.00	1.00	1.00	1.00	1.00	1.00	.	1.00	1.00	1.00
VAN seg1	yes	All	0.80	0.50	0.50	0.50	0.50	0.50	0.67	1.00	0.33	1.00	0.33	1.00
VAN seg1	yes	Normal	1.00	.	1.00	1.00	1.00	1.00	1.00	.	1.00	.	1.00	1.00
VAN seg1	yes	Reverse	0.75	0.50	0.50	0.33	0.33	0.33	0.67	0.33	0.33	0.00	0.00	0.75
VAN seg1	yes	Strslip	1.00	1.00	1.00	1.00	1.00	1.00	1.00	1.00	1.00	1.00	1.00	1.00
MEX seg1	no	All	0.00	0.00	0.33	0.33	0.00	0.00	0.00	0.50	1.00	1.00	0.00	1.00

MEX seg1	no	Normal	0.00	0.00	0.50	0.00	0.00	0.00	0.00	1.00	1.00	1.00	0.00	1.00
MEX seg1	no	Reverse	.	.	.	.	.	.	.	.	.	.	0.00	0.00
MEX seg1	no	Strslip	.	.	.	.	.	.	.	.	.	.	0.00	0.00
MEX seg1	yes	All	0.00	0.00	0.25	0.50	0.00	0.33	0.50	1.00	0.50	0.50	0.00	1.00
MEX seg1	yes	Normal	0.00	0.00	0.33	0.33	0.00	0.00	0.00	1.00	1.00	1.00	0.00	1.00
MEX seg1	yes	Reverse	0.00	0.00	0.00	.	0.00	1.00	1.00	1.00	0.00	0.00	0.00	1.00
MEX seg1	yes	Strslip	.	.	.	.	.	.	.	.	.	.	0.00	0.00
MEX seg2	no	All	0.00	0.00	0.00	0.00	0.00	0.00	0.00	0.00	0.00	0.00	0.00	0.00
MEX seg2	no	Normal	.	.	0.00	0.00	0.00	0.00	.	.	.	.	0.00	0.00
MEX seg2	no	Reverse	0.00	0.00	0.00	0.00	0.00	0.00	0.00	0.00	0.00	0.00	0.00	0.00
MEX seg2	no	Strslip	.	.	.	.	.	.	.	.	.	.	0.00	0.00
MEX seg2	yes	All	0.00	0.33	0.33	0.00	0.00	0.00	0.00	0.00	0.00	0.00	0.00	0.33
MEX seg2	yes	Normal	0.00	0.00	0.00	0.00	0.00	0.00	0.00	0.00	.	0.00	0.00	0.00
MEX seg2	yes	Reverse	0.00	0.00	0.00	0.00	0.00	0.00	0.00	0.00	0.00	0.00	0.00	0.00
MEX seg2	yes	Strslip	.	.	.	.	.	.	.	.	.	.	0.00	0.00
MEX seg3	no	All	0.17	0.20	0.33	0.40	0.50	0.50	0.33	0.50	0.00	0.00	0.00	0.50
MEX seg3	no	Normal	.	.	.	.	.	.	.	.	.	.	0.00	0.00
MEX seg3	no	Reverse	0.00	0.00	0.50	0.00	1.00	1.00	0.50	1.00	0.00	0.00	0.00	1.00
MEX seg3	no	Strslip	0.50	0.50	1.00	1.00	1.00	1.00	1.00	1.00	1.00	1.00	0.50	1.00
MEX seg3	yes	All	0.10	0.11	0.29	0.43	0.60	0.40	0.40	0.67	0.00	0.33	0.00	0.67
MEX seg3	yes	Normal	0.00	0.00	0.00	0.00	0.00	0.00	0.00	0.00	0.00	0.00	0.00	0.00
MEX seg3	yes	Reverse	0.00	0.00	0.33	0.00	0.50	0.50	0.50	0.50	0.00	0.00	0.00	0.50
MEX seg3	yes	Strslip	0.20	0.20	0.25	0.20	0.33	0.50	0.33	0.25	0.50	1.00	0.20	1.00
SUM seg1	no	All	.	.	.	.	.	.	.	.	.	.	0.00	0.00
SUM seg1	no	Normal	.	.	.	.	.	.	.	.	.	.	0.00	0.00
SUM seg1	no	Reverse	.	.	.	.	.	.	.	.	.	.	0.00	0.00
SUM seg1	no	Strslip	.	.	.	.	.	.	.	.	.	.	0.00	0.00
SUM seg1	yes	All	.	.	.	.	.	.	.	.	.	.	0.00	0.00
SUM seg1	yes	Normal	.	.	.	.	.	.	.	.	.	.	0.00	0.00
SUM seg1	yes	Reverse	.	.	.	.	.	.	.	.	.	.	0.00	0.00
SUM seg1	yes	Strslip	.	.	.	.	.	.	.	.	.	.	0.00	0.00
SUM seg2	no	All	.	.	.	.	.	.	.	.	.	.	0.00	0.00
SUM seg2	no	Normal	.	.	.	.	.	.	.	.	.	.	0.00	0.00
SUM seg2	no	Reverse	.	.	.	.	.	.	.	.	.	.	0.00	0.00

SUM seg2	no	Strslip	.	.	.	.	.	.	.	.	.	.	0.00	0.00
SUM seg2	yes	All	.	0.00	0.00	0.00	.	0.00	0.00	0.00	0.00	0.00	0.00	0.00
SUM seg2	yes	Normal	.	.	.	.	.	.	.	.	.	.	0.00	0.00
SUM seg2	yes	Reverse	.	.	0.00	0.00	0.00	0.00	0.00	0.00	0.00	.	0.00	0.00
SUM seg2	yes	Strslip	.	.	.	.	.	.	.	.	.	.	0.00	0.00
SUM seg3	no	All	0.19	0.11	0.17	0.27	0.11	0.22	0.38	0.20	0.17	0.33	0.11	0.38
SUM seg3	no	Normal	0.67	0.67	0.50	0.50	0.50	0.50	0.50	0.50	1.00	0.50	0.50	1.00
SUM seg3	no	Reverse	0.63	0.50	0.50	0.67	0.33	0.33	0.33	0.33	0.33	0.33	0.33	0.67
SUM seg3	no	Strslip	0.22	0.15	0.20	0.20	0.11	0.29	0.43	0.43	0.43	0.50	0.11	0.50
SUM seg3	yes	All	0.27	0.11	0.15	0.25	0.11	0.22	0.25	0.40	0.40	0.50	0.11	0.50
SUM seg3	yes	Normal	0.67	0.75	0.50	0.50	0.50	0.50	0.50	0.50	0.50	0.50	0.50	0.75
SUM seg3	yes	Reverse	0.56	0.50	0.40	0.50	0.25	0.50	0.50	0.50	0.50	0.50	0.25	0.56
SUM seg3	yes	Strslip	0.19	0.13	0.18	0.20	0.11	0.25	0.38	0.43	0.43	0.25	0.11	0.43
SAM seg1	no	All	1.00	1.00	1.00	1.00	1.00	1.00	1.00	1.00	1.00	1.00	1.00	1.00
SAM seg1	no	Normal	1.00	.	.	.	.	.	.	.	.	.	1.00	1.00
SAM seg1	no	Reverse	.	.	.	.	.	.	.	.	.	.	0.00	0.00
SAM seg1	no	Strslip	0.00	0.00	1.00	0.00	1.00	.	0.00	.	.	.	0.00	1.00
SAM seg1	yes	All	0.25	0.33	0.67	0.33	1.00	0.50	0.50	1.00	1.00	1.00	0.25	1.00
SAM seg1	yes	Normal	1.00	.	.	.	.	.	.	.	.	.	1.00	1.00
SAM seg1	yes	Reverse	0.00	0.00	0.00	0.00	0.00	0.00	0.00	0.00	0.00	0.00	0.00	0.00
SAM seg1	yes	Strslip	0.00	0.00	1.00	0.00	1.00	0.00	0.00	0.00	0.00	.	0.00	1.00
SAM seg2	no	All	0.00	0.00	0.00	0.00	0.00	0.00	.	0.00	0.00	.	0.00	0.00
SAM seg2	no	Normal	.	.	.	.	.	.	.	.	.	.	0.00	0.00
SAM seg2	no	Reverse	0.00	.	.	0.00	0.00	.	.	0.00	0.00	.	0.00	0.00
SAM seg2	no	Strslip	.	.	.	.	.	.	.	.	.	.	0.00	0.00
SAM seg2	yes	All	0.33	0.50	0.50	0.50	0.50	0.67	0.67	0.50	0.50	1.00	0.33	1.00
SAM seg2	yes	Normal	0.00	0.00	0.00	0.00	0.00	0.00	0.00	.	0.00	0.00	0.00	0.00
SAM seg2	yes	Reverse	0.00	0.00	0.00	0.50	0.00	0.00	1.00	1.00	0.00	.	0.00	1.00
SAM seg2	yes	Strslip	.	.	.	.	.	.	.	.	.	.	0.00	0.00
SAM seg3	no	All	0.00	0.00	0.00	0.00	0.00	0.00	0.00	0.00	0.00	0.00	0.00	0.00
SAM seg3	no	Normal	0.00	0.00	0.00	0.00	0.00	0.00	0.00	0.00	0.00	0.00	0.00	0.00
SAM seg3	no	Reverse	.	.	.	.	.	.	.	.	.	.	0.00	0.00
SAM seg3	no	Strslip	0.00	0.00	1.00	1.00	1.00	1.00	1.00	1.00	1.00	1.00	0.00	1.00
SAM seg3	yes	All	0.00	0.00	0.00	0.00	0.00	0.00	0.00	0.00	0.00	0.00	0.00	0.00

SAM seg3	yes	Normal	0.00	0.00	0.00	0.00	0.00	0.00	0.00	0.00	0.00	0.00	0.00	0.00
SAM seg3	yes	Reverse	0.00	0.00	0.00	0.00	0.00	.	0.00	0.00	0.00	.	0.00	0.00
SAM seg3	yes	Strslip	0.00	0.00	1.00	1.00	1.00	1.00	1.00	1.00	1.00	1.00	0.00	1.00
SAM seg4	no	All	0.00	0.00	0.00	0.00	0.00	0.00	0.00	0.00	0.00	0.00	0.00	0.00
SAM seg4	no	Normal	0.00	0.00	0.00	0.00	0.00	0.00	0.00	0.00	0.00	0.00	0.00	0.00
SAM seg4	no	Reverse	0.00	0.00	0.00	0.00	0.00	0.00	0.00	0.00	0.00	0.00	0.00	0.00
SAM seg4	no	Strslip	.	.	.	.	.	.	.	.	.	.	0.00	0.00
SAM seg4	yes	All	0.00	0.00	0.00	0.00	0.00	0.00	0.00	0.00	0.00	0.00	0.00	0.00
SAM seg4	yes	Normal	.	.	0.00	0.00	0.00	0.00	0.00	0.00	0.00	0.00	0.00	0.00
SAM seg4	yes	Reverse	0.00	0.00	0.00	0.00	0.00	0.00	0.00	0.00	0.00	0.00	0.00	0.00
SAM seg4	yes	Strslip	0.00	.	0.00	0.00	0.00	.	0.00	.	0.00	0.00	0.00	0.00

C.2 Supplementary figures: Geographic location of subduction segments analyzed in this study.

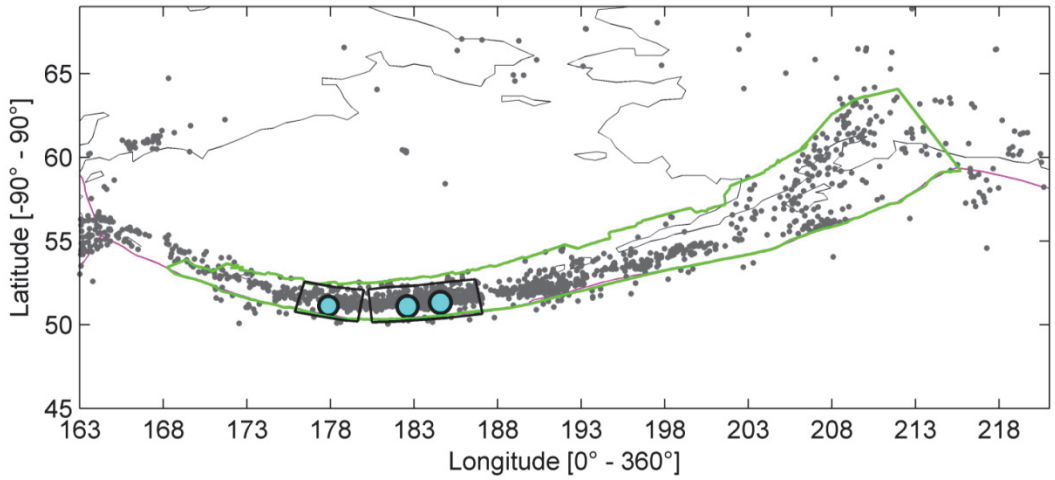

Figure 7.1: Map of the Alaska-Aleutians subduction region showing in light blue the epicenters of subduction earthquakes ≥ M_w 7.7 identified in the catalog (Table 4.1 in main manuscript). The black boxes are the near-field segments of those events. From right to left the segments are ALU_seg1 and ALU_seg2 (Table 4.2 in main manuscript). The green polygon encloses the boundary of the Slab1.0 model. In gray are shown the earthquakes recorded by the Global CMT catalog.

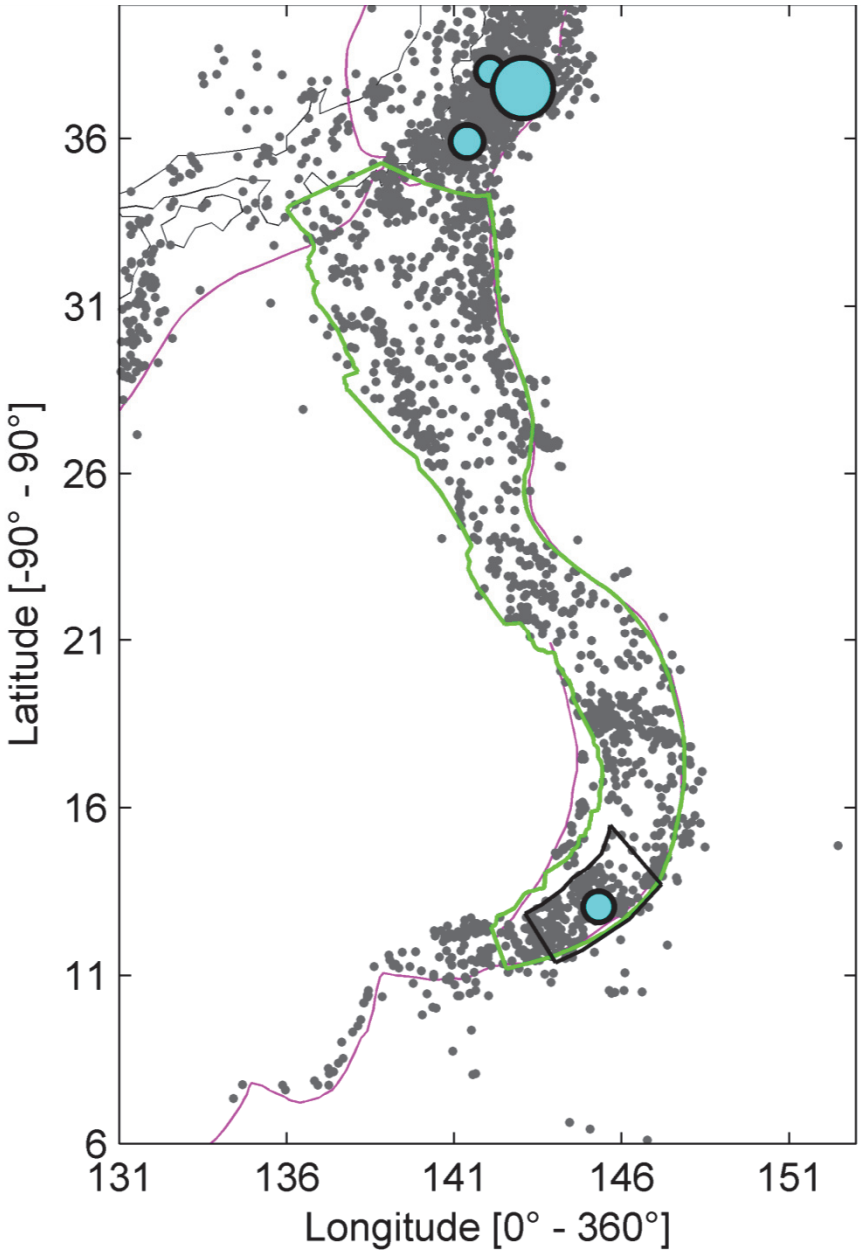

Figure 7.2: Map of the Izu-Bonin subduction region showing in light blue the epicenters of subduction earthquakes ≥ M_w 7.7 identified in the catalog (Table 4.1 in main manuscript). The black box is the near-field segment IZU_seg1 determined for the event (Table 4.2 in main manuscript). The green polygon encloses the boundary of the Slab1.0 model. In gray are shown the earthquakes recorded by the Global CMT catalog.

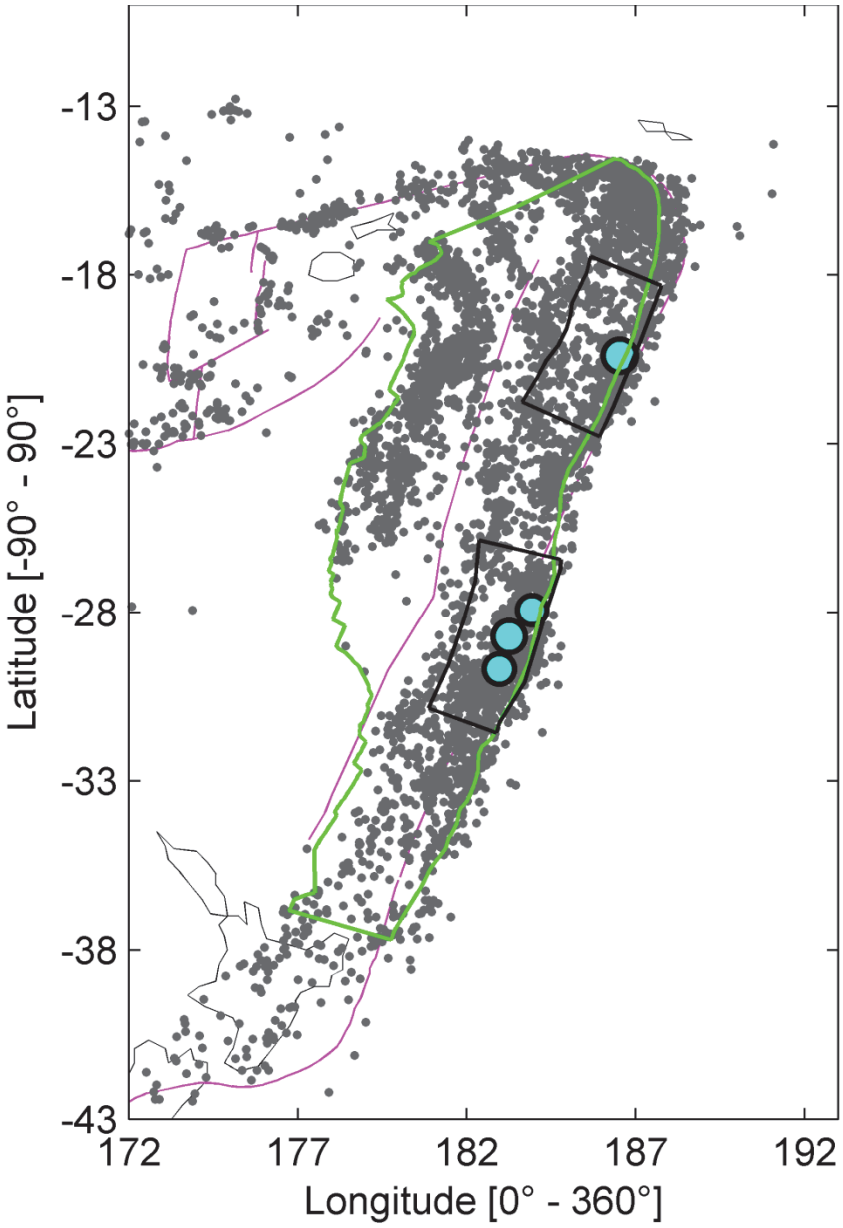

Figure 7.3: Map of the Kermadec-Tonga subduction region showing in light blue the epicenters of subduction earthquakes ≥ M_w 7.7 identified in the catalog (Table 4.1 in main manuscript). The black boxes are the near-field segments of those events. From top to bottom the segments are KER_seg1 and KER_seg2 (Table 4.2 in main manuscript).The green polygon encloses the boundary of the Slab1.0 model. In gray are shown the earthquakes recorded by the Global CMT catalog.

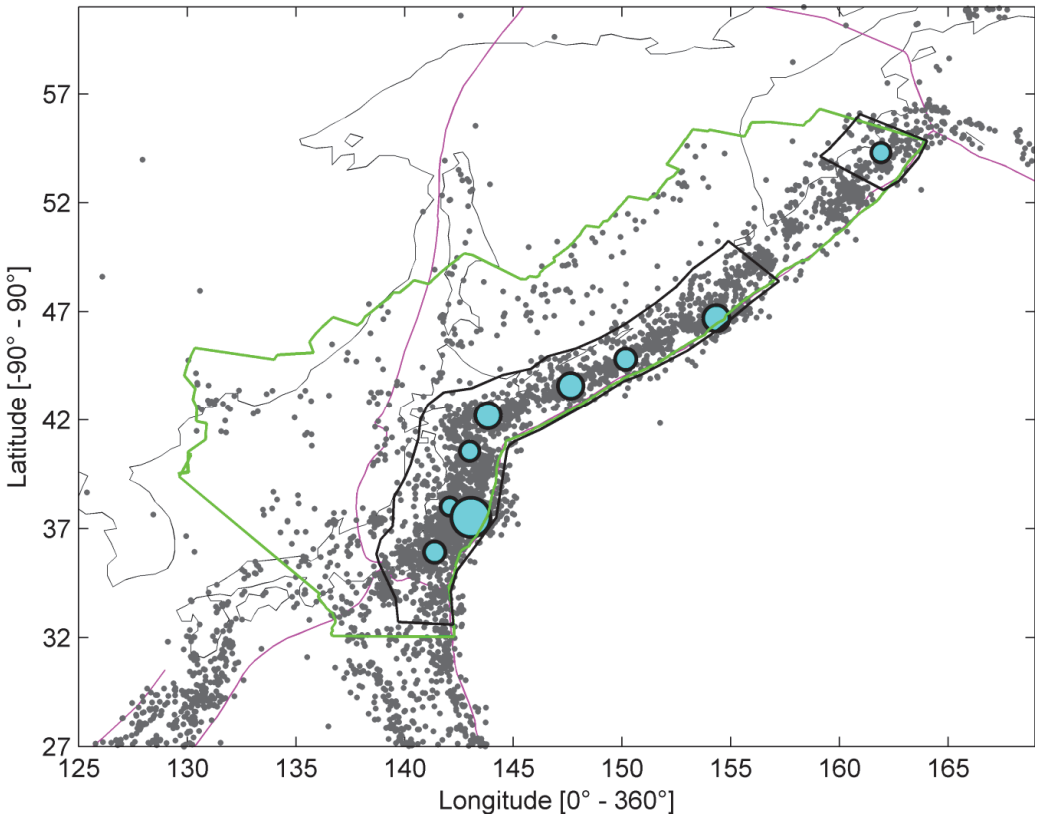

Figure 7.4: Map of the Kamchatka-Kurils-Japan subduction region showing in light blue the epicenters of subduction earthquakes ≥ M_w 7.7 identified in the catalog (Table 4.1 in main manuscript). The black boxes are the near-field segments of those events. From top to bottom the segments are KUR_seg1 and KUR_seg2 (Table 4.2 in main manuscript).The green polygon encloses the boundary of the Slab1.0 model. In gray are shown the earthquakes recorded by the Global CMT catalog.

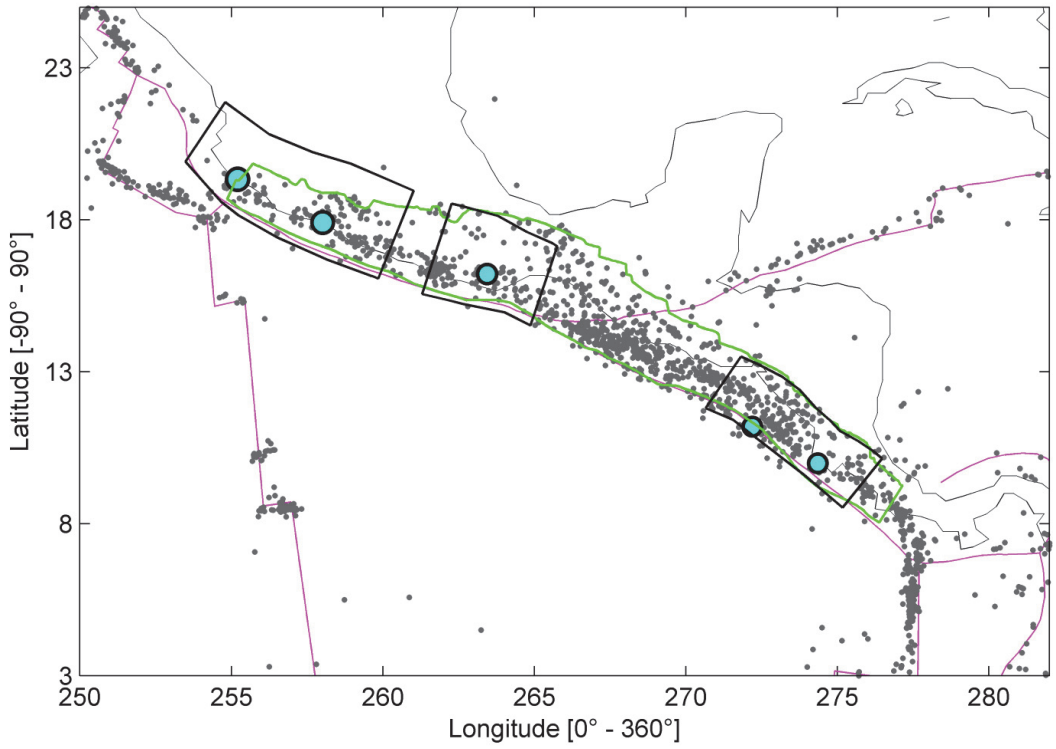

Figure 7.5: Map of the Central America subduction region showing in light blue the epicenters of subduction earthquakes ≥ M_w 7.7 identified in the catalog (Table 4.1 in main manuscript). The black boxes are the near-field segments of those events. From right to left the segments are MEX_seg1, MEX_seg2 and MEX_seg3 (Table 4.2 in main manuscript).The green polygon encloses the boundary of the Slab1.0 model. In gray are shown the earthquakes recorded by the Global CMT catalog.

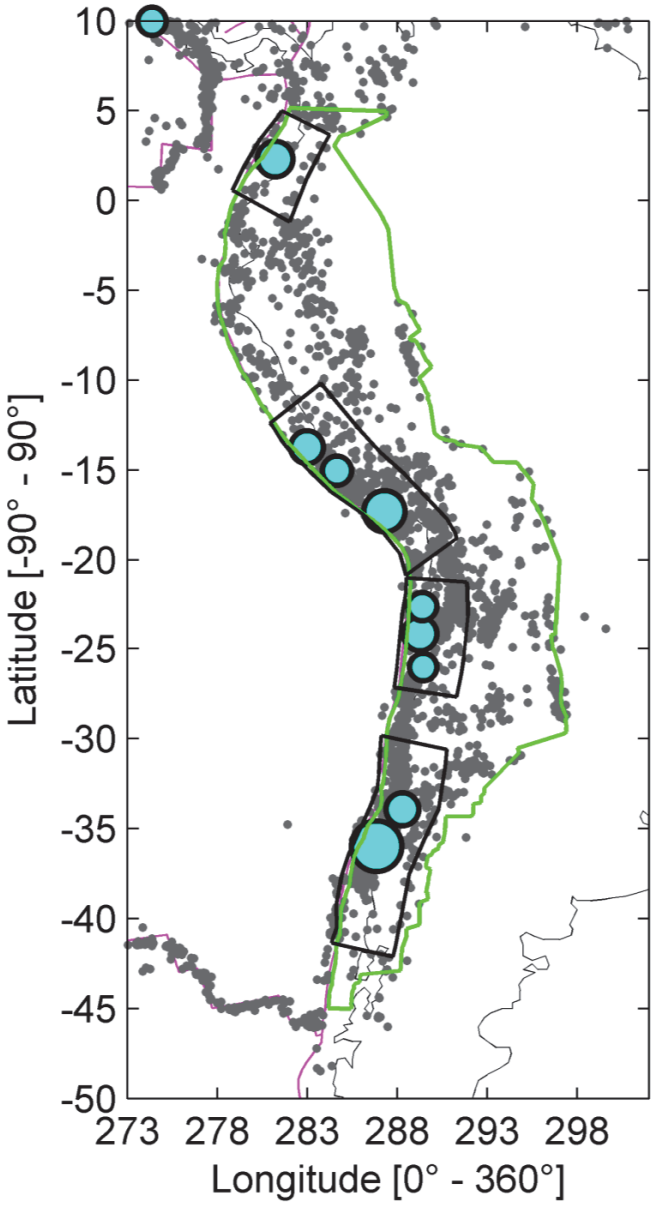

Figure 7.6: Map of the South America subduction region showing in light blue the epicenters of subduction earthquakes ≥ M_w 7.7 identified in the catalog (Table 4.1 in main manuscript). The black boxes are the near-field segments of those events. From bottom to top the segments are SAM_seg1, SAM_seg2, SAM_seg3 and SAM_seg4 (Table 4.2 in main manuscript).The green polygon encloses the boundary of the Slab1.0 model. In gray are shown the earthquakes recorded by the Global CMT catalog.

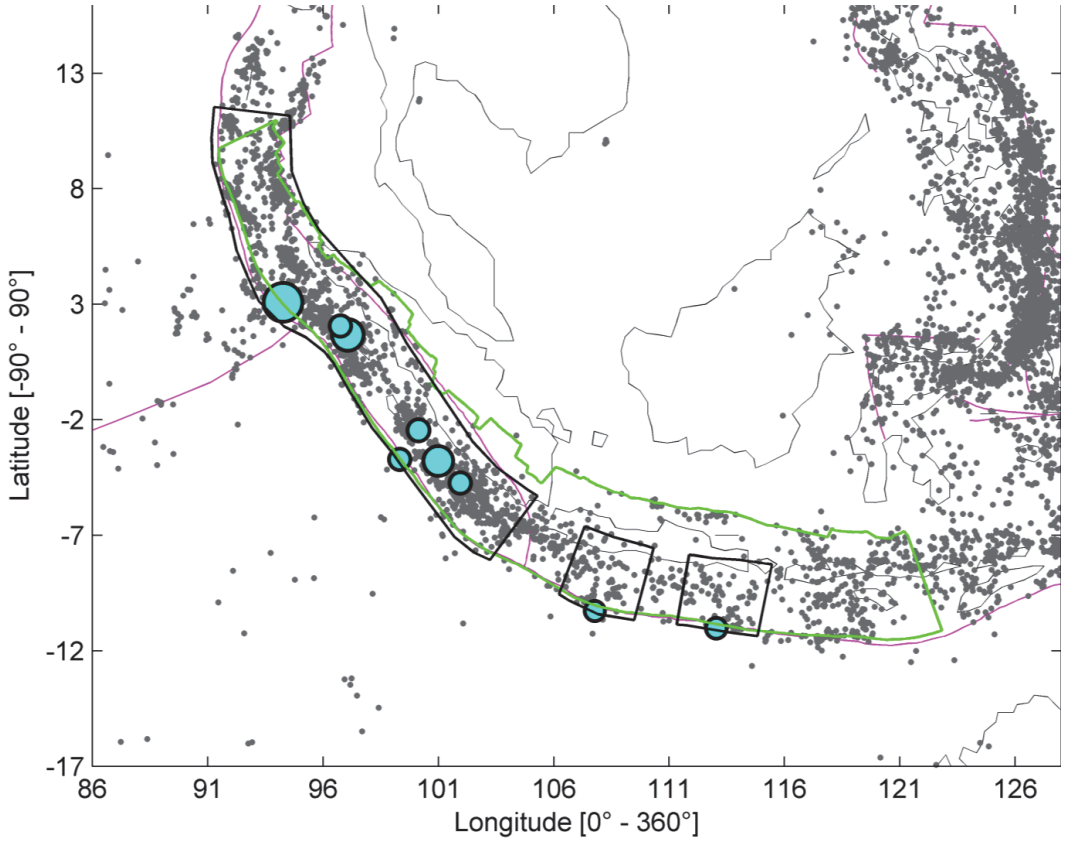

Figure 7.7: Map of the Sumatra-Java subduction region showing in light blue the epicenters of subduction earthquakes ≥ M_w 7.7 identified in the catalog (Table 4.1 in main manuscript). The black boxes are the near-field segments of those events. From right to left the segments are SUM_seg1, SUM_seg2, and SUM_seg3 (Table 4.2 in main manuscript).The green polygon encloses the boundary of the Slab1.0 model. In gray are shown the earthquakes recorded by the Global CMT catalog.

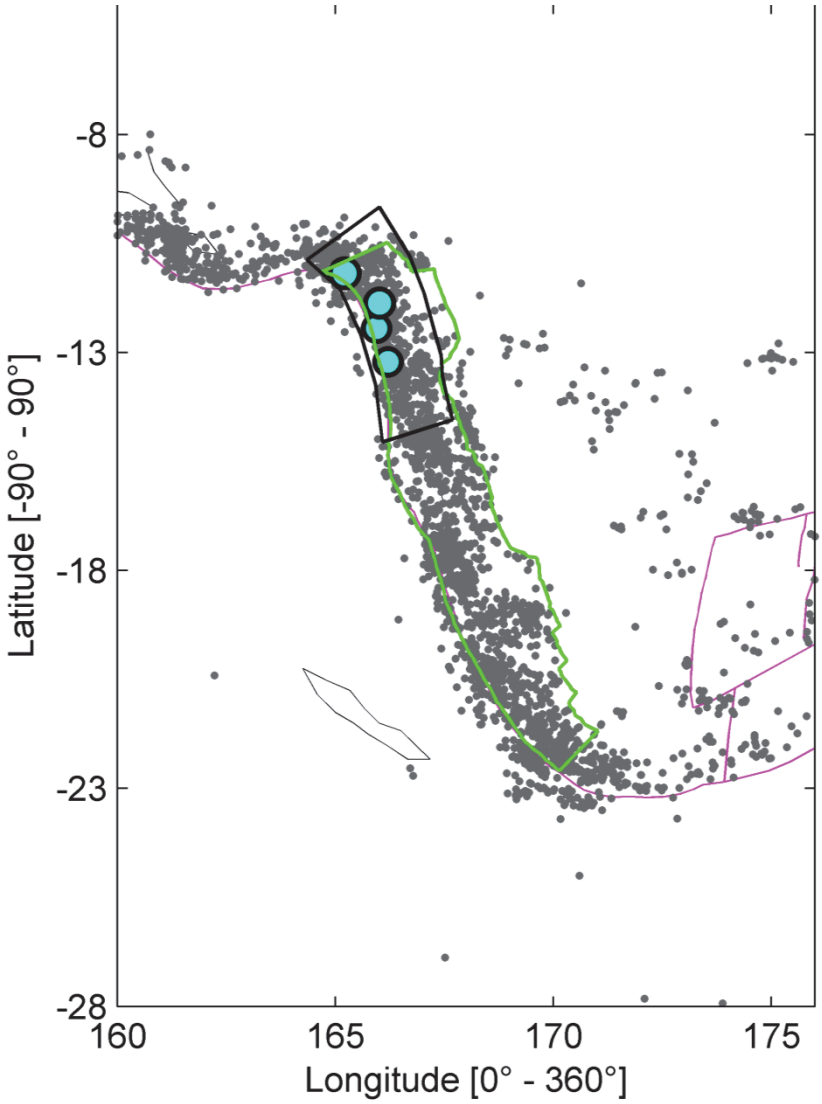

Figure 7.8: Map of the Santa Cruz Islands-Vanuatu-Loyalty Islands subduction region showing in light blue the epicenters of subduction earthquakes ≥ M_w 7.7 identified in the catalog (Table 4.1 in main manuscript). The black box is the near-field segment VAN_seg1 determined for the event (Table 4.2 in main manuscript). The green polygon encloses the boundary of the Slab1.0 model. In gray are shown the earthquakes recorded by the Global CMT catalog.

APPENDIX D

MATLAB CODES USED FOR ANALYSIS OF UPPER PLATE AND MEGATHRUST SEISMICITY OVER FOREARC REGIONS WORLDWIDE (SUPPLEMENTAL TO CHAPTER 4)

Over the course of my PhD I have produced numerous Matlab codes to resolve scientific problems involving extensive datasets as well as methods and algorithms used in structural geology and geophysics. Specifically in Chapter 4, all the processing and analysis of the seismic data from the Global CMT catalog was fully automated through a series of codes which I detail in the following section, providing the complete Matlab routines.

D.1 SolverEQsFilter.m

This routine is the main code used to filter the earthquakes from the Global CMT catalog that fall inside the SLAB1.0 regions. Also, the code is used to separate between upper plate events from earthquakes that fall inside the slab according to the geometries provided in this model. Parameters such as the depth tolerance above and below the SLAB1.0 surface, as well as angular tolerance of strike and dip of the megathrust plane can be modified in order to better discriminate events which location or geometry of their nodal planes may indicate subduction, thrust faulting. Inside SolverEQsFilter.m there are two functions, GetSlab1.m and cmt2slab.m which I will detailed in the next two sections. The code uses the data available at the SLAB1.0 webpage from the USGS: http://earthquake.usgs.gov/data/slab/.

```
clear all
close all

%Input data
file_slabdata='kur_slab1.0_clip.xyz';
file_slabstr='kur_slab1.0_strclip.xyz';
file_slabdip='kur_slab1.0_dipclip.xyz';
file_slaboutline='kur_slab1.0.clip';
file_allCMT='WorldCMT_jan1976_may2013_53cols.xls';
file_coordsyst='NED';
grid_elem=0.05;
halfwidth_slabUP=10;
% halfwidth_slabLP=25;
strike_tol=15;
dip_tol=15;
depth_seismo=65;

%The following goes into the names of the files depending on the
%seismogenic depth used for the upper plate, the upper tolerance
range
%above the Slab1.0 surface or upper half width, and strike and dip
%tolerance.
text_hwUP=num2str(halfwidth_slabUP);
text_seis=num2str(depth_seismo);
text_striketol=num2str(strike_tol);
text_diptol=num2str(dip_tol);
fileext='.dat';                     %Extensions of files to save

display(' ');
display(' ');
display([upper(file_slabdata(1:3)),' SLAB1.0 region']);
display('  Parameters used :');
display(['   * Depth seismogenic zone = ',text_seis,'km']);
display(['   * UP tol = ',text_hwUP,'km,',',  strike tol =
',text_striketol,...
    'deg,',',  dip tol = ',text_diptol,'deg']);


tic
display(' ');
display('1. Acquiring Slab1.0 data =');
%Get 5-column Slab Cell and Matrix containing lat, long, slab depth,
slab
%strike and slab dip inside the specific Slab1.0 region, consistent
with
%CMT coordinate system (NED system)
[SLABcell,SLABmat,OUT_NED]=GetSlab1(file_slabdata,file_slabstr,file_s
labdip,file_slaboutline);
toc

tic
display(' ');
display('2. Acquiring all EQs. inside the Slab1.0 region and plotting
=');
```

```
%Get 17-column cell and 15-column matrix of CMT earthquakes since
1976
%inside the specific Slab1.0 region. Column fields are:
%lat(1),lat_err(2),long(3),long_err(4),depth(5),depth_err(6),str1(7),
dip1
%(8),rake1(9),str2(10),dip2(11),rake2(12),sc(13),iexp(14),SerDate(15)
,date
%(16),DepthType(17). For now only works in NED coordinate system!
(which is
%the coordinate system reported by Global CMT).
[cmtslabCell,cmtslabMat]=cmt2slab(file_allCMT,file_slaboutline,file_c
oordsyst);
toc

tic
display(' ');
display('3. Creating main grid =');

%Limits of rectangular grid containing Sab1.0 region.
W_Limit=min(OUT_NED(:,2));
E_Limit=max(OUT_NED(:,2));
N_Limit=max(OUT_NED(:,1));
S_Limit=min(OUT_NED(:,1));

%Construct main grid for Slab1.0 region and 3 matrices with depth,
strike
%and dip of Slab (zi, stri, dipi).
[xi yi]=meshgrid((S_Limit-1):grid_elem:(N_Limit+1),(W_Limit-
1):grid_elem:(E_Limit+1));
zi=griddata(SLABmat(:,1),SLABmat(:,2),SLABmat(:,3),xi,yi);
stri=griddata(SLABmat(:,1),SLABmat(:,2),SLABmat(:,4),xi,yi);
dipi=griddata(SLABmat(:,1),SLABmat(:,2),SLABmat(:,5),xi,yi);
toc

nEQsVec=size(cmtslabCell);      %Number of EQs inside the Slab1.0
region
nEQs=nEQsVec(1);

%Main loop throughout all EQs inside Slab1.0 region to get logical
vector
%that separate UP events (logical vector component =1) from rest of
events
%(which are the intraslab)
logic_UP=zeros(nEQs,1);

tic
display(' ');
display('4. Main loop, filtering upper plate from slab events =');

for i=1:nEQs

    %%% PRE FILTER CALCULATIONS

    %Slab depth at ith EQ epicenter location
```

```
    z_epi=interp2(xi,yi,zi,cmtslabMat(i,8),cmtslabMat(i,43));
    %Strike Slab at ith EQ epicenter location
    str_epi=interp2(xi,yi,stri,cmtslabMat(i,8),cmtslabMat(i,43));
    %Dip Slab at ith EQ epicenter location
    dip_epi=interp2(xi,yi,dipi,cmtslabMat(i,8),cmtslabMat(i,43));
    %Dip direction Slab at ith EQ epicenter location
    dipdir_epi=str_epi+90;
    if dipdir_epi>360
        dipdir_epi=dipdir_epi-360;
    end

    dipdirCMT1=cmtslabMat(i,37)+90;  %Dip direction plane 1 of ithEQ
    if dipdirCMT1>360
        dipdirCMT1=dipdirCMT1-360;
    end
    dipdirCMT2=cmtslabMat(i,40)+90; %Dip direction plane 2 of ithEQ
    if dipdirCMT2>360
        dipdirCMT2=dipdirCMT2-360;
    end

    %Absolute difference between ithEQ dip and Slab dip at ithEQ
epicenter
    %location for both nodal planes
    dipdiff1=abs(dip_epi-cmtslabMat(i,38));
    dipdiff2=abs(dip_epi-cmtslabMat(i,41));

    %Absolute difference between ithEQ dip direction and Slab dip
    %direction at ithEQ epicenter location for both nodal planes
    dipdirdiff1=abs(dipdir_epi-dipdirCMT1);
    if dipdirdiff1>180
        dipdirdiff1=360-dipdirdiff1;
    end
    dipdirdiff2=abs(dipdir_epi-dipdirCMT2);
    if dipdirdiff2>180
        dipdirdiff2=360-dipdirdiff2;
    end



    %%% FILTER OF UPPER PLATE EARTHQUAKES

    %Filter out from UP for very shallow Slab regions.
    if z_epi<=halfwidth_slabUP
        logic_UP(i)=0;

    %Filter out earthquakes deeper than seismogenic zone defined by
input
    %depth
    elseif cmtslabMat(i,12)>=depth_seismo
        logic_UP(i)=0;

    %Filter out earthquakes deeper than slab depth
    elseif cmtslabMat(i,12)>=z_epi
        logic_UP(i)=0;
```

```
    %Filter in very shallow events compared to Slab depth
    elseif cmtslabMat(i,12)<=(z_epi-
(halfwidth_slabUP+(halfwidth_slabUP/2)))
        logic_UP(i)=1;

    %Filter in or out events shallower than upper limit of Slab
depending
    %on their kinematics (normal=negative rake) and geometry of
thrust
    %focal mechanisms which coincide approximately with geomotry of
Slab
    %(strike and dip)
    elseif cmtslabMat(i,12)<=(z_epi-halfwidth_slabUP)
        if cmtslabMat(i,39)<0 || cmtslabMat(i,42)<0      %rakes
            logic_UP(i)=1;
        else
            %Events with similar fault geometry to Slab
            if (dipdiff1<=dip_tol && dipdirdiff1<=strike_tol) ||...
                    (dipdiff2<=dip_tol && dipdirdiff2<=strike_tol)
                logic_UP(i)=0;
            else
                logic_UP(i)=1;
            end
        end
%     elseif cmtslabMat(i,5)>(z_epi-
(halfwidth_slabUP+(halfwidth_slabUP/2)))...
%             && cmtslabMat(i,5)<=(z_epi-halfwidth_slabUP)

    %Filter in normal events above the slab plus half of the
half_width
    %inputed
    elseif (cmtslabMat(i,12)<=(z_epi-(halfwidth_slabUP/2))) &&...
            (cmtslabMat(i,39)<0 || cmtslabMat(i,42)<0)
        logic_UP(i)=1;

    else
        logic_UP(i)=0;
    end

end
logic_UP=logical(logic_UP);
toc

tic
display(' ');
display('5. Creating final data matrices =');

%Upper plate earthquakes
CMT_SLAB_UP=cmtslabCell(logic_UP,:);
nEQsUP_Vec=size(CMT_SLAB_UP);
nEQsUP=nEQsUP_Vec(1);
CMT_SLAB_UP_mat=[cell2mat(CMT_SLAB_UP(:,4:8)),...
    cell2mat(CMT_SLAB_UP(:,10:17)),cell2mat(CMT_SLAB_UP(:,19:53))];
```

```
%Slab earthquakes all
CMT_SLAB_SLAB=cmtslabCell(~logic_UP,:);
nEQsSLAB_Vec=size(CMT_SLAB_SLAB);
nEQsSLAB=nEQsSLAB_Vec(1);
CMT_SLAB_SLABmat=[cell2mat(CMT_SLAB_SLAB(:,4:8)),...

cell2mat(CMT_SLAB_SLAB(:,10:17)),cell2mat(CMT_SLAB_SLAB(:,19:53))];

%Slab earthquakes above seismogenic zone
Slab_above_seismo=CMT_SLAB_SLABmat(:,12)<=depth_seismo;
CMT_SLAB_SEIS=CMT_SLAB_SLAB(Slab_above_seismo,:);
nEQsSLABseism_Vec=size(CMT_SLAB_SEIS);
nEQsSLABseism=nEQsSLABseism_Vec(1);
CMT_SLAB_SEISmat=[cell2mat(CMT_SLAB_SEIS(:,4:8)),...

cell2mat(CMT_SLAB_SEIS(:,10:17)),cell2mat(CMT_SLAB_SEIS(:,19:53))];

toc


% figure
%
plot(OUT_NED(:,2),OUT_NED(:,1),cmtslabMat(:,3),cmtslabMat(:,1),'.g');

% Check:
% http://stackoverflow.com/questions/5212573/saving-matlab-graphs-in-
a-specific-resolution
% http://www.mathworks.com/matlabcentral/fileexchange/23629
% https://sites.google.com/site/oliverwoodford/software/export_fig

% Change ceil for round


%%% CREATING FIGURES AND SAVING FIGURE FILES
tic
display(' ');
display('6. Ploting and saving figures =');

h1=figure;
plot(OUT_NED(:,2),OUT_NED(:,1),'k',CMT_SLAB_UP_mat(:,43),CMT_SLAB_UP_
mat(:,8),'.r');
axis([round(W_Limit-5) round(E_Limit+5) round(S_Limit-5)
round(N_Limit+5)])
daspect([1 1 1])
grid on
title({['Upper Plate EQs Jan1976-Apr2013.
',upper(file_slabdata(1:3)),' Slab1.0'];...
    ['(tolUP:',text_hwUP,', seisdepth:',text_seis,',
tolstr:',text_striketol,', toldip:',text_diptol,')']})
xlabel('Longitude (0 to 360° scale)')
ylabel('Latitude (-90 to 90° scale)')
set(gca,'XTick',round(W_Limit-5):5:round(E_Limit+5))
```

```
set(gca,'YTick',round(S_Limit-5):5:round(N_Limit+5))

%The following is from Emma's post in:
%http://www.mathworks.com/matlabcentral/newsreader/view_thread/314017
%check also:
%http://stackoverflow.com/questions/5150802/how-to-save-a-plot-into-
a-pdf-file-without-a-large-margin-around
%and:
%http://www.mathworks.com/help/matlab/creating_plots/automatic-axes-
resize.html#f1-32665
ti = get(gca,'TightInset');
set(gca,'Position',[ti(1) ti(2) 1-ti(3)-ti(1) 1-ti(4)-ti(2)]);
set(gca,'units','centimeters')
pos = get(gca,'Position');
ti = get(gca,'TightInset');
set(gcf, 'PaperUnits','centimeters');
set(gcf, 'PaperSize', [pos(3)+ti(1)+ti(3) pos(4)+ti(2)+ti(4)]);
set(gcf, 'PaperPositionMode', 'manual');
set(gcf, 'PaperPosition',[0 0 pos(3)+ti(1)+ti(3)
pos(4)+ti(2)+ti(4)]);

%Saving figures h1
saveas(h1,['CMT_',upper(file_slaboutline(1:3)),'_tolUP',text_hwUP,'_s
eisdepth',...

text_seis,'_tolstr',text_striketol,'_toldip',text_diptol,'_UP.fig'],'
fig')
print(h1,'-
depsc',['CMT_',upper(file_slaboutline(1:3)),'_tolUP',text_hwUP,'_seis
depth',...
    text_seis,'_tolstr',text_striketol,'_toldip',text_diptol,'_UP'])
print(h1,'-dtiff','-
r600',['CMT_',upper(file_slaboutline(1:3)),'_tolUP',text_hwUP,'_seisd
epth',...
    text_seis,'_tolstr',text_striketol,'_toldip',text_diptol,'_UP'])

% W_Limit=min(OUT_NED(:,2));
% E_Limit=max(OUT_NED(:,2));
% N_Limit=max(OUT_NED(:,1));
% S_Limit=min(OUT_NED(:,1));



h2=figure;
plot(OUT_NED(:,2),OUT_NED(:,1),'k',CMT_SLAB_SEISmat(:,43),CMT_SLAB_SE
ISmat(:,8),'.b');
axis([round(W_Limit-5) round(E_Limit+5) round(S_Limit-5)
round(N_Limit+5)])
daspect([1 1 1])
grid on
title({['Lower Plate EQs Jan1976-Apr2013.
',upper(file_slabdata(1:3)),' Slab1.0'];...
    ['(tolUP:',text_hwUP,', seisdepth:',text_seis,',
tolstr:',text_striketol,', toldip:',text_diptol,')']})
xlabel('Longitude (0 to 360° scale)')
```

```
ylabel('Latitude (-90 to 90° scale)')
set(gca,'XTick',round(W_Limit-5):5:round(E_Limit+5))
set(gca,'YTick',round(S_Limit-5):5:round(N_Limit+5))

%Same than h1
ti = get(gca,'TightInset');
set(gca,'Position',[ti(1) ti(2) 1-ti(3)-ti(1) 1-ti(4)-ti(2)]);
set(gca,'units','centimeters')
pos = get(gca,'Position');
ti = get(gca,'TightInset');
set(gcf, 'PaperUnits','centimeters');
set(gcf, 'PaperSize', [pos(3)+ti(1)+ti(3) pos(4)+ti(2)+ti(4)]);
set(gcf, 'PaperPositionMode', 'manual');
set(gcf, 'PaperPosition',[0 0 pos(3)+ti(1)+ti(3)
pos(4)+ti(2)+ti(4)]);

%Saving figures h2
saveas(h2,['CMT_',upper(file_slaboutline(1:3)),'_tolUP',text_hwUP,'_s
eisdepth',...

text_seis,'_tolstr',text_striketol,'_toldip',text_diptol,'_LP.fig'],'
fig')
print(h2,'-
depsc',['CMT_',upper(file_slaboutline(1:3)),'_tolUP',text_hwUP,'_seis
depth',...
    text_seis,'_tolstr',text_striketol,'_toldip',text_diptol,'_LP'])
print(h2,'-dtiff','-
r600',['CMT_',upper(file_slaboutline(1:3)),'_tolUP',text_hwUP,'_seisd
epth',...
    text_seis,'_tolstr',text_striketol,'_toldip',text_diptol,'_LP'])


h3=figure;
plot(OUT_NED(:,2),OUT_NED(:,1),'k',CMT_SLAB_SLABmat(:,43),CMT_SLAB_SL
ABmat(:,8),'.b');
axis([round(W_Limit-5) round(E_Limit+5) round(S_Limit-5)
round(N_Limit+5)])
daspect([1 1 1])
grid on
title({['Lower Plate EQs Jan1976-Apr2013.
',upper(file_slabdata(1:3)),' Slab1.0'];...
    ['(tolUP:',text_hwUP,', tolstr:',text_striketol,',
toldip:',text_diptol,')']})
xlabel('Longitude (0 to 360° scale)')
ylabel('Latitude (-90 to 90° scale)')
set(gca,'XTick',round(W_Limit-5):5:round(E_Limit+5))
set(gca,'YTick',round(S_Limit-5):5:round(N_Limit+5))

%Same than h1
ti = get(gca,'TightInset');
set(gca,'Position',[ti(1) ti(2) 1-ti(3)-ti(1) 1-ti(4)-ti(2)]);
set(gca,'units','centimeters')
pos = get(gca,'Position');
ti = get(gca,'TightInset');
```

```
set(gcf, 'PaperUnits','centimeters');
set(gcf, 'PaperSize', [pos(3)+ti(1)+ti(3) pos(4)+ti(2)+ti(4)]);
set(gcf, 'PaperPositionMode', 'manual');
set(gcf, 'PaperPosition',[0 0 pos(3)+ti(1)+ti(3)
pos(4)+ti(2)+ti(4)]);

%Saving figures h3
saveas(h3,['CMT_',upper(file_slaboutline(1:3)),'_tolUP',text_hwUP,'_t
olstr',...
    text_striketol,'_toldip',text_diptol,'_LP.fig'],'fig')
print(h3,'-
depsc',['CMT_',upper(file_slaboutline(1:3)),'_tolUP',text_hwUP,'_tols
tr',...
    text_striketol,'_toldip',text_diptol,'_LP'])
print(h3,'-dtiff','-
r600',['CMT_',upper(file_slaboutline(1:3)),'_tolUP',text_hwUP,'_tolst
r',...
    text_striketol,'_toldip',text_diptol,'_LP'])

toc

% figure
%
plot(OUT_NED(:,2),OUT_NED(:,1),CMT_SLAB_SL_mat(:,3),CMT_SLAB_SL_mat(:
,1),'.k');


%%% SAVING DATA FILES
tic
display(' ');
display('7. Saving files =');

filename1 = ['CMT_',upper(file_slaboutline(1:3)),'_allEQs',fileext];
fid1 = fopen(filename1, 'w');
fprintf(fid1,...

'%s\t%s\t%s\t%s\t%s\t%s\t%s\t%s\t%s\t%s\t%s\t%s\t%s\t%s\t%s\t%s\t%s\t%s\t
%s\t%s\t%s\t%s\t%s\t%s\t%s\t%s\t%s\t%s\t%s\t%s\t%s\t%s\t%s\t%s\t%s\t%s\t%
s\t%s\t%s\t%s\t%s\t%s\t%s\t%s\t%s\t%s\t%s\t%s\t%s\t%s\t%s\t%s\t%s\t%s\t%s
\t%s\n',...

'catalog','date','time','lat','long','depth','M1','M2','name','c_time
',...

'c_time_err','c_lat','c_lat_err','c_long','c_long_err','c_depth','c_d
epth_err',...

'depth_type','iexp','Mrr','Mrr_err','Mtt','Mtt_err','Mpp','Mpp_err','
Mrt',...

'Mrt_err','Mrp','Mrp_err','Mtp','Mtp_err','eval1','plg1','azi1','eval
2',...
```

```
'plg2','azi2','eval3','plg3','azi3','sc','str1','dip1','rake1','str2'
,'dip2',...
    'rake2','c_longAZI','SerDate','Mo','Mo_err','Mw','Mw_err');

for row1=1:nEQs
    fprintf(fid1, ...

'%s\t%s\t%s\t%4.2f\t%4.2f\t%4.2f\t%4.1f\t%4.1f\t%s\t%4.2f\t%4.2f\t%4.
2f\t%4.2f\t%4.2f\t%4.2f\t%4.2f\t%4.2f\t%s\t%d\t%4.2f\t%4.2f\t%4.2f\t%
4.2f\t%4.2f\t%4.2f\t%4.2f\t%4.2f\t%4.2f\t%4.2f\t%4.2f\t%4.2f\t%4.2f\t
%3d\t%3d\t%4.2f\t%3d\t%3d\t%4.2f\t%3d\t%3d\t%4.2f\t%3d\t%3d\t%3d\t%3d
\t%3d\t%3d\t%4.2f\t%8d\t%4.3f\t%4.3f\t%4.3f\t%4.3f\n', ...
        cmtslabCell{row1,:});
end
fclose(fid1);


filename2 =
['CMT_',upper(file_slaboutline(1:3)),'_tolUP',text_hwUP,'_seisdepth',
...

text_seis,'_tolstr',text_striketol,'_toldip',text_diptol,'_UP',fileex
t];
fid2 = fopen(filename2, 'w');
fprintf(fid2,...

'%s\t%s\t%s\t%s\t%s\t%s\t%s\t%s\t%s\t%s\t%s\t%s\t%s\t%s\t%s\t%s\t%s\t%s\t
%s\t%s\t%s\t%s\t%s\t%s\t%s\t%s\t%s\t%s\t%s\t%s\t%s\t%s\t%s\t%s\t%s\t%s\t%
s\t%s\t%s\t%s\t%s\t%s\t%s\t%s\t%s\t%s\t%s\t%s\t%s\t%s\t%s\t%s\t%s\t%s\t%s
\t%s\n',...

'catalog','date','time','lat','long','depth','M1','M2','name','c_time
',...

'c_time_err','c_lat','c_lat_err','c_long','c_long_err','c_depth','c_d
epth_err',...

'depth_type','iexp','Mrr','Mrr_err','Mtt','Mtt_err','Mpp','Mpp_err','
Mrt',...

'Mrt_err','Mrp','Mrp_err','Mtp','Mtp_err','eval1','plg1','azi1','eval
2',...

'plg2','azi2','eval3','plg3','azi3','sc','str1','dip1','rake1','str2'
,'dip2',...
    'rake2','c_longAZI','SerDate','Mo','Mo_err','Mw','Mw_err');

for row2=1:nEQsUP
    fprintf(fid2, ...

'%s\t%s\t%s\t%4.2f\t%4.2f\t%4.2f\t%4.1f\t%4.1f\t%s\t%4.2f\t%4.2f\t%4.
2f\t%4.2f\t%4.2f\t%4.2f\t%4.2f\t%4.2f\t%s\t%d\t%4.2f\t%4.2f\t%4.2f\t%
4.2f\t%4.2f\t%4.2f\t%4.2f\t%4.2f\t%4.2f\t%4.2f\t%4.2f\t%4.2f\t%4.2f\t
```

```
%3d\t%3d\t%4.2f\t%3d\t%3d\t%4.2f\t%3d\t%3d\t%4.2f\t%3d\t%3d\t%3d\t%3d
\t%3d\t%3d\t%4.2f\t%8d\t%4.3f\t%4.3f\t%4.3f\t%4.3f\n', ...
        CMT_SLAB_UP{row2,:});
end
fclose(fid2);


filename3 =
['CMT_',upper(file_slaboutline(1:3)),'_tolUP',text_hwUP,'_seisdepth',
...

text_seis,'_tolstr',text_striketol,'_toldip',text_diptol,'_LP',fileex
t];
fid3 = fopen(filename3, 'w');
fprintf(fid3,...

'%s\t%s\t%s\t%s\t%s\t%s\t%s\t%s\t%s\t%s\t%s\t%s\t%s\t%s\t%s\t%s\t%s\t%s\t
%s\t%s\t%s\t%s\t%s\t%s\t%s\t%s\t%s\t%s\t%s\t%s\t%s\t%s\t%s\t%s\t%s\t%s\t%
s\t%s\t%s\t%s\t%s\t%s\t%s\t%s\t%s\t%s\t%s\t%s\t%s\t%s\t%s\t%s\t%s\t%s\t%s
\t%s\n',...

'catalog','date','time','lat','long','depth','M1','M2','name','c_time
',...

'c_time_err','c_lat','c_lat_err','c_long','c_long_err','c_depth','c_d
epth_err',...

'depth_type','iexp','Mrr','Mrr_err','Mtt','Mtt_err','Mpp','Mpp_err','
Mrt',...

'Mrt_err','Mrp','Mrp_err','Mtp','Mtp_err','eval1','plg1','azi1','eval
2',...

'plg2','azi2','eval3','plg3','azi3','sc','str1','dip1','rake1','str2'
,'dip2',...
    'rake2','c_longAZI','SerDate','Mo','Mo_err','Mw','Mw_err');
for row3=1:nEQsSLABseism
    fprintf(fid3, ...

'%s\t%s\t%s\t%4.2f\t%4.2f\t%4.2f\t%4.1f\t%4.1f\t%s\t%4.2f\t%4.2f\t%4.
2f\t%4.2f\t%4.2f\t%4.2f\t%4.2f\t%4.2f\t%s\t%d\t%4.2f\t%4.2f\t%4.2f\t%
4.2f\t%4.2f\t%4.2f\t%4.2f\t%4.2f\t%4.2f\t%4.2f\t%4.2f\t%4.2f\t%4.2f\t
%3d\t%3d\t%4.2f\t%3d\t%3d\t%4.2f\t%3d\t%3d\t%4.2f\t%3d\t%3d\t%3d\t%3d
\t%3d\t%3d\t%4.2f\t%8d\t%4.3f\t%4.3f\t%4.3f\t%4.3f\n', ...
        CMT_SLAB_SEIS{row3,:});
end
fclose(fid3);


filename4 =
['CMT_',upper(file_slaboutline(1:3)),'_tolUP',text_hwUP,'_tolstr',...
    text_striketol,'_toldip',text_diptol,'_LP',fileext];
fid4 = fopen(filename4, 'w');
fprintf(fid4,...
```

```
'%s\t%s\t%s\t%s\t%s\t%s\t%s\t%s\t%s\t%s\t%s\t%s\t%s\t%s\t%s\t%s\t%s\t%s\t
%s\t%s\t%s\t%s\t%s\t%s\t%s\t%s\t%s\t%s\t%s\t%s\t%s\t%s\t%s\t%s\t%s\t%s\t%
s\t%s\t%s\t%s\t%s\t%s\t%s\t%s\t%s\t%s\t%s\t%s\t%s\t%s\t%s\t%s\t%s\t%s\t%s
\t%s\n',...

'catalog','date','time','lat','long','depth','M1','M2','name','c_time
',...

'c_time_err','c_lat','c_lat_err','c_long','c_long_err','c_depth','c_d
epth_err',...

'depth_type','iexp','Mrr','Mrr_err','Mtt','Mtt_err','Mpp','Mpp_err','
Mrt',...

'Mrt_err','Mrp','Mrp_err','Mtp','Mtp_err','eval1','plg1','azi1','eval
2',...

'plg2','azi2','eval3','plg3','azi3','sc','str1','dip1','rake1','str2'
,'dip2',...
    'rake2','c_longAZI','SerDate','Mo','Mo_err','Mw','Mw_err');
for row4=1:nEQsSLAB
    fprintf(fid4, ...

'%s\t%s\t%s\t%4.2f\t%4.2f\t%4.2f\t%4.1f\t%4.1f\t%s\t%4.2f\t%4.2f\t%4.
2f\t%4.2f\t%4.2f\t%4.2f\t%4.2f\t%4.2f\t%s\t%d\t%4.2f\t%4.2f\t%4.2f\t%
4.2f\t%4.2f\t%4.2f\t%4.2f\t%4.2f\t%4.2f\t%4.2f\t%4.2f\t%4.2f\t%4.2f\t
%3d\t%3d\t%4.2f\t%3d\t%3d\t%4.2f\t%3d\t%3d\t%4.2f\t%3d\t%3d\t%3d\t%3d
\t%3d\t%3d\t%4.2f\t%8d\t%4.3f\t%4.3f\t%4.3f\t%4.3f\n', ...
        CMT_SLAB_SLAB{row4,:});
end
fclose(fid4);

toc
```

D.2 GetSlab1.m

This function works inside SolverEQsFilter.m and is used to parse data from the Global CMT catalog contained in an Excel input file called in the main code ('WorldCMT_jan1976_may2013_53cols.xls'). This routine transforms the data in cell-arrays which are easier to handle in Matlab.

```
function [SLABcell_NED,SLABmat_NED,OUT_NED] =
GetSlab1(file_slabdata,file_slabstr,file_slabdip,file_slaboutl)

% %%%Uncomment to operate as simple code and no function.
% file_slabdata='sam_slab1.0_clip.xyz';
% file_slabstr='sam_slab1.0_strclip.xyz';
% file_slabdip='sam_slab1.0_dipclip.xyz';
% file_slaboutl='sam_slab1.0.clip';


SLABmat_ENU_raw=importdata(file_slabdata);
StrMat_ENU=importdata(file_slabstr);
DipMat_ENU=importdata(file_slabdip);

negStr=StrMat_ENU(:,3)<0;
negDip=DipMat_ENU(:,3)<0;

StrMat_ENU(negStr,3)=360+StrMat_ENU(negStr,3);
DipMat_ENU(negDip,3)=DipMat_ENU(negDip,3)*-1;


SLABmat_ENU_raw=[SLABmat_ENU_raw(:,1), SLABmat_ENU_raw(:,2),
SLABmat_ENU_raw(:,3), StrMat_ENU(:,3), DipMat_ENU(:,3)];
SLABmat_NED_raw=[SLABmat_ENU_raw(:,2),SLABmat_ENU_raw(:,1),SLABmat_EN
U_raw(:,3)*-1, StrMat_ENU(:,3), DipMat_ENU(:,3)];

% %Analysis without filtering out the NaN values reported on Slab1.0.
In that
% %way the process to obtain the Cell array might be faster but I
don't know
% %if the NaNs will affect the later computations.
% SLABmat_NED=SLABmat_NED_raw;
% SLABcell_NED=num2cell(SLABmat_NED);

OUT_ENU_raw=importdata(file_slaboutl);
OUT_ENU=[OUT_ENU_raw(:,1), OUT_ENU_raw(:,2)];
OUT_NED=[OUT_ENU(:,2), OUT_ENU(:,1)];
```

```
%Analysis filtering the Slab1.0 data inside the boundary polygos. In
this
%way the computation is much longer

in=inpolygon(SLABmat_NED_raw(:,1),SLABmat_NED_raw(:,2),OUT_NED(:,1),O
UT_NED(:,2));

SLABmat_NED=SLABmat_NED_raw(in,:);
SLABmat_NED_outs=SLABmat_NED_raw(~in,:);

SLABcell_NED=num2cell(SLABmat_NED);
```

D.3 cmt2slab.m

The cmt2slab.m function works inside SolverEQsFilter.m. The specific task of this function is to filter earthquakes that fall inside the SLAB1.0 regions boundaries available at http://earthquake.usgs.gov/data/slab/. The outputs of this routine are sown in figures which are saved as eps and tiff files.

```
function [cmtslabCell,cmtslabMat] =
cmt2slab(file_cmt,file_slabout,NED_ENU)

% file_cmt='CMT_jan76-apr13.xls';
% file_slabout='sam_slab1.0.clip';
% NED_ENU='NED';


%Longitude is in 0 to 360 nomenclature.
[num,text,raw]=xlsread(file_cmt);
[a b]=size(raw);
nEQ=a;

%long_mat=cell2mat(raw(:,3));




%47-columns cell array with all the
AllEQsCell_NED=raw;
AllEQsMat_NED=[cell2mat(AllEQsCell_NED(:,4:8)),...

cell2mat(AllEQsCell_NED(:,10:17)),cell2mat(AllEQsCell_NED(:,19:53))];

% AllEQsCell_NED=raw;
% AllEQsCell_NED(:,3)=long_cell;
% AllEQsCell_NED=[AllEQsCell_NED,raw(:,3)];
% AllEQsMat_NED=cell2mat(AllEQsCell_NED(:,1:15));
% AllEQsMat_NED=[AllEQsMat_NED,long_mat_raw];

OUT_ENU_raw=importdata(file_slabout);
OUT_ENU=[OUT_ENU_raw(:,1), OUT_ENU_raw(:,2)];
OUT_NED=[OUT_ENU(:,2), OUT_ENU(:,1)];

if strcmp(NED_ENU,'NED')
```

```
%
in=inpolygon(AllEQsMat_NED(:,1),AllEQsMat_NED(:,3),OUT_NED(:,1),OUT_N
ED(:,2));

%In the CMT earthquakes data Matrix (no Cell!) the Centroid Lat is in
8ith
%column and the Azimutal Long in the 45th.

in=inpolygon(AllEQsMat_NED(:,8),AllEQsMat_NED(:,43),OUT_NED(:,1),OUT_
NED(:,2));
    cmtslabMat=AllEQsMat_NED(in,:);
    cmtslabMat_outs=AllEQsMat_NED(~in,:);
    cmtslabCell=AllEQsCell_NED(in,:);



    h=figure;
%
plot(OUT_NED(:,2),OUT_NED(:,1),'r',AllEQsMat_NED(~in,3),AllEQsMat_NED
(~in,1),'.k',AllEQsMat_NED(in,3),AllEQsMat_NED(in,1),'.g');


plot(OUT_NED(:,2),OUT_NED(:,1),'r',AllEQsMat_NED(~in,43),AllEQsMat_NE
D(~in,8),'.k',AllEQsMat_NED(in,43),AllEQsMat_NED(in,8),'.g');
    axis([0 360 -90 90])
    daspect([1 1 1])
    grid on
    title({'World Earthquakes Jan1976-May2013 from GCMT
Catalog';[upper(file_slabout(1:3)),' Slab1.0 Region in Green']})
    xlabel('Longitude [0° - 360°]')
    ylabel('Latitude [-90° - 90°]')
    set(gca,'YTick',-90:30:90)
    set(gca,'XTick',0:30:360)

    %The following is from Emma's post in:

%http://www.mathworks.com/matlabcentral/newsreader/view_thread/314017
    %check also:
    %http://stackoverflow.com/questions/5150802/how-to-save-a-plot-
into-a-pdf-file-without-a-large-margin-around
    %and:
    %http://www.mathworks.com/help/matlab/creating_plots/automatic-
axes-resize.html#f1-32665
    ti = get(gca,'TightInset');
    set(gca,'Position',[ti(1) ti(2) 1-ti(3)-ti(1) 1-ti(4)-ti(2)]);
    set(gca,'units','centimeters')
    pos = get(gca,'Position');
    ti = get(gca,'TightInset');
    set(gcf, 'PaperUnits','centimeters');
    set(gcf, 'PaperSize', [pos(3)+ti(1)+ti(3) pos(4)+ti(2)+ti(4)]);
    set(gcf, 'PaperPositionMode', 'manual');
    set(gcf, 'PaperPosition',[0 0 pos(3)+ti(1)+ti(3)
pos(4)+ti(2)+ti(4)]);
```

```
    saveas(h,['CMT_WorldEQs_jan1976-
may2013_',upper(file_slabout(1:3)),'.fig'],'fig')
    print(h,'-depsc',['CMT_WorldEQs_jan1976-
may2013_',upper(file_slabout(1:3))])
    print(h,'-dtiff','-r600',['CMT_WorldEQs_jan1976-
may2013_',upper(file_slabout(1:3))])

%%% The ENU section needs to be corrected
else
    AllEQsMat_ENU=AllEQsMat_NED;

AllEQsMat_ENU(:,1:5)=[AllEQsMat_NED(:,3:4),AllEQsMat_NED(:,1:2),AllEQ
sMat_NED(:,5)*-1];


in=inpolygon(AllEQsMat_ENU(:,1),AllEQsMat_ENU(:,3),OUT_ENU(:,1),OUT_E
NU(:,2));

    cmtslabMat=AllEQsMat_ENU(in,:);
    cmtslabMat_outs=AllEQsMat_ENU(~in,:);

    cmtslabCell=raw;

cmtslabCell(:,1:5)=[raw(in,3:4),AllEQsCell_ENU(in,1:2),AllEQsMat_ENU(
in,5)*-1];

    figure

plot(OUT_ENU(:,1),OUT_ENU(:,2),AllEQsMat_ENU(in,1),AllEQsMat_ENU(in,3
),'.r',AllEQsMat_ENU(~in,1),AllEQsMat_ENU(~in,3),'.b');



end
```

D.4 cmt2Kostrov.m

This function calculates a moment tensor summation of earthquakes from the individual components of the tensors reported by the CMT catalog.

```
function [e_tot_NED,e_tot_ENU]=cmt2Kostrov(filename,mu,Vol)

%This function opens the text file with your EQs. (Ex: 'my EQs.txt')
and
%allows you to input different volumnes (Vol in m^3) and shear
modulus (mu
%in Pa).
%Each row of the file corresponds to an individual EQ and needs to
contain the
%following information (as the gCMT psmeca output format), separated
by tabs or single spaces:
%long lat depth mrr mtt mpp mrt mrp mtp iexp  (10 columns)
%Don't use a header for the columns in the first row.

%creted by Felipe Aron, Cornell U.

fidMT=fopen(filename);
i=0;

%The following creates an n-length cell array (n is the number of
EQs)
%containing each row of your EQs file. Then creates a n-by-10 matrix
%with the numerical values of the moment tensor (columns 4 to 9).
%Column 1-3 are long, lat and depth, and column 10 the exponent
(dyne-cm)
while ~feof(fidMT)
    i=i+1;
    rawMT_C{i}=fgetl(fidMT);
    raw_MT(i,:)=str2num(rawMT_C{i}(:,:));   %not sure if this step is
always necesary,
                                            %but fgetl normally gives
a string vector
                                            %which needs to be
transformed to numbers.
end
fclose(fidMT);
n=size(raw_MT);         %Number of earthquakes in your file

% Tansforms the Moment tensors from [dyne-cm] (gCMT output) to [N-m].
for j=1:n(1)
    MT(j,:)=(raw_MT(j,4:9))*((10^((raw_MT(j,10))))/(1e7));
end
```

```
%Transformation of original rtp coordinate system to geographics.
%Cell arrays (n-EQs elements) with moment matrices ENU and NED.
for j=1:n(1)
    MT_ENU{j}=[MT(j,3),-MT(j,6),MT(j,5);-MT(j,6),MT(j,2),-
MT(j,4);MT(j,5),...
        -MT(j,4),MT(j,1)];
    MT_NED{j}=[MT(j,2),-MT(j,6),MT(j,4);-MT(j,6),MT(j,3),-
MT(j,5);MT(j,4),...
        -MT(j,5),MT(j,1)];
end

%Moment tensor summation (NED and ENU)

Sum_MT_NED=zeros(3,3);
Sum_MT_ENU=zeros(3,3);
for j=1:n(1)
    Sum_MT_NED=[Sum_MT_NED+MT_NED{j}];
    Sum_MT_ENU=[Sum_MT_ENU+MT_ENU{j}];
end

%Finally, after having the summation of moments, the code calculates
the
%total strain tensors (3x3 matrix) for the NED and ENU coordinate
systems.

e_tot_NED=Sum_MT_NED/(2*mu*Vol);
e_tot_ENU=Sum_MT_ENU/(2*mu*Vol);

%After you have the total  strain tensors, which are the outputs of
this function,
%you can use the eig or eigs functions in matlab to get the 3
eigenvalues and
%3 eigenvectors, which correspond to the principal axes of the
strain. You have
%to be sure which eigenvalue (magnitude of each principal axis)
corresponds
%to each eigenvector. Finally, remember that the 2 tensors are in
different
%coordinate systems, so treat the components of the vectors
accordingly.

%Enjoy!
```

D.5 RuptFilter.m

This routine filters the seismic data from the CMT catalog which falls inside the near-field segments defined in Chapter 4. It also produced figures and files containing the results of the filtering process.

```
tic
display(' ');
display('1. Clear all =');
clear all
close all
toc


tic
display(' ');
display('2. Importing & preparing data =');

%%% The next 4 paragraphs need to be modified with the correct name
of the
%%% slab region.

%Doesn't read headlines! xls file has to start with first data line
file_cmt_UP='CMT_VAN_tolUP10_seisdepth65_tolstr15_toldip15_UP.xls';
[num,text,UP_CMT_cell]=xlsread(file_cmt_UP);
[n_UPeqs,bb1]=size(UP_CMT_cell);
UP_CMT_mat=[cell2mat(UP_CMT_cell(:,4:8)),cell2mat(UP_CMT_cell(:,10:17
)),...
    cell2mat(UP_CMT_cell(:,19:53))];

%Doesn't read headlines! xls file has to start with first data line
file_cmt_LP='CMT_VAN_tolUP10_seisdepth65_tolstr15_toldip15_LP.xls';
[num,text,LP_CMT_cell]=xlsread(file_cmt_LP);
[n_LPeqs,bb2]=size(LP_CMT_cell);
LP_CMT_mat=[cell2mat(LP_CMT_cell(:,4:8)),cell2mat(LP_CMT_cell(:,10:17
)),...
    cell2mat(LP_CMT_cell(:,19:53))];

file_slab1_clip='van_slab1.0.clip';
clip_ENU=importdata(file_slab1_clip);
clip_NED=[clip_ENU(:,2), clip_ENU(:,1)];

%%% This input cell contains the names of all the rupture segments
%%% identified at each slab region. The individual cells contain a
string
```

```
%%% vector with the name of the files containing the polygon. The
number of
%%% cells is the number of segments.
%%% e.g.1:
file_rupt_segs={'sum_seg1.txt','sum_seg2.txt','sum_seg3.txt'}
%%% e.g.2: file_rupt_segs={'izu_seg1.txt'}

file_rupt_segs={'van_seg1.txt'};
[aa,n_ruptures]=size(file_rupt_segs);
%%% End of input section slab data files

%Limits of rectangular grid containing Sab1.0 region.
W_Limit=min(clip_NED(:,2));
E_Limit=max(clip_NED(:,2));
N_Limit=max(clip_NED(:,1));
S_Limit=min(clip_NED(:,1));

load coast
lat_coast_mat=lat;
lat_coast_cell=num2cell(lat_coast_mat);
%0-360° longitude
long_coast_mat=long;
neg_long=long<0;
long_coast_mat(neg_long)=360+long(neg_long);
close360=long_coast_mat>359;
long_coast_mat(close360)=NaN;
lat_coast_mat(close360)=NaN;
long_coast_cell=num2cell(long_coast_mat);

platebound=importdata('TectonicPlates.txt');
lat_plates=platebound(:,2);
long_plates=platebound(:,1);
%0-360° longitude
neg_long_plates=long_plates<0;
long_plates(neg_long_plates)=360+long_plates(neg_long_plates);

%Doesn't read headlines! xls file has to start with first data line
[num_W,text_W,World_EQs_cell]=xlsread('WorldCMT_jan1976_may2013_53col
s.xls');
World_EQs_mat=[cell2mat(World_EQs_cell(:,4:8)),...

cell2mat(World_EQs_cell(:,10:17)),cell2mat(World_EQs_cell(:,19:53))];

SubdEQs=importdata('WorldSubdEQs_7.7&greater_Matlab.txt');
%0-360° longitude
neg_long_subd=SubdEQs(:,4)<0;
SubdEQs(neg_long_subd,4)=360+SubdEQs(neg_long_subd,4);
max_SubdEQ=max(SubdEQs(:,6));
min_SubdEQ=min(SubdEQs(:,6));

symbol_sizes=350*(exp(SubdEQs(:,6)))/(exp(9.5));

%Arrays to be used inside the following loop
All_UP_inrupts_cell={};
```

```
All_UP_inrupts_mat=[];

All_LP_inrupts_cell={};
All_LP_inrupts_mat=[];

All_ruptures_clip_NED=[];
NaN_vec=[NaN,NaN];

toc


tic
display(' ');
display('3. Main loop to save data files and produce plot-ready
arrays =');

for i=1:n_ruptures

    file_rupture=[file_rupt_segs{i}];
    rupture_ENU_raw=importdata(file_rupture);

    lat_rupture=rupture_ENU_raw(:,2);
    long_rupture=rupture_ENU_raw(:,1);
    %0-360° longitude
    neg_long_rupture=long_rupture<0;

long_rupture(neg_long_rupture)=360+long_rupture(neg_long_rupture);

    rupture_ENU=[long_rupture, lat_rupture];
    rupture_NED=[lat_rupture, long_rupture];

%     eval([file_rupture(1:8) '_NED' ' =rupture_NED;'])


in_UP=inpolygon(UP_CMT_mat(:,8),UP_CMT_mat(:,43),lat_rupture,long_rup
ture);
    In_rupt_UP_mat=UP_CMT_mat(in_UP,:);
    %cmtslabMat_outs=AllEQsMat_NED(~in,:);
    In_rupt_UP_cell=UP_CMT_cell(in_UP,:);


in_LP=inpolygon(LP_CMT_mat(:,8),LP_CMT_mat(:,43),lat_rupture,long_rup
ture);
    In_rupt_LP_mat=LP_CMT_mat(in_LP,:);
    %cmtslabMat_outs=AllEQsMat_NED(~in,:);
    In_rupt_LP_cell=LP_CMT_cell(in_LP,:);

    %Cell and matrix arrays containing the filtered EQs. in all
rupture
    %segments identified in the specific slab region.
    All_UP_inrupts_cell=[All_UP_inrupts_cell;In_rupt_UP_cell];
    All_UP_inrupts_mat=[All_UP_inrupts_mat;In_rupt_UP_mat];
```

```
    All_LP_inrupts_cell=[All_LP_inrupts_cell;In_rupt_LP_cell];
    All_LP_inrupts_mat=[All_LP_inrupts_mat;In_rupt_LP_mat];

    %Ruptures polygons

All_ruptures_clip_NED=[All_ruptures_clip_NED;rupture_NED;NaN_vec];

    [nEQs_UP colsUP]=size(In_rupt_UP_cell);      %Number of UP EQs
inside the rupture region
    [nEQs_LP colsLP]=size(In_rupt_LP_cell);      %Number of LP EQs
inside the rupture region

    % Saving files
    filename1 = [file_cmt_UP(5:8),'UP',file_rupture(4:8),'.out'];
    fid1 = fopen(filename1, 'w');
    fprintf(fid1,...

'%s\t%s\t%s\t%s\t%s\t%s\t%s\t%s\t%s\t%s\t%s\t%s\t%s\t%s\t%s\t%s\t%s\t%s\t
%s\t%s\t%s\t%s\t%s\t%s\t%s\t%s\t%s\t%s\t%s\t%s\t%s\t%s\t%s\t%s\t%s\t%s\t%
s\t%s\t%s\t%s\t%s\t%s\t%s\t%s\t%s\t%s\t%s\t%s\t%s\t%s\t%s\t%s\t%s\t%s\t%s
\t%s\n',...

'catalog','date','time','lat','long','depth','M1','M2','name','c_time
',...

'c_time_err','c_lat','c_lat_err','c_long','c_long_err','c_depth','c_d
epth_err',...

'depth_type','iexp','Mrr','Mrr_err','Mtt','Mtt_err','Mpp','Mpp_err','
Mrt',...

'Mrt_err','Mrp','Mrp_err','Mtp','Mtp_err','eval1','plg1','azi1','eval
2',...

'plg2','azi2','eval3','plg3','azi3','sc','str1','dip1','rake1','str2'
,'dip2',...
        'rake2','c_longAZI','SerDate','Mo','Mo_err','Mw','Mw_err');

    for row1=1:nEQs_UP
        fprintf(fid1, ...

'%s\t%s\t%s\t%4.2f\t%4.2f\t%4.2f\t%4.1f\t%4.1f\t%s\t%4.2f\t%4.2f\t%4.
2f\t%4.2f\t%4.2f\t%4.2f\t%4.2f\t%4.2f\t%s\t%d\t%4.2f\t%4.2f\t%4.2f\t%
4.2f\t%4.2f\t%4.2f\t%4.2f\t%4.2f\t%4.2f\t%4.2f\t%4.2f\t%4.2f\t%4.2f\t
%3d\t%3d\t%4.2f\t%3d\t%3d\t%4.2f\t%3d\t%3d\t%4.2f\t%3d\t%3d\t%3d\t%3d
\t%3d\t%3d\t%4.2f\t%8d\t%4.3f\t%4.3f\t%4.3f\t%4.3f\n', ...
            In_rupt_UP_cell{row1,:});
    end
    fclose(fid1);


    filename2 = [file_cmt_LP(5:8),'LP',file_rupture(4:8),'.out'];
    fid2 = fopen(filename2, 'w');
    fprintf(fid2,...
```

```
'%s\t%s\t%s\t%s\t%s\t%s\t%s\t%s\t%s\t%s\t%s\t%s\t%s\t%s\t%s\t%s\t%s\t%s\t
%s\t%s\t%s\t%s\t%s\t%s\t%s\t%s\t%s\t%s\t%s\t%s\t%s\t%s\t%s\t%s\t%s\t%s\t%
s\t%s\t%s\t%s\t%s\t%s\t%s\t%s\t%s\t%s\t%s\t%s\t%s\t%s\t%s\t%s\t%s\t%s\t%s
\t%s\n',...

'catalog','date','time','lat','long','depth','M1','M2','name','c_time
',...

'c_time_err','c_lat','c_lat_err','c_long','c_long_err','c_depth','c_d
epth_err',...

'depth_type','iexp','Mrr','Mrr_err','Mtt','Mtt_err','Mpp','Mpp_err','
Mrt',...

'Mrt_err','Mrp','Mrp_err','Mtp','Mtp_err','eval1','plg1','azi1','eval
2',...

'plg2','azi2','eval3','plg3','azi3','sc','str1','dip1','rake1','str2'
,'dip2',...
        'rake2','c_longAZI','SerDate','Mo','Mo_err','Mw','Mw_err');

    for row2=1:nEQs_LP
        fprintf(fid2, ...

'%s\t%s\t%s\t%4.2f\t%4.2f\t%4.2f\t%4.1f\t%4.1f\t%s\t%4.2f\t%4.2f\t%4.
2f\t%4.2f\t%4.2f\t%4.2f\t%4.2f\t%4.2f\t%s\t%d\t%4.2f\t%4.2f\t%4.2f\t%
4.2f\t%4.2f\t%4.2f\t%4.2f\t%4.2f\t%4.2f\t%4.2f\t%4.2f\t%4.2f\t%4.2f\t
%3d\t%3d\t%4.2f\t%3d\t%3d\t%4.2f\t%3d\t%3d\t%4.2f\t%3d\t%3d\t%3d\t%3d
\t%3d\t%3d\t%4.2f\t%8d\t%4.3f\t%4.3f\t%4.3f\t%4.3f\n', ...
            In_rupt_LP_cell{row2,:});
    end
    fclose(fid2);

end
toc


%%% CREATING FIGURES AND SAVING FIGURE FILES
tic
display(' ');
display('4. Ploting and saving figures =');

%Upper plate events
h1=figure;
plot(long_coast_mat,lat_coast_mat,'k','LineWidth',.25);
hold on
plot(long_plates,lat_plates,'m');
hold on
plot(World_EQs_mat(:,43),World_EQs_mat(:,8),'o','MarkerSize',2,...
    'MarkerFaceColor',[.4 .4 .4],'MarkerEdgeColor',[.4 .4 .4]);
hold on
scatter(SubdEQs(:,4),SubdEQs(:,3),symbol_sizes,'fill','LineWidth',1.5
,'MarkerEdgeColor','k','MarkerFaceColor',[0 1 1]);
```

```
hold on
plot(clip_NED(:,2),clip_NED(:,1),'-g','LineWidth',1);
hold on
plot(All_ruptures_clip_NED(:,2),All_ruptures_clip_NED(:,1),'-
k','LineWidth',1);
hold on
plot(All_UP_inrupts_mat(:,43),All_UP_inrupts_mat(:,8),'o','MarkerSize
',3.5,...
    'MarkerFaceColor','r','MarkerEdgeColor','r');
hold off

axis([round(W_Limit-5) round(E_Limit+5) round(S_Limit-5)
round(N_Limit+5)])
daspect([1 1 1])
grid off
%title({'World Earthquakes Jan1976-May2013 from GCMT Catalog';'
Slab1.0 Region in Green'})
xlabel('Longitude [0° - 360°]')
ylabel('Latitude [-90° - 90°]')
set(gca,'XTick',round(W_Limit-5):5:round(E_Limit+5))
set(gca,'YTick',round(S_Limit-5):5:round(N_Limit+5))

%The following is from Emma's post in:
%http://www.mathworks.com/matlabcentral/newsreader/view_thread/314017
%check also:
%http://stackoverflow.com/questions/5150802/how-to-save-a-plot-into-
a-pdf-file-without-a-large-margin-around
%and:
%http://www.mathworks.com/help/matlab/creating_plots/automatic-axes-
resize.html#f1-32665
ti = get(gca,'TightInset');
set(gca,'Position',[ti(1) ti(2) 1-ti(3)-ti(1) 1-ti(4)-ti(2)]);
set(gca,'units','centimeters')
pos = get(gca,'Position');
ti = get(gca,'TightInset');
set(gcf, 'PaperUnits','centimeters');
set(gcf, 'PaperSize', [pos(3)+ti(1)+ti(3) pos(4)+ti(2)+ti(4)]);
set(gcf, 'PaperPositionMode', 'manual');
set(gcf, 'PaperPosition',[0 0 pos(3)+ti(1)+ti(3)
pos(4)+ti(2)+ti(4)]);

name_file=[file_cmt_UP(1:8),'UP_segs'];
%Saving figures h1
saveas(h1,name_file,'fig')
print(h1,'-depsc',name_file)
print(h1,'-dtiff','-r600',name_file)


%Lower plate events
h2=figure;
plot(long_coast_mat,lat_coast_mat,'k','LineWidth',.25);
hold on
plot(long_plates,lat_plates,'m');
hold on
```

```
plot(World_EQs_mat(:,43),World_EQs_mat(:,8),'o','MarkerSize',2,...
    'MarkerFaceColor',[.4 .4 .4],'MarkerEdgeColor',[.4 .4 .4]);
hold on
scatter(SubdEQs(:,4),SubdEQs(:,3),symbol_sizes,'fill','LineWidth',1.5
,'MarkerEdgeColor','k','MarkerFaceColor',[0 1 1]);
hold on
plot(clip_NED(:,2),clip_NED(:,1),'-g','LineWidth',1);
hold on
plot(All_ruptures_clip_NED(:,2),All_ruptures_clip_NED(:,1),'-
k','LineWidth',1);
hold on
plot(All_LP_inrupts_mat(:,43),All_LP_inrupts_mat(:,8),'o','MarkerSize
',3.5,...
    'MarkerFaceColor','b','MarkerEdgeColor','b');
hold off

axis([round(W_Limit-5) round(E_Limit+5) round(S_Limit-5)
round(N_Limit+5)])
daspect([1 1 1])
grid off
%title({'World Earthquakes Jan1976-May2013 from GCMT Catalog';'
Slab1.0 Region in Green'})
xlabel('Longitude [0° - 360°]')
ylabel('Latitude [-90° - 90°]')
set(gca,'XTick',round(W_Limit-5):5:round(E_Limit+5))
set(gca,'YTick',round(S_Limit-5):5:round(N_Limit+5))

%The following is from Emma's post in:
%http://www.mathworks.com/matlabcentral/newsreader/view_thread/314017
%check also:
%http://stackoverflow.com/questions/5150802/how-to-save-a-plot-into-
a-pdf-file-without-a-large-margin-around
%and:
%http://www.mathworks.com/help/matlab/creating_plots/automatic-axes-
resize.html#f1-32665
ti = get(gca,'TightInset');
set(gca,'Position',[ti(1) ti(2) 1-ti(3)-ti(1) 1-ti(4)-ti(2)]);
set(gca,'units','centimeters')
pos = get(gca,'Position');
ti = get(gca,'TightInset');
set(gcf, 'PaperUnits','centimeters');
set(gcf, 'PaperSize', [pos(3)+ti(1)+ti(3) pos(4)+ti(2)+ti(4)]);
set(gcf, 'PaperPositionMode', 'manual');
set(gcf, 'PaperPosition',[0 0 pos(3)+ti(1)+ti(3)
pos(4)+ti(2)+ti(4)]);

name_file=[file_cmt_LP(1:8),'LP_segs'];
%Saving figures h2
saveas(h2,name_file,'fig')
print(h2,'-depsc',name_file)
print(h2,'-dtiff','-r600',name_file)


%Subduction Earthquakes Mw>7.7
```

```
h3=figure;
plot(long_coast_mat,lat_coast_mat,'k','LineWidth',.25);
hold on
plot(long_plates,lat_plates,'m');
hold on
plot(World_EQs_mat(:,43),World_EQs_mat(:,8),'o','MarkerSize',2,...
    'MarkerFaceColor',[.4 .4 .4],'MarkerEdgeColor',[.4 .4 .4]);
hold on
scatter(SubdEQs(:,4),SubdEQs(:,3),symbol_sizes,'fill','LineWidth',1.5
,'MarkerEdgeColor','k','MarkerFaceColor',[0 1 1]);
hold on
plot(clip_NED(:,2),clip_NED(:,1),'-g','LineWidth',1);
hold on
plot(All_ruptures_clip_NED(:,2),All_ruptures_clip_NED(:,1),'-
k','LineWidth',1);
hold on

axis([round(W_Limit-5) round(E_Limit+5) round(S_Limit-5)
round(N_Limit+5)])
daspect([1 1 1])
grid off
%title({'World Earthquakes Jan1976-May2013 from GCMT Catalog';'
Slab1.0 Region in Green'})
xlabel('Longitude [0° - 360°]')
ylabel('Latitude [-90° - 90°]')
set(gca,'XTick',round(W_Limit-5):5:round(E_Limit+5))
set(gca,'YTick',round(S_Limit-5):5:round(N_Limit+5))

%The following is from Emma's post in:
%http://www.mathworks.com/matlabcentral/newsreader/view_thread/314017
%check also:
%http://stackoverflow.com/questions/5150802/how-to-save-a-plot-into-
a-pdf-file-without-a-large-margin-around
%and:
%http://www.mathworks.com/help/matlab/creating_plots/automatic-axes-
resize.html#f1-32665
ti = get(gca,'TightInset');
set(gca,'Position',[ti(1) ti(2) 1-ti(3)-ti(1) 1-ti(4)-ti(2)]);
set(gca,'units','centimeters')
pos = get(gca,'Position');
ti = get(gca,'TightInset');
set(gcf, 'PaperUnits','centimeters');
set(gcf, 'PaperSize', [pos(3)+ti(1)+ti(3) pos(4)+ti(2)+ti(4)]);
set(gcf, 'PaperPositionMode', 'manual');
set(gcf, 'PaperPosition',[0 0 pos(3)+ti(1)+ti(3)
pos(4)+ti(2)+ti(4)]);

name_file=[file_cmt_UP(1:8),'SubdEQs'];
%Saving figures h3
saveas(h3,name_file,'fig')
print(h3,'-depsc',name_file)
print(h3,'-dtiff','-r600',name_file)

toc
```

D.6 RuptStatsSolver

This routine is the main code which performs the statistical analysis shown in Chapter 4. It uses two other subfunctions named: TimeSerBins.m and EQsStats.m, which I detail in the last two sections of this supplemental. The outputs of this code are figures and text files containing the results of the different calculation discussed in Chapter 4.

```
tic
display(' ');
display('1. Clear all =');
clear all
close all
toc


tic
display(' ');
display('2. Input parameters, file names & preparing data =');

date_in='1976/01/01';
date_end='2013/05/31';

SubReg='KUR';
Segmt='seg2';

binsize=1000;
tol_bin_percent=20;         % Percentage of binsize.

EventsIDXS_file=[SubReg,'_SubdEQs_IDXs_',Segmt,'.dat'];

Events_file='WorldSubdEQs_7.7&greater_Matlab.txt';

World_SubdEQs=importdata(Events_file);

FIX={'no','yes'};

kinematics={'all','reverse','strslip','normal'};
[aa,n_runs]=size(kinematics);

EQS_file_UP=[SubReg,'_UP_',Segmt,'.xls'];
EQS_file_LP=[SubReg,'_LP_',Segmt,'.xls'];
```

```
toc

tic
display(' ');
display('3. Getting bins of time series =');

[n_bins,time_range,DatesSubdEQs,SegmSubdEQs,breakes,bins_mids,bins_ti
me,bins_mins,bins_maxs]=...

TimeSerBins(date_in,date_end,binsize,tol_bin_percent,EventsIDXS_file,
Events_file);
toc

tic
display(' ');
display(sprintf ('4. Running statistics for the segment =\n Outer
loop: FIX events no & yes \n Inner loop: all, reverse, strike-slip &
normal'));
tic

for j=1:2

    FixType=FIX{j};
    for i=1:n_runs



[bins_EQSTATs_UP,SerDates_UP,NO_EQs_bins_UP,bins_EQevents_UP]=...

EQsStats(n_bins,bins_mins,bins_maxs,bins_time,FixType,kinematics{i},E
QS_file_UP);


[bins_EQSTATs_LP,SerDates_LP,NO_EQs_bins_LP,bins_EQevents_LP]=...

EQsStats(n_bins,bins_mins,bins_maxs,bins_time,FixType,kinematics{i},E
QS_file_LP);

        KineType=kinematics{i};

        eval(['bins_EQSTATs_UP_' KineType '_FIX' FixType '
=bins_EQSTATs_UP;'])
        eval(['SerDates_UP_' KineType '_FIX' FixType '
=SerDates_UP;'])
        eval(['NO_EQs_bins_UP_' KineType '_FIX' FixType '
=NO_EQs_bins_UP;'])
        eval(['bins_EQevents_UP_' KineType '_FIX' FixType '
=bins_EQevents_UP;'])

        eval(['bins_EQSTATs_LP_' KineType '_FIX' FixType '
=bins_EQSTATs_LP;'])
        eval(['SerDates_LP_' KineType '_FIX' FixType '
=SerDates_LP;'])
```

```
        eval(['NO_EQs_bins_LP_' KineType '_FIX' FixType '
=NO_EQs_bins_LP;'])
        eval(['bins_EQevents_LP_' KineType '_FIX' FixType '
=bins_EQevents_LP;'])


    end

end


n_bins_range=1;

[Diffs_Mo_FIXno,Diffs_Mo_FIXyes]=...
    NormMoDiffs(n_bins,n_bins_range,...
    bins_EQSTATs_UP_normal_FIXno,bins_EQSTATs_UP_normal_FIXyes,...
    bins_EQSTATs_UP_strslip_FIXno,bins_EQSTATs_UP_strslip_FIXyes,...
    bins_EQSTATs_UP_reverse_FIXno,bins_EQSTATs_UP_reverse_FIXyes);

toc


% %%% CREATING FIGURES AND SAVING FIGURE FILES
tic
display(' ');
display('4. Ploting and saving figures =');


% color_bar=[1 0 0;1 0.5 1;0.5 0.5 1;0 0 1];

%color_bar(1)=Normal fault (red)
%color_bar(2)="Weird" fault (black)
%color_bar(3)=Strike-slip fault (cream)
%color_bar(4)=Reverse fault (blue)
color_bar1=[1 0 0;0 0 0;1 1 0.6;0 0 1];
color_bar2=[0 0 1;1 1 0.6;1 0 0];
path_outputs='D:\Users\Felipe Aron\Documents\P h D   a t   C O R N E
L L\P A P E R  Global search\MATLAB\New CODES_2-20-2014\Outputs from
RuptStatsSolver.m';

%%% Some ideas for plotting. Use the NaN approach with plotyy graphs.

%%% bins_EQSTATs matrices components (columns):

%(1) Simple scalar moment summation per bin.
%(2) Simple scalar moment rate per bin based on (1).
%(3) Scalar moment from tensor summation per bin.
%(4) Error of (3).
%(5) Mw per bin calculated from (3).
%(6) Error of (5)
%(7) Number of earthquakes per bin.
```

```
%(8) Plunge of P-axis per bin from moment tensor summation. Empties
are NaN
%(9) Plunge of T-axis per bin from moment tensor summation (idem
NaN).
%(10) Plunge of N-axis per bin from moment tensor summation (idem
NaN).
%(11) Color code of bin (normal=1, strslip=3, reverse=4) (idem NaN).
%(12) Moment tensor summation per bin only for normal faults (idem
NaN).
%   Should be same as (3) for 'bins_EQSTATs_...' variables obtained
in
%   RuptStatsSolver.m file containing 'normal' in name.
%(13) Moment tensor summation per bin only for reverse faults (idem
NaN).
%   Should be same as (3) for 'bins_EQSTATs_...' variables obtained
in
%   RuptStatsSolver.m file containing 'reverse' in name.
%(14) Moment tensor summation per bin only for strslip faults (idem
NaN).
%   Should be same as (3) for 'bins_EQSTATs_...' variables obtained
in
%   RuptStatsSolver.m file containing 'strslip' in name.


%%%%%%%%%%%%%%%%%%%%%%%%%%%%%%%%%%%%%%%%%%%%%%%%%%%%%%%%%%%%%%%%%%%%%%%
%%%%%%
%%% FIGURE 1
% For publication files format
h1=figure('units','inches','position',[3 0.5 8 6.5]);
% Alternative visualization on full screen Matlab window
% h1=figure('units','normalized','outerposition',[0.04 0.05 0.9
0.95]);

set(gcf,'color',[1 1 1])

%%% subplot(3,1,1)
subplot('Position',[0.08 0.66 0.8 0.28])
%Time series of stacked moment per bin for upper plate events the
three
%independent kinematics (tri-color stacked bars). FIX=no.

y1=bins_EQSTATs_UP_reverse_FIXno(:,3);
y2=bins_EQSTATs_UP_strslip_FIXno(:,3);
y3=bins_EQSTATs_UP_normal_FIXno(:,3);

Y=[y1,y2,y3];
tot_Mo_all=y1+y2+y3;
max_Yvalue=max(tot_Mo_all);
half_max_Yvalue=max_Yvalue/2;

bar(bins_mids,Y,1.1,'stacked');
colormap(color_bar2);

set(gca,'XLim',[0 time_range])
```

```
set(gca,'XTick',0:3000:time_range)
% set(hAx(1),'XTickLabel','')
set(gca,'YAxisLocation','right')
if max_Yvalue>0
    set(gca,'YLim',[0 max_Yvalue])
    set(gca,'YTick',0:half_max_Yvalue:max_Yvalue)
    Y_str=sprintf('%0.1E|',0:half_max_Yvalue:max_Yvalue);
    Y_str = strrep(Y_str, 'E+0','E+');
    Y_str = strrep(Y_str, 'E-0','E-');
    set(gca,'YTickLabel',Y_str)
end

leg_handle=legend('reverse','strike-slip','normal');
% title_handle = get(leg_handle,'Title');
% set(title_handle,'String','Kinematics')
% set(leg_handle,'Location','Best')

%legend(...,'Location','location') location is
[left,bottom,width,height]
set(leg_handle, 'Position', [0.08,0.87,.03,.1]);
%set(leg_handle,'EdgeColor',[1 1 1])
set(leg_handle, 'Box', 'off')
set(leg_handle, 'Color', 'none')

title({['Upper Plate EQs Time Series ',EventsIDXS_file(1:3),' Segment
',EQS_file_UP(11),...
    ' (FIX= ',FIX{1},', Bin size= ',num2str(binsize),'
days)']},'fontweight','bold')
%xlabel(['Days [',date_in,' (0) - ',date_end,' (13665)]'])
ylabel('Moment [dyne-cm]','fontweight','bold')


%%% subplot(3,1,2)
subplot('Position',[0.08 0.44 0.8 0.18])
% bar(bins_mids_ALL,bins_nEQs_ALL_UP,'g')
bar_h=bar(bins_mids,bins_EQSTATs_UP_all_FIXno(:,7),1.1,'k');

set(gca,'XLim',[0 time_range])
set(gca,'XTick',0:3000:time_range)
set(gca,'XTickLabel','')

% title({['Upper Plate EQs Time Series ',EventsIDXS_file(1:3),'
Segment ',EQS_file_UP(11)]})
% xlabel(['Days [',date_in,' (0) - ',date_end,' (13665)]'])
ylabel('Number of Events / Bin','fontweight','bold')


%%% subplot(3,1,3)
subplot('Position',[0.08 0.07 0.8 0.28])

bar_h=bar(bins_mids,bins_EQSTATs_LP_reverse_FIXyes(:,3),1.1);
set(bar_h,'FaceColor',color_bar2(1,:));
```

```
max_Yvalue=max(bins_EQSTATs_LP_reverse_FIXyes(:,3));
half_max_Yvalue=max_Yvalue/2;

set(gca,'XLim',[0 time_range])
set(gca,'XTick',0:3000:time_range)
% set(hAx(1),'XTickLabel','')
set(gca,'YAxisLocation','right')
if max_Yvalue>0
    set(gca,'YLim',[0 max_Yvalue])
    set(gca,'YTick',0:half_max_Yvalue:max_Yvalue)
    Y_str=sprintf('%0.1E|',0:half_max_Yvalue:max_Yvalue);
    Y_str = strrep(Y_str, 'E+0','E+');
    Y_str = strrep(Y_str, 'E-0','E-');
    set(gca,'YTickLabel',Y_str)
end

title({['Subduction EQs Time Series ',EventsIDXS_file(1:3),' Segment
',EQS_file_UP(11)]},'fontweight','bold')
xlabel(['Days [',date_in,' (0) - ',date_end,'
(13665)]'],'fontweight','bold')
ylabel('Moment [dyne-cm]','fontweight','bold')


%D:\Users\Felipe Aron\Documents\P h D   a t   C O R N E L L\P A P E R
%Global search\MATLAB\New CODES_2-20-2014\Outputs from
RuptStatsSolver.m
filename=[EventsIDXS_file(1:3),EQS_file_UP(7:11),'_Mo_Nr_UpFIX',FIX{1
}];
path_filename=fullfile(path_outputs,filename);

%Saving figures h1
saveas(h1,path_filename,'fig')
print(h1,'-depsc',path_filename)
print(h1,'-dtiff','-r600',path_filename)
%%%%%%%%%%%%%%%%%%%%%%%%%%%%%%%%%%%%%%%%%%%%%%%%%%%%%%%%%%%%%%%%%%%%%%%
%%%%%%


%%%%%%%%%%%%%%%%%%%%%%%%%%%%%%%%%%%%%%%%%%%%%%%%%%%%%%%%%%%%%%%%%%%%%%%
%%%%%%
%%% FIGURE 2
% For publication files format
h2=figure('units','inches','position',[3 0.5 8 6.7]);
% Alternative visualization on full screen Matlab window
% h1=figure('units','normalized','outerposition',[0.04 0.05 0.9
0.95]);
set(gcf,'color',[1 1 1])


%%% subplot(4,1,1)
subplot('Position',[0.12 0.76 0.8 0.2])

y1=bins_EQSTATs_UP_reverse_FIXno(:,3);
```

```
y2=bins_EQSTATs_UP_strslip_FIXno(:,3);
y3=bins_EQSTATs_UP_normal_FIXno(:,3);

Y=[y1,y2,y3];
tot_Mo_all=y1+y2+y3;
max_Yvalue=max(tot_Mo_all);
half_max_Yvalue=max_Yvalue/2;

% % y = {rand(x, 1) * 100; (-0:(0.8)/(x-1):0.8)'};
% % fn1=@(x,y) bar(x , y, 0.3, 'FaceColor','r');
% % fn2=@(x,y) bar(x , y, 0.3, 'FaceColor','b');
% % [ax, hbar1, hbar2]=plotyy(1:2:6, y{1},2:2:6,y{2} ,fn1,fn2);

% bar(bins_mids,Y,1.1,'stacked');
% colormap(color_bar2);
stackedbar = @(x, A) bar(x,A,1.1,'stack');
colormap(color_bar2);

[hAx,hLine1,hLine2]=plotyy(bins_mids,Y,bins_mids,...
    bins_EQSTATs_LP_reverse_FIXyes(:,5),stackedbar,'stem');

set(hLine2,'LineStyle','-
','color','g','marker','*','LineWidth',1.25,'MarkerEdgeColor','g','Ma
rkerFaceColor','none','MarkerSize',11)

set(hAx(1),'XLim',[0 time_range])
set(hAx(1),'XTick',0:3000:time_range)
set(hAx(1),'XTickLabel','')
if max_Yvalue>0
    set(hAx(1),'YLim',[0 max_Yvalue])
    set(hAx(1),'YTick',0:half_max_Yvalue:max_Yvalue)
    Y_str=sprintf('%0.1E|',0:half_max_Yvalue:max_Yvalue);
    Y_str = strrep(Y_str, 'E+0','E+');
    Y_str = strrep(Y_str, 'E-0','E-');
    set(hAx(1),'YTickLabel',Y_str)
end

set(hAx(2),'YLim',[7.5 9.5])
set(hAx(2),'YTick',7.5:0.5:10,'fontweight','bold')
set(hAx(2),'YColor','g')
set(hAx(2),'XLim',[0 time_range])
set(hAx(2),'XTick',[])
set(hAx(2),'XTickLabel','')

leg_handle=legend(hLine1,'reverse','strike-slip','normal');
% title_handle = get(leg_handle,'Title');
% set(title_handle,'String','Kinematics')
%legend(...,'Location','location') location is
[left,bottom,width,height]
% set(leg_handle, 'Position', [0.08,0.87,.03,.1]);
set(leg_handle,'Location','Best')
set(leg_handle, 'Box', 'off')
set(leg_handle, 'Color', 'none')
```

```
title({['Upper Plate EQs Time Series ',EventsIDXS_file(1:3),' Segment
',EQS_file_UP(11),...
    ' (FIX= ',FIX{1},', Bin size= ',num2str(binsize),'
days)']},'fontweight','bold')
%xlabel(['Days [',date_in,' (0) - ',date_end,' (13665)]'])
%ylabel('Moment [dyne-cm]','fontweight','bold')
% xlabel(['Days [',date_in,' (0) - ',date_end,' (13665)]'])
% ylabel(hAx(1),'Moment [dyne-cm]','fontweight','bold')
% ylabel(hAx(2),'Mw Subduction Earthquake','fontweight','bold')


%%% subplot(4,1,2)
subplot('Position',[0.12 0.53 0.8 0.2])

% y1=bins_EQSTATs_UP_reverse_FIXno(:,3);
% y2=bins_EQSTATs_UP_strslip_FIXno(:,3);

% % y = {rand(x, 1) * 100; (-0:(0.8)/(x-1):0.8)'};
% % fn1=@(x,y) bar(x , y, 0.3, 'FaceColor','r');
% % fn2=@(x,y) bar(x , y, 0.3, 'FaceColor','b');
% % [ax, hbar1, hbar2]=plotyy(1:2:6, y{1},2:2:6,y{2} ,fn1,fn2);

% stackedbar = @(x, A) bar(x,A,1.1,'stack');
% colormap(color_bar2);

max_Yvalue=max(bins_EQSTATs_UP_normal_FIXno(:,3));
half_max_Yvalue=max_Yvalue/2;

[hAx,hLine1,hLine2]=plotyy(bins_mids,bins_EQSTATs_UP_normal_FIXno(:,3
),bins_mids,...
    bins_EQSTATs_LP_reverse_FIXyes(:,5),'bar','stem');

set(hLine1,'FaceColor',color_bar2(3,:));
set(hLine1,'BarWidth',1.1);
%set(hLine1,'stack');
%set(hLine1,'FaceColor',color_bar2);
set(hLine2,'LineStyle','-
','color','g','marker','*','LineWidth',1.25,'MarkerEdgeColor','g','Ma
rkerFaceColor','none','MarkerSize',11)

% set(hAx_i(1),'XLim',[0 14000])
% set(hAx_i(2),'XLim',[0 14000])

set(hAx(1),'XLim',[0 time_range])
set(hAx(1),'XTick',0:3000:time_range)
set(hAx(1),'XTickLabel','')
if max_Yvalue>0
    set(hAx(1),'YLim',[0 max_Yvalue])
    set(hAx(1),'YTick',0:half_max_Yvalue:max_Yvalue)
    Y_str=sprintf('%0.1E|',0:half_max_Yvalue:max_Yvalue);
    Y_str = strrep(Y_str, 'E+0','E+');
    Y_str = strrep(Y_str, 'E-0','E-');
    set(hAx(1),'YTickLabel',Y_str)
```

```
end

set(hAx(2),'YLim',[7.5 9.5])
set(hAx(2),'YTick',7.5:0.5:10,'fontweight','bold')
set(hAx(2),'XLim',[0 time_range])
set(hAx(2),'XTick',[])
set(hAx(2),'XTickLabel','')
set(hAx(2),'YColor','g')

% leg_handle=legend(hLine1,'normal');
% % title_handle = get(leg_handle,'Title');
% % set(title_handle,'String','Kinematics')
%
% %legend(...,'Location','location') location is
[left,bottom,width,height]
% % set(leg_handle, 'Position', [0.08,0.87,.03,.1]);
% set(leg_handle,'Location','Best')
%
% %set(leg_handle,'EdgeColor',[1 1 1])
% set(leg_handle, 'Box', 'off')
% set(leg_handle, 'Color', 'none')

% title({['Upper Plate EQs Time Series ',EventsIDXS_file(1:3),'
Segment ',EQS_file_UP(11),...
%     ' (FIX= ',FIX{1},', Bin size= ',num2str(binsize),'
days)']},'fontweight','bold')
% xlabel(['Days [',date_in,' (0) - ',date_end,' (13665)]'])
ylabel(hAx(1),'Moment [dyne-cm] Upper Plate
Events','fontweight','bold')
ylabel(hAx(2),'Mw Subduction EQs.','fontweight','bold')


%%% subplot(4,1,3)
subplot('Position',[0.12 0.3 0.8 0.2])

% y1=bins_EQSTATs_UP_reverse_FIXno(:,3);
% y2=bins_EQSTATs_UP_strslip_FIXno(:,3);

% % y = {rand(x, 1) * 100; (-0:(0.8)/(x-1):0.8)'};
% % fn1=@(x,y) bar(x , y, 0.3, 'FaceColor','r');
% % fn2=@(x,y) bar(x , y, 0.3, 'FaceColor','b');
% % [ax, hbar1, hbar2]=plotyy(1:2:6, y{1},2:2:6,y{2} ,fn1,fn2);

% stackedbar = @(x, A) bar(x,A,1.1,'stack');
% colormap(color_bar2);

max_Yvalue=max(bins_EQSTATs_UP_reverse_FIXno(:,3));
half_max_Yvalue=max_Yvalue/2;

[hAx,hLine1,hLine2]=plotyy(bins_mids,bins_EQSTATs_UP_reverse_FIXno(:,
3),bins_mids,...
    bins_EQSTATs_LP_reverse_FIXyes(:,5),'bar','stem');
```

```
set(hLine1,'FaceColor',color_bar2(1,:));
set(hLine1,'BarWidth',1.1);
%set(hLine1,'stack');
%set(hLine1,'FaceColor',color_bar2);
set(hLine2,'LineStyle','-
','color','g','marker','*','LineWidth',1.25,'MarkerEdgeColor','g','Ma
rkerFaceColor','none','MarkerSize',11)

% set(hAx_i(1),'XLim',[0 14000])
% set(hAx_i(2),'XLim',[0 14000])

set(hAx(1),'XLim',[0 time_range])
set(hAx(1),'XTick',0:3000:time_range)
set(hAx(1),'XTickLabel','')
if max_Yvalue>0
    set(hAx(1),'YLim',[0 max_Yvalue])
    set(hAx(1),'YTick',0:half_max_Yvalue:max_Yvalue)
    Y_str=sprintf('%0.1E|',0:half_max_Yvalue:max_Yvalue);
    Y_str = strrep(Y_str, 'E+0','E+');
    Y_str = strrep(Y_str, 'E-0','E-');
    set(hAx(1),'YTickLabel',Y_str)
end

set(hAx(2),'YLim',[7.5 9.5])
set(hAx(2),'YTick',7.5:0.5:10,'fontweight','bold')
set(hAx(2),'XLim',[0 time_range])
set(hAx(2),'XTick',[])
set(hAx(2),'XTickLabel','')
set(hAx(2),'YColor','g')

% set(hAx(1),'fontweight','bold')
%set(gca,'YAxisLocation','right')
%set(hAx_i(1),'YLim',[4.9 7.4])
%set(hAx_i(1),'YTick',5:0.5:7.5)
% set(hAx(1),'box','off')

% leg_handle=legend(hLine1,'reverse');
% % title_handle = get(leg_handle,'Title');
% % set(title_handle,'String','Kinematics')
% %legend(...,'Location','location') location is
[left,bottom,width,height]
% % set(leg_handle, 'Position', [0.08,0.87,.03,.1]);
% set(leg_handle,'Location','Best')
% %set(leg_handle,'EdgeColor',[1 1 1])
% set(leg_handle, 'Box', 'off')
% set(leg_handle, 'Color', 'none')

% title({['Upper Plate EQs Time Series ',EventsIDXS_file(1:3),'
Segment ',EQS_file_UP(11),...
%     ' (FIX= ',FIX{1},', Bin size= ',num2str(binsize),'
days)']},'fontweight','bold')
% xlabel(['Days [',date_in,' (0) - ',date_end,' (13665)]'])
% ylabel(hAx(1),'Moment [dyne-cm]','fontweight','bold')
% ylabel(hAx(2),'Mw','fontweight','bold')
```

```
%%% subplot(4,1,4)
subplot('Position',[0.12 0.065 0.8 0.2])

% y1=bins_EQSTATs_UP_reverse_FIXno(:,3);
% y2=bins_EQSTATs_UP_strslip_FIXno(:,3);

% % y = {rand(x, 1) * 100; (-0:(0.8)/(x-1):0.8)'};
% % fn1=@(x,y) bar(x , y, 0.3, 'FaceColor','r');
% % fn2=@(x,y) bar(x , y, 0.3, 'FaceColor','b');
% % [ax, hbar1, hbar2]=plotyy(1:2:6, y{1},2:2:6,y{2} ,fn1,fn2);

% stackedbar = @(x, A) bar(x,A,1.1,'stack');
% colormap(color_bar2);

max_Yvalue=max(bins_EQSTATs_UP_strslip_FIXno(:,3));
half_max_Yvalue=max_Yvalue/2;

[hAx,hLine1,hLine2]=plotyy(bins_mids,bins_EQSTATs_UP_strslip_FIXno(:,
3),bins_mids,...
    bins_EQSTATs_LP_reverse_FIXyes(:,5),'bar','stem');

set(hLine1,'FaceColor',color_bar2(2,:));
set(hLine1,'BarWidth',1.1);
%set(hLine1,'stack');
%set(hLine1,'FaceColor',color_bar2);
set(hLine2,'LineStyle','-
','color','g','marker','*','LineWidth',1.25,'MarkerEdgeColor','g','Ma
rkerFaceColor','none','MarkerSize',11)

% set(hAx_i(1),'XLim',[0 14000])
% set(hAx_i(2),'XLim',[0 14000])

set(hAx(1),'XLim',[0 time_range])
set(hAx(1),'XTick',0:3000:time_range)
% set(hAx(1),'XTickLabel','')
if max_Yvalue>0
    set(hAx(1),'YLim',[0 max_Yvalue])
    set(hAx(1),'YTick',0:half_max_Yvalue:max_Yvalue)
    Y_str=sprintf('%0.1E|',0:half_max_Yvalue:max_Yvalue);
    Y_str = strrep(Y_str, 'E+0','E+');
    Y_str = strrep(Y_str, 'E-0','E-');
    set(hAx(1),'YTickLabel',Y_str)
end

set(hAx(2),'YLim',[7.5 9.5])
set(hAx(2),'YTick',7.5:0.5:10,'fontweight','bold')
set(hAx(2),'XLim',[0 time_range])
set(hAx(2),'XTick',[])
set(hAx(2),'XTickLabel','')
set(hAx(2),'YColor','g')
```

```
% leg_handle=legend(hLine1,'strike-slip');
% % title_handle = get(leg_handle,'Title');
% % set(title_handle,'String','Kinematics')
% %legend(...,'Location','location') location is
[left,bottom,width,height]
% % set(leg_handle, 'Position', [0.08,0.87,.03,.1]);
% set(leg_handle,'Location','Best')
% %set(leg_handle,'EdgeColor',[1 1 1])
% set(leg_handle, 'Box', 'off')
% set(leg_handle, 'Color', 'none')

% title({['Upper Plate EQs Time Series ',EventsIDXS_file(1:3),'
Segment ',EQS_file_UP(11),...
%     ' (FIX= ',FIX{1},', Bin size= ',num2str(binsize),'
days)']},'fontweight','bold')
%xlabel(['Days [',date_in,' (0) - ',date_end,' (13665)]'])
%ylabel('Moment [dyne-cm]','fontweight','bold')
xlabel(['Days [',date_in,' (0) - ',date_end,'
(13665)]'],'fontweight','bold')
% ylabel(hAx(1),'Moment [dyne-cm]','fontweight','bold')
% ylabel(hAx(2),'Mw','fontweight','bold')

%D:\Users\Felipe Aron\Documents\P h D   a t   C O R N E L L\P A P E R
%Global search\MATLAB\New CODES_2-20-2014\Outputs from
RuptStatsSolver.m
filename=[EventsIDXS_file(1:3),EQS_file_UP(7:11),'_Mo_UpALL_UpFIX',FI
X{1}];
path_filename=fullfile(path_outputs,filename);

%Saving figures h2
saveas(h2,path_filename,'fig')
print(h2,'-depsc',path_filename)
print(h2,'-dtiff','-r600',path_filename)
%%%%%%%%%%%%%%%%%%%%%%%%%%%%%%%%%%%%%%%%%%%%%%%%%%%%%%%%%%%%%%%%%%%%%%%
%%%%%%



%%%%%%%%%%%%%%%%%%%%%%%%%%%%%%%%%%%%%%%%%%%%%%%%%%%%%%%%%%%%%%%%%%%%%%%
%%%%%%
%%% FIGURE 3
% For publication files format
h3=figure('units','inches','position',[3 0.5 8 6.5]);
% Alternative visualization on full screen Matlab window
% h1=figure('units','normalized','outerposition',[0.04 0.05 0.9
0.95]);

set(gcf,'color',[1 1 1])

% subplot(3,1,1)
subplot('Position',[0.08 0.66 0.8 0.28])
%Time series of stacked moment per bin for upper plate events the
three
%independent kinematics (tri-color stacked bars). FIX=yes.
```

```
y1=bins_EQSTATs_UP_reverse_FIXyes(:,3);
y2=bins_EQSTATs_UP_strslip_FIXyes(:,3);
y3=bins_EQSTATs_UP_normal_FIXyes(:,3);

Y=[y1,y2,y3];
tot_Mo_all=y1+y2+y3;
max_Yvalue=max(tot_Mo_all);
half_max_Yvalue=max_Yvalue/2;

bar(bins_mids,Y,1.1,'stacked');
colormap(color_bar2);

set(gca,'XLim',[0 time_range])
set(gca,'XTick',0:3000:time_range)
% set(hAx(1),'XTickLabel','')
set(gca,'YAxisLocation','right')
if max_Yvalue>0
    set(gca,'YLim',[0 max_Yvalue])
    set(gca,'YTick',0:half_max_Yvalue:max_Yvalue)
    Y_str=sprintf('%0.1E|',0:half_max_Yvalue:max_Yvalue);
    Y_str = strrep(Y_str, 'E+0','E+');
    Y_str = strrep(Y_str, 'E-0','E-');
    set(gca,'YTickLabel',Y_str)
end

leg_handle=legend('reverse','strike-slip','normal');
% title_handle = get(leg_handle,'Title');
% set(title_handle,'String','Kinematics')
% set(leg_handle,'Location','Best')

%legend(...,'Location','location') location is
[left,bottom,width,height]
set(leg_handle, 'Position', [0.08,0.87,.03,.1]);
%set(leg_handle,'EdgeColor',[1 1 1])
set(leg_handle, 'Box', 'off')
set(leg_handle, 'Color', 'none')

title({['Upper Plate EQs Time Series ',EventsIDXS_file(1:3),' Segment
',EQS_file_UP(11),...
    ' (FIX= ',FIX{2},', Bin size= ',num2str(binsize),'
days)']},'fontweight','bold')
%xlabel(['Days [',date_in,' (0) - ',date_end,' (13665)]'])
ylabel('Moment [dyne-cm]','fontweight','bold')


% subplot(3,1,2)
subplot('Position',[0.08 0.44 0.8 0.18])
% bar(bins_mids_ALL,bins_nEQs_ALL_UP,'g')
bar_h=bar(bins_mids,bins_EQSTATs_UP_all_FIXyes(:,7),1.1,'k');

set(gca,'XLim',[0 time_range])
set(gca,'XTick',0:3000:time_range)
set(gca,'XTickLabel','')
```

```
% title({['Upper Plate EQs Time Series ',EventsIDXS_file(1:3),'
Segment ',EQS_file_UP(11)]})
% xlabel(['Days [',date_in,' (0) - ',date_end,' (13665)]'])
ylabel('Number of Events / Bin','fontweight','bold')


% subplot(3,1,3)
subplot('Position',[0.08 0.07 0.8 0.28])

bar_h=bar(bins_mids,bins_EQSTATs_LP_reverse_FIXyes(:,3),1.1);
set(bar_h,'FaceColor',color_bar2(1,:));

max_Yvalue=max(bins_EQSTATs_LP_reverse_FIXyes(:,3));
half_max_Yvalue=max_Yvalue/2;

set(gca,'XLim',[0 time_range])
set(gca,'XTick',0:3000:time_range)
% set(hAx(1),'XTickLabel','')
set(gca,'YAxisLocation','right')
if max_Yvalue>0
    set(gca,'YLim',[0 max_Yvalue])
    set(gca,'YTick',0:half_max_Yvalue:max_Yvalue)
    Y_str=sprintf('%0.1E|',0:half_max_Yvalue:max_Yvalue);
    Y_str = strrep(Y_str, 'E+0','E+');
    Y_str = strrep(Y_str, 'E-0','E-');
    set(gca,'YTickLabel',Y_str)
end

title({['Subduction EQs Time Series ',EventsIDXS_file(1:3),' Segment
',EQS_file_UP(11)]},'fontweight','bold')
xlabel(['Days [',date_in,' (0) - ',date_end,'
(13665)]'],'fontweight','bold')
ylabel('Moment [dyne-cm]','fontweight','bold')


%D:\Users\Felipe Aron\Documents\P h D   a t   C O R N E L L\P A P E R
%Global search\MATLAB\New CODES_2-20-2014\Outputs from
RuptStatsSolver.m
filename=[EventsIDXS_file(1:3),EQS_file_UP(7:11),
'_Mo_Nr_UpFIX',FIX{2}];
path_filename=fullfile(path_outputs,filename);

%Saving figures h3
saveas(h3,path_filename,'fig')
print(h3,'-depsc',path_filename)
print(h3,'-dtiff','-r600',path_filename)
%%%
```

```
%%% FIGURE 4
% For publication files format
h4=figure('units','inches','position',[3 0.5 8 6.7]);
% Alternative visualization on full screen Matlab window
% h1=figure('units','normalized','outerposition',[0.04 0.05 0.9
0.95]);
set(gcf,'color',[1 1 1])


%%% subplot(4,1,1)
subplot('Position',[0.12 0.76 0.8 0.2])

y1=bins_EQSTATs_UP_reverse_FIXyes(:,3);
y2=bins_EQSTATs_UP_strslip_FIXyes(:,3);
y3=bins_EQSTATs_UP_normal_FIXyes(:,3);

Y=[y1,y2,y3];
tot_Mo_all=y1+y2+y3;
max_Yvalue=max(tot_Mo_all);
half_max_Yvalue=max_Yvalue/2;

% % y = {rand(x, 1) * 100; (-0:(0.8)/(x-1):0.8)'};
% % fn1=@(x,y) bar(x , y, 0.3, 'FaceColor','r');
% % fn2=@(x,y) bar(x , y, 0.3, 'FaceColor','b');
% % [ax, hbar1, hbar2]=plotyy(1:2:6, y{1},2:2:6,y{2} ,fn1,fn2);

% bar(bins_mids,Y,1.1,'stacked');
% colormap(color_bar2);
stackedbar = @(x, A) bar(x,A,1.1,'stack');
colormap(color_bar2);

[hAx,hLine1,hLine2]=plotyy(bins_mids,Y,bins_mids,...
    bins_EQSTATs_LP_reverse_FIXyes(:,5),stackedbar,'stem');

set(hLine2,'LineStyle','-
','color','g','marker','*','LineWidth',1.25,'MarkerEdgeColor','g','Ma
rkerFaceColor','none','MarkerSize',11)

%%%
set(hAx(1),'XLim',[0 time_range])
set(hAx(1),'XTick',0:3000:time_range)
set(hAx(1),'XTickLabel','')
if max_Yvalue>0
    set(hAx(1),'YLim',[0 max_Yvalue])
    set(hAx(1),'YTick',0:half_max_Yvalue:max_Yvalue)
    Y_str=sprintf('%0.1E|',0:half_max_Yvalue:max_Yvalue);
    Y_str = strrep(Y_str, 'E+0','E+');
    Y_str = strrep(Y_str, 'E-0','E-');
    set(hAx(1),'YTickLabel',Y_str)
end
%%%

set(hAx(2),'YLim',[7.5 9.5])
```

```
set(hAx(2),'YTick',7.5:0.5:10,'fontweight','bold')
set(hAx(2),'YColor','g')
set(hAx(2),'XLim',[0 time_range])
set(hAx(2),'XTick',[])
set(hAx(2),'XTickLabel','')

leg_handle=legend(hLine1,'reverse','strike-slip','normal');
% title_handle = get(leg_handle,'Title');
% set(title_handle,'String','Kinematics')
%legend(...,'Location','location') location is
[left,bottom,width,height]
% set(leg_handle, 'Position', [0.08,0.87,.03,.1]);
set(leg_handle,'Location','Best')
set(leg_handle, 'Box', 'off')
set(leg_handle, 'Color', 'none')

title({['Upper Plate EQs Time Series ',EventsIDXS_file(1:3),' Segment
',EQS_file_UP(11),...
    ' (FIX= ',FIX{2},', Bin size= ',num2str(binsize),'
days)']},'fontweight','bold')
%xlabel(['Days [',date_in,' (0) - ',date_end,' (13665)]'])
%ylabel('Moment [dyne-cm]','fontweight','bold')
% xlabel(['Days [',date_in,' (0) - ',date_end,' (13665)]'])
% ylabel(hAx(1),'Moment [dyne-cm]','fontweight','bold')
% ylabel(hAx(2),'Mw Subduction Earthquake','fontweight','bold')


%%% subplot(4,1,2)
subplot('Position',[0.12 0.53 0.8 0.2])

% y1=bins_EQSTATs_UP_reverse_FIXno(:,3);
% y2=bins_EQSTATs_UP_strslip_FIXno(:,3);

% % y = {rand(x, 1) * 100; (-0:(0.8)/(x-1):0.8)'};
% % fn1=@(x,y) bar(x , y, 0.3, 'FaceColor','r');
% % fn2=@(x,y) bar(x , y, 0.3, 'FaceColor','b');
% % [ax, hbar1, hbar2]=plotyy(1:2:6, y{1},2:2:6,y{2} ,fn1,fn2);

% stackedbar = @(x, A) bar(x,A,1.1,'stack');
% colormap(color_bar2);

max_Yvalue=max(bins_EQSTATs_UP_normal_FIXyes(:,3));
half_max_Yvalue=max_Yvalue/2;

[hAx,hLine1,hLine2]=plotyy(bins_mids,bins_EQSTATs_UP_normal_FIXyes(:,
3),bins_mids,...
    bins_EQSTATs_LP_reverse_FIXyes(:,5),'bar','stem');

set(hLine1,'FaceColor',color_bar2(3,:));
set(hLine1,'BarWidth',1.1);
%set(hLine1,'stack');
%set(hLine1,'FaceColor',color_bar2);
```

```
set(hLine2,'LineStyle','-
','color','g','marker','*','LineWidth',1.25,'MarkerEdgeColor','g','Ma
rkerFaceColor','none','MarkerSize',11)

set(hAx(1),'XLim',[0 time_range])
set(hAx(1),'XTick',0:3000:time_range)
set(hAx(1),'XTickLabel','')
if max_Yvalue>0
    set(hAx(1),'YLim',[0 max_Yvalue])
    set(hAx(1),'YTick',0:half_max_Yvalue:max_Yvalue)
    Y_str=sprintf('%0.1E|',0:half_max_Yvalue:max_Yvalue);
    Y_str = strrep(Y_str, 'E+0','E+');
    Y_str = strrep(Y_str, 'E-0','E-');
    set(hAx(1),'YTickLabel',Y_str)
end

set(hAx(2),'YLim',[7.5 9.5])
set(hAx(2),'YTick',7.5:0.5:10,'fontweight','bold')
set(hAx(2),'XLim',[0 time_range])
set(hAx(2),'XTick',[])
set(hAx(2),'XTickLabel','')
set(hAx(2),'YColor','g')

% leg_handle=legend(hLine1,'normal');
% % title_handle = get(leg_handle,'Title');
% % set(title_handle,'String','Kinematics')
% %legend(...,'Location','location') location is
[left,bottom,width,height]
% % set(leg_handle, 'Position', [0.08,0.87,.03,.1]);
% set(leg_handle,'Location','Best')
% %set(leg_handle,'EdgeColor',[1 1 1])
% set(leg_handle, 'Box', 'off')
% set(leg_handle, 'Color', 'none')

% title({['Upper Plate EQs Time Series ',EventsIDXS_file(1:3),'
Segment ',EQS_file_UP(11),...
%     ' (FIX= ',FIX{1},', Bin size= ',num2str(binsize),'
days)']},'fontweight','bold')
% xlabel(['Days [',date_in,' (0) - ',date_end,' (13665)]'])
ylabel(hAx(1),'Moment [dyne-cm] Upper Plate
Events','fontweight','bold')
ylabel(hAx(2),'Mw Subduction EQs.','fontweight','bold')


%%% subplot(4,1,3)
subplot('Position',[0.12 0.3 0.8 0.2])

% y1=bins_EQSTATs_UP_reverse_FIXno(:,3);
% y2=bins_EQSTATs_UP_strslip_FIXno(:,3);

% % y = {rand(x, 1) * 100; (-0:(0.8)/(x-1):0.8)'};
% % fn1=@(x,y) bar(x , y, 0.3, 'FaceColor','r');
% % fn2=@(x,y) bar(x , y, 0.3, 'FaceColor','b');
% % [ax, hbar1, hbar2]=plotyy(1:2:6, y{1},2:2:6,y{2} ,fn1,fn2);
```

```
% stackedbar = @(x, A) bar(x,A,1.1,'stack');
% colormap(color_bar2);

max_Yvalue=max(bins_EQSTATs_UP_reverse_FIXyes(:,3));
half_max_Yvalue=max_Yvalue/2;

[hAx,hLine1,hLine2]=plotyy(bins_mids,bins_EQSTATs_UP_reverse_FIXyes(:
,3),bins_mids,...
    bins_EQSTATs_LP_reverse_FIXyes(:,5),'bar','stem');

set(hLine1,'FaceColor',color_bar2(1,:));
set(hLine1,'BarWidth',1.1);
%set(hLine1,'stack');
%set(hLine1,'FaceColor',color_bar2);
set(hLine2,'LineStyle','-
','color','g','marker','*','LineWidth',1.25,'MarkerEdgeColor','g','Ma
rkerFaceColor','none','MarkerSize',11)

set(hAx(1),'XLim',[0 time_range])
set(hAx(1),'XTick',0:3000:time_range)
set(hAx(1),'XTickLabel','')
if max_Yvalue>0
    set(hAx(1),'YLim',[0 max_Yvalue])
    set(hAx(1),'YTick',0:half_max_Yvalue:max_Yvalue)
    Y_str=sprintf('%0.1E|',0:half_max_Yvalue:max_Yvalue);
    Y_str = strrep(Y_str, 'E+0','E+');
    Y_str = strrep(Y_str, 'E-0','E-');
    set(hAx(1),'YTickLabel',Y_str)
end

set(hAx(2),'YLim',[7.5 9.5])
set(hAx(2),'YTick',7.5:0.5:10,'fontweight','bold')
set(hAx(2),'XLim',[0 time_range])
set(hAx(2),'XTick',[])
set(hAx(2),'XTickLabel','')
set(hAx(2),'YColor','g')

% leg_handle=legend(hLine1,'reverse');
% % title_handle = get(leg_handle,'Title');
% % set(title_handle,'String','Kinematics')
% %legend(...,'Location','location') location is
[left,bottom,width,height]
% % set(leg_handle, 'Position', [0.08,0.87,.03,.1]);
% set(leg_handle,'Location','Best')
% %set(leg_handle,'EdgeColor',[1 1 1])
% set(leg_handle, 'Box', 'off')
% set(leg_handle, 'Color', 'none')

% title({['Upper Plate EQs Time Series ',EventsIDXS_file(1:3),'
Segment ',EQS_file_UP(11),...
%     ' (FIX= ',FIX{1},', Bin size= ',num2str(binsize),'
days)']},'fontweight','bold')
% xlabel(['Days [',date_in,' (0) - ',date_end,' (13665)]'])
```

```
% ylabel(hAx(1),'Moment [dyne-cm]','fontweight','bold')
% ylabel(hAx(2),'Mw','fontweight','bold')


%%% subplot(4,1,4)
subplot('Position',[0.12 0.065 0.8 0.2])

% y1=bins_EQSTATs_UP_reverse_FIXno(:,3);
% y2=bins_EQSTATs_UP_strslip_FIXno(:,3);

% % y = {rand(x, 1) * 100; (-0:(0.8)/(x-1):0.8)'};
% % fn1=@(x,y) bar(x , y, 0.3, 'FaceColor','r');
% % fn2=@(x,y) bar(x , y, 0.3, 'FaceColor','b');
% % [ax, hbar1, hbar2]=plotyy(1:2:6, y{1},2:2:6,y{2} ,fn1,fn2);

% stackedbar = @(x, A) bar(x,A,1.1,'stack');
% colormap(color_bar2);

max_Yvalue=max(bins_EQSTATs_UP_strslip_FIXyes(:,3));
half_max_Yvalue=max_Yvalue/2;

[hAx,hLine1,hLine2]=plotyy(bins_mids,bins_EQSTATs_UP_strslip_FIXyes(:
,3),bins_mids,...
    bins_EQSTATs_LP_reverse_FIXyes(:,5),'bar','stem');

set(hLine1,'FaceColor',color_bar2(2,:));
set(hLine1,'BarWidth',1.1);
%set(hLine1,'stack');
%set(hLine1,'FaceColor',color_bar2);
set(hLine2,'LineStyle','-
','color','g','marker','*','LineWidth',1.25,'MarkerEdgeColor','g','Ma
rkerFaceColor','none','MarkerSize',11)

set(hAx(1),'XLim',[0 time_range])
set(hAx(1),'XTick',0:3000:time_range)
% set(hAx(1),'XTickLabel','')
if max_Yvalue>0
    set(hAx(1),'YLim',[0 max_Yvalue])
    set(hAx(1),'YTick',0:half_max_Yvalue:max_Yvalue)
    Y_str=sprintf('%0.1E|',0:half_max_Yvalue:max_Yvalue);
    Y_str = strrep(Y_str, 'E+0','E+');
    Y_str = strrep(Y_str, 'E-0','E-');
    set(hAx(1),'YTickLabel',Y_str)
end

set(hAx(2),'YLim',[7.5 9.5])
set(hAx(2),'YTick',7.5:0.5:10,'fontweight','bold')
set(hAx(2),'XLim',[0 time_range])
set(hAx(2),'XTick',[])
set(hAx(2),'XTickLabel','')
set(hAx(2),'YColor','g')

% leg_handle=legend(hLine1,'strike-slip');
```

```
% % title_handle = get(leg_handle,'Title');
% % set(title_handle,'String','Kinematics')
% %legend(...,'Location','location') location is
[left,bottom,width,height]
% % set(leg_handle, 'Position', [0.08,0.87,.03,.1]);
% set(leg_handle,'Location','Best')
% %set(leg_handle,'EdgeColor',[1 1 1])
% set(leg_handle, 'Box', 'off')
% set(leg_handle, 'Color', 'none')

% title({['Upper Plate EQs Time Series ',EventsIDXS_file(1:3),'
Segment ',EQS_file_UP(11),...
%     ' (FIX= ',FIX{1},', Bin size= ',num2str(binsize),'
days)']},'fontweight','bold')
%xlabel(['Days [',date_in,' (0) - ',date_end,' (13665)]'])
%ylabel('Moment [dyne-cm]','fontweight','bold')
xlabel(['Days [',date_in,' (0) - ',date_end,'
(13665)]'],'fontweight','bold')
% ylabel(hAx(1),'Moment [dyne-cm]','fontweight','bold')
% ylabel(hAx(2),'Mw','fontweight','bold')

%D:\Users\Felipe Aron\Documents\P h D   a t   C O R N E L L\P A P E R
%Global search\MATLAB\New CODES_2-20-2014\Outputs from
RuptStatsSolver.m
filename=[EventsIDXS_file(1:3),EQS_file_UP(7:11),'_Mo_UpALL_UpFIX',FI
X{2}];
path_filename=fullfile(path_outputs,filename);

%Saving figures h4
saveas(h4,path_filename,'fig')
print(h4,'-depsc',path_filename)
print(h4,'-dtiff','-r600',path_filename)
%%%%%%%%%%%%%%%%%%%%%%%%%%%%%%%%%%%%%%%%%%%%%%%%%%%%%%%%%%%%%%%%%%%%%%%
%%%%%%



%%%%%%%%%%%%%%%%%%%%%%%%%%%%%%%%%%%%%%%%%%%%%%%%%%%%%%%%%%%%%%%%%%%%%%%
%%%%%%
%%% FIGURE 5
% For publication files format
h5=figure('units','inches','position',[3 0.5 8 6.5]);
% Alternative visualization on full screen Matlab window
% h1=figure('units','normalized','outerposition',[0.04 0.05 0.9
0.95]);

set(gcf,'color',[1 1 1])

% subplot(3,1,1)
subplot('Position',[0.1 0.66 0.8 0.28])

bar_h=bar(bins_mids,bins_EQSTATs_UP_normal_FIXno(:,5),1.5);
set(bar_h,'FaceColor',color_bar2(3,:));
hold on
```

```
bar_h=bar(bins_mids,bins_EQSTATs_UP_strslip_FIXno(:,5),1);
set(bar_h,'FaceColor',color_bar2(2,:));

bar_h=bar(bins_mids,bins_EQSTATs_UP_reverse_FIXno(:,5),0.5);
set(bar_h,'FaceColor',color_bar2(1,:));

axis([0 time_range 4.9 7.4])
%set(gca,'XLim',[0 time_range])
set(gca,'XTick',0:3000:time_range)
set(gca,'YAxisLocation','right')

leg_handle=legend('normal','strike-slip','reverse');
% title_handle = get(leg_handle,'Title');
% set(title_handle,'String','Kinematics')
% set(leg_handle,'Location','Best')
%legend(...,'Location','location') location is
[left,bottom,width,height]
set(leg_handle, 'Position', [0.08,0.87,.03,.1]);
%set(leg_handle,'EdgeColor',[1 1 1])
set(leg_handle, 'Box', 'off')
set(leg_handle, 'Color', 'none')

title({['Upper Plate EQs Time Series ',EventsIDXS_file(1:3),' Segment
',EQS_file_UP(11),...
    ' (FIX= ',FIX{1},', Bin size= ',num2str(binsize),'
days)']},'fontweight','bold')
%xlabel(['Days [',date_in,' (0) - ',date_end,' (13665)]'])
ylabel('Mw','fontweight','bold')
grid on

hold off


% subplot(3,1,2)
subplot('Position',[0.1 0.44 0.8 0.18])
% bar(bins_mids_ALL,bins_nEQs_ALL_UP,'g')
bar_h=bar(bins_mids,bins_EQSTATs_UP_all_FIXno(:,7),1.1,'k');

set(gca,'XLim',[0 time_range])
set(gca,'XTick',0:3000:time_range)
set(gca,'XTickLabel','')

% title({['Upper Plate EQs Time Series ',EventsIDXS_file(1:3),'
Segment ',EQS_file_UP(11)]})
% xlabel(['Days [',date_in,' (0) - ',date_end,' (13665)]'])
ylabel('Number of Events / Bin','fontweight','bold')


% subplot(3,1,3)
subplot('Position',[0.1 0.07 0.8 0.28])

bar_h=bar(bins_mids,bins_EQSTATs_LP_reverse_FIXyes(:,5),1.1);
set(bar_h,'FaceColor',color_bar2(1,:));
```

```
axis([0 time_range 5.0 9.5])

% set(gca,'XLim',[0 time_range])
set(gca,'XTick',0:3000:time_range)

title({['Subduction EQs Time Series ',EventsIDXS_file(1:3),' Segment
',EQS_file_UP(11)]},'fontweight','bold')
xlabel(['Days [',date_in,' (0) - ',date_end,'
(13665)]'],'fontweight','bold')
ylabel('Mw','fontweight','bold')
grid on


%D:\Users\Felipe Aron\Documents\P h D   a t   C O R N E L L\P A P E R
%Global search\MATLAB\New CODES_2-20-2014\Outputs from
RuptStatsSolver.m
filename=[EventsIDXS_file(1:3),EQS_file_UP(7:11),'_Mw_Nr_UpFIX',FIX{1
}];
path_filename=fullfile(path_outputs,filename);

%Saving figures h5
saveas(h5,path_filename,'fig')
print(h5,'-depsc',path_filename)
print(h5,'-dtiff','-r600',path_filename)
%%%%%%%%%%%%%%%%%%%%%%%%%%%%%%%%%%%%%%%%%%%%%%%%%%%%%%%%%%%%%%%%%%%%%%%
%%%%%%


%%%%%%%%%%%%%%%%%%%%%%%%%%%%%%%%%%%%%%%%%%%%%%%%%%%%%%%%%%%%%%%%%%%%%%%
%%%%%%
%%% FIGURE 6
% For publication files format
h6=figure('units','inches','position',[3 0.5 8 6.5]);
% Alternative visualization on full screen Matlab window
% h1=figure('units','normalized','outerposition',[0.04 0.05 0.9
0.95]);

set(gcf,'color',[1 1 1])

% subplot(3,1,1)
subplot('Position',[0.1 0.66 0.8 0.28])

bar_h=bar(bins_mids,bins_EQSTATs_UP_normal_FIXyes(:,5),1.5);
set(bar_h,'FaceColor',color_bar2(3,:));
hold on

bar_h=bar(bins_mids,bins_EQSTATs_UP_strslip_FIXyes(:,5),1);
set(bar_h,'FaceColor',color_bar2(2,:));

bar_h=bar(bins_mids,bins_EQSTATs_UP_reverse_FIXyes(:,5),0.5);
set(bar_h,'FaceColor',color_bar2(1,:));
```

```
axis([0 time_range 4.9 7.4])
%set(gca,'XLim',[0 time_range])
set(gca,'XTick',0:3000:time_range)
set(gca,'YAxisLocation','right')

leg_handle=legend('normal','strike-slip','reverse');
% title_handle = get(leg_handle,'Title');
% set(title_handle,'String','Kinematics')
% set(leg_handle,'Location','Best')
%legend(...,'Location','location') location is
[left,bottom,width,height]
set(leg_handle, 'Position', [0.08,0.87,.03,.1]);
%set(leg_handle,'EdgeColor',[1 1 1])
set(leg_handle, 'Box', 'off')
set(leg_handle, 'Color', 'none')

title({['Upper Plate EQs Time Series ',EventsIDXS_file(1:3),' Segment
',EQS_file_UP(11),...
    ' (FIX= ',FIX{2},', Bin size= ',num2str(binsize),'
days)']},'fontweight','bold')
%xlabel(['Days [',date_in,' (0) - ',date_end,' (13665)]'])
ylabel('Mw','fontweight','bold')
grid on

hold off


% subplot(3,1,2)
subplot('Position',[0.1 0.44 0.8 0.18])
% bar(bins_mids_ALL,bins_nEQs_ALL_UP,'g')
bar_h=bar(bins_mids,bins_EQSTATs_UP_all_FIXyes(:,7),1.1,'k');

set(gca,'XLim',[0 time_range])
set(gca,'XTick',0:3000:time_range)
set(gca,'XTickLabel','')

% title({['Upper Plate EQs Time Series ',EventsIDXS_file(1:3),'
Segment ',EQS_file_UP(11)]})
% xlabel(['Days [',date_in,' (0) - ',date_end,' (13665)]'])
ylabel('Number of Events / Bin','fontweight','bold')


% subplot(3,1,3)
subplot('Position',[0.1 0.07 0.8 0.28])

bar_h=bar(bins_mids,bins_EQSTATs_LP_reverse_FIXyes(:,5),1.1);
set(bar_h,'FaceColor',color_bar2(1,:));

axis([0 time_range 5.0 9.5])

% set(gca,'XLim',[0 time_range])
set(gca,'XTick',0:3000:time_range)
```

```
title({['Subduction EQs Time Series ',EventsIDXS_file(1:3),' Segment
',EQS_file_UP(11)]},'fontweight','bold')
xlabel(['Days [',date_in,' (0) - ',date_end,'
(13665)]'],'fontweight','bold')
ylabel('Mw','fontweight','bold')
grid on


%D:\Users\Felipe Aron\Documents\P h D   a t   C O R N E L L\P A P E R
%Global search\MATLAB\New CODES_2-20-2014\Outputs from
RuptStatsSolver.m
filename=[EventsIDXS_file(1:3),EQS_file_UP(7:11),'_Mw_Nr_UpFIX',FIX{2
}];
path_filename=fullfile(path_outputs,filename);

%Saving figures h6
saveas(h6,path_filename,'fig')
print(h6,'-depsc',path_filename)
print(h6,'-dtiff','-r600',path_filename)
%%%%%%%%%%%%%%%%%%%%%%%%%%%%%%%%%%%%%%%%%%%%%%%%%%%%%%%%%%%%%%%%%%%%%%%
%%%%%%


%%%%%%%%%%%%%%%%%%%%%%%%%%%%%%%%%%%%%%%%%%%%%%%%%%%%%%%%%%%%%%%%%%%%%%%
%%%%%%
%%% FIGURE 7
% For publication files format
h7=figure('units','inches','position',[3 0.5 8 5]);
%location is [left,bottom,width,height]
% Alternative visualization on full screen Matlab window
% h1=figure('units','normalized','outerposition',[0.04 0.05 0.9
0.95]);
set(gcf,'color',[1 1 1])


%%% subplot(2,1,1)
subplot('Position',[0.12 0.54 0.8 0.39])

y1=bins_EQSTATs_UP_reverse_FIXno(:,3);
y2=bins_EQSTATs_UP_strslip_FIXno(:,3);
y3=bins_EQSTATs_UP_normal_FIXno(:,3);

Y=[y1,y2,y3];
tot_Mo_all=y1+y2+y3;
max_Yvalue=max(tot_Mo_all);
half_max_Yvalue=max_Yvalue/2;

% % y = {rand(x, 1) * 100; (-0:(0.8)/(x-1):0.8)'};
% % fn1=@(x,y) bar(x , y, 0.3, 'FaceColor','r');
% % fn2=@(x,y) bar(x , y, 0.3, 'FaceColor','b');
% % [ax, hbar1, hbar2]=plotyy(1:2:6, y{1},2:2:6,y{2} ,fn1,fn2);

% bar(bins_mids,Y,1.1,'stacked');
```

```
% colormap(color_bar2);
stackedbar = @(x, A) bar(x,A,1.1,'stack');
colormap(color_bar2);

[hAx,hLine1,hLine2]=plotyy(bins_mids,Y,bins_mids,...
    bins_EQSTATs_LP_reverse_FIXyes(:,5),stackedbar,'stem');

set(hLine2,'LineStyle','-
','color','g','marker','*','LineWidth',1.25,'MarkerEdgeColor','g','Ma
rkerFaceColor','none','MarkerSize',11)

set(hAx(1),'XLim',[0 time_range])
set(hAx(1),'XTick',0:3000:time_range)
set(hAx(1),'XTickLabel','')
if max_Yvalue>0
    set(hAx(1),'YLim',[0 max_Yvalue])
    set(hAx(1),'YTick',0:half_max_Yvalue:max_Yvalue)
    Y_str=sprintf('%0.1E|',0:half_max_Yvalue:max_Yvalue);
    Y_str = strrep(Y_str, 'E+0','E+');
    Y_str = strrep(Y_str, 'E-0','E-');
    set(hAx(1),'YTickLabel',Y_str)
end

set(hAx(2),'YLim',[7.5 9.5])
set(hAx(2),'YTick',7.5:0.5:10,'fontweight','bold')
set(hAx(2),'YColor','g')
set(hAx(2),'XLim',[0 time_range])
set(hAx(2),'XTick',[])
set(hAx(2),'XTickLabel','')

leg_handle=legend(hLine1,'reverse','strike-slip','normal');
% title_handle = get(leg_handle,'Title');
% set(title_handle,'String','Kinematics')
%legend(...,'Location','location') location is
[left,bottom,width,height]
% set(leg_handle, 'Position', [0.08,0.87,.03,.1]);
set(leg_handle,'Location','Best')
set(leg_handle, 'Box', 'off')
set(leg_handle, 'Color', 'none')

title({['Upper Plate EQs Time Series ',EventsIDXS_file(1:3),' Segment
',EQS_file_UP(11),...
    ' (FIX= ',FIX{1},', Bin size= ',num2str(binsize),'
days)']},'fontweight','bold')
%xlabel(['Days [',date_in,' (0) - ',date_end,' (13665)]'])
%ylabel('Moment [dyne-cm]','fontweight','bold')
% xlabel(['Days [',date_in,' (0) - ',date_end,' (13665)]'])
ylabel(hAx(1),'Moment [dyne-cm] Upper Plate
Events','fontweight','bold')
ylabel(hAx(2),'Mw Subduction EQs.','fontweight','bold')


%%% subplot(2,1,2)
subplot('Position',[0.12 0.09 0.8 0.39])
```

```
% y1=bins_EQSTATs_UP_reverse_FIXno(:,3);
% y2=bins_EQSTATs_UP_strslip_FIXno(:,3);

% % y = {rand(x, 1) * 100; (-0:(0.8)/(x-1):0.8)'};
% % fn1=@(x,y) bar(x , y, 0.3, 'FaceColor','r');
% % fn2=@(x,y) bar(x , y, 0.3, 'FaceColor','b');
% % [ax, hbar1, hbar2]=plotyy(1:2:6, y{1},2:2:6,y{2} ,fn1,fn2);

% stackedbar = @(x, A) bar(x,A,1.1,'stack');
% colormap(color_bar2);

max_Yvalue=max(bins_EQSTATs_UP_all_FIXno(:,7));
half_max_Yvalue=max_Yvalue/2;

[hAx,hLine1,hLine2]=plotyy(bins_mids,bins_EQSTATs_UP_all_FIXno(:,7),b
ins_mids,...
    bins_EQSTATs_LP_reverse_FIXyes(:,5),'bar','stem');

set(hLine1,'FaceColor','k');
set(hLine1,'BarWidth',1.1);
%set(hLine1,'stack');
%set(hLine1,'FaceColor',color_bar2);
set(hLine2,'LineStyle','-
','color','g','marker','*','LineWidth',1.25,'MarkerEdgeColor','g','Ma
rkerFaceColor','none','MarkerSize',11)

set(hAx(1),'XLim',[0 time_range])
set(hAx(1),'XTick',0:3000:time_range)
% set(hAx(1),'XTickLabel','')

if max_Yvalue>0 && max_Yvalue<=7
    set(hAx(1),'YLim',[0 max_Yvalue])
    set(hAx(1),'YTick',0:1:max_Yvalue)
%     Y_str=sprintf('%0.1E|',0:half_max_Yvalue:max_Yvalue);
%     Y_str = strrep(Y_str, 'E+0','E+');
%     Y_str = strrep(Y_str, 'E-0','E-');
%     set(hAx(1),'YTickLabel',Y_str)
elseif max_Yvalue>7 && max_Yvalue<=15
    set(hAx(1),'YLim',[0 max_Yvalue])
    set(hAx(1),'YTick',0:2:max_Yvalue)
elseif max_Yvalue>15 && max_Yvalue<=39
    set(hAx(1),'YLim',[0 max_Yvalue])
    set(hAx(1),'YTick',0:5:max_Yvalue)
elseif max_Yvalue>39 && max_Yvalue<=79
    set(hAx(1),'YLim',[0 max_Yvalue])
    set(hAx(1),'YTick',0:10:max_Yvalue)
elseif max_Yvalue>79 && max_Yvalue<=150
    set(hAx(1),'YLim',[0 max_Yvalue])
    set(hAx(1),'YTick',0:20:max_Yvalue)
elseif max_Yvalue>150
    set(hAx(1),'YLim',[0 max_Yvalue])
    set(hAx(1),'YTick',0:50:max_Yvalue)
end
```

```
set(hAx(2),'YLim',[7.5 9.5])
set(hAx(2),'YTick',7.5:0.5:10,'fontweight','bold')
set(hAx(2),'XLim',[0 time_range])
set(hAx(2),'XTick',[])
set(hAx(2),'XTickLabel','')
set(hAx(2),'YColor','g')

% leg_handle=legend(hLine1,'normal');
% % title_handle = get(leg_handle,'Title');
% % set(title_handle,'String','Kinematics')
%
% %legend(...,'Location','location') location is
[left,bottom,width,height]
% % set(leg_handle, 'Position', [0.08,0.87,.03,.1]);
% set(leg_handle,'Location','Best')
%
% %set(leg_handle,'EdgeColor',[1 1 1])
% set(leg_handle, 'Box', 'off')
% set(leg_handle, 'Color', 'none')

% title({['Upper Plate EQs Time Series ',EventsIDXS_file(1:3),'
Segment ',EQS_file_UP(11),...
%     ' (FIX= ',FIX{1},', Bin size= ',num2str(binsize),'
days)']},'fontweight','bold')
xlabel(['Days [',date_in,' (0) - ',date_end,'
(13665)]'],'fontweight','bold')
ylabel(hAx(1),'Number of Events / Bin','fontweight','bold')
ylabel(hAx(2),'Mw Subduction EQs.','fontweight','bold')

%D:\Users\Felipe Aron\Documents\P h D   a t   C O R N E L L\P A P E R
%Global search\MATLAB\New CODES_2-20-2014\Outputs from
RuptStatsSolver.m
filename=[EventsIDXS_file(1:3),EQS_file_UP(7:11),'_MoALL_NrALL_UpFIX'
,FIX{1}];
path_filename=fullfile(path_outputs,filename);

%Saving figures h7
saveas(h7,path_filename,'fig')
print(h7,'-depsc',path_filename)
print(h7,'-dtiff','-r600',path_filename)
%%%%%%%%%%%%%%%%%%%%%%%%%%%%%%%%%%%%%%%%%%%%%%%%%%%%%%%%%%%%%%%%%%%%%%%
%%%%%%


%%%%%%%%%%%%%%%%%%%%%%%%%%%%%%%%%%%%%%%%%%%%%%%%%%%%%%%%%%%%%%%%%%%%%%%
%%%%%%
%%% FIGURE 8
% For publication files format
h8=figure('units','inches','position',[3 0.5 8 5]);
%location is [left,bottom,width,height]
% Alternative visualization on full screen Matlab window
% h1=figure('units','normalized','outerposition',[0.04 0.05 0.9
0.95]);
```

```
set(gcf,'color',[1 1 1])


%%% subplot(2,1,1)
subplot('Position',[0.12 0.54 0.8 0.39])

y1=bins_EQSTATs_UP_reverse_FIXyes(:,3);
y2=bins_EQSTATs_UP_strslip_FIXyes(:,3);
y3=bins_EQSTATs_UP_normal_FIXyes(:,3);

Y=[y1,y2,y3];
tot_Mo_all=y1+y2+y3;
max_Yvalue=max(tot_Mo_all);
half_max_Yvalue=max_Yvalue/2;

% % y = {rand(x, 1) * 100; (-0:(0.8)/(x-1):0.8)'};
% % fn1=@(x,y) bar(x , y, 0.3, 'FaceColor','r');
% % fn2=@(x,y) bar(x , y, 0.3, 'FaceColor','b');
% % [ax, hbar1, hbar2]=plotyy(1:2:6, y{1},2:2:6,y{2} ,fn1,fn2);

% bar(bins_mids,Y,1.1,'stacked');
% colormap(color_bar2);
stackedbar = @(x, A) bar(x,A,1.1,'stack');
colormap(color_bar2);

[hAx,hLine1,hLine2]=plotyy(bins_mids,Y,bins_mids,...
    bins_EQSTATs_LP_reverse_FIXyes(:,5),stackedbar,'stem');

set(hLine2,'LineStyle','-
','color','g','marker','*','LineWidth',1.25,'MarkerEdgeColor','g','Ma
rkerFaceColor','none','MarkerSize',11)

set(hAx(1),'XLim',[0 time_range])
set(hAx(1),'XTick',0:3000:time_range)
set(hAx(1),'XTickLabel','')
if max_Yvalue>0
    set(hAx(1),'YLim',[0 max_Yvalue])
    set(hAx(1),'YTick',0:half_max_Yvalue:max_Yvalue)
    Y_str=sprintf('%0.1E|',0:half_max_Yvalue:max_Yvalue);
    Y_str = strrep(Y_str, 'E+0','E+');
    Y_str = strrep(Y_str, 'E-0','E-');
    set(hAx(1),'YTickLabel',Y_str)
end

set(hAx(2),'YLim',[7.5 9.5])
set(hAx(2),'YTick',7.5:0.5:10,'fontweight','bold')
set(hAx(2),'YColor','g')
set(hAx(2),'XLim',[0 time_range])
set(hAx(2),'XTick',[])
set(hAx(2),'XTickLabel','')

leg_handle=legend(hLine1,'reverse','strike-slip','normal');
% title_handle = get(leg_handle,'Title');
```

```
% set(title_handle,'String','Kinematics')
%legend(...,'Location','location') location is
[left,bottom,width,height]
% set(leg_handle, 'Position', [0.08,0.87,.03,.1]);
set(leg_handle,'Location','Best')
set(leg_handle, 'Box', 'off')
set(leg_handle, 'Color', 'none')

title({['Upper Plate EQs Time Series ',EventsIDXS_file(1:3),' Segment
',EQS_file_UP(11),...
    ' (FIX= ',FIX{2},', Bin size= ',num2str(binsize),'
days)']},'fontweight','bold')
%xlabel(['Days [',date_in,' (0) - ',date_end,' (13665)]'])
%ylabel('Moment [dyne-cm]','fontweight','bold')
% xlabel(['Days [',date_in,' (0) - ',date_end,' (13665)]'])
ylabel(hAx(1),'Moment [dyne-cm] Upper Plate
Events','fontweight','bold')
ylabel(hAx(2),'Mw Subduction EQs.','fontweight','bold')


%%% subplot(2,1,2)
subplot('Position',[0.12 0.09 0.8 0.39])

% y1=bins_EQSTATs_UP_reverse_FIXno(:,3);
% y2=bins_EQSTATs_UP_strslip_FIXno(:,3);

% % y = {rand(x, 1) * 100; (-0:(0.8)/(x-1):0.8)'};
% % fn1=@(x,y) bar(x , y, 0.3, 'FaceColor','r');
% % fn2=@(x,y) bar(x , y, 0.3, 'FaceColor','b');
% % [ax, hbar1, hbar2]=plotyy(1:2:6, y{1},2:2:6,y{2} ,fn1,fn2);

% stackedbar = @(x, A) bar(x,A,1.1,'stack');
% colormap(color_bar2);

max_Yvalue=max(bins_EQSTATs_UP_all_FIXyes(:,7));
half_max_Yvalue=max_Yvalue/2;

[hAx,hLine1,hLine2]=plotyy(bins_mids,bins_EQSTATs_UP_all_FIXyes(:,7),
bins_mids,...
    bins_EQSTATs_LP_reverse_FIXyes(:,5),'bar','stem');

set(hLine1,'FaceColor','k');
set(hLine1,'BarWidth',1.1);
%set(hLine1,'stack');
%set(hLine1,'FaceColor',color_bar2);
set(hLine2,'LineStyle','-
','color','g','marker','*','LineWidth',1.25,'MarkerEdgeColor','g','Ma
rkerFaceColor','none','MarkerSize',11)

set(hAx(1),'XLim',[0 time_range])
set(hAx(1),'XTick',0:3000:time_range)
% set(hAx(1),'XTickLabel','')
if max_Yvalue>0 && max_Yvalue<=7
```

```
    set(hAx(1),'YLim',[0 max_Yvalue])
    set(hAx(1),'YTick',0:1:max_Yvalue)
%     Y_str=sprintf('%0.1E|',0:half_max_Yvalue:max_Yvalue);
%     Y_str = strrep(Y_str, 'E+0','E+');
%     Y_str = strrep(Y_str, 'E-0','E-');
%     set(hAx(1),'YTickLabel',Y_str)
elseif max_Yvalue>7 && max_Yvalue<=15
    set(hAx(1),'YLim',[0 max_Yvalue])
    set(hAx(1),'YTick',0:2:max_Yvalue)
elseif max_Yvalue>15 && max_Yvalue<=39
    set(hAx(1),'YLim',[0 max_Yvalue])
    set(hAx(1),'YTick',0:5:max_Yvalue)
elseif max_Yvalue>39 && max_Yvalue<=79
    set(hAx(1),'YLim',[0 max_Yvalue])
    set(hAx(1),'YTick',0:10:max_Yvalue)
elseif max_Yvalue>79 && max_Yvalue<=150
    set(hAx(1),'YLim',[0 max_Yvalue])
    set(hAx(1),'YTick',0:20:max_Yvalue)
elseif max_Yvalue>150
    set(hAx(1),'YLim',[0 max_Yvalue])
    set(hAx(1),'YTick',0:50:max_Yvalue)
end

set(hAx(2),'YLim',[7.5 9.5])
set(hAx(2),'YTick',7.5:0.5:10,'fontweight','bold')
set(hAx(2),'XLim',[0 time_range])
set(hAx(2),'XTick',[])
set(hAx(2),'XTickLabel','')
set(hAx(2),'YColor','g')

% leg_handle=legend(hLine1,'normal');
% % title_handle = get(leg_handle,'Title');
% % set(title_handle,'String','Kinematics')
%
% %legend(...,'Location','location') location is
[left,bottom,width,height]
% % set(leg_handle, 'Position', [0.08,0.87,.03,.1]);
% set(leg_handle,'Location','Best')
%
% %set(leg_handle,'EdgeColor',[1 1 1])
% set(leg_handle, 'Box', 'off')
% set(leg_handle, 'Color', 'none')

% title({['Upper Plate EQs Time Series ',EventsIDXS_file(1:3),'
Segment ',EQS_file_UP(11),...
%     ' (FIX= ',FIX{1},', Bin size= ',num2str(binsize),'
days)']},'fontweight','bold')
xlabel(['Days [',date_in,' (0) - ',date_end,'
(13665)]'],'fontweight','bold')
ylabel(hAx(1),'Number of Events / Bin','fontweight','bold')
ylabel(hAx(2),'Mw Subduction EQs.','fontweight','bold')

%D:\Users\Felipe Aron\Documents\P h D   a t   C O R N E L L\P A P E R
%Global search\MATLAB\New CODES_2-20-2014\Outputs from
RuptStatsSolver.m
```

```
filename=[EventsIDXS_file(1:3),EQS_file_UP(7:11),'_MoALL_NrALL_UpFIX'
,FIX{2}];
path_filename=fullfile(path_outputs,filename);

%Saving figures h8
saveas(h8,path_filename,'fig')
print(h8,'-depsc',path_filename)
print(h8,'-dtiff','-r600',path_filename)
%%%%%%%%%%%%%%%%%%%%%%%%%%%%%%%%%%%%%%%%%%%%%%%%%%%%%%%%%%%%%%%%%%%%%%%%%%%%
%%%%%%

toc
```

D.7 TimeSerBins.m

The function TimeSerBins.m works inside RuptStatsSolver.m and discretize the time series of the near field segments in bins of equal size. Also can be used to re-arrange the time space in a way that a great subduction earthquakes (>7.7) identified in the catalog always set the starting time of one of the bins of the series. See Chapter 4 for more details.

```
function
[n_bins,time_range,DatesSubdEQs,SegmSubdEQs,breakes,bins_mids,bins_ti
me,bins_mins,bins_maxs] =
TimeSerBins(date_in,date_end,binsize,tol_bin_percent,EventsIDXS_file,
Events_file)
%TIMESERBINS generates a time series of discretized bins with breaks
%at specific dates given by subduction earthquakes greater than 7.7.

% date_in='1976/01/01';
% date_end='2013/05/31';
%
% binsize=300;
% tol_bin_percent=20;         % Percentage of binsize.
%
% EventsIDXS_file='SAM_SubdEQs_IDXs_seg1.dat';
%
% Events_file='WorldSubdEQs_7.7&greater_Matlab.txt';

SubdEQidxs=importdata(EventsIDXS_file);
World_SubdEQs=importdata(Events_file);

tol_bin=binsize+(binsize*(tol_bin_percent/100));
t_end_TOT=datenum(date_end,'yyyy/mm/dd');
t_in_TOT=datenum(date_in,'yyyy/mm/dd');
t_range_TOT=t_end_TOT-t_in_TOT;
time_range=t_range_TOT;

[cc,n_SubdEQ]=size(SubdEQidxs);

%0-360° longitude
neg_long_subd=World_SubdEQs(:,4)<0;
World_SubdEQs(neg_long_subd,4)=360+World_SubdEQs(neg_long_subd,4);
max_SubdEQ=max(World_SubdEQs(:,6));
min_SubdEQ=min(World_SubdEQs(:,6));

DatesSubdEQs=World_SubdEQs(SubdEQidxs,2)';
```

```
SegmSubdEQs=World_SubdEQs(SubdEQidxs,:);

breakes=[];

if n_SubdEQ==1

    breakes=DatesSubdEQs;

else

    breakes(1)=DatesSubdEQs(1);
    pairs=0;

    for i=2:n_SubdEQ
        difference=DatesSubdEQs(i)-DatesSubdEQs(i-1);
        if difference<tol_bin
            pairs=pairs+1;
        else
            breakes=[breakes,DatesSubdEQs(i)];
        end
    end

end

%Final breakes vector contains day "zero" and the last serial date of
the
%catalog as well.
breakes=[0,breakes,t_range_TOT];

[dd,n_breakes]=size(breakes);

bins_maxs=[];
bins_mins=[];
bins_mids=[];
bins_time=[];

for j=2:n_breakes

    n_bins_BEF_raw=(breakes(j)-breakes(j-1))/binsize;
    rem_BEF_raw=rem((breakes(j)-breakes(j-1)),binsize);
    n_norm_bins_BEF=floor(n_bins_BEF_raw);

    if breakes(j)-breakes(j-1) <= tol_bin
        bins_mids_BEF=round((breakes(j)+breakes(j-1))/2);
        bins_mins_BEF=breakes(j-1);

        if j==n_breakes
            bins_maxs_BEF=breakes(j);
        else
            bins_maxs_BEF=breakes(j)-1;
        end
```

```
        bins_time_BEF=bins_maxs_BEF-bins_mins_BEF;

        bins_maxs=[bins_maxs,bins_maxs_BEF];
        bins_mins=[bins_mins,bins_mins_BEF];
        bins_mids=[bins_mids,bins_mids_BEF];
        bins_time=[bins_time,bins_time_BEF];

    else

        if rem_BEF_raw <= (binsize*(tol_bin_percent/100))
            bins_mins_BEF=breakes(j-1):binsize:(breakes(j)-
rem_BEF_raw-binsize);

            bins_maxs_BEF=breakes(j-1)+binsize-1:binsize:(breakes(j)-
rem_BEF_raw-1);
            bins_maxs_BEF(n_norm_bins_BEF)=breakes(j)-1;

            bins_mids_BEF=round((bins_maxs_BEF+bins_mins_BEF)/2);

            bins_time_BEF=bins_maxs_BEF-bins_mins_BEF;

            bins_maxs=[bins_maxs,bins_maxs_BEF];
            bins_mins=[bins_mins,bins_mins_BEF];
            bins_mids=[bins_mids,bins_mids_BEF];
            bins_time=[bins_time,bins_time_BEF];

        else
            bins_mins_BEF=breakes(j-1):binsize:(breakes(j)-
rem_BEF_raw);

            bins_maxs_BEF=(breakes(j-1)+binsize-
1):binsize:(breakes(j)-rem_BEF_raw-1);

            if j==n_breakes
                bins_maxs_BEF=[bins_maxs_BEF,breakes(j)];
            else
                bins_maxs_BEF=[bins_maxs_BEF,(breakes(j)-1)];
            end

            bins_mids_BEF=round((bins_maxs_BEF+bins_mins_BEF)/2);

            bins_time_BEF=bins_maxs_BEF-bins_mins_BEF;

            bins_maxs=[bins_maxs,bins_maxs_BEF];
            bins_mins=[bins_mins,bins_mins_BEF];
            bins_mids=[bins_mids,bins_mids_BEF];
            bins_time=[bins_time,bins_time_BEF];
        end
    end

end
[dd,n_bins]=size(bins_mids);
```

D.8 EQsStats.m

Finally, the function EQsStats.m, which works inside RuptStatsSolver.m, estimates all the variables analyzed in Chapter 4 from the distribution of time bins selected. These variables are the number of earthquakes and the total moment and moment magnitude per bin.

```
function
[bins_EQSTATs,SerDates_UP,NO_EQs_bins_UP,bins_EQevents_ALL_UP] =...

EQsStats(n_bins,bins_mins_ALL,bins_maxs_ALL,bins_time_ALL,fix_depth,k
inematics,EQS_filename)
%EQTSTATS generates a time series of discretized in
%%% The next 2 lines of code need to be modified which the correct
name of
%%% the slab region and number of segments.
%%% IMPORTANT!: Names of all variables contain either the string 'UP'
or
%%% 'ALL', inherited from a previous version of the code which
%%% analyzed both upper plate and lower plate EQs in the same run
(See file
%%% RuptStats_BACK3.m).

% n_bins=n_bins;
% FIX='no';       % FIX= 'yes' or 'no'.
% KINE='all';     % KINE= 'all', 'normal', 'reverse' or 'strslip'.
% EQS_file='SAM_UP_seg1.xls';

%n_bins=n_bins;
FIX=fix_depth;       % FIX= 'yes' or 'no'.
KINE=kinematics;     % KINE= 'all', 'normal', 'reverse' or 'strslip'.
EQS_file=EQS_filename;


%Reads headlines! xls file has to start with headline

[num,text,UP_EQs_cell]=xlsread(EQS_file);
UP_EQs_cell=UP_EQs_cell(2:end,:);
[n_UPeqs,aa]=size(UP_EQs_cell);
UP_EQs_mat=[cell2mat(UP_EQs_cell(:,4:8)),cell2mat(UP_EQs_cell(:,10:17
)),...
    cell2mat(UP_EQs_cell(:,19:53))];


if strcmp(FIX,'no')
```

```
    logic_UP=ones(n_UPeqs,1);
%     logic_LP=ones(n_LPeqs,1);

    for m=1:n_UPeqs
        depth_type=UP_EQs_cell{m,18};
        if strcmp(depth_type,'FIX')
            logic_UP(m)=0;
        end
    end

%     for n=1:n_LPeqs
%         depth_type=LP_EQs_cell{n,18};
%         if strcmp(depth_type,'FIX')
%             logic_LP(n)=0;
%         end
%     end

    logic_UP=logical(logic_UP);
%     logic_LP=logical(logic_LP);

    UP_EQs_cell=UP_EQs_cell(logic_UP,:);
    UP_EQs_mat=UP_EQs_mat(logic_UP,:);

    [n_UPeqs,aa]=size(UP_EQs_cell);

%     LP_EQs_cell=LP_EQs_cell(logic_LP,:);
%     LP_EQs_mat=LP_EQs_mat(logic_LP,:);

end


%%% Separating Normal, Reverse or Strike-slip on upper plate
logic_SS=zeros(n_UPeqs,1);
logic_Nor=zeros(n_UPeqs,1);
logic_Rev=zeros(n_UPeqs,1);

for n=1:n_UPeqs
    T=UP_EQs_cell{n,33};
    N=UP_EQs_cell{n,36};
    P=UP_EQs_cell{n,39};

    if (P<45) && (T<45) && (N<45)
        logic_SS(n)=1;
    elseif N>45
        logic_SS(n)=1;
    elseif T>45
        logic_Rev(n)=1;
    elseif P>45
        logic_Nor(n)=1;
    end
end
```

```
logic_SS=logical(logic_SS);
logic_Nor=logical(logic_Nor);
logic_Rev=logical(logic_Rev);

if strcmp(KINE,'normal')
    UP_EQs_cell=UP_EQs_cell(logic_Nor,:);
    UP_EQs_mat=UP_EQs_mat(logic_Nor,:);
elseif strcmp(KINE,'reverse')
    UP_EQs_cell=UP_EQs_cell(logic_Rev,:);
    UP_EQs_mat=UP_EQs_mat(logic_Rev,:);
elseif strcmp(KINE,'strslip')
    UP_EQs_cell=UP_EQs_cell(logic_SS,:);
    UP_EQs_mat=UP_EQs_mat(logic_SS,:);
end


% tic
% display(' ');
% display('3. Main loop to save data files and produce plot-ready
arrays =');

%%% STATISTICS

bins_NaNs=zeros(n_bins,1);
bins_NaNs(:,:)=NaN;

% Initialization of all variables.
SerDates_UP=cell2mat(UP_EQs_cell(:,49));
NO_EQs_bins_UP=0;

bins_EQevents_ALL_UP=cell(1,n_bins);

bins_scMom_ALL_UP=zeros(n_bins,1);

bins_MomRate_ALL_UP=zeros(n_bins,1);

bins_Mo_ALL_UP=zeros(n_bins,1);

bins_MoErr_ALL_UP=zeros(n_bins,1);

bins_Mw_ALL_UP=zeros(n_bins,1);

bins_MwErr_ALL_UP=zeros(n_bins,1);

bins_nEQs_ALL_UP=zeros(n_bins,1);

bins_plungeP_ALL_UP=bins_NaNs;

bins_plungeT_ALL_UP=bins_NaNs;

bins_plungeN_ALL_UP=bins_NaNs;
```

```
bins_color_ALL_UP=bins_NaNs;

bins_MoNormal_ALL_UP=bins_NaNs;

bins_MoReverse_ALL_UP=bins_NaNs;

bins_MoSSlip_ALL_UP=bins_NaNs;

for k=1:n_bins

    idxs_datesrange_UP=find(SerDates_UP>=bins_mins_ALL(k) &
SerDates_UP<=bins_maxs_ALL(k));
    if isempty(idxs_datesrange_UP)
        NO_EQs_bins_UP= NO_EQs_bins_UP+1;

    else
        [numb_EQs_bin_UP,ee]=size(idxs_datesrange_UP);

        bins_nEQs_ALL_UP(k)=numb_EQs_bin_UP;

        bins_EQevents_ALL_UP{1,k}=UP_EQs_cell(idxs_datesrange_UP,:);


scMom_vec_raw_UP=cell2mat(UP_EQs_cell(idxs_datesrange_UP,50));
        iexp_vec_UP=cell2mat(UP_EQs_cell(idxs_datesrange_UP,19));

        scMom_vec_UP=(scMom_vec_raw_UP).*(10.^(iexp_vec_UP));

        bins_scMom_ALL_UP(k)=sum(scMom_vec_UP);

        bins_MomRate_ALL_UP(k)=bins_scMom_ALL_UP(k)/bins_time_ALL(k);

        %Moment tensor components Mrr(20), Mrr_err(21), Mtt(22),
        %Mtt_err(23), Mpp(24), Mpp_err(25), Mrt(26), Mrt_err(27),
Mrp(28),
        %Mrp_err(29), Mtp(30), Mtp_err(31)

        MomTen_mat_raw_UP=cell2mat(UP_EQs_cell(idxs_datesrange_UP,[20
22 24 26 28 30]));

MomTen_mat_error_UP=cell2mat(UP_EQs_cell(idxs_datesrange_UP,[21 23 25
27 29 31]));

        MT_UP=zeros(numb_EQs_bin_UP,6);
        MT_UP_error=zeros(numb_EQs_bin_UP,6);
        MT_UP_error_sq=zeros(numb_EQs_bin_UP,6);
%         Sum_MT_UP_NED=zeros(3,3);
%         Sum_MT_UP_NED_err=zeros(3,3);

        for l=1:numb_EQs_bin_UP

MT_UP(l,:)=(MomTen_mat_raw_UP(l,:)).*(10.^(iexp_vec_UP(l)));
```

```
MT_UP_error(l,:)=(MomTen_mat_error_UP(l,:)).*(10.^(iexp_vec_UP(l)));
            MT_UP_error_sq(l,:)=MT_UP_error(l,:).^2;

%              MT_UP_NED=[MT_UP(l,2),-MT_UP(l,6),MT_UP(l,4);-
MT_UP(l,6),...
%                  MT_UP(l,3),-MT_UP(l,5);MT_UP(l,4),-
MT_UP(l,5),MT_UP(l,1)];
%              Sum_MT_UP_NED=Sum_MT_UP_NED+MT_UP_NED;
        end

        MT_UP_sum=sum([MT_UP;zeros(1,6)]);
        MT_UP_err_sum=sqrt(sum([MT_UP_error_sq;zeros(1,6)]));

        Sum_MT_UP_NED=[MT_UP_sum(2),-MT_UP_sum(6),MT_UP_sum(4);...
            -MT_UP_sum(6),MT_UP_sum(3),-MT_UP_sum(5);...
            MT_UP_sum(4),-MT_UP_sum(5),MT_UP_sum(1)];


Sum_MT_UP_NED_err=[MT_UP_err_sum(2),MT_UP_err_sum(6),MT_UP_err_sum(4)
;...
            MT_UP_err_sum(6),MT_UP_err_sum(3),MT_UP_err_sum(5);...
            MT_UP_err_sum(4),MT_UP_err_sum(5),MT_UP_err_sum(1)];

        a=(((MT_UP_sum(1))^2)+((MT_UP_sum(2))^2)+...
        ((MT_UP_sum(3))^2)+(2*(MT_UP_sum(4))^2)+...
        (2*(MT_UP_sum(5))^2)+(2*(MT_UP_sum(6))^2));

        bins_Mo_ALL_UP(k)=(sqrt(a))/sqrt(2);

        bins_MoErr_ALL_UP(k)=(1/2)*(sqrt(3/a))*...
            (sqrt(((2*MT_UP_sum(1)*MT_UP_err_sum(1))^2)+...
            ((2*MT_UP_sum(2)*MT_UP_err_sum(2))^2)+...
            ((2*MT_UP_sum(3)*MT_UP_err_sum(3))^2)+...
            ((4*MT_UP_sum(4)*MT_UP_err_sum(4))^2)+...
            ((4*MT_UP_sum(5)*MT_UP_err_sum(5))^2)+...
            ((4*MT_UP_sum(6)*MT_UP_err_sum(6))^2)));

        bins_Mw_ALL_UP(k)=((2/3)*(log10(bins_Mo_ALL_UP(k))))-10.7;

bins_MwErr_ALL_UP(k)=((2/3)*(1/((bins_Mo_ALL_UP(k))*log(10))))*(bins_
MoErr_ALL_UP(k));


        [V_UP,D_UP]=eig(Sum_MT_UP_NED);
        [min_eval_UP,min_idx_UP]=min(min(D_UP));
        [max_eval_UP,max_idx_UP]=max(max(D_UP));

        Null_search_UP=[NaN,NaN,NaN];

Null_search_UP([min_idx_UP,max_idx_UP])=[min_idx_UP,max_idx_UP];
        null_idx_UP=find(isnan(Null_search_UP));
```

```
        TP_P_UP=cart2spher(V_UP(1,min_idx_UP),V_UP(2,min_idx_UP),...
            V_UP(3,min_idx_UP));
        plunge_P_UP=TP_P_UP(2);

        TP_T_UP=cart2spher(V_UP(1,max_idx_UP),V_UP(2,max_idx_UP),...
        V_UP(3,max_idx_UP));
        plunge_T_UP=TP_T_UP(2);


TP_N_UP=cart2spher(V_UP(1,null_idx_UP),V_UP(2,null_idx_UP),...
        V_UP(3,null_idx_UP));
        plunge_N_UP=TP_N_UP(2);

        bins_plungeP_ALL_UP(k)=plunge_P_UP;
        bins_plungeT_ALL_UP(k)=plunge_T_UP;
        bins_plungeN_ALL_UP(k)=plunge_N_UP;


        if (plunge_P_UP<45) && (plunge_T_UP<45) && (plunge_N_UP<45)
            bins_color_ALL_UP(k)=3;

        elseif plunge_N_UP>45
            bins_color_ALL_UP(k)=3;

        elseif plunge_T_UP>45
            bins_color_ALL_UP(k)=4;

        elseif plunge_P_UP>45
            bins_color_ALL_UP(k)=1;

        end


%         if (plunge_N_UP>plunge_P_UP && plunge_N_UP>plunge_T_UP)
%
%             if plunge_P_UP>plunge_T_UP
%                 bins_color_ALL_UP(k)=2;
%             else
%                 bins_color_ALL_UP(k)=3;
%             end
%
%         elseif (plunge_P_UP>plunge_T_UP) &&
(plunge_P_UP>plunge_N_UP)
%             bins_color_ALL_UP(k)=1;
%
%         else
%             bins_color_ALL_UP(k)=4;
%         end


    end

end
```

```
normidx=find(bins_color_ALL_UP==1);
bins_MoNormal_ALL_UP(normidx,:)=bins_Mo_ALL_UP(normidx,:);

revidx=find(bins_color_ALL_UP==4);
bins_MoReverse_ALL_UP(revidx,:)=bins_Mo_ALL_UP(revidx,:);

ssidx=find(bins_color_ALL_UP==3);
bins_MoSSlip_ALL_UP(ssidx,:)=bins_Mo_ALL_UP(ssidx,:);

%Final statistics matrix per bin.
bins_EQSTATs=[bins_scMom_ALL_UP,bins_MomRate_ALL_UP,bins_Mo_ALL_UP,..
.

bins_MoErr_ALL_UP,bins_Mw_ALL_UP,bins_MwErr_ALL_UP,bins_nEQs_ALL_UP,.
..
    bins_plungeP_ALL_UP,bins_plungeT_ALL_UP,bins_plungeN_ALL_UP,...
    bins_color_ALL_UP,bins_MoNormal_ALL_UP,bins_MoReverse_ALL_UP,...
    bins_MoSSlip_ALL_UP];
```